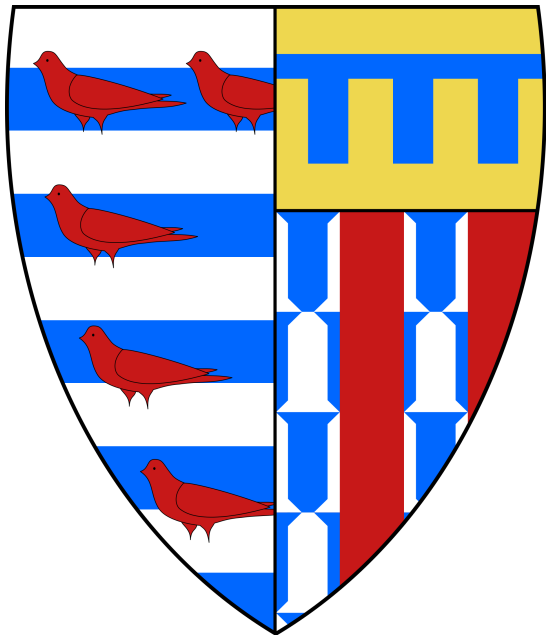
Improving the understanding of the influence of emissions of biogenic volatile organic compounds on climate.



James Michael Weber

Supervisor:
Dr. Alex Archibald

Department of Chemistry
University of Cambridge

This dissertation is submitted for the degree of
Doctor of Philosophy

Pembroke College October 2021

Declaration

This thesis is the result of my own work and includes nothing which is the outcome of work done in collaboration except as declared in the preface and specified in the text. It is not substantially the same as any work that has already been submitted before for any degree or other qualification except as declared in the preface and specified in the text. It does not exceed the prescribed word limit for the Physics and Chemistry Degree Committee.

James Weber

October 2021

Acknowledgments

I am grateful to a considerable number of people for their support and advice during my PhD. My greatest thanks go to my supervisor Dr Alex Archibald for his excellent guidance, expertise, and unwavering support as well as to Dr Scott Archer-Nicholls for his advice, time, and assistance during my PhD. Dr Paul Griffiths and Dr Luke Abraham have also been extremely generous in giving up time to help with a range of issues and I extend thanks to all members of the Centre for Atmospheric Science for making me feel so welcome.

Among my student colleagues a special mention is necessary for Youngsub Matthew Shin who has provided superb technical advice, been a steady PhD partner from day one, and a good friend. Johnny Staunton-Sykes, Lihang Pan and Seb Hickman were enthusiastic members of the inaugural G6 cricket league and good friends while I was also lucky to work with Glen Chua who always made the office a cheerful place. Andrea, Risa, Le, Zosia, Lauren, Ben, Jayaprakash, Michelle, Jason, Seb and Lorrie have all been excellent colleagues and I only wish we could have spent more time in the office.

I am grateful for the help of Dr Torsten Berndt, Dr Cat Scott, Dr Michael Jenkin, Dr Tom Bannan, Dr Christoph Knote, Dr Hamish Gordon and Dr Gerd Folberth.

Away from academia, I am indebted to fellow Pembroke PhD student Emilie Wigdor for her friendship and support, as well as my undergraduate friends Jim Phillips, Matt Hudson, Jack Capel-Shyu and Adam Barker, among others, and Jess Veldmeyer. I must also mention PCAFC with whom I have enjoyed 7 happy seasons, many fun nights at The Alma and made more questionable decisions to leave my area as a goalkeeper than I care to mention.

And lastly, I cannot thank my parents enough for their resolute support and kindness during my PhD. I am very grateful for everything they have done for me.

Abstract

The feedback between the emissions of biogenic volatile organic compounds (BVOCs), atmospheric composition and climate is a key component of the Earth System. However, there remains uncertainty as to its magnitude and sign. An important factor is the gas phase chemistry of BVOCs since this influences atmospheric oxidising capacity and thus radiative forcing from CH_4, O_3, aerosol and clouds. Recent advances in the understanding of BVOC oxidation chemistry, which reduce the oxidant depletion typically simulated with enhanced BVOCs, are considered in very few climate models and their impact on the BVOC feedback has not been assessed. More attention has been paid to the impacts of BVOCs solely on organic aerosol which only leads to a partial description of BVOCs' climatic impact.

This thesis assesses the requirements for a BVOC chemical mechanism to be "state-of-the-art", given the recent advances in chemical understanding. I further examine how updating the description of BVOC chemistry affects firstly simulated atmospheric composition and secondly the climatic impact of BVOCs. BVOC climatic impact and feedback is calculated from the climatic response to a doubling of BVOC emissions using the standard and state-of-the-art mechanisms in a pre-industrial atmosphere with a focus on the gas and aerosol phase changes.

Updates to chemistry in the state-of-the-art mechanism result in greater terrestrial boundary layer OH and improved model performance against observations compared to standard mechanisms. The net radiative forcing and feedback from increasing BVOC emissions is positive in both mechanisms considered. Negative forcing from enhanced aerosol scattering is outweighed by positive forcings from O_3 and CH_4 increases and aerosol-cloud interactions, the latter contrary to past studies. However, the magnitude of the forcing (feedback) is 43% smaller when the state-of-the-art mechanism is used. This is attributed to the lower oxidant depletion which yields smaller increases in CH_4 and smaller decreases in cloud droplet number concentration via the suppression of H_2SO_4 production from gas phase SO_2 oxidation. Therefore, the pre-industrial climate is only about half as sensitive to a change in BVOC emissions with the state-of-the-art mechanism, highlighting the significant influence of simulated chemistry. The sensitivity to the chemical mechanism is comparable to the variation in BVOCs' climatic impact across multiple climate models, suggesting inter-model variation in simulated chemistry, often overlooked, is important for understanding model uncertainty.

Finally, a further development to the state-of-the-art mechanism describing the production of highly oxygenated organic molecules (HOMs) from α-pinene is presented, representing a new way for BVOCs to influence climate and the first semi-explicit HOM mechanism suitable for climate models. The α-pinene-HOM mechanism captures experimentally observed dependencies of HOMs on isoprene, NO_x and temperature, while also agreeing with previous suggestions that nucleation from HOMs is likely to be more influential in a pre-industrial atmosphere. CRI-HOM provides a basis for further improving understanding of the BVOC-climate feedback.

The model updates and analysis presented in this thesis will allow important policy-relevant questions, including those regarding climate change mitigation strategies, to be addressed in a more comprehensive manner.

Table of Contents

List of Figures

List of Tables

Abbreviations

Thesis Aims and Research Questions

Personal Paper References and Author Contributions

1. Introduction

1.1 Atmospheric Composition and Climate

1.2 Tropospheric Chemistry

1.2.1 Daytime Chemistry

1.2.1.1 NO_x-limited and VOC-limited regions

1.2.2 Nighttime Chemistry

1.2.3 Atmospheric Oxidising Capacity

1.2.4 Chemistry in Climate Models

1.3 Atmospheric Aerosol

1.3.1 Aerosol Composition

1.3.2 Aerosol Size Distribution

1.3.3 Aerosols in Climate Models

1.3.4 Aerosol Direct Radiative Effect

1.3.5 Aerosol Indirect Radiative Effect

1.4 BVOCs

1.4.1 BVOC Emissions

1.4.1.1 Modelling BVOC emissions

1.4.2 Isoprene Chemistry

1.4.2.1 ISOPOO H-shifts and HO_x-recycling

1.4.2.2 Modelling Isoprene Chemistry

1.4.2.3 Impact of HO_x-recycling

1.4.3 Isoprene SOA

1.4.4 α-pinene and β-pinene Chemistry

1.4.4.1 Autoxidation

1.4.4.2 Dimerisation

1.4.4.3 Modelling α-pinene and β-pinene Chemistry

1.4.5 α-pinene and β-pinene SOA

1.4.5.1 HOMs and SOA

1.4.6 Oxidants and the Location of SOA Production

1.5 Climatic Impacts and Feedbacks

1.5.1 Feedback Factor

1.6 Thesis Structure

2. The influence of different chemical mechanisms on atmospheric composition

Abstract

2.1 Introduction

2.2. Development of CS2 - incorporation of CRI v2.2 into UKCA

2.3. Model Runs

- 2.3.1 Short runs for model-observation comparisons
- 2.3.2 Longer runs for mechanistic intercomparison
- 2.3.3 Biogenic Emissions

2.4 Comparison with Observations

- 2.4.1 Ozone
- 2.4.2 HO_x
- 2.4.3 Isoprene
  - 2.4.3.1 Isoprene Surface Measurements
  - 2.4.3.2 Isoprene Flight Measurements
  - 2.4.3.3 Isoprene Columns
- 2.4.4 Isoprene Oxidation Products
- 2.4.5 Isoprene Nitrate, IEPOX and HPALDs
- 2.4.6 Monoterpenes (MT)

2.5. Comparison to CRI-STRAT and CRI-STRAT 2

- 2.5.1 O_x
  - 2.5.1.1. O_x Budget
  - 2.5.1.2 O_x production
  - 2.5.1.3 O_x loss
- 2.5.2 HO_x
- 2.5.3 BVOCs
- 2.5.4 HPALDs and IEPOX
- 2.5.5 NO_y
- 2.5.6 Impacts on Aerosols
- 2.5.7 Summary and synthesis

2.6 Conclusion

3. The influence of chemical mechanism on the climatic impact of BVOCs

3.1 Introduction and Summary

3.1.1 BVOC Forcing and Feedbacks

3.1.2 Chemical Mechanisms

3.2 Methods

3.2.1 Model Description and Simulations

3.2.2 Aerosol Modelling

3.2.3 ERF and Feedback Calculation

3.2.4 Forcing Decomposition

3.3 Results

3.3.1 Gas Phase Chemistry

3.3.1.1 NO_y

3.3.1.2 O_3

3.3.1.3 HO_x, CH_4 & H_2O_2

3.3.1.4 BVOCs

3.3.2 Aerosol

3.3.2.1 Secondary Organic Aerosol

3.3.2.2 Primary Organic Aerosol

3.3.2.3 Sulphate Aerosol

3.3.3.4 Aerosol Number Concentrations

3.3.3.5 Aerosol Optical Depth

3.3.3.6 Cloud properties

3.4 Forcing and Feedback Factors

3.4.1 Clear-clean forcing

3.4.1.1 O_3

3.4.1.2 CH_4

3.4.2 Aerosol Direct Effect

3.4.3 Aerosol-Cloud Interactions

3.4.4 Sum of Forcing Components

3.4.5 Feedback Factors

3.4.6 Implications

3.4.6.1 Influence of atmospheric state

3.5 Conclusion

3.5.1 Wide reaching role of oxidants

3.5.2 Chemistry in the context of inter-model differences

4. CRI-HOM: A novel chemical mechanism for simulating highly oxygenated organic molecules (HOMs) in global chemistry–aerosol–climate models

Abstract

4.1 Introduction

4.2 Mechanism Development

4.2.1 Ozonolysis

4.2.2 OH oxidation

4.2.3 Peroxy Radical + Peroxy Radical Interactions

4.2.3.1 Large Peroxy Radical Pool

4.2.3.2 Medium and Small Peroxy Radical Pools

4.2.4 HOM Loss Mechanisms

4.3 Mechanism Optimisation and Validation

4.3.1 Comparison to Experimental Data

4.3.1.1 Varying α-pinene Experiment

4.3.1.2 Varying Isoprene Experiment

4.3.1.3 Simulation of Accretion Products

4.3.2 HOM yield variation with temperature and NO_x

4.3.3 Comparison to CRI v2.2

4.3.3.1 Peroxy Radicals and HOMs

4.3.3.2 Closed Shell and non-HOM Species

4.4 Simulation of HOM Vertical Profiles

4.4.1 Nucleation Rates

4.5 Conclusions

5. Conclusions and Future Work

5.1. How does the transition from a standard chemical mechanism to a state-of-the-art chemical mechanism affect simulated atmospheric composition?

5.2. How does the transition from a standard chemical mechanism to a state-of-the-art chemical mechanism affect the climatic impact of BVOCs and how might this help to explain the variation in the climatic impact of BVOCs between models?

5.3. How can the chemistry of HOM formation from BVOCs be described in a form suitable for global climate modelling?

5.4 Future Work

5.4.1 Model development

5.4.1.1 HOMs and PBN

5.4.1.2 Isoprene SOA

5.4.1.3 Sulphur Chemistry

5.4.2 Using Current Modelling Capabilities

5.4.2.1 Influence of the chemical mechanism on other climate feedbacks

5.4.2.2 The influence of atmospheric state on BVOC climatic impact

5.4.2.3 The impact of co-located changes to physical parameters

References

Appendix A

Appendix B

Appendix C

Appendix D

List of Figures

Chapter 1

Figure 1.1 – IPCC AR6 gas phase forcing, associated GSAT change and total aerosol forcing.

Figure 1.2 – O_3 NO_x-VOC Isopleth

Figure 1.3 – Schematic of ARI and ACI

Figure 1.4 – Isoprene emission projections

Figure 1.5 – Oxidation mechanism of isoprene + OH from Wennberg et al (2018)

Figure 1.6 – 1,6 H-shift mechanism for isoprene hydroxy peroxy radical

Figure 1.7 – Mechanistic differences between ST and CS2 for OH + isoprene

Figure 1.8 – Autoxidation of peroxy radical from α-pinene ozonolysis

Figure 1.9 – Formation of 20-carbon dimer from α-pinene-derived peroxy radical

Figure 1.10 – BVOC radiative efficiency across a range of previous studies

Chapter 2

Figure 2.1 – Surface mechanism-observation comparisons for OH, O_3, isoprene, monoterpenes and isoprene oxidation products.

Figure 2.2 – Vertical mechanism-observation profiles for comparison

Figure 2.3 – Isoprene column values from observation and mechanism-observation comparison.

Figure 2.4 – Zonal mean and low altitude differences in O_3 between CS and CS2.

Figure 2.5 – Zonal mean differences in O_x production, loss and net production between CS and CS2.

Figure 2.6 – Zonal mean and low altitude differences in OH between CS and CS2 and impact of isoprene chemistry.

Figure 2.7 – Zonal mean and low altitude isoprene concentrations in CS and CS2 and isoprene oxidation flux.

Figure 2.8 – Zonal mean and low altitude concentrations of HPALDs and IEPOX in CS2.

Figure 2.9 – Zonal means differences in NO_y components between CS and CS2

Figure 2.10 – Zonal mean fluxes of Sec_Org production and SO_2 + OH oxidation in CS and difference between CS and CS2.

Chapter 3

Figure 3.1 – BVOC feedback schematic from Sporre et al (2019)

Figure 3.2 – Mechanistic differences in NO_2 and PANs; response of NO_2 column and zonal mean NO_x.

Figure 3.3 – Mechanistic differences in O_3; response of O_3 column and zonal mean O_3.

Figure 3.4 – Mechanistic differences in OH; response of zonal mean HO_x and CH_4 oxidation.

Figure 3.5 – Mechanistic differences in OH and HO_2 production fluxes.

Figure 3.6 – Global lifetimes of Isoprene and Monoterpenes.

Figure 3.7 – Sec_Org production vertical profiles and zonal means, SOA zonal mean and global SOA accumulation mode column.

Figure 3.8 – Response of column fluxes of SO_2 + OH and H_2SO_4 nucleation

Figure 3.9 – Responses of AOD, accumulation mode number concentration and size.

Figure 3.10 – CDNC, ERF, $SARF_{O3}$ and IRF_{DRE}

Figure 3.11 – Forcing, radiative efficiency and feedback factors from ST and CS2 mechanisms.
Figure 3.12 – BVOC feedback schematic from Chapter 3
Figure 3.13 – BVOC radiative efficiency comparing previous studies and this work.

Chapter 4

Figure 4.1 – Schematic of additions to α-pinene ozonolysis pathway.
Figure 4.2 – Schematic of additions to α-pinene + OH pathway
Figure 4.3 – Observed and modelled O3RO2 and OHRO2 concentrations with fixed isoprene.
Figure 4.4 – Observed and modelled O3RO2, OHRO2 and isoprene RO2 concentrations with increasing isoprene.
Figure 4.5 – Observed and modelled 20-carbon and 15-carbon dimers with increasing isoprene.
Figure 4.6 – HOM yields and HOM concentrations with varying NO_x and temperature.
Figure 4.7 – Simulated HOM vertical profiles in Hyytiala, Finland and the Amazon.
Figure 4.8 – Vertical nucleation rate profiles from sulphuric acid activation and pure biogenic nucleation in pre-industrial and present-day atmospheres.

List of Tables

Chapter 2

Table 2.1 – Comparison of the CRI-STRAT and CRI-STRAT 2 chemical mechanisms

Table 2.2 – Species added and removed from the CS mechanism in the development of the CRI-Strat 2 mechanism.

Table 2.3 – Details of observational datasets considered

Table 2.4 – Shorter runs performed for mechanism-observational comparisons.

Table 2.5 – Longer runs performed for CRI mechanism comparison

Table 2.6 – O_x diagnostics for CS and CS2

Table 2.7 – Tropospheric average HO_x parameters for CS and CS2.

Table 2.8 – NO_y budget and NO_y deposition fluxes for CS and CS2

Chapter 3

Table 3.1 – Summary of simulations considered.

Table 3.2 – BVOC burdens and oxidation flux breakdowns.

Table 3.3 – SOA and SO4 aerosol burdens and lifetimes.

Table 3.4 – Forcing and feedback factors.

Chapter 4

Table 4.1 – Summary of new species added for CRI-HOM.

Table 4.2 – Summary of products from updated peroxy radical pool.

Table 4.3 – Simulations performed for testing CRI-HOM.

Table 4.4 – Autoxidation coefficients determined from optimisation.

Table 4.5 – Observed and modelled concentrations.

Abbreviations

ACI	Aerosol-cloud interactions
AIE	Aerosol indirect effect
AOD	Aerosol optical depth
ARI	Aerosol-radiation interactions
BVOC	Biogenic volatile organic compound
CCN	Cloud condensation nuclei
CDNC	Cloud droplet number concentration
CMIP6	Coupled Model Intercomparison Project phase 6
CRI	Common Representative Intermediate
CWS	Cloud-weighted Susceptibility
CS	CRI-Strat
CS2	CRI-Strat 2
DHP-RO_2	Dihydroperoxide carbonyl peroxy radical
DRE	Direct radiative effect
ELVOC	Extremely low volatility organic compound
ERF	Effective radiative forcing
GCM	Global Circulation Model
HC5	Isoprene-derived hydroxy carbonyl
HMML	Hydroxymethylmethyl-α-lactone
HOM	Highly oxygenated organic molecule
HPALD	Hydroperoxy aldehyde
IEPOX	Isoprene epoxy diol
IHN	Isoprene hydroxy nitrate
ISOPOO	Isoprene hydroxy peroxy radical
ISOPOOH	Isoprene hydroxy hydroperoxide
LW	Longwave
NH	Northern Hemisphere
SH	Southern Hemisphere
SSP	Shared Socio-economic Pathways
SST	Sea-Surface Temperature
ST	Strat-Trop
SVOC	Semi-volatile organic compound
SW	Shortwave
TOA	Top-of-atmosphere
UKCA	United Kingdom Chemistry and Aerosols model
UKESM1	United Kingdom Earth System Model version 1

Thesis Structure and Aims

The chemical composition of the atmosphere plays an important role in determining the energy balance of the Earth system and thus climate. This PhD aims to assess the climatic influence of a key component of the Earth system: the emission of biogenic volatile organic compounds (BVOCs) from terrestrial vegetation. This is performed by firstly assessing how different descriptions of BVOC chemistry affect simulated atmospheric composition and then examining how this translates to the influence BVOCs have on climate. Finally, I describe the development and evaluation of the first chemical mechanism which simulates the latest developments in BVOC-aerosol chemistry and will enable the United Kingdom Earth System Model (UKESM) to become one of the most advanced Earth System models.

Research Questions

I aim to answer four questions in this thesis.

1. What does a chemical mechanism need to be state-of-the-art in its description of BVOCs?

2. How does the transition from a standard chemical mechanism to a state-of-the-art chemical mechanism affect simulated atmospheric composition?

3. How does the transition from a standard chemical mechanism to a state-of-the-art chemical mechanism affect the climatic impact of BVOCs and how might this help explain the variation in the climatic impact of BVOCs between models?

4. How can the chemistry of HOM formation from BVOCs be described in a form suitable for global climate modelling?

Each question is answered by a chapter of this thesis and, in doing so, I aim to make an important contribution to the scientific community's understanding of how BVOCs influence atmospheric composition and climate while also providing a basis for further research. The final chapter summarises my findings.

Appendix Structure

The first four chapters in this thesis each have an associated Appendix labelled A-D. Figures, tables and sections in the appendices are denoted in the main text with the Appendix name and number (e.g., Fig A1 is in Appendix A).

Personal Paper References and Author Contributions

Chapters 2 and 4 are published papers where I am the first author. Below, I provide the references and, as required by the Degree Committee for the faculty of Physics and Chemistry, a full summary of the author contributions for each paper.

Chapter 2

The results from this chapter were published in Geoscientific Model Development in August 2021. (The only addition for this thesis is Section B7 of Appendix B).

Weber, J., Archer-Nicholls, S., Abraham, N. L., Shin, Y. M., Bannan, T. J., Percival, C. J., Bacak, A., Artaxo, P., Jenkin, M., Khan, M. A. H., Shallcross, D. E., Schwantes, R. H., Williams, J., and Archibald, A. T.: Improvements to the representation of BVOC chemistry–climate interactions in UKCA (v11.5) with the CRI-Strat 2 mechanism: incorporation and evaluation, Geosci. Model Dev., 14, 5239–5268, https://doi.org/10.5194/gmd-14-5239-2021, 2021.

The incorporation of the CRI-Strat 2 mechanism into UKCA by modification of the UKCA source code was carried out by James Weber with support from Scott Archer-Nicholls and Luke Abraham and advice from Alex Archibald, Youngsub Matthew Shin, Michael Jenkin, Anwar Khan and Dudley Shallcross. James Weber set up and ran all model simulations and carried out all the data analysis. Observational comparison experiments were designed and carried out by James Weber with advice from Scott Archer-Nicholls, Luke Abraham and Alex Archibald. Mechanism intercomparison comparison experiments were designed by James Weber with advice from Scott Archer-Nicholls, Luke Abraham and Alex Archibald and carried out by James Weber. Tom Bannan, Carl Percival, Asan Bacak and Paulo Artaxo compiled and supplied the ZF2 Brazil observational data and Tom Bannan wrote the field campaign description in Appendix B. Rebecca Schwantes advised on the SEAC^{4}RS data and analysis. James Weber interpreted the ZF2 Brazil, Borneo, ATTO, FAAM, GABRIEL and SEAC^{4}RS observational data with advice from Scott Archer-Nicholls, Luke Abraham, Alex Archibald and Jonathan Williams. James Weber wrote the paper. All co-authors discussed the results and commented on the paper.

In addition to this paper, James Weber lodged the CRI-Strat 2 mechanism in the trunk of the Unified Model for version 12.0 with the help of Luke Abraham and Scott Archer-Nicholls, making it available for all users of UKCA and UKESM1. The additional documentation describing the key features of CRI-Strat 2 and how to use it is given in Unified Model Documentation Paper 084: United Kingdom Chemistry and Aerosol (UKCA) Technical Description (https://code.metoffice.gov.uk/doc/um/latest/papers/umdp_084.pdf).

The publication in Geoscientific Model Development is also intended to serve as documentation for the CRI-Strat 2 mechanism and the influence of the new chemistry so that UKCA and UKESM1 users can make a well-informed decision about whether they want to use this chemistry scheme.

Data Availability:

The description of the Z2F field campaign is given Appendix B4 and the observational data is available at https://doi.org/10.17863/CAM.65133 (Weber and Bannan, 2021).

The observational data from the SEAC4RS flight campaign is available at https://www-air.larc.nasa.gov/cgi-bin/ArcView/seac4rs?MERGE=1#60_SECOND.DC8_MRG (Chen., 2016) [Last access 9th April 2021]

The observational data from the ATTO tower is available to download at https://www.attodata.org. Specific datasets used were https://www.attodata.org/ddm/data/Showdata/72, https://www.attodata.org/ddm/data/Showdata/73, https://www.attodata.org/ddm/data/Showdata/74 and https://www.attodata.org/ddm/data/Showdata/77 (Yáñez-Serrano., 2020) [Last access 1st April 2021)

The observational data from the FAAM aircraft is available at http://data.ceda.ac.uk/badc/op3/data/op3-aircraft and Borneo data can be found at http://data.ceda.ac.uk/badc/op3/data. last access: 27 March 2021; Natural Environment Research Council et al., 2010).

Data tables of the full CRI-Strat 2 mechanism and the mechanisms used in the sensitivity test described in this paper are included in Appendix B. The CRI v2.2 mechanism can be viewed and downloaded from http://cri.york.ac.uk.

Chapter 4

The results from this chapter were published in Atmospheric Chemistry and Physics in September 2020
Weber, J., Archer-Nicholls, S., Griffiths, P., Berndt, T., Jenkin, M., Gordon, H., Knote, C., and Archibald, A. T.: CRI-HOM: A novel chemical mechanism for simulating highly oxygenated organic molecules (HOMs) in global chemistry–aerosol–climate models, Atmos. Chem. Phys., 20, 10889–10910, https://doi.org/10.5194/acp-20-10889-2020, 2020.

James Weber wrote the CRI-HOM mechanism with advice from Alex Archibald, Scott Archer-Nicholls and Michael Jenkin. The modelling experiments were designed and carried out by James Weber with advice from Alex Archibald, Scott Archer-Nicholls, Paul Griffiths, Michael Jenkin, Hamish Gordon and Christoph Knote. The model optimisation experiments used laboratory flow cell data from experiments performed by Torsten Berndt. James Weber wrote the paper with advice from Alex Archibald and all co-authors discussed the results and commented on the paper.

During my PhD I also led a study looking at the climatic impact of emission reductions associated with the COVID19 pandemic and published a paper in GRL. However, as this is largely separate from my PhD research, this is not included in this thesis.

Weber, J., Shin, Y.M., Staunton Sykes, J., Archer-Nicholls, S., Abraham, N.L. and Archibald, A.T.: Minimal climate impacts from short-lived climate forcers following emission reductions related to the COVID-19 pandemic. *Geophysical Research Letters*, *47*, p2020GL090326, https://doi.org/10.1029/2020GL090326, 2020.

1. Introduction

In this chapter, I first provide a summary of the role atmospheric composition has on climate. I further consider how isoprene and monoterpenes influence atmospheric composition, including detailing the most recent advances in the understanding of their oxidation pathways, to answer the first question of this thesis by describing what a chemical mechanism needs to be "state-of-the-art" for these species. Finally, I review the current understanding of how biogenic volatile organic compounds (BVOCs) influence climate via perturbations to atmospheric composition and the associated climatic feedbacks. I also show how the three chapters of original research, Chapters 2-4, build upon current understanding.

1.1 Atmospheric Composition and Climate

Earth's atmosphere is primarily made up of nitrogen (N_2, 78%), oxygen (O_2, 21%), argon (Ar, 1%) and water vapour, which can range from ~0% to 3%. A huge number of chemical species make up less than 1% and are collectively termed trace gases. These include carbon dioxide (CO_2), methane (CH_4) and Nitrous Oxide (N_2O) which, along with water vapour, ozone (O_3), certain chlorofluorocarbons (CFCs) and hydrochlorofluorocarbons (HCFCs) and sulphur hexafluoride (SF_6), are the major greenhouse gases (GHGs). The atmosphere also comprises a range of aerosols; liquid or solid particles suspended in air, with sizes ranging from ~3 nm to ~10 μm with a diverse range of chemical compositions (Section 1.3).

Earth's climate is controlled by the balance of incoming solar radiation (F_{in}) and outgoing radiation (F_{out}), comprising shortwave radiation directly reflected by the atmosphere and surface and long wave radiation emitted by the atmosphere and surface. The balance, F (Eq1.1), can be considered as the net incoming flux.

$$F = F_{in} - F_{out} \quad (1.1)$$

The interaction of radiation with the atmosphere depends on its composition: the concentrations of radiatively-active gas phase chemical species and aerosol. Therefore, a change to atmospheric composition, driven by anthropogenic activities or natural events, will change this balance and thus climate. A change to this balance is called radiative forcing (ΔF) and may be defined as the change to net incoming radiative flux at either the top of the atmosphere (TOA) or the tropopause, depending on the type of forcing under consideration. The resulting change in surface temperature, ΔT, can be related to the radiative forcing (Eq 1.2).

$$\Delta T = \lambda \Delta F \quad (1.2)$$

Where λ relates the change in temperature to a change in the net incoming flux and is known as the climate sensitivity parameter. In reality the presence of feedbacks within the Earth System makes this response more complicated and this is discussed in Section 1.5.1.

All GHGs absorb longwave radiation emitted by the surface and re-emit into the atmosphere, reducing total outgoing radiation that escapes to space (F_{out}). Therefore, an increase in GHGs will cause a positive radiative forcing, while secondary effects may amplify (e.g., additional O_3 production from CH_4) or oppose (e.g., O_3 destruction from CFCs) the primary positive forcing. The gas phase secondary effects relevant in the troposphere are considered further in Section 1.2. Aerosol can also perturb the balance by scattering or absorbing radiation directly (Section 1.3.4) or influencing cloud properties (Section 1.3.5).

The individual forcings from radiatively-active components including GHGs and aerosols are shown in Figure 1.1. Considering the period 1850 and 2019, which may be considered as showing the difference between pre-industrial (PI) and present day (PD) conditions, changes to GHGs have led to a positive forcing of 3.118 ± 0.258 Wm^{-2} while changes to aerosol have resulted in a negative forcing of -1.11 ± 0.38 Wm^{-2} (Forster et al., 2021). The net positive radiative forcing of ~2 Wm^{-2} has driven increases in global mean surface temperature of 1.09 ± 0.14 K (Gulev et al., 2021).

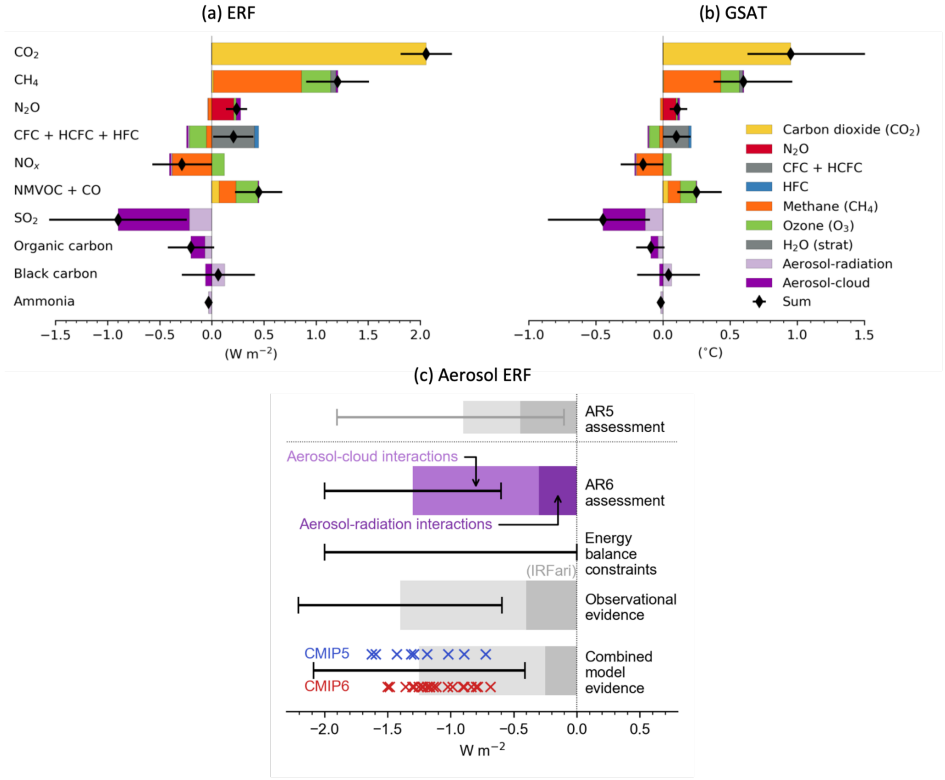


Figure 1.1. (a) Effective radiative forcing (ERF) from PI-to-PD changes for different components of atmospheric composition and (b) corresponding change in global mean surface air temperature (GSAT) from the IPCC 6th Assessment Report (AR6). (c) Total aerosol ERF and ARI and ACI components (see Sections 1.3.4 and 1.3.5) from the IPCC AR5 and AR6 assessments, observational evidence for aerosol forcing and simulated aerosol ERF from the 5th and 6th Coupled Model Intercomparison Projects (CMIP5, CMIP6) run for AR5 and AR6 respectively. Figures adapted from IPCC AR6 (Naik et al., 2021; Forster et al., 2021).

To understand how climate will change in the future, it is necessary to understand the likely changes in atmospheric composition and how these changes will impact the atmosphere's radiative balance. This requires an understanding of the fundamental processes which control atmospheric composition and I describe those relevant to this thesis in the following sections.

1.1.1 Climate Modelling

The scale and complexity of the Earth System means describing it requires a computational model. The earliest models, termed Global Circulation Models (GCM), focused predominantly on the physics of the atmosphere and oceans. Over time additional components such as atmospheric chemistry, aerosol, interactive land surface (e.g. vegetation) and sea-ice have been added (Fig A1). When these components are coupled, the model may be considered an Earth System Model (ESM) (e.g. UKESM1; Walters et al., 2019) but, to reduce computational cost and noise from interacting components, models are often run with just a single active component such as the atmosphere in this work. Each component is divided into cells in which relevant processes (e.g. chemical reactions) are simulated for a given period of time (the model's timestep) before energy and matter is transferred between adjacent cells. These models allow investigation into how the whole Earth System, or one component, would respond to a given perturbation such as increasing CO_2 from PI to PD concentrations. Model simulation of chemistry (Section 1.2.4), aerosols (Section 1.3.3), BVOC emissions (Section 1.4.1) and BVOCs (Sections 1.4.2.3, 1.4.4.3) and previous model studies investigating the climatic impact of BVOCs (Section 1.5) are discussed throughout Chapter 1.

1.2 Tropospheric Chemistry

The troposphere contains ~90% of the atmosphere's mass and is the region of greatest interest here as only a very small fraction of BVOCs and their oxidation products persist long enough to enter the stratosphere. To understand how BVOCs influence atmospheric composition, it is necessary to consider first the most influential reactions of tropospheric chemistry.

1.2.1 Daytime Chemistry

Tropospheric chemistry differs from the stratosphere because the attenuation of high frequency radiation in the stratosphere means the intensity of radiation with wavelengths <290 nm is negligible in the troposphere (Hobbs, Ch 4). As a result, the photolysis of O_2 does not happen. Rather the central process in tropospheric daytime chemistry is the photolysis of O_3 which yields the excited species $O(^1D)$ (Eq 1.3) or the ground state $O(^3P)$ (Eq 1.4).

$$O_3 + h\nu \rightarrow O_2 + O(^1D) \;\; \lambda < 310 \text{ nm} \quad (1.3)$$

$$O_3 + h\nu \rightarrow O_2 + O(^3P) \;\; \lambda < 1180 \text{ nm} \quad (1.4)$$

Eq 1.4 and 1.5 represent a null cycle since O_3 is rapidly reformed:

$$O(^3P) + O_2 + M \rightarrow O_3 + M \quad (1.5)$$

Where M represents a third body (N_2 or O_2) which removes additional energy.

$O(^1D)$ can be quenched to $O(^3P)$ via reaction with O_2 (Eq. 1.6) and N_2 (Eq. 1.7) (returning to the null cycle) or yield the highly reactive hydroxyl radical OH upon reaction with H_2O (Eq. 1.8) which constitutes a loss of O_3. OH production via this route, termed primary production, depends on the relative rates of the quenching and OH-forming reactions and therefore the concentration of water vapour (specific humidity) and the rate constants. The impact of the uncertainty in these rate constants is illustrated in Chapter 2.

$$O(^1D) + O_2 \rightarrow O(^3P) + O_2 \quad (1.6)$$
$$O(^1D) + N_2 \rightarrow O(^3P) + N_2 \quad (1.7)$$
$$O(^1D) + H_2O \rightarrow OH + OH \quad (1.8)$$

OH is the major daytime oxidant in the troposphere and, globally averaged, its major reaction partners are CO (~70%) and CH_4 (~15%) (Holmes., 2018). In an unpolluted atmosphere, typically considered as one with low concentrations of nitrogen oxides (NO_x = NO + NO_2), OH's reaction with CO leads to a net loss of O_3 and interconversion of OH and HO_2, collectively termed HO_x.

$$OH + CO \rightarrow CO_2 + H \quad (1.9)$$
$$H + O_2 + M \rightarrow HO_2 + M \quad (1.10)$$
$$HO_2 + O_3 \rightarrow 2O_2 + OH \quad (1.11)$$

$$\text{net: } CO + O_3 \rightarrow CO_2 + O_2$$

However, in more polluted regions with greater concentrations of NO, Eq 1.11, which destroys O_3, can be outcompeted by Eq. 1.12. Assuming an O_3 concentration of 30 ppbv, Eq 1.11 can start to compete with Eq 1.10 when NO reaches ~7.5 ppt.

$$HO_2 + NO \rightarrow NO_2 + OH \quad (1.12)$$

This is important as the rapid photolysis of NO_2 (lifetime ~100 s) leads to the production of O_3 via Eq 1.13 and Eq. 1.5.

$$NO_2 + h\nu \rightarrow NO + O(^3P) \quad (1.13)$$

By oxidising NO to NO_2 without the destruction of O_3, Eq. 1.11 breaks the null cycle of Eq. 1.13, 1.5 and 1.14 where photolysis of NO_2 results in no net change to O_3.

$$NO + O_3 \rightarrow NO_2 + O_2 \text{ (1.14)}$$

OH is also the major oxidant of the GHG CH_4. Therefore CH_4 atmospheric lifetime, and its radiative impact, is closely linked to the concentration of OH. In the clean atmosphere, oxidation of CH_4 leads to a loss of HO_x with the soluble methyl hydroperoxide (CH_3OOH) readily lost via wet deposition.

$$CH_4 + OH \rightarrow CH_3 + H_2O \text{ (1.15)}$$
$$CH_3 + O_2 + M \rightarrow CH_3O_2 + M \text{ (1.16)}$$
$$CH_3O_2 + HO_2 \rightarrow CH_3OOH + O_2 \text{ (1.17)}$$

However, in the presence of NO_x, the methyl peroxy radical (CH_3O_2) reacts with NO forming NO_2 and the alkoxy radical CH_3O which decomposes to formaldehyde (HCHO) and HO_2 (Eq 1.20, 1.21).

$$CH_4 + OH \rightarrow CH_3 + H_2O \text{ (1.18)}$$
$$CH_3 + O_2 + M \rightarrow CH_3O_2 + M \text{ (1.19)}$$
$$CH_3O_2 + NO \rightarrow CH_3O + NO_2 \text{ (1.20)}$$
$$CH_3O + O_2 \rightarrow HCHO + HO_2 \text{ (1.21)}$$

The two conversions of NO to NO_2 (Eq. 1.12 and 1.20) mean two O_3 molecules can be produced from this sequence. HCHO photolysis can produce two additional molecules of HO_2 and thus O_3 via Eq. 1.12 and 1.13.

$$HCHO + h\nu \rightarrow HCO + H \text{ (1.22)}$$
$$H + O_2 + M \rightarrow HO_2 + M \text{ (1.23)}$$
$$HCO + O_2 \rightarrow CO + HO_2 \text{ (1.24)}$$

The CO from Eq. 1.24 can react via Eq. 1.9 to form one more HO_2 and thus one more O_3 (total of five). HCHO can also react with OH (Eq 1.25) to yield HCO which, via Eq 1.24, facilitates the production of two more molecules of O_3 (total of four) via Eq 1.12 and the oxidation of CO.

$$HCHO + OH \rightarrow HCO + H_2O \text{ (1.25)}$$

This chemistry can be generalised to the oxidation by OH of larger VOCs, such as the BVOCs considered in this thesis, to form a peroxy radical, RO_2 (Eq 1.26, 1.27).

$$RH + OH \rightarrow R + H_2O \text{ (1.26)}$$
$$R + O_2 + M \rightarrow RO_2 + M \text{ (1.27)}$$

In low NO_x environments, the RO_2 will react with HO_2 to form a peroxide (Eq. 1.28) which is readily lost via deposition, constituting a loss of HO_x and O_3.

$$RO_2 + HO_2 \rightarrow ROOH + O_2 \text{ (1.28)}$$

In environments with higher NO_x, reformation of NO_2 and the formation of HO_2 will facilitate net O_3 production.

$$RO_2 + NO \rightarrow RO + NO_2 \text{ (1.29)}$$
$$RO + O_2 \rightarrow R'CHO + HO_2 \text{ (1.30)}$$
$$HO_2 + NO \rightarrow NO_2 + OH \text{ (1.31)}$$

Crucially, the carbonyl R'CHO (where the R' moiety has one fewer carbon and two fewer hydrogens than R the in RO_2) can react further with OH or by photolysis, yielding further peroxy radicals, i.e., $R'O_2$, facilitating further O_3 production. This is the central principle of the Common Representative Intermediates chemistry mechanism (Jenkin et al., 2008; Watson et al., 2008; Utembe et al., 2009), the central mechanism of this thesis. The maximum number of O_3 molecules which can be produced from a VOC during its oxidation by OH into CO_2 and H_2O is equivalent to the number of NO to NO_2 conversions which can occur. In an alkane, this corresponds to the total number of C-C and C-H bonds assuming all closed-shell intermediates also react with OH. Thus, CH_4 can produce four molecules of O_3 when HCHO reacts with OH, while C_2H_6 can produce seven molecules. It should be noted that if HCHO were to undergo photolysis instead of reaction with OH, an extra molecule of O_3 would be produced.

The reaction of RO_2 + NO can also yield organonitrates, $RONO_2$ (Eq. 1.32), which act as temporary reservoirs of NO_x. Organonitrate photolysis or reaction with OH can reform NO_2.

$$RO_2 + NO + M \rightarrow RONO_2 + M \text{ (1.32)}$$

Acyl peroxy radicals can also react with NO_2 to form a peroxy acyl nitrate species, the most common of which, $C_2H_3O_3NO_2$ (Eq 1.33), is termed PAN.

$$CH_3C(O)O_2 + NO_2 + M \rightarrow CH_3C(O)O_2NO_2 + M \text{ (1.33)}$$

PAN and the other peroxy acyl nitrate species also act as reservoirs of NO_x and their role in transporting NO_x away from source regions is considered further in Chapter 3.

1.2.1.1 NO_x-limited and VOC-limited regions

Increasing NO_x will not always lead to greater O_3 production. This can be understood by considering the concept of NO_x-limited and VOC-limited regimes. In much of the atmosphere, the addition of NO_x will drive O_3 production via the reactions of NO with peroxy radicals, principally HO_2 and CH_3O_2 (Eq 1.12, 1.20). Such a regime is NO_x-limited; adding more NO_x will increase O_3 production (Fig 1.2, lower right region). By contrast, in areas of high NO_x with an insufficient supply of peroxy radicals to react with NO, formation of nitric acid ($HONO_2$) via reaction 1.34, which terminates the catalytic cycle, becomes important and results in NO_x loss via

deposition. As the production of NO_2 often destroys O_3 (Eq 1.14) and the rapid photolysis of NO_2 leads to O_3 reformation. Eq 1.34 represents a loss of O_3.

$$OH + NO_2 + M \rightarrow HONO_2 + M \quad (1.34)$$

In this case additional NO_x will not increase O_3 (Fig 1.2, upper left region), rather NO_x and HO_x are sequestered to $HONO_2$ and lost via deposition. However, the addition of VOCs will increase the supply of peroxy radicals and thus O_3 production; such a regime is therefore VOC-limited.

This complex non-linear chemistry and the role of NO_x reservoirs have important consequences for the global tropospheric O_3 distribution. Many regions with high NO emissions are VOC-limited and the termination reaction (Eq 1.34) restricts the ozone production efficiency (OPE), defined as the average number of O_3 molecules a single NO molecule can produce by cycling catalytically between NO and NO_2. However, the formation of PANs, organonitrates and other NO_x reservoirs, which differ from $HONO_2$ in that they are not rapidly removed from the atmosphere but are transported to less polluted regions, changes this. Once a NO_2 molecule is liberated from these species in a less polluted (NO_x-limited) region, it can undergo many more NO to NO_2 conversions and produce many more molecules of O_3 (higher OPE) than would have occurred in the VOC-limited regime.

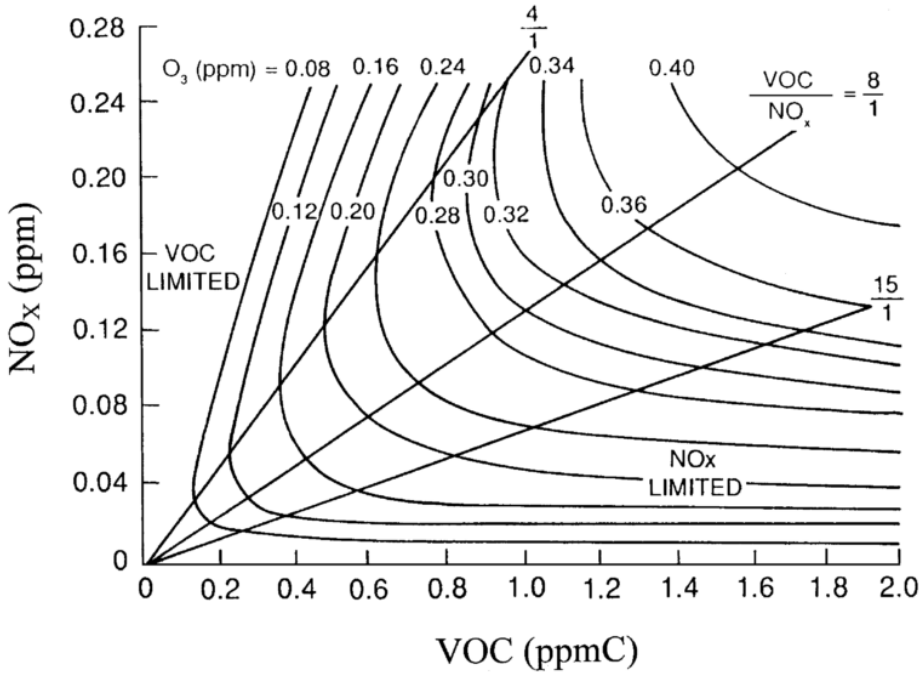


Figure 1.2. Maximum O_3 as a function of NO_x and volatile organic compound (VOC) concentrations. Taken from (Jenkin and Clemitshaw, 2000)

Thus, NO_x reservoirs can increase the global O_3 burden by increasing global OPE. This has impacts on climate via the total O_3 burden but also the fact that O_3 is a more efficient GHG (in terms of the forcing per unit

concentration change) in the upper tropical tropopause than at the surface (Lacis et al., 1990). The description of NO_x reservoirs in chemical mechanisms is therefore important for the O_3 distribution. The impact of such differences between a standard and state-of-the-art chemical mechanism on atmospheric composition and climate is considered in Chapters 2 and 3.

The significant PI-to-PD increase in NO emissions has contributed to the PD's greater modelled tropospheric O_3 burden (44% increase, Griffiths et al., 2021) with an attendant positive forcing of ~0.15 Wm^{-2} (Fig 1.1(a)). However, the increases in NO_x have also increased tropospheric OH via O_3 photolysis and HO_2 + NO, increasing the oxidation of CH_4 with an attendant negative forcing of about -0.4 Wm^{-2} (Fig 1.1(a)). This results in a negative net forcing from NO_x-driven changes to gas phase atmospheric composition. The change to oxidants also affects the forcing from aerosol and clouds (Section 1.3.4, 1.3.5 & 1.4.6).

1.2.2 Nighttime Chemistry

At night the lack of O_3 and NO_2 photolysis means the concentrations of OH and NO drop to almost zero, meaning production of O_3 cannot occur. Ozonolysis of certain alkenes and decomposition of subsequent Criegee Intermediates can produce OH (e.g, Khan et al., 2018) but in most locations NO_3, present at very low concentrations during the day due to rapid photolysis (Eq. 1.35, 1.36), and O_3 are the dominant oxidants.

$$NO_3 + h\nu \rightarrow NO + O_2 \quad (1.35)$$

$$NO_3 + h\nu \rightarrow NO_2 + O(^3P) \quad (1.36)$$

NO_3 is produced by the reaction of O_3 and NO_2 (Eq 1.37).

$$O_3 + NO_2 \rightarrow NO_3 + O_2 \quad (1.37)$$

In the context of organic chemistry, NO_3 is particularly reactive with carbon-carbon double bonds and therefore reacts rapidly with isoprene and monoterpenes (Atkinson & Aery., 2003). Attack of NO_3 into the double bond yields an $-ONO_2$ group on one carbon and a peroxy radical. Thus, these pathways lead to the quick addition of multiple heteroatoms which can lower the molecule's volatility and favour partitioning to the aerosol phase.

NO_3 also reacts with NO_2 to form an equilibrium with N_2O_5 (Eq 1.38).

$$NO_3 + NO_2 + M \leftrightharpoons N_2O_5 + M \quad (1.38)$$

The rapid heterogeneous hydrolysis of N_2O_5 (Eq 1.39) forms $HONO_2$ whose subsequent loss via deposition represents a loss of total reactive nitrogen (NO_x)

$$N_2O_5\,(g) + H_2O\,(l) \rightarrow 2HONO_2(aq)\ \text{(Eq 1.39)}$$

1.2.3 Atmospheric Oxidising Capacity

The oxidising capacity of the atmosphere is controlled by the burdens of the major gas phase oxidants (O_3, OH and NO_3) and H_2O_2, an important aqueous phase oxidant. The concentrations of these oxidants influence CH_4 concentrations (via reaction with OH), the processing of other volatile organic compounds and the formation of organic aerosol (Section 1.3.1). The oxidation of SO_2 to form sulphate aerosol also depends on oxidant concentrations (Section 1.3.1).

Sections 1.2.1 and 1.2.2 have described the key processes which control O_3 concentrations, specifically the role of NO_x and VOCs in net O_3 production or loss, and by extension the concentrations of OH, NO_3 and H_2O_2 (via the self reaction of HO_2 or during oxidation of VOCs like isoprene).

Therefore the emissions of NO_x and VOCs, which have increased between the PI and PD due to enhanced anthropogenic contributions (e.g., Thornhill et al., 2021a), play a major role in atmospheric oxidising capacity. For example, when comparing two PI atmospheres with PI and PD emissions of NO_x and VOCs, Karset et al (2018) found the oxidising capacity of the PD atmosphere to be much higher with important consequences for aerosol formation and dispersion, a key feature of Chapter 3.

The importance of oxidants is a central theme of this thesis. Chemical processes affecting the oxidising capacity during isoprene oxidation are detailed in Section 1.4.2 and the role of oxidants on the climatic impact of BVOCs is discussed in Sections 1.4.6 and 1.5.

1.2.4 Chemistry in Climate Models

Atmospheric chemistry is described in climate models by a set of reactions - a chemical mechanism - which the model converts into a series of differential equations and solves for each timestep in each grid cell to calculate the concentration of the chemical species. Initial conditions for each timestep are determined by the results of the previous timestep, the inflow and outflow of chemical species and physical parameters such as temperature, pressure and incident radiation. Emissions of certain chemical species are included to simulate a range of sources including anthropogenic activities (e.g., fossil fuel combustion), terrestrial biogenic regions (this thesis' major focus), oceans and biomass burning. These emissions are typically added into the lowest grid cell level although some models include emissions into higher grid cells to simulate chimneys and emissions from aircraft. Physical processes which affect certain chemical species such as deposition or photolysis are also simulated.

A major challenge in simulating chemistry is condensing the huge number of chemical reactions and species which occur in the atmosphere to a level which the model's solver can process on a feasible timescale while still capturing the key processes which determine atmospheric composition. For example, the Strat-Trop (ST) chemical

mechanism (Archibald et al., 2020a) in UKESM1 considers 87 species and 305 reactions while the more comprehensive CRI-Strat 2 (CS2) mechanism (Chapter 2), has 228 species and 766 reactions. As a result, CS2's runtime is 90% longer. These mechanisms are compared in Chapters 2 and 3.

The concentrations of radiatively-active chemical species are also considered by the modules within climate models which simulate radiation within the atmosphere.

1.3 Atmospheric Aerosols

Atmospheric aerosols also influence the radiative balance of the atmosphere. Aerosols are emitted directly from the Earth's surface (primary aerosols) or formed in the atmosphere (secondary aerosols). The chemical composition and size of aerosols strongly influence how they interact with radiation and contribute to clouds.

1.3.1 Aerosol Composition

The chemical composition of most aerosols can be categorised as sulphate (SO_4), black carbon (BC), organic matter (OM), nitrate, ammonium, mineral dust (DU) and sea salt (SS) (Hobbs, Ch 6). Aerosol particles will typically contain a mixture of these components. In this thesis, particular attention is paid to organic carbon aerosol and SO_4 aerosol since the secondary production of these components is closely tied to the climatic impacts of BVOCs.

SO_4 aerosol contains the sulphate anion (SO_4^{2-}) and is formed in the atmosphere by the oxidation of SO_2 which is emitted by fossil fuel combustion and volcanos and produced in the atmosphere by oxidation of dimethyl sulphide (DMS) which is emitted by biogenic sources (Simpson et al., 1999). Oxidation of SO_2 can occur in the gas phase by OH, yielding sulphuric acid (H_2SO_4), after several intermediate steps. H_2SO_4's low volatility allows it to condense on to existing aerosol particles or nucleate new particles by clustering with water, termed binary homogeneous nucleation (Benson et al., 2008), amines ("ternary inorganic", e.g., Dunne et al., 2016; Lehtipalo et al., 2018) and oxidised organic species ("ternary organic"; Section 1.4.5). SO_2 can also be oxidised in aqueous aerosol or cloud droplets by O_3 and H_2O_2 (Turnock et al., 2019). Thus the atmospheric oxidising capacity (Section 1.2.3) has a strong influence on SO_4 aerosol production as well as controlling how SO_2 contributes to the aerosol size distribution. Gas phase oxidation of SO_2 can add new small particles, via nucleation, while aqueous phase oxidation of SO_2 only adds mass to existing particles; the impact is discussed in Section 1.3.5.

Primary organic aerosol (POA) is emitted by biomass burning and anthropogenic activities and contains partially oxidised carbon (compared to BC aerosol which contains highly reduced carbon). Organic carbon aerosol can also be formed in the atmosphere, termed Secondary Organic Aerosol (SOA), where the gas phase oxidation of volatile organic compounds such as the biogenic species isoprene and monoterpenes and the predominantly anthropogenic species xylene yields more highly oxidised products (e.g., Hallquist et al., 2009; Shrivistava et al., 2017). These products can partition to the aerosol phase either due to their lower volatility or via reactive uptake (Claeys & Maenhaut., 2021). In addition to nucleation by clustering with sulphuric acid and amines, the most

highly oxidised organic products can also participate in new particle formation either on their own or with an ion generated by cosmic rays, termed pure biogenic nucleation (PBN) (Kirkby et al., 2011; Dunne et al., 2016). SOA from isoprene and monoterpenes, including developments in understanding of the chemistry which facilitate PBN, is discussed further in Section 1.4.5.

Like SO_4 aerosol, the necessity of gas phase oxidation means the location of SOA's formation, contribution to the aerosol size distribution and lifetime are dependent on local oxidant concentrations. Thus, oxidants play an important role in determining the climatic impact of SOA (Section 1.4.6) and this forms a central part of this thesis' examination of the climatic impact of BVOCs, (Chapter 3).

1.3.2 Aerosol Size Distribution

Aerosol particles are typically categorised into four size modes based on diameter, d: nucleation (d < 10 nm), Aitken (10 nm < d < 100 nm), accumulation (100 nm < d < 1 μm) and coarse (d > 1 μm), although the precise range of size bins can vary (Hobbs Ch 6, Mann et al., 2010). Nucleation mode aerosols tend to have the highest number concentration (reaching 10^6 cm^{-3}) followed by the Aitken mode with concentrations typically between 10^3 cm^{-3} (remote marine regions) to 10^5 cm^{-3} (polluted regions) (Hobbs, Ch 6). However, these modes contribute little to the total mass, surface area or volume concentrations of aerosol. Despite being present at lower number concentrations (10-10^3 cm^{-3}), the accumulation mode contributes a much greater fraction of the total aerosol mass, volume and surface area concentration. Coarse mode particles are found at much lower concentrations (~1-10 cm^{-3}), but often contain a substantial fraction of the aerosol mass and volume concentrations due to their size.

Aerosol mass can be transferred between modes by several processes. Condensation of low volatility species can grow small particles while coagulation of smaller particles yields larger particles. Aerosol particles can also be removed from the atmosphere by pathways including loss to water droplets in clouds (nucleation scavenging), precipitation (impaction scavenging) or dry deposition (Mann et al., 2010). The surface area contribution is particularly important because it determines which mode low volatility species condense on to and thus how the aerosol size distribution is perturbed by a change in condensable vapours (e.g., by a change in BVOC emissions). This is discussed further in Section 1.4.6 and Chapter 3.

1.3.3 Aerosols in Climate Models

Aerosols are treated in a similar way to chemical species in many climate models. In UKESM1 the aerosol scheme GLOMAP-mode (Mann et al., 2010) considers the number of aerosol particles in each size mode and the mass of each component (SO_4, SOA etc.) in each mode. Aerosol processes such as condensation, nucleation, coagulation, deposition and scavenging are combined with primary aerosol emissions and treated in the same way as chemical reactions: after each timestep the aerosol number and component masses of each mode are updated. Given this thesis' focus on chemistry, a full description of these processes is beyond the scope but is given in Mann et al (2010).

Aerosols are also considered by the modules within climate models which simulate the interaction of radiation with the atmosphere, both in terms of the direct interaction of aerosols with radiation (Section 1.3.4) and the interaction of aerosol with clouds (Section 1.3.5).

1.3.4 Aerosol Direct Radiative Effect

Aerosols can influence the radiative budget of the atmosphere by interacting directly with radiation via scattering or absorption, termed the aerosol Direct Radiative Effect (DRE) or aerosol-radiation interaction (ARI) (Bellouin et al., 2020).

The strength of this interaction is strongly dependent on aerosol size. Under the Mie regime, aerosol particles which are comparable in size to the wavelength of incident radiation interact most strongly with it and for visible light this corresponds to particles in the accumulation mode (Hobbs, Ch 4). Therefore, a perturbation to the aerosol distribution which increases the number of accumulation mode particles will have the strongest impact on the DRE (e.g., Sporre et al., 2020).

The aerosol's chemical composition is also important with regard to whether the aerosol scatters or absorbs the incident radiation. Scattering aerosols cool the climate while absorbing aerosols warm (Fig 1.3(a-d)). SO_4 aerosol is an efficient scatter of radiation while BC aerosol is the strongest absorber. In a multi-model study where PD emissions of SO_2, BC and POA were separately applied to a PI atmosphere and compared to an unperturbed PI simulation, Thornhill et al (2021a) found the mean forcing from the changes to the DRE was -0.36 Wm^{-2} for SO_2 (cooling from enhanced scattering) but +0.28 Wm^{-2} for BC (warming from greater absorption). This result is also seen in Figure 1.1(a). Organic matter aerosol (total POA and SOA) is typically a scattering aerosol with the PI-to-PD change in POA emissions yielding a forcing from DRE changes of -0.09 Wm^{-2} (Thornhill et al., 2021a).

The total extinction of incident radiation in a vertical column by scattering or absorption by aerosol can be described by the aerosol optical depth (AOD) and is considered in Chapter 3.

The CMIP6 multi-model mean PI-to-2019 net instantaneous forcing from aerosol DRE changes is -0.2±0.20 Wm^{-2} (Forster et al., 2021) (Fig 1.1(c)). (This forcing includes the effects of aerosols scattering and absorbing radiation but not the effects of absorbing aerosols, typically BC, on cloud formation, often called the semi-direct effect.)

1.3.5 Aerosol Indirect Radiative Effect

Aerosols can also influence the radiation budget indirectly by affecting cloud properties in processes collectively termed aerosol-cloud interactions (ACI). The most important pathways are the impacts on cloud albedo, called the first aerosol indirect effect (1st AIE) or Twomey effect (Twomey., 1974), and on cloud lifetime, the second aerosol indirect effect (2nd AIE) (Albrecht., 1989).

Aerosol size and composition are important for ACI. In air masses which are supersaturated with respect to water vapour, aerosol particles can serve as cloud condensation nuclei (CCN) as water condenses onto their surface and grows the particle to form a cloud droplet; a process called activation. This only happens for particles with sizes at the upper end of the Aitken mode and above because the saturation vapour pressure of water over a curved surface (the atmospheric vapour pressure which must be exceeded for net condensation and thus droplet growth to occur) is higher than over a flat surface: the Kelvin effect (Hobbs, Ch 7). This effect is stronger for smaller particles given their greater radius of curvature and means that the water vapour concentrations required for their growth far exceed those typically found in the atmosphere. The Kelvin effect is opposed by the reduction in saturation vapour pressure above an aqueous solution by the presence of solute ions (Raoult's Law). The net effect, Kohler's Law, describes the ratio of the saturation vapour pressure over an aerosol particle's curved surface with the saturation vapour pressure over a flat surface and, for a certain aerosol composition, gives the maximum saturation vapour pressure required for the CCN to be activated.

The 1st AIE refers to the dependence of cloud albedo (ratio of reflected to incident radiation) to the cloud droplet number concentration (CDNC) in the liquid water path. A higher CDNC will result in greater albedo and more reflection of incoming solar radiation (a cooling effect). For a constant LWC, this means the cloud droplet effective radius (r_{eff}) will decrease. Therefore, if the aerosol distribution is perturbed such that a greater number of aerosol particles can activate into cloud droplets, typically by growth of smaller particles into larger particles, cloud albedo will increase (Appendix A1 for derivation). The increase in albedo for a given increase in CDNC is inversely proportional to the initial CDNC and highest in clouds with an initial albedo of 0.5 (Twomey., 1991).

The 2nd AIE is also linked to the CDNC since smaller cloud droplets grow less efficiently via collision-coalescence into sizes sufficient for precipitation than larger particles. Therefore, a cloud with greater CDNC will tend to have a longer lifetime.

The importance of CDNC on ACI leads to a dependence on oxidant concentrations via the contribution of SOA and SO_4 aerosol. This is particularly true in the case of SO_4 aerosol given the different pathways by which SO_2 can contribute to aerosol. Gas phase oxidation of SO_2 yields H_2SO_4 which can grow existing particles or nucleate new particles while aqueous phase oxidation only adds mass to existing particles (Section 1.3.1). Suppression of the OH oxidation pathway reduces new particle formation and consequently the number of particles which grow to CCN sizes and become cloud droplets. For example, when PD CH_4 concentrations were applied to a PI atmosphere in O'Connor et (2021), depletion of OH reduced CDNC and led to a global forcing from the shortwave (SW) ACI of +0.5 Wm^{-2}, ~70% of the forcing from CH_4 acting as a GHG.

The CMIP6 multi-model mean PI-to-2019 net forcing from changes to ACI is -0.86±0.57 Wm^{-2} (Forster et al., 2021) (Fig 1.1(c)), ~3.5× stronger than the ARI.

The forcing from changes to the ARI and ACI (net -1.11 ± 0.38 Wm^{-2}) represent the greatest uncertainty in PI-to-PD radiative forcing (Gulev et al., 2021) (Fig 1.1(c)). Reduction in this uncertainty is important since it will improve the understanding of the net anthropogenic forcing and thus predictions of future climate change.

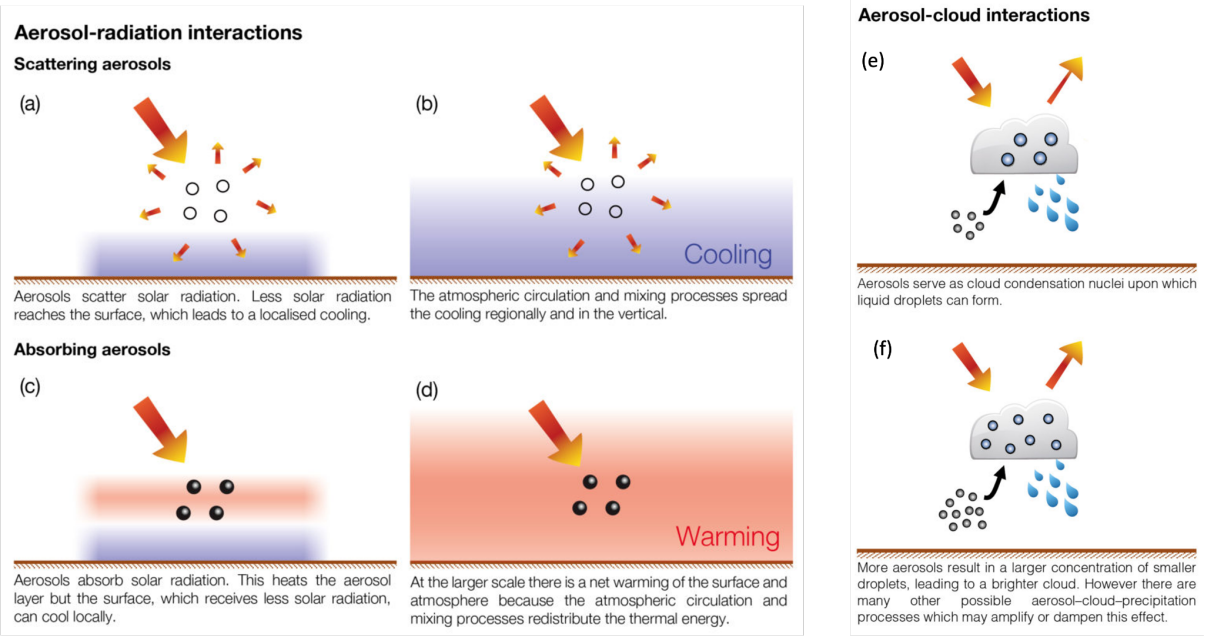


Figure 1.3. Schematic showing the climatic impact of ARI, including cooling from scattering aerosol (a,b) and warming from absorbing aerosol (c,d), and ACI (e,f). Red/orange arrows show the flow of radiation. Adapted from AR5 Boucher et al (2013).

1.4 BVOCs

BVOCs comprise a huge range of organic species emitted by the biosphere. In this thesis, I consider BVOCs emitted by vegetation with a focus on isoprene (2-methyl-1,3-butadiene) and the monoterpenes α-pinene and β-pinene ($C_{10}H_{16}$). Isoprene is the most widely emitted non-methane VOC (~600 TgC yr^{-1}) while total emissions of the monoterpenes are ~95 TgC yr^{-1} with α- and β-pinene comprising ~50% of this (Sindelarova et al., 2014). By reacting with O_3, OH and NO_3 to yield a range of products including RO_2, NO_x reservoirs and SOA precursors, these BVOCs influence atmospheric composition (including O_3, OH and CH_4) and climate. The understanding of the chemical reactions of isoprene and monoterpene oxidation and their contribution to SOA has advanced considerably over the last decade and an accurate description is critical for modelling the influence these species have on atmospheric composition.

However, just as BVOCs influence atmospheric composition and climate, the emissions of BVOCs (E_{BVOC}) are also strongly affected by atmospheric conditions. Therefore, to understand the role BVOCs will have on future climate, it is necessary to consider both how they respond to climate change and how they will impact climate and I review both in the following sections.

1.4.1 BVOC Emissions

Isoprene emissions are highest in the tropical rainforests of Amazonia, central Africa and southeast Asia. Monoterpene emissions are high in these locations as well as the boreal forests of North America, Scandinavia and Siberia (Sindelarova et al., 2014). The emissions of isoprene and monoterpenes exhibit complex dependencies on a range of atmospheric variables.

Isoprene emissions increase exponentially with temperature up to ~38°C before declining (Kesselmeier & Staudt., 1999) while also showing a strong positive dependence on photosynthetic radiation (PAR) (Sharkey and Monson., 2017) and therefore a diel cycle. This is because isoprene, unlike monoterpenes, is not stored in plants and so emissions cease rapidly after production stops at night. Increasing CO_2 can increase isoprene emissions by fertilising new vegetation (Zhu et al., 2016) but also inhibit isoprene production within plants (Heald et al., 2009).

Monoterpene emissions also exhibit an exponential temperature dependence (Kesselmeier & Staudt., 1999) but a much weaker dependence on CO_2. The dependency on PAR is more complex than for isoprene because in many plant species a fraction of monoterpenes emissions comes from storage pools, and is light independent, while the remainder arises from recently synthesised compounds and does show a light dependence (Kesselmeier & Staudt., 1999). The relative contributions from storage pools and denovo production varies between tree species.

Aerosol perturbations which enhance diffuse radiation (e.g., from biomass burning) can increase E_{BVOC} (Rap et al., 2018) while droughts, floods and changes to the hydrological cycle will affect BVOC production in a multitude of ways (Jardine et al., 2015, Sheil., 2018). Land use change, often driven by anthropogenic activities such as deforestation, will also change E_{BVOC} (Squire et al., 2015).

These variables are predicted to change in the future scenarios considered in the Scenario Model Intercomparison Project (ScenarioMIP; O'Neill et al., 2016). The ScenarioMIP pathways combine different socioeconomic projections from the Shared Socioeconomic Pathways (SSP) framework with the climate change mitigation targets based on the Representative Concentration Pathways (RCPs) (van Vuuren et al., 2011) to provide estimates for how the Earth System may evolve under a given set of assumptions about societal change up to 2100. For example, the change in forested area from the 2010 to 2100 ranges from +7% in SSP1 (a more sustainable future), to -15% in SSP3 where environmental challenges are considered low priority (Fig A2; Riahi et al., 2017). The typical nomenclature is "SSP[SSP number][RCP number]" such that SSP370 is a combination of SSP3 (a fossil-fuel driven pathway) and RCP7.0 where the PI-to-2100 radiative forcing is 7 Wm^{-2}.

1.4.1.1 Modelling BVOC Emissions

To capture the influence of climate on E_{BVOC}, climate models typically calculate E_{BVOC} by considering simulated temperature, photosynthesis, CO_2 and land surface. UKESM1 considers land surfaces ranging from ice and desert (where E_{BVOC} are zero) to various vegetation types which produce BVOCs at different rates. Schemes like iBVOC in UKESM1 (Pacifico et al., 2011) combine these parameters to generate E_{BVOC} for each grid cell for each

timestep, allowing external perturbations (e.g., CO_2 increases) to influence E_{BVOC}; critical for capturing biosphere-climate feedbacks.

Several modelling studies have considered how E_{BVOC} have changed between the PI and PD and will evolve in future climate scenarios. Pacifico et al (2012) simulated PI isoprene emissions to be 26% (~120 TgC) higher than in the PD while under the RCP8.5 scenario, emissions in 2100 were very similar to PD levels with CO_2 inhibition offsetting the increase from higher temperatures. Factoring in projected land use change between the PD and 2095 while using iBVOC, Squire et al (2015) found that reductions to isoprene emissions from CO_2 inhibition and land use change outweighed increases from higher temperatures and CO_2 fertilisation with a net reduction of 55%.

Most models simulate an increase in emissions up to 2100 albeit with variation between different ScenarioMIP pathways (Fig 1.4(a)). There also remains significant inter-model variation in E_{BVOC} within a given pathway (Fig 1.4(b)) due to differences in the isoprene emission parameterisation scheme and land use cover. Compared to the PI-to-PD reduction of isoprene emissions in UKESM1, other CMIP6 models which use the alternative Model of Emissions of Gases and Aerosols from Nature (MEGAN) scheme to calculate isoprene emissions simulate little change (Fig 1.4(b)) (Cao et al., 2021).

Between 2015 and 2100, all models simulate increases in SSP370 with the dominant driver increasing temperatures. UKESM1 predicts the smallest increase in emissions due to CO_2 inhibition which is nearly twice as strong as the other models (Cao et al., 2021). Differences in CO_2 inhibition are also apparent when considering the increase in E_{BVOC} with temperature following an instantaneous quadrupling of CO_2 ($4xCO_2$, Eyring et al., 2016), relevant for quantifying the BVOC feedback (Section 1.5). UKESM1's increase is ~¼ of the 5-model mean (Thornhill et al., 2021b) and 7× smaller than NorESM2's increase.

While further constraining the influence of atmospheric conditions on E_{BVOC} is not this thesis' focus, the uncertainty in how E_{BVOC} will change in future and the implications for climate is important and highlighted further in Section 1.5.1.

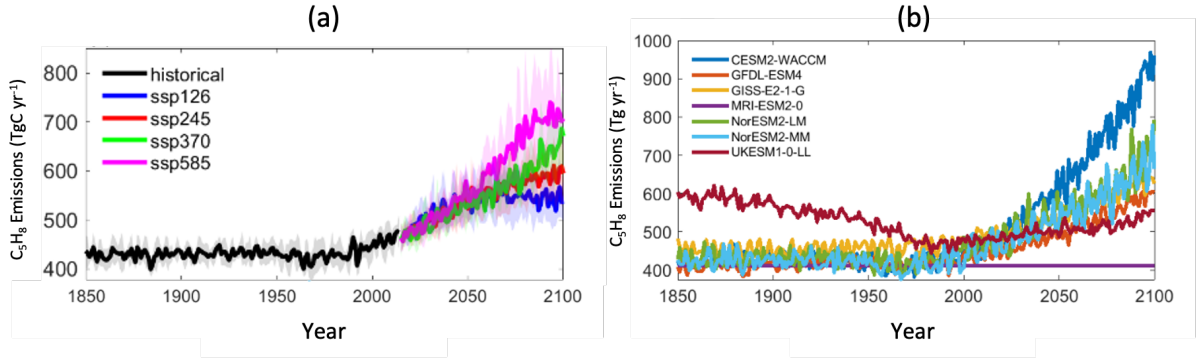


Figure 1.4. (a) Multi-model mean isoprene emissions from historical simulations (1850-2014) and various ScenarioMIP simulations (2015-2100) from climate models GFDL-ESM4, GISS-E2-1-G, NorESM2-LM and NorESM2-MM (shading shows 1 standard deviation of multi-model spread). (b) Isoprene emissions from historical simulations (1850-2014) and ScenarioMIP simulation SSP370 (2015-2100) from different climate models. Note the different units in (a) and (b). Plots taken from Cao et al (2021).

1.4.2 Isoprene Chemistry

Isoprene's gas phase oxidation has been studied extensively due to isoprene's significant influence on atmospheric composition in terrestrial tropical regions. A key challenge has been reconciling the low bias of simulated OH in many chemical mechanisms in low NO_x, high isoprene environments compared to observations (e.g., Butler et al., 2008). This low bias arises in part from the omission of reaction pathways which regenerate OH and have only been verified in the last decade. In this section I describe isoprene oxidation chemistry and the recent advances in understanding while relating these to the ST and CS2 chemical mechanisms, the key mechanisms examined in this thesis. CS2 is based on the CRI v2.2 mechanism (Jenkin et al., 2019a), in turn derived from the Master Chemical Mechanism (MCM) v3.3.1 (Jenkin et al., 2015).

Reaction with OH accounts for ~85% of isoprene oxidation and acts as a major sink for OH in isoprene-rich regions. Isoprene's terminal carbons are the dominant locations (>99%) for OH's attack with branching ratios of 63% and 39% for attack at the 1-carbon (adjacent the methyl group) and 4-carbon positions respectively (Wennberg et al., 2018) (Fig 1.5). The resulting allylic radical isomerises rapidly via the addition and loss of an O_2 molecule to form monounsaturated species with the peroxy radical and hydroxy groups separated by two (β isomer) or four (δ isomer) carbons, collectively termed ISOPOO (Fig 1.5).

The β isomers dominate (>90%) over most atmospheric conditions (Jenkin et al., 2019a). The δ isomers are further differentiated by those where the two oxygenated groups are in the trans ($E\delta$) or cis ($Z\delta$) conformation. Reaction of the $\beta, E\delta$ and $Z\delta$ RO_2 with HO_2 predominantly yields isomers of the isoprene hydroxy hydroperoxide (ISOPOOH). Reactions of NO and NO_3 with the β isomer yields methyl vinyl ketone (MVK), methacrolein (MACR) and isomers of the isoprene hydroxy nitrate (IHN) while the δ RO_2 yields IHN and a range of other products. Reactions with other RO_2 yield MVK, MACR and HCHO as the major products. In the last decade, additional isomerisation pathways of certain ISOPOO isomers have been discovered. ST and CS2 differ in this regard and this is discussed in Section 1.4.2.1.

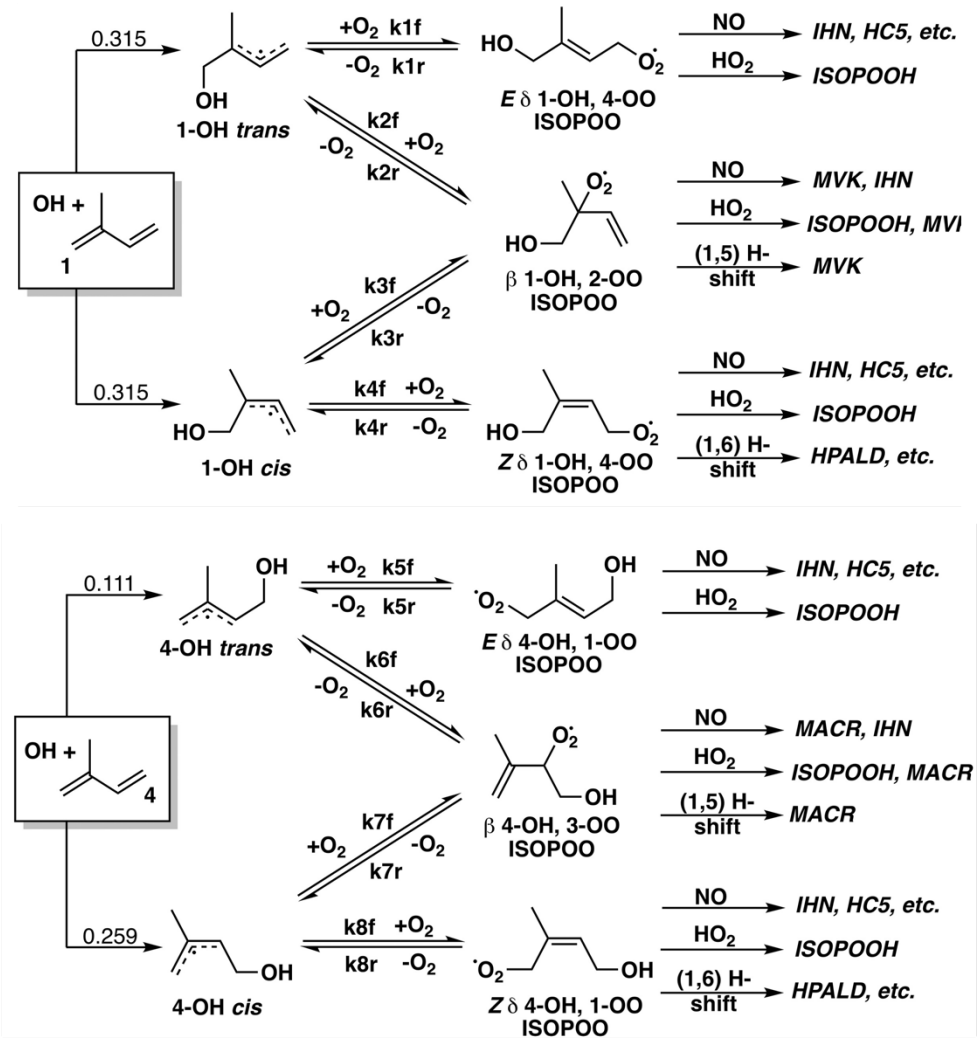


Figure 1.5. Oxidation mechanism of isoprene + OH for OH-attack at the 1 (upper) and 4 (lower) carbon positions. Numbers on arrows show branching ratios for each pathway and kxr and kxf refer to rate constants for O_2 addition and loss respectively. HC5 is a hydroxy carbonyl. Taken from Wennberg et al (2018).

Ozonolysis destroys ~10% of isoprene with major products of MVK, MACR and HCHO (Wennberg et al., 2018). The ozonolysis schemes of ST and CS2 are similar. The methyl acyl radical, CH_3CO_3, the precursor to PAN, is also produced at a ~10% yield and its importance is discussed in Chapter 3.

Oxidation by NO_3 accounts for ~5% of isoprene destruction and is more important at night (Section 1.2.2) when isoprene concentrations are lower. ST assumes 100% IHN production but the reality is more complicated. NO_3 oxidation of isoprene produces a nitrated peroxy radical which can isomerise between β and δ isomers, like ISOPOO, before reacting with HO_2, NO, NO_3 and other RO_2 (Vereecken et al., 2021). CS2 simulates the formation of a single nitrated RO_2, representing the β and δ isomers, which then forms a nitrated hydroperoxide from HO_2 and unsaturated nitrated carbonyls from NO, NO_3 and RO_2. The difference between ST and CS2 is important because these products are NO_x reservoirs and their transport and subsequent release of NO_x can lead to O_3

production in remote regions. The products in CS2 react differently and therefore have different lifetimes to the single IHN of ST and thus the extent of NO_x transport differs between the mechanisms.

The chlorine radical is a minor isoprene sink (Wennberg et al., 2018) but is not considered in ST and CS2.

1.4.2.1 ISOPOO H-shifts and HO_x-recycling

The major development in oxidation chemistry over the last decade has been the theoretical prediction (Peeters et al., 2009) and subsequent laboratory observation (Crounse et al., 2011) of an intramolecular reaction pathway which certain ISOPOO isomers undergo. This is a 1,6 H-shift reaction of $Z\delta$ RO_2 where the peroxy radical moiety abstracts the hydrogen adjacent to the hydroxy group (Fig 1.6). The resulting allylic radical can form two different RO_2 (A,B Fig 1.6) depending on to which carbon the incoming O_2 bonds. These RO_2 can decompose into a dihydroperoxide carbonyl RO_2 (DHP-RO_2) (A) which can decompose further, producing OH and CO, or a hydroperoxy aldehyde (HPALD) (B) and HO_2, . These processes are crucial as they regenerate HO_x directly and indirectly via subsequent reactions. The rapid photolysis of HPALDs yields two molecules of HO_x as well as another unsaturated carbonyl which also produces HO_x when photolysed. The regeneration of HO_x from these processes is termed "HO_x-recycling".

The competitiveness of the 1,6 H-shift increases with temperature and depends on the concentrations of the bimolecular reaction partners (Teng et al., 2017). At a bimolecular lifetime (τ_{bimol}) of 10^3 s, corresponding to pristine conditions (reaction partner concentrations of ~1-5 ppt), ~90% of $Z\delta$ 4-OH,1-OO ISOPOO and ~40% $Z\delta$ 1-OH,4-OO ISOPOO undergo a 1,6 H-shift (Wennberg et al., 2018). By contrast, when τ_{bimol}=10 s, representing more polluted regions (reaction partner concentrations of ~100-500 ppt), < 3% of all $Z\delta$ ISOPOO undergoes a 1,6 H-shift. This chemistry is therefore most influential in low NO_x conditions such as those found over Amazonia in the present day or more widely in the PI atmosphere; precisely the conditions where older mechanisms were low biased for OH.

Some of the β RO_2 isomers can also undergo a 1,5 H-shift forming HCHO, OH and MACR or MVK (Wennberg et al., 2018) (Fig A3), regenerating HO_x.

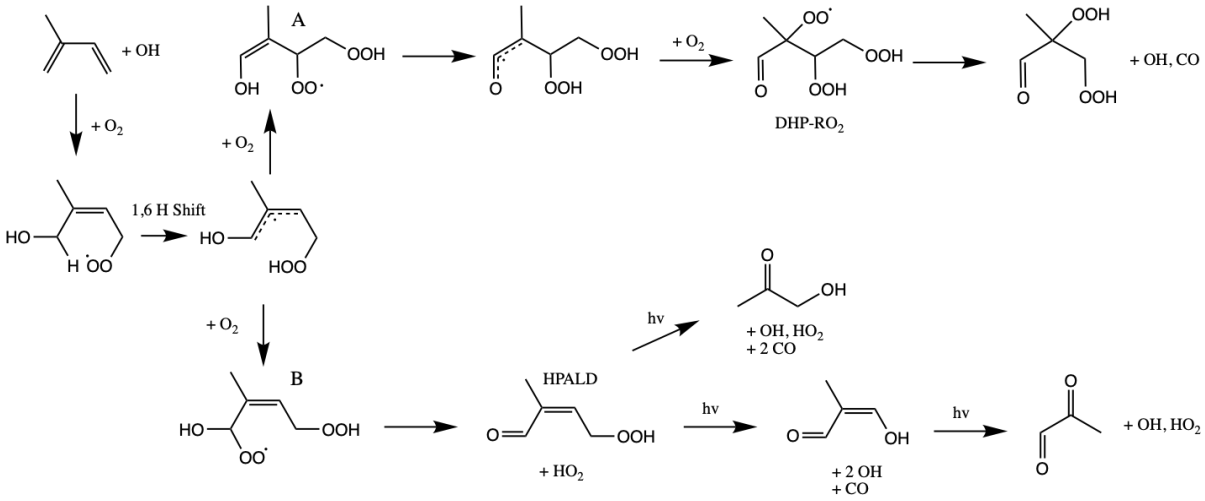


Figure 1.6. Simplified sequence for production of HPALD and DHP-RO_2 from one possible Zδ ISOPOO (Zδ1-OH, 4-OO) and subsequent reactions which regenerate HO_x. Adapted from Wennberg et al (2018).

HO_x-recycling does occur in higher NO_x regions via the production of HO_2 from the reaction of NO or NO_3 with ISOPOO and the photolysis of the major products, MACR and MVK, but this is greatly limited in low NO_x conditions. These two H-shifts and the subsequent chemistry increase the level of HO_x-recycling in low NO_x conditions considerably and thus reduces isoprene's depletion of OH (Chapter 2).

1.4.2.2 Modelling Isoprene Chemistry

The challenge of reducing isoprene's oxidation pathway to a form suitable for climate models is considerable: in the near-explicit Master Chemical Mechanism (MCM) v3.3.1, isoprene oxidation comprises 1926 reactions and 602 species. Reduction is performed by lumping multiple isomers into a single species and omitting short-lived species and minor pathways.

The relatively small differences between ST and CS2 for the oxidation of isoprene by O_3 and NO_3 have been discussed in Section 1.4. However, these mechanisms differ more when it comes to the most important pathway, oxidation by OH, as shown in Figure 1.7. Both mechanisms use a single species to represent all ISOPOO isomers. This species reacts with the traditional bimolecular reaction partners of HO_2 (forming a lumped ISOPOOH species), NO and NO_3 (forming MACR, MVK and a lumped IHN) and other RO_2 (forming MACR and MVK and HCHO). Crucially for this thesis however, CS2 also includes additional isomerisation pathways of ISOPOO (Section 1.4.2.1). The 1,6 H-shift forms a single HPALD species, representing the different HPALD isomers which can be formed (Fig 1.6 shows one route), and a single DHP-RO_2 species. These react further to regenerate HO_x while the 1,5 H-shift forms OH, MACR and MVK. Chapter 2 and Appendix B provides a comprehensive description of the isoprene mechanism in CS2.

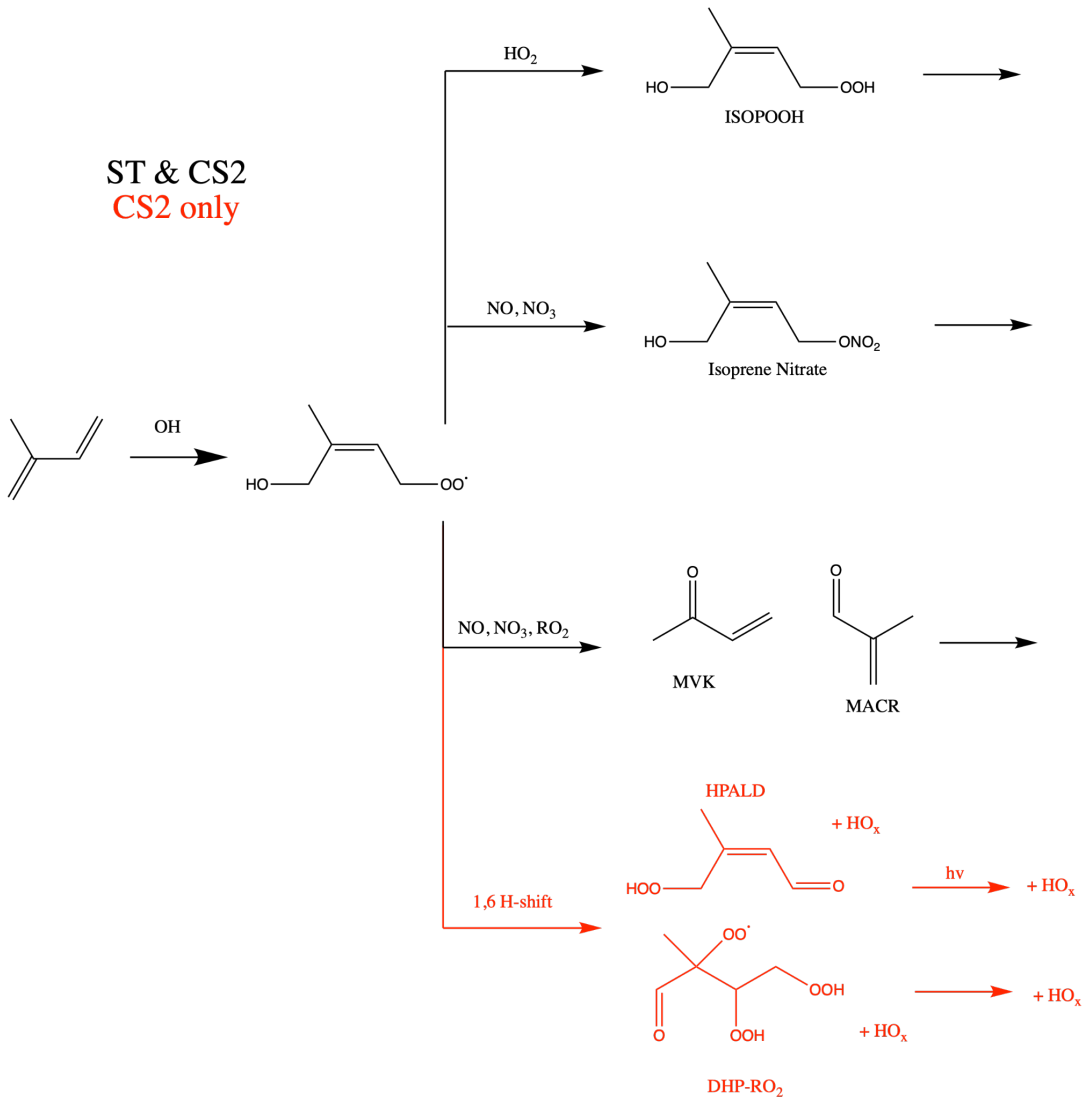


Figure 1.7. Mechanistic differences for OH + isoprene between ST and CS2. Only one isomer from OH + isoprene (Zδ1-OH, 4-OO) is considered and the 1,5 H-shift is omitted. Reactions in both mechanisms are shown in black and reactions unique to CS2 are in red.

The updates to chemistry in CS2 do not result in a perfect mechanism: there remains uncertainty in several key processes including the photolysis frequency of HPALDs (e.g., Schwantes et al., 2020) and the description of organonitrates, important for O_3 production (Wennberg et al., 2018). The reduced nature of CS2 also necessitates omission of minor reaction pathways and lumping of chemical species. Nevertheless, the addition of the isomerisation reactions and other developments in CS2 represent a major improvement over standard mechanisms such as ST and allows the isoprene chemistry within CS2 to be considered state-of-the-art at present.

1.4.2.3 Impact of HO_x-recycling

Limited assessment has been performed using climate models into the knock-on impacts of enhanced isoprene HO_x-recycling for wider atmospheric composition and climate, particularly via the oxidation of CH_4 and the

formation of SOA-precursors. Archibald et al (2011) simulated the isomerisation chemistry and subsequent HPALD photolysis by producing OH directly at a fixed yield from an ISOPOO unimolecular reaction to represent HO_x regeneration. This approach increased PD tropospheric burdens of O_3 and OH by 8% and 17% respectively with the greater OH reducing CH_4 lifetime by 14%.

More comprehensive mechanisms developed over the last few years which capture the influence of bimolecular reactions partners and temperature have also started to investigate the impact of this chemistry. Using the CalTech reduced isoprene scheme (Bates et al., 2019) in GEOS-CHEM, Møller et al (2019) found that ~30% of all ISOPOO undergo at least one H-shift and the inclusion of H-shift reactions increased boundary layer OH by up to a factor of three in the Amazonian planetary boundary layer (PBL). In the STOCHEM model using CRI v2.2, Jenkin et al (2019) simulated increases of terrestrial tropical OH exceeding 30% while Khan et al (2020) showed the addition of ISOPOO H-shift reactions decreased the global isoprene burden by 17% and CH_4 lifetime by 0.5 years.

Thus, the choice of chemical mechanism for isoprene has important consequences for wider atmospheric composition and climate. However, a comprehensive comparison of two fully interactive mechanisms in a coupled chemistry-climate model, including a rigorous assessment against observational data, has yet to be performed. In Chapter 2 I present the incorporation and evaluation of the CS2 mechanism into UKCA and compare it to the ST mechanism and its predecessor, CRI-Strat (CS) (Archer-Nicholls et al., 2021).

1.4.3 Isoprene SOA

Isoprene can also influence climate by contributing to SOA. For example, isoprene is responsible for ~20% of all organic aerosol in the Amazon (Schulz et al., 2018). While the influence of isoprene's chemical description is the major focus of this research, the link between chemistry and SOA means the key aerosol processes, and the limitations of the current modelling approaches, must be considered.

Isoprene contributes to SOA via the formation of derivatives which can partition into the aerosol phase due to volatility (typically species with multiple hydroperoxide or nitrate groups) or by reactive uptake. The isoprene epoxy diol (IEPOX) is the major SOA contributor at low NO_x (Surratt et al., 2010; Claeys and Maenhaut., 2021) while species including HMML (hydroxymethylmethyl-α-lactone) and nitrated isoprene derivatives contribute at high NO_x (Sato., 2008; Claeys and Maenhaut., 2021). IEPOX partitions to the aerosol phase via reactive uptake (Gaston et al., 2014; Nguyen et al., 2014; Schwantes et al., 2019) with chemical markers (tetrols) found in droplets (e.g., Allan et al., 2014). Isoprene is also a major source of methylglyoxal and glyoxal (47% and 79% of global production respectively) which can contribute to aerosol by uptake (Fu et al., 2008).
As the glyoxal species are commonplace in most mechanisms and IEPOX and HMML are explicitly represented in more detailed chemical mechanisms like CS2, it would appear possible to simulate isoprene's contributions to SOA explicitly. However, the reactive uptake of IEPOX and HMML exhibits significant dependence on the aerosol pH, water content and sulphuric acid content (Claeys and Maenhaut., 2021). Diagnosing the aerosol pH

is currently beyond the capability of UKESM1 and so accurately modelling explicit formation of isoprene SOA is beyond the scope of this study.

Numerous experiments to determine isoprene SOA yield have demonstrated dependencies on NO_x, relative humidity, and aqueous phase pH among other factors with measured mass yields ranging from <0.5% to ~10% (Marais et al., 2016). A common approach in climate models is for isoprene oxidation to produce an inert tracer at a fixed yield, alongside other chemical species, which is then transferred to the aerosol phase (e.g. Sec_Org in UKESM1, Mulcahy et al., 2020). Molar yields are typically around 1-5%, values chosen to represent the most relevant atmospheric conditions, but this approach doesn't capture the full influence of NO_x, humidity and pH. The use of a volatility basis set (VBS), which lumps species into bins based on their volatility before partitioning to the aerosol phase (e.g. Donahue et al., 2011), represents a step up in complexity but still does not capture the full influence of external factors. Important areas for further work are discussed in Section 5.4.1.2.

1.4.4 α-pinene and β-pinene Chemistry

The oxidation of α-pinene and β-pinene also yields RO_2 and understanding of the subsequent chemistry has advanced considerably over the last decade. These developments have also centered on the prediction (eg., Kurtén et al., 2015) of intramolecular H-shifts, prompted by laboratory observations (Ehn et al., 2012; Ehn et al., 2014) of pinene derivatives with multiple oxygenated groups forming much more quickly than would have been possible via bimolecular reaction routes. The isomerisation reactions of these RO_2, termed autoxidation, compete with the standard bimolecular reactions with NO, NO_3, HO_2 and other RO_2 (Jenkin., 2004).

1.4.4.1 Autoxidation

The ozonolysis of α-pinene yields a Criegee intermediate which can decompose to form four possible RO_2 (Fig A4) (Kurtén et al., 2015). These RO_2 can react with bimolecular reaction partners (HO_2, NO, NO_3 and RO_2) but also undergo an intramolecular H-shift involving the abstraction of hydrogen atoms from other parts of the molecule by the peroxy radical group (Fig 1.8). This H-shift typically yields a hydroperoxide group and an alkyl radical which rapidly forms another peroxy radical. The rate of this process depends on the molecular structure (Kurtén et al., 2015), functionalisation (Bianchi et al., 2019) and exhibits a strong positive temperature dependence (Quéléver et al., 2019). In conditions where the RO_2 bimolecular lifetime is long, autoxidation can rapidly add multiple hydroperoxide groups to the molecule, lowering its volatility (Kurtén et al., 2016).

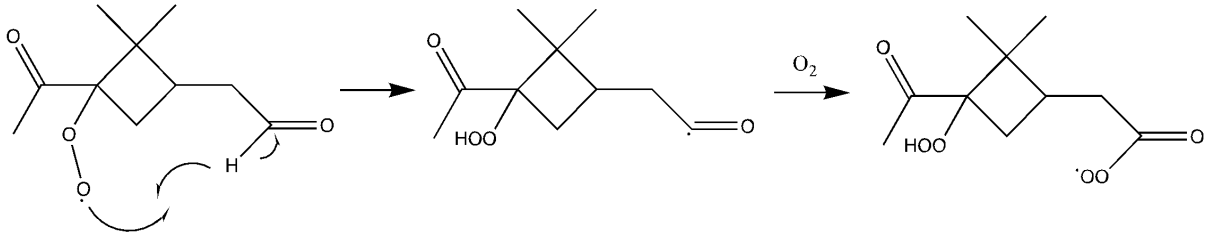


Figure 1.8. Autoxidation of one of the peroxy radicals formed from α-pinene ozonolysis. Adapted from Kirkby et al (2016).

Once enough oxygens have been added and the RO_2 forms a closed shell species via bimolecular reaction, the species may be termed a Highly Oxygenated Organic Molecule (HOM). Bianchi et al (2019) proposed the definition of a HOM to be a species formed in the gas phase via autoxidation containing at least six oxygens and, while arbitrary, this definition captures the main features of pinene-derived RO_2 reactivity and is used here. The reaction of α-pinene with OH also yields peroxy radicals (Fig A5), one of which can undergo autoxidation (Xu et al., 2018) (Fig A6).

Experimental HOMs yields from α-pinene + O_3 have been in the range 1.2-7 % (Jokinen et al., 2015, Kirkby et al., 2016). HOMs derived from the α-pinene + OH pathway have also been observed (Jokinen et al., 2015, Berndt et al., 2018a) albeit at lower yields of 0.44-1.2% (Ehn et al., 2012, Jokinen et al., 2015) and their formation mechanism has received less attention. β-pinene exhibits lower measured HOM yields (0.12% from O_3, 0.58 % from OH). Most attention has therefore been paid to α-pinene as well as other endocyclic species such as limonene which has an even higher HOM yield (5-17%, Ehn et al., 2012; Jokinen et al., 2015) but whose emissions are lower (Sindelarova et al., 2014).

1.4.4.2 Dimerisation

The other major development in this area has involved the formation of accretion products, also called dimers. These are formed from the reaction of two large RO_2 species via the creation of a peroxide linkage (ROOR) connecting the two RO_2 backbones (Fig 1.9). If formed from pinene-derived RO_2, the resultant dimers typically contain ~20 carbons and, along with the high numbers of oxygen atoms, this makes them even more involatile (Kurtén et al., 2016) than HOMs which have not undergone dimerisation (often termed HOM monomers). The understanding of dimer formation is relatively limited since such a pathway is non-existent for the RO_2 + RO_2 reactions of smaller species such as the methyl peroxy radical (CH_3O_2). Indeed, the rate constant for dimer formation has been measured to increase with RO_2 functionality (suggesting that the presence of heteroatoms may stabilise the transition state) and is also much larger (16-80x) for 10-carbon RO_2 than for 5-carbon RO_2 derived from isoprene (Berndt et al., 2018a, Berndt et al., 2018b). Accordingly 15-carbon dimers from the cross reaction of isoprene and pinene-derived RO_2 have been detected (Fig 1.9) but the formation rate constant is lower (Berndt et al., 2018b). The importance of dimerisation for aerosol is discussed in Section 1.4.5.1.

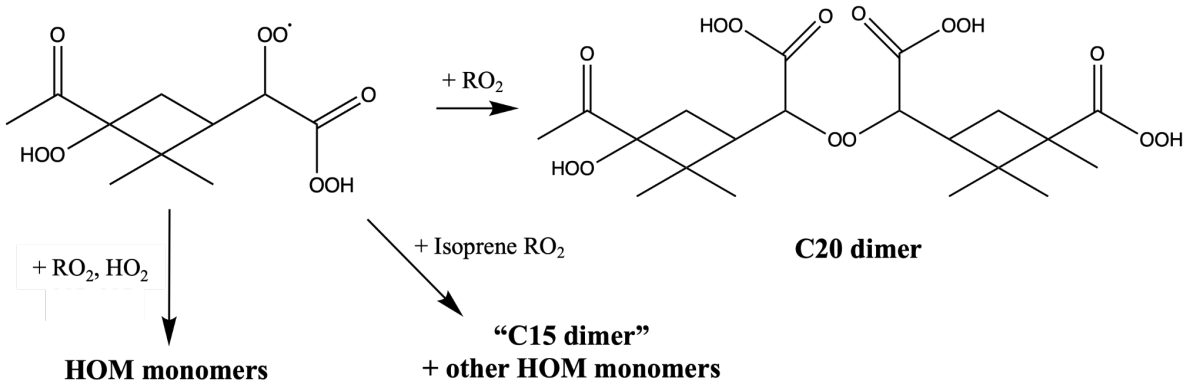


Figure 1.9. Formation of 20-carbon dimer and other pathways available to an oxidised RO_2 derived from α-pinene ozonolysis. Adapted from Kirkby et al (2016).

1.4.4.3 Modelling α-pinene and β-pinene Chemistry

As with isoprene, the full oxidation scheme of α-pinene and β-pinene is too complex for a climate model. In the MCM the fully explicit degradation of these species involves >1500 reactions and >500 species (Jenkin., 2004). To reduce computational cost and given monoterpene emissions are ~1/5 of isoprene emissions, some mechanisms such as ST only consider the contribution of these species to aerosol (Section 1.4.5) with no chemically-active species produced from oxidation. However, this does not conserve mass and means monoterpenes act as sinks of oxidants which, given their many C-C and C-H bonds and attendant ability to produce multiple molecules of O_3 in the presence of NO_x (Eq 1.29-1.31), is not accurate. The CRI mechanisms such as CS2 feature more comprehensive α-pinene and β-pinene chemistry with peroxy radicals produced from their oxidation, allowing the fundamental chemistry discussed in Section 1.2 to be simulated. Lumping of multiple products in a single species and omission of minor reaction pathways is again used but, crucially, autoxidation and dimerisation are not included due to their very recent discovery. The treatment of α-pinene chemistry, including the addition of these processes in the CRI-HOM mechanisms, is discussed in Chapter 4.

1.4.5 α-pinene and β-pinene SOA

Experimental SOA mass yields from pinenes have ranged from 6% to 50% (Ng et al., 2007). Common approaches in climate models follow that for isoprene (Section 1.4.3) with chemically-inert species formed at a fixed yield from monoterpene oxidation (e.g., 14.3% in UKESM1) which are transferred to the aerosol phase. Some schemes have introduced nucleation from monoterpene oxidation products with H_2SO_4 (Sporre et al., 2020 and Chapter 3) as well as using multiple tracers to distinguish between semi-volatile organic compounds (SVOCs) which just condense onto existing aerosol and extremely low volatile organic species (ELVOCs) which can also participate in nucleation (e.g. Sengupta et al., 2021). However, this approach also suffers from the same inability to capture the influence of other factors including temperature and NO_x (Ng et al., 2007) as well the more recently discovered interactions between isoprene and monoterpenes (McFiggans et al., 2019).

1.4.5.1 HOMs and SOA

The processes of autoxidation and dimerisation leads to HOMs which have lower volatility than the species formed from bimolecular reactions (typically the only products featured in the chemical mechanisms currently used in models). Most HOMs have sufficiently low volatility to partition to the aerosol phase but HOMs only comprise a small fraction of total SOA (HOM yield is lower than total SOA yield). However, unlike most of the monoterpene oxidation products which contribute to SOA, some HOMs, particularly dimers, have such low volatility that they can nucleate new particles; the key process by which HOMs can influence climate. Awareness of organic-mediated nucleation of new particles by clustering with sulphuric acid (e.g., Metzger et al., 2010) and with amines as well (Dunne et al., 2016) has existed for some time but, crucially, certain HOMs are sufficiently involatile to nucleate particles without these partners, termed Pure Biogenic Nucleation (PBN), often induced by cosmic ions which stabilise the clusters (Kirkby et al., 2016).

This has significant implications for new particle formation in low-sulphur atmospheres such as the PI where previous assumptions that H_2SO_4 was required for all new particle formation resulted in low aerosol number concentrations. Producing HOMs at fixed yields directly from monoterpene oxidation, Gordon et al (2016) showed the inclusion of PBN increased PI CCN concentrations by up to 100% in terrestrial tropical regions. Consequently, the negative forcing associated with the PI-to-PD increase in cloud albedo driven by increased anthropogenic emissions of aerosols and aerosol precursors was 27% smaller when PBN was included. Since the negative aerosol cloud forcing partially offsets the positive forcing from GHGs (Fig 1.1), this finding has important ramifications for the understanding of climate sensitivity as it would imply that the PI-to-PD warming may have been achieved with a larger net positive forcing. If this is the case, the climate sensitivity may be lower than previously estimated, which would imply less future warming due to increased GHG concentrations.

Gordon et al (2016) represents a useful first investigation into the impact of HOMs on climate but the fixed yield approach means many important chemical and physical feedbacks are not captured. These include the significant suppression of HOM formation by lower temperatures (Quéléver et al., 2019) and NO_x (Lehtipalo et al., 2019). Indeed, increasing NO_x will (up to a point) increase HOM production via increases to O_3 and OH (Section 1.2.1) in the Gordon et al (2016) approach. Isoprene does not form HOMs (Jokinen et al., 2015) but can disrupt HOM formation from larger BVOCs. Kiendlar-Scharr et al (2009) identified isoprene's ability to inhibit new particle formation by suppressing OH while Berndt et al (2018a) also showed the suppression of highly oxidised RO_2 derived from α-pinene + OH when isoprene concentrations were increased in a flow tube. McFiggans et al (2019) further demonstrated that in addition to suppressing OH, isoprene could also disrupt the formation of HOM dimers via $RO_2 + RO_2$ reactions by providing smaller RO_2 which could compete with this reaction. This was also observed in separate experiments by Heinritzi et al (2020) and has implications for new particle formation since the 20-carbon dimers are more efficient at nucleating new particles (Simon et al., 2020). The impact of isoprene on HOMs, via OH suppression and dimerisation disruption, illustrates the complex interactions between BVOCs and the influence that the chemical mechanism can have on aerosol.

Capturing these interactions is vital to producing an accurate description of HOMs and their influence on climate and requires HOM formation to be represented within a wider chemical mechanism that is also simple enough to be run in a climate model. However, the complexity of oxidation pathways and the large number of isomeric oxidation products makes this challenging. A near explicit MCM add-on for HOM formation just from α-pinene developed by Roldin et al (2019) included over 1700 reactions, making it ~3x larger than the entire CS2 mechanism and too complex for UKCA. The CRI-HOM mechanisms presented in Chapter 4 aims to capture the key processes of HOM formation while being concise enough for use in climate models. In this regard, CRI-HOM may be considered state-of-the-art for HOM chemistry at present.

1.4.6 Oxidants and the Location of SOA Production

The role of oxidants in producing low volatility organic products which contribute to existing aerosols and, in some cases, participate in new particle formation has been discussed in the context of isoprene and monoterpene oxidation. However, oxidants play a further role by determining where these SOA precursors form in the atmosphere in relation to their source regions and thus the impact the resulting SOA has on climate via the DRE and ACI.

Greater oxidant concentrations reduce the dispersion of BVOCs before they are oxidised to form SOA precursors. Sporre et al (2020) found that removing isoprene emissions in the EC-Earth model led to higher OH concentrations (no isoprene-OH sink) and much greater production of SOA (from monoterpene oxidation) closer to source and less SOA dispersion. By contrast, this was not simulated in NorESM and ECHAM because their use of prescribed oxidants meant the removal of isoprene had no impact on OH.

The location of precursor formation is also important because it affects how the SOA precursor perturbs the aerosol size and number distribution: the accumulation mode tends to dominate in the tropical PBL and the Aitken mode in the free troposphere. This is climatically relevant because if SOA precursors contribute to growth of Aitken mode particles such that the number of accumulation mode particles increases, as would occur in the free troposphere, the change to aerosol DRE is likely to be greater as the accumulation mode scatters solar radiation more strongly. By contrast, if the SOA precursors mostly contribute to growth of existing accumulation mode particles, as would occur in the PBL, the change in the DRE is likely to be smaller. Sporre et al (2020) also highlighted the importance of the change to the aerosol distribution: across the three models a doubling of SOA yield from BVOCs led to increases in the DRE's magnitude (negative forcing) but the smallest increase was found in the model which simulated the smallest increase in the accumulation mode number concentration (ECHAM). Increasing the number of accumulation mode particles can also increase CCN and cloud albedo, resulting in a stronger negative forcing from the AIE (Sporre et al., 2020). The background aerosol distribution and the description of aerosol size distribution can differ substantially between models and is a major driver of inter-model differences in the simulated climatic impact of BVOCs (Sporre et al., 2020).

SOA formed at higher altitude (i.e. after greater dispersion of precursors) also has a longer lifetime and a greater climatic impact. As in Sporre et al (2020), Karset et al (2018) demonstrated that a less oxidising atmosphere

resulted in greater dispersion of aerosol precursors and enhancements to aerosol number concentrations in the more remote troposphere where the lower background aerosol concentrations meant additional aerosol had a greater effect and led to a stronger negative AIE (Chen et al., 2016). Oxidant changes can also perturb the AIE via the SO_4 aerosol production pathways (Section 1.3.5).

1.5 Climatic impacts and feedbacks of BVOCs

Section 1.4 reviewed the recent developments to the understanding of isoprene and pinene oxidation chemistry, demonstrating how they may have important consequences for the climatic impact of BVOCs compared to past estimates via changes to oxidants and aerosol. In this section, I summarise recent work examining the climatic impact and feedback between BVOCs and climate.

A perturbation to E_{BVOC} will influence climate by changing CH_4 (commonly diagnosed by changes to lifetime, τ_{CH_4}), O_3, DRE and AIE. Figure 1.10 shows the radiative efficiency, ϕ_{BVOC} (forcing per unit change in E_{BVOC}), from a range of recent experiments. These find that an increase in E_{BVOC} typically results in a negative forcing from aerosol changes and positive forcing from changes to gas phase species. The considerable variation between studies reflects differences in experimental setup, period (PI vs PD) and, most importantly, model descriptions for aerosol, clouds and chemistry. Chapter 3 helps to constrain the influence of differences arising from the modelled chemistry.

Across NorESM, ECHAM and EC-Earth (Fig 1.10(a)), Sporre et al (2020) showed isoprene and, separately, monoterpene emissions led to negative forcings from the change in DRE (i.e., emissions provided a cooling) but a larger, more varied response in the AIE (emissions typically provided a cooling). This was attributed to differences in the models' aerosol and cloud parameterisations, background aerosol concentrations and the ability of oxidants to respond to emission changes, highlighting the major influence of these parameterisations. Forcings from DRE and AIE changes associated with E_{BVOC} increases were also negative in comparable studies from Sporre et al (2019) (Fig 1.10(b)), Scott et al (2018a) (Fig 1.10(d)) and most models in Thornhill et al (2021b) (Section 1.5.1, Fig 1.10(e)), albeit with considerable variation in magnitude.

The changes to O_3 and CH_4 have been simulated to offset the negative forcing from aerosol and clouds. Unger (2014a) (Fig 1.10(c)) found the presence of E_{BVOC} led to a net positive forcing in the PI (0.6 Wm^{-2}) and PD (0.4 Wm^{-2}), with the forcings from increases in O_3 and CH_4 and reduction in SO_4 aerosol outweighing the negative forcing from enhanced SOA.

Conversely, Scott et al (2018) found that reducing E_{BVOC} (-73%) in a PD global deforestation scenario led to a warming (the presence of E_{BVOC} cooled the atmosphere) with the positive forcing from reduced DRE and AIE outweighing the negative forcing from lower O_3 and CH_4; further highlighting the uncertainty as to whether E_{BVOC} warm or cool the Earth.

The influence of climate on BVOC emissions (Section 1.4.1) and the impact that BVOCs in turn can have on climate leads to a feedback loop where a given perturbation to climate perturbs BVOC emissions and the BVOC-driven change to atmospheric composition may augment (positive feedback) or oppose (negative feedback) the original climatic perturbation.

Kulmala et al (2004) proposed that increases in global temperature and CO_2 would likely result in increases of E_{BVOC} and organic aerosol, leading to cooling (i.e. a negative feedback). Spanning future scenarios with surface warmings of 1.8-4.8 K, Carslaw et al (2010) documented predicted increases in SOA aerosol burden of 25-150% between the PD and 2100 (with associated radiative forcing from the DRE of -0.04 to -0.24 Wm^{-2}), supporting the theory of a negative feedback from enhanced SOA. Applying conditions of $2xCO_2$ and 2080 sea-surface temperature (SSTs) and comparing simulations where E_{BVOC} were fixed or allowed to respond climate, Sporre et al (2019) found E_{BVOC} were 63% higher when they could respond compared to when the feedback was prevented. The attendant 53% higher increase in SOA burden led to a -0.49 Wm^{-2} negative forcing (predominantly from enhanced cloud forcing) compared to the no-feedback scenario, equivalent to ~13% of the positive forcing from the increased CO_2 (Fig 1.10(b)). However, the use of prescribed oxidants prevented chemical feedbacks from influencing aerosol production (a point addressed in Chapter 3) or the radiative impact of CH_4 and O_3 which have been shown by more comprehensive models to offset, to a greater or lesser extent, the cooling from aerosol (Unger., 2014a; Thornhill et al., 2021b).

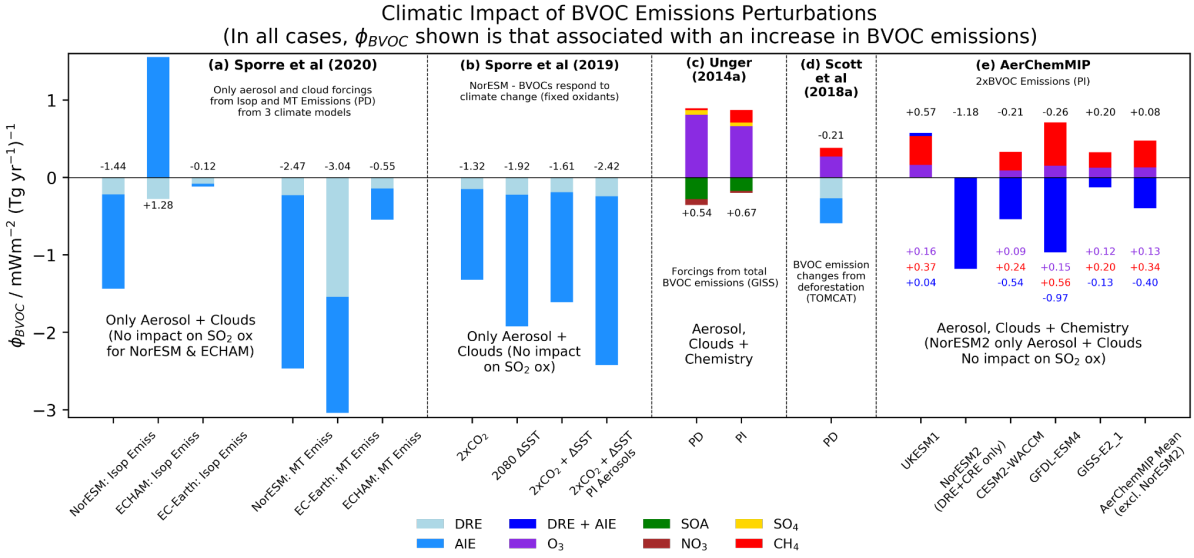


Figure 1.10. Components of BVOC radiative efficiency (ϕ_{BVOC}) in previous studies. Note that for comparison purposes, the sign of some values has been reversed so that all ϕ_{BVOC} correspond to an increase in emissions. For the AerChemMIP experiments only the total aerosol (DRE +AIE) radiative efficiency was available. The total aerosol radiative efficiency is shown alongside the individual DRE and AIE components for simulations in this chapter for ease of comparison. Black values correspond to the net ϕ_{BVOC} while coloured values in (e,f) relate to the O_3, CH_4 and total aerosol components.

1.5.1 Feedback Factor

The magnitude of climate feedbacks can be quantified by the feedback factor, α. The feedback factor for BVOCs, α_{BVOC}, is the forcing arising from a change in E_{BVOC} accompanying a change in surface temperature. A positive value of α_{BVOC} indicates BVOCs augment warming (positive feedback) while a negative value indicates they oppose the warming.

Considering just aerosol effects in a PD atmosphere, Scott et al (2018b) calculated a negative feedback (α_{BVOC}= -0.06 Wm^{-2} K^{-1}). However, as with Sporre et al (2019), the use of fixed oxidants prevented assessment of the impact of changes to GHGs O_3 and CH_4 and the influence of oxidants on aerosols.

A multi-model calculation of α_{BVOC} was performed as part of the Aerosol Chemistry Model Intercomparison Project (AerChemMIP) (Collins et al., 2017) and documented in Thornhill et al (2021b). The definition of the feedback factor used in Thornhill et al (2021b) and in Chapter 3 can be derived by extending Eq 1.2.

Consider an atmosphere which is perturbed by an increase in CO_2. This increases the net incoming radiative flux at the TOA, constituting a positive forcing, ΔF, and a temperature increase, ΔT. However, the increase in temperature leads to changes in a range of physical and chemical processes in the atmosphere, for example E_{BVOC}, which lead to changes in atmospheric composition (e.g., CH_4 concentration) and in turn changes the net incoming radiative flux. These changes modify the initial forcing ΔF to yield the actual forcing ΔN according to Eq 1.40 (Gregory et al., 2004).

$$\Delta N = \Delta F + \alpha \Delta T \quad (1.40)$$

The climate feedback parameter, α, represents the rate of change of the TOA radiative imbalance (ΔN) with respect to the global mean change in surface temperature and can be decomposed into individual feedback terms, α_i, arising from changes to different climate variables, C_i (Eq 1.41).

$$\alpha = \frac{d\Delta N}{d\Delta T} = \sum_i \frac{\partial \Delta N}{\partial \Delta C_i} \frac{\partial \Delta C_i}{\partial \Delta T} = \sum_i \alpha_i \quad (1.41)$$

In this study the climate variable of interest is E_{BVOC}, and the corresponding feedback factor, α_{BVOC} (Eq.1.42).

$$\alpha_{BVOC} = \frac{\partial \Delta N}{\partial \Delta E_{BVOC}} \frac{\partial \Delta E_{BVOC}}{\partial \Delta T} = \phi_{BVOC} \gamma_{BVOC} \quad (1.42)$$

Where the radiative efficiency of BVOC emissions, ϕ_{BVOC}, typically has units of Wm^{-2} $(Tg\ yr^{-1})^{-1}$ and γ_{BVOC} is the change in E_{BVOC} per unit change in surface temperature ($Tg\ yr^{-1}\ K^{-1}$).

ϕ_{BVOC} is calculated by dividing the radiative forcing by the change in E_{BVOC}. γ_{BVOC} is diagnosed from a simulation where CO_2 is instantaneously quadrupled (abrupt4xCO_2; Eyring et al., 2016) from which the change in E_{BVOC} per unit temperature change is then calculated.

In the AerChemMIP study, the climate models UKESM1, NorESM2 (non-interactive chemistry), GFDL-ESM4, CESM2-WACCM and GISS-E2-1 simulated 30-year PI timeslice runs with control and doubled (2xE_{BVOC}) emissions of isoprene and monoterpenes. The feedback factor for each model was calculated and decomposed into the contributions from changes to aerosol (in this case the sum of the DRE and AIE), O_3 and CH_4 lifetime (τ_{CH_4}) denoted here as α_{aer}, α_{O_3} and $\alpha_{\tau_{CH_4}}$ respectively.

Doubling E_{BVOC} increases O_3, leading to a positive O_3 forcing and thus positive α_{O_3} (mean 0.011 ± 0.004 Wm^{-2} K^{-1}). The universal increase in τ_{CH_4} with 2xE_{BVOC} across the models due to BVOCs depleting OH resulted in a positive $\alpha_{\tau_{CH_4}}$ of 0.031±0.018 Wm^{-2} K^{-1}, nearly three times larger than that from O_3.

UKESM1 yielded the lowest α_{O_3} and $\alpha_{\tau_{CH_4}}$(~1/2 and 1/3 of the model-multi mean (MMM) respectively). However, the radiative efficiencies (ϕ_{BVOC}) from O_3 and τ_{CH_4}in UKESM1 were consistent with the other models (Fig 1.10(e))): the difference in α_{O_3} and $\alpha_{\tau_{CH_4}}$ arose from UKESM1 predicting significantly smaller values of γ_{BVOC} (1/4 of the MMM), illustrating the impact of the uncertainty in γ_{BVOC} between models (Section 1.4.1).

By contrast, the forcing from aerosol changes (DRE and AIE) was negative for all models (-0.24 to -0.69 Wm^{-2}) except for UKESM1 (+0.03 Wm^{-2}). This significant variation (Fig 1.10(e)) is likely to come from both differences in model aerosol schemes but also the description of atmospheric chemistry via aerosol-chemistry coupling. Understanding the response in UKESM1, including why its forcing is much smaller than the other models, and the role chemistry plays in the variation of aerosol forcing is a key aim of Chapter 3

The net feedback factors, combining, O_3, CH_4 and aerosol, range from -0.038 Wm^{-2} K^{-1} (GFDL) to +0.022 Wm^{-2} K^{-1} (GISS) with UKESM1 on the higher end (+0.018 Wm^{-2} K^{-1}). This inter-model variation highlights the uncertainty as to whether BVOCs warm or cool the planet. Furthermore, the case of NorESM2, which had an (aerosol-only) feedback factor of -0.28 Wm^{-2} K^{-1} (>7x larger than the next strongest response), and easily the largest negative aerosol forcing (>2x MMM), also illustrates the importance of including the whole response, not just aerosols, since without a consideration of the chemistry, one could reach the conclusion that BVOCs are more efficient at cooling the planet than they likely are. This is discussed further in Section 3.5.1.

The AerChemMIP inter-model variation and variation between other studies illustrates the substantial uncertainty in how BVOCs influence climate. There is also a lack of detailed analysis into the mechanisms by which BVOCs influence climate, particularly involving changes to atmospheric chemistry. Chapter 3 builds on this by providing a detailed analysis of the atmospheric composition response to a 2xE_{BVOC} perturbation and uses two different chemical mechanisms to assess the sensitivity to the description of key chemical processes.

1.6 Thesis Structure

Chapter 2 presents the incorporation and evaluation of the CS2 mechanism in UKCA to assess the impact of the state-of-the-art isoprene chemistry (Section 1.4.2) on atmospheric composition. This evaluation includes comparison of model data generated using CS2, the previous CRI mechanism, CS, and UKCA's standard chemical mechanism, ST, against observational data for isoprene, monoterpenes, OH, O_3 and a range of other species. A global comparison between CS and CS2, along with sensitivity tests, isolates the impacts of the differences between the CS and CS2.

Chapter 3 progresses the assessment of the influence of chemistry with a detailed analysis of how BVOCs influence climate and the strength of the associated feedback. This is performed using control and 2xE_{BVOC} simulations with two different chemical mechanisms, ST and CS2, which differ significantly in the sophistication of the simulated BVOC chemistry and therefore respond differently to an E_{BVOC} perturbation.

Chapter 4 builds on recent developments in HOM chemistry and presents the CRI-HOM mechanism. CRI-HOM includes the updates to α-pinene chemistry described in Sections 1.4.4 and 1.4.5 and is state-of-the-art in this respect, while being sufficiently concise for use in a global climate model. This chapter includes the description of the fundamental chemistry used to build the mechanism, the optimisation of the key mechanistic parameters, the testing of influence of NO_x and temperature on HOM formation and a first assessment of the different impacts it would have on PI andPD atmospheres.

I summarise my findings and consider the most important areas for future research in Chapter 5.

2. The influence of different chemical mechanisms on atmospheric composition

As discussed in Section 1.4.2, the understanding of the chemical mechanism of isoprene oxidation has advanced considerably over the last decade. The theoretical prediction and subsequent observation of the isomerisation of certain isoprene peroxy radicals to yield products which regenerate HO_x, termed HO_x-recycling, and thus reduce the suppression of oxidants by isoprene has been a major development, particularly in the attempt to reconcile the low bias of OH seen in many models over isoprene-rich, NO_x-poor regions.

However, the assessment of the impact of this chemistry in global climate models such as UKCA has been relatively limited, principally because, until recently, there did not exist mechanisms which could both accurately describe this chemistry, which consists of hundreds of reactions, and were sufficiently concise to be suitable for GCMs. The CRI v2.2 tropospheric chemistry mechanism (Section 1.4.2) represents one of the first mechanisms which fulfils these criteria. The previous version of the CRI mechanism, CRI v2, whose tropospheric chemistry is based on the MCM v3.2 and does not include isoprene HO_x-recycling, was incorporated into UKCA as the CRI-Strat (CS) mechanism (Archer-Nicholls et al., 2021) as an alternative to the simpler Strat-Trop (ST) mechanism.

In this chapter I answer the question:

How does the transition from a standard chemical mechanism to a state-of-the-art chemical mechanism affect simulated atmospheric composition?

I first describe the incorporation of CRI v2.2 into UKCA to give the CRI-Strat 2 (CS2) mechanism which includes stratospheric and tropospheric chemistry. Then the performance of the CS, CS2 and ST mechanisms in UKCA is assessed via comparison to multiple observational datasets for BVOCs and other important species, including surface data from the Amazon and Borneo, flight campaign data from the Amazon, Borneo and the southeast USA and isoprene column satellite observations. Finally, a broader mechanism intercomparison is performed between CS and CS2, including sensitivity tests.

While featuring more comprehensive tropospheric chemistry than the ST mechanism, CS is considered the "standard" mechanism for the global mechanism comparison section as it does not contain the state-of-the-art improvements to isoprene chemistry, among other things, featured in CS2. The decision to compare CS to CS2 also complements the previous comparison of ST and CS (Archer-Nicholls et al., 2021) with the two studies providing a full documentation of the three mechanisms available for UKCA and UKESM1.

This chapter was published in Geoscientific Model Development.

Abstract

We present the first incorporation of the Common Representative Intermediates version 2.2 tropospheric chemistry mechanism, CRI v2.2, combined with stratospheric chemistry, into the global chemistry-climate United Kingdom Chemistry and Aerosols (UKCA) model to give the CRI-Strat 2 mechanism. A rigorous comparison of CRI-Strat 2 with the earlier version, CRI-Strat, is performed in UKCA in addition to an evaluation of three mechanisms, CRI-Strat 2, CRI-Strat and the standard UKCA chemical mechanism, StratTrop vn1.0, against a wide array of surface and airborne chemical data.

CRI-Strat 2 comprises a state-of-the-art isoprene scheme, optimised against the MCM v3.3.1, which includes isoprene peroxy radical isomerisation, HO_x-recycling through the addition of photolabile hydroperoxy aldehydes (HPALDs) and IEPOX formation. CRI-Strat 2 also features updates to several rate constants for the inorganic chemistry including the reactions of inorganic nitrogen and $O(^1D)$.

The update to the isoprene chemistry in CRI-Strat 2 increases OH over the lowest 500m in tropical forested regions by 30-50%, relative to CRI-Strat, leading to an improvement in model-observation comparisons for surface OH and isoprene relative to CRI-Strat and StratTrop. Enhanced oxidants also cause a 25% reduction in isoprene burden and an increase in oxidation fluxes of isoprene and other biogenic volatile organic compounds (BVOCs) at low altitudes with likely impacts on subsequent aerosol formation, atmospheric lifetime, and climate.

By contrast, updates to the rate constants of $O(^1D)$ with its main reactants relative to CRI-Strat reduces OH in much of the free troposphere, producing a 2% increase in the methane lifetime, and increases the tropospheric ozone burden by 8%, primarily from reduced loss via $O(^1D) + H_2O$. The changes to inorganic nitrogen reaction rate constants increase the NO_x burden by 4% and shift the distribution of nitrated species closer to that simulated by StratTrop.

CRI-Strat 2 is suitable for multi-decadal model integrations and the improved representation of isoprene chemistry provides an opportunity to explore the consequences of HO_x-recycling in the United Kingdom Earth System Model (UKESM1). This new mechanism will enable a re-evaluation of the impact of BVOCs on the chemical composition of the atmosphere and probe further the feedback between the biosphere and the climate.

2.1 Introduction

Isoprene (2-methyl-1,3-butadiene) makes up 70 % of all non-methane BVOC emissions with annual average emissions of 594 ± 34 TgC yr^{-1} over the period 1980-2010 (Sindelarova et al., 2014). Isoprene's rapid chemical oxidation in the atmosphere by OH, O_3 and NO_3 directly affects the tropospheric oxidising capacity, ozone burden and the processing of other trace gases like methane (e.g. Archibald et al, 2011, Khan et al., 2020) while also serving as an important source of secondary organic aerosol (SOA) (e.g., Scott et al., 2014, Kelly et al., 2018, Claeys and Maenhaut., 2021). Thus, isoprene has substantial effects on the radiative balance of the atmosphere, both directly via production of SOA and ozone, and indirectly via its changes to the oxidising capacity of the

atmosphere influencing methane lifetime and production of other aerosol species such as from oxidation of monoterpenes and SO_2 (Unger., 2014, Makkonnen et al., 2012, Sporre et al., 2020) An accurate representation of isoprene chemistry in climate models is essential to understanding the feedbacks between the biosphere and the rest of the Earth system and thus capturing isoprene's climatic impact.

However, the treatment of isoprene in the chemistry schemes of many climate models is outdated or oversimplified (e.g. Squire et al., 2015). The last decade has seen significant advances in our understanding of the isoprene oxidation pathway, principally the concept of rapid, intramolecular hydrogen shifts (H-shifts), also termed isomerisation reactions, in the isoprene hydroxy peroxy radicals (frequently termed ISOPOO). Predictions from theoretical work (Peeters et al., 2009, Peeters et al., 2014) and observations (Crounse et al., 2011; Teng et al., 2017; Wennberg et al., 2018) have established this pathway to be competitive with the traditional bimolecular reactions of the peroxy radical with NO, NO_3, HO_2 and RO_2 in certain conditions such as low NO_x(=NO + NO_2) environments. These H-shifts reactions lead to the production of HO_x(=OH + HO_2) either directly or indirectly following the degradation of the isomerisation products (e.g., Archibald et al., 2011, Jenkin et al., 2015, Wennberg et al., 2018).

This process, termed HO_x-recycling, has been shown to be important for low-NO_x, high-isoprene regions of the atmosphere (Butler et al., 2008, Lelieveld et al., 2008). By adding a simple, fixed yield OH production pathway from ISOPOO to represent OH production from hydroperoxy aldehydes (HPALDs), Archibald et al (2011) simulated an 8-18% increase in tropospheric O_3 burden while the tropospheric OH burden increased by 17% in the present day (PD) and by 50% in a pre-industrial (PI) atmosphere featuring 1860 emissions of key chemical species such as NO_x, CO and isoprene. Consequently, the lifetime of methane was predicted to decrease by between 11% (in a future climate scenario) and 35% (in the PI). This illustrated the significant impact that such a process could have on our understanding of the PI atmosphere (and the radiatively active components therein), and thus the PD-PI change and climate sensitivity. While the greatest change to the chemistry was simulated in the boundary layer (BL), convection of isoprene and its oxidation products into the free troposphere resulted in this added chemistry having global impacts.

The effect on oxidants from HO_x-recycling influences the lifetimes of isoprene and other BVOCs such as monoterpenes and thus the extent of their dispersion and the location of the subsequent SOA formation. Karset et al. (2018) found that when lower oxidant fields were applied to the PI atmosphere isoprene, monoterpenes, SO_2 and other key aerosol precursors were more dispersed from their sources, reaching higher altitudes and enhancing particle number concentration in the remote free troposphere. The radiative impact of the resulting aerosols was greater due to their enhanced lifetime (from slower deposition) and the highly non-linear relationship between aerosol number and cloud forcing where the addition of a given concentration of aerosol has a much greater impact in remote regions where the background concentration of aerosol is smaller (Chen et al., 2016). The importance of oxidants to BVOCs and aerosol was also shown in Sporre et al (2020) where models with an interactive oxidant scheme simulated a BVOC-driven depletion of oxidants and attendant greater dispersion of BVOCs and their oxidation products (including SOA precursors). In contrast, a prescribed oxidant approach saw BVOC oxidation confined far more to source regions, reducing dispersion.

Change to oxidant fields also perturb the oxidation pathways of SO_2. In the United Kingdom Chemistry and Aerosols (UKCA) model, SO_2 can be oxidised in the gas phase by OH to yield H_2SO_4 or in the aqueous phase by O_3 or H_2O_2 (Mulcahy et al., 2020). This has consequences for the aerosol mass and number distributions because only H_2SO_4 can nucleate new particles in UKCA, therefore amplifying the gas phase pathway over the aqueous pathways leads to a greater number of smaller aerosols. Thus, uneven changes to these pathways can alter the size and number distribution of the aerosol population, affecting the radiative properties of aerosols and clouds. Decreases in OH in other UKCA studies (Weber et al., 2020a, O'Connor et al., 2021) have resulted in simulated reductions in particle number concentration and cloud droplet number concentration. The resulting negative cloud radiative forcing is smaller in magnitude as the lower cloud droplet number concentration (CDNC) makes the clouds less "bright" (Twomey., 1974). The impact of different oxidant schemes on the burden and lifetime of DMS, an important SO_2 precursor, and the impact to sulphate aerosol transport is highlighted by Mulcahy et al. (2020).

While Archibald et al (2011) used a relatively simple approach to simulate HO_x-recycling, further advances in the chemical understanding have led to a near explicit representation of HO_x-recycling being incorporated into comprehensive mechanisms including the Master Chemical Mechanism (MCM v3.3.1) (Jenkin et al., 2015), the CalTech isoprene scheme (Wennberg et al., 2018). However, such mechanisms are far too large for use in global chemistry-climate models.

There exist a few reduced mechanisms featuring this state-of-the-art isoprene chemistry suitable for use in chemistry-climate models including the CalTech reduced isoprene scheme (Bates et al., 2019), the MAGRITTE v1.1 model (Müller et al., 2019), the Mainz Organic Mechanism (Sander et al., 2019), the updated ECHAM-MESSy (Novelli et al., 2020) and the Common Representative Intermediates mechanism v2.2 (CRI v2.2) (Jenkin et al., 2019a), the focus of this work. The CRI v2.2 is an update to the Common Representative Intermediate v2.1 mechanism (Jenkin et al., 2008, Utembe et al., 2010, Watson et al., 2008) and was developed from the fully explicit Master Chemical Mechanism (MCM) version 3.3.1 (Jenkin et al., 2015) which describes the degradation of organic compounds in the troposphere. In the CRI framework, species are lumped together into surrogate molecules whose reactivity is optimised against the fully explicit MCM. A description of CRI v2.2 is given in Jenkin et al. (2019a). The CRI v2.1, along with the corresponding stratospheric chemistry, has already been incorporated into UKCA as CRI-Start (CS) (Archer-Nicholls et al., 2021) as an alternative to the simpler but more widely used STRAT-TROP (ST) chemistry scheme (Archibald et al., 2020a), the scheme used for UKESM's contributions to CMIP6 (e.g. Sellar et al., 2020, Thornhill et al., 2021b).

Using the reduced Caltech Isoprene Mechanism, which includes H-shifts of ISOPOO in GEOS-CHEM, Bates et al (2019) simulated significant increases in OH (>100%) and HO_2 (up to 50%) over the Amazon and other forested tropical regions as a result of the HO_x-recycling. After implementing updated rate constants for isoprene H-shifts in GEOS-CHEM Møller et al. (2019) also found that globally around 30% of all isoprene peroxy radicals undergo at least one H-shift reaction resulting in an OH yield of 47% per isoprene molecule and that adding all isoprene H-shift reactions increased boundary layer OH by up to a factor of three in the Amazon. Using CESM/CAM-

CHEM and the MOZART-TS2 mechanism, Schwantes et al (2020) showed reasonable agreement for some isoprene oxidation products over the Southeast USA.

Jenkin et al. (2019a), using CRI v2.2 in the STOCHEM Lagrangian chemistry-transport model, showed the significant influence of HO_x recycling in CRI v2.2 simulating a 6.4% increase in the tropospheric OH burden relative to the CRI v2.1 and increases of surface OH of 20-50% over much of the forested tropical regions. Khan et al. (2020), using the same setup, also simulated enhanced surface OH and attendant decreases in methane lifetime (0.5 years) and isoprene burden (17%).

However, while the reduced mechanisms featuring HO_x-recycling chemistry have been tested in chemistry-climate models, less work has been done in terms of multi-species comparison to observations and detailed analysis of the effect to global atmospheric composition. This study introduces the CS2, based on CRIv2.2 and expanded with stratospheric chemistry, as a mechanism in UKCA, evaluates its performance against observational data, and compares its output and key processes to the related CS mechanism and well-established ST mechanism. By providing a wide-ranging comparison to observations and a detailed description of the changes CS2 causes to global and regional atmospheric chemistry, this current work builds on the existing literature to develop further our understanding of the consequences of HO_x-recycling.

2.2. Development of CS2 - incorporation of CRI v2.2 into UKCA

It is important to note that the CRI v2.2 mechanism, like the CRI v2.1 mechanism, is strictly a tropospheric chemistry scheme. In developing the whole atmosphere mechanism CS, Archer-Nicholls et al (2021) merged the CRI v2.1 mechanism with the Stratospheric chemistry scheme (Morgenstern et al., 2009) in UKCA (Table 2.1) to allow this scheme to be used within UKESM1 (Sellar et al., 2019). The same approach was taken in this work with the Stratospheric scheme unchanged and tropospheric scheme switched from CRI v2.1 to CRI v2.2. Therefore, to differentiate the "CRI v2.2" mechanism used in UKCA in this work from the solely tropospheric CRI v2.2 mechanism described on the CRI v2.2 website (http://cri.york.ac.uk/), the UKCA mechanism will henceforth be referred to as CRI-Strat 2 (CS2) (Table 2.1). A full description of the changes made to CS to update it to CS2 is given in the Appendix B1.1 while a summary of the changes is now discussed.

CS2 features a significant update to isoprene oxidation chemistry relative to CS with the incorporation of 1,6 and 1,4 H-shift reactions of isoprene peroxy radicals as well as an update to the organonitrate scheme (as detailed in Jenkin et al., 2019a). CS2 also features updates to multiple reaction rate constants (which were out of date in CS (Archer-Nicholls et al., 2021)) to the best of our understanding as documented in the IUPAC Task Group on Atmospheric Chemical Kinetic Data Evaluation (http://iupac.pole-ether.fr/). Changes were implemented to the rate constants of the reactions of $O(^1D)$ with H_2O, O_2 and N_2; rate constants of multiple inorganic nitrogen reactions such as those forming species with the peroxy acyl nitrate moiety, termed PAN-type, and $HONO_2$ and the HO_2+NO reaction and the rate constants of organic peroxy radicals (RO_2) with NO and NO_3. These updates ensure consistency between the CS2 mechanism incorporated in UKCA and that described on the CRI v2.2

website (http://cri.york.ac.uk/). The photolysis of glyoxal, formaldehyde and propionaldehyde was also updated (see Section B6).

CS2 has 9 more species than CS (Tables 2.1, 2.2) as well as 46 additional bimolecular reactions, 12 additional photolysis reactions and 8 additional uni/termolecular reactions (Table 2.1). This leads to a modest increase in runtime (6%) compared with CS whose runtime was already ~75% greater than ST. Incorporation of CS2 into UKCA involved extensive use of the UM-UKCA virtual machine environment (Abraham et al., 2018).

Table 2.1. Comparison of the CRI-STRAT and CRI-STRAT 2 chemical mechanisms

	CRI-STRAT (CS)	**CRI-STRAT 2 (CS2)**
Tropospheric Chemistry Scheme	CRI v2.1	CRI v2.2
Stratospheric Chemistry Scheme	Stratospheric chemistry	Stratospheric chemistry
No. of Species	219	228
No. of Bimolecular Reactions	536	582
No. of Termolecular Reactions	36	44
No. of Photolysis Reactions	128	140

The main update to the isoprene chemistry is the inclusion of 1,6 and 1,4 H-shift reactions of the isoprene peroxy radical (termed RU14O2 in CRI nomenclature). The 1,6 H-shift process is well studied (Peeters et al., 2009, Crounse et al., 2011, Teng et al., 2017, Wennberg et al., 2018) and follows the $k_{bulk1,6H}$ rate coefficient described in Jenkin et al. (2019a), capturing the dependence of isomerisation on both temperature and the rates of reaction of RU14O2 with the standard bimolecular partners (NO, NO_3, HO_2 and RO_2). This pathway yields hydroperoxy aldehydes (HPALDs, termed HPUCARB12 in CS2) and dihydroperoxy carbonyls peroxy radicals (DHPR12O2). The photolysis of the highly photolabile HPALD (HPUCARB12), and its product HUCARB9 (unsaturated hydroxy carbonyl), are key routes for HO_x regeneration.

The production of the isoprene epoxy diol (IEPOX) from the isoprene hydroperoxide (RU14OOH) and the hydroxymethyl-methyl-a-lactone (HMML) also represent important updates (Jenkin et al., 2019a). IEPOX and HMML are known SOA precursors (Nguyen et al., 2014; Nguyen et al 2017; Allan et al., 2014) and so their addition may enable a more explicit representation of SOA formation within the CRI framework, as opposed to the current framework whereby SOA formation is represented by the condensation on existing aerosol of a single inert tracer, Sec_Org, which is made from monoterpene oxidation (Mann et al., 2010; Mulcahy et al., 2020). This is beyond the scope of this paper but will be a focus of future work.

The introduction of HPUCARB12 and HUCARB9 necessitates a careful update to the FASTJX photolysis scheme used by UKCA (Telford et al., 2013). The cross-sectional dependence of wavelength for HPALDs is assumed to be the same as methacrolein (Peeters et al., 2009, Wennberg et al., 2018, Schwantes et al., 2020) but with a significantly larger quantum yield (QY). Prather (2015) recommends a QY of 0.003 for methacrolein and Liu et al (2017) a QY of 0.55 for HPALDs (both used by Wennberg et al., 2018). To implement the photolysis of these new species, the photolysis frequency of HPUCARB12 was taken to be the photolysis frequency for methacrolein scaled by the ratio of the QY of HPALDs to the QY of methacrolein, the same approach used by Schwantes et al (2020) for δ-HPALDs. A scaling of 0.5 was applied to the photolysis frequency of HUCARB9 in agreement with the MCM v3.3.1.

In addition to the updates to isoprene chemistry, CRIv2.2 has had the rate coefficients for many organic and inorganic reactions updated to bring the mechanism into agreement with the MCM v3.3.1 and IUPAC. These affect the overall chemistry in three major ways. The first involves the major reactions of the excited oxygen radical, $O(^1D)$. The rate constants of $O(^1D)$ with H_2O, O_2 and N_2 changed by -3%, -1% and +20% respectively to bring them into agreement with the current IUPAC values (http://iupac.pole-ether.fr). This also means the rate constant of $O(^1D)$ with N_2 became much closer (within ±1.5%) to that used in ST (Archibald et al., 2020a) and rate constants for the reactions with O_2 and H_2O also move closer to those used by ST. The result of this is a reduction in the fraction of $O(^1D)$ reacting with H_2O by 10-15%, thus lowering OH production while also reducing O_x loss via this pathway.

The second involves multiple inorganic reactions of nitrated species. The formation rate constants for PAN-type species (species with peroxyacyl nitrate functionality), $HONO_2$, HO_2NO_2 and N_2O_5 changed by around -45%, -15%, -45% and +50-75% in the troposphere respectively. The change for PAN brought its formation rate constant much closer to that used in ST (within ±7%) and this was also the case for $HONO_2$ and HO_2NO_2 formation. The rate constant of HO_2 + NO, the single biggest production source of O_x, decreased by 4%.

Finally, the rate constants for most RO_2 + NO and RO_2 + NO_3 reactions have been changed by +12.5% and -8%, respectively while maintaining the same temperature dependence. This is likely to have a smaller impact that the other chemistry changes but, at the margins, will make reactions with NO more competitive with the isomerisation reactions of the ISOPOO.

The implementation of CRI v2.2 by Khan et al (2020) in STOCHEM model, while including the updates to isoprene chemistry and the RO_2 + NO and RO_2 + NO_3 reactions, did not feature updates to the rate constants for $O(^1D)$ with H_2O, O_2 and N_2 or the inorganic nitrogen reactions. Therefore, even in low altitude terrestrial conditions where isoprene HO_x-recycling tends to dominate the change in OH, comparison between Khan et al (2020) and the results of this work must be caveated with the changes to the inorganic chemistry.

In addition to the chemistry changes, updates are made to the photolysis of several species. Two additional photolysis reactions of glyoxal (CARB3 in the CRI mechanisms) were added as well as updates to the photolysis parameters for HCHO and EtCHO (propionaldehyde). The wavelength bins of the product of cross-section and

quantum yield used by FAST-JX (Telford et al., 2013) used were updated to the v7.3 values from Prather (2015) for HCHO and EtCHO. The photolysis of CARB3, which had previously been estimated in CS by a scaling of HCHO photolysis (Archer-Nicholls et al., 2021), is replaced with the glyoxal photolysis for 999 hPa from v7.3 of Prather (2015). This reaction does exhibit a modest pressure dependence but one which has not been incorporated into FAST-JX at the current time.

In addition to the changes to the chemistry and photolysis, updates to the wet deposition scheme were implemented to both CS and CS2 schemes. The previous approach of applying parameters for standard surrogate for other species with the same functional groups (e.g. EtOOH was used for most hydroperoxides), as described in Archer-Nicholls et al (2021), was updated to use either data for the precise species (taken from Schwantes et al., 2020) or a more closely related-surrogate. The changes to the wet deposition parameters are detailed in Table B1 of Appendix B and, as they were applied to both CS and CS2 mechanisms, they are unlikely to have a significant influence on the inter-mechanism difference. No changes were made to the dry deposition scheme in this work.

Table 2.2. Species added and removed from the CS mechanism in the development of the CRI-Strat 2 mechanism.

Added Species	**Species Functionality**	**MCM v3.3.1 equivalent**
HPUCARB12	Hydroperoxy aldehyde (HPALD)	C5HPALD1, C5HPALD2
HUCARB9	Unsaturated hydroxy carbonyl	HMVK, HMAC
IEPOX	Isoprene epoxy diol	IEPOXA
HMML	Hydroxymethyl-methyl-a-lactone	HMML
DHPCARB9	Dihydroperoxy carbonyl	DHPMEK,
DHPR12OOH	Trihydroperoxy carbonyl	C536OOH
DHCARB9	Dihydroxy carbonyl	HO12CO3C4
RU12NO3	Hydroxy carbonyl nitrate	C57NO3
RU10NO3	Hydroxy carbonyl nitrate	MVKNO3, MACRNO3
DHPR12O2	Dihydroperoxy carbonyl peroxy radical	C536O2
MACO3	Unsaturated acyl peroxy radical	MACO3
RU10AO2	Hydroxy carbonyl peroxy radical	MACRO2
Removed Species		**MCM v3.2 equivalent**
RU12PAN	PAN-type species with at least one hydroxy group	C5PAN19
TNCARB11	Alkyl carbonyl	N/A
TNCARB12	Alkyl carbonyl	N/A

2.3. Model Runs

All model runs were performed using the United Kingdom Chemistry and Aerosols Model (UKCA) run at a horizontal resolution of 1.25° × 1.875° with 85 vertical levels up to 85 km (Walters et al., 2019) and the GLOMAP-mode aerosol scheme which simulates sulfate, sea salt, BC, organic matter, and dust but not currently nitrate aerosol (Mulcahy et al., 2020). In this setup, the inert chemical tracer Sec_Org, which condenses irreversibly onto existing aerosol, was produced at a 26% yield solely from reactions of α-pinene and β-pinene with O_3, OH and NO_3 with the enhanced yield applied to account for a lack of SOA formation from isoprene or anthropogenic species (Mulcahy et al., 2020).

The runs in this work fell into two distinct categories. Firstly, short runs (generally 1-2 months, Table 2.3) with higher frequency (hourly) output using the ST, CS and CS2 chemical mechanisms were performed to evaluate each mechanism's performance against the observational data. Secondly, longer runs (2-5 years, Table 2.4) with

monthly output using the CS and CS2 chemical mechanisms (or variants of CS2 for sensitivity tests) were conducted to facilitate a rigorous comparison of the global chemical composition (Table 2.4).

Temperature and horizontal wind fields were nudged (Telford et al., 2013) in all model runs to atmospheric reanalyses from ECMWF (Dee et al., 2011) to constrain the simulations to consistent meteorology, thus preventing diverging meteorology adding to the differences resulting from the chemical mechanisms and replicating as closely as possible the atmospheric conditions experienced when the observations were recorded. Nudging only occurred above ~1200 m in altitude and thus the majority of the planetary boundary layer was not nudged. The model runs were atmosphere-only with prescribed sea surface temperatures (SSTs). CO_2 is not emitted but set to a constant field while methane, CFCs and N_2O are prescribed with constant lower boundary conditions, all at 2014 levels (Archibald et al., 2020a).

The emissions used in this study are the same as those from Archer-Nicholls et al (2021) and are those developed for the Coupled-Model Intercomparison Project 6 (CMIP6) (Collins et al., 2017). Anthropogenic and biomass burning emissions data for CMIP6 are from the Community Emissions Data System (CEDS), as described by Hoesly et al. (2018). For the short runs, timeseries anthropogenic and biomass burning emissions were used for all ST runs and all CRI runs up to 2015. For the runs done for comparison to observational data recorded at the ZF2 site near Manaus in 2016 (see Tables 2.3, 2.5) , timeslice 2014 emissions were used due to a lack of post-2015 CRI emissions although the impact of the difference is expected to be minimal.

All longer runs used time slice 2014 emissions for anthropogenic and biomass burning emissions. Oceanic emissions were from the POET 1990 dataset (Olivier et al., 2003) and all biogenic emissions except isoprene and monoterpenes (see Section 3.3) were based on 2001-2010 climatologies from Model of Emissions of Gases and Aerosols from Nature under the Monitoring Atmospheric Composition and Climate project (MEGAN-MACC) (MEGAN) version 2.1 (Guenther et al., 2012) and are discussed further in Section 3.3. A full description of the emission sources for each emitted species is given in Table B2.

All mechanisms used the same raw emissions data. However, the additional emitted species required by CS and CS2 means the total mass of emitted organic compounds is greater in CS and CS2 and the lumping of species for emissions is also different. The approach and consequences are discussed in Archer-Nicholls et al (2021).

2.3.1 Short runs for model-observation comparisons

The runs performed for comparison to observations are detailed in Table 2.3 and correspond to an observational dataset described in Section 2.4 and Table 2.5. All runs were spun-up for a minimum of three months. For most of the runs, hourly model output was used so as to allow for detailed comparison with observations. The only exception were the runs performed for the comparison to the Isoprene Column data ("Isoprene Column" Table 2.3) where monthly means were used.

2.3.2 Longer runs for mechanistic intercomparison

The longer runs (Table 2.4) were designed with the primary aim of examining the consequences of the mechanism changes between CS and CS2 and followed an approach similar to that used by Archer-Nicholls et al (2021). These runs also served a secondary purpose as they enabled longer term comparison to observations for several species. We ran two 5 years nudged runs (1 year spin up, 4 years analysis) with the CS and CS2 mechanisms. In addition, five 2-year sensitivity runs (1 year spin up, 1 year analysis) were performed to analyse the impact of the individual changes to the isoprene scheme, the $O(^1D)$ reactions, inorganic nitrogen reactions, the RO_2+NO/NO_3 reactions and the photolysis reactions as discussed in Section 2.2. These sensitivity tests featured mechanisms based on the CS2 mechanism but each had a different feature which was reverted to that found in CS.

CS2_O1D used the old rate constants from CS for the reaction of $O(^1D)$ with N_2, O_2 and H_2O. CS2_inorgN used the rate constants from CS for the formation of $HONO_2$, HO_2NO_2, PANs, HONO and N_2O_5 as well as for the reactions of HO_2 + NO, OH+$MeONO_2$, OH+ PAN and OH+MPAN.

CS2_isoprene followed as closely as possible the isoprene reactions from CS with the major change being the omission of the isomerisation reactions of RU14O2 and subsequent production of HPALDs and other species which are key for HO_x recycling.

In CS2_RO2_N, the rate constants for the RO_2 + NO and RO_2 + NO_3 reactions were reverted to those used in CS which led to a 12.5% decrease and 8% increase, respectively for the vast majority of these reactions. Where branching ratios changed between CS and CS2, the CS2 branching ratios were maintained and the rate constants scaled accordingly.

Finally, CS2_photo used the parameters and reactions from CS for the photolysis of CARB3 (glyoxal), HCHO and EtCHO and was performed to evaluate the impact of update to photolysis (see Appendix B6).

Each sensitivity test, when compared to the CS2 run, provides information as to the impact of the change of the respective section of the mechanism (when taken in isolation); for example, the impact of the changes to the rate coefficients of $O(^1D)$'s reactions is examined by comparing the CS2 and CS2_O1D runs.

A full description of the changes to reactions and rate constants for each sensitivity test is given in Appendix B Section 2. The changes to the photolysis were found to have a minimal effect on atmospheric composition compared with the other sensitivity tests and is described entirely in Appendix B. The analysis of the longer runs is discussed in Section 2.5.

Table 2.3. Location, reference, time period and species measured in observational data sets and corresponding modelling approach. For the ZF2 Brazil, ATTO, Borneo, GABRIEL, FAAM and SE4C^{4}RS datasets, model data was filtered to select only the same days as observational data.

Dataset (Location / Coordinates)	Reference	Dates of Measurement	Measurement Details	Species Considered	Corresponding model run (Table 2.3 unless stated)
ZF2 Brazil Field Campaign, Amazon (-2.60°, -60.21°, 60 km NNW of Manaus)	Appendix B4	June-July 2016	1-minute intervals 30 m above ground (above tree canopy)	O_3, CO, SO_2, NO_2, isoprene, monoterpenes, benzene	ZF2 Brazil
Instant ATTO Tower, Amazon (-2.14° , -59.00°, 150 km NE of Manaus)	Yannez-Serrano et al (2015)	February 2013, September 2013 and February 2014	16-minute intervals at multiple heights (0.05 m, 0.5 m, 4 m, 12 m, 25 m, 38m, 53m and 79 m)	Isoprene, monoterpenes, MVK, MACR, ISOPOOH, acetone	ATTO
GAW Station, Borneo (5.0°, 117.5°)	Hewitt et al (2010), Whalley et al (2011), Edwards et al (2013)	April-July 2008	10-minute intervals	OH, HO_2, O_3, isoprene, monoterpene, HCHO, CO, MeCHO, acetone MACR, MVK, PAN, NO_2	Borneo
GABRIEL Aircraft Campaign (Suriname, Guyana and French Guiana)	Butler et al (2008)	October 2005	Daytime aircraft sampling ~0.3-8 km at 30 second intervals	O_3, NO, HCHO, CO, acetone, isoprene, MACR, MVK	GABRIEL
FAAM Aircraft Campaign, Borneo	Hewitt et al (2010)	July 2008	Daytime aircraft sampling ~0.3-7 km at 5 min intervals	O_3, isoprene, CO	FAAM
SE4C^{4}RS Flight Campaign (Southeast United States)	Toon et al (2016)	August - September 2013	Daytime aircraft sampling up to 12 km at 1 min intervals	O_3, CO, Isoprene, ISOPOOH, HPALDs, IEPOX, isoprene nitrate	SEAC^{4}RS
Global Isoprene Columns	Wells et al (2020)	Jan, April, Jul & Oct 2013	Global monthly mean isoprene column values	Isoprene	Isoprene Column

Table 2.4. Shorter runs performed for mechanism-observation comparisons. Identical biogenic (2001-2010 MEGAN-MACC climatology, iBVOC for isoprene and MT) and ocean (1990 timeslice) for each run unless otherwise stated.

Run Name	Mechanisms Tested	Period(s)	Observational Reference
ATTO	ST, CS, CS2	Feb 2013, Sept 2013, Feb 2014	Yáñez-Serrano et al (2015)
ZF2 Brazil	ST, CS, CS2	June 2016	Appendix B4
Borneo	ST, CS, CS2	April-May, June-July 2008	Hewitt et al (2010), Whalley et al (2011), Edwards et al (2013)
GABRIEL	ST, CS, CS2	October 2005	Butler et al (2008)
FAAM	ST, CS, CS2	July 2008	Hewitt et al (2010)
Isoprene Column	ST, CS, CS2	Jan, April, Jul & Oct 2013	Wells et al (2020)
SEAC^{4}RS	CS2	August-September 2013	Toon et al (2016)

Table 2.5. Longer runs performed for CRI mechanism comparison. Identical emissions for each run (anthropogenic and biomass timeslice 2014, biogenic 2001-2010 MEGAN-MACC climatology, oceanic 1990 timeslice)

Name	Base Mechanism	Total Length (after spin up)	Alterations from base mechanism
CS	CRI-STRAT	5 years	None
CS2	CRI-STRAT 2	5 years	None
CS2_O1D	CS2	2 years	Rate constants for $O(^1D)$ with H_2O, O_2 and N_2 set to values in CS
CS2_inorgN	CS2	2 years	Rate constants for $HONO_2$, HO_2NO_2, N_2O_5, PAN formation, HO_2 + NO and $MeONO_2$ + OH set to values in CS
CS2_isoprene	CS2	2 years	Isoprene chemistry set to that in CS
CS2_RO2_N	CS2	2 years	Rate constants for RO_2 + NO and RO_2 + NO_3 reactions reverted to CS values
CS2_photo (Appendix B6)	CS2	2 years	Photolysis of CARB3, HCHO and EtCHO reverted to that from CS

2.3.3 Biogenic Emissions

This work used the interactive Biogenic Volatile Organic Compound (iBVOC) emissions system (Pacifico et al., 2012) for isoprene and monoterpenes, the standard approach for UKESM's contributions to CMIP6 (Sellar et al., 2019). Emissions of isoprene and monoterpenes are calculated interactively based on temperature, photosynthetically active radiation (PAR) and plant functional type for each grid cell. While a diel cycle for isoprene is standard in UKESM, iBVOC has the advantage of also simulating a diel cycle of emissions for monoterpenes, leading to improved model performance relative to observation (see Section 2.4). The dependence on temperature and PAR means that emissions of BVOCs differ slightly between runs and thus between mechanisms. However, nudging inhibits considerably divergence of surface temperature between comparative runs and so the differences between emissions were <5% and typically 1-2%, significantly smaller than the differences caused by the mechanisms. Monoterpenes emissions were speciated in a 2:1 α-pinene : β-pinene ratio as used in Archer-Nicholls et al (2021).

There are temporal and spatial disparities between using iBVOC emissions and offline emissions, such as the MEGAN-MACC dataset ((Sindelarova et al., (2014), as used by Archer-Nicholls et al., (2021)), which could affect conclusions about mechanism-observational biases. These differences are discussed in more detail in Appendix B3. In short, for the ZF2 Brazil, ATTO and Borneo sites for the periods considered, the isoprene and MT emissions were higher when using the iBVOC approach than for MEGAN-MACC (Figs. B1, B2).

2.4. Comparison with Observations

The shorter UKCA models runs listed in Table 2.3 were used to evaluate mechanism performance against 6 high frequency observational datasets (3 surface/near-surface and 3 aircraft campaigns) from the Amazon, Borneo and the South East USA, all important regions for BVOC production. In addition, satellite-derived isoprene columns (Wells et al., 2020) were compared to model output (Isoprene Column, Table 2.3). Monthly mean data from the longer CS and CS2 runs (Table 2.4) for O_3, CO and $HONO_2$ were also compared to a range of observational data. A summary of the observation datasets is given in Table 2.3 and locations of the surface and airborne campaigns shown in Fig B3.

Diel profiles for multiple species were calculated from the three surface/near-surface sites and the vertical profiles were calculated from the ATTO site.

The three flight campaigns considered were the October 2005 Amazon GABRIEL campaign (Butler et al., 2008), the July 2008 Borneo Facility for Airborne Atmospheric Measurements (FAAM) (Hewitt et al., 2010) and the Studies of Emissions and Atmospheric Composition, Clouds and Climate Coupling by Regional Surveys ($SEAC^4RS$) flight campaign over the South East USA in August - September 2013 (Toon et al., 2016). Hourly model output corresponding to the days and times of the flights was used for the mechanism-observation comparison for each campaign. Model and observational data were binned into 250m/500m altitude bins and median values for the variables of interest across the whole region for a given altitude bin were considered. For

the SEAC^{4}RS comparison, observational data were also filtered to exclude urban plumes (NO_2>4 ppb), fire plumes (acetonitrile>0.2 ppb) and stratospheric air (O_3/CO > 1.25) while missing data were not used and data flagged as a lower limit of detection were set to zero as done in Schwantes et al (2020). Estimated limits of detection are shown for relevant species for the GABRIEL and FAAM campaigns.

The performance of each mechanism is now described for the key species e.g. O_3, HO_x, isoprene, certain isoprene oxidation products and monoterpenes. A brief commentary about other species including $HONO_2$, CO, PAN, HCHO, MeCHO, EtCHO and acetone is given in Appendix B.

2.4.1 Ozone

CS2 exhibits a modest increase in O_3 (~1-2 ppb) over CS at all surface sites (Fig. 2.1), exacerbating the existing high surface bias of CS, whose drivers were discussed in Archer-Nicholls et al (2021), and the smaller high bias of ST. On a diel basis, the mechanisms are able to replicate the shape of the diel cycle at the ZF2 site (with similar diel profiles at the ATTO site) but perform less well in Borneo, simulating pronounced diel cycles with a high bias compared to much more muted cycles from observation.

An increase of ~1-4 ppb relative to CS is also exhibited by CS2 for monthly mean O_3 when both mechanisms are compared to observational data at 10 locations from pole to pole at 4 pressure levels (250, 500, 750 and 900 hPa) (Fig. B4). CS2 reduces the low bias in polar regions but increases CS's high bias in the tropics and Eastern US.

Model high biases are also observed from flight data comparisons (Figs. 2.2(b,f), B6(a)). In the Amazon, where the observed and modelled NO vertical profiles agree well (Fig. B6(e)), there is little difference between the three mechanisms. Each exhibits the greatest high bias at low and a smaller high bias in the free troposphere. CS2 exhibits a high bias of 15-20 ppb for the SEAC^{4}RS campaign (Fig. B6(d))), with perhaps some influence from the low altitude NO_2 model high bias. In Borneo, all mechanisms exhibit a roughly consistent high bias of ~20 ppb for ST increasing to 30 ppb for CS2. Interestingly, all the mechanisms simulate a significant low bias for NO_2 (Fig. B6(f)) which may indicate biomass burning events which are not simulated, something which might be expected to promote higher ozone concentrations.

2.4.2 HO_x

Modelled surface OH increases in all locations from ST through CS to CS2 with a significant increase in midday OH from CS to CS2 (Fig. 2.1). In Borneo, OH is consistently low biased in the three mechanisms but the best comparison is exhibited by CS2 where the mean diel bias compared to ST and CS decreases by 43-50% and 24-40%, respectively over the period considered. The drivers of the HO_x change are explored further in Section 2.5.

Surface HO_2 isalso simulated to increase in all locations from ST to CS to CS2. Significant high bias is simulated in Borneo (the only observational dataset) (Fig. B7) for the CRI mechanisms, including at night. The simulated ratio of HO_2 to OH is highly biased in all mechanisms. However, it is best simulated in CS2, indicating that the

increase in OH is much larger than that for HO_2. It should be noted that none of the mechanisms at present include the heterogenous reactions of HO_2 and their inclusion, which will be addressed in future work, should reduce the HO_2 high bias.

The comparison of modelled HO_x to observation is complicated by large discrepancies in key reaction partners. Relative to observed values of 100-130 ppb, CO in ST in Borneo is highly biased by 13 ppb and 27 ppb while CO in the CRI mechanisms exhibits larger biases of ~35-50 ppb and ~50-60 ppb during April-May and June-July, respectively (Fig. B7). These high biases would enhance modelled HO_2 at the expense of OH, potentially explaining the modelled low biases in OH. Indeed, the OH model low bias is greater in the June-July period. This highlights the complexity of model-observation comparisons: the CRI mechanisms may well simulate secondary CO production from isoprene more accurately than ST but other model biases, for example in emissions of CO, NO and isoprene, can lead to the CRI mechanisms appearing worse. Nevertheless, if the CO high bias is reduced in future, we might reasonably assume the modelled OH will improve still further.

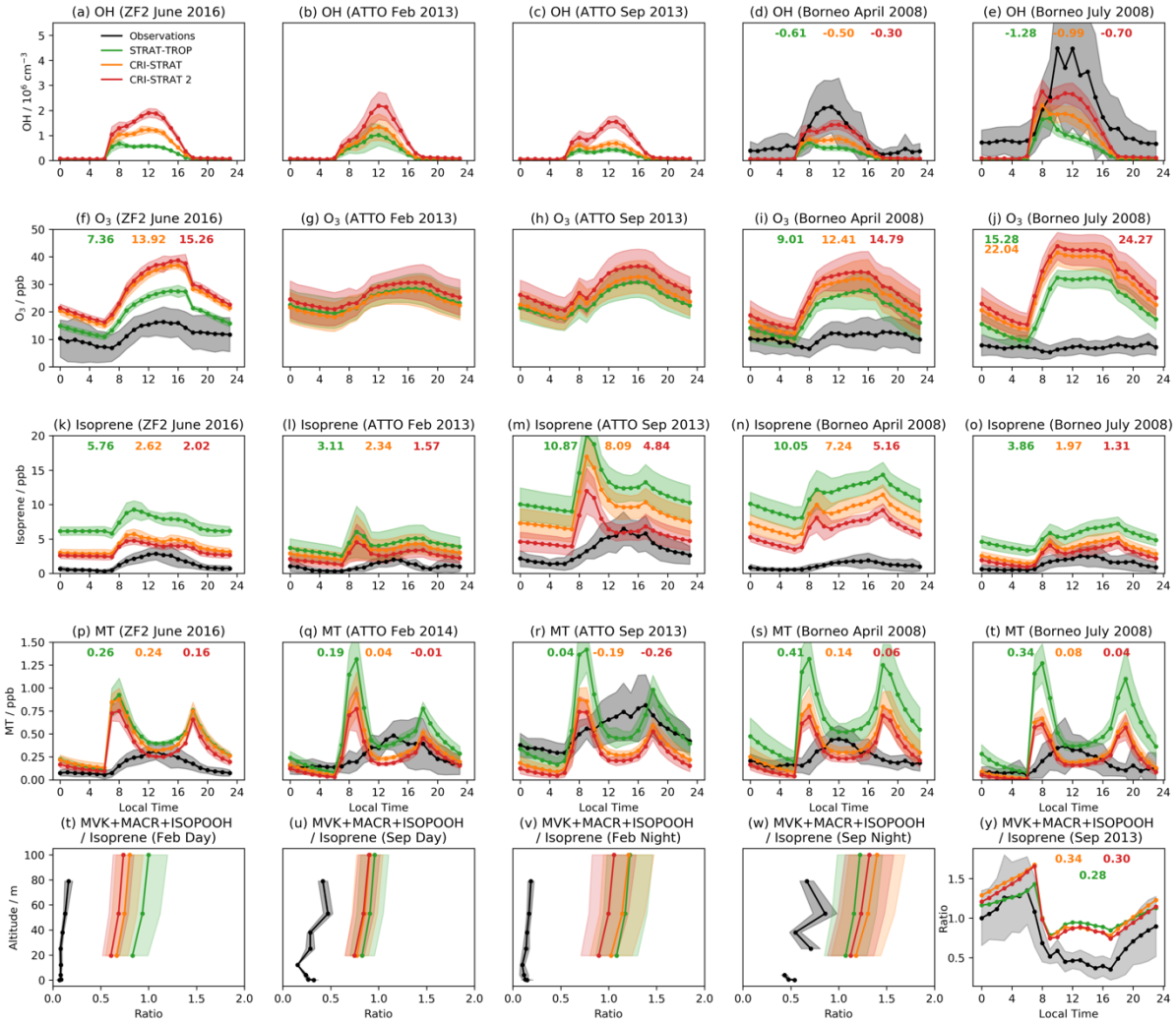


Figure 2.1. Mean diel cycles of observed and modelled OH (top row), O_3 (2nd row), Isoprene (3rd row) and MT (MT=α-pinene + β-pinene for the CRI mechanisms) (4th row) at the three surface/near surface sites considered. The bottom row shows the vertical profile of the ratio of the isoprene oxidation products MVK+MACR+ISOPOOH to isoprene for daytime (0900-1500 LT) and nighttime (2100-0300 LT) periods and the diel profile of the ratio at 53 m (all from ATTO tower). Shading indicates ±1 standard deviation from the mean and the numbers in bold show the mean diel model bias (model - observations) for species/locations where observations were recorded.

2.4.3 Isoprene

Modelled isoprene from all three mechanisms was compared to surface observations, flight campaign data and isoprene columns measured by satellite.

2.4.3.1 Isoprene Surface Measurements

CS2 yields the best model-observation comparison for surface isoprene on a daily basis in all locations (Fig. 2.2. (k-o)). CS2 reduces the high bias in the diel profiles by 50-60% relative to ST and 20-40% to CS at the ZF2, ATTO and Borneo sites, driven by the elevated OH concentrations

In most locations the model simulates, to a greater or less extent, a "twin peak" isoprene profile with a sharp rise around 7:00 LT and a second, smaller peak at 19:00 LT. This was most pronounced in the Amazon dry season (ATTO Sept 2013). The morning peak is likely to be due to a combination of the sharp rise in simulated isoprene emissions which starts at 6:00-7:00 am LT, outweighing the concurrent rise in OH, and an underestimation in the model of the rate of BL height growth which can trap isoprene close to the surface, causing a buildup. By contrast, observed isoprene concentrations exhibit a much slower morning growth reaching a peak in early afternoon. While the "out-of-phase" nature of the profiles is unlikely to be the sole driver of model-observation difference, it will play a role since isoprene chemistry occurs on the time scale of ~1-2 hours and atmospheric oxidising capacity varies throughout the day.

Over the lowest 80 m at the ATTO site, all mechanisms are high biased in the daytime (9:00-15:00) and nighttime (21:00-3:00) (Fig. B8 (a-d)) with CS2 exhibiting the smallest bias but produce similar isoprene vertical gradients to observations. The effect of boundary layer height was further considered by looking separately at the periods 6:00-8:00 LT and 17:00-19:00 LT (Fig. B8 (e-h)). In contrast to the daytime and nighttime periods, during the 6:00-8:00 period the simulated isoprene gradient is significantly more negative than the observation, indicating less vertical mixing and similar results are seen with the MT profile (Fig. B8 (m-p)). This is most noticeable in September where the largest morning peak is seen in the diel profile for both species and lends support to the theory that the simulated BL height is not increasing as quickly as in reality, leading to more isoprene and MT being trapped at low altitude. Smaller differences between observed and simulated isoprene and MT vertical gradients are seen during 17:00-19:00 LT, coinciding with smaller evening peaks in the diel profiles. This suggests the reduction in BL height is more accurately simulated than the morning increase.

The major drivers of the remaining model-observation difference are likely to be the concentrations of oxidants (despite the increases seen in CS2, OH remains low biased in Borneo) and the emissions of isoprene (including the modelled vs. actual diel cycle). The concentrations of isoprene and other species also vary significantly through and above the tree canopy, as shown by the ATTO measurements (Fig. B8), and the global model resolution is not high enough to resolve the vertical gradient of species in the canopy. When testing the CRI v2.2 in STOCHEM-CRI with isoprene emissions from the MEGAN-MACC inventory, Khan et al (2020) noted that halving the isoprene emissions reduced the model-observation disagreement significantly and attributed the model high bias in their work to high biases in the emissions of isoprene.

2.4.3.2 Isoprene Flight Measurements

Model-observation comparisons of isoprene vertical-profiles extending into the boundary layer and into the free troposphere reveal quite a different story from the surface analysis (Fig 2.2 (a, e, h)).

Despite being high biased at the surface and at low altitude, simulated isoprene vertical profiles over the Amazon and Borneo rapidly show a low bias as altitude increases. There are likely two reasons for this. The first is the vertical mixing, already discussed in relation to the isoprene and MT surface diel cycles. Secondly, for the Amazon and Borneo campaigns only estimated detection limits (0.1 ppb in both cases) could be used. This has the effect of biasing the median of the observational data to higher values as very low values are ignored. In the SEAC^{4}RS campaign, all data points flagged as below the detection limit were set to zero, mitigating this issue. The enhanced oxidative capacity of CS2 at low altitude results in the lowest simulated vertical concentrations among the three mechanisms but the general low bias above the surface is an issue faced by all mechanisms, suggesting it is not just down to modelling of the chemistry.

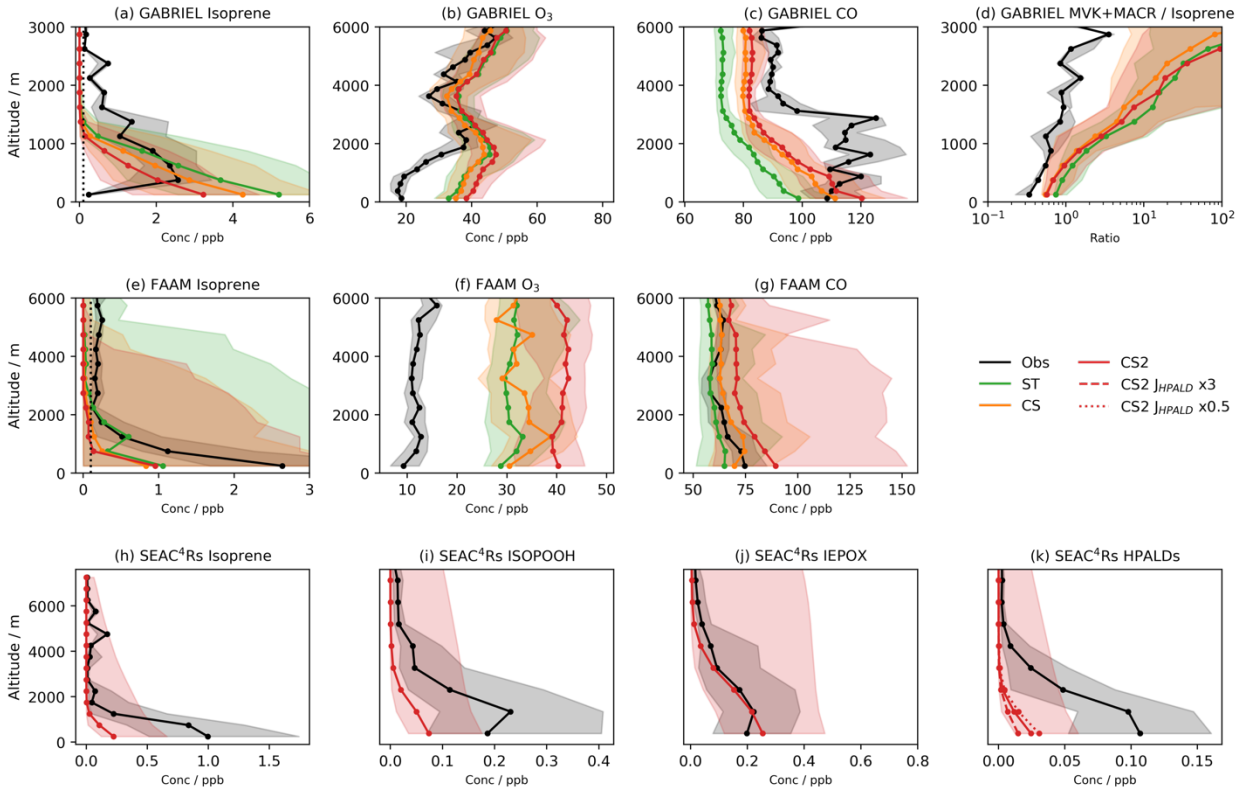


Figure 2.2. Median observed and model concentrations for the GABRIEL campaign in the Amazon for (a) Isoprene, (b) O_3, (c) CO and (d) the ratio of the isoprene oxidation products MVK+MACR to isoprene. Median observed and model concentrations for the FAAM campaign over Borneo for (e) isoprene, (f) O_3 and (g) CO. Median observed and model concentrations for the SEAC^{4}RS campaign over the South East USA for (h) isoprene, (i) isoprene hydroperoxide (ISOPOOH), (j) the isoprene epoxy diol (IEPOX) and (k) hydroperoxy aldehydes (HPALDs). SEAC^{4}RS observational data is also filtered to exclude urban plumes (NO_2>4 ppb), fire plumes (acetonitrile>0.2 ppb) and stratospheric air (O_3/CO > 1.25) as done in Schwantes et al (2020). Shading shows IQR, black dotted lines (a, e) show estimated limits of detection for isoprene and J_{HPALD}x3 and J_{HPALD}x0.5 lines in (k) show results of the scaling the HPALD photolysis frequency by 3 and 0.5, respectively. Note the logarithmic horizontal scale for (d).

2.4.3.3 Isoprene Columns

To consider isoprene on a global scale, monthly modelled isoprene columns for all mechanisms are compared to satellite observations from January, April, July and October 2013 (Wells et al., 2020) (Fig. 2.3).

Significant variation in model bias is exhibited between the mechanisms with ST exhibiting the highest isoprene columns and CS2 the lowest. In South America CS2 exhibits the smallest bias while the ST columns are over double the observed values for April and July. CS and CS2 exhibit the smallest biases in Africa and Southeast Asia respectively. The low biases in North America (~ 0.7-1.5×10^{15} molecules cm^{-2}), Europe (~ 0.5-2.7 ×10^{15}

molecules cm^{-2}) and Central Asia (~ 0.1-1.1 $\times 10^{15}$ molecules cm^{-2}) are quite consistent across the mechanisms and, in some cases almost equal in magnitude to the observed columns, which suggests the bias is driven more by insufficient emissions rather than the chemistry scheme in these locations.

CS and CS2 yield lower isoprene columns and generally smaller model biases than ST. This comparison highlights the significant influence of the different chemistry schemes on the simulated isoprene column and thus the considerable challenges of determining isoprene emissions via top-down approaches using back-calculation from observed concentrations or column values: different chemistry schemes will lead to different emission estimates.

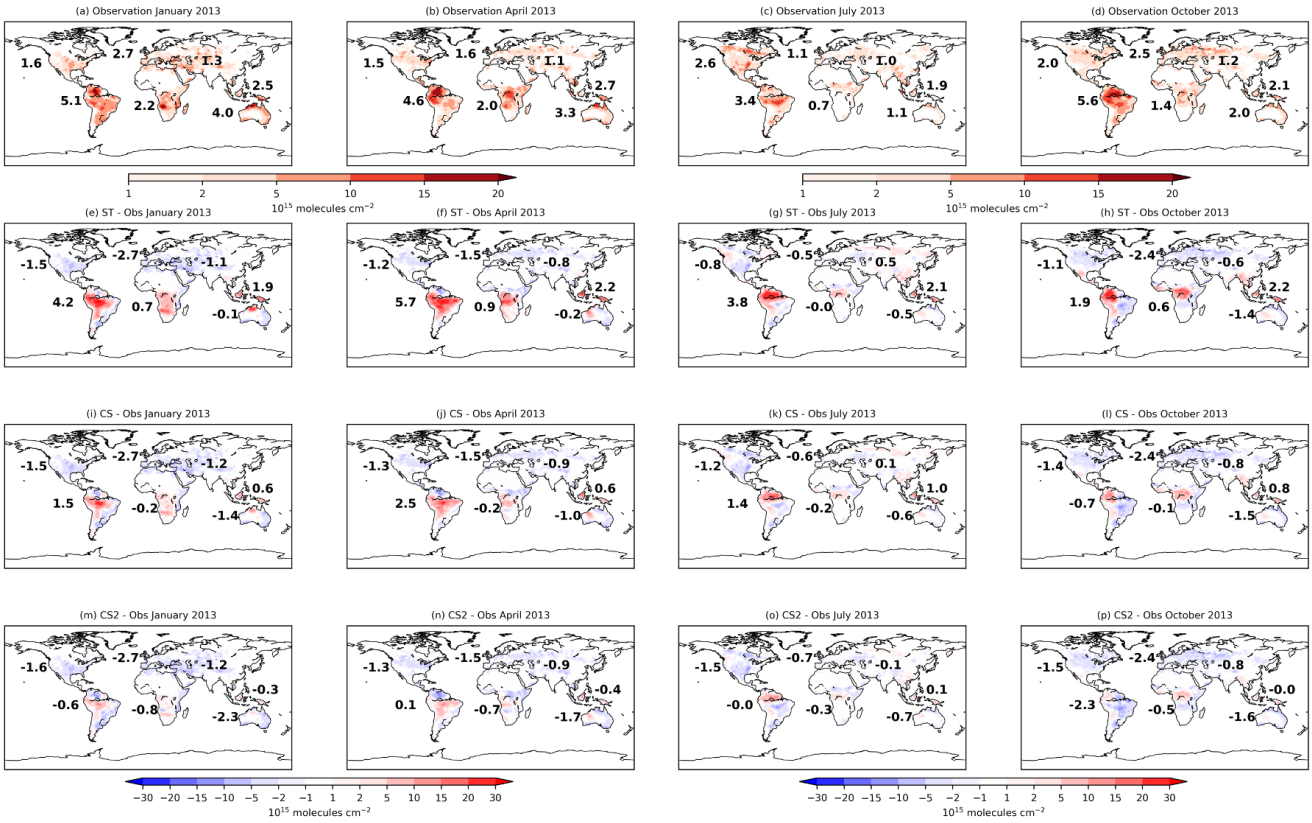


Figure 2.3. Monthly mean isoprene column values from the Global Isoprene Column observational dataset (Wells et al., 2020) for (a) January, (b) April, (c) July and (d) October 2013. Model bias (model-observation) using (d-h) ST (i-l) CS, and (m-p) CS2. Numbers in (a-d) show area-weighted mean model column values and in (e-p) model bias for individual terrestrial regions (number in North Atlantic refers to Europe and South Atlantic to Africa).

2.4.4 Isoprene Oxidation Products

During the GABRIEL flight campaign, the major isoprene oxidation products MACR and MVK were measured via PTRMS.At the ATTO tower, isoprene oxidation products were also measured via PTRMS but in this case were defined as the sum of MACR, MVK and ISOPOOH (Yáñez-Serrano et al., 2015) and, to avoid confusion,

we refer explicitly to the isoprene oxidation products as either MVK+MACR (for Gabriel) and as MVK+MACR+ISOPOOH (ATTO). In each case, the observational data are compared with model data.
At the ATTO site, all mechanisms are largely high biased for MVK+MACR+ISOPOOH but CS2 produces the best comparison to observations for both diel and vertical profiles (Figs. 2.1, B9, B11). CS2 also yields the smallest high bias for the ratio of MVK+MACR+ISOPOOH to isoprene (a metric less sensitive to discrepancies between actual and modelled isoprene emissions) in the Amazon (Figs. 2.1, B9, B11). Despite the greater oxidising capacity of the PBL in the CS2 simulations, the MVK+MACR+ISOPOOH concentrations are lower. This is attributed to the fact that in the relatively low NO_x environment around the ATTO tower, the isomerisation reactions of the isoprene peroxy radical are particularly important and favour the production of HPALDs and other species over MACR, MVK and ISOPOOH.

Relative to the GABRIEL flight data (Fig. 2.2(d)), the ratio of MVK+MACR to isoprene is high biased in all mechanisms albeit with the CRI mechanisms exhibiting a smaller bias than ST.

2.4.5 Isoprene Nitrate, IEPOX and HPALDs

The isoprene oxidation products HPALDs and IEPOX, unique to the CS2 mechanism in this study, are compared, along with isoprene, ISOPOOH and the isoprene nitrate (Fig. B6), to observational data from the SEAC^{4}RS campaign over the Southeast USA. Modelled isoprene (Fig 2.2(h)) exhibits a significant low bias, in line with the isoprene column analysis (Fig 2.3) and is attributed to insufficient emissions. Unsurprisingly, ISOPOOH (Fig 2.2(i)), the isoprene nitrate (Fig. B4(c))) and HPALDs (Fig. 2.2(j)) are also low biased. However, IEPOX (Fig 2.2(j)) compares favorably to observation.

The apparent good performance of IEPOX, despite the significant low biases of isoprene and its direct precursor ISOPOOH, is likely to be due to a missing sink to the aerosol phase. IEPOX is readily lost to aerosol by reactive uptake (Nguyen et al., 2014, Nguyen et al., 2017, Allan et al., 2014); a process featured in Schwantes et al (2020) (who simulated lower IEPOX concentrations) but not in UKCA. The rate constant for IEPOX's production from ISOPOOH is ~30% lower than that used by a mechanism of similar complexity, MOZART TS2 (Schwantes et al., 2020) while IEPOX's loss via OH has a similar rate constant to MOZART TS2. Including reactive uptake of IEPOX in future updates may reduce this high bias. The processing of IEPOX is unlikely to affect HO_x-recycling as much as HPALDs, however its importance to SOA formation means it will be a focus of future work.

The low bias of HPALDs, also simulated to a lesser extent in Schwantes et al (2020) who used isoprene emissions from the MEGAN v2.1, is important given its role in HO_x-recycling via photolysis. There remains uncertainty in HPALD photolysis frequency. In this work simulated HPALD destruction is dominated by reaction with OH and photolysis which are roughly equal ascending to 2.5 km whereupon OH's importance grows rapidly at the expense of photolysis. To test the impact of photolysis uncertainty on the bias, two further runs were performed with the photolysis frequency of HPALDs scaled by 0.5 and 3, respectively. These tests change HPALD concentrations in the lowest 2 km by +30% and -50% (Fig. 2.2(k)), respectively, suggesting concentration of HPALDs is dependent on the photolysis frequency of HPALDs, which is not currently well constrained.

Interestingly, these scaling tests only change low altitude OH by ~2-3% in the south east USA, suggesting the uncertainty in HPALD photolysis from the current approach may not have a huge impact on oxidants in this region although this may in part be due to the modelled isoprene and HPALD low biases (Fig. 2.2(h,k)). Furthermore, the fact that the modelled photolysis frequency of methacrolein here is low biased by a factor of 2.5-3 (not shown) suggests that, if further changes to the HPALD frequency are made in future, any potential reductions in methacrolein frequency should be scrutinised carefully. Nevertheless, constraining HPALD photolysis further will be a key focus of future work. A lack of OH measurements prevents attempts to constrain the OH loss pathway.

Evaluating HPALD production is also challenging since observations of ISOPO2 were not measured. Over the relevant temperatures, the rate constant for HPALD production in CS2 is 6-14 time greater than the equivalent used by Schwantes et al (2020) which would, if anything, make a low bias less likely. The sensitivity of HPALD production to the concentrations of the bimolecular reaction partners of ISOPO2 (e.g. NO) can also lead to resolution issues with the model: regions with high and low NO concentration treated as a single region within the model (model grids can be up to ~125 km wide at the equator) with moderate [NO], suppressing HPALD formation (see Schwantes et al., 2020). A commentary on the global distribution of HPALDs and IEPOX is given in Section 2.5.

2.4.6 Monoterpenes (MT)

Simulated surface diel monoterpene profiles (Fig. 2.1) are characterised by early morning and evening peaks which are not present in observations. As discussed in relation to the isoprene diel cycle, the morning peak is probably caused by a combination of the simulated emissions increasing too early and a delayed evolution of the simulated BL height, trapping large quantities of monoterpenes close to the surface (Fig. B8). The evening peak coincides with a reduction of simulated OH to near zero and therefore is probably driven by oxidant reduction as well as a reduction in the BL height. Around midday the mechanisms do a better job in most locations with the lower values in the CRI mechanisms driven by the greater oxidant concentrations. In 4 of the 5 locations, CS2 yields the smallest model bias although is it acknowledged that other issues, such as the BL dynamics, need attention.

2.5. Comparison of CRI-STRAT and CRI-STRAT 2

The performance of the CS mechanism to the simpler ST mechanism was discussed in detail in Archer-Nicholls et al (2021). Here we describe chemical composition of the atmosphere simulated by CS2 relative to that from CS using the longer model runs summarised in Table 2.5. Particular attention is paid to O_3 and its production and loss fluxes, HO_x, isoprene and monoterpenes, the isoprene oxidation productions IEPOX and HPALDs, nitrated species (NO_y) and the potential impacts on aerosols. Changes to CO and HCHO are discussed in Appendix B5.

2.5.1 O_x

As in Archer-Nicholls et al (2021), the change to O_3 was analysed by considering the sum of odd oxygen, NO_2 and its reservoir species, termed O_x, and defined in Eq 2.1.

$$O_x = O + O_3 + NO_2 + 3N_2O_5 + 2NO_3 + HONO_2 + HO_2NO_2 + PANs \quad (2.1)$$

Tropospheric O_3 burden increases by 8% from 328 Tg in CS to 354 Tg in CS2. Much of the free troposphere exhibits increases of 2-6 ppb (~6-14%) in O_3 with large parts of the tropical troposphere increasing by more than 4 ppb (Fig 2.1). This increase is driven chiefly by a 1.3% decrease in O_x chemical destruction, resulting in an 12% increase in net chemical O_x production. The sensitivity tests (Table B4) reveal the update to the isoprene mechanism only has a minor effect on O_3 burden (~2 Tg decrease) while the changes to $O(^1D)$ and inorganic nitrogen reactions each yield increases of 17 Tg (when considered in isolation) with greater impacts in the lower and upper troposphere, respectively (Fig B16). The changes to the O_3 burden in the sensitivity tests do not sum to the total 26 Tg increase from CS to CS2 which indicates a degree of interplay between the different updates, an unsurprising result given ozone's central role in tropospheric chemistry.

O_x lifetime, defined as the ratio of O_x burden (B_{Ox}) to the sum of chemical (L_{Ox}) and physical (D_{Ox}) O_x loss fluxes (Eq 2.2) (Young et al., 2018, Archibald et al., 2020b), increase by 8% to 18.8 days in CS2, while ozone production efficiency (OPE), defined as moles of O_x produced (P_{Ox}) per mole of NO_x emitted (E_{NO}) (Eq 2.3) (Archer-Nicholls et al., 2021) increases negligibly from 33.74 to 33.78.

$$\tau_{O_x} = \frac{B_{O_x}}{L_{O_x} + D_{O_x}} \quad (2.2)$$

$$OPE = \frac{P_{O_x}}{E_{NO}} \quad (2.3)$$

O_3 below 500 m increases across almost the entire globe with increases of 2-4 ppb (~5-7.5%) over much of Europe, Africa and the Americas and 4-5 ppb over India and China (Fig 2.4), exacerbating the existing high bias in CS (Archer-Nicholls et al., 2021). The sensitivity tests allow this change to be partially decomposed into the different drivers (Fig B13). The update to isoprene chemistry produces localised increases in O_3 over the tropical forested regions of South America, Africa and East Asia of 2-4 ppb: the increase in O_x production via HO_2 + NO and MeO_2 + NO outweigh the reduction in the non-methyl peroxy radicals (RO_2 + NO) pathway (discussed later). While comparison to Khan et al (2020) is difficult given the multiple mechanistic differences, O_x production from RO_2 + NO also decreased in their study. The changes to $O(^1D)$ also yield an increase in >1 ppb across the entire globe (due to reduced O_x loss via $O(^1D) + H_2O$) with a larger increase (2-3 ppb) encompassing ~20S-40N. The change to inorganic nitrogen also leads to terrestrial increases of 2-4 ppb from increased O_x production via HO_2 + NO and RO_2 + NO.

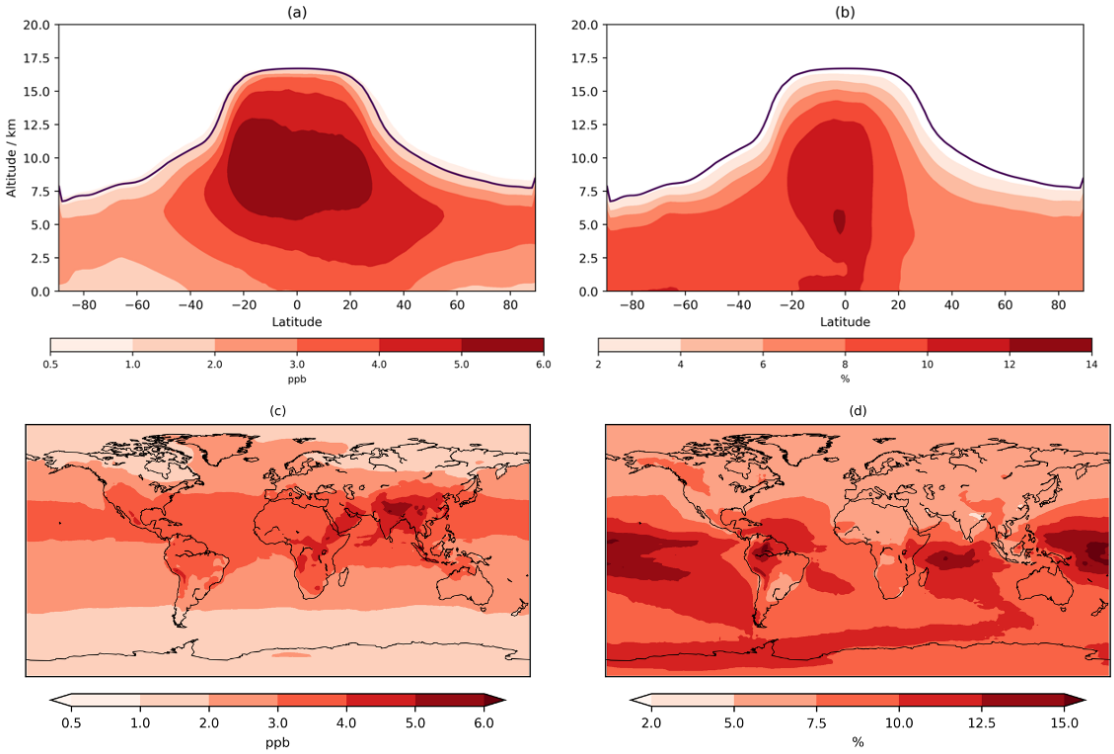


Figure 2.4. Annual mean tropospheric zonal (a, b) and lowest 500 m (c, d) change in O_3 mixing ratio (CS2 - CS). Purple line in zonal mean shows average height of tropopause.

2.5.1.1. O_x Budget

O_x production and loss fluxes for CS and CS2 are given in Table 2.6 and the breakdown for the sensitivity tests is given in Table B4. O_x production decreases in CS2 in much of the tropical and SH BL and lower free troposphere but increases in the NH midlatitude BL and tropical high troposphere while O_x loss decreases strongly in the tropical BL and lower free troposphere (Fig 2.5). Despite the modest changes to total O_x production and loss fluxes, the story is more complicated than it first appears due to offsetting changes to the key chemical production and loss fluxes.

2.5.1.2 O_x production

The HO_2 + NO pathway represents the largest absolute increase of O_x production (3.2%, Table 2.6) with particular increases in the NH tropics and mid latitude boundary layer and tropical upper troposphere (Fig B12). The drivers of this change are complex: the low altitude increases are driven by the significant increases in HO_2 (Fig 2.6), which exceed 5% in places, while at higher altitude the increase is attributed to a localised 15-20% rise in NO. The sensitivity tests suggest the change to the isoprene scheme (CS2_isoprene) is a key driver in the rise of low altitude HO_2 (and thus the flux) while the change to the inorganic nitrogen reactions (CS2_inorgN) also contribute to the increased flux at low altitudes and are chiefly responsible for the increase at higher altitudes.

However, the increase in HO_2 + NO is offset by a decrease in the NO + RO_2 flux (15.4%, Table 2.6) where RO_2 comprises all peroxy radicals except the methyl peroxy radical, MeO_2. This reduction is strongest in the tropical BL and low free troposphere and driven by a significant decrease in the RO_2 burden (32%). This burden reduction arises from the isomerisation pathways which inhibit the conversion of the isoprene-derived peroxy radical, RU14O2, to the other peroxy radicals RU12O2 and RU10O2 (via reactions with standard partners such as NO and NO_3) by providing competing routes which yield other species whose degradation pathways do not produce further RO_2 (Khan et al., 2020). For example, the HPALDs produced are photolysed to hydroxy acetone and unsaturated hydroxy carbonyls which further degrade producing mostly closed-shell products and HO_2. This rapid reaction pathway for RU14O2 sees its burden decrease by 35% in CS2 compared to CS and tropical low altitude mixing ratios decline by over 30%. Similar declines in the RO_2 + NO flux (15%) and RO_2 burden (33%) are seen for CS2 relative to the CS2_isoprene sensitivity test, providing strong evidence that the change to isoprene is driving the change in RO_2. Khan et al (2020) also simulated a reduction in RO_2 burden (and a corresponding drop in O_3 production via this pathway) although their decrease of 6.5% is less than half the equivalent value (including MeO_2) of 15% in this work, likely due to the other differences between the mechanisms used in their work and this study (see Section 2.1).

The fluxes of NO with HO_2, MeO_2 and RO_2 account for over 99.5% of total O_x production in both mechanisms and the changes in other pathways are an order of magnitude smaller in absolute terms. The reduction in the rate constant for OH + $MeONO_2$ (Section 2.1) reduces O_x production from organic nitrate oxidation significantly while also driving the increase in O_x production from organic nitrate photolysis. The addition of the photolysis of isoprene hydroxy nitrate and the other nitrates RU12NO3 and RU10NO3 make smaller contributions.

Table 2.6. Annual mean O_x diagnostics for CRI-STRAT, CRI-STRAT 2 and difference between mechanisms (percentage changes in parentheses). UKESM1 CMIP6 1995-2004 using ST: chemical production = 5315 Tg year^{-1}, chemical loss = 4476 Tg year^{-1}, dry deposition = 867 Tg year^{-1} (Griffiths et al., 2021). Entries in bold show total production, loss and deposition and entries in plain text show individual components of these production, loss and deposition.

	CS	**CS2**	**CS2 - CS**
O_3 Burden (Tg)	328	354	26 (7.9%)
O_x Lifetime (days)	17.4	18.8	1.4 (8.0%)
OPE	33.74	33.78	0.05 (0.1%)
Chemical Production (Tg year^{-1})	**6572**	**6582**	**10 (0.1%)**
HO_2 + NO	4099	4322	132 (3.2%)
MeOO + NO	1573	1583	10 (0.6%)
NO + RO_2	849	717	-131 (-15.4%)
Other	51	49	-1 (-2.8%)
Chemical Loss (Tg year^{-1})	**5834**	**5757**	**-77 (1.3%)**
$O(^1D)$ + H_2O	3157	2928	-229 (-7.2%)
HO_2 + O_3	1666	1819	152 (9.1%)
OH + O_3	740	796	57 (7.6%)
O_3 + Alkene	166	101	-65 (-39.2%)
Other	105	113	8 (10.1%)
Deposition (Tg year^{-1})	**1133**	**1207**	**76 (6.5%)**
O_3 Dry Dep	942	1018	77 (8.0%)
NO_y dep	191	189	-3 (1.3%)
Inferred STT (Tg year^{-1})	395	384	-13 (-3.3%)

2.5.1.3 O_x loss

The change in O_x chemical destruction is dominated by the reduction in $O(^1D) + H_2O$ reaction (7.2%) which accounts for 54% of O_x loss in CS but only 49% in CS2. In the sensitivity run CS2_O1D, which uses the same $O(^1D)$ rate constants as CS, the $O(^1D)+H_2O$ flux accounts for 54% of O_x chemical loss. As this reaction involves water, the change is strongest in the tropical BL and low free troposphere (Fig B14).

The increase in O_x loss via $HO_2 + O_3$ (9.1%, Table 2.6) is driven predominantly by changes to the inorganic nitrogen and $O(^1D)$ reactions while the isoprene scheme is simulated to have little impact. O_x loss via $OH + O_3$ also increases (7.6%) despite the decrease in free troposphere HO_x with the new isoprene chemistry and revised inorganic nitrogen reactions simulated to play important roles. O_x destruction from O_3 + alkene reactions decline significantly (39%) yet increase at very low altitudes (<500 m) before decreasing at higher altitudes. This altitude dependence may arise from the enhanced O_3 low altitude driving a greater O_3 + alkene flux but, at higher altitudes, the depletion of the VOCs by O_3 and the elevated OH, means O_3 destruction is lower.

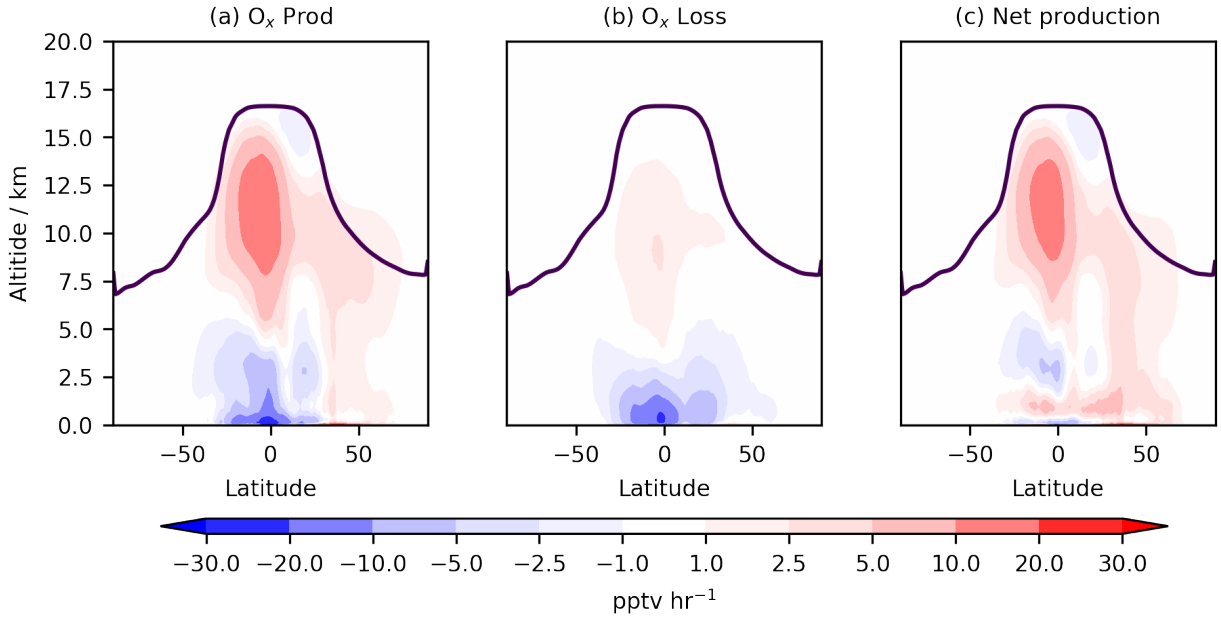


Figure 2.5. Annual zonal mean change in (a) total O_x production flux, (b) total O_x chemical loss flux and (c) net O_x chemical production flux. Purple line indicates mean tropopause height.

5.2 HO_x

The change to OH shows significant spatial and altitudinal variation, increasing at low altitude over land but decreasing over the oceans and in much of the free troposphere. This stems from the different drivers of OH concentrations and their relative importance in different regions.

At low altitude, the terrestrial increases in OH (Fig. 2.6(c,d)) are revealed by the sensitivity tests to be driven predominantly by the isoprene scheme: a clear illustration of impact of the HO_x-recycling chemistry (Fig B15).

The inorganic nitrogen changes make a smaller contribution to the low latitude OH increase while the $O(^1D)$ changes reduce low altitude OH but this effect is only noticeable over the oceans.

This significant increase in low terrestrial altitude OH is of particular interest in the context of BVOCs and their impact on the chemical composition of the atmosphere. Concentrations in the lowest 500 m increase by 2-3 × 10^5 cm^{-3} (30-50%) in much of the Amazon with similar changes seen in other tropical regions and the Southeast USA; regions with the greatest emissions of isoprene and BVOCs. The boreal forest regions in North America and Eurasia exhibit modest increases of up to 10% in places since isoprene emissions are lower (Fig B15). The influence of the updated isoprene chemistry is further apparent when the HO_x production flux from two of the key new HO_x-recycling pathways - photolysis of the HPALD and hydroxy unsaturated carbonyl (HUCARB9) species - is compared to that from $O(^1D) + H_2O$ (Fig 2.6(f)). Over the Amazon and other tropical regions, HO_x flux from this pathway amounts to 20-40% of that from $O(^1D) + H_2O$. The difference in BVOC-driven depletion of oxidant concentrations at low altitudes will be even more pronounced when CS2 is compared with ST which exhibited even lower tropical low altitude HO_x (e.g., Fig. 9, Archer-Nicholls et al., 2021).

However, in much of the free troposphere, OH decreases by 2-10% relative to CS due to the changes made to the $O(^1D)$ rate constants (Fig. B16) which reduces the fraction of $O(^1D)$ reacting with H_2O (Fig. 2.6(a)). This general decline is reversed in the upper tropical troposphere (10-15 km) where OH increases by up to 15%, driven by an increase in NO stemming from the update to inorganic nitrogen reactions and a smaller contribution from the updated isoprene chemistry (Fig. B16). These free troposphere changes partially reverse the changes simulated between CS and ST (Fig. 6, Archer-Nicholls et al., 2021). In that comparison, tropical free troposphere OH (~2-6 km) increased in CS relative to ST by 0.5-2×10^5 cm^{-3} while here CS2 yields a decrease in the same location of 0.25-1×10^5 cm^{-3} compared to CS. In the upper tropical troposphere, CS decreased OH by 1-4×10^5 cm^{-3} relative to ST while CS2 exhibits an increase of 0.25-1.5×10^5 cm^{-3} in the same region compared to CS. Thus, the distribution of free troposphere OH in CS2 is more similar to that in ST than the CS distribution is.

Overall, the reduction in the free troposphere OH outweighs the increases elsewhere with the tropospheric air mass-weighted concentration and burden of OH decreasing in CS2 by 1.5% and 0.49% respectively. (Note that the fractional change in tropospheric OH burden is equivalent to the fractional change in the average tropospheric OH concentration, not the air mass-weighted OH concentration which gives greater weight to OH at low altitude.) This is in sharp contrast to the 6.4% increase in burden simulated by Khan et al (2020). However, in the CS2_O1D sensitivity test the OH burden increases by 6.6 % relative to CS allowing us to be confident that this discrepancy between Khan et al (2020) and this work is down predominantly to the differing $O(^1D)$ rate constants. Despite the increase in surface OH, the net reduction in tropospheric OH yields a 2.3% increase in methane lifetime from 7.43 to 7.60 years (Table 2.7), also in contrast to the 0.5 years decrease in methane lifetime simulated by Khan et al (2020). However, the isolated change to isoprene chemistry, given by the comparison of CS2 and CS2_isoprene, causes a methane lifetime decreases of 2.2% due to the enhanced low altitude OH.

Table 2.7. Tropospheric average HO_x parameters for CS and CS2.

	CS	**CS2**	**CS2 – CS**
[OH] / 10^6 cm^{-3}	1.355	1.334	-0.021 (1.5%)
$[HO_2]$ / 10^8 cm^{-3}	0.990	0.988	-0.002 (0.2%)
[OH] / $[HO_2]$ (%)	1.369	1.349	-0.02 (1.5%)
CH_4 lifetime w.r.t. OH / years	7.43	7.60	0.17 (2.3%)

HO_2 also increases at low altitude (up to 6-8% at the surface, Fig 2.6(b)), driven primarily by the new isoprene chemistry, yet this increase extends much further into the free troposphere than OH, reaching nearly 5 km above the equator. HO_2 decreases in the rest of the free troposphere, partially from $O(^1D)$ changes, and does not exhibit the high increase shown by OH, rather declining by 6-8% in the tropical high troposphere resulting in a burden decrease of 0.7%. The greater increase in low altitude HO_2 (than for OH) is likely to be due in part to co-located increases in CO of 3-6 ppb (Appendix B and Fig B21(a)).

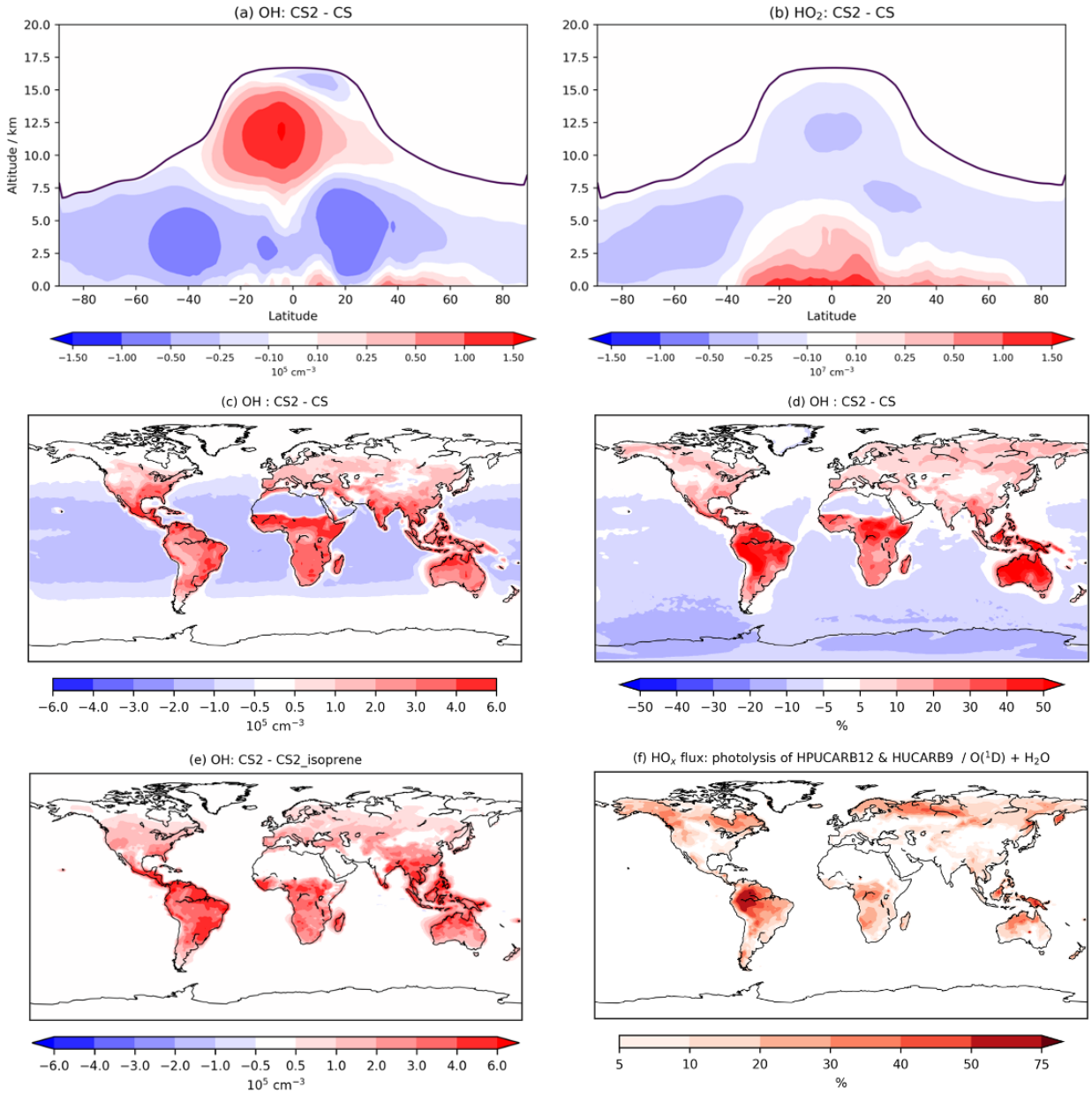


Figure 2.6. Annual zonal mean changes in (a) OH and (b) HO_2 between CS2 and CS, (c) absolute and (d) percentage in change in OH in lowest ~500 m of atmosphere, (e) the change in OH in lowest 500 m between the CS2 and CS2_isoprene sensitivity test and (f) HO_x production flux from HPUCARB12 and HUCARB9 photolysis as a percentage of HO_x from $O(^1D) + H_2O$ (right, bottom). Purple lines indicate average height of tropopause.

2.5.3 BVOCs

The interactive nature of iBVOC emissions led to average isoprene emissions being 0.36 Tg yr^{-1} (0.06%) lower in CS2 while monoterpene emissions were 0.05 Tg yr^{-1} (0.05%) lower. However, these differences are dwarfed by the reductions in the burdens of isoprene, α-pinene and β-pinene of 26%, 18% and 24%, respectively.

Isoprene mixing ratios averaged over the lowest ~ 100m decrease by 1-3 ppb (~10-30%) in large parts of South America, Africa and South East Asia (Fig 2.7). The greater terrestrial low altitude HO_x increases the OH-initiated oxidative flux of isoprene by 3.5 %, attributable almost entirely to the updated isoprene scheme. However, this is actually outweighed by a 23% decrease in isoprene destruction by O_3 while oxidation via NO_3 increased by 3.7%. Despite the modest global increase, isoprene oxidation is confined even more to low altitude regions (Fig 2.7), a feature also simulated by Karset et al (2018) (Fig 2.8). This also results in lower mixing ratios throughout the whole troposphere (Fig. 2.7).

α-pinene's chemical destruction by OH, O_3 and NO_3 changed by 7.5%, -6.3% and -0.8% respectively leading to a total flux increase of 0.05 Tg yr^{-1} (+0.05%). The corresponding changes for β-pinene with OH, O_3 and NO_3 were 3.2%, -4.3% and -0.2% with a total increase of 0.70 Tg yr^{-1} (1.5%).

The reductions to these BVOC burdens are greater than those simulated by Khan et al (2020) of 17%, 4% and 9% for isoprene, α-pinene's and β-pinene respectively. However, Khan et al (2020) simulated a reduction in O_3 over tropical regions and a much smaller increase in NO_3 burden (1%) which would have resulted in significantly lower BVOC destruction fluxes, particularly for the monoterpenes. As discussed in Section 2.4, CS2 simulates a reduction in the model high bias of surface isoprene and, to a lesser extent, monoterpenes, compared to CS and ST.

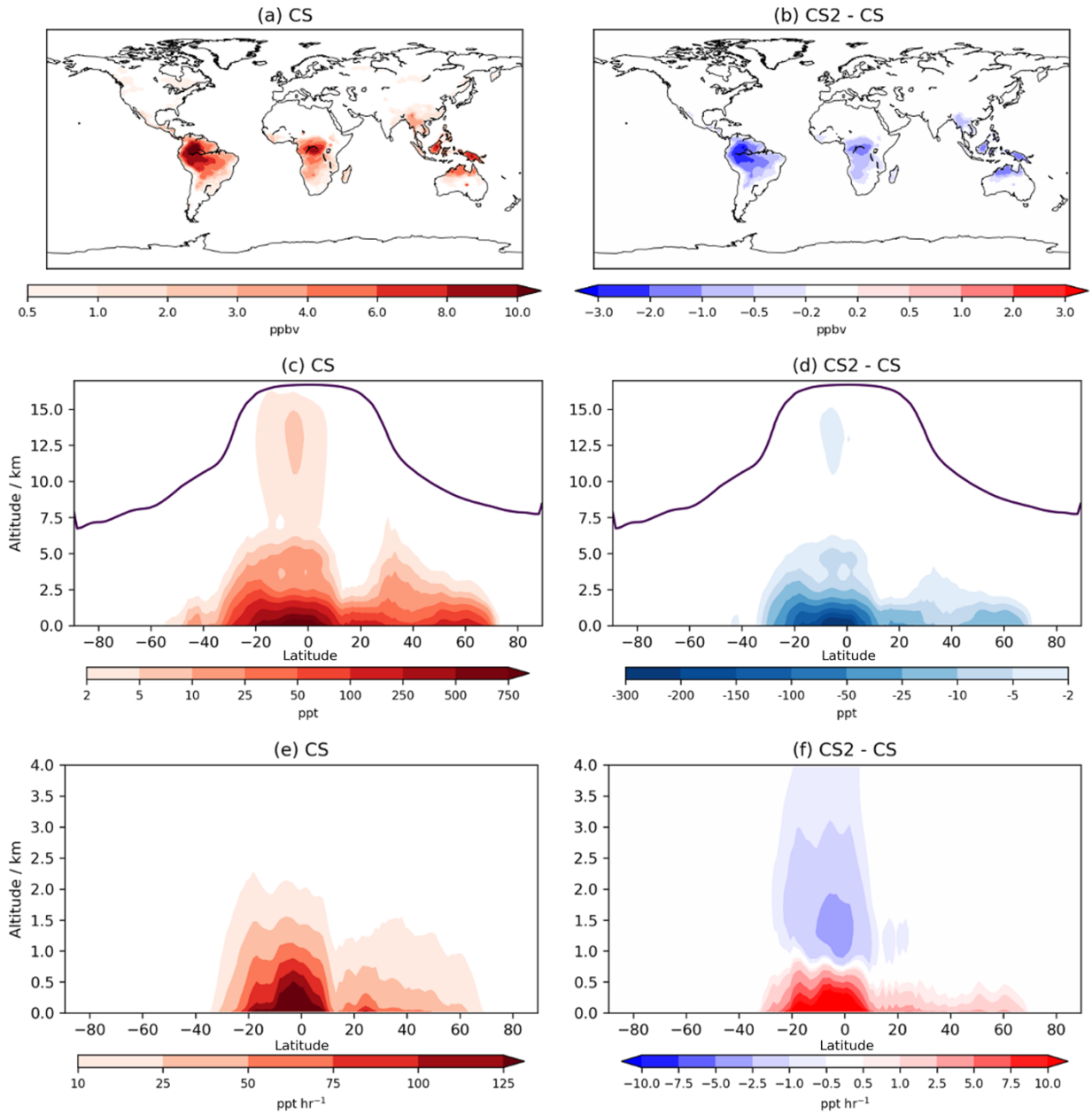


Figure 2.7. Annual mixing ratio of isoprene averaged over the lowest ~ 100 m (a) in CS and (b) the difference between CS2 and CS. Annual zonal mean mixing ratios in (c) CS and (d) difference between CS2 and CS (note the log scales used for colour maps). Annual average total oxidation flux of isoprene (e) in CS and (f) the difference between CS2 and CS.

2.5.4 HPALDs and IEPOX

While a comparison cannot be made between CS and CS2 for HPALDs and IEPOX, their importance for HO_x-recycling and SOA formation respectively means examining their global distribution is still useful. Both species follow the surface distribution of isoprene closely (Fig. 2.8) with IEPOX concentrations typically an order of magnitude greater than HPALDs, something also reflected in their burdens (0.39 Tg and 0.02 Tg, respectively). As discussed in Section 2.4, loss of IEPOX to aerosol via reactive uptake is not currently modelled and simulated

concentrations will decrease once this process is included. Indeed, accurate modelling of IEPOX and its contribution to SOA has been suggested to be important in future climate scenarios (Jo et al., 2021) which highlights the benefits of including IEPOX in CS2 but also the need for careful consideration of how aerosol uptake is modelled. Simulated advection up to the upper tropical troposphere is clearly seen in the DJF zonal means with potentially important consequences for IEPOX-derived SOA which has been observed in the lower troposphere in flight campaigns (e.g. Allan et al., 2014).

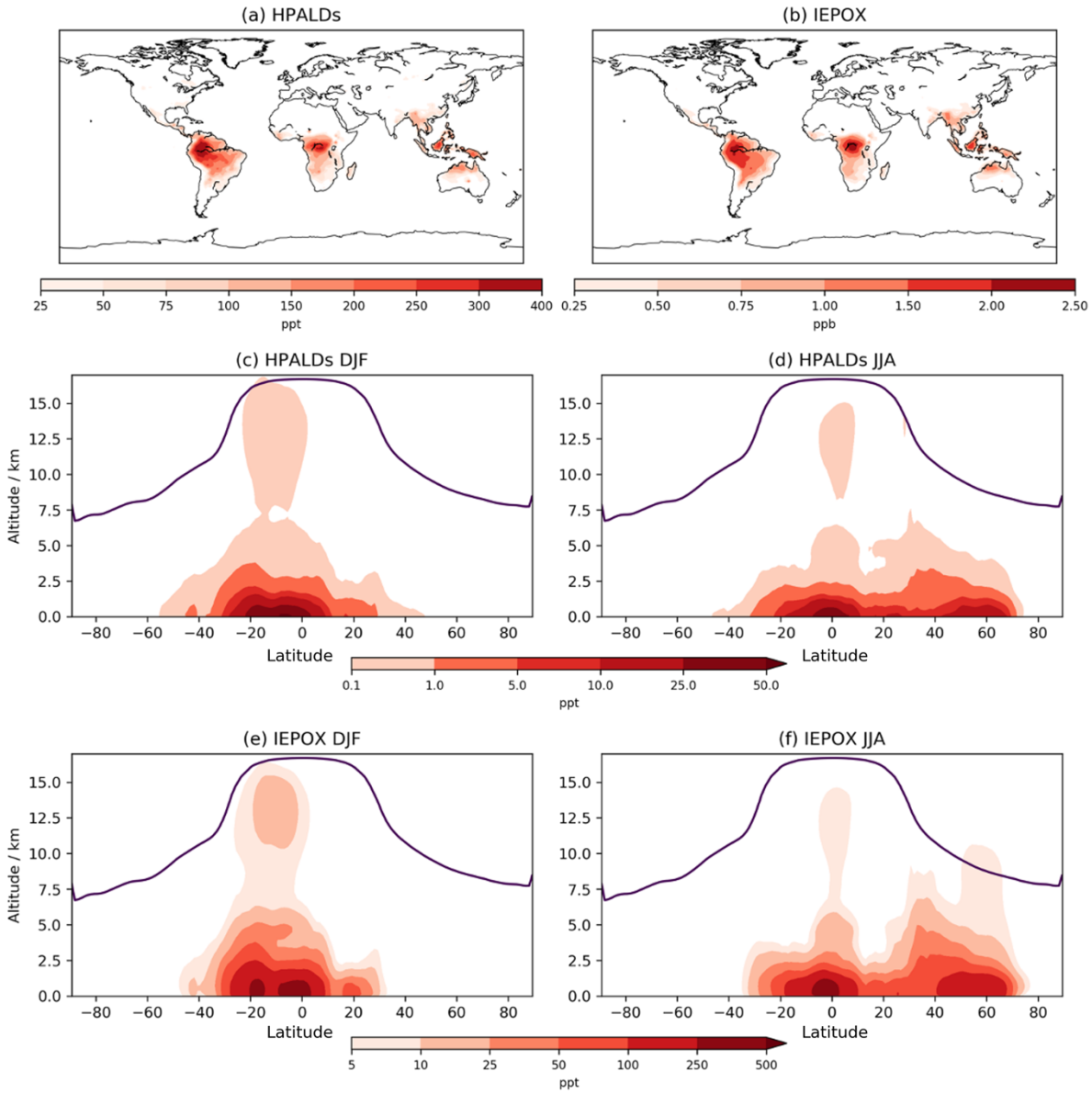


Figure 2.8. Annual mean mixing ratios for (a) HPALDs and (b) IEPOX (upper panels) over lowest ~100 m. DJF and JJA zonal mean mixing ratios for HPALDs (c, d) and IEPOX (e,f), note differing scales for HPALD and IEPOX plots and log scales for (c-f).

2.5.5 NO_y

The distribution of nitrated products (NO_y) between reactive (NO_x) and reservoir species (NO_z) changes between CS and CS2 and is detailed in Table 2.8. Here we use the standard definitions of NO_x, NO_z and NO_y (Archer-Nicholls et al., 2021) (Eq. 2.4, 2.5, 2.6):

$$NO_x = NO + NO_2 \quad (2.4)$$

$$NO_z = NO_3 + 2N_2O_5 + HONO_2 + HO_2NO_2 + ClONO_2 + BrONO_2 + PANs + RONO_2 + CH_3O_2NO_2 + \text{Nitrophenols} \quad (2.5)$$

$$NO_y = NO_x + NO_z \quad (2.6)$$

($RONO_2$ comprises alkyl nitrates, hydroxy nitrates and hydroperoxy nitrates while PANs comprises all species with the peroxyaceyl nitrate functionality).

The NO_y burden decreases by 4.8% (in terms of mass of N), driven primarily by a 20% decline in PANs. However, the NO_x burden increases by 4% with the widespread increase in the tropical high troposphere of 10-20 ppt (up to 25%) outweighing the reduction in the NH midlatitude PBL (10-50 ppt, 1-2.5%) (Fig 2.9(a)). The increase in NO_x and the reduction in NO_y leads to the fraction of NO_y as reactive Nitrogen increasing by 9% and the associated increases to the O_3 production, particularly in the free troposphere, are identified in Section 2.5.1. The sensitivity tests revealed the high-altitude NO_x rise to be driven predominantly by the change to the inorganic nitrogen with a smaller contribution from the updated isoprene scheme (Fig. B17).

The 6% reduction in NO_z burden is dominated by the decrease in PANs which exceeds 40 ppt in most of the 40N-40S troposphere (Fig. 2.9(e)). The decrease in the PANs formation rate constant discussed in Section 2.2 is not the principal driver of this reduction despite reducing by 40% in much of the troposphere. For the single year used for the sensitivity tests, the PANs burden in CS2_inorgN (featuring the larger formation rate constant) (0.292 TgN) is much closer to that in CS2 (0.290 TgN) than in CS (0.364 TgN). A more important factor is the reduction in the PAN-precursor acyl peroxy radical ($MeCO_3$), driven by the updated isoprene chemistry, whose burden decreases by over 20% in both CS2 and the sensitivity test CS2_inorgN. This dependency is clearly illustrated by the fact that the isolated change to the inorganic nitrogen reactions (CS2_inorgN) only produces a small decrease to low altitude PANs while the change to isoprene scheme (CS2_isoprene) yields a much larger decrease in PANs in spatial agreement with the CS2-CS difference (Fig. B18). The PANs burden of 0.317 TgN in the CS2_isoprene test is also closer to that in CS. However, the change in PANs between CS2 and CS is still larger than that simulated from the isolated isoprene chemistry change alone which suggests there are some synergistic effects occurring.

Table 2.8. Burdens of NO_y and its constituent species, NO_x emissions, NO_y deposition and inferred Stratosphere-to-Troposphere (STT) transport of NO_y. Values in parentheses for burdens show the fraction

of total NO_y burden represented by each constituent and, for deposition diagnostics, the fraction of total NO_y deposition represented by each pathway.

	CS	**CS2**	**CS2 – CS**
NO_y burden / TgN	**1.088**	**1.036**	**-0.052**
NO_x burden / TgN	0.118 (10.9%)	0.123 (11.9%)	0.005
NO_z burden / TgN	0.972 (89.2%)	0.914 (88.1%)	-0.058
$HONO_2$ burden / TgN	0.523 (48.0%)	0.521 (50.3%)	-0.002
Other inorganic NO_z burden / TgN	0.020 (1.8%)	0.014 (1.4%)	-0.006
PANs burden / TgN	0.367 (33.7%)	0.292 (28.2%)	-0.075
$RONO_2$ burden / TgN	0.044 (4.0%)	0.070 (6.7%)	0.026
MeO_2NO_2 burden / TgN	0.008 (0.8%)	0.008 (0.7%)	-0.0007
Nitrophenols burden / TgN	0.009 (0.9%)	0.009 (0.9%)	-0.0005
NOx Emissions / TgN $year^{-1}$	**55.65**	**55.65**	**0**
Total NOy Deposition / TgN $year^{-1}$	**62.12**	**62.35**	**0.23**
Inferred STT / TgN $year^{-1}$	**6.47**	**6.70**	**0.23**
NO_x Deposition / TgN $year^{-1}$	6.32 (10.2 %)	6.30 (10.1 %)	-0.02
$HONO_2$ Wet Deposition / TgN $year^{-1}$	29.01 (46.6%)	29.26 (46.8 %)	0.25
$HONO_2$ Dry Deposition / TgN $year^{-1}$	21.66 (34.9 %)	21.79 (35.0 %)	0.13
Other Inorganic NOy Deposition / TgN $year^{-1}$	1.21 (2.0 %)	0.96 (1.5 %)	-0.25
PANs / TgN $year^{-1}$	2.45 (3.9%)	1.93 (3.1 %)	-0.52
$RONO_2$ Deposition / TgN $year^{-1}$	1.41 (2.3 %)	2.03 (3.2 %)	0.62
Nitrophenols Deposition / TgN $year^{-1}$	0.08 (0.1 %)	0.07 (0.1 %)	-0.01

The 0.4% increase in $HONO_2$, including increases of up to 30 ppt in the tropical mid troposphere (Fig. 2.9(d)), is driven more by the update to the isoprene scheme than the change to inorganic nitrogen reactions (Fig. B19).

The 59% increase in $RONO_2$ burden in CS2 is predominantly due to the significant reduction in the rate constant for the OH-initiated destruction of $MeONO_2$, the principal organonitrate, which brings CS2 into agreement with STRAT-TROP and the most recent IUPAC value. At 290 K, the rate constant is 18 times lower in CS2 and at 250 K 50 times lower, yielding a 3-fold MeONO2 burden increase. The update to the isoprene scheme, when isolated,

actually reduces $RONO_2$, despite the introduction of the two new organic nitrates (RU12NO3 and RU10NO3). As discussed in the context of the RO_2 burden, this is driven by the added competition from the RU14O2 isomerisation reactions: the flux of the RU14O2 + NO reaction is 15% lower in CS2 than CS. The increase in $RONO_2$ is simulated to be 10-20 ppt in the tropical lower altitude and 2-10 ppt for the rest of the troposphere (Fig. 2.9(f), B20).

With the significant drop in PANs as a fraction of NO_y (34% to 28%) and the increase in $HONO_2$ and NO_x, the breakdown of NO_y in CS2 is closer to that in ST (Archer-Nicholls et al., 2021). The increase in $RONO_2$ is the only major exception to this since ST, which only has two organonitrate species (isoprene nitrate and $MeONO_2$), has a lower $RONO_2$ burden than CS.

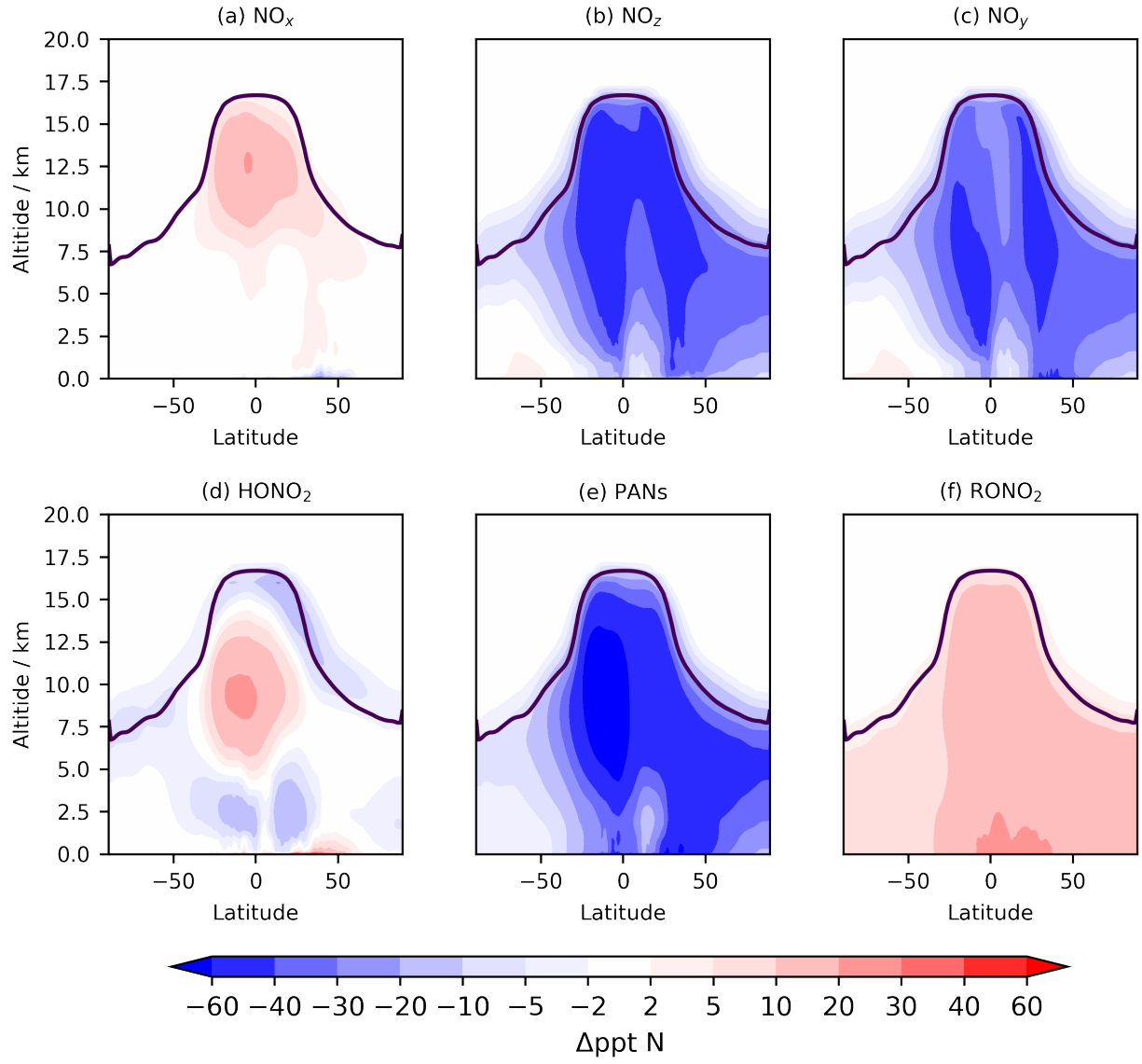


Figure 2.9. Tropospheric annual zonal mean change in (a) NO_x, (b) NO_z, (c) NO_y, (d) $HONO_2$, (e) PANs and (d) $RONO_2$ between CS2 and CS. Purple line shows average tropopause height.

2.5.6 Impacts on Aerosols

A key area of future research with the CRI mechanisms will be on their influence on aerosols. The spatial changes to oxidants are also likely to influence secondary organic aerosol (SOA) formation, as discussed in Section 1. In UKCA, SOA is produced from the tracer Sec_Org, a surrogate for the oxidised products of α-pinene and β-pinene which adds to existing organic aerosol with an optional boundary layer nucleation scheme involving Sec_Org and H_2SO_4 based on Metzger et al (2010) also available. The Sec_Org burden decreases by 7% in CS2 with noticeable annual variation (DJF -10%, JJA -4%). Despite the burden decrease, within the lowest 500m in the tropics Sec_Org mass concentration increases by 2-10%, driven by an increase its production from α-pinene and β-pinene (Fig. 2.10(a,b)). Above this region, Sec_Org production and mass concentration decrease and so it appears the greater low altitude oxidative capacity in CS2 leads to greater production of Sec_Org within the boundary layer but lower concentrations above it. This is likely to have an impact on SOA distribution (and lifetime) since deposition and loss to the aerosol phase is greater in the boundary layer due to the steep decline in aerosol surface aerosol density with altitude. Further detailed analysis involving the fluxes of Sec_Org to aerosol and the resulting changes to size and number distributions are beyond the scope of this work but examining wider consequences for SOA, in the context of the BVOC-mediated feedback between the biosphere and climate, will form a key area of future research. It is also worth noting an even more pronounced perturbation to SOA may be seen if isoprene is allowed to produce Sec_Org which is a more realistic approach to simulating SOA (e.g. Scott et al., 2014) and will be explored in future work.

The global perturbation to the oxidation pathways of SO_2, another important aerosol precursor, are more modest. From CS to CS2, the oxidative fluxes of SO_2 with OH, H_2O_2 and O_3 change by +0.9%, +0.02% and 1.7%, respectively while the tropospheric sulphate aerosol burden decreases by just 2.3%. However, as with isoprene oxidation and Sec_Org production, the burden change belies the more complex perturbations occurring. The increased oxidants at lower altitude and reduction at greater altitudes result in gas phase SO_2 oxidation increasing by 2.5-10% in the tropical and midlatitude PBL yet decreasing at higher altitudes (Fig. 2.10(c,d)). This effect is expected to be even more pronounced when CS2 is compared to ST which simulates even lower low altitude OH than CS (Archer-Nicholls et al., 2021) and has been the standard mechanism for investigations into aerosol-oxidant coupling in UKCA (Thornhill et al., 2021b, Weber et al., 2020a, O'Connor et al., 2021). Therefore, the mechanism-driven changes to oxidants are likely to have consequences for both SOA and sulphate aerosol. While a full investigation into oxidant aerosol coupling is beyond the scope of this paper, it will form a central part of future work with the CRI mechanisms.

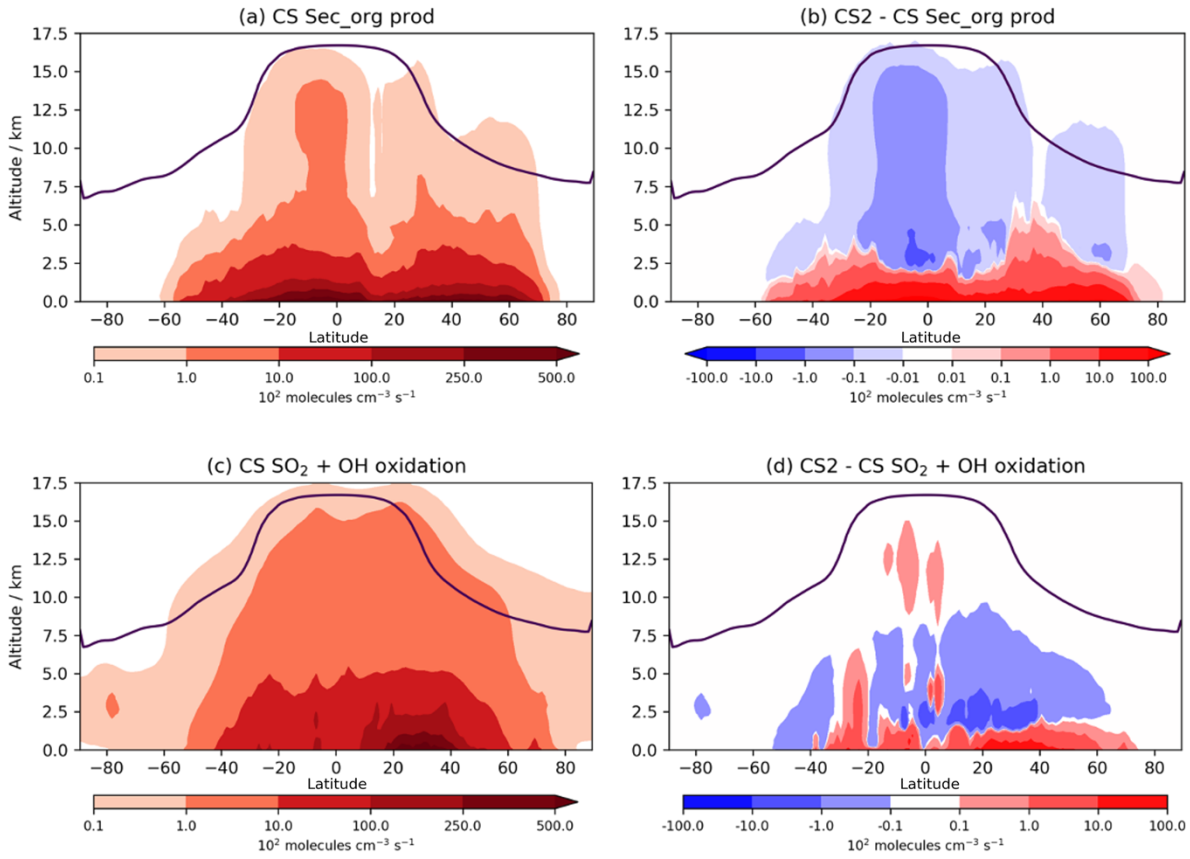


Figure 2.10. Tropospheric annual zonal mean production flux of Sec_Org in (a) CS and (b) difference between CS2 and CS. Annual zonal mean flux of SO_2 + OH in (c) CS and (d) difference between CS2 and CS.

2.5.7 Summary and synthesis

The key changes between CS and CS2, driven by the multiple chemistry changes, can be summarised as follows:

1. O_x production increases marginally in CS2 but a larger decrease in O_x destruction, driven by a significant reduction in the $O(^1D) + H_2O$ flux, leads to a greater O_3 tropospheric burden and mixing ratios.
2. The update to the isoprene chemistry increases low altitude tropical HO_x but the reduction in OH production from $O(^1D) + H_2O$ results in lower HO_x concentrations in much of the free troposphere, increasing methane lifetime.
3. The update to the inorganic nitrogen reactions increases NO_x as a fraction of NO_y with a significant increase in the upper tropical free troposphere and a co-located increase in OH. The PAN burden decreases by 20%.
4. The increase in boundary layer oxidative capacity reduces the burden of BVOCs and confines their oxidation even more to low altitude with likely consequences for aerosol production and lifetime.

2.6 Conclusion

The radiative impact of isoprene, via its influence on atmospheric chemical composition and organic aerosol, means an accurate description of its chemistry is crucial for advancing our understanding of pre-industrial, present day and future atmospheres. In this study we describe the incorporation of the Common Representative Intermediates chemistry scheme version 2.2 (CRI v2.2), along with accompanying stratospheric chemistry, into the global chemistry-climate model UKCA to create the mechanism CRI-Strat 2 (CS2). The introduction of CS2 into UKCA facilitates a semi-explicit description of HO_x-recycling chemistry during isoprene oxidation via the isomerisation of isoprene peroxy radicals to produce HPALDs which yield HO_x upon photolysis. This is a key process for reconciling the model low bias of HO_x in low NO_x, BVOC-rich regions. In addition, CS2 also features updates to the rate constants of the reactions of $O(^1D)$, inorganic nitrogen and organic peroxy radicals with NO and NO_3, bringing the mechanism into agreement with the most recent IUPAC values. CS2 is one of the first mechanisms with this functionality suitable for long term climate integrations.

A rigorous comparison using UKCA with CS2 and two other chemical mechanisms, STRAT-TROP (ST) (the standard chemistry mechanism used in UKESM1's contributions to CMIP6 experiments) and CRI-STRAT (CS) (which has tropospheric chemistry from an earlier version of the CRI, CRI v2.1), is performed against high frequency surface and airborne observational data from BVOC-rich regions for multiple chemical species including O_3, OH, HO_2, isoprene and monoterpenes and isoprene oxidation production. The HO_x-recycling in CS2 results in significantly enhanced surface diel OH (up to 50% higher than CS at midday) in the Amazon and Borneo (improving model low bias), leading to improved modelling of diel and vertical isoprene profiles and reducing the mean 24-hour bias by 50-60% and 20-40% relative to ST and CS, respectively across the locations considered. However, CRI-Strat 2 exacerbates the existing isoprene model low bias away from the surface, suggesting potential issues with model vertical convection. CS and CS2 yield smaller isoprene column biases compared to observations than ST, in line with the surface and free troposphere observational comparisons, while also illustrating the significant influence the chemical mechanism has on modelled column. This comparison also highlights the significant influence the different chemistry schemes have on the simulated isoprene column and thus the considerable challenges of determining isoprene emissions via back-calculation.

The low altitude high biases for O_3 in CS increase modestly (1-2 ppb) in CS2. Simulated monoterpene concentrations are high biased at the surface at most of the locations considered with CS2 returning the smallest bias. As with isoprene, simulated monoterpenes display sharp morning and evening peaks which are believed to be due to boundary layer height issues. Model high bias of IEPOX and the low bias of HPALDS suggests further investigation of the key processes of loss to aerosol for IEPOX and HPALD photolysis frequency are needed.

In addition to observational comparisons, a detailed comparison of UKCA model output using CS and CS2 is performed, complementing the earlier comparison of ST and CS (Archer-Nicholls et al., 2021). Sensitivity tests are also performed to help isolate the drivers of the differences between CS and CS2. CS2 simulates an 8% increase in tropospheric O_3 burden driven primarily by reduced O_x loss as the changes to rate constants of $O(^1D)$ with H_2O, O_2 and N_2 mean that a smaller fraction of $O(^1D)$ reacts with H_2O to produce OH. Low altitude O_3 increased by 2-4 ppb over much of the globe, driven predominantly by changes to the $O(^1D)$ and inorganic

nitrogen reactions. More broadly, the widespread influence of the changes the rate constants of $O(^1D)$ and multiple inorganic nitrogen species highlights the importance of having accurate information for these parameters.

Relative to CS, low altitude OH increases over terrestrial regions, exceeding 50% in some tropical forested regions, primarily due to the influence of HO_x-recycling from isoprene. However, OH decreases over the oceans and in much of the free troposphere driven by updates to the rate constants of $O(^1D)$'s reactions with H_2O, O_2 and N_2. As a result, methane lifetime increases by 2.3%in stark contrast to previous studies using CRI v2.2 in the STOCHEM model which did not make changes to $O(^1D)$ and inorganic nitrogen reactions. When the changes to isoprene chemistry are isolated, methane lifetime decreases by 2.2%, qualitatively in line with previous studies. The addition of isomerisation pathways in the updated isoprene scheme reduces the methyl (7%) and non-methyl peroxy (36%) radical burdens.

The distribution of nitrated species (NO_y) in CS2 is closer to that simulated in ST than CS is, with a significant reduction (20%) in the burden of PANs which is driven by a reduction in the precursor RO_2. The NO_x burden increased by 4%.

The increase in low altitude OH reduced the burdens of isoprene (26%) and monoterpenes (18-24%) and the extent of their dispersion: more oxidation takes place in the boundary layer where loss of oxidation products such as the lumped SOA precursor Sec_Org to existing aerosol is likely to be greater. Enhanced SO_2 oxidation in the boundary layer is also simulated. These changes are likely to have implications for SOA and sulphate aerosol, particularly as CS has already been shown to have a more highly oxidising boundary layer than ST. Therefore, the difference between CS2 and ST (the mechanism used to explore chemical-aerosol coupling in UKESM1 in CMIP6 experiments), is likely to be significant and will be the subject of future work.

The addition of CS2 also lays the groundwork for the incorporation of a novel chemistry scheme which describes the formation of the highly oxidised organic molecules (HOMs) derived from biogenic species such as α-pinene (e.g. CRI-HOM, Weber et al., 2020b). HOMs are crucial for new particle formation without sulphuric acid (Kirkby et al., 2016, Simon et al., 2020), a process which is an important source of new particles in the Amazonian free troposphere (Zhao et al., 2020) and has been simulated to have consequences for our understanding of pre-industrial aerosol burden (Gordon et al., 2016). The influence of isoprene in HOM production (Kiendler-Schaar et al., 2009, McFiggans et al., 2019, Heinritzi et al., 2020) can also be captured by addition of CRI-HOM making UKCA one of the very first global chemistry-climate models to feature a semi-explicit representation of HOMs and enabling further investigation into the climatic impact of the interaction between BVOCS. Long chain terpenes addition to CS2 are also planned including sesquiterpenes, which may reduce the surface ozone high bias and form HOMs, and improvements to the uptake of oxidised species to plant surfaces.

While certain elements of the CRI-STRAT 2 mechanism in UKCA such as the ozone high bias remain problematic, its incorporation represents a major step forward in our ability to simulate isoprene chemistry in low NO_x environments. The simulated changes to oxidants in CRI-Strat 2 will affect the atmosphere's radiative balance by perturbing certain greenhouse gases and aerosols and investigating the impact will be a major topic of

future work. In particular, the feedback between the biosphere and climate, mediated by BVOCS, will be evaluated using multiple mechanisms to assess their influence. CRI-Strat 2 can be taken up for use, alongside other mechanisms, to further our understanding of the wide-ranging impact BVOCs have on climate.

3. The influence of the chemical mechanism on the climatic impact of BVOCs

3.1 Introduction and Summary

Chapter 2 described the incorporation and evaluation of the CS2 chemical mechanism in UKCA, compared model output from CS2, CS and ST to observational data in BVOC-rich regions and examined how mechanistic differences led to differences in the global atmospheric composition in CS and CS2.

The mechanistic variations between ST and CS2 are likely to lead to differences in the simulated climatic impact of BVOCs given the central role of oxidants and aerosol, prompting investigation into the extent to which differences in chemistry may be responsible for the inter-model variation of BVOCs' climatic impact (Section 1.5 and Fig 1.10). For example, the comparisons of CS and ST (Archer-Nicholls et al., 2021) and of CS2 with ST (Chapter 2 and Appendix B7) indicate that the increase in present day tropical terrestrial OH is even higher from ST to CS2 than CS to CS2, with implications for SOA-precursor production among others.

Building on the understanding of how and why CS2 differs from standard mechanisms (i.e., ST and CS) presented in Chapter 2, I consider the two-part question: "How does the transition from a standard chemical mechanism (ST) to a state-of-the-art chemical mechanism (CS2) affect the climatic impact of BVOCs and how might this help to explain the inter-model variation in the climatic impact of BVOCs?"

Focusing on the forcings from changes to O_3, CH_4, aerosol scattering and clouds, I find that increasing BVOC emissions leads to a net positive forcing, and thus positive feedback, in both ST and CS2. Positive forcings from enhanced O_3 and CH_4 and cloud changes outweigh the negative forcing from greater aerosol scattering. However, the magnitude of the net forcing is 43% smaller in CS2. This is attributed to a smaller reduction in atmospheric oxidising capacity in CS2 with higher BVOC emissions which leads to a smaller increase in CH_4 and smaller reduction in CDNC (differences in the forcings from O_3 and aerosol scattering are smaller). Comparing the difference in net forcing and the individual components between the two mechanisms to the inter-model variation of AerChemMIP (Fig 1.10(e)) suggests that differences in chemical mechanism may play an important role in different model responses for O_3 and CH_4 but, unsurprisingly, a smaller role in the aerosol forcing. I now describe the experiments performed, present a detailed analysis into the atmospheric composition response for each mechanism and relate this to the radiative forcing and thus climatic impact of BVOCs.

3.1.1 BVOC Feedbacks

As discussed in Chapter 1, the emissions of BVOCs influence the chemical composition of the troposphere and, by reactions with OH, O_3 and NO_3, directly affect the tropospheric oxidising capacity and the abundance of the radiatively-active species O_3 and CH_4 (Section 1.4, and Archibald et al., 2011). BVOCs also serve as important sources of SOA and affect the formation of sulphate aerosol, influencing the Earth's radiation budget via the scattering or absorption of solar radiation (aerosol direct radiative effect, DRE) (Bellouin et al., 2020) and aerosol-cloud interactions (Naik et al., 2021). Aerosols also increase incident diffuse radiation and so photosynthesis,

enhancing carbon sequestration (Rap et al., 2018). Thus, E_{BVOC} affect climate, but simultaneously climatic and atmospheric conditions such as CO_2, temperature, photosynthetically active radiation (PAR) and precipitation also have strong impacts on E_{BVOC} (Section 1.4.1).

This interdependence between E_{BVOC} and climate leads to a feedback loop, quantified by the feedback factor (Section 1.5). For example, considering increases in E_{BVOC} from enhanced CO_2 and temperature in an atmosphere with prescribed oxidants, Sporre et al (2019) found a negative feedback from enhanced organic aerosol (Fig 3.1). The AerChemMIP study of Thornhill et al (2021b) decomposed the radiative impacts of BVOCs in five climate models into those from changes to O_3, CH_4 and aerosol (combining the aerosol direct and indirect effects) and calculated feedback factors for each component, highlighting the considerable inter-model variation in the feedback's sign and size. This chapter's results are compared to AerChemMIP in Section 3.5.2.

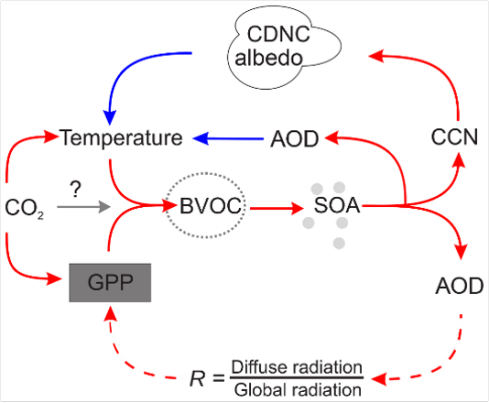


Figure 3.1 Feedback diagram taken directly from Sporre et al (2019) from experiments where enhanced CO_2 and temperature drove increases in E_{BVOC} but oxidants were prescribed. This means forcings and feedbacks arose only from changes to organic aerosol. Red lines indicate an increasing relationship and blue lines a decreasing relation (e.g., higher CO2 drives higher temperatures). The lower red line is dashed to indicate the reduced role of changes in diffuse radiation on gross primary production (GPP). The question mark indicates the uncertainty regarding the net effect of elevated CO_2 levels on E_{BVOC} due to the opposing effects of CO_2 fertilisation and isoprene inhibition.

3.1.2 Chemical Mechanisms

Several modelling studies have examined the influence of varying the yield and production pathways of SOA on its burden, properties (e.g., size distribution) and climatic impact (Scott et al., 2014, Kelly et al., 2018, Sporre et al., 2020). However, the influence of the description of atmospheric chemistry (i.e. the chemical mechanism) on the climatic impact of BVOCs has received much less attention yet is likely to be just as important given the central role which atmospheric oxidising capacity plays in the magnitude of the gas phase (CH_4, O_3, e.g. Archibald et al., 2011) and aerosol forcing components (e.g. Karset et al., 2018). By conducting identical experiments in UKESM1 using two different chemical mechanisms with the same SOA production pathways and aerosol scheme, this work complements previous, aerosol-focused studies, by assessing both how the description of chemistry affects simulated PI atmospheric composition, and the simulated feedback between E_{BVOC} and climate.

The chemical mechanisms used in this study are Strat-Trop (ST) and CRI-Strat 2 (CS2) (Chapter 2; Weber et al., 2021). ST is used because it is the standard chemical mechanism for UKESM1 and was used for UKESM1's contributions to CMIP6, including AerChemMIP (Fig 1.10(e)). Thus ST serves as a benchmark while CS2 is used as it includes a more comprehensive description of tropospheric chemistry and, crucially for this study, state-of-the-art isoprene chemistry. CS2 features ~3x as many chemical species as ST, including 4 additional emitted species. ST and CS2 have very similar schemes for stratospheric chemistry.

As discussed in Section 1.4, ST features relatively outdated isoprene chemistry from Poschl et al (2000) where oxidation by OH yields ISOPOO. ISOPOO subsequently produces the isoprene hydroperoxide (ISOPOOH) from reaction with HO_2 and HCHO and MACR as the major products from reaction with NO, NO_3 and other peroxy radicals (RO_2). CS2 includes this chemistry but also the updates detailed in Section 1.4.2 where ISOPOO can also undergo a 1,6 H-shift, forming HPALDs and HO_x, and a 1,5 H-shift yielding MACR and OH. The chemistry resulting from the 1,6 H-shifts, including the photolysis of HPALDs (and its products) regenerate HO_x. As a result, the significant surface isoprene high bias simulated by ST in BVOC rich regions (driven by a depletion of OH which exhibits a corresponding low bias) is significantly improved in CS2 (Section 2.4 and Fig B24(f)).

Monoterpene chemistry also differs between ST and CS2. In ST, the single monoterpene tracer, MT, is oxidised by OH, O_3 and NO_3 but only produces the chemically inert tracer Sec_Org which contributes to aerosol. Thus, MT acts as an oxidant sink. In CS2, separate tracers for α-pinene and β-pinene are used. These produce Sec_Org at the same yield as ST but also produce species which undergo further chemical reactions, affecting oxidant budgets and O_3 production (full description in Appendix B2). While neither approach conserves mass, CS2 is more realistic since only a fraction of MT actually contributes to aerosol (SOA yield <<100%; Ng et al., 2007) and the large number of C-C and C-H bonds means MT can have an important impact on regional concentrations of O_3 (Section 1.2.1) and HO_x, something missed in ST.

The influence of oxidants on the gas phase forcing agents CH_4 and O_3, and direct and indirect aerosol forcing via aerosol-oxidant coupling is discussed in Chapter 1. The comparisons between CS and CS2 (in Chapter 2), between ST and CS (Archer-Nicholls et al., 2021) and ST and CS2 (Appendix B) have shown that CS2 and ST simulate significantly different oxidant fields, particularly in BVOC-rich regions. Therefore it is reasonable to expect the simulated climatic impact of an E_{BVOC} perturbation will differ between the mechanisms yet the complex and potentially offsetting nature of the drivers of the forcing components means it is not clear how the responses will differ. The aim of this chapter is to assess how and why the responses of atmospheric composition to an E_{BVOC} perturbation differ between the two mechanisms and understand how this affects the climatic impact of BVOCs. In turn, this will provide a better understanding of how BVOCs influence climate and the role they may play in future climate change.

In Section 3.2 I discuss the model setup, simulations performed, updates to the SOA scheme and the methodology for calculating the forcing components. I examine the changes to the gas phase chemistry and aerosol in Section

3.3 and in Section 3.4 calculate the forcing and feedback factors and provide a link to the atmospheric composition changes.

3.2 Methods

3.2.1 Model Description & Simulations

Four 45-year PI timeslice simulations (15 years spin up, 30 years analysis) were run using the UKESM1-AMIP setup at a horizontal resolution of 1.25° × 1.875° with 85 vertical levels up to 85 km (Walters et al., 2019). All simulations had interactive stratospheric and tropospheric chemistry using either the ST or the CS2 mechanism. The simulations used the GLOMAP-mode aerosol scheme which simulates sulfate (SO_4), sea-salt (SS), black carbon (BC), primary organic aerosol (POA), secondary organic aerosol (SOA) and dust but not currently nitrate aerosol (Mann et al., 2010; Mulcahy et al., 2020). In this setup, the model tracks the mass concentration of each mode present in each component (e.g. SO_4 nucleation mode) and the total particle number concentration for the nucleation, Aitken (soluble and insoluble), accumulation and coarse modes. Improvements were made to the SOA scheme for this work (Section 3.2.3). Updates to the dry deposition of SO_2 over wet surfaces (Hardacre et al., 2021) were also included.

Emissions of well-mixed greenhouse gases, such as CH_4 and CO_2, were not simulated; rather, prescribed lower boundary conditions (LBC) at PI levels were applied for CO_2 (284 ppm), CH_4 (802 ppb) and N_2O (273 ppb), consistent with the control runs of UKESM1's contributions to AerChemMIP (Collins et al., 2017).

The four main runs (Table 3.1) consisted of two baseline runs, ST_{con} and $CS2_{con}$, and two perturbed runs, ST_{2x} and $CS2_{2x}$, where emissions of monoterpene and isoprene were doubled. A fifth simulation, $CS2_{ST,\,isop}$, which uses the CS2 mechanism and control E_{BVOC} but with ST isoprene chemistry was run for 4 years (1 year spin up, 3 year analysis) to help isolate the impact of the isoprene chemistry from the other differences between the ST and CS2 mechanisms (e.g. different VOC emissions). In addition, the two runs comprising UKESM1's contribution to the 2xBVOC experiment of AerChemMIP (Thornhill et al., 2021b), denoted as ACM_{con} and ACM_{2x} and collectively ACM, are used for a small number of comparisons (I did not set up or execute ACM_{con} and ACM_{2x}).

The setup of these runs followed the AerChemMIP protocol (Collins et al., 2017) to allow calculation of the ERF in the manner recommended by Forster et al (2016). Fields for sea surface temperatures (SSTs), sea-ice, ocean biogeochemistry and vegetation (leaf area index, land cover fraction and canopy height) were taken from monthly mean climatologies derived from 30 years of output of the UKESM1 fully-coupled pre-industrial control experiment (Sellar et al., 2019). Timeslice PI anthropogenic and biomass burning emissions were taken from the CEDS dataset from Hoesly et al (2018) and van Marle et al (2017) respectively. While the atmosphere-only setup with fixed SSTs does constrain the wider Earth System response (e.g., aerosol-driven changes to PAR cannot change land cover via vegetation fertilisation), it reduces the noise which would occur with a coupled ocean. Critically it makes this study's results directly comparable to the BVOC simulations of AerChemMIP (Fig

1.10(e)), allowing assessment of the role of simulated chemistry in explaining inter-model variation (Section 3.5.2).

All biogenic emissions, except isoprene and MT, were based on 2001-2010 climatologies from Model of Emissions of Gases and Aerosols from Nature under the Monitoring Atmospheric Composition and Climate project (MEGAN-MACC) version 2.1 (Guenther et al., 2012). Oceanic emissions were from the POET 1990 dataset (Olivier et al., 2003).

As in UKESM1's runs for AerChemMIP, isoprene and MT emissions were calculated using iBVOC (Pacifico et al., 2012) which calculates the emissions interactively based on temperature, CO_2, plant functional type and photosynthetically active radiation (PAR) (Section 1.4.1.1). The use of iBVOC allows for a more faithful estimate of pre-industrial emissions of biogenic species compared to using present-day emissions inventories since iBVOC takes into account the PI land use (less deforestation in the PI) and atmospheric conditions such as lower CO_2. In the CS2 runs, MT emissions calculated by iBVOC were split into α-pinene and β-pinene in a 2:1 ratio as in previous CRI studies (Chapter 2).

As discussed in Archer-Nicholls et al (2021), emissions of VOCs are higher in CS2. Monoterpenes account for an extra 124 TgC yr^{-1} of reactive carbon. There are smaller differences in other biogenic (~30 TgC yr^{-1}), anthropogenic (~5.5 TgC yr^{-1}) and biomass burning (~23 TgC yr^{-1}) emissions. Oceanic emissions are almost identical. The impacts of these additional emissions are considered in Section 3.3.

The rate constant for the reaction of MT + NO_3 in ST was corrected from $1.19 \times 10^{-12} e^{925/T}$ to $1.19 \times 10^{-12} e^{490/T}$, bringing it into line with the IUPAC preferred value (https://iupac-aeris.ipsl.fr/htdocs/datasheets/pdf/NO3_VOC9_NO3_apinene.pdf, last access 14th September 2021) for α-pinene on which the ST tracer MT is based. This reduces the rate constant by ~80% but, as NO_3 is a minor sink for isoprene and monoterpenes in the PI, it does not have a huge impact on aerosol formation.

Table 3.1. Model runs performed for this study (ST_{con}, ST_{2x}, $CS2_{con}$, $CS2_{2x}$, $CS2_{ST,isop}$) and UKESM1's contribution to AerChemMIP (ACM_{con}, ACM_{2x}) discussed in Thornhill et al (2021b). BHN is binary homogeneous nucleation ($H_2SO_4 + H_2O$) and BLN is boundary layer nucleation following Metzger et al (2010). (All runs were spun up for 15 years unless otherwise stated.)

Run	Mechanism	Length / years	E_{BVOC} Scaling	SOA Scheme (molar yield)	Nucleation Mechanisms
ST_{con}	ST	30	1x	13% Sec_Org_{MT} 3% Sec_Org_{Isop}	BHN, BLN w/ Sec_Org_{MT}
ST_{2x}	ST	30	2x	13% Sec_Org_{MT} 3% Sec_Org_{Isop}	BHN, BLN w/ Sec_Org_{MT}
$CS2_{con}$	CS2	30	1x	13% Sec_Org_{MT} 3% Sec_Org_{Isop}	BHN, BLN w/ Sec_Org_{MT}
$CS2_{2x}$	CS2	30	2x	13% Sec_Org_{MT} 3% Sec_Org_{Isop}	BHN, BLN w/ Sec_Org_{MT}
$CS2_{ST,isop}$	CS2 with ST isoprene chemistry	3 (1 spin up)	1x	13% Sec_Org_{MT} 3% Sec_Org_{Isop}	BHN, BLN w/ Sec_Org_{MT}
ACM_{con}	ST	30	1x	26% Sec_Org_{MT}	BHN only
ACM_{2x}	ST	30	2x	26% Sec_Org_{MT}	BHN only

3.2.2 Aerosol Modelling

The non-standard approach of tracking POA and SOA separately adopted here facilitated a more detailed investigation into how changes in the chemistry affected SOA compared to ACM simulations where POA and SOA were lumped. In addition, two other important improvements to the SOA aerosol scheme were implemented specifically for this study: SOA production from isoprene and organic-mediated new particle formation.

In the UKESM1 contributions to AerChemMIP (e.g. Thornhill et al., 2021a, 2021b), the inert Sec_Org tracer was produced solely from monoterpene oxidation at a molar yield of 26% (Mulcahy et al., 2020) and did not participate in new particle formation. The 26% yield, significantly higher than in past studies (e.g. Scott et al., 2014; Sporre et al., 2019), was doubled from the standard molar yield of 13% (Spracklen et al., 2005) to account for the absence of SOA from isoprene and anthropogenic sources yet has undergone little evaluation.

Multiple experimental and observational studies have shown that isoprene contributes to SOA (e.g., Marais et al., 2016 and Section 1.4.3) and the absence of SOA production from isoprene leads to a high bias in SOA production in boreal regions, where monoterpene emissions are higher, and a low bias in tropical regions which have the highest isoprene emissions (Sindelarova et al., 2014). The strong vertical mixing in the tropics means SOA in the tropics can be transported into the middle and upper troposphere (Williamson et al., 2019; Zhao et al., 2020), leading to differences in the SOA global distributions between the MT-only approach and the Isoprene + MT approach of this study.

Isoprene's contribution to SOA is largely through the species IEPOX, HMML, glyoxal and methylglyoxal (Section 1.4.3) and while CS2 features all of these species, ST does not. Therefore, to model SOA from isoprene, a molar Sec_Org yield of 1.5% (mass yield of 3.3%) was applied, consistent with previous UKCA studies (Scott et al., 2014; Kelly et al., 2018) and in line with observed SOA mass yields from isoprene (e.g. Kroll et al., 2005, 2006). The molar yield from monoterpenes reverted to 13%.

I have also included the nucleation of new particles via the clustering of the Sec_Org tracer from monoterpenes and H_2SO_4, based on the Metzger et al (2010) boundary layer nucleation (BLN) scheme. Scott et al (2014), using a 13% molar yield of Sec_Org from MT, showed that BLN significantly improved UKCA's performance of aerosol number concentration against measurements in the boreal forest. Ranjithkumar et al (2021) found that including BLN when using a 26% molar yield of Sec_Org from MT improved the aerosol number concentration and condensation sink in UKCA over the Atlantic and Pacific. While the inclusion of this scheme represents an update in BVOC modelling relative to the UKESM1 contributions to AerChemMIP (Thornhill et al., 2021b), at present it only operates in the model boundary layer and does not capture the formation of new particles in the free troposphere, an observed process which may have important consequences for the global aerosol distribution (Williamson et al., 2019; Zhao et al., 2020). PBN (nucleation from HOMs without sulphuric acid; Section 1.4.5.1) was not simulated but is discussed in Chapter 4 and Future Work (Section 5.4.1.1).

Since the products of isoprene oxidation are too volatile to participate in nucleation, the inclusion of both SOA from isoprene and BLN meant I needed to further modify UKESM1's aerosol code to consider two Sec_Org tracers: a tracer from MT oxidation (Sec_Org_{MT}) which can undergo condensation and nucleation (Eq. 3.1, 3.3), and a separate tracer from isoprene oxidation (Sec_Org_{ISOP}) which can only undergo condensation (Eq. 3.2).

$$MT + O_x \rightarrow 0.13\ Sec_Org_{MT} \rightarrow \text{Condensation or Nucleation} \quad (3.1)$$

$$Isoprene + O_x \rightarrow 0.015\ Sec_Org_{Isop} \rightarrow \text{Condensation} \quad (3.2)$$

$$J = k[H_2SO_4][Sec_Org_{MT}] \text{ where } k = 5 \times 10^{-13} s^{-1} \quad (3.3)$$

($O_x = OH, O_3$ or NO_3)

A similar approach has been used in a few studies using prescribed oxidants (e.g., Scott et al., 2018a,b) but this chapter represents the first time it has been used with fully interactive chemistry in UKESM1. It is an improvement over past approaches since it allows isoprene to contribute to existing SOA at a yield consistent with literature while also allowing MT to contribute to both nucleation and condensation, something not possible with a single Sec_Org tracer. It also brings the aerosol setup closer to the approach used in three other Earth System models: NorESM, EC-Earth and ECHAM where the Sec_Org_{MT} tracer is analogous to the ELVOC tracer (which participates in condensation and nucleation) and the Sec_Org_{ISOP} tracer is similar to L/SVOC tracer which only condenses (Sporre et al, 2020).

Scott et al (2014), Sporre et al (2020) and Sengupta et al (2021) have shown the significant influence that uncertainty in aerosol parameters, including yield and PBN, can have. This chapter does not aim to tackle these issues. Rather I have chosen aerosol parameters which are the most scientifically acceptable within the parameter-space previously explored and applied them consistently across all runs, thus ensuring the differences between runs are due solely to the simulated chemistry.

3.2.3 Forcing and Feedback Calculation

The key metrics in this study are the forcings arising from the $2xE_{BVOC}$ perturbations with each mechanism and the associated feedback factors. The methodology for calculating the feedback factor is given in Section 1.5.

The radiative efficiency of BVOCs, ϕ_{BVOC}, used for the feedback factor calculation for each mechanism is calculated by dividing the forcing from the simulation pairs (ST_{con}, ST_{2x} and $CS2_{con}$, $CS2_{2x}$) by the change in emissions from the $2xE_{BVOC}$ perturbations (~870 Tg yr^{-1}). The forcings are defined in Section 3.2.4. The use of ERF allows the inclusion of stratospheric temperature adjustments but also rapid adjustments in the troposphere including temperature, water vapour, clouds and land surface temperature (Chung and Soden., 2015, O'Connor et al., 2021).

3.2.4 Forcing decomposition

For each mechanism pair, the ERF is defined as the difference in TOA net radiative flux (Eq 3.4).

$$\mathrm{ERF} = \Delta \mathrm{N} = \mathrm{N_{2x}} - \mathrm{N_{con}} \quad (3.4)$$

Where N_{con} (Eq 3.5) and N_{2x} (Eq 3.6) represent the net incoming radiative flux for the control and $2xE_{BVOC}$ simulations respectively.

$$\mathrm{N_{con}} = \mathrm{N_{con,in}} - \mathrm{N_{con,out}} \quad (3.5)$$
$$\mathrm{N_{2x}} = \mathrm{N_{2x,in}} - \mathrm{N_{2x,out}} \quad (3.6)$$

Following the approach of Ghan (2013) and O'Connor et al (2021), the ERF can be decomposed into aerosol direct radiative effects (IRF_{DRE}) (Eq 3.7), aerosol-cloud effects (CRE) (Eq 3.8), and clear-sky effects (ERF_{CS}) (Eq 3.9).

$$\mathrm{IRF_{DRE}} = \Delta(\mathrm{N} - \mathrm{N_{clean}}) \quad (3.7)$$
$$\mathrm{CRE} = \Delta\left(\mathrm{N_{clean}} - \mathrm{N_{clear,clean}}\right) \quad (3.8)$$
$$\mathrm{ERF_{CS}} = \Delta\left(\mathrm{N_{clear,clean}}\right) \quad (3.9)$$

N_{clean} is the net flux excluding scattering and absorption by aerosols while $N_{clear,clean}$ is the net flux excluding scattering and absorption by aerosols and clouds. Thus, the IRF_{DRE} corresponds to the difference in net TOA radiative flux due solely to the scattering and absorption of aerosols (Section 1.3.4). The IRF_{DRE} also includes changes to land surface albedo but these are negligible here given the atmosphere-only setup of this work. The CRE is the forcing arising from changes to the interaction of cloud and radiation via aerosol indirect effects (Section 1.3.5). The clear-sky component corresponds to forcing arising from changes to absorption and emission of radiation by gas phase species.

The prescribed surface concentration of CH_4 in the model setup significantly constrains the response of CH_4 concentrations to oxidant perturbations and thus the radiative effect. However, the change in CH_4 concentration which would have occurred had surface CH_4 concentration not been constrained can be diagnosed by considering the change in CH_4 lifetime using Eq 3.10.

$$\frac{\Delta C}{C} = \left(\frac{\Delta \tau}{\tau} + 1\right)^{f} - 1 \quad (3.10)$$

Where C is the CH_4 concentration, $\Delta C$the change in CH_4 concentration which would have occurred following a perturbation if the surface concentration were allowed to respond, τ the methane lifetime (Appendix C1), $\Delta\tau$ the difference in lifetime between two simulations and f the feedback of CH_4 on its own lifetime (Fiore et al., 2009) taken as 1.28 for the PI (O'Connor et al., 2021). The forcing due to the change in CH_4 concentration was then calculated using the approach in Etminan et al (2016) using the baseline concentrations of CH_4 and N_2O of 802 ppb and 273 ppb respectively. Following Thornhill et al (2021b), this forcing was then scaled by 1.52 to account for the additional chemical production of O_3 and stratospheric water vapour.

Unlike CH_4, O_3 concentrations can respond to changes in E_{BVOC} and the resulting forcing is included in the clear sky forcing component, ERF_{CS}. The forcing due to ozone was also isolated using the radiative kernel from Skeie et al (2020) as in Thornhill et al (2021b).

3.3 Results

The simulations provide insight into how the chemical composition of the simulated PI atmosphere changes on the transition from a standard to state-of-the-art chemical mechanism (via comparison of ST_{con} and $CS2_{con}$) and, more importantly for this thesis, how the atmospheric and climatic responses to a doubling of E_{BVOC} differ between ST and CS2 (via side-by-side comparison of ST_{con} vs. ST_{2x} and $CS2_{con}$ vs. $CS2_{2x}$).

The mechanism acronyms ST or CS2 refer to a particular detail of the mechanism (e.g. "the OH + CH_4 rate constant in ST"). The individual runs are denoted with the mechanism acronym and subscript (e.g. ST_{con}) while the terms ST_{Δ} and $CS2_{\Delta}$ refer to the change between control and 2xE_{BVOC} simulations for a given parameter (i.e.,

"the change in O_3 in ST_Δ" refers to the change in O_3 between ST_{con} and ST_{2x}) (Eq 3.11, 3.12, 3.13). The same logic is used for ACM_{con} and ACM_{2x} (Eq 3.13).

As this study examines how the chemical mechanism affects the atmospheric response to $2xE_{BVOC}$, it is necessary to consider the difference between $CS2_\Delta$ and ST_Δ. This "difference of differences" is shown in Eq 3.14.

$$ST_\Delta = ST_{2x} - ST_{con} \quad (3.11)$$

$$CS2_\Delta = CS2_{2x} - CS2_{con} \quad (3.12)$$

$$ACM_\Delta = ACM_{2x} - ACM_{con} \quad (3.13)$$

$$CS2_\Delta - ST_\Delta = (CS2_{2x} - CS2_{con}) - (ST_{2x} - ST_{con}) \quad (3.14)$$

3.3.1 Gas Phase Chemistry

From a climatic perspective, the most important changes to the gas phase chemical composition of the atmosphere involve the oxidants O_3 and OH. O_3 acts as a GHG, with its radiative efficiency (forcing per unit change in concentration) greatest around the tropical tropopause (TT) (Lacis et al., 1990), as well as a major oxidant of monoterpenes which produce SOA. OH is the major oxidant of isoprene, another SOA precursor, as well as the key determinant of CH_4 lifetime which, as discussed in Section 3.2.4, is used to diagnose the change in CH_4 concentration and thus radiative forcing. OH and O_3 also oxidise SO_2 to form SO_4 aerosol in the gas phase and aqueous phase respectively with the important difference of these reactions on the aerosol distribution discussed in Section 1.3.2. Thus, the responses of the two mechanisms to $2xE_{BVOC}$ are driven primarily by the changes in O_3, HO_y(=HO_x + H_2O_2) and nitrated species (NO_y), the latter a key factor in O_3 transport. Therefore, to understand the climatically relevant changes, it is necessary to understand how the mechanism differs in these components (and their coupling) both in the baseline simulations and then in response to $2xE_{BVOC}$.

3.3.1.1 NOy

Reactive nitrogen (NO_x = NO + NO_2) and the less reactive reservoir species (NO_z), collectively termed NO_y (Section 2.5.5), play a central role in determining how BVOCs influence atmospheric composition. Local NO_x concentrations control the production of O_3 from BVOC-derived peroxy radicals (RO_2) oxidising NO to NO_2 (Section 1.2).

The partitioning of NO_x into NO_z affects the local NO_x concentration available for local ozone production, total NO_y loss via deposition and the transport of NO_z to more remote regions where it can form O_3 more efficiently (higher OPE). The major components of NO_z are $HONO_2$ (~70-75%), which serves as a sink for NO_x (and HO_x) due to its rapid loss via deposition, and the peroxyacyl nitrates, collectively termed PANs (the major constituent, $C_2H_3NO_5$, is referred to as PAN hereafter) (~13-20%) which are formed from reaction of NO_2 with BVOC

derivatives (e.g. $MeCO_3$) and act as long-range transporters of NO_x. ST includes PAN, MPAN ($C_4H_5NO_5$) and PPAN ($C_2H_6NO_6$) while CS2 also features PHAN ($C_2H_3NO_6$) and RTN26PAN which is produced from pinonaldehyde, an α-pinene oxidation product. PANs are destroyed by OH and thermal decomposition. PAN and PPAN are photolysed in both mechanisms and MPAN is only photolysed in ST. The influence of NO_y on O_3 in turn affects OH and thus CH_4 processing and aerosol formation.

Therefore, understanding the differences in the NO_y distribution between the baseline experiments and the response to $2xE_{BVOC}$ is critical to understanding the changes to atmospheric composition and climate.

ST_{con} vs. $CS2_{con}$

The tropospheric NO_y burden is 10% lower in $CS2_{con}$ than ST_{con}, primarily due to smaller burdens of PANs (-41%) and NO_x (-12.5%). NO_x is lower in $CS2_{con}$ throughout much of the troposphere by >10%, exceeding 20% at the poles and tropical upper troposphere with the only exception the tropical middle troposphere where it is 5-15% higher (Fig C1(a,b)). The differences in NO_y are driven by the partitioning between NO_x and the major NO_z components PANs and $HONO_2$. The NO_x lifetime with respect to these species (τ_{NOx_PANs}, $\tau_{NO_x_HONO_2}$; Eq 3.15, 3.16), and the lifetimes for NO_x reformation (τ_{PANs_NOx}, $\tau_{HONO_2_NOx}$; Eq 3.17, 3.18) or loss via deposition (τ_{PANs_dep}, $\tau_{HONO_2_dep}$; Eq 3.19, 3.20) can be used to assess the partitioning.

$$\tau_{NO_x_PANs} = \frac{B_{NO_x}}{F_{NOx \rightarrow PANs}} \quad (3.15)$$

$$\tau_{NO_x_HONO_2} = \frac{B_{NO_x}}{F_{NOx \rightarrow HONO_2}} \quad (3.16)$$

$$\tau_{PANs_NO_x} = \frac{B_{PANs}}{F_{PANs \rightarrow NO_x}} \quad (3.17)$$

$$\tau_{HONO_2_NO_x} = \frac{B_{HONO_2}}{F_{HONO_2 \rightarrow NO_x}} \quad (3.18)$$

$$\tau_{PANs_dep} = \frac{B_{PANs}}{F_{PANs\ Dep}} \quad (3.19)$$

$$\tau_{HONO_2_dep} = \frac{B_{HONO_2}}{F_{HONO_2\ Dep}} \quad (3.20)$$

Where, for a given region, B_A is the burden of species A and $F_{A \rightarrow B}$ is the flux of process of A → B.

The warm temperatures of the tropical PBL yield a short τ_{PANs_NOx} (~1 hr in lowest 1 km) and make PANs an inefficient NO_x reservoir. However, vertical transport into the colder tropical middle troposphere can increase τ_{PANs_NOx}. Between 4-6 km in the tropics, τ_{PANs_NOx} is ~2 days in ST_{con} and $CS2_{con}$. Both mechanisms simulate a maximum in the PANs concentration in the tropical mid troposphere although PANs are lower in $CS2_{con}$ throughout the whole troposphere for several reasons.

The PANs formation rate constant, k_{FPAN}, is ~5% lower in CS2 in the tropical PBL, where the bulk of PANs production occurs, while the thermal decomposition rate constant, k_{BPAN}, is 30-40% higher in the same region (i.e. faster decomposition). In addition, the concentration of $MeCO_3$, the precursor for PAN and thus the most important PANs precursor, is also significantly lower in $CS2_{con}$ (-60%) in the tropical PBL, attributed in part to the greater flux of $OH + C_5H_8$ at the expense of $O_3 + C_5H_8$ (Table 3.2), the latter a key $MeCO_3$ production pathway. The greater fraction of isoprene reacting with OH in $CS2_{con}$ is a direct result of higher OH in $CS2_{con}$ from isoprene HO_x-recycling and greater primary production (Section 3.3.4). As a result, loss of NO_x to PANs in the tropical PBL is slower in $CS2_{con}$ ($\tau_{PANs_NOx}$is 74% longer in $CS2_{con}$) and NO_x reformation from PANs is faster (τ_{PANs_NOx} is 25% shorter in $CS2_{con}$). These reinforcing factors result in lower net PANs production in $CS2_{con}$ and so less PANs, and thus reservoirs of NO_x, are transported into the free troposphere.

Accordingly, $CS2_{con}$ simulates lower PANs columns (and low altitude PANs) and higher NO_2 columns (>10% over Amazonia) over the major BVOC emission regions (Fig 3.2(a,b)). Regions further from BVOC emission sources (e.g. tropical oceanic regions) exhibit lower NO_2 columns (5-10%), characteristic of lower transport of NO_x away from sources.

Within the PBL, the greatest difference in PANs occurs over Africa since NO emissions are highest there given biomass burning. In the same region, $CS2_{con}$ exhibits much higher $HONO_2$ concentrations (>30% in central Africa) (Fig C1(c,d)) and more rapid loss of NO_x to $HONO_2$ ($\tau_{NOx_HONO_2}$ is 18% shorter). Thus, the lower sequestration of NO_x into PANs in $CS2_{con}$, coupled with the co-located higher OH concentrations, results in more $HONO_2$ despite CS2's rate constant for $HONO_2$ formation, k_{OH+NO_2}, being 10-15% lower in the tropical PBL. $HONO_2$ acts an efficient sink of NO_x via deposition ($\tau_{HONO_2_NOx}$~17 days compared to $\tau_{HONO_2_dep}$~30 hours the tropical PBL) whereas PANs do not. Total $HONO_2$ deposition is 0.78 TgN yr^{-1} higher in $CS2_{con}$ while PANs deposition is only 0.17 TgN yr^{-1} lower, helping to explain $CS2_{con}$'s lower NO_x and NO_y burdens as well as the lower NO_x in much of the free troposphere. Organonitrates ($RONO_2$), including $MeONO_2$ and isoprene hydroxy nitrate, are higher in $CS2_{con}$ than ST_{con} over the major emissions regions but these are of secondary importance to the role of PANs.

In the tropical mid troposphere (~4-6 km), loss of NO_x to PANs is more important than to $HONO_2$ ($\tau_{NOx_PANs} < \tau_{NOx_HONO2}$) and the higher NO_x in $CS2_{con}$ arises because less NO_x is sequestered to PANs: τ_{NOx_PANs} is much longer in $CS2_{con}$ than ST_{con} (11.4 vs 5.2 hours).

In the tropical upper troposphere (10-15 km), the importance of NO_x loss to $HONO_2$ ($\tau_{NOx_HONO_2}$ = 4.9 days in ST_{con} and 3.8 days in $CS2_{con}$) becomes comparable to loss to PANs (τ_{NOx_PANs} = 2.2 days in ST_{con} and 5.4 days

in $CS2_{con}$). Identifying the drivers of $CS2_{con}$'s lower NO_x is difficult. Greater loss in $CS2_{con}$ to $HONO_2$ arises in part from a 10-15% greater k_{OH+NO_2}. Furthermore, the longer τ_{PANs_NOx} (26 days in $CS2_{con}$ vs. 6 days in ST_{con}), primarily due to lower photolytic destruction, means more N remains in PANs reservoir.

2xE_{BVOC}

Following 2xE_{BVOC}, NO_2 columns decrease in regions of high E_{BVOC}, and increase over more remote regions (Fig. 3.2(c,d)), characteristic of greater increase in BVOC-derived RO_2 sequestering NO_x into PANs and $RONO_2$ (particularly over Africa) and subsequent greater transport of NO_z by these reservoir species. These changes are larger in ST_Δ than $CS2_\Delta$, indicating a greater increase in reservoir formation and transport.

In the lowest ~5 km, NO_x decreases over the major biogenic regions with attendant increases in PANs and $RONO_2$. However, the sink of NO_x to $HONO_2$ decreases, driven by the additional BVOCs suppressing HO_x (and thus OH + NO_2). Accordingly, in the lowest 2 km in the tropics $\tau_{NOx_HONO_2}$ increases by 18% in ST_Δ and 22% in $CS2_\Delta$ and $HONO_2$ deposition decreases by 10% in both, yielding higher NO_y burdens. The chain length of NO_x (Eq 3.21), which describes the number of O_3-producing reactions per termination reaction, also increases due to reduced loss to $HONO_2$, rising by 100-150% in the PBL over the major emission regions. This means a greater fraction of NO_x partitions to reservoirs (rather than sinks) and can be transferred to more remote regions, resulting in a global increase in NO_x in the lowest ~ 5km (Fig. 3.2(e,f)).

$$\text{length} = \frac{\sum F_{NO+RO_2}}{F_{OH+NO_2 \rightarrow HONO_2}} \quad (3.21)$$

However, the lower temperatures of the middle and upper troposphere (and the longer τ_{PANs_NOx} which makes PANs a more efficient reservoir) leads to lower NO_x throughout this region with both mechanisms exhibiting more than a 30% decrease, exceeding 40% in places in ST_Δ (Fig. 3.2(e,f)).

The increase in PANs arises from the increase in BVOC-derived precursors (e.g. $MeCO_3$). This comes predominantly from the doubling of BVOC emissions but is amplified by the increase in the fraction of isoprene undergoing ozonolysis (and thus producing $MeCO_3$) in both mechanisms at the expense of OH-initiated oxidation. This shift is due to OH-depletion and the greater depletion in ST_Δ leads to a 28% greater increase in $MeCO_3$ production via this process in ST_Δ (Section 3.3.4). The greater propensity to form PANs in ST and greater increase in PANs-precursors in ST_Δ leads to a greater reduction in τ_{NOx_PANs} (46% in ST_Δ vs. 40% in $CS2_\Delta$) and greater PANs burden increase (0.25 TgN, 66% vs 0.14 TgN, 61%). This is reflected in the large reductions in NO_x in ST_Δ (Fig 3.2(e,f)).

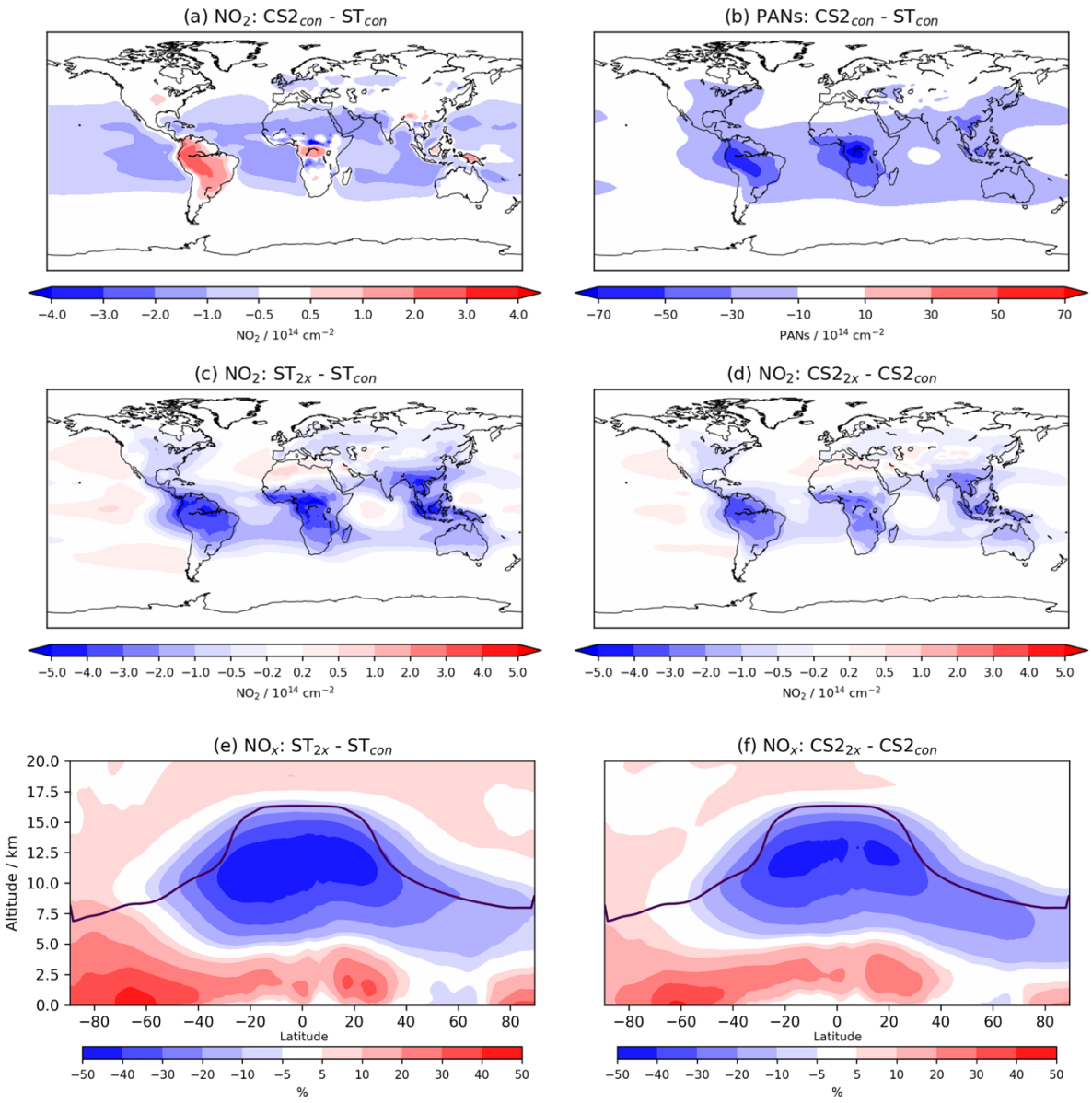


Figure 3.2. Difference in (a) NO_2 and (b) PANs columns between ST_{con} and $CS2_{con}$. Changes in NO_2 columns for (c) ST_{Δ} and (d) $CS2_{\Delta}$. Percentage changes in zonal mean NO_x for (e) ST_{Δ} and (f) $CS2_{\Delta}$.

3.3.1.2 O_3

The PD comparisons between ST, CS and CS2 (Archer-Nicholls et al., 2021, Chapter 2 (Fig 2.4) and Appendix B7) showed that CS2 simulates greater low altitude O_3 (< 500 m) than ST over much of the northern hemisphere (NH) and terrestrial southern hemisphere (Fig B24(b)) as well as higher O_3 in the NH free troposphere up to ~10 km (Fig B24(d)).

ST_{con} vs. $CS2_{con}$

The PD low altitude O_3 is higher in CS and CS2 than ST over NH terrestrial regions due to the CRI mechanisms' greater emissions of VOCs, particularly those with major anthropogenic contributions (43 TgC yr^{-1} higher in CS2) such as aromatics which are not considered in ST (Table 3 Archer-Nicholls et al., 2021 and Appendix B7).

However, in the PI the lower anthropogenic emissions of such species means the difference in total VOC emissions is smaller (~5.5 TgC yr^{-1} higher in CS2) and, coupled with lower anthropogenic NO emissions, this leads to a smaller difference (<1 ppb) in low altitude O_3 between ST_{con} and $CS2_{con}$ in much of the NH.

The greatest difference occurs over central Africa. This region has the highest NO emissions and is also where a substantial fraction of the higher emissions of monoterpenes (124 TgC yr^{-1}) and other biogenic species (30 TgC yr^{-1}) is located. Consequently, O_3 in $CS2_{con}$ is 10-15 ppb (30-40%) higher in central Africa while over the oceans O_3 is 1-3 ppb (5-10%) lower (Fig C2). This spatial variation is also seen in the tropospheric O_3 columns (Fig. 3.3).

The trend of greater tropical terrestrial O_3 and lower remote O_3 in $CS2_{con}$ follows the pattern of lower PANs production which results in greater NO_2 columns over the biogenic regions (Fig 3.2(a)), and thus O_3 production, but less transport of O_3-precursors to remote regions, contributing to the lower O_3 column (Fig 3.3(b)).

Vertically, O_3 in $CS2_{con}$ is 1-4 ppb (4-6%) lower in much of the free troposphere (Fig. 3.3(a)), broadly following the spatial difference in NO_x and leading to a lower tropospheric burden (275 Tg vs. 288 Tg). The large differences in NO_x (50-70 ppt, 20-30%) between ST_{con} and $CS2_{con}$ simulated around the TT yield the largest differences in O_3 with $CS2_{con}$ 6-10 ppb (6-10%) lower than ST_{con}.

2xE_{BVOC}

Doubling E_{BVOC} perturbs O_3 directly by increasing its chemical loss by reaction with BVOCs, and indirectly by changing the concentrations of HO_x and RO_2, which can produce or destroy O_3, depending on the local concentration of NO_x. Tropospheric burden increases of 9.7 Tg (3.4%) in ST_Δ and 11.4 Tg (4.2%) in $CS2_\Delta$ are simulated.

In both mechanisms, the tropospheric column O_3 decreases over the major biogenic emission regions but this is offset by increases over oceanic and some terrestrial regions where biogenic emissions are lower (Fig. 3.3(c,d)). The reduction over biogenic regions is greater in ST_Δ partly due to the greater increase in the fraction (and absolute flux) of BVOCs reacting with O_3 rather than OH (due to greater OH-depletion in ST_Δ, Section 3.3.3) coupled with the fact that, unlike in CS2, MT in ST destroys O_3 without producing any RO_2 which could reform O_3 (Section 3.1.2). The other driver is the aforementioned greater increase in PANs in ST_Δ which results in lower local NO_2 columns. The spatial reductions in NO_2 column (Fig 3.2(c,d)) and tropospheric O_3 column (Fig 3.3(c,d)) match well, particularly the greater reduction which occurs over the tropical Atlantic in ST_Δ but not in $CS2_\Delta$. ST_Δ's greater increases in O_3 and NO_2 in remote regions (e.g. Pacific) also indicate greater long range transport of NO_x.

This is important because the OPE in such remote regions will be higher than that in the BVOC emission regions and so more O_3 will be produced per molecule of NO.

Vertically, $2xE_{BVOC}$ results in increases of 1-5 ppb in much of the PBL and lower free troposphere (Fig. 3.3(e,f)), driven by NO_x increases from reduced $HONO_2$ formation. In the tropical mid troposphere, ST_Δ exhibits an decrease in O_3 of 2-5 ppb while reductions are <1 ppb in $CS2_\Delta$ coinciding with the larger decrease NO_x in ST_Δ attributed to a greater sequestration to PANs (Fig 3.2(e,f)).

From a climatic perspective, the most important region of change is the tropical tropopause (TT) where O_3's radiative efficiency is greatest (Lacis et al., 1990). The increase in O_3 at the TT is ~10 ppb greater in ST_Δ than $CS2_\Delta$ but, as with the differences in ST_{con} and $CS2_{con}$, identifying the drivers of the larger response in ST_Δ is difficult. Despite the substantial reduction in NO_x in the upper tropical troposphere (Fig 3.2(e,f)), O_3 production via NO + HO_2 and NO + RO_2 around the TT is higher in ST_{2x} and $CS2_{2x}$ than their corresponding baseline runs. This comes from greater increases in co-reactants concentrations: HO_2 is 40% higher around the TT (exceeding 50% in places in ST_Δ) (Fig 3.4(e,f)), outweighing the decreases in NO_x. The chain length also increases by more in ST_Δ (120%) than $CS2_\Delta$ (60%) in this region.

In this region HO_2 production increases by more in ST_Δ than $CS2_\Delta$, primarily due to greater photolysis of peroxide and carbonyls such as HCHO (Fig 3.5(f) shows $CS2_\Delta$ - ST_Δ). The high-altitude increase of these organic species is greater in ST_Δ due to the greater depletion of oxidants at low altitude (Section 3.3.1.3) and the consequent greater dispersal that the BVOCs and their oxidation products can undergo before destruction. In $CS2_\Delta$, the smaller reduction in oxidants means that these species do not ascend as far; as a result the increase in HO_2 production from carbonyl and peroxide photolysis increases by more in $CS2_\Delta$ than ST_Δ in the mid tropical troposphere where O_3's radiative efficiency is lower. The climatic impact is discussed in Section 3.4.1.1.

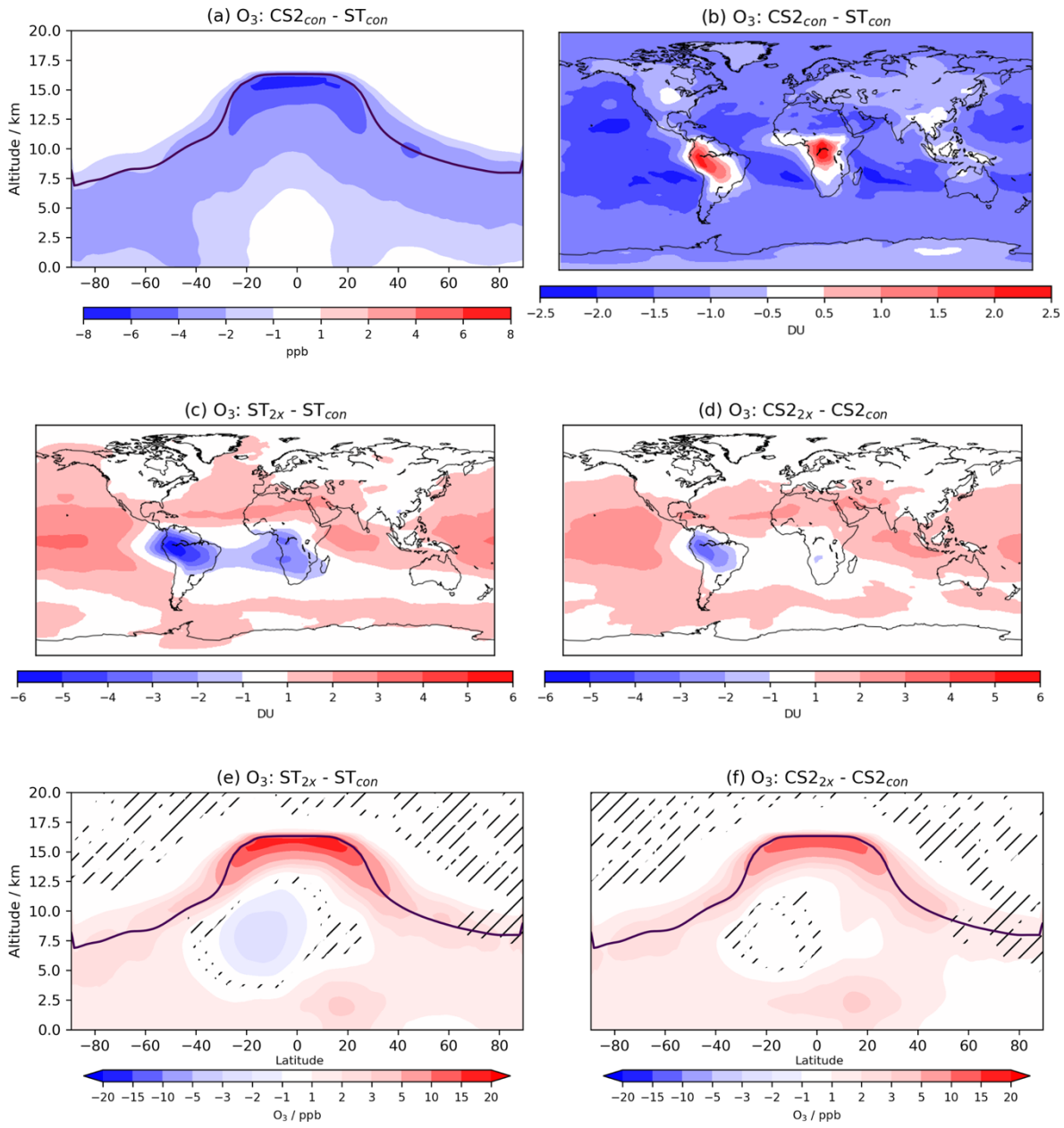


Figure 3.3. Difference in (a) zonal mean O_3 and (b) O_3 column between ST_{con} and $CS2_{con}$. Changes in O_3 columns for (c) ST_{Δ} and (d) $CS2_{\Delta}$. Changes in zonal mean tropospheric O_3 for (e) ST_{Δ} and (f) $CS2_{\Delta}$. Shading in (e,f) shows regions that are statistically insignificant at the 95% confidence level.

3.3.1.3 HO_x, CH_4 and H_2O_2

As discussed in Section 1.2.1, the bulk of OH production comes from $O(^1D)$ (primary production; Eq 3.22) and HO_2 + NO (Eq 3.23). While BVOCs destroy OH via direct reaction with subsequent HO_x removal via processes like hydroperoxide deposition, OH and HO_2 can be produced from BVOC oxidation products such as H_2O_2 and other hydroperoxides (ROOH) and carbonyls (Eqs 3.24, 3.25). The major HO_x-recycling processes of CS2's new isoprene chemistry are included in Eq 3.24.

$$O(^1D) + H_2O \rightarrow OH + OH \quad (3.22)$$

$$HO_2 + NO \rightarrow OH + NO_2 \quad (3.23)$$

$$ROOH + h\nu \rightarrow OH + \text{other products} \quad (3.24)$$

$$ROOH \text{ or carbonyl} + h\nu \rightarrow HO_2 + \text{other products} \quad (3.25)$$

ST_{con} vs. $CS2_{con}$

Low altitude (<500 km) OH in $CS2_{con}$ is considerably higher than ST_{con} in the major biogenic emission regions of Amazonia (0.1-0.5×10^6 cm^{-3}, 100-250%), central Africa (0.5-1.0×10^6 cm^{-3}, 100-150%) and Southeast Asia (0.1-0.5×10^6 cm^{-3}, ~200%). OH is also higher over the secondary emission regions of North America (50-100%) and Eurasia (50-100%) (Fig 3.4(a)). There are several drivers of this difference.

Over Amazonia, $CS2_{ST,\ isop}$ reveals the updated isoprene chemistry is responsible for about half the increase in low altitude OH (Fig C3(a,b)) with the other half coming from greater primary production (Eq 3.22; Fig C3(e,f)) from the higher O_3 (Figs 3.3(b), C2) and higher secondary production arising from the higher VOC emissions. As discussed in Section 3.1, the dominant contributor to the higher VOC emissions in the CS2 simulations is monoterpenes because monoterpene oxidation in ST only contributes aerosol and acts as an oxidant sink.

Over central Africa, where NO emissions are much higher, the updated isoprene chemistry is responsible for only around ~¼ of the higher OH in $CS2_{con}$. The greater primary and secondary production (Eq 3.23), which stem from the lower sequestration of NO_x to PANs and greater VOC emissions in $CS2_{con}$, are more important over Africa. $CS2_{con}$ simulates lower oceanic OH concentrations (0.1-0.5×10^6 cm^{-3}, 10-25%), caused by lower O_3 and primary production (Figs C2, C3(e,f)).

In the tropical mid-troposphere, OH is 2-3×10^5 cm^{-3} (10-20%) higher in $CS2_{con}$ (Fig 3.4(b)). $CS2_{ST,\ isop}$ reveals the primary driver is not the higher secondary production from isoprene (Fig C3(c,d))), but greater fluxes of HO_2 + NO (+15-20%), which shows very similar spatial change to OH (Fig 3.5(a)). There is a smaller contribution from the photolysis of H_2O_2 and ROOH (Eq. 3.24) (Fig 3.5(b)). The yield of H_2O_2 from isoprene ozonolysis in CS2 (38.5%) is much higher than in ST (9%) while α-pinene and β-pinene in CS2 also produce H_2O_2 directly during ozonolysis at yields of 17.5% and 20% respectively (MT in ST produces none). The oxidation of α-pinene and β-pinene also yields a range of other peroxides.

The greater HO_2+NO flux arises from a 4.5% greater rate constant in CS2, 5-15% higher NO_x (due to greater sequestration of NO_x to PANs in ST_{con}) (Fig C1) and higher HO_2 (4-6% in most of the troposphere, rising to >10% in the tropical lower troposphere). As discussed in Section 2.5.2 and Appendix B7, CS2 simulates greater HO_2 in the tropical PBL and low troposphere due to a combination of the updated chemistry and higher VOC emissions. Analysis of the major HO_2 production terms reveals the photolysis of hydroperoxides and carbonyls (also

produced by pinene oxidation in CS2) is much larger in $CS2_{con}$ than ST_{con} in the tropical PBL and lower troposphere, contributing to the higher HO_2 (Fig 3.5(e)). The increase in HO_2 + NO in the lower free troposphere also occurs almost exclusively over land, further evidence that it is driven by the reactions of BVOCs and their derivatives.

The different OH distributions simulated by ST_{con} and $CS2_{con}$ influence the processing of CH_4. The LBC means the CH_4 burdens from the ST and CS2 simulations differ by less than 0.1% and so the differences in CH_4 + OH flux are determined by OH concentration and the rate constant, k_{OH+CH4}, whose strong positive temperature dependence restricts the bulk of CH_4 oxidation to the warm lower tropical troposphere (k_{OH+CH4} is 5-6x greater at 3 km than 12.5 km in the tropics). The difference in the k_{OH+CH4} expressions used by ST and CS2 is greatest at low temperatures (k_{OH+CH4} in CS2 is 7.6% higher at 240 K) but reduces to 3% at 273 K and 1% at 290 K. Therefore, within the PBL and lower tropical troposphere, where temperatures are typically 270-300K, the difference in k_{OH+CH4} plays a smaller role and the variation in CH_4 oxidation flux between ST_{con} and $CS2_{con}$ is controlled primarily by the difference in OH. Accordingly, the CH_4 lifetime, τ_{CH_4} (Appendix C1 for definition), in $CS2_{con}$ of 7.70 years is 3% lower than ST_{con} (7.92 years), driven by a greater tropospheric flux of CH_4 + OH.

The variation in terrestrial and oceanic OH between ST_{con} and $CS2_{con}$ (Fig 3.4(a)) also leads to differences. In the lowest 1 km where ~19% of all tropospheric CH_4 oxidation occurs, $CS2_{con}$'s higher terrestrial OH concentrations result in a 25% greater methane oxidation flux (2.1 Tg yr^{-1}) over land, offsetting almost entirely the lower flux (-7.2%) over the oceans. In other words, without the isoprene HO_x-recycling and other terrestrial low altitude processes discussed earlier, global low altitude CH_4 oxidation flux would be higher in ST_{con}.

A larger difference is simulated in the free troposphere where CH_4 oxidation flux is 7.3% greater in $CS2_{con}$ between 2.5 and 10 km, and >10% higher in the equatorial lower troposphere. The k_{OH+CH4} difference plays only a minor role: in the region with the largest flux difference (-2° S, ~3.5 km), k_{OH+CH4} in CS2 is 3% higher yet the flux is 15% higher. Rather the flux difference is driven by higher OH in the tropical lower and mid troposphere in $CS2_{con}$ (Fig 3.4(b)), arising from greater secondary production in a region where temperatures are sufficiently high for CH_4 oxidation to be important.

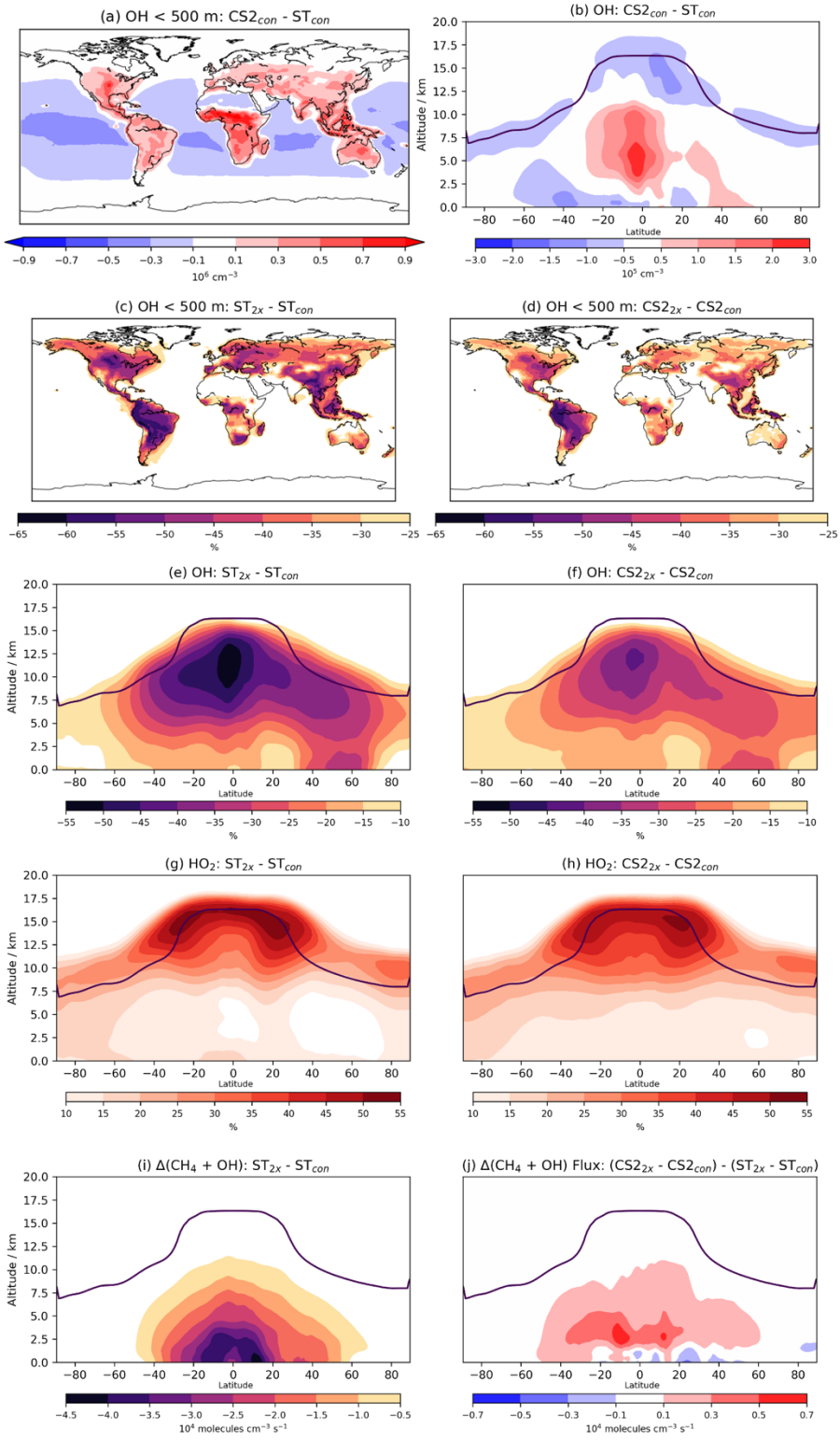


Figure 3.4. Difference in (a) low altitude OH and (b) zonal mean OH between ST_{con} and $CS2_{con}$. Average change in OH < 5 km (c) ST_{Δ} and (d) $CS2_{\Delta}$, zonal mean OH for (e) ST_{Δ} and (f) $CS2_{\Delta}$ and zonal mean HO_2 for (g) ST_{Δ} and (h) $CS2_{\Delta}$. Zonal mean change in OH + CH_4 flux for (i) ST_{Δ} and (j) difference in change in OH + CH_4 flux between ST_{Δ} and $CS2_{\Delta}$.

$2xE_{BVOC}$

Doubling E_{BVOC} depletes OH in the tropical PBL and throughout the free troposphere (Fig 3.4(c-f)) while HO_2 increases (Fig 3.4(g,h)).

In the tropical terrestrial PBL and lower free troposphere, the decrease in OH is driven by increases in the fluxes of OH with BVOCs and secondary CO, the latter in particular driving the increase in HO_2. By contrast, in the upper troposphere where the largest absolute and relative OH decreases are simulated, the reduction in NO_x due to sequestration into reservoirs (chiefly PANs) reduces OH production via reaction of HO_2 + NO.

While both mechanisms exhibit the same response in the PBL and free troposphere, the relative reduction in OH is smaller in $CS2_\Delta$. In the upper troposphere this is due to the smaller reduction in NO_x (Fig 3.2(e,f)) from the less efficient sequestration into PANs. However, the cold temperatures of this region make it less important for CH_4 oxidation. In the warmer terrestrial PBL, the lower relative reduction in $CS2_\Delta$ comes from, among other things, the enhanced HO_x-recycling from isoprene which reduces the magnitude of the OH sink.

In the tropical PBL and tropical free troposphere, of particular interest for CH_4 oxidation given the higher temperatures, OH decreases by >65% (>55%) and >50% (>35%) over Amazonia and Africa respectively in ST_Δ ($CS2_\Delta$) (Fig 3.4(c,d)) leading to zonally-averaged reductions of >25% in ST_Δ compared to ~20% in $CS2_\Delta$. These mechanistic differences arise from a greater increase in OH production in $CS2_\Delta$, driven by increases in H_2O_2 and ROOH photolysis extending up from the PBL into the lower troposphere, and HO_2 + NO in the lower free troposphere (Fig 3.5(c,d)).

Greater increases in H_2O_2 in $CS2_\Delta$ (Fig C8(a-d)) stem in part from the much higher yield from BVOC oxidation, as previously mentioned, and the greater increase in reactive carbon emissions from monoterpenes (124 TgC yr^{-1} in $CS2_\Delta$, zero in ST_Δ). CS2's inclusion of pinene oxidation also means HO_2 (and thus HO_2 + NO) increases by a greater amount in $CS2_\Delta$ via direct production and indirectly via the production of carbonyls and peroxides whose photolysis yields HO_2 in the lower free troposphere (Eq 3.25, Fig 3.5(e,f)).

Consequently, $2xE_{BVOC}$ yields increases in τ_{CH_4} of 25.7% (2.03 yr) for ST_Δ and 21.2 % (1.63 yr) for $CS2_\Delta$, via decreases in CH_4 oxidation by OH (-22.9% and -19.5% respectively). The climatic implications are discussed in Section 3.4.1.2.

In addition to secondary OH production, the increases in H_2O_2 are important for SO_4 aerosol. The aqueous phase oxidation of SO_2 by H_2O_2 is a major pathway for SO_4 aerosol production, accounting for ~50% of all SO_2 oxidation in ST_{con} and $CS2_{con}$. An increase to this pathway (at the expense of the gas phase oxidation of SO_2) will change the aerosol size distribution since it adds mass to existing aerosol without increasing aerosol number (Section 1.3.2). The impact of this change in the context of SO_4 aerosol is discussed in Section 3.3.3.3.

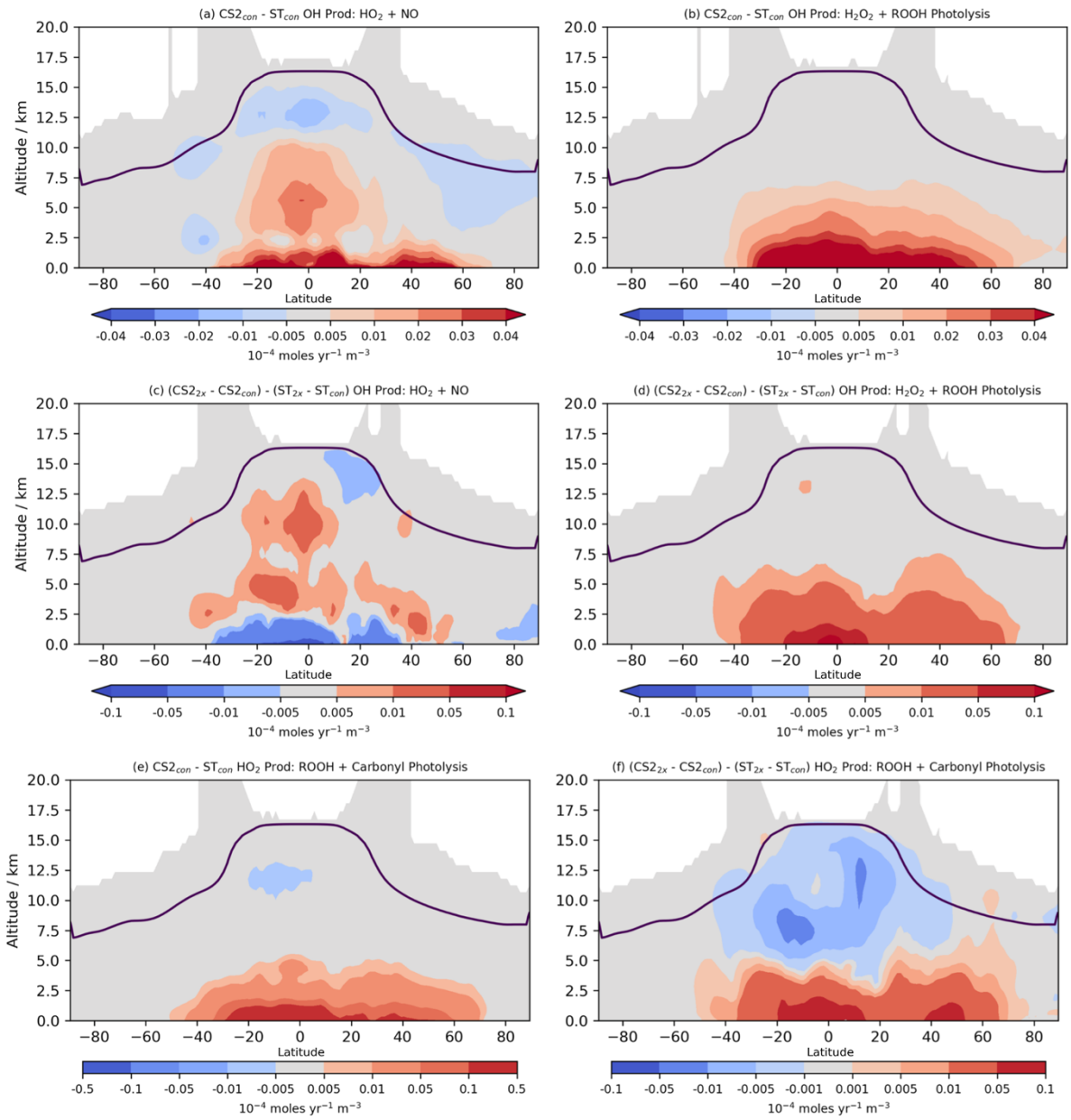


Figure 3.5. Zonal mean difference between $CS2_{con}$ and ST_{con} for OH production from (a) HO_2 + NO and (b) H_2O_2 and other peroxides. Zonal mean difference between ST_{Δ} and $CS2_{\Delta}$ for OH production from (c) HO_2 + NO and (d) H_2O_2 and other peroxides. (e) Zonal mean difference between $CS2_{con}$ and ST_{con} for HO_2 production from peroxide and carbonyl photolysis. (f) Zonal mean difference between ST_{Δ} and $CS2_{\Delta}$ for HO_2 production from peroxide and carbonyl photolysis. [Note different scales]

3.3.1.4 BVOCs

Significant global and regional differences are simulated in the processing of isoprene and monoterpenes between the mechanisms. The isoprene burden (0.53 Tg) in $CS2_{con}$ is roughly half that of ST_{con} (1.07 Tg) and a similar ratio is simulated between $CS2_{2x}$ (1.69 Tg) and ST_{2x} (3.50 Tg) (Table 3.2). The lower isoprene burden in $CS2_{con}$ is attributed to the greater OH concentrations in the high BVOC emission regions given OH's role as the dominant oxidant of isoprene: OH is responsible for 87% of isoprene oxidation in $CS2_{con}$ compared to 78% in ST_{con}.

Consequently, isoprene's global lifetime in $CS2_{con}$ (6.1 hr) is half that in ST_{con} (12.4 hr) (Fig 3.6), indicating that isoprene will undergo less dispersion from source regions before oxidation in $CS2_{con}$ with an attendant reduction in SOA dispersion. Isopene's lifetime in $CS2_{con}$ also agrees with Karset et al (2018) who calculated a 6.0 hr global lifetime.

$2xE_{BVOC}$ in both mechanisms leads to over a 3-fold increase in isoprene burden (~225%), illustrating isoprene's feedback on its own lifetime by acting as a sink for OH, analogous to CH_4's feedback on its own lifetime (Fiore et al., 2009; Holmes., 2018). Isoprene lifetime's increases by less in absolute (8.2 hr vs. 3.7 hr) and relative (66% vs. 61%) terms in $CS2_{\Delta}$ due to the smaller reductions in OH (Fig 3.4(c,d)) which dampen the impact of $2xE_{BVOC}$ (Fig 3.6). This also leads to a smaller increase in isoprene dispersion in $CS2_{\Delta}$ and the consequences for SOA are discussed in Section 3.3.2.1.

The fraction of isoprene destroyed by OH decreases from 87% to 83% ($CS2_{\Delta}$) and 78% to 72% (ST_{Δ}) and a greater fraction of isoprene undergoes ozonolysis instead. As discussed in Section 3.3.1.1, this has important consequences for O_3 and NO_x, both directly as the isoprene sink for O_3 increases disproportionately, and indirectly via the NO_y distribution since $MeCO_3$, the precursor of PAN, is produced directly from isoprene ozonolysis with a yield of ~10% in both mechanisms. The greater increase in $O_3 + C_5H_8$ in ST_{Δ} (246 vs. 157 Tg yr^{-1}) results in a greater 28% increase in $MeCO_3$ production from isoprene ozonolysis, contributing to the greater increase in PANs in ST_{Δ} and resulting O_3 distribution (Section 3.3.1.2).

Unlike isoprene, the burdens and lifetimes of MT are more similar in ST_{con} (5.1 hr) and $CS2_{con}$ (4.6 hr) (Fig 3.6(d), Table 3.2), both agreeing reasonably well with 5.3 hr of Karset et al (2018). Similar increases in burdens and lifetimes following $2xE_{BVOC}$ are also simulated. This degree of similarity comes from the greater importance of ozonolysis (low altitude O_3 differs by less in relative terms between mechanisms) and reduced dominance of OH (which exhibits much greater mechanistic disparity).

Nevertheless, the fraction of MT oxidised by OH is noticeably higher in $CS2_{con}$ and $CS2_{2x}$ with a corresponding shorter lifetime with respect to OH (Fig 3.6(e). This arises partly from CS2's higher local OH concentrations but also to the partitioning of monoterpene into two species. β-pinene's exocyclic double bond is less reactive with O_3 thanα-pinene's endocyclic double bond. β-pinene's rate constants with OH and O_3 are ~40% higher and ~80% lower respectively than for α-pinene while the MT tracer in ST simply has the rate constants of α-pinene. Thus, while 2/3 of the monoterpene mass in CS2 reacts in a similar way to the MT tracer in ST, the other 1/3 greatly favours reaction with OH over O_3, shifting the overall distribution more towards OH, resulting in monoterpene having longer lifetimes with respect to O_3 in the CS2 simulations.

Table 3.2. BVOC burdens and reaction flux breakdowns. Values in parentheses show percentage change relative to respective control simulation and values in square brackets show difference between $CS2_{con}$ and ST_{con}. Rounding means some percentage values do not sum to 100.

	ST_{con}	**ST_{2x}**	**CS_{con}**	**$CS2_{2x}$**
C_5H_8 burden / Tg	1.07	3.48 (+225%)	0.53 [-49.5%]	1.69 (+219%)
MT burden / Tg	0.082	0.214 (+161%)	0.074 [-9.8%]	0.200 (+170%)
Global C_5H_8 Oxidation breakdown (% OH, O_3, NO_3)	78 / 21 / 1	72 / 28 / 1	87 / 12 / 1	83 / 16 / 1
MT Oxidation breakdown (% OH, O_3, NO_3)	29 / 66 / 4	20 / 77 / 3	52 / 43 / 5	44 / 52 / 4

Regional analysis of Amazonia and Africa further illustrates the mechanistic differences. In both regions the fraction of isoprene destroyed by OH is 10 percentage points higher in CS2 than ST in the PBL, increasing to over 20 percentage points for monoterpene species (Fig C5). As the other major oxidant, the O_3 fraction mirrors OH. NO_3 is a minor sink for C_5H_8 but more influential for the monoterpenes, contributing 5-10% in the African PBL where NO_x is higher.

The enhanced oxidising capacity in the CS2 simulations and shorter lifetimes lead to lower BVOC dispersion and a greater fraction of isoprene and, to a lesser extent, MT being oxidised at low altitude. For example, over Amazonia 71% of all isoprene oxidation occurs within the lowest 1 km in $CS2_{con}$ compared to only 57% in ST_{con}. This flux difference is equivalent to 5% of the total global isoprene oxidation flux in ST_{con}. A similar pattern is simulated over Africa.

The suppression of oxidants and increases in BVOC lifetimes with $2xE_{BVOC}$ leads to greater BVOC dispersion. The fraction of isoprene oxidised in the lowest 1 km over Amazonia decreases in both mechanisms but remains higher in $CS2_{2x}$ (63%) than ST_{2x} (55%). This has direct consequences for SOA via the formation of the condensable Sec_Org tracers: 72% (63%) of all Sec_Org production over Amazonia occurs within the lowest ~1 km in $CS2_{con}$ ($CS2_{2x}$), compared to 62% (55%) in ST_{con} (ST_{2x}) (Fig. 3.7(a)) with this trend also simulated over Africa and throughout the tropical PBL (Fig 3.7(b-d)). The implications for SOA are discussed in Section 3.3.2.1.

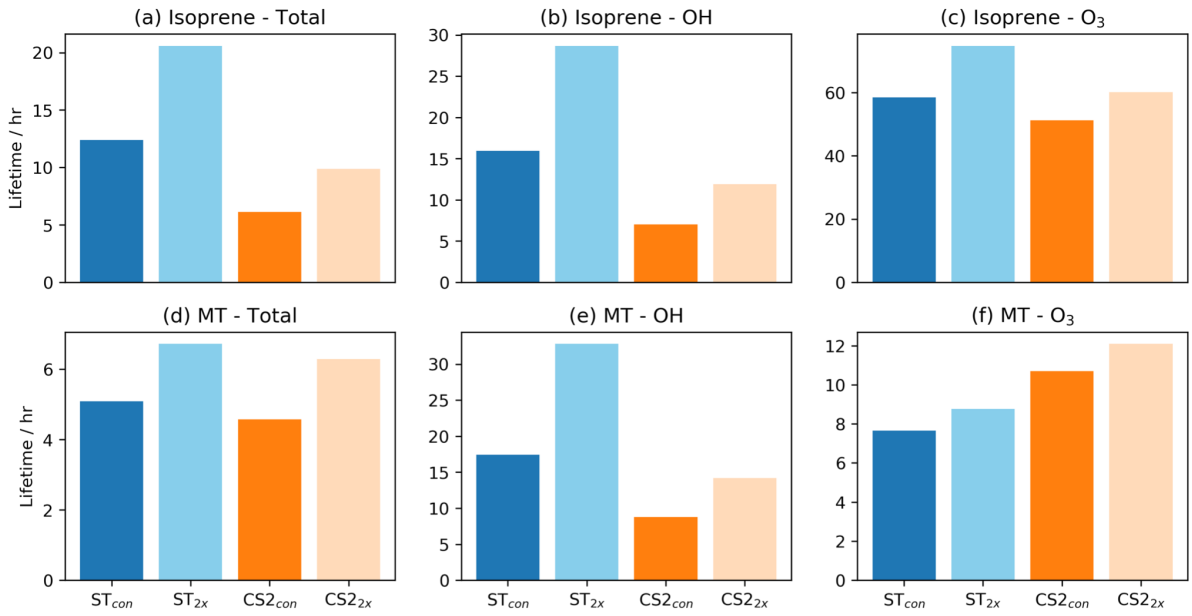


Figure 3.6. Global average lifetimes of isoprene (a) and monoterpene (d) and lifetimes with respect to (b,e) OH and (c,f) O_3. Note different vertical scales.

3.3.2 Aerosol

The differences between ST and CS2 have knock-on effects for the formation and growth of both SOA and SO_4 aerosol. The SOA and SO_4 aerosol burdens are 11% and 32% lower respectively in $CS2_{con}$ than ST_{con} with negligible differences in the burdens of sea-salt (SS), black carbon (BC) or primary organic carbon (POA) aerosol (Tables 3.3, C1). The aerosol response to a doubling of E_{BVOC} is unsurprisingly dominated by SOA burden increases of 120% in ST_{Δ} and 115% in $CS2_{\Delta}$ as well as decreases of 7-10% in the burdens of SO_4, POA and BC in both mechanisms. In this section I discuss how the differences in chemistry influence the aerosol in the control runs and the response to $2xE_{BVOC}$.

Table 3.3. SOA and SO_4 components burdens and lifetimes. Values in parentheses show percentage change in $2xE_{BVOC}$ experiment relative to corresponding control run. Values in square brackets show the percentage difference between ST_{con} and $CS2_{con}$.

Burden / Tg	ST_{con}	ST_{2x}	$CS2_{con}$	$CS2_{2x}$
SOA	0.524	1.161 (+121%)	0.471 [-11.4%]	1.010 (+114%)
SO_4	0.829	0.759 (-8.4%)	0.561 [-32.3%]	0.519 (-7.5%)
Lifetime / days				
SOA	4.42	4.96 (+12.2%)	3.98 [-10.0%]	4.27 (+7.3%)
SO_4	6.14	5.88 (-4.2 %)	5.58 [-9.1%]	5.19 (-7.0%)

3.3.2.1 SOA

Section 3.3.1.4 showed how the greater oxidising capacity of CS2 leads to greater production of Sec_Org at low altitude. This in turn impacts where and how Sec_Org contributes to SOA which is important for SOA's climatic impact (Sporre et al., 2020 and Section 1.4.6).

ST_{con} vs. $CS2_{con}$

The mechanistic variation in the location of Sec_Org production leads to greater condensation fluxes of Sec_Org to the SOA Aitken and accumulation modes in $CS2_{con}$ below ~1km and lower fluxes above this (Fig C6(a,b)). In addition, a greater fraction of Sec_Org condenses on to the accumulation mode in $CS2_{con}$ (65% vs. 61%) at the expense of the Aitken mode (33% vs. 37%), particularly over Amazonia (Fig C7(ab)), because the accumulation mode number concentration is greatest in the tropical boundary layer whereas the Aitken mode number concentration peaks in the tropical mid troposphere. Growing Aitken particles to accumulation mode size (and to a lesser extent growing the size of existing accumulation mode particles) will increase the aerosol DRE, since accumulation mode particles are more efficient scatters of solar radiation than Aitken mode particles, and can also lead to a more negative AIE by increasing the number of CCN. Adding mass to SOA at higher altitudes will also lead to a longer SOA lifetime.

The vertical differences in Sec_Org production, and thus condensation to aerosol, result in $CS2_{con}$ simulating more SOA at low altitude over the tropics and NH mid latitudes but less in the free troposphere (Fig 3.7(e)) and an 11.4% smaller SOA burden (B_{SOA}) (Table 3.2). The bulk of the B_{SOA} difference between $CS2_{con}$ and ST_{con} occurs

in the Aitken mode (30% difference) (Table C2) whose concentration is lower in $CS2_{con}$ throughout almost the whole troposphere, driven in part by the lower fraction of Sec_Org which condenses on the Aitken mode in $CS2_{con}$. The accumulation mode exhibits a much smaller burden difference (-0.3%) but also substantial spatial heterogeneity: greater concentrations at low altitude in $CS2_{con}$, particularly in the tropics, and lower concentrations in the free troposphere; direct results of the location of Sec_Org production.

The differences in the location of Sec_Org production and SOA concentration are reflected in the SOA lifetime which is 10% shorter in $CS2_{con}$ (3.98 days) than in ST_{con} (4.42 days). The Aitken mode lifetime in $CS2_{con}$ (3.04 days) is 22% shorter than in ST_{con} (3.89 days), primarily due to a 30% shorter lifetime with respect to condensational growth to the accumulation mode. This is caused by the higher Sec_Org concentrations in the PBL in $CS2_{con}$ (i.e. closer to the BVOC emission source) which allow the Aitken mode to grow to accumulation mode size more rapidly. By contrast, in ST_{con} more condensation to the Aitken mode occurs above the PBL (Fig C6(a)) where the Aitken mode number concentration is higher and so the Sec_Org mass is distributed between a greater number of particles, leading to fewer particles reaching accumulation mode size and an attendant longer Aitken mode lifetime.

2xE_{BVOC}

A doubling of E_{BVOC} leads to more than a doubling of B_{SOA} (ST_{Δ} 121%, $CS2_{\Delta}$ 114%) as a greater fraction of BVOC oxidation occurs further from source and at higher altitude due to oxidant depletion (Fig 3.7(a-d)) and longer BVOC lifetimes (Fig 3.6). The greater dispersion results in increases in τ_{SOA} with the greater oxidant suppression in ST_{Δ} (Fig 3.5) yielding a larger lifetime increase (0.54 days, 12.2%) than $CS2_{\Delta}$ (0.29 days, 7.3%).

The fraction of Sec_Org condensing on to the accumulation mode (68% ST_{2x}, 73% $CS2_{2x}$) increases at the expense of the Aitken mode (30% ST_{2x}, 26% $CS2_{2x}$) driven in part by a small increase (2-5%) in the tropical PBL accumulation number concentration and a reduction in Aitken mode number concentrations (from enhanced growth and coagulation to the accumulation mode). Over Amazonia and Africa, $CS2_{\Delta}$ exhibits a greater increase in flux to the accumulation mode and a smaller increase in the flux to the Aitken mode than ST_{Δ} (Fig C7(c,d)) since the greater oxidant depletion in ST_{Δ} allows greater dispersion of BVOCs.

ST_{Δ} and $CS2_{\Delta}$ exhibit ~10% decreases in the nucleation mode burden due to increased condensational growth and loss to the coagulation sink but substantial increases in the Aitken (91-97%) and accumulation (123-134%) modes, albeit with larger increases for ST_{Δ}. The fact that the Aitken mode burden increases by <100% and the accumulation mode by >100% is indicative of the shift towards the accumulation mode in both mechanisms as Aitken mode particles grow to accumulation mode size.

The lifetime of the accumulation mode SOA, of particular interest given its ability to influence climate by scattering solar radiation and acting as CCN, increases by 10.4 hours (13%) in ST_{Δ} but only 5.4 hours (6.7%) in $CS2_{\Delta}$. The larger increase in ST_{Δ} occurs in part from the greater increase in vertical dispersion of Sec_Org in

ST_{Δ} which leads to a greater increase in the condensational flux onto Aitken mode aerosol above the PBL (Fig C6(c)) which can then grow to accumulation mode size.

Accordingly, the increase in the transfer of SOA mass from the Aitken mode to the accumulation mode by Aitken mode growth is higher in ST_{Δ} than $CS2_{\Delta}$ above the PBL (Fig C6(f)) and the resultant accumulation mode particles have a longer lifetime, facilitating greater dispersion from major BVOC emission regions. This is seen by the larger increases in SOA accumulation mode column (ACC_{SOA_COL}) over the southern Atlantic, Indian ocean and eastern Pacific in ST_{Δ} (Fig 3.7(h)). By contrast, close to emission sources the increase in ACC_{SOA_COL} is greater in $CS2_{\Delta}$. The climatic implications are discussed in Section 3.4.2.

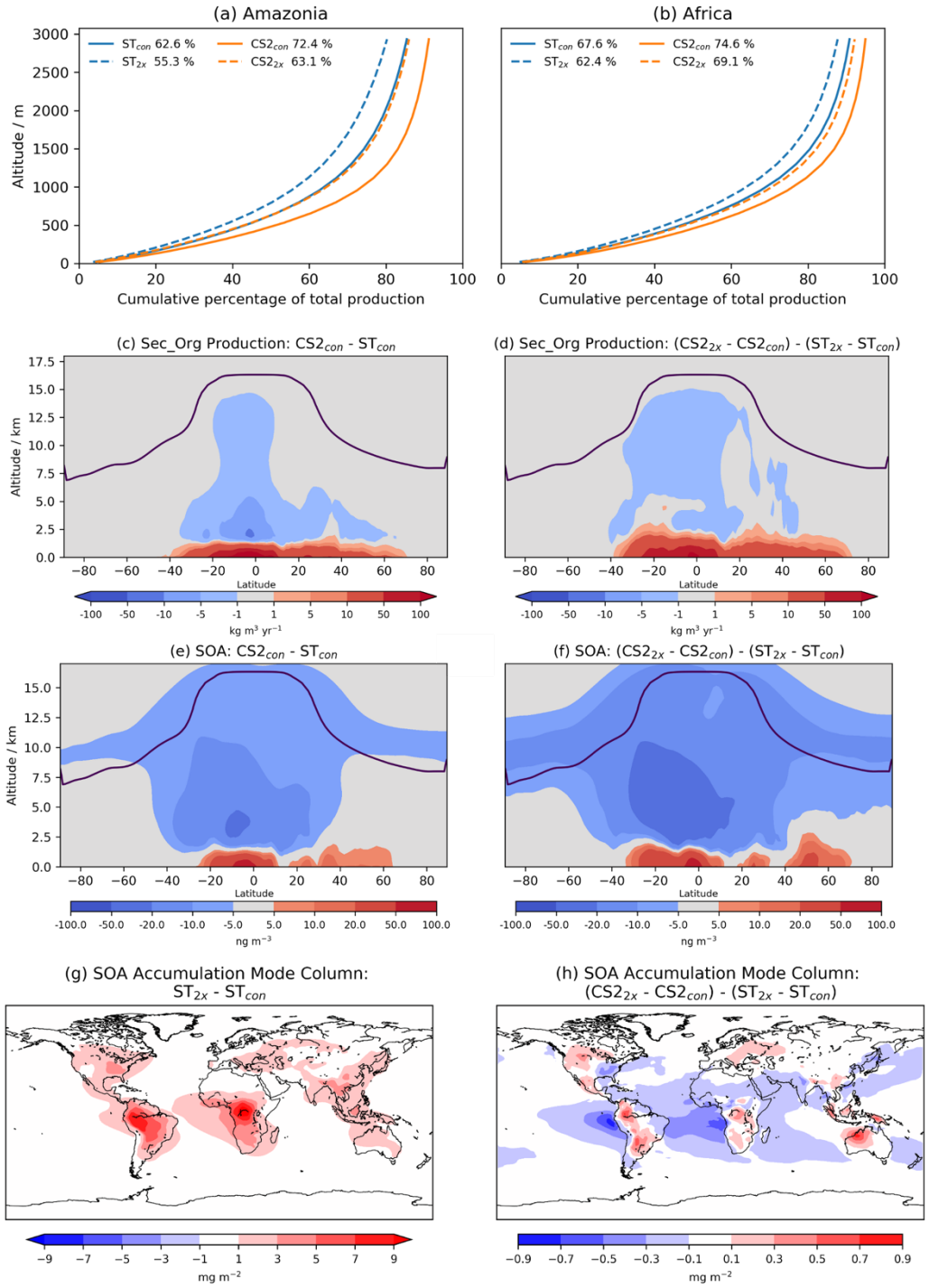


Figure 3.7. Cumulative fraction of Sec_Org production with altitude over (a) Amazonia and (b) Central Africa. (c) Zonal mean difference in Sec_Org production flux between ST_{con} and $CS2_{con}$ and (d) zonal mean difference in Sec_Org production flux between ST_{Δ} and $CS2_{\Delta}$. Zonal mean (e) difference in SOA concentration between ST_{con} and $CS2_{con}$ and (f) difference between ST_{Δ} and $CS2_{\Delta}$ for SOA concentration. (g) Change in accumulation mode SOA column (AC_{CSOA}) for ST_{Δ} and (h) difference between ST_{Δ} and $CS2_{\Delta}$ for accumulation mode SOA column.

3.3.2.2 Primary Organic Aerosol

Primary organic carbon aerosol (POA) is tracked separately to SOA to allow the effects of oxidant-aerosol chemistry on SOA to be isolated. The POA burdens (B_{POA}) in ST_{con} and $CS2_{con}$ are unsurprisingly very similar, differing by <0.02%, as the same POA emissions were used and POA is not directly affected by chemistry. Both mechanisms exhibit a ~10% reduction in B_{POA} (~0.08 Tg) with $2xE_{BVOC}$ (~13% of the B_{SOA} increase) driven by a ~32% reduction in the Aitken mode burden which outweighs a 7% increase in the accumulation mode burden. POA lifetime decreases from 5.7 days to 5.2 days in ST_{Δ} and $CS2_{\Delta}$.

The reduction in the Aitken mode is dominated by an increased transfer of mass to the accumulation mode driven by the additional Sec_Org. While Sec_Org does not contribute directly to the mass of the POA component, it adds mass and thus size to each aerosol mode, allowing Aitken mode particles to grow to accumulation mode size.

3.3.2.3 Sulphate Aerosol

ST_{con} vs. $CS2_{con}$

In the PI the major sources of SO_2 and thus SO_4 are oceanic DMS emissions and volcanic SO_2 emissions. In this study, the latter are found in central America, Sicily and southeast Asia. While the simulations use the same emissions of SO_2 and DMS, the SO_4 burden (B_{SO4}) in $CS2_{con}$ is 32% lower than ST_{con} (Tables 3.2 & C2). A major reason is that in ST 100% of DMS forms SO_2 via direct reaction with OH, NO_3 and $O(^3P)$, omitting intermediate steps, while in CS2 the more complex DMS oxidation mechanism includes branching points where species which do not contribute to SO_4 can form instead of SO_2.

In CS2 $MeSO_2$, an intermediate in the DMS oxidation pathway, can form SO_2 via a unimolecular reaction or $MeSO_3$ via reaction with O_3 or NO_2. At temperatures and reaction partner concentrations characteristic of the tropical and mid-latitude marine PBL, $MeSO_2$ forms SO_2 at yields of 40-70%. The product of the other $MeSO_2$ reaction pathways, $MeSO_3$, can produce H_2SO_4 (which forms SO_4) with yields of 30-70% or methyl sulphonic acid (MSA) which does not contribute to SO_4 aerosol at present, providing a route for the diversion of mass away from SO_4 formation. By contrast, the production of MSA in ST does not compete with any pathways which contribute to SO_4 aerosol. Rather the oxidation of DMS by OH produces MSA and SO2 both at 100% yield and thus at present does not conserve sulphur.

Given the focus on BVOCs, a full comparison of DMS chemistry and SO_4 formation is beyond the scope of this study. However, understanding the impact of the description of DMS chemistry from the basic approach in ST to the more detailed, yet still simplified scheme in CS2, is important, particularly given the discovery of new species which may contribute to aerosol formation and growth (e.g., Veres et al., 2020). This is discussed in Future Work (Section 5.4.1.3).

$2xE_{BVOC}$

$2xE_{BVOC}$ reduces B_{SO4} by 8.4% (0.07 Tg) in ST_{Δ} and 7.5% (0.04 Tg) in $CS2_{\Delta}$ with SO_4 lifetime decreasing by 0.12 days (2.2%) ST_{Δ} and 0.27 days (5.4%) in in $CS2_{\Delta}$.

In addition to the decreased burden, the BVOC-driven change to oxidants also perturbs the pathways for SO_4 formation. In both mechanisms gas phase reaction of SO_2 with OH yields H_2SO_4 which can condense onto existing aerosol or nucleate new particles while aqueous phase reaction with O_3 or H_2O_2 only adds mass to existing particles (Section 1.3.1). BVOC-driven OH depletion reduces the flux of SO_2 forming H_2SO_4 by a greater amount in ST_{Δ} than $CS2_{\Delta}$ (2.9 Tg yr^{-1} (21.8%) vs. 2.0 Tg yr^{-1} (20.8%)) with the same trend exhibited by decreases in new particle formation flux: 0.025 Tg yr^{-1} (ST_{Δ}) and 0.014 Tg yr^{-1} ($CS2_{\Delta}$). Unsurprisingly these fluxes exhibit the greatest absolute decreases close to the major volcanic SO_2 source but the proximity of the central American and southeast Asian sources to major biogenic emission regions facilitates noticeable coupling between BVOC-driven oxidant reductions and SO_4 formation. This is shown by decreases in the column fluxes of SO_2 + OH and nucleation from H_2SO_4 of 45% (35%) and >70% (>50%) in ST_{Δ} ($CS2_{\Delta}$) respectively over Amazonia with the decreases extending eastwards over the South Atlantic (Fig 3.8).

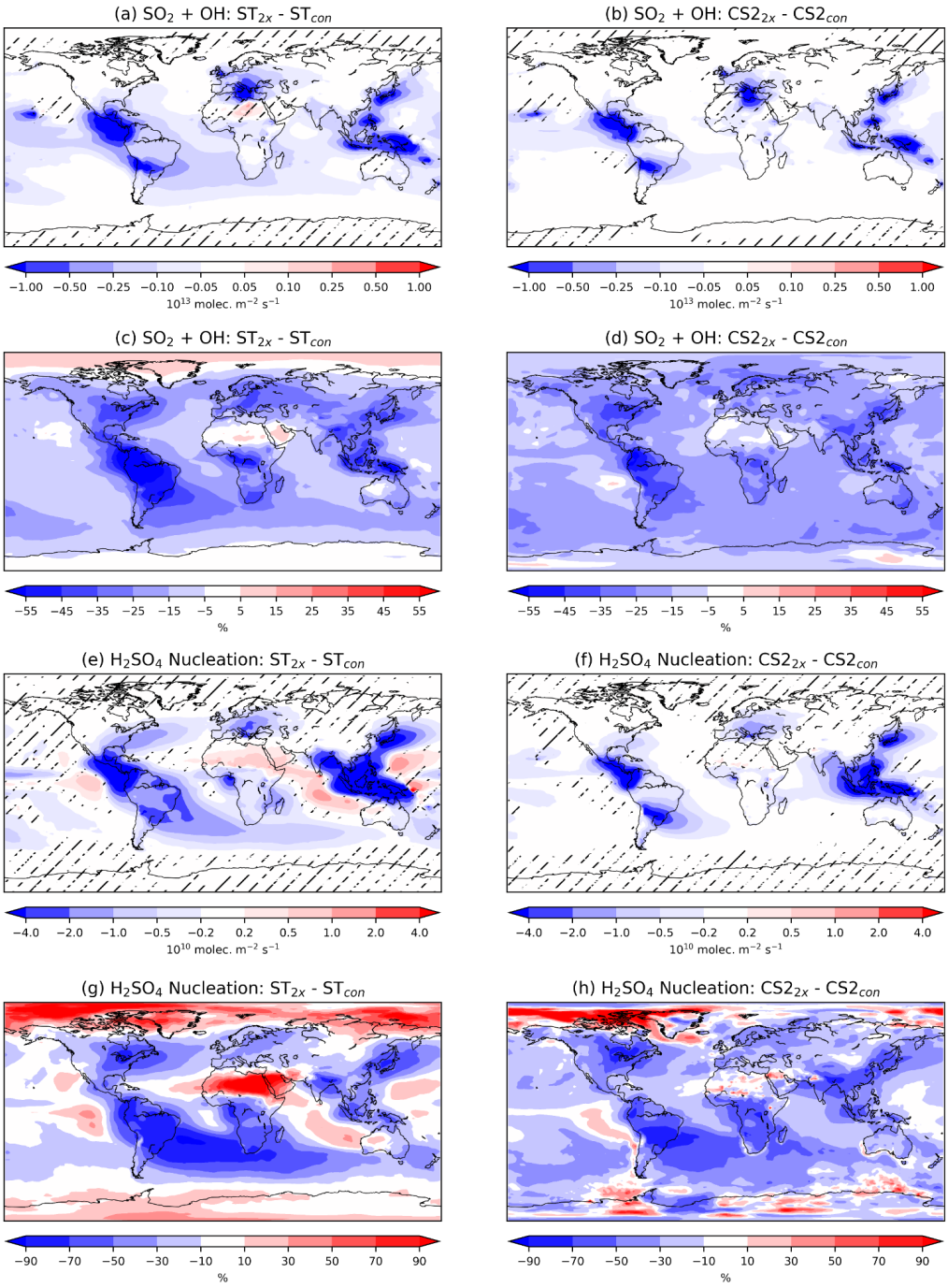


Figure 3.8. Absolute (a,b) and percentage changes (c,d) in SO_2 + OH column fluxes for ST_Δ and $CS2_\Delta$. Absolute (e,f) and percentage (g,h) changes in H_2SO_4 nucleation column fluxes for ST_Δ and $CS2_\Delta$.

The increases in H_2O_2 concentrations in both mechanisms (Fig C8(a-d)), discussed in Section 3.3.1.3, also play a role in the reduction of SO_2 + OH by increasing the flux through the competing H_2O_2 + SO_2 aqueous phase oxidation pathway (the change to O_3 + SO_2 is small). The increase in H_2O_2 concentration is much smaller in absolute and relative terms in ST_Δ and so, based solely on the changes to H_2O_2, a smaller relative increase in the H_2O_2 + SO_2 flux would be expected in ST_Δ. However, ST_Δ simulates a larger absolute and relative increase in H_2O_2 + SO_2 (Fig C8(e-h)), in agreement with the greater suppression of the SO_2 + OH pathway due to larger OH

decreases in ST_{Δ}. In other words, the larger decrease in OH (and thus SO_2 + OH) in ST_{Δ} outweighs the greater increase in H_2O_2 in $CS2_{\Delta}$ and means that ST_{Δ} exhibits the greater increase in H_2O_2 + SO_2 flux.

The net result is a shift towards having fewer, large particles at the expense of a greater number of smaller particles since the H_2O_2 + SO_2 flux predominantly adds mass to accumulation mode particles. ST_{Δ} exhibits a greater reduction in Aitken SO_4 burden than $CS2_{\Delta}$ (0.074 Tg, 26% vs. 0.037 Tg, 20%) as well as an increase in the SO_4 accumulation mode (+1.6%) compared to a small decrease in $CS2_{\Delta}$ (-0.8%). Decreases in Aitken SO_4 column and total Aitken aerosol number column are also greater and more widespread in ST_{Δ} (Fig C9) while the increase in size of accumulation mode particles is larger in ST_{Δ} across almost the whole globe, also indicative of a shift to having more mass in the accumulation mode at the expense of the Aitken mode (Fig 3.9).

3.3.3.4 Aerosol Number Concentrations

$CS2_{con}$ simulates lower nucleation ($N_{nuc,}$ 20-40%), Aitken ($N_{ait,}$ 20-40%) and accumulation (N_{acc}, 5-10%) mode number concentrations than ST_{con} in the upper tropical troposphere, lower tropical troposphere and PBL respectively, largely mirroring the differences in SO_4 and SOA mass concentrations.

Following 2xE_{BVOC}, both mechanisms simulate similar spatial reductions in N_{nuc} (20-40%) in the free troposphere. N_{ait} and Aitken mode number column exhibit decreases (greater in ST_{Δ}) (Fig C9), driven by the reduction in SO_4 Aitken mode and condensational growth to accumulation mode from the enhanced Sec_Org.

Conversely, N_{acc} and accumulation mode column (N_{acc_col}) increase throughout the troposphere with the largest increases over the terrestrial tropics (Fig 3.9(a)), aligning reasonably well with the increase in SOA accumulation mode column (Fig 3.7(g)).

The difference in the N_{acc_col} responses for ST_{Δ} and $CS2_{\Delta}$ (Fig 3.9(c,d)) can be explained by considering the changes to SOA and SO_4. Over the major BVOC emission regions, the smaller increase in N_{acc} in $CS2_{\Delta}$ arises from the greater increase in condensation flux to the accumulation mode (Fig C7) and smaller increase to the Aitken mode compared to ST_{Δ} as the smaller reduction in oxidising capacity in $CS2_{\Delta}$ leads to greater production of SOA at low altitude than in ST_{Δ}. Thus more of the extra Sec_Org in $CS2_{2x}$ goes into making the existing accumulation particles bigger (hence co-located larger increase in accumulation mode size (Fig 3.9(d))) than in ST_{2x} where more Sec_Org goes to growing Aitken mode particles to accumulation mode size, leading to greater increases in N_{acc}. ST_{Δ}'s larger increase in N_{acc_col} extends over the central Atlantic from Africa (Fig 3.9(b)), following the co-located larger increases in ACC_{SOA_COL} in ST_{Δ} (Fig 3.7(h)) which arise from the greater dispersion of SOA.

By contrast, further away from the major BVOC emission regions, the mechanisms' responses are reversed with $CS2_{\Delta}$ exhibiting greater increases in N_{acc_col} (e.g., south Atlantic, Fig 3.9(d)). This comes from the aforementioned smaller reduction in Aitken mode number concentrations in $CS2_{\Delta}$ (Fig C9) which allows a greater number of Aitken mode particles to grow to accumulation mode size. In ST_{Δ}, much more mass is added directly to the

accumulation mode via the aqueous phase oxidation of SO_2 + H_2O_2. The increase in mass transfer to the accumulation mode via this process is 48% greater in ST_Δ than $CS2_\Delta$ and this results in a greater increase in accumulation mode size in ST_Δ (Fig 3.9(f)).

3.3.3.5 Aerosol Optical Depth

The differences in simulated aerosol number concentration and size between the control simulations and between each mechanism's response affect the interaction of aerosol with radiation. This can be described with the aerosol optical depth (AOD) (Section 1.3.4). Between the control simulations, lower SO_4 concentrations in $CS2_{con}$ result in a lower AOD compared to ST_{con} over oceanic regions while over the major E_{BVOC} regions $CS2_{con}$ simulates slightly greater AOD (1-5%).

Following $2xE_{BVOC}$, statistically significant AOD increases (95% confidence) are simulated over most terrestrial regions with the largest rises over Africa (30-40%) and Amazonia (>70%) in both mechanisms (Fig 3.9(e,f)). The total AOD response is driven almost exclusively by the accumulation mode and the larger fractional increase over Amazonia arises from a combination of a greater absolute increase in E_{BVOC} and the fact that the greater biomass burning emissions in Africa result in a higher AOD baseline from BC and POA aerosol.

The AOD exhibits similar increases in ST_Δ and $CS2_\Delta$ directly over the major emission regions despite the smaller increase in N_{acc_col} in $CS2_\Delta$. Given the strong influence of the N_{acc} on the AOD, it is not entirely clear why such a similar increase is simulated.

An interesting feature of the AOD away from the major biogenic emission regions is the more widespread increase in ST_Δ over the central Atlantic which closely aligns with the greater increase in N_{acc_col} (Fig. 3.7(a,b)) and SOA accumulation mode column mass (ACC_{SOA}) (Fig. 3.7(g,h)), strongly suggesting this is from the greater increase in SOA dispersion in ST_Δ. While these increases are small in absolute terms (0.01-0.05) compared to those over BVOC-rich regions (e.g. 0.15-0.2 over Africa), the substantial fractional increase (10-20%) and the low baseline AOD mean such changes can have radiative effects which are disproportionate to the change in AOD (i.e. adding a small amount of additional aerosol to a low baseline can have a large impact). The climatic impact is discussed in Section 3.4.3.

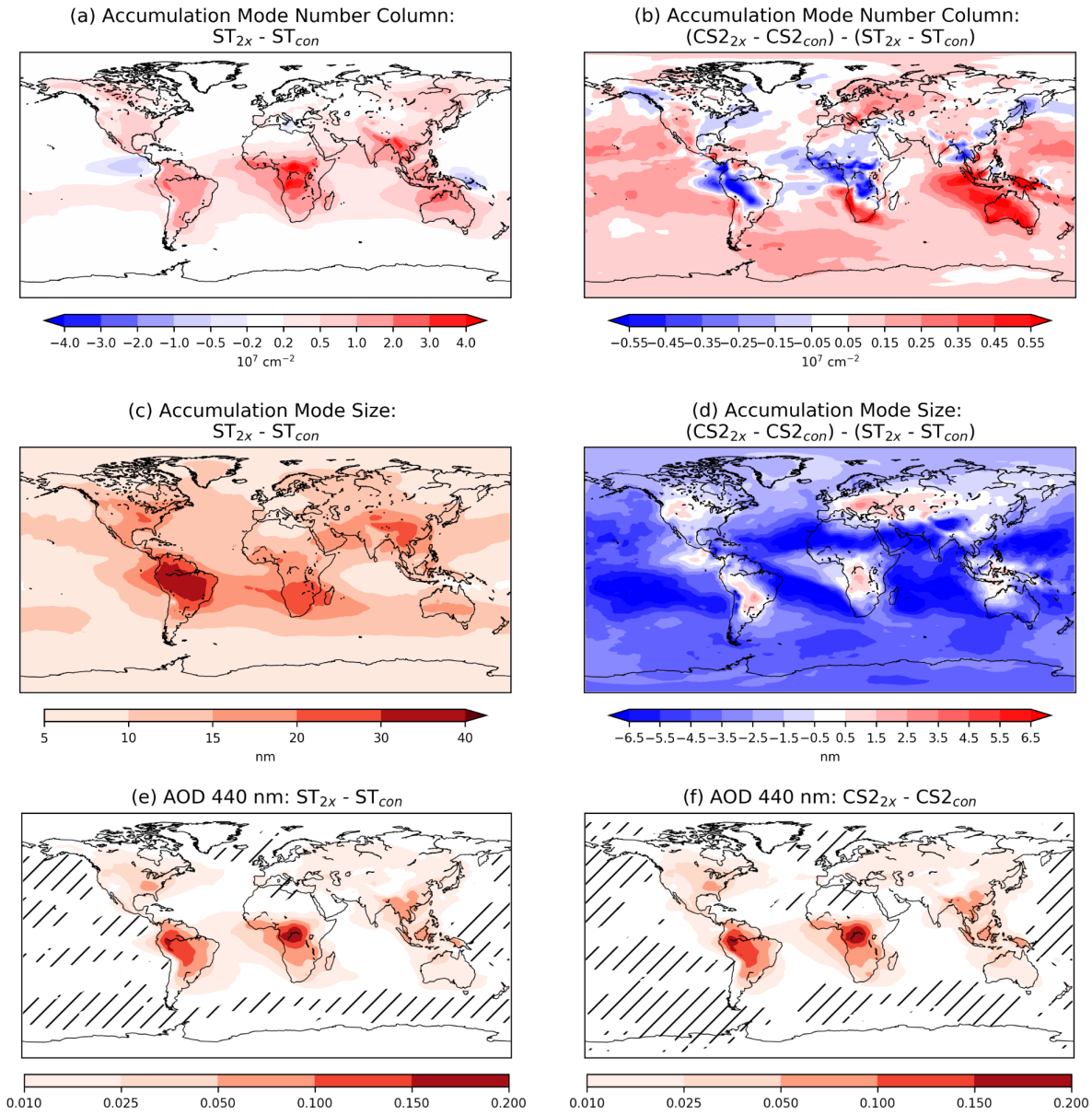


Figure 3.9. Change in (a) accumulation mode number column (N_{acc_col}) in ST_{Δ} and (b) difference in change in accumulation mode number column between $CS2_{\Delta}$ and ST_{Δ}. (c) Change in accumulation mode size for ST_{Δ} and (f) change in accumulation mode size between $CS2_{\Delta}$ and ST_{Δ}. Change in total AOD at 440 nm for (e) ST_{Δ} and (f) $CS2_{\Delta}$. Hatching shows regions where change is statistically insignificant at 95% confidence level.

3.3.3.6 Cloud properties

Changes to the aerosol size and number distributions influence cloud properties, namely CDNC and cloud droplet effective radius (r_{eff}), and thus the magnitude of the cloud radiative effect (CRE) (Section 1.3.5).

Both mechanisms simulate global decreases to CDNC (-2.6% ST_{Δ}, -1.2% $CS2_{\Delta}$) (Fig. 3.10(a,b)) and increases to r_{eff} (0.36% ST_{Δ}, 0.05% $CS2_{\Delta}$) (Fig C10). CDNC reductions over oceanic regions outweigh increases over biogenic regions.

Over Amazonia and Africa, statistically significant (95%) increases are simulated in the CDNC column with larger gains in $CS2_{\Delta}$ (6-10%) than ST_{Δ} (2-6%) (Figs 3.10(c,d), C10(c,d)). Co-located decreases in r_{eff}, also larger in $CS2_{\Delta}$, are simulated (Fig C10(a,b)). The increases in CDNC spread from Africa over the central Atlantic and are closely aligned with increases in ACC_{SOA} (Fig 3.7), N_{acc_col} and AOD (Fig 3.9), suggesting the CDNC increases are a result of the enhanced SOA.

By contrast, ST_{Δ} simulates statistically significant decreases to CDNC (2-10%) over the south Atlantic, stretching east towards Australia and off the west coast of Central and South America. $CS2_{\Delta}$ exhibits a much weaker response in both regions. A key driver of the CDNC reductions over much of the SH is the oxidant-driven suppression of H_2SO_4 production and thus new particle formation, simulated in both mechanisms but greater in ST_{Δ} (Section 3.3.2.3, Fig C8). The reduction of CDNC following a depletion of OH was also demonstrated by O'Connor et al (2021) in the context of CH_4-driven OH reductions when simulations with PI and PD levels of CH_4 were compared. This change reduces Aitken mode number concentrations (Fig C9) and thus the number of particles which can activate to cloud droplets (some Aitken mode particles can act as CCN in the remote troposphere; Sporre et al., 2020). Accordingly, the flux of SO_4 Aitken mass activating as cloud droplets decreases by a greater amount in ST_{Δ} (1.2 Tg yr^{-1}, 25%) than $CS2_{\Delta}$ (0.7 Tg yr^{-1}, 18%).

The increase in CDNC over Amazonia and decrease over most oceanic regions and around the central American volcanic region are in reasonable spatial agreement with the multi-model mean from AerChemMIP (Fig S3, Thornhill et al., 2021b).

3.4 Forcing and Feedback Factors

In this section the components of the forcing arising from the $2xE_{BVOC}$ perturbation for each mechanism and the corresponding feedback factors are calculated.

Table 3.4. Forcing and feedback factors. Uncertainties in forcings are the errors in the 30-year mean with additional scalings of 1.14 and 1.15 for $SARF_{O3}$ and τ_{CH_4} respectively. Calculation of the errors is explained in Appendix C2.

Forcing / mWm^{-2}	**ST_{2x} - ST_{con}**	**$CS2_{2x}$ - $CS2_{con}$**
ERF_{CS} (excl. CH_4)	141 ± 26	106 ± 23
IRF_{DRE}	-260 ± 18	-244 ± 15
ΔCRE	183 ± 30	91 ± 28
$SARF_{O_3}$ (offline)	100 ± 12	92 ± 9
τ_{CH_4} (offline)	275 ± 2	230 ± 2
$IRF_{DRE} + \Delta CRE + SARF_{O_3} + \tau_{CH_4}$	**298 ± 37**	**169 ± 33**
Feedback Factor / mWm^{-2} K^{-1}		
α_{DRE}	-9.8 ± 0.9	-9.0 ± 0.8
α_{DRE}	6.9 ± 1.2	3.3 ± 1.1
$\alpha_{SARF_{O_3}}$	3.8 ± 0.5	3.4 ± 0.4
$\alpha_{\tau_{CH_4}}$	10.3 ± 0.7	8.5 ± 0.5
α_{Total}	**10.2± 1.7**	**6.2 ± 1.5**

3.4.1 Clear-Clean Forcing

The online clear-clean forcing (excluding CH_4), termed ERF_{CS}, is positive for ST_Δ (141±20 mWm^{-2}) and $CS2_\Delta$ (106±18 mWm^{-2}) with the LW component (ST_Δ 112 mWm^{-2}, $CS2_\Delta$ 87 mWm^{-2}) unsurprisingly dominating given the increases in O_3. The LW component shows a general positive trend over the tropics, in agreement with the increases in O_3 around the TT (Fig. 3.3) where its radiative efficiency is greatest.

3.4.1.1 Ozone

As in Thornhill et al (2021b), the stratospherically-adjusted O_3 radiative forcing ($SARF_{O3}$) is calculated using the O_3 kernel from Skeie et al (2020). Kernel analysis highlights the heterogeneity of O_3 radiative efficiency and thus the importance of where the O_3 change occurs. This is illustrated by comparing the radiative impact of the 2-3 ppb O_3 reduction in the mid tropical troposphere (~7 km; 300-400 hPa) and 15-20 ppb increase around the TT (15km; 100-200 hPa) in ST_Δ (Fig 3.3(e)). In number concentration terms, the 2-3 ppb reduction is roughly half the magnitude of the 15-20 ppb increase yet the radiative impact of the increase is 4-5×greater (Fig 3.10(g,h)).

Therefore, $CS2_\Delta$, which simulates a smaller O_3 reduction in the mid tropical troposphere but a smaller increase around the TT, yields an 8% smaller $SARF_{O3}$ (92±9 mWm^{-2}) than ST_Δ (100±12 mWm^{-2}). This is despite $CS2_\Delta$

exhibiting a 17.5% larger increase in O_3 tropospheric burden (1.7 Tg). The kernel $SARF_{O3}$ is dominated by the LW contribution with very small SW contributions (1.5-1.8 mWm^{-2}). The corresponding feedback factors are 3.8 ± 0.5 mWm^{-2} K^{-1} for ST_Δ and 3.4 ± 0.4 mWm^{-2} K^{-1} for $CS2_\Delta$.

The net $SARF_{O3}$ for ST_Δ (100±12 mWm^{-2}) is within the uncertainty range of the value from Thornhill et al (2021b) (120±20 mWm^{-2}). The changes to the MT + NO_3 rate constant, isoprene SOA and organic-mediated nucleation I implemented are likely to have led to the difference. The $SARF_{O3}$ from ST_Δ and $CS2_\Delta$ are closer to those from GFDL (70±10 mWm^{-2}) and CESM2 (60±10 mWm^{-2}) and further from the outlier value of 230±20 mWm^{-2} from GISS. The role of differences in simulated chemistry in helping to explain the intermodal variation is considered in Section 3.5.2.

The ERF_{CS}, diagnosed directly from the simulations and dominated by the O_3 forcing, and the $SARF_{O3}$, calculated using simulations' O_3 fields and the radiative kernel of Skeie et al (2020), differ. A major is reason is because the kernel was generated using cloud, water vapour, temperature and GHG fields from 2003 not the PI. Furthermore, the kernel had a much coarser resolution, particularly in the vertical where it has only 32 levels compared to UKESM's 85.

3.4.1.2 Methane

The forcing from the increase in τ_{CH_4} with $2xE_{BVOC}$ is ~2.5x larger than $SARF_{O3}$ and the difference between ST_Δ and $CS2_\Delta$ is greater. Increases in τ_{CH_4} of 2.03 years (25.7%) and 1.63 years (21.2%) in ST_Δ and $CS2_\Delta$ respectively (following reductions in airmass-weighted mean OH of 27% and 22% respectively) correspond to hypothetical concentrations increases of 276 ppb (34%) and 226 ppb (28%) respectively and forcings of 275±2 mWm^{-2} and 230±2 mWm^{-2}. Respective feedback factors of 10.3 ± 0.7 $mWm^{-2}K^{-1}$ and 8.4 ± 0.5 $mWm^{-2}K^{-1}$ illustrate both the greater role CH_4 plays in the climatic impact of BVOCs (compared to O_3) but also the 16% lower sensitivity to BVOC-τ_{CH_4}-driven warming of the PI atmosphere in UKCA when $CS2_\Delta$ is used rather than ST_Δ.

Comparing the change in τ_{CH_4} per unit E_{BVOC} to the other models used in AerChemMIP (Table 12, Thornhill et al., 2021b) reveals ST_Δ (0.030 % (Tg_{VOC} yr^{-1})$^{-1}$) to be similar to GFDL and CESM2 (0.030 and 0.035 % (TgVOC yr^{-1})$^{-1}$) while the smaller depletion of oxidants in CS2 leads to lower sensitivity (0.024 % (Tg_{VOC} yr^{-1})$^{-1}$). GISS (0.018 % (Tg_{VOC} yr^{-1})$^{-1}$) remains the model with the lowest sensitivity but this unsurprising given its larger O_3 increase will likely buffer OH depletion more via increased primary OH production.

(Note the calculation of CH_4 forcing from the AerChemMIP simulations of Thornhill et al (2021b) did not include soil loss (lifetime of 120 years) and stratospheric loss (lifetime of 160 years) but they are included in this study for completeness. This means the baseline τ_{CH_4} are smaller in this study and the fractional increase slightly larger, increasing the calculated CH_4 forcing.)

3.4.2 Aerosol Direct Effect

Both mechanisms simulate negative global mean forcing from increases to the aerosol DRE (ST_{Δ} -0.260 Wm^{-2}, $CS2_{\Delta}$ -0.244 Wm^{-2}). The strongest forcing occurs over Amazonia and central Africa (-1.5 to - 2.5 Wm^{-2}) (Fig 3.10 (i,j)), the regions with the largest increases in AOD, while more moderate negative forcing is also simulated over regions of southeast Asia and north America; all statistically significant (95%). The important MT emission regions of the NH boreal forests exhibit negligible negative forcing in ST_{Δ} and only a small negative forcing in $CS2_{\Delta}$.

In contrast to the similar IRF_{DRE} over Amazonia and Africa, the negative forcing away from the major emission regions is stronger in ST_{Δ}. This is seen most clearly over the central and southern Atlantic (and to a lesser extent around southeast Asia) where the stronger negative forcing extending from Africa towards South America aligns well with ST_{Δ}'s larger increases in AOD and accumulation mode SOA column, indicating the greater increase in SOA dispersion of ST_{Δ} is a key driver.

While the forcing in this region is small relative to that in the major emission regions, the large areas affected means the global impact is important: the mean IRF_{DRE} over oceanic regions is 13% larger in ST_{Δ} than $CS2_{\Delta}$, while over land it is <1% smaller. A parallel can be drawn with Sporre et al (2020) where EC-Earth simulated greater SOA dispersion following a doubling of SOA yields than NorESM, contributing to the negative IRF_{DRE} in EC-Earth being twice as strong as in NorESM.

While the focus of this chapter is to assess the influence of the different descriptions of BVOC chemistry, the impact of differences in the description of aerosol formation can also be identified by comparing the response of the ACM simulations with ST_{Δ}. Here the major difference is the switch from ACM's MT-only SOA scheme (2x yield and no organic-mediated BLN) to the more realistic approach of this study where isoprene and MT can produce SOA (Section 3.2.2). The MT-only SOA approach in ACM leads to a stronger negative forcing over the boreal forest regions but lower forcing over the tropical forests and the Atlantic (Fig C11). The global mean IRF_{DRE} is 23% smaller (-0.199 Wm^{-2}) than ST_{Δ}. Some of this difference can be attributed to the fact that the increase in SOA production is ~11% smaller in ACM_{Δ} due to the MT-only production but this comparison also highlights the sensitivity to different aerosol schemes (e.g., Scott et al., 2014; Sporre et al., 2020).

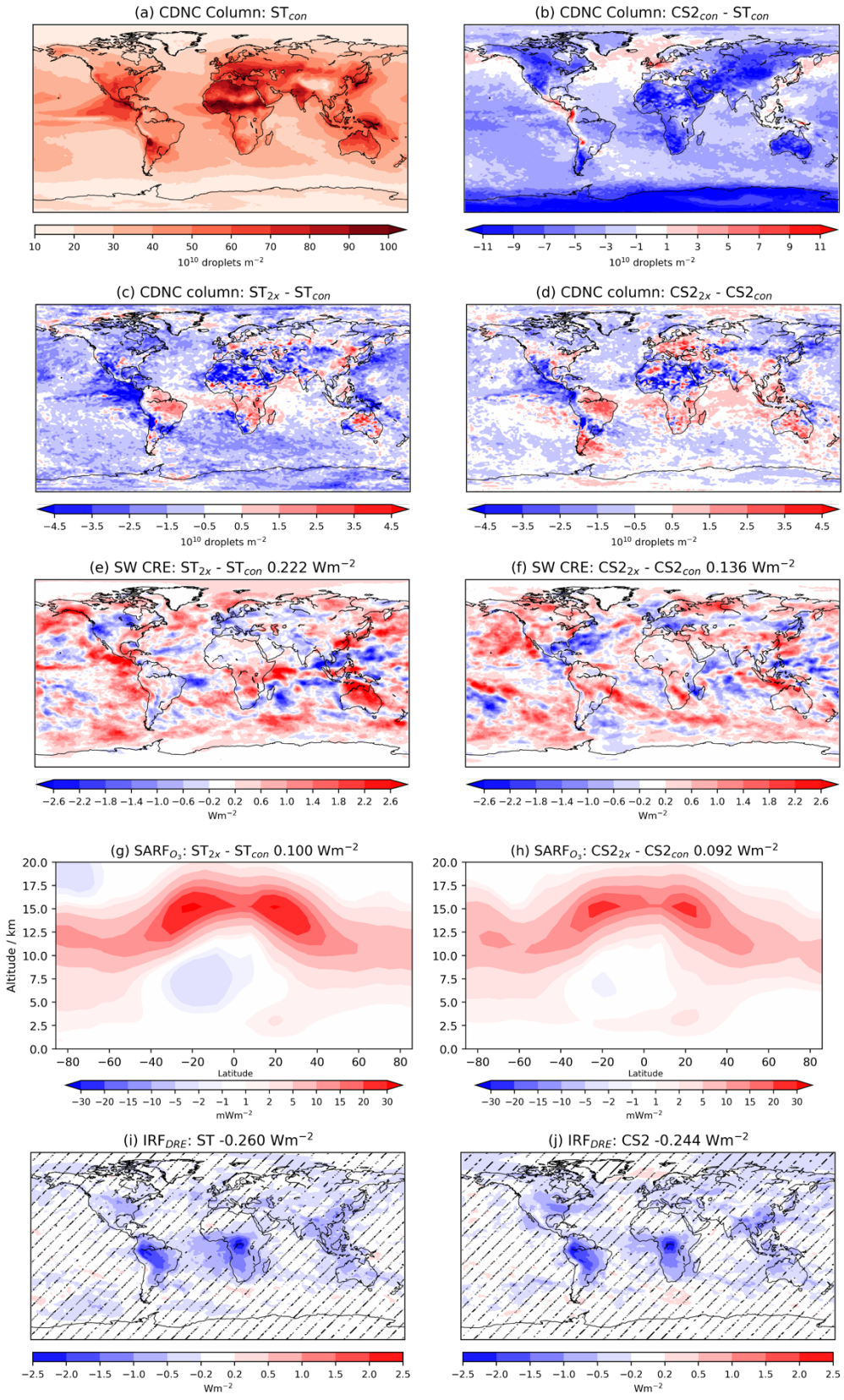


Figure 3.10. Cloud droplet for (a) ST_{con} and (b) $CS2_{con}$ - ST_{con}. Change in cloud droplet column number for (c) ST_{Δ} and (d) $CS2_{\Delta}$. SW CRE forcing for (e) ST_{Δ} and (f) $CS2_{\Delta}$. $SARF_{O3}$ forcing for (g) ST_{Δ} and (h) $CS2_{\Delta}$. IRF_{DRE} forcing for (i) ST_{Δ} and (j) $CS2_{\Delta}$. Values in titles for (e-j) are area-weighted global means.

3.4.3 Aerosol-Cloud Interactions

The global CRE is twice as large for ST_{Δ} as $CS2_{\Delta}$ (0.183 vs. 0.091 Wm^{-2}) with the difference arising almost exclusively in the positive SW term (ST_{Δ} 0.222 Wm^{-2}, $CS2_{\Delta}$ 0.137 Wm^{-2}) which dominates over the smaller negative LW term (ST_{Δ} -0.040 Wm^{-2}, $CS2_{\Delta}$ -0.037 Wm^{-2}) and suggests the major CRE driver is a change in cloud albedo. The corresponding increase in r_{eff} may also lead to decreases in cloud lifetime (2nd AIE; Section 1.3.5).

Over Amazonia, the shift to higher concentrations of smaller cloud droplets (higher CDNC, smaller r_{eff}) (Fig 3.10 (c,d)), more pronounced in $CS2_{\Delta}$, would be expected to lead to enhanced cloud albedo (Twomey., 1974). However, the co-located negative CRE is weak with contributions from both LW and SW components. The maximum increase in CDNC is located in eastern Amazonia while the AOD and DRE increases are greatest in western Amazonia which may reflect the longer timescale required for aerosol particles to grow and activate into cloud droplets which allows for greater transport.

Conversely, several large oceanic regions, particularly in ST_{Δ}, including the south Atlantic stretching east towards Australia exhibit positive SW CRE (Fig 3.10(e,f)). While some of these areas of positive SW CRE do align with the areas of CDNC reduction, and CDNC reduction is likely to reduce cloud albedo and thus drive a positive SW CRE (Section 1.3.5, Appendix A and O'Connor et al., 2021), I cannot be certain of the correlation between the two.

Overall, it appears that the reduction in CDNC from H_2SO_4 suppression outweighs the effect of SOA increases and drives the attendant positive forcing in both mechanisms. It is perhaps unexpected that this effect is larger in ST_{Δ} because $CS2_{con}$ simulates lower CDNC over much of the Southern Ocean, Atlantic and Pacific (exceeding 10% in places) (Fig 3.10(a,b)). The lower baseline concentration means the cloud albedo is likely to be more sensitive to a given absolute reduction in CDNC (Section 1.3.5, Appendix A1) which would favour a stronger positive CRE in $CS2_{\Delta}$. However, this is outweighed by the impact of the greater change of oxidants and the larger absolute reduction in SO_4 aerosol in ST_{Δ}, highlighting again the influence of the chemical mechanism.

ACM_{Δ} simulates a similar CRE to ST_{Δ} (0.183 vs 0.177 Wm^{-2}). Overall, ACM_{Δ}'s smaller IRF_{DRE} (than ST_{Δ}) is almost entirely offset by the CRE, leading to a negligible total aerosol forcing (-0.02 Wm^{-2}), in line with Thornhill et al (2021b). In other words, UKESM1's small total aerosol forcing comes from a near complete offset of the forcing from changes to direct and indirect effects. (It should be noted the total aerosol forcing is calculated in a different way in Thornhill et al (2021b) with it defined as the total forcing minus the $SARF_{O3}$, hence the small positive value of 0.03 Wm^{-2} for UKESM1 in AerChemMIP).

The general finding that changes in organic aerosol have a strong influence on IRF_{DRE} but a weak influence on CRE (e.g., over Amazonia) is characteristic of UKESM1, having been exhibited in the multi-model comparison of Thornhill et al (2021a). In that study, applying PD POA emissions to a PI atmosphere (perturbing the organic

aerosol but not the chemistry) led to a negative IRF_{DRE} in UKESM1 which was twice as large as all other CMIP6 models considered but a negative CRE which was 2-3x smaller. A contributing factor is likely to be the current approach of assigning a hygroscopicity parameter of zero to organic aerosol. A value of 0.1 is recommended (Petters and Kreidenweiss., 2007) and has been used in some non-UKCA GLOMAP studies (e.g., Scott et al., 2014). This illustrates the influence of aerosol and cloud parameterisations on the climatic impact of BVOCs which have been identified as important drivers of inter-model differences (Sporre et al., 2020, and Sections 1.5 & 1.6).

3.4.4 Sum of Forcing Components

The positive forcings from the CRE, $SARF_{O3}$ and CH_4 outweigh the negative IRF_{DRE} forcing to yield net positive forcings for both mechanisms. However, net $CS2_{\Delta}$ forcing is 43% smaller than ST_{Δ}, driven primarily by the 50% smaller CRE and 16% smaller CH_4 forcings.

3.4.5 Feedback Factors

Feedback factors, the forcing arising from the change in E_{BVOC} accompanying a unit change in surface temperature (Section 1.5.1), are calculated for the O_3, CH_4, CRE and IRF_{DRE} forcings and summed to give to the total feedback factor of BVOCs on climate (Table 3.4). The smaller forcings in $CS2_{\Delta}$, particularly from CRE and CH_4, lead to a 43% (±13%) lower total feedback factor. Both mechanisms yield positive feedback factors, in line with UKESM1's contribution to AerChemMIP.

3.4.6 Implications

While the feedback factor allows determination of the forcing arising from a change in E_{BVOC} following a unit change in surface temperature, the uncertainty in the E_{BVOC} change with temperature (γ_{BVOC}) and the impact of other E_{BVOC}-drivers means care must be taken in the application of the feedback factor.

For a 1.1 K increase (approximate PI-to-PD change) with no change to use change or atmospheric composition, the feedback factors would correspond to an additional forcing of 13 mWm^{-2} in ST and 7 mWm^{-2} in CS2, 0.65% and 0.37% respectively of the ~2 Wm^{-2} net PI-to-PD forcing. UKESM1 simulates the smallest γ_{BVOC} in AerChemMIP (~¼ of the multi model mean, Section 1.4.1) which leads to a smaller feedback factor. However, even with an increase of a factor of 4, the total forcing would be no more than a few percent of the net PI-to-PD forcing.

When UKESM1's PI-to-PD change in E_{BVOC} (including the impact of land use change, CO_2 and temperature (Fig 1.4, Cao et al., 2021)) is considered, the ~20% (170 Tg yr^{-1}) reduction can be combined with the calculated radiative efficiencies (ST_{Δ} 0.347 mWm^{-2} (Tg $yr^{-1})^{-1}$, $CS2_{\Delta}$ 0.187 mWm^{-2} (Tg $yr^{-1})^{-1}$) to yield negative forcings of 60 mWm^{-2} and 33 mWm^{-2} for ST and CS2 respectively (3% and 1.6% of the net PI-to-PD forcing).

3.4.6.1 Influence of atmospheric state

The changes which have occurred to atmospheric composition and background aerosol from the PI to the PD are also likely to have an effect on the climatic impact of BVOCs.

Higher PD CH_4 and N_2O concentrations mean the forcing per unit change in CH_4 concentration is ~35% lower (Etminan et al., 2016). Higher background aerosols concentrations will change regional sensitivity to aerosol perturbation (Sporre et al., 2020) while greater NO_x is likely to increase O_3 production although the forcing's strong dependence on the location of O_3 change means the net climatic impact may be less intuitive. The influence of atmospheric composition is discussed in detail in Section 5.4.1.2 in the context of future work and while the complex interactions make it hard to predict the net effect, the approach in this chapter, building on AerChemMIP, provides a basis for investigating the climatic impact of BVOCs in other atmospheres.

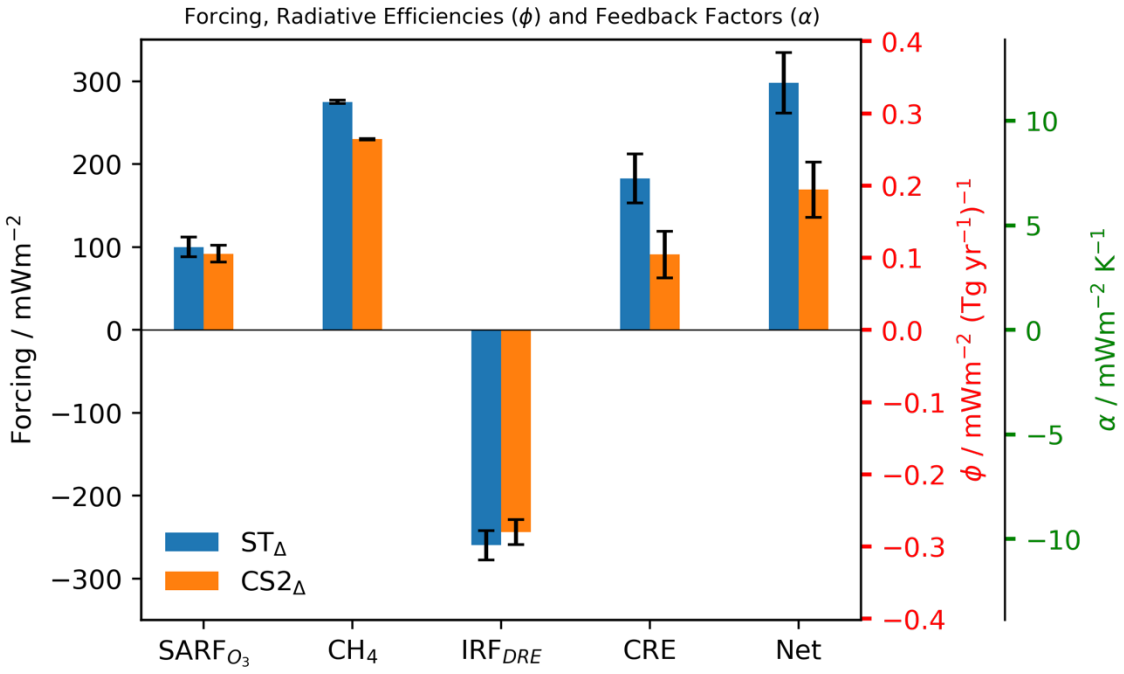


Figure 3.11. Forcing, BVOC radiative efficiency (ϕ) and feedback factor (α) for each component and net result for ST$_\Delta$ and CS2$_\Delta$.

3.5 Conclusion

Understanding the feedback of BVOCs on climate is important because anthropogenic factors (and some climate change mitigation strategies) are projected to alter these emissions in future climate scenarios. I have shown that within a single climate model, with a consistent aerosol scheme, the forcing and feedback of E_{BVOC} in a PI atmosphere is positive when using either the standard simplistic ST chemical mechanism, or the state-of-the-art BVOC mechanism CS2. However, the choice of chemical mechanism strongly influences the magnitude of the forcing/feedback: CS2$_\Delta$ yields a forcing/feedback which is 45% smaller than ST$_\Delta$ (Fig 3.11), implying that the PI atmosphere is only about half as sensitive to a change in E_{BVOC} when a state-of-the-art BVOC

chemistry mechanism is used compared to the standard mechanism. This is important because most prior work on the climatic impact of BVOCs has focused on the influence of BVOC-aerosol parameterisations. This current study complements such work by highlighting the significant influence of the simulated chemistry and, by extension, the importance of accurately representing chemistry within models used for climate change predictions.

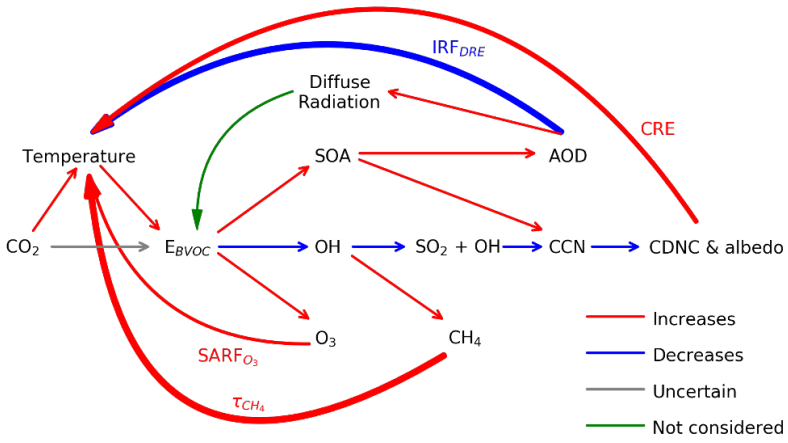


Figure 3.12. Feedback diagram from this study with varying E_{BVOC} and interactive oxidants. Curved arrows indicate feedbacks with the thickness of the arrows proportional to size of the feedback for ST_{Δ}. Note that the feedback from enhanced diffuse radiation was not considered as the constraints on the land surface prevented this change from having an effect.

Figure 3.12(a) shows the interactions considered in this study. The strongest forcing responses arise from the IRF_{DRE} (negative) and increase in CH_4 lifetime (positive) while overall the positive forcings from O_3, CH_4 lifetime and CRE outweigh the negative IRF_{DRE} (Fig. 3.10). However, for each component, the magnitude of the forcing in $CS2_{\Delta}$ is smaller. The smaller oxidant depletion in $CS2_{\Delta}$ leads to smaller increases in O_3 around the TT and smaller reductions to CH_4 oxidation flux. The increase in SOA occurs at lower altitudes than in ST_{Δ}, resulting in less dispersion and thus scattering while the smaller reduction in gas phase SO_2 oxidation yields lower decreases in CDNC and a smaller positive CRE.

The offsetting of IRF_{DRE} with the O_3, CH_4 and CRE forcings reduces the magnitude of the resulting feedback factors in both cases such that the additional forcings associated with the PI-to-PD temperature or land use changes are only a few percent of the ~2 Wm^{-2} net PI-to-PD forcing.

This study omits other parts of the wider Earth system response. A study using a fully coupled land surface model with unconstrained SSTs would complement the current work by allowing assessment of the impact of diffuse radiation on the land surface (e.g., by vegetation fertilisation; Rap et al., 2018). The inclusion of HOMs and pure biogenic nucleation using the mechanism presented in Chapter 4 would also improve understanding

into this pathway's influence (Future Work Section 5.4.1.1). Assessing the influence that atmospheric state (e.g., temperature, NO_x, SO_2, background aerosol) has on the magnitude of the BVOC forcing/feedback is also considered further (Section 5.4.2). Nevertheless, by decomposing the response into the key forcing components and examining the influential processes in each case, this study provides a basis for the investigation of E_{BVOC} and climate in other scenarios while illustrating the considerable influence that simulated chemistry can have on climate.

Moving beyond the E_{BVOC} feedback, this suggests assessment may be required into the extent to which other natural chemistry-climate feedbacks are dependent on the chemistry scheme.

3.5.1 Wide reaching role of oxidants

The contribution of SO_4 aerosol changes to the CRE response (Section 3.4.3) highlights the subtle but important difference between the IRF_{DRE} and CRE from a perturbation to E_{BVOC} with interactive oxidants (as in this study) and the IRF_{DRE} and CRE from a perturbation to SOA, the latter typically achieved either by scaling the SOA production yield (e.g. Scott et al., 2014) or perturbing E_{BVOC} with prescribed oxidants (Sporre et al., 2019; Sporre et al., 2020). In the latter case, only the IRF_{DRE} and CRE from SOA are impacted, typically yielding a negative feedback if SOA yield or E_{BVOC} are increased. As discussed in Sections 1.5 & 3.1, Sporre et al (2019) found the total negative aerosol forcing following the increase in BVOCs accompanying a doubling of CO_2 offset 13% of the positive forcing from the CO_2 increase, rising to 20% when PI aerosol emissions were used (Figs 3.1, 3.12(b)). This substantial offsetting, eye-catching for policy makers, arises from a very strong positive dependence of E_{BVOC} with temperature (NorESM2 has the highest among AerChemMIP models) causing a large increase in SOA which yields negative forcing from the IRF_{DRE} and CRE with no accompanying positive forcings from changes to CH_4, O_3 or SO_4 aerosol.

By contrast, Figure 3.11 reveals the more complex story when interactive oxidants are used, including the significant perturbations to the lifecycle of SO_4 aerosol. The attendant net positive CRE in this study from increased E_{BVOC} (where impact of SO_4 changes far outweigh the impact of SOA changes) leads to the opposite conclusion to that of Sporre et al (2019) (and the NorESM contribution to AerChemMIP) and illustrates the need to perform simulations which capture as much of the full atmospheric response as possible. This is particularly important in the context of BVOCs and other policy-relevant topics since incorrectly diagnosing their effects on climate could lead to implementation of ineffective or even counterproductive policies.

3.5.2 The role of chemistry in explaining inter-model differences

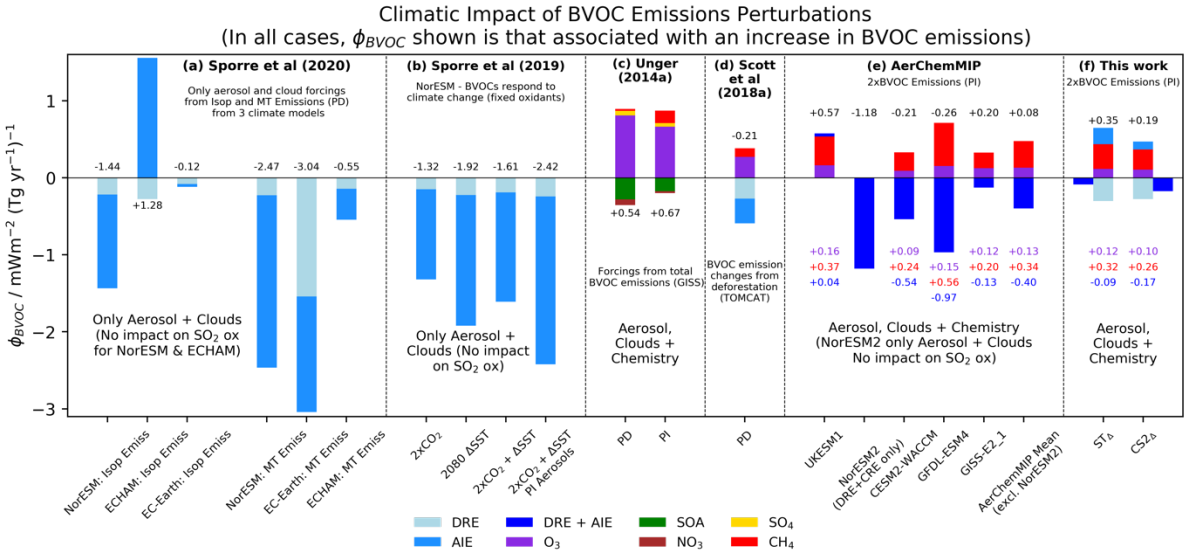


Figure 3.13. Components of BVOC radiative efficiency (ϕ_{BVOC}) in previous studies and this work. Note that for comparison purposes, the sign of some values has been reversed so that all ϕ_{BVOC}correspond to an increase in emissions. For the AerChemMIP experiments only the total aerosol (DRE +AIE) radiative efficiency was available. The total aerosol radiative efficiency is shown alongside the individual DRE and AIE components for simulations in this chapter (f) for ease of comparison. Black values correspond to the net ϕ_{BVOC} while coloured values in (e,f) relate to the O$_3$, CH$_4$ and total aerosol components.

The differing climatic responses in ST$_\Delta$ and CS2$_\Delta$ and the key drivers (i.e., the effect of different simulated chemistry) provides some insight into the causes of inter-model variation. Figure 3.13 (extension of Fig 1.10) shows the results of this chapter in the context of previous studies (Section 1.5). It reveals that the (still considerable) 43% change in net ϕ_{BVOC} from ST$_\Delta$ to CS2$_\Delta$ (0.16 mWm^{-2} (Tg yr^{-1})$^{-1}$) is smaller than the inter-model variation in ϕ_{BVOC} from AerChemMIP.

However, when ϕ_{BVOC} is decomposed into its O$_3$ (ϕ_{O_3}), CH$_4$ (ϕ_{CH_4}) and total aerosol (DRE + AIE) (ϕ_{aer}) components, it is clear the changes in ϕ_{O_3} (0.02 mWm^{-2} (Tg yr^{-1})$^{-1}$) and ϕ_{CH_4} (0.06 mWm^{-2} (Tg yr^{-1})$^{-1}$) are more comparable to the variations in the corresponding components in the AerChemMIP runs (std. dev: ϕ_{O_3} 0.03 mWm^{-2} (Tg yr^{-1})$^{-1}$; ϕ_{CH_4} 0.14 mWm^{-2} (Tg yr^{-1})$^{-1}$) i.e. the difference in chemical mechanism is likely to be a major contributor to the inter-model variation for O$_3$ and CH$_4$. This makes sense as these gas phase species are strongly influenced by the chemical mechanism employed (e.g., Chapter 2 and Archer-Nicholls et al., 2021). By contrast, while the ST$_\Delta$ to CS2$_\Delta$ change in ϕ_{aer} (0.08 mWm^{-2} (Tg yr^{-1})$^{-1}$) highlights the influence of chemistry (via oxidants) on aerosol, the change is considerably smaller than the variation between total aerosol components in AerChemMIP (std. dev 0.39 mWm^{-2} (Tg yr^{-1})$^{-1}$, excluding NorESM2), suggesting the differences in chemical mechanisms alone are unlikely to explain the ϕ_{aer} variation exhibited by the AerChemMIP runs. Again, this is unsurprising because the treatment of aerosol and clouds and the background aerosol concentrations, which differ between models, have been identified as major sources of inter-model discrepancy (Sporre et al., 2020 and Section 1.5). Scott et al (2014) also showed the influence of the finer details of an aerosol scheme such as the pathway(s) for nucleation and inclusion of aerosol ageing: these also differ between

models. To this end, comparison of the total aerosol forcing in ACM_{Δ} and ST_{Δ} (calculated using Eqs 3.7, 3.8) reveals that switching from MT-only SOA with no BLN to SOA from isoprene and MT with BLN (Table 3.1) leads to ϕ_{aer}decreasing by 0.064 mWm^{-2} $(Tg\ yr^{-1})^{-1}$; comparable to the difference between ST_{Δ} and $CS2_{\Delta}$. In other words, even changing the SOA sources within the same aerosol scheme and chemical mechanism has a noticeable impact on ϕ_{aer}, highlighting ϕ_{aer}'s sensitivity to factors which certainly differ between models and will contribute to the inter-model variation. Variations in BVOC emission locations (e.g., iBVOC vs. MEGAN-MACC; Fig B2) and model dynamical schemes are also influential given the importance of the vertical mixing of BVOCs for tropospheric oxidising capacity and aerosol dispersion.

Nevertheless, the substantial influence the changes to SO_4 aerosol and CDNC have on the SW CRE and thus total aerosol forcing in UKESM1, making it much smaller than that from CESM2 and GFDL, suggest further analysis into the coupling between BVOCs, oxidants and SO_4 aerosol as a possible driver of inter-model variation is warranted. For example, the chemistry or aerosol parameterisations in CESM2 and GDFL may be such that the BVOC-driven changes to SO_4 aerosol and CDNC are small and/or inconsequential from a forcing perspective, leading to larger net negative total aerosol forcing driven primarily by the change in SOA. Understanding why models differ in this regard, and the strength of their respective approaches, would further help constrain the climatic influence of BVOCs.

Decomposing the total aerosol forcing of each AerChemMIP model into the IRF_{DRE} and CRE components (required data is not currently publically available) and examining the variation in the global mean and spatial distribution of each component would be informative. Both components will exhibit inter-model variation given the different model parameterisations for organic aerosol and sulphate aerosol which lead to different forcings from direct and indirect effects. For example, as discussed in Section 3.4.3, organic aerosol is a stronger scatter in UKESM1 (greater IRF_{DRE}) than many other CMIP6 models but much weaker in its indirect radiative effect (Thornhill et al., 2021a) and this may contribute to the lower total aerosol forcing evident in all UKESM1 runs in Fig 3.13(e,f). However, the comparison may also highlight other differences indicative of oxidant-aerosol coupling (or lack thereof). For example, the comparison of SO_4 production, CDNC and SW CRE away from major emission regions may provide information regarding the importance of SO_4 aerosol changes.

Another area to explore is the spatial relationship between CDNC changes and the cloud-weighted susceptibility (CWS), a dimensionless parameter relating the SW CRE to a CDNC change at a given location (Karset et al., 2018). For a certain change in CDNC, a higher CWS leads to a larger SW CRE. Variations in cloud microphysics schemes mean the spatial variation in CWS will differ between models. Some models will simulate CDNC changes in regions with higher CWS (and thus a larger SW CRE) while the CDNC change in the other models may coincide with areas of lower CWS (yielding a smaller SW CRE), potentially helping to explain inter-model variation.

4. CRI-HOM: A novel chemical mechanism for simulating highly oxygenated organic molecules (HOMs) in global chemistry–aerosol–climate models

Chapter 2 illustrated the impact the choice of chemical mechanism has on atmospheric composition and how updates to simulated isoprene chemistry improved model performance for OH, isoprene and monoterpenes relative to observations. Chapter 3 built on this by identifying how the choice of chemical mechanism influences the climatic impact of BVOC emissions and the magnitude of the resulting biosphere-climate feedback.

However, to isolate the differences in simulated atmospheric composition and climatic impact to those arising from the differences in the ST, CS and CS2 mechanisms, Chapters 2 or 3 did not include a consideration of how BVOCs can contribute to aerosol via HOM formation. HOMs can influence climate by contributing to existing aerosol or nucleating new particles with and without sulphuric acid (Section 1.4). This suggests their inclusion would be of particular importance in low sulphur atmospheres such as the PI (Gordon et al., 2016).

Compared to isoprene chemistry, the understanding of HOM formation mechanisms is more limited (Section 1.4.4). There remains uncertainty in the dependence of the autoxidation reaction rate constants on molecular structure, functionalisation and temperature as well as the influence of NO_x and other bimolecular reaction partners (e.g., Bianchi et al., 2019). The modelling of HOMs is therefore less established than for isoprene chemistry. The near-explicit HOM mechanism of Roldin et al (2019) is too large for UKCA and fixed yield approaches (e.g., Gordon et al., 2016) do not fully capture chemical feedbacks such as the influence of oxidants, NO_x, competing bimolecular reaction pathways or the experimentally observed suppression of HOMs by isoprene (McFiggans at al., 2019) (Section 1.4.5.1). Including the impact of these additional factors is vital to produce an accurate description of HOMs and their influence on climate. Therefore, to assess the influence of HOMs on the climatic impact of BVOCs, a chemical mechanism describing HOM formation suitable for a global climate model must first be developed.

This chapter answers the question: How can the chemistry of HOM formation from BVOCs be described in a form suitable for global climate modelling?

I present the development and evaluation of CRI-HOM, the first semi-explicit HOM model suitable for incorporation into UKCA. I describe the fundamental chemistry used to build the mechanism, the optimisation of the key mechanistic parameters, the testing of influence of NO_x and temperature on HOM formation and a first assessment of the impacts it would have on PI and PD atmospheres. CRI-HOM provides a basis for investigating the impact of HOMs from α-pinene on aerosol and climate in UKCA as well as a methodology for incorporating HOMs from other species such as anthropogenic VOCs in future work.

This chapter was published in Atmospheric Chemistry and Physics.

Abstract

We present here results from a new mechanism, CRI-HOM, which we have developed to simulate the formation of highly oxygenated organic molecules (HOMs) from the gas phase oxidation of α-pinene, one of the most widely emitted BVOCs by mass. This concise scheme adds 12 species and 66 reactions to the Common Representative Intermediates (CRI) mechanism v2.2 Reduction 5 and enables the representation of semi-explicit HOM treatment suitable for long term global chemistry-aerosol-climate modelling, within a comprehensive tropospheric chemical mechanism. The key features of the new mechanism are (i) representation of the autoxidation of peroxy radicals from the hydroxyl radical and ozone-initiated reactions of α-pinene, (ii) formation of multiple generations of peroxy radicals, (iii) formation of accretion products (dimers) and (iv) isoprene-driven suppression of accretion product formation, as observed in experiments. The mechanism has been constructed through optimisation against a series of flow tube laboratory experiments. The mechanism predicts a HOM yield of 2-4.5% under conditions of low to moderate NO_x, in line with experimental observations, and reproduces qualitatively the decline in HOM yield and concentration at higher NO_x. The mechanism gives a HOM yield that also increases with temperature, in line with observations, and our mechanism compares favourably to some of the limited observations of [HOM] observed in the boreal forest in Finland and in the southeast USA.

The reproduction of isoprene-driven suppression of HOMs is a key step forward as it enables global climate models to capture the interaction between the major BVOC species, along with the potential climatic feedbacks. This suppression is demonstrated when the mechanism is used to simulate atmospheric profiles over the boreal forest and rainforest; different isoprene concentrations result in different [HOM] distributions, illustrating the importance of BVOC interactions in atmospheric composition and climate. Finally, particle nucleation rates calculated from [HOM] in present day and pre-industrial atmospheres suggest that "sulphuric acid free" nucleation can compete effectively with other nucleation pathways in the boreal forest, particularly in the pre-industrial, with important implications for the aerosol budget and radiative forcing.

4.1 Introduction

Aerosols play an important role in the Earth system by affecting the Earth's radiative balance as well as local air quality and thus human health (Carslaw et al., 2010). Aerosols can interact directly with solar radiation through scattering or absorption and indirectly by influencing cloud properties by seeding cloud droplets as well as increasing cloud albedo (Forster et al., 2007; Twomey., 1974). Thus, aerosols change the balance between the energy received from the Sun and the energy emitted from the planet at the top of the atmosphere. However, a major uncertainty in climate change predictions arises from aerosols and aerosol-cloud interactions (Stocker et al., 2013). This arises in part from a lack of understanding of pre-industrial (PI) aerosol and it is the change in aerosol burden from the PI to the present day (PD) which determines the effective radiative forcing (ERF) of aerosols. As PI aerosols sources are almost exclusively natural, an understanding of natural sources and the associated aerosol formation processes is essential if better predictions for climate change are to be made.

An important formation route for aerosols is oxidation of volatile organic compounds which form lower volatility

species that can partition into the aerosol phase or nucleate new particles (Kirkby et al., 2016; Shrivastava et al., 2017). Recently it has been established that the oxidation of organic compounds can lead to the formation of "highly oxygenated organic molecules" (HOMs) (Mentel et al., 2014; Ehn et al., 2014; Kurtén et al., 2016; Bianchi et al., 2019) (also referred to as "highly oxidised multifunctional organic compounds; Ehn et al., 2012) which are formed by multiple intramolecular oxidation steps, termed autoxidation (Crounse et al., 2013; Bianchi et al., 2019). Autoxidation typically involves the abstraction by a peroxy radical of a hydrogen atom bonded to a carbon elsewhere on the molecule resulting in an alkyl radical and hydroperoxide group. The alkyl radical reacts rapidly with atmospheric oxygen to form a new peroxy radical, ultimately reducing the species' volatility and enabling particle formation/condensation. HOMs are defined as closed-shell species with at least 6 oxygens formed by initial atmospheric oxidation and subsequent autoxidation steps (Bianchi et al., 2019). HOM formation has been observed from anthropogenic species (Berndt et al., 2018a) and biogenic species such as α-pinene (Molteni et al., 2019; Berndt et al., 2018b). The semi-explicit mechanism described for the first time in this paper describes the formation of HOMs from α-pinene in a form suitable for global modelling studies. This provides a framework for incorporating a comprehensive description of pure biogenic nucleation into a global model and, ultimately, allowing for a more rigorous description of aerosol formation and the climatic consequences. α-pinene is considered as it is the most widely studied and widely emitted monoterpene (~32 TgC yr^{-1}, Sindelarova et al., 2014) and, with measured HOM yields around 3-10 % (Ehn et al., 2014; Jokinen et al. 2015), has the potential to produce 2-7 Tg HOM yr^{-1} with the range arising from uncertainties in emissions, HOM yield and difference in mass between the precursor BVOC and the HOMs which will have at least 6 additional oxygen atoms but in some cases, considerably more. HOM yields from β-pinene (the second most widely emitted monoterpene, Sindelarova et al., 2014) and isoprene (the most widely emitted BVOC, Sindelarova et al., 2014) are negligible (Ehn et al., 2014). Limonene has emissions around 25% of α-pinene (Sindelarova et al., 2014) and is likely to have a higher HOM yield (Ehn et al., 2014; Jokinen et al., 2015) although a much wider range of values have been reported than for α-pinene. Limonene thus may have the potential to produce a similar mass of HOM as α-pinene and its consideration may be an area of future work. Emissions of anthropogenic VOCs account for ~10% of total VOC emissions (Guenther et al., 1995), roughly the same quantity as monoterpene emissions, and, as no species have HOM yields above 2.5% (Ehn et al., 2014; Jokinen et al., 2015; Kirkby et al., 2016; Bianchi et al., 2019), the contribution of anthropogenic VOCs to HOM is likely to be significantly smaller. Nevertheless, the speciation of anthropogenic VOCs in the CRI v2.2 mechanism means that addition of HOMs from these sources will be possible and, from an urban air quality perspective, very important.

Nucleation of new particles from sulphuric acid is an important means of new particle formation (NPF) in the atmosphere (Kulmala et al., 1998). Sulphuric acid can also form new particles with oxidised organic species (Riccobono et al., 2015). However, extremely involatile HOMs can participate in NPF, without necessarily needing a sulphuric acid seed in a process termed pure biogenic nucleation (PBN) (Kirkby et al., 2016, Gordon et al., 2016). Despite playing important roles in aerosol formation and growth, the relatively recent discovery of HOMs and the complexity of their formation means that their role in particle formation and contribution to aerosol has been assessed in very few global model studies (Gordon et al., 2016, Zhu et al., 2019). The ability of PBN to change atmospheric aerosol loading by providing a route to particle formation without sulphuric acid has been illustrated (Gordon et al., 2016) with this effect particularly important in the PI atmosphere, where lower SO_2

emissions resulted in greater sensitivity of aerosol loading to alternative formation routes (i.e. including PBN) and a higher simulated aerosol burden than previous studies. As a result, Gordon et al (2016) calculated that the cloud radiative forcing from the PI to PD was 27% lower than previous estimates. Meanwhile, Zhu et al (2019), highlighting the fact that many chemistry schemes fail to reproduce nucleation rates in low sulphuric acid concentrations, showed the complex effect PBN has in the PI and PD with a more complicated mechanism but one which also omitted autoxidation and accretion product formation. Including PBN in a global chemistry-aerosol scheme resulted in a much larger increase in the magnitude of the (negative) aerosol indirect effect (AIE) in the PI than the PD. This has potentially important consequences as it means that the effective radiative forcing (ERF) of aerosols from the PI to PD may be smaller than previously expected. This in turn would mean that climate sensitivity is lower than previously thought as aerosols are offsetting a smaller amount of warming arising from the enhanced concentrations of greenhouse gases than previously thought, with implications for predictions of future climate change as well.

The peroxy radicals produced from α-pinene oxidation by OH or O_3 have been observed to undergo autoxidation under typical atmospheric conditions (Ehn et al., 2014; Jokinen et al., 2014; Berndt et al., 2016; Berndt et al., 2018b). The autoxidation competes with the bimolecular reaction of peroxy radicals with NO, NO_3, HO_2 and other peroxy radicals and its yield is thus dependent on background atmospheric composition. Therefore, an accurate description of HOMs requires consideration of NO_x and oxidant concentrations as well as autoxidation; indeed, elevated NO_x has been observed to suppress HOM formation (Lehtipalo et al., 2018). The first order rate constants for autoxidation can vary over several orders of magnitude ($\sim 10^{-6} - 10^{2}$ s^{-1}) depending on nearby functional groups (Otkjær et al., 2018; Bianchi et al., 2019; Crounse et al., 2013; Xu et al., 2018; Kurten et al., 2015). Autoxidation rates also exhibit a significant positive temperature dependence (Jenkin et al., 2019b; Bianchi et al., 2019) and HOM yield has been observed to be highly temperature dependent (Quéléver et al., 2019). Thus, the overall competitiveness of autoxidation is dependent on the background atmospheric composition and ambient temperature as well as the molecule undergoing oxidation.

In addition to autoxidation, the formation of HOM accretion products (also called dimers; Kurtén et al., 2016; Bianchi et al., 2019) by reactions between two peroxy radicals has been observed to be significant with large peroxy radicals (Kirkby et al., 2016; Berndt et al., 2018a; Berndt et al., 2018b; Jenkin et al., 2019b; Molteni et al., 2019). These species are predicted to be more involatile than 10-carbon HOMs (also termed monomers; Kurtén et al., 2016) with important implications for new particle formation and contributions to SOA. In established schemes such as the Master Chemical Mechanism (MCM) (Jenkin et al., 1997; Saunders et al., 2003), the Common Representative Intermediates (CRI) (Utembe et al., 2010; Watson et al., 2008; Jenkin et al., 2008; Jenkin et al., 2019a) and the Chemistry of the Stratosphere and Troposphere (Strat-Trop) used in the climate model UKCA (United Kingdom Chemistry and Aerosol) (Archibald et al., 2020), formation of accretion products is not included as it was previously considered negligible or too complex to include. However, experimental work suggests that accretion product formation is a competitive pathway for larger peroxy radicals, such as those formed from α-pinene (Berndt et al., 2018b; Molteni et al., 2019; Simon et al., 2020) and indeed becomes more favourable with increasing functionality and size; the rate coefficient for the accretion reaction between two α-pinene derived

peroxy radicals was observed to be 16-80× greater (depending on the extent of oxidation) than for the analogous reaction between two isoprene derived peroxy radicals (Berndt et al., 2018a; Berndt et al., 2018b).

The mechanistic treatment of HOMs in numerical models has varied considerably from simple fixed-yield approximations (Gordon et al., 2016) through basic mechanisms linked to a volatility basis set (Schervish et al., 2019) to more explicit descriptions based on the MCM featuring either a limited subset of HOMs without accretion product formation or autoxidation (Zhu et al., 2019) or a near explicit description involving over 1700 reactions (Roldin et al., 2019). Whilst the addition of PBN represents an important process level improvement in models, the approaches discussed above all have some degree of limitation. As well as omitting accretion product formation, simpler models (Gordon et al., 2016; Schervish et al., 2019) do not fully capture the influence of oxidant levels, NO_x or temperature while the more explicit schemes (Zhu et al., 2019; Roldin et al., 2019) are too computationally expensive for long term climate studies. Furthermore, none of the schemes include the relatively novel observation of suppression via reactive RO_2 cross reactions (McFiggans et al., 2019), although this has been identified as an important area for future research (Zhu et al., 2019; Roldin et al., 2019) and is addressed in this work.

New experimental evidence suggests that isoprene may suppress the formation of the most involatile accretion products and thus the smallest aerosol particles (Berndt et al., 2018b; McFiggans et al., 2019; Heinritzi et al., 2020) and reproducing the effect of isoprene has been identified as an important requirement for future mechanisms (Roldin et al., 2019). This inhibition is driven firstly by isoprene scavenging OH radicals (Lee et al., 2016; Kiendler-Scharr et al., 2009; Berndt et al, 2018b), thus reducing the formation of large peroxy radicals by reaction of α-pinene with OH. The second driver is the scavenging of the 10-carbon α-pinene peroxy radicals (C10RO2) by isoprene peroxy radicals (C5RO2) and the other smaller peroxy radicals from species such as CO and CH_4 (McFiggans et al., 2019). These C10RO2 could otherwise form 20-carbon accretion products (Eq 4.1) which are predicted to be highly involatile (Kurtén et al., 2016). The reaction of isoprene peroxy radicals with the α-pinene radicals produces the 15-carbon accretion product (C15d) (Eq 4.2) as well as closed shell species (C10 and C5) (Eq 4.3) and alkoxy radicals (C10RO and C5RO) (Eq 4.4) which isomerise or fragment (Jenkin et al, 2019b).

$$\mathrm{C10RO_2} + \mathrm{C10RO_2} \rightarrow \mathrm{C20d} + \mathrm{O_2} \quad (4.1)$$

$$\mathrm{C10RO_2} + \mathrm{C5RO_2} \rightarrow \mathrm{C15d} + \mathrm{O_2} \quad (4.2)$$

$$\mathrm{C10RO_2} + \mathrm{C5RO_2} \rightarrow \mathrm{C10} + \mathrm{C5} + \mathrm{O_2} \quad (4.3)$$

$$\mathrm{C10RO_2} + \mathrm{C5RO_2} \rightarrow \mathrm{C10RO} + \mathrm{C5RO} + \mathrm{O_2} \quad (4.4)$$

This inhibition affects the aerosol size distribution (an important parameter for the radiative forcing of aerosol., Zhu et al., 2019) by favouring the growth of larger existing aerosol particles by promoting the production of smaller, more volatile species which can partition to pre-existing aerosol rather than the nucleation of new

particles from larger, less volatile species. This has the potential to have important consequences for future predictions of SOA and the negative feedback proposed to exist between biogenic VOC emissions and atmospheric temperature (Kulmala et al., 2004; Carslaw et al., 2010; Sporre et al., 2018). Such predictions, based on the modelled increases in isoprene and monoterpene emissions in a warmer climate (Kulmala et al., 2013; Sporre et al., 2019) have not considered the potential perturbation to NPF and atmospheric aerosol loading by isoprene and the changes in radiative forcing which may result. Reassessing the sign and size of this feedback by coupling the chemistry scheme described in this work to an aerosol scheme within a global climate model is a key long-term aim of this work.

In this study we describe our work developing a new mechanism sufficiently concise for global chemistry climate models that can simulate the process of autoxidation, the formation of HOMs from α-pinene and the influence of isoprene. In Section 4.2 the development of the mechanism from the principles of gas phase chemistry is described and in Section 4.3 we discuss mechanism optimisation and validation against experimental data and the parent mechanism, CRI v2.2. In Section 4.4, the mechanism is used to simulate atmospheric HOM profiles and explore implications for new particle formation. Finally, in Section 4.5, conclusions for further work are drawn.

4.2 Mechanism Development

The new mechanism builds on the Common Representative Intermediates (CRI) scheme version 2.2 Reduction 5 (Jenkin et al., 2019a) (hereafter the "base mechanism"), developed from the fully explicit Master Chemical Mechanism (MCM) version 3.3.1 (Jenkin et al., 2015) which describes the degradation of organic compounds in the troposphere. In the CRI framework, species are lumped together into surrogate molecules whose behaviour is optimised against the fully explicit MCM. The CRI v2.2 R5 mechanism describes the degradation of α-pinene, β-pinene, isoprene and 19 other emitted VOC species.

The updates we have made to the base mechanism to produce the new HOM-forming functionality include the addition of autoxidation of α-pinene oxidation products and a more detailed peroxy radical pool scheme. These changes enable the formation of 10-carbon, 15-carbon and 20-carbon HOMs and add 12 species and 66 reactions to the base mechanism. The new chemical mechanisms for ozonolysis and OH oxidation are shown in Figure 4.1 and Figure 4.2 respectively. We now describe the changes made to the base mechanism to incorporate HOM chemistry in more detail.

4.2.1 Ozonolysis

To simulate the autoxidation reactions formed from ozonolysis, 5 new peroxy radical species were added to the base mechanism. The peroxy radicals formed from ozonolysis of α-pinene and subsequent autoxidation steps are collectively termed "O3RO2". In the base mechanism, α-pinene reacts with ozone to produce the single lumped peroxy radical RN18AO2 and acetone. This single mechanistic step represents multiple chemical steps, with RN18AO2 representing a 6 or 7 carbon species. In addition, TNCARB26 (closed shell carbonyl species) and RCOOH25 (pinonic acid) arise from the reaction of Criegee intermediates with water. The yields of these species,

17.5% and 2.5% respectively, remain unchanged from the CRI v2.2 mechanism and are well supported in the literature (IUPAC Task Group on Atmospheric Chemical Kinetic Data Evaluation, Atkinson and Arey., 2003; Johnson and Marston et al., 2008). RN18AO2 goes on to react with standard peroxy radical reaction partners; HO_2 forming hydroperoxides; NO and NO_3 forming alkoxy radicals; and the peroxy radical pool forming alkoxy radicals, carbonyls and alcohols, as described in (Jenkin et al., 2019b).

In our new mechanism, RN18AO2 is replaced with the tracers RN26BO2 and RTN24O2. RN26BO2 represents the 10-carbon peroxy radicals formed directly from the cleavage of the ozonide and subsequent addition of atmospheric oxygen, which can then undergo autoxidation. RTN24O2, a species already in the CRI mechanism, represents the 9 carbon peroxy radical species (MCM species C96O2) which is also formed from ozonolysis but does not undergo autoxidation in this mechanism. RN26BO2 is termed "1st generation" as it has undergone one oxidation step and it can undergo autoxidation to form the 2nd, 3rd, 4th and lumped higher generation species, termed RN25BO2O2, RN24BO4O2, RN23BO4O2 and RNxBOyO2 species respectively (RNxBOyO2 does not undergo further autoxidation but does undergo all the other reactions). In the base mechanism, the first number featured in a species' name is an index which refers to the number of NO-to-NO_2 conversions possible, which depends on the number of C-C and C-H bonds. During the H-shift step of autoxidation, a C-H bond is usually broken to produce the alkyl radical which then forms the peroxy radical from atmospheric oxygen and so each autoxidation step reduces the index by one while the number of oxygens is increased by 2. For example, the autoxidation of the 2nd generation O3RO2 to 3rd generation is expressed by Eq 4.5.

$$\mathrm{RN25BO2O2} \rightarrow \mathrm{RN24BO4O2} \quad (4.5)$$

Each generation of peroxy radical also undergoes bimolecular reactions. Reaction with HO_2 produces a hydroperoxide species; for the 2nd and later generations, the product is classified as a HOM (C10z) as they fulfil the criteria discussed by Bianchi et al (2019), while for the 1st generation species the resulting hydroperoxide is RTN26OOH, a species already present in the CRI (Eq 4.6).

$$\mathrm{RNaBObO2} + \mathrm{HO_2} \rightarrow \mathrm{RTN26OOH\ or\ C10z} \quad (4.6)$$

Reaction with NO and NO_3 yields nitrates or alkoxy radicals and accurately representing the behaviour of these products is crucial to reproducing the effect of NO_x on HOM formation. Alkoxy radicals are not represented explicitly due to their rapid reactions which, typically for alkoxy radicals formed from larger peroxy radicals, are decomposition or isomerisation. Decomposition produces two smaller species, one closed shell and one peroxy radical while isomerisation produces a more functionalised peroxy radical via an alkyl radical intermediate with one fewer oxygen than would have been added via autoxidation. Faced with very limited data and the fact that the precise fate of an alkoxy radical will depend considerably on molecular structure and neighbouring groups, a branching ratio 50:50 for decomposition and isomerisation was adopted. Sensitivity tests perturbing the branching ratio between 75:25 and 25:75 were performed to probe the consequences of this uncertainty. These tests suggested the precise value of this branching ratio within this range did not affect the fitting of rate coefficients for autoxidation and accretion product formation (Section 4.3.1). These branching ratio perturbations did lead to

changes in HOM yield (Fig. D4(b)) and are discussed in more detail in Section 4.3.2. The decomposition products are existing CRI species CARB16 and RN10O2 or RN9O2 and the isomerisation product is the next generation peroxy radical as shown in the example reaction (Eq 4.7).

$$\mathrm{RN25BO2O2} + \mathrm{NO} \rightarrow 0.5\mathrm{RN24BO4O2} + 0.5\mathrm{CARB16} + 0.5\mathrm{RN9O2} \quad (4.7)$$

A schematic of the additions made to the CRI for the ozonolysis scheme is shown in Figure 4.1.

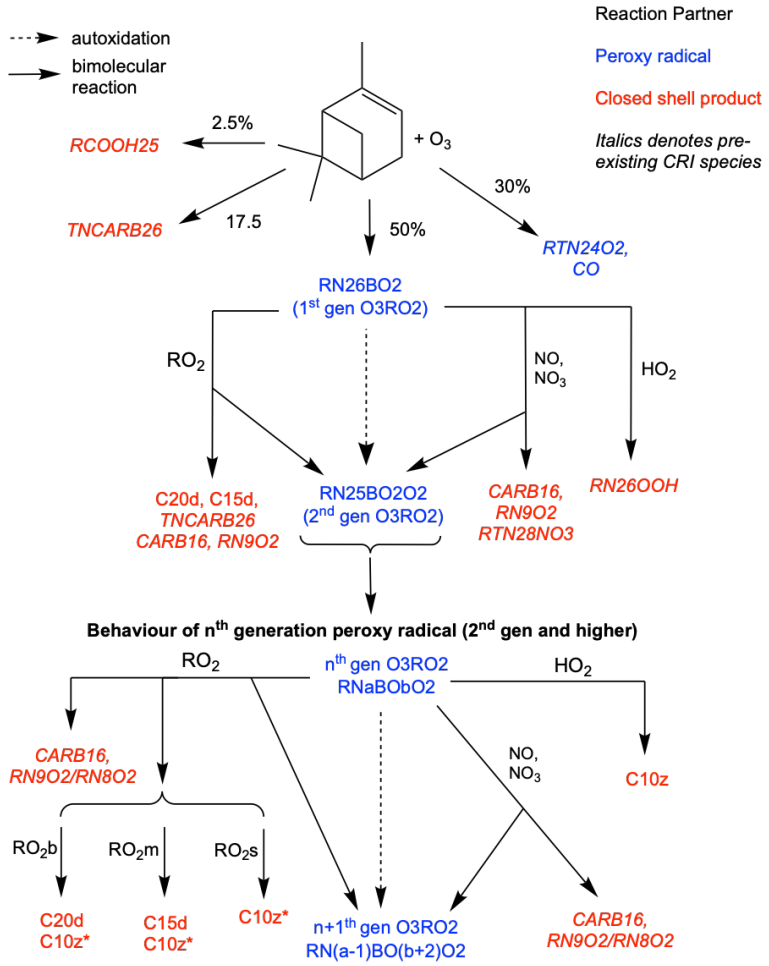


Figure 4.1. Schematic of additions to CRI v2.2 to represent autoxidation and HOM formation via ozonolysis of α-pinene. HOMs (C10z, C15d, C20d) can be produced via reaction of the O3RO2 with HO_2 and RO_2 while reaction with NO, NO_3 and RO_2 can produce alkoxy radicals which can fragment or isomerise. New species introduced in this scheme are denoted by normal font, existing species by italics. The RO_2 pool is split into subsections covering big (RO_2b), medium (RO_2m) and small (RO_2s) peroxy radicals to facilitate addition of accretion product formation.

4.2.2 OH oxidation

Autoxidation through the OH initiated oxidation pathway resulted in the addition of 6 new species, including 5 new peroxy radicals. The peroxy radicals formed from OH oxidation of α-pinene and subsequent autoxidation steps are termed "OHRO2". The single peroxy radical RTN28O2 in the base mechanism is replaced by RTN28AO2, representing the two species which do not undergo autoxidation (APINAO2 and APINBO2 in the MCM), and RTN28BO2 (MCM APINCO2) which can undergo autoxidation to form higher generation peroxy radicals (Xu et al., 2018). The 2nd and 3rd generation OHRO2 are represented explicitly (RTN27BO2O2 and RTN26BO4O2) and all 4th generation and higher species are lumped together as RTNxBOyO2 for mechanistic simplicity. The chemical treatment of RTN28AO2 is the same as the original CRI species RTN28O2 while all other OHRO2 (except RTNxBOyO2) can undergo autoxidation (Eq 4.8).

$$\mathrm{RTNaBObO2} \rightarrow \mathrm{RTN(1-a)BO(b+2)O2} \quad (4.8)$$

Reaction of the 1st and 2nd generation OHRO2 (RTN28BO2 and RTN27BO2O2) with HO_2 yields the hydroperoxide RTN28OOH which is not classified as a HOM due to insufficient oxygens. The HOM produced by all later generation OHRO2 is termed C10x (Eq 4.9).

$$\mathrm{RTNaBObO2} + \mathrm{HO_2} \rightarrow \mathrm{RTN28OOH\ or\ C10x} \quad (4.9)$$

Reaction with NO and NO_3 is treated in the same manner as O3RO2 except for RTN28BO2 which follows the reaction of the analogous species APINCO2 in the MCM. A schematic of the additions made to the base mechanism for the OH oxidation scheme is shown in Fig. 4.2.

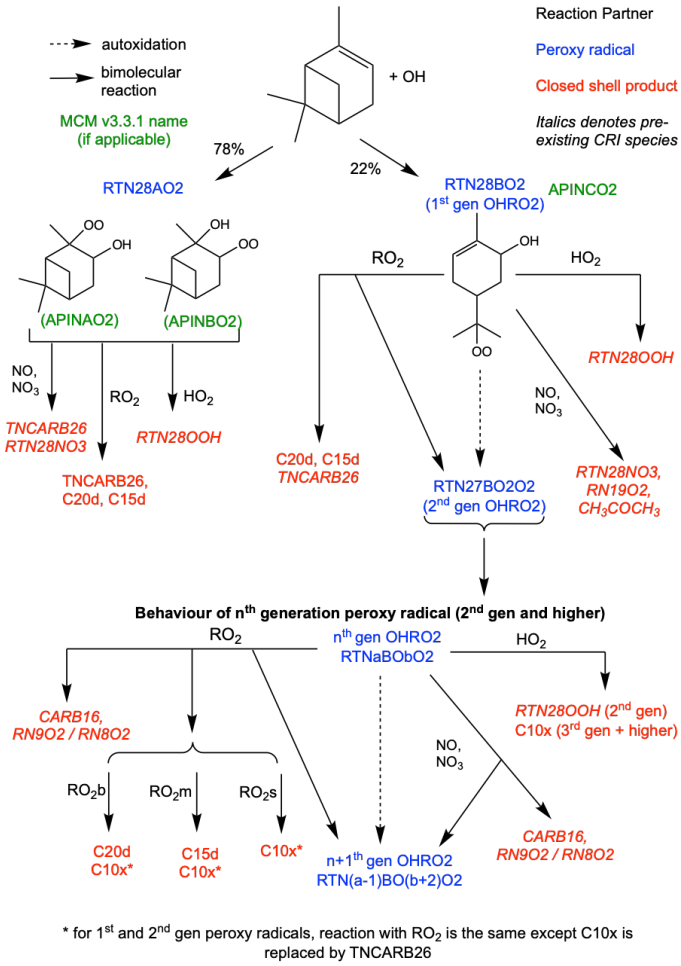


Figure 4.2. Schematic of additions to CRI v2.2 to represent autoxidation and HOM formation via OH oxidation. HOMs can be produced via reaction with HO_2 and RO_2 while reaction with NO, NO_3 and RO_2 can produce alkoxy radicals which can fragment or isomerise. The RO_2 pool is split into subsections covering big (RO_2b), medium (RO_2m) and small (RO_2s) peroxy radicals to facilitate addition of accretion product formation.

The pathway initiated by reaction of α-pinene with NO_3 was not considered in this work but is identified as an area for future work. A summary of the peroxy radical species in the two pathways is given in Table 4.1 and a full mechanistic description is provided in Appendix D.

4.2.3 Peroxy Radical + Peroxy Radical Interactions

Reactions between peroxy radicals can result in the formation of two alkoxy radicals (Eq 4.10), a carbonyl and an alcohol (Eq 4.11) or accretion product (Eq 4.12) (Jenkin et al., 2019b).

$$RO_2 + R'O_2 \rightarrow RO + R'O + O_2 \quad (4.10)$$

$$RO_2 + R'O_2 \rightarrow R_{-H}O + R'OH + O_2 \text{ or } R'_{-H}O + ROH + O_2 \quad (4.11)$$

$$RO_2 + R'O_2 \rightarrow ROOR' + O_2 \quad (4.12)$$

Rather than represent every possible RO_2-RO_2 reaction combination, the base mechanism uses a peroxy radical pool. Each peroxy radical undergoes a unimolecular reaction with a first order rate coefficient determined by the total peroxy radical concentration and the geometric mean of the self-reaction rates of the methyl peroxy radical and radical of interest (Jenkin et al., 2019b).

Table 4.1. Summary of new species added in HOM mechanism. The removal of species RN18AO2 and RTN28O2 results in a net increase of 12 species.

Species	**Classification**	**Origin**	**MCM v3.3.1 equivalent**
RN26BO2	1st generation RO_2	Ozonolysis	C107O2, C109O2
RN25BO2O2	2nd generation RO_2	Ozonolysis	N/A
RN24BO4O2	3rd generation RO_2	Ozonolysis	N/A
RN23BO6O2	4th generation RO_2	Ozonolysis	N/A
RNxBOyO2	Lumped 5th and higher generation RO_2	Ozonolysis	N/A
RTN28AO2	1st generation RO_2 (no autoxidation)	Ozonolysis	APINAO2, APINBO2
RTN28BO2	1st generation RO_2 (autoxidation possible)	OH oxidation	APINCO2
RTN27BO2O2	2nd generation RO_2	OH oxidation	N/A
RTN26BO4O2	3rd generation RO_2	OH oxidation	N/A
RTNxBOyO2	Lumped 4th and higher generation RO_2	OH oxidation	N/A
C10z	10-carbon HOM	Ozonolysis	N/A
C10x	10-carbon HOM	OH oxidation	N/A
C15d	15-carbon HOM	Ozonolysis and OH oxidation	N/A
C20d	20-carbon HOM	Ozonolysis and OH oxidation	N/A

While computationally efficient, such a mechanism fails to represent the effect of peroxy radical size on the distribution of products. While negligible for small peroxy radicals, accretion product formation is more

favourable when larger, more functionalised peroxy radicals react (Berndt et al., 2018b; Schervish et al., 2019). To describe the reactions between the differently sized peroxy radicals, we have split the single peroxy radical pool into three pools for small (<4 carbons), medium (4-7 carbons) and big (>7 carbons) peroxy radicals. Each big peroxy radical reacts separately with each peroxy radical pool while, to minimise the total number of reactions, all small peroxy radicals react with the total pool as accretion product formation is much less favourable (Jenkin et al., 2019b). Medium peroxy radicals are discussed below. The use of large and medium peroxy radical pools allows for improved representation of the competition between peroxy radicals with different reactivity in our new mechanism and is a substantial improvement over the base mechanism.

Table 4.2 summarises the products for a specific peroxy radical reacting with the different peroxy radical pools. As discussed previously, alkoxy radials were not simulated explicitly, rather they decomposed into closed shell products and peroxy radicals. A full list of the contents of each peroxy radical pool is given in Appendix D.

Table 4.2. Summary of possible products formed for a particular peroxy radical reacting with the big, medium and small peroxy radical pools. (*Result depends on extent to which the reacting RO_2 has been oxidised prior to RO_2-RO_2 reaction. Products from some of less oxidised RO_2 may not qualify as HOMs and are assigned to the most relevant non-HOM CRI species.)

Size of reacting RO_2	Product of reaction with big pool	Product of reaction with medium pool	Product of reaction with small pool
Big (>7 C, e.g. RN26BO2)	C20 HOM accretion product C10 HOM / Existing CRI species* Peroxy radical	C15 HOM accretion product C10 HOM / Existing CRI species* Peroxy radical	C10 HOM / Existing CRI species* Peroxy radical
Medium (4-7 C, e.g. RU14O2)	Closed shell, alkoxy radical		
Small (<4 C, e.g. CH3O2)	Closed shell species, alkoxy radical (no change from CRI v2.2 treatment)		

In practice, the alkoxy radicals formed from the reaction of isoprene-derived peroxy radicals (which are likely to dominate the medium size pool) with other peroxy radicals decompose rapidly into the major products: closed shell carbonyls methyl vinyl ketone and methacrolein (UCARB10) and the minor product hydroxy vinyl carbonyl (UCARB12) (Jenkin et al., 2015). The accretion of isoprene-derived peroxy radicals has been measured to be over an order of magnitude slower than the accretion of peroxy radicals derived from α-pinene (Berndt et al., 2018b), supporting the theory that accretion product formation becomes more favourable with increasing peroxy radical size. Therefore, to limit complexity, all medium peroxy radicals in the mechanism simply react with the total peroxy radical pool and their accretion product formation was ignored.

4.2.3.1 Large Peroxy Radical Pool

The reaction of a large peroxy radical with the large peroxy radical pool ($RO2_b$) can produce an accretion product (Eq 4.13), closed species (Eq 4.14) or an alkoxy radical (Eq 4.15) (Jenkin et al., 2019b) which then reacts as

discussed in sections 4.2.1 and 4.2.2. Note that a single C10RO2 species will produce half a C20d accretion product for the purposes of mass conservation.

$$\mathrm{C10RO_2} + \mathrm{RO2_b} \rightarrow 0.5\mathrm{C20d} + \mathrm{O_2} : \mathrm{k_{13}} \quad (4.13)$$

$$\mathrm{C10RO_2} + \mathrm{RO2_b} \rightarrow \mathrm{C10\,z/C\,10\,x/TNCARB\,26} : \mathrm{k_{14}} \quad (4.14)$$

$$\mathrm{C10RO_2} + \mathrm{RO2_b} \rightarrow \mathrm{C10RO} : \mathrm{k_{15}} \quad (4.15)$$

The rate coefficient for C20d formation, k_{13}, increased with the extent of oxidation of the reacting peroxy radical. This was done to simulate the observed behaviour that accretion product formation becomes faster as the reacting peroxy radicals become more functionalised (Berndt et al., 2018a; Berndt et al., 2018b). Thus, the reaction forming C20d from the 1st generation peroxy radicals had a lower rate coefficient than the analogous reactions involving higher generation RO2 species (reactions 21, 23, 25, 27, 29, 46, 63, 64, 65 and 66 in the Appendix D). The rate coefficients used, 0.4-3.6×10^{-11} cm^3 $molecule^{-1}$ s^{-1} were derived from fitting against experimental data (Berndt et al., 2018b) and, as discussed in Section 4.3.1.3, and were in line with the range measured by Berndt et al (2018b) (0.97-7.9×10^{-11} cm^3 $molecule^{-1}$ s^{-1}). This resulted in Eq 4.13 being more important that Eq 4.14 and Eq 4.15 which had rate coefficients based on literature (Molteni et al., 2019; Roldin et al., 2019) up to an order of magnitude lower.

The rate coefficient for the formation of the closed shell species from O3RO2, k_{14}, was taken as the mean of the rate coefficients measured by Molteni et al (2019) (1.68×10^{-12} cm^3 $molecule^{-1}$ s^{-1}). The rate coefficient for alkoxy radical formation, k_{15}, was assumed to have the same value as k_{14} (i.e. a 50:50 branching ratio between these pathways). This value is close to the value of closed shell : alkoxy radical of 40:60 ratio suggested for primary and secondary peroxy radicals by Jenkin et al (2019b) but further from the 20:80 suggested for tertiary peroxy radicals. However, sensitivity tests where the mechanism was run with branching ratios of 40:60 and 20:80 revealed that the precise values of this branching ratio within this range did not affect the fitting of rate coefficients for autoxidation and accretion product formation (Section 4.3.1). These branching ratio perturbations led to negligible changes in HOM yield (Section 4.3.2, Simulation C) which were much smaller than the range in the HOM yield simulated to arise from the uncertainty in the autoxidation temperature dependence and are therefore considered to be of minor importance (Table D6).

The rate coefficients for formation of closed shell species and alkoxy radicals from OHRO2 with $RO2_b$ were taken from Roldin et al (2019).

4.2.3.2 Medium and Small Peroxy Radical Pools

Reaction of a large peroxy radical with the medium peroxy radical pool ($RO2_m$) can produce a 15-carbon accretion product (Eq 4.16), closed shell species (Eq 4.17) or an alkoxy radical (Eq 4.18) which is not modelled explicitly but rather decomposes rapidly into another closed shell product and peroxy radical.

$$C10RO_2 + RO2_m \rightarrow 0.667C15d + O_2 : k_{16} \quad (4.16)$$

$$C10RO_2 + RO2_m \rightarrow C10\,z/C\,10\,x/TNCARB\,26 : k_{17} \quad (4.17)$$

$$C10RO_2 + RO2_m \rightarrow C10RO : k_{18} \quad (4.18)$$

In a manner similar to C20d formation, the rate coefficient for C15d formation, k_{16}, in the mechanism increases with the extent of oxidation of the reacting large peroxy radical; the reaction forming C15d from the 1st gen peroxy radicals had a lower rate coefficient than the analogous reactions involving higher generation RO_2 species (reactions 36, 37, 38, 39, 40, 47, 71, 72, 73 and 74 in Appendix D). The fitting of k_{16} rate coefficients to experimental data is discussed in Section 4.3.1.3. The chosen fitted values of 1.8-7.5×10^{-12} cm^3 $molecule^{-1}$ s^{-1} were lower than the range measured by Berndt et al (2018b) (1.2-3.6×10^{-11} cm^3 $molecule^{-1}$ s^{-1}).

Reaction of a large peroxy radical with the small peroxy radical pool ($RO2_s$) produces a closed shell species or an alkoxy radical, in a manner analogous to Eq 4.17, Eq 4.18.

4.2.4 HOM Loss Mechanisms

The number of different molecules falling under the C10x, C10z, C15d and C20d umbrellas is huge, making the treatment of loss processes complex. Losses will occur via chemical or photolytic degradation as well as to condensation to aerosol, to the nucleation sink and dry and wet deposition. Physical loss is believed to be the major sink for HOM (Maso et al., 2002; Petäjä et al., 2009; Tan et al., 2018; Wu et al., 2018; Bianchi et al., 2019). For simplicity, in the simulations below, we ignore wet and dry deposition but do include loss to the condensation sink for modelling simulations C and D (Table 4.3).

Chemical losses of HOMs are highly uncertain. It is suggested that HOMs will react with OH (Bianchi et al., 2019). In this mechanism, OH reacts with C10x, C10z, C15d and C20d with the rate coefficient of the large hydroperoxide, RTN28OOH, used to produce the smaller closed shell CRI species CARB10 and CARB15 as well as UCARB10 (lumped methacrolein and methyl vinyl ketone) for 15-carbon dimers. This rate coefficient was 2.38×10^{-11} $molecules^{-1}$ cm^3 s^{-1} and, considering suggestions that the rate coefficient of OH with HOM could be higher (Bianchi et al., 2019), sensitivity tests increasing the rate coefficient to 1×10^{-10} $molecules^{-1}$ cm^3 s^{-1} were performed but no material effect was observed. Photolysis of peroxide and carbonyl linkages produce alkoxy radicals which behave as previously described. Photolysis frequencies are taken from the MCM (Jenkin et al., 1997, Saunders et al., 2003). Given the small concentrations of HOMs we predict that uncertainty in these gas phase loss processes are likely to have small impacts on the general features of tropospheric chemistry (i.e. OH reactivity or ozone production).

Physical loss is believed to be the major sink for HOM (Dal Maso et al., 2002; Petäjä et al., 2009; Tan et al., 2018; Wu et al., 2018; Bianchi et al., 2019). Loss to the condensation sink presents a complex challenge. The saturation vapour pressure will vary considerably (Kurtén et al., 2016) for HOMs, even within the C10 umbrella, affecting

the fraction which partition to the aerosol phase. Furthermore, some HOMs are likely to have aldehyde and alcohol moieties which will enhance their removal via reactive uptake into the aerosol phase, particularly if it is aqueous. When using our new mechanism in different simulations (Table 4.3), condensation sinks have been set to fixed values or values taken from literature.

Having described the additions and changes made to the base mechanism to develop our new mechanism, we now discuss the optimisation and validation of the mechanism.

4.3 Mechanism Optimisation and Validation

Here we discuss the optimisation of the new mechanism and its validation. In total 4 simulations were performed with the mechanism as detailed in Table 4.3.

Table 4.3. Simulations used for developing and testing new mechanism

Simulation	Purpose	Mechanism Version(s)	Conditions
A: Flow cell experiment	Optimise mechanism by fitting autoxidation coefficients and rate coefficients for accretion product formation	Temperature independent mechanism	297 K, $NO_x < 10^8$ cm^{-3}, dark 26 ppb O_3, initial α-pinene concentration varied
B: Flow cell experiment	Optimise mechanism by fitting autoxidation coefficients and rate coefficients for accretion product formation	Temperature independent mechanism	297 K, NOx < 10^8 cm^{-3}, dark 80 ppb O_3, 15.6 ppb α-pinene concentration, initial isoprene concentration varied
C: Chamber Experiment	HOM yield	Temperature dependent mechanisms with autoxidation activation energies of 6000K, 9000K and 12077K	270 K, 290 K or 310 K α-pinene 15 ppb, O_3 40 ppb NO, NO_2 varied from 0.01-10 ppb
D: Tropical Boundary Layer Experiment	Compare new mechanism with concentrations predicted by CRI v2.2	Temperature independent and all temperature dependent mechanisms	8 day run with diurnally varying photolysis, temperature (298±4 K), α-pinene and isoprene emissions Multiple runs performed with scaled NO and α-pinene emissions (Appendix D)

4.3.1 Comparison to Experimental Data

There exists a limited amount of experimental data which provides an insight into the behaviour of the multiple generations of peroxy radicals produced from ozonolysis and OH-oxidation of α-pinene (Berndt et al., 2018b). Using a flow cell, Berndt measured the concentration of α-pinene-derived peroxy radicals produced by ozonolysis (O3RO2) and OH oxidation (OHRO2) and 20-carbon (C20d) and 15-carbon (C15d) accretion products at the end of the flow tube using a chemical ionisation-atmospheric pressure interface-time of flight (CI-APi-TOF) mass spectrometer and a chemical ionisation-time of flight (CI3-TOF) mass spectrometer. The observed peroxy radicals spanned several generations of autoxidation, namely the 1^{st}-4^{th} generation for O3RO2 species and 1^{st}-3^{rd} generation for OHRO2. Berndt et al (2018b) also calculated rate coefficients for accretion product formation using the observation that accretion product concentration increased linearly with time with an assumed uncertainty no greater than a factor of 3. Reagent ions used in the CI-APi-TOF were $C_3H_7NH_3^+$, CH_3COO^- and NO_3^- and in the CI3-TOF NH_4^+. The flow tube experiments lasted for 7.9 s, at which point the flow was sampled by the mass spectrometers. Reactions proceeded under dark conditions at 1 atm and 297 K under low [NO_x] ($<10^8$ cm^{-3}). The low concentrations of bimolecular reaction partners HO_2 and NO meant that multiple autoxidation steps could occur in the reaction time.

Flow tubes operating under laminar flow are easily modelled using box models as there are very few complications to consider in terms of mixing and wall loss and no new particle formation was observed. A box model version of the mechanism was compiled in the BOXMOX framework (Knote et al., 2015). The experimental data allowed the autoxidation coefficients of the peroxy radical species and the rate coefficients of accretion product formation to be constrained. The concentrations of peroxy radicals and accretion products in the box model were evaluated at the end of the 7.9 s reaction period and compared with experiments. A process of iterative adjustment to autoxidation and accretion product formation rate coefficients in the mechanism was performed to produce the best reproduction of the experimental data by the mechanism.

Two experiments from Berndt et al (2018b) were considered. In the first experiment, flow tube runs were performed with varying initial concentrations of α-pinene (3-50 ppb) with initial O_3 at 28 ppb (Simulation A). In the second experiment, runs were performed with fixed initial α-pinene (15.6 ppb) and O_3 (80 ppb) but with initial isoprene concentrations varying from 0-60 ppb (Simulation B). Comparison to this experimental data facilitated examination of the model's ability to reproduce the concentration of HOM-precursors and accretion products with and without isoprene as well as at moderate and high O_3 mixing ratios.

An important parameter in the mechanism was the yield of RN26BO2 from α-pinene ozonolysis. This yield is uncertain, and it was found to affect the autoxidation coefficients required to reproduce the experimental data for the O3RO2 species. To constrain it, a first-order autoxidation rate coefficient of 0.206 s^{-1} for RN26BO2 was imposed, based on theoretical analysis of the α-pinene ozonolysis system (Kurtén et al., 2015), and the yield adjusted until the mechanism was able to achieve the best possible fit to the data. This resulted in a yield of 50% for RN26BO2 and 30% for RTN24O2. However, this remains a source of uncertainty and warrants further investigation. The low NO_x conditions meant that the autoxidation coefficients dominated the concentration of later generation O3RO2 and OHRO2 and, from this starting point, the autoxidation rate coefficients for later

generations were fitted against experimental data over multiple rounds of optimisation (Table 4.4). The autoxidation coefficient for the 1st generation OHRO2, RTN28BO2, was taken as 2.1 s^{-1} based on Xu et al (2018). An estimation of the uncertainty in the autoxidation is also provided in Table 4.4. These values were calculated by adjusting the autoxidation rate coefficients one at a time to determine the maximum and minimum values of an autoxidation rate coefficient for which the corresponding peroxy radical would fall within the experimental uncertainty region. This approach neglects any cross-sensitivities through the joint uncertainty in several rate coefficients. A full Monte Carlo uncertainty analysis addressing this issue is beyond the scope of this manuscript but would make a valuable follow up for future work in this field. Therefore, the autoxidation rate coefficient uncertainties are large as the experimental error uncertainties are large.

The autoxidation coefficients in Table 4.4 are higher than those considered in the theoretical study of Schervish et al (2019) but closer to the values measured by Zhao et al (2018) and the values suggested by Roldin et al (2019). The mechanism using the autoxidation coefficients from Table 4.4 predicted the lumped higher generation species (5th generation for O3RO2, 4th generation for OHRO2) at concentrations higher than observed in the work by Berndt et al (2018b). This suggests there may be additional, currently unknown loss processes for the more highly oxidised peroxy radical species which are not incorporated in this work. Additional loss processes would likely reduce the fitted autoxidation coefficients because they would provide an additional sink for the RO_2 species which does not lead to the production of the next generation RO_2. Therefore, the autoxidation coefficients determined in this work are likely to be upper limits but further insight into this is not possible with the data currently available. This is a key area for further study**.**

Table 4.4. Autoxidation coefficients for peroxy radicals after fitting to experimental data (at 297 K) with estimated uncertainty. ([a]Taken from Xu et al., 2018)

Generation	**O3RO2 / s^{-1}**	**OHRO2 / s^{-1}**
1st	0.206 (+0.025/ -0.04)	2.1[a]
2nd	1.7 (+1.1/-0.4)	2.1 (+1.6 / -0.2)
3rd	1.7 (+1.1/-0.4)	0.25 (+0.3 /-0.1)
4th	1.6 (+0.8/ -0.5)	N/A

Unfortunately, the flow tube studies of Berndt et al (2018b) lack observations to constrain the full chemical space simulated by the box model. In particular there were no measurements of OH, HO_2 or NO. The effect of the uncertainty in the initial experimental concentrations of NO, HO_2 and OH on the modelled concentrations of O3RO2, OHRO2 and accretion products and thus fitted the autoxidation coefficients and accretion product formation rates coefficients was investigated with a series of sensitivity tests. Initial conditions of 10^6 cm^{-3} for OH and 4 ppt for HO_2 were used. NO and NO_2 were initialised at 4 ppt, based on the purity of the flow gas (personal communication with T. Berndt). For HO_2, NO and NO_2 sensitivity simulations indicated that increases of 10 ppt (250% increase) and decreases of 3 ppt (75% decrease) did not lead to deviations in the concentrations of RO_2 or accretion products sufficient to warrant a change in the rate coefficients for autoxidation or accretion

product formation. Initial OH concentration had negligible effect (<5% change) on O3RO2, OHRO2 and C20d when varied over 10^5 – 2×10^6 cm^{-3} (90 % decrease, 100 % increase).

4.3.1.1 Varying α-pinene Experiment

In Simulation A, the mechanism was used to simulate various experiments with increasing initial mixing ratios of α-pinene with a fixed mixing ratio of 26 ppb of O_3. The modelled 1st-4th generation O3RO2 species (Fig. 4.3(b)) agreed well with the observed concentrations, with all the model results falling within experimental uncertainty bounds (although we note these are large).

The model was also able to reproduce the 2nd and 3rd gen OHRO2 species well (Fig. 4.3(a)) but struggled with the 1st generation OHRO2 species, overestimating it by a factor of 10, despite reproducing the general trend of variation with α-pinene. The experimental measurements of 1st generation OHRO2 concentration from Berndt et al (2018b) were believed to be underestimated by about a factor of 5 (Fig. D3). This suggests the model overprediction of the concentration of OHRO2 may be about a factor of 2. The cause of the discrepancy between modelled and measured 1st generation OHRO2 remains unclear. The rate coefficient for the production of the 1st generation OHRO2 has undergone extensive evaluation and the same coefficient is used in the CRI v2.2 parent mechanism which has been optimised against the MCM. Sensitivity tests perturbing the branching ratio between RTN28AO2 and RTN28BO2 revealed that even doubling the fraction of RTN28BO2, a significant deviation from literature (Berndt et al., 2016; Pye et al., 2018), had negligible effect as did changing initial [OH] by +100 % / -90%. Another explanation is the presence of additional unknown loss processes not currently included in the model, but in the absence of additional data, no further insights can be made at this time. More importantly, the 1st generation OHRO2 does not form HOM itself and so it is unlikely to have a significant impact on HOM concentration. Furthermore, the modelled 1st generation OHRO2 was dominated by RTN28AO2, the species which does not autoxidise to form later generation RO_2. Nevertheless, this remains an important area for future work but one where more data is needed for additional constraints to be put in place.

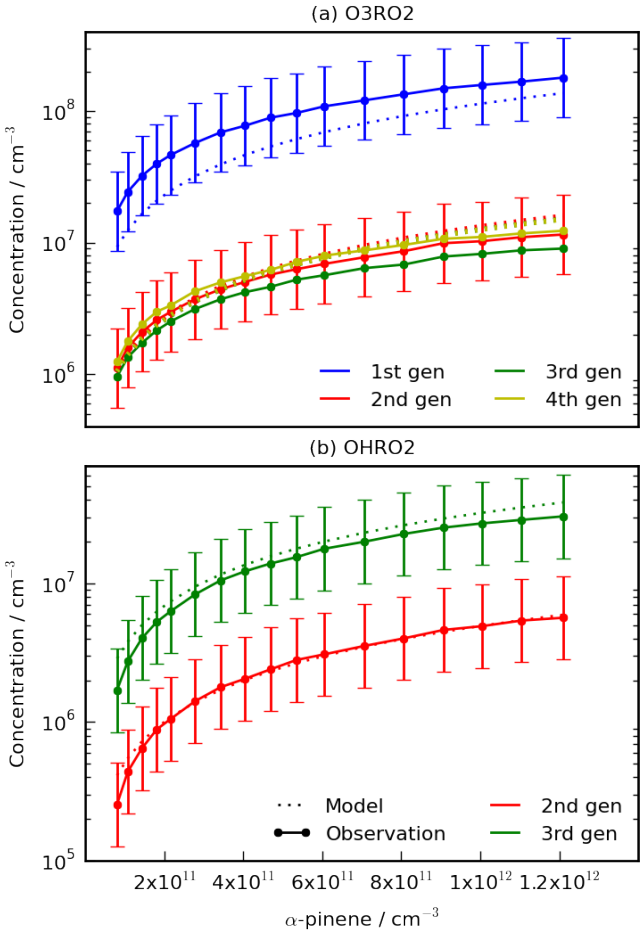


Figure 4.3. Comparison of the HOM-precursors (a) O3RO2 and (b) OHRO2 produced by the model and from Berndt et al (2018b) for experiments performed with different initial concentrations of α-pinene (Simulation A). The model reproduces the increase in O3RO2 and 2nd and 3rd generation OHRO2 with initial α-pinene well. The model struggled to reproduce concentrations of the 1st generation OHRO2 (not shown). Note that the error shown is the experimental error from Berndt et al (2018b) and the error bars for the 3rd and 4th generation O3RO2 species are of very similar size to the error bars of the 2nd generation species but have been omitted for clarity.

4.3.1.2 Varying Isoprene Experiment

In Simulation B, varying initial concentrations of isoprene were employed under conditions of fixed initial mixing ratios of α-pinene (15.6 ppb) and O_3 (80 ppb). The model was able to reproduce the observed decline in the 2nd and 3rd generation OHRO2 species (Fig. 4.4(a)) with increasing isoprene while also reproducing the minor decrease in the O3RO2 species (Fig. 4.4(b)). The decline in OHRO2 mirrored the modelled decrease in OH, providing a strong indication that OH scavenging by isoprene is playing a major role in decrease in OHRO2, as suggested by McFiggans et al (2019), also highlighting the need for better understanding of HO_x-recycling during isoprene oxidation.

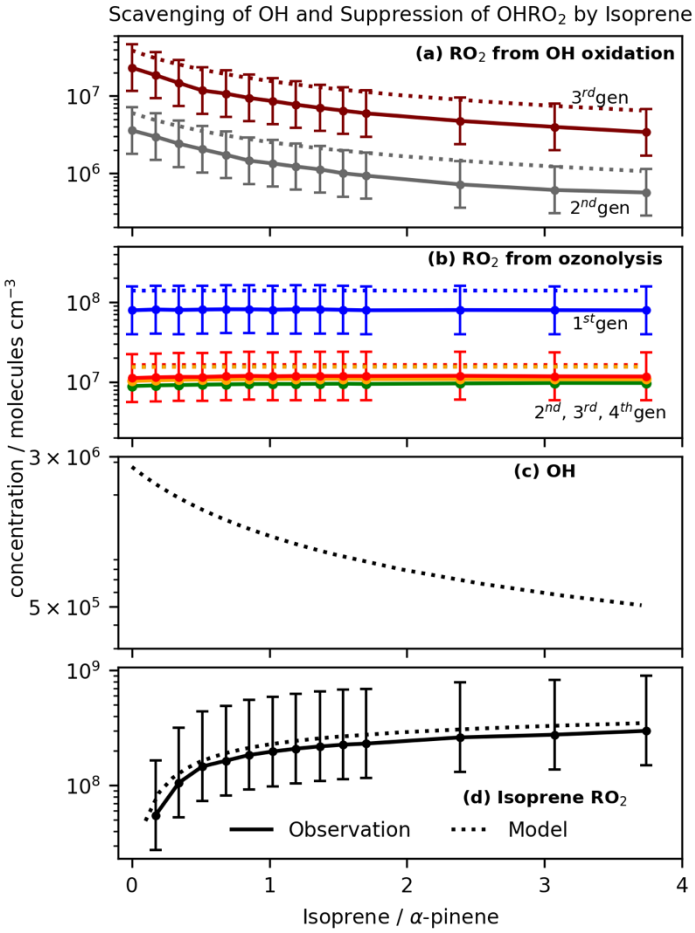


Figure 4.4. Observed and modelled variation for Simulation B of OHRO2 (a), O3RO2 (b), OH (c) and the peroxy radical formed from isoprene oxidation (d) with increasing isoprene (observed data from Berndt et al., 2018b). The model is able to reproduce the decrease in OHRO2 as well as their concentrations. The fractional decline of OHRO2 mirrors that observed in the OH concentration, suggesting the major driver is OH scavenging. The error shown is the experimental error from Berndt et al (2018b).

4.3.1.3 Simulation of Accretion Products

The 20-carbon accretion products were measured in both the isoprene-free, varying α-pinene experiment (Simulation A) and, separately, under conditions of constant α-pinene and varying isoprene (Simulation B). The rate coefficients for 20-carbon accretion product formation were fitted against experimental data (Berndt et al., 2018b) and incorporated the increase in propensity to form accretion products with RO_2 oxidation.

The species with the lowest functionality, the 1st generation OHRO2 (RTN28AO2 and RTN28BO2), which contain only 3 oxygens, had the lowest value of k_{13} (0.4×10^{-11} cm^3 molecule^{-1} s^{-1}) while the 1st generation O3RO2 (RN26BO2) with 4 oxygens had $k_{13}=0.97\times10^{-11}$ cm^3 molecule^{-1} s^{-1}, its self-reaction rate coefficient determined by Berndt et al (2018b). The most functionalised species for O3RO2 (RNxBOyO2) and OHRO2 (RTNxBOyO2) were assigned values of k_{13} of 3.6×10^{-11} cm^3 molecule^{-1} s^{-1} and 3.5×10^{-11} cm^3 molecule^{-1} s^{-1} respectively. The fitted

rate coefficients used were in line with the range 0.97-7.9×10^{-11} cm^3 $molecule^{-1}$ s^{-1} (with an uncertainty no greater than a factor of 3) measured by Berndt et al (2018b) and the full list of values is given in the reaction list in Appendix D. This reproduced, within experimental error, the total observed C20d concentrations for both experiments (Fig. 4.5 and Fig. D1) as well as the RO_2 in Simulations A and B. Sensitivity studies which scaled all k_{13} values by the same factor before rerunning Simulation B and comparing the output to experimental data suggested that variations in the C20d formation rate coefficients of +100 % / -35 % spanned the experimental uncertainty (Table D6).

Using values of k_{13} = 0.1-3×10^{-12} cm^3 $molecule^{-1}$ s^{-1}, as suggested by Roldin et al (2019) for C20d formation, produced C20d concentrations lower than those observed (Fig D1) while values of 1-8×10^{-10} cm^3 $molecule^{-1}$ s^{-1} from Molteni et al (2019) produced values which were higher than observation.

The rate coefficients for 15-carbon accretion product formation, fitted against experimental data, also increased with the extent of oxidation of the reacting peroxy radical. Values of k_{16} ranging from 1.2×10^{-12} cm^3 $molecule^{-1}$ s^{-1} for the least oxidised RO_2 to 5×10^{-12} cm^3 $molecule^{-1}$ s^{-1} for the most oxidised species reproduced observed levels of the C15d accretion product (Fig. 4.5 and Fig. D2) from the constant α-pinene and variable isoprene experiments (as in Fig. 4.4) and were lower than the values measured by Berndt (1.3-2.3×10^{-11} cm^3 $molecule^{-1}$ s^{-1} with an uncertainty no greater than a factor of 3). Sensitivity studies which scaled all k_{13} values by the same factor before rerunning Simulation B and comparing the output to experimental data suggested that variations in the C15d formation rate coefficients of ±50 % spanned the experimental uncertainty (Table D6).

Figure 4.5 shows that the decrease in 20-carbon accretion products with increasing isoprene far outweighs the increase in 15-carbon accretion products. The mechanism reproduces the general trend of suppression of total accretion product concentration with increasing initial isoprene concentration. This finding is in good agreement with McFiggans et al (2019) and highlights a key component of the new mechanism which simple mechanisms (e.g. Gordon et al., 2016) will miss. This net decrease in accretion products concentrations is driven in part by OH scavenging (and the subsequent reduction in OHRO2 (Fig. 4.4)). In this work this was the major driver of C20d decrease. However, suppression was also observed due to scavenging of C10RO2 by isoprene-derived RO_2 as observed by McFiggans et al (2019). The influence of smaller peroxy radicals such as that from methane on accretion product formation (McFiggans et al., 2019) will be an area of future investigation.

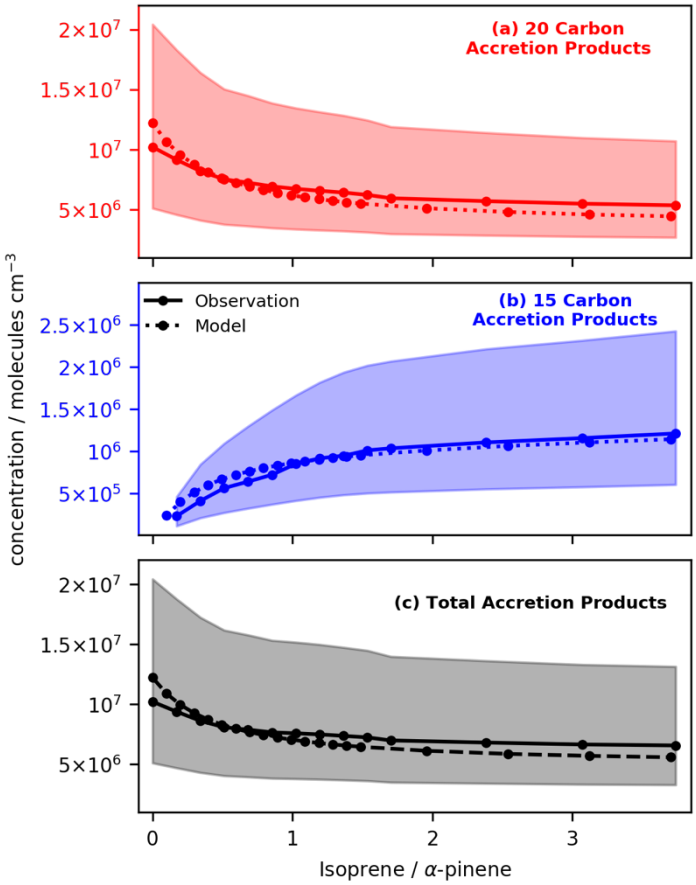


Figure 4.5. Variation in Simulation B of observed and modelled concentrations of (a) C20d, (b) C15d and (c) total accretion products with isoprene at fixed initial concentrations of α-pinene (observed data from Berndt et al (2018b)). The modelled data falls within the experimental uncertainty shown by the pale red, blue and grey regions. The model reproduces the observed decrease in C20 accretion products and increase in C15 accretion products well. Furthermore, the model reproduces qualitatively the result observed by McFiggans et al (2019) that addition of isoprene reduces the total accretion products concentration with potentially important implications for total aerosol burden and particle size distribution.

4.3.2 HOM yield variation with temperature and NO_x

Autoxidation reactions have significant positive temperature dependencies (Praske et al., 2018, Bianchi et al., 2019, Jenkin et al., 2019b). Accordingly, HOM yields are expected to be highly temperature sensitive. Quéléver et al (2019) recorded a 50-fold increase in HOM yield at 293 K relative to 273 K. This temperature variation cannot be attributed to the temperature dependence of the initial oxidation of α-pinene as the rate coefficient of ozonolysis increases only 17% between 273 K and 293 K while the reactions with OH and NO_3 exhibit negative temperature dependencies. Frege et al (2018) measured a decrease in O:C ratio values in HOMs with reducing temperatures, attributing this to a reduction in autoxidation.

Variation in peroxy radical structure and functionality will result in different generation peroxy radicals having different barriers to autoxidation (Bianchi et al., 2019). A few modelling studies have considered the temperature dependencies of the autoxidation rate coefficient in peroxy radical from α-pinene derivatives. Schervish et al (2019) considered a simple approach where all generations of peroxy radicals from α-pinene ozonolysis had a fixed activation energy of 62.4 or 66.5 KJ mol^{-1} (θ = 7500-8000 K when rate coefficient is expressed as $k=Ae^{-\theta/T}$), while noting that a reduction in barriers to autoxidation with increasing functionality is plausible but so far unproven. By contrast, Roldin et al (2019) considered a higher activation energy of 100.4 KJ mol^{-1} (θ = 12077 K) based on the theoretical work of Kurtén et al (2015) which identified activation energies of 90-120 KJ mol^{-1} for α-pinene.

Given the lack of additional literature in this area, 3 versions of the new mechanism were created to probe the effects of temperature and activation energy on HOM yield and subsequent evolution. In each mechanism all autoxidation reactions (for O3RO2 and OHRO2) had the same activation energy while all non-autoxidation rate coefficients were the same across mechanisms (Table D2). Activation barriers of θ = 6000 K, θ = 9000 K and θ = 12077 K were chosen as they included the range suggested by Roldin et al (2019) and Schervish et al (2019) and the mechanism versions termed HOM_{6000}, HOM_{9000} and HOM_{12077} respectively. For the temperature dependent versions, the pre-exponential factor of the autoxidation coefficient (Table D5) was adjusted so that the autoxidation coefficients were the same at 297 K as those derived from the comparison to experimental data from Berndt et al (2018b) (Table 4.4). It is recognised that the autoxidation steps are likely to have different activation energies, but this analysis provides a first approximation of the influence of activation energy on HOM formation.

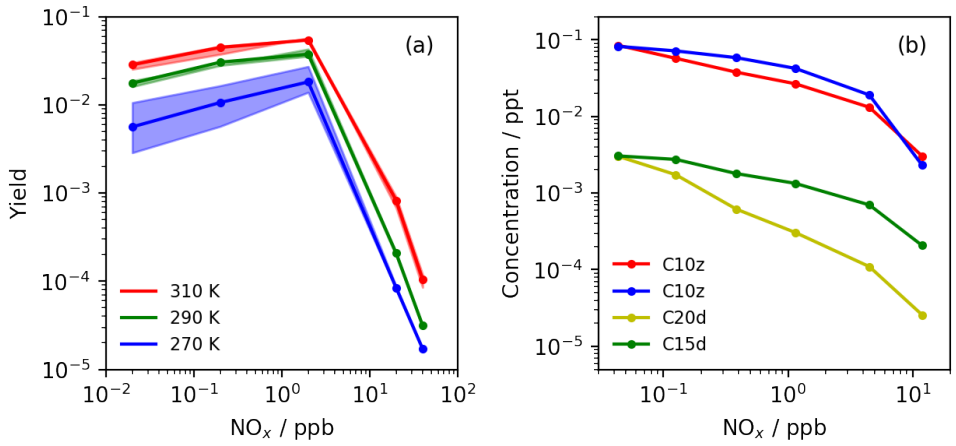


Figure 4.6. (a) Maximum modelled HOM yields (C10x and C10z) exhibiting significant decline under high NO_x conditions (Simulation C). The spread in the modelled yield between HOM mechanisms (HOM_{6000}, HOM_{9000} and HOM_{12077}), shown by the shaded regions, indicates the lower sensitivity to autoxidation activation energy at temperatures above ~290 K. (b) Observed HOM concentrations from 8-day tropical PBL run (Simulation D) showing decrease in concentration for all HOM species with NO_x. Under tropical PBL conditions, negligible difference was observed between HOM mechanisms due to daytime temperatures exceeding 300 K.

In a simulation modelling an instantaneous injection of α-pinene (Simulation C), the HOM yield for the 10-carbon species, individually and in total (yields defined in Appendix D) were calculated with the three different temperature dependencies (HOM_{6000}, HOM_{9000} and HOM_{12077}) at temperatures of 270 K, 290 K and 310 K for initials conditions of α-pinene 15 ppb, O_3 40 ppb and OH at 10^6 cm^{-3} and a temperature independent condensation sink of 2×10^{-3} s^{-1}.

Figure 4.6(a) shows the results from the simulations performed with initial concentrations of NO and NO_2 of 0.01-10 ppb. These simulations showed that the 10-carbon HOM yield tends to increase slightly from very low (0.02 ppb) to moderate (2 ppb) NO_x and before starting to decrease with increasing NO_x thereafter. This behaviour is likely to be due to the inclusion in the mechanism of the isomerisation pathway via reaction with NO which yields the next generation peroxy radical. This pathway has been suggested as an important route for forming more highly oxidised derivatives of α-pinene due to the potential rapid ring-opening mechanism involving alkoxy radicals and the cyclobutyl ring found in α-pinene ozonolysis products (Rissanen et al., 2015). Figure 4.6(a) indicates that the absolute yield is also sensitive to temperature, with the highest yields simulated at the highest temperatures. At low temperatures (blue data), the uncertainty in autoxidation temperature dependence has the greatest effect while at high temperature this feature is muted. The increase in yield with temperature is in qualitative agreement with observation (Quéléver et al., 2019, Simon et al., 2020).

The model predicted total HOM yields at 290 K of 1.9±0.2 % (0.01 ppb NO) to 3.9±0.5% (1 ppb NO), with the quoted range resulting from the range of temperature dependencies considered. This is within the ranges previously suggested by Jokinen et al (2015) (1.7-6.8 %) and close to the values from Ehn et al (2014) (3.5-10.5 %) and Sarnela et al (2018) (3.5-6.5%) while lower than Roldin et al (2019) (~7%). In addition, the HOM yield at 270 K of ~0.6-1.9 % compared favourably with the yield of ~2% determined by Roldin et al (2019). This suggests that the mechanism is doing a good job at simulating HOM yield. The slight low bias may be in part due the values of k_{14} and k_{15} which were shown to influence the HOM yield relatively strongly. Sensitivity tests involving doubling and halving of the rate coefficients produced HOM yield changes of around +65% and -40% respectively while preserving the general dependencies on NO_x and temperature (Fig. D4(a)) (Table D6). This area of uncertainty will be the focus of future work.

The HOM yield showed negligible sensitivity to the alkoxy radical decomposition-isomerisation branching ratio below 200 ppt of NO_x and around ±0.7 percentage points (~20 %) at 2 ppb NO_x. However, this range was encompassed by the range arising from autoxidation temperature dependence uncertainty. Above 2 ppb NO_x, this ratio had greater influence as NO reactions with RO_2 started to compete more efficiently with autoxidation, but this coincided with the sharp drop in HOM yield (Fig. D4(b)). Therefore, while further work is needed to develop the isomerisation-decomposition branching ratio description, it is unlikely to have a significant influence in the low-NO_x conditions where HOM are predicted to be most prevalent and in these conditions the uncertainty in temperature dependence of autoxidation is predicted to have a larger effect.

4.3.3 Comparison to CRI v2.2

The ability of the new mechanism to reproduce the concentrations of key atmospheric species from the CRI v2.2 under different emissions of NO_x and α-pinene was assessed using an 8 day box modelling run (Simulation D). Over the majority of emissions space, O_3 differed by less than 0.05 ppb (0.1%), OH by less than 0.4% and NO by less than 2.5 ppt (0.4%) (Fig. D6-D8) with similar (or better) agreement for other important species (Fig. D9-D17). Acetone was routinely underpredicted (Fig. D18) by between a factor of ~14 at 50 ppt NO_x and by ~20 % at 2-10 ppb of NO_x but this did not result in significant deviation between the base mechanism and new mechanism for O_3 or OH. This indicates that the basic features of atmospheric chemistry, such as HO_x recycling processes added in the CRI v2.2, which have been shown to have important consequences for atmospheric composition (Jenkin et al., 2019a), are preserved in the new mechanism.

4.3.3.1 Peroxy Radicals and HOMs

As our model simulations indicate, and as has previously been observed (Lehtipalo et al., 2018), at higher concentrations of NO_x there is inhibition of HOM formation with the principal driver being the reaction of NO with peroxy radicals occurring at a rate outcompeting autoxidation. While reaction with NO can in part aid HOM formation by increasing the isomerisation pathway, the fragmentation pathway (forming smaller species) and formation of non-HOM nitrates leads to a reduction in total HOM. Accordingly, all these mechanisms predict a decrease in HOM concentration with increasing NO_x (Fig. 4.6(b)). Furthermore, very little difference is observed between the different HOM mechanisms, suggesting that uncertainty in the activation energy may not be too great an impediment to understanding general HOM behaviour, at least at the temperatures considered.

However, it should be remembered that, at present, the HOM tracers in the mechanism represent a range of species with varying levels of oxidation. For example, C10z corresponds to HOMs formed from 2nd to 5th O3RO2 generations of O3RO2 and C10x to HOMs from all generations of OHRO2. The predicted concentrations of different generations of O3RO2 (Fig. D19) and OHRO2 (Fig. D20) were also observed to decrease with NO_x with little difference between different HOM mechanisms. Furthermore, the most abundant peroxy radicals for both pathways were the lumped highest generation species, highlighting the potential issue of lack of loss processes for the most highly oxidised RO_2 species as was encountered when fitting parameters to flow cell data.

4.3.3.2 Closed Shell and non-HOM Species

In the base mechanism, α-pinene oxidation predominantly leads to the formation of the closed shell species CARB16 and TNCARB26 (carbonyls) and RN18NO3 and RTN28NO3 (nitrates). Whilst the base mechanism has been optimised against the MCM, these pathways have not themselves been tuned extensively to reproduce concentrations observed in experimental systems. These species are still present in the new mechanism but the concentrations of RTN28NO3 and TNCARB26 are predicted to be slightly lower than in the base mechanism (Fig. D21) while CARB16 is simulated as being much lower in concentration than in the base mechanism at low NO_x with the difference attributed to the added competition from the autoxidation pathways.

The nitrate species formed from RN18AO2 in the base mechanism, RN18NO3, is significantly lower in the HOM

mechanism. Nitrate yield is a complicated topic, not least because the MCM predicts that the peroxy radicals C107O2 and C109O2, which are used to represent the 1st generation O3RO2 in part (RN26BO2), do not form nitrate upon reaction with NO or NO_3. Importantly this does not affect the O_3 and OH concentrations, but this should be an area that future work addresses.

4.4 Simulation of HOM Vertical Profiles

Given the success of the mechanism in simulating the laboratory flow tube experiments and its ability to capture the sensitivity of HOMs to changes in the reactivity of the peroxy radical pool, we focus now on using the scheme to simulate tropospheric conditions to investigate, to first order, how the scheme would predict ambient HOM concentrations. Here we focus on using our new mechanism to simulate the surface [HOMs] and the vertical profile of [HOMs]. We also look at the effect of the simulated HOMs on nucleation rates in the lower troposphere.

The vertical profiles of HOMs over the boreal forest near Hyttalia in Finland (61º 9' N, 23º 4' E) and near Manaus in the Amazon rainforest (-2º 35' N, 60º 12' W) were investigated along with surface concentrations representative of Brent, Alabama (32.903°N, 87.250°W). For each altitude level, the sensitivity simulations were performed with three different activation energies for the autoxidation steps (HOM_{6000}, HOM_{9000} and HOM_{12077}). Vertical transport was neglected - a different box model was run at each vertical level with the inputs being the output of a simulation with the UKCA model (Archibald et al., 2019) sampled at 14:00 LT (photolysis frequencies were adjusted to account for the solar zenith angle but not for altitude variation). Hourly concentration data from UKCA were provided for O_3, OH, isoprene, α-pinene, HO_2, NO, NO_2, NO_3, N_2O_5, temperature and pressure for 16th June averaged over 2010-2014, from the grid boxes in UKCA corresponding to the respective locations discussed above, and supplemented with monthly mean concentrations of a further 23 species (Table D3) with the concentration of certain species adjusted to observations (Kuhn et al., 2007 and Table 4.5) and scaled vertically to account for biases in the UKCA output. The scaled values of isoprene and α-pinene showed reasonable agreement with observations taken up to 80 m in altitude at the ATTO tower (Yáñez-Serrano et al., 2015). Modelled isoprene fell within 0.5 ppb of observation taken at 2 pm in June while modelled monoterpene were within 0.1 ppb of observation, well within the observational standard deviation in both cases (Fig. D22). HOM condensation sinks (CS) (equal for all HOM species) discussed in Lee et al (2016) (Table D4) were used at the surface and scaled using the modelled vertical profile of aerosol surface area density. Sensitivity studies revealed that the output of the 1D box modelling shows significant sensitivity of [HOMs] to the magnitude and profile of the CS (Fig. D22). Therefore, we can suggest that our simulated vertical profiles be regarded as illustrative as more work is required to identify if the condensation sink should be species dependent.

Table 4.5 summarises the comparison of our model simulations of near surface [HOMs] compared to observations. In the boreal forest in Hyytiala, the range of predicted 10-carbon [HOM] falls at the higher end of the mean observational range and well below the maximum observed concentrations (1-1.5 ppt) (Roldin et al., 2019). The predicted 20-carbon accretion product concentration is around double the mean observational range and well below the maximum observed values (0.6-0.7 ppt). In Alabama, the model produces a reasonable value given that the observation dataset includes 9-carbon species not considered in the model at present. The model results in

Table 4.5 provide strong support that when implemented in a global chemistry climate model, our new scheme should perform well if the underlying emissions of BVOCs and NO_x and the CS are well simulated.

Table 4.5. Observed and modelled concentrations after adjustment of model input. The model performs well in comparison to observed [HOM] at Hyytiala. ([a]Roldin et al., 2019, [b]Lee et al., 2016, [c]Ranges given accounts for factor of 2 uncertainty in observed concentrations, [d]Includes concentrations from C9 species ($C_9H_{14-20}O_{4-10}$) and C10 species ($C_{10}H_{16-22}O_{4-10}$), [e]Model was run with surface conditions in May for comparison to data from Roldin et al., 2019. [f]Range arises from model runs using range of CS values suggested in Lee et al., 2016)

Location	Species Adjusted to Observations	Mean observed concentrations at relevant time of day / ppt[c]	Model concentrations with input adjusted to observations / ppt[e]
Hyytiala[a]	Monoterpene	10-carbon HOM: 0.2-0.8 (mean 0.4) 20-carbon accretion product: 0.04-0.16 (mean 0.08)	10-carbon HOM: 0.75-0.85 20-carbon accretion product: 0.28-0.30
Alabama[b]	Monoterpene, Isoprene, OH, O3	C9 & C10[d]: 30	C10[f]: 4.5-13.3

Figure 4.7 shows the concentrations of the different HOMs from the box model version as a function of altitude above Hyytiala and over the Amazon rainforest near Manaus. In both locations, the 10-carbon HOM profiles roughly mirror α-pinene with roughly equal abundance of the species from ozonolysis and OH oxidation. HOM from OH showed a significantly greater sensitivity to temperature, diverging from the HOM from O_3 at around 5 km in Hyytiala and 8 km in the Amazon due to the elevated temperature profile. This was attributed to the requirement for 1st generation OHRO2 to undergo two autoxidation steps before HOMs can be formed (Section 4.2.2) while 1st generation O3RO2 only need to undergo one autoxidation step and thus have a weaker temperature dependence. This effect only becomes noticeable at temperatures below ~250 K when autoxidation ceases to compete effectively with bimolecular reactions. In spite of higher [BVOCs], the considerably higher CS in the Amazon region (Lee et al., 2016) resulted in lower [HOM] within the boundary layer than at Hyytiala, while the warmer temperatures also resulted in a negligible dependence on the activation energy in the lowest 4 km (i.e. the shaded areas are smaller in Fig. 4.7(b) than in Fig. 4.7(a)).

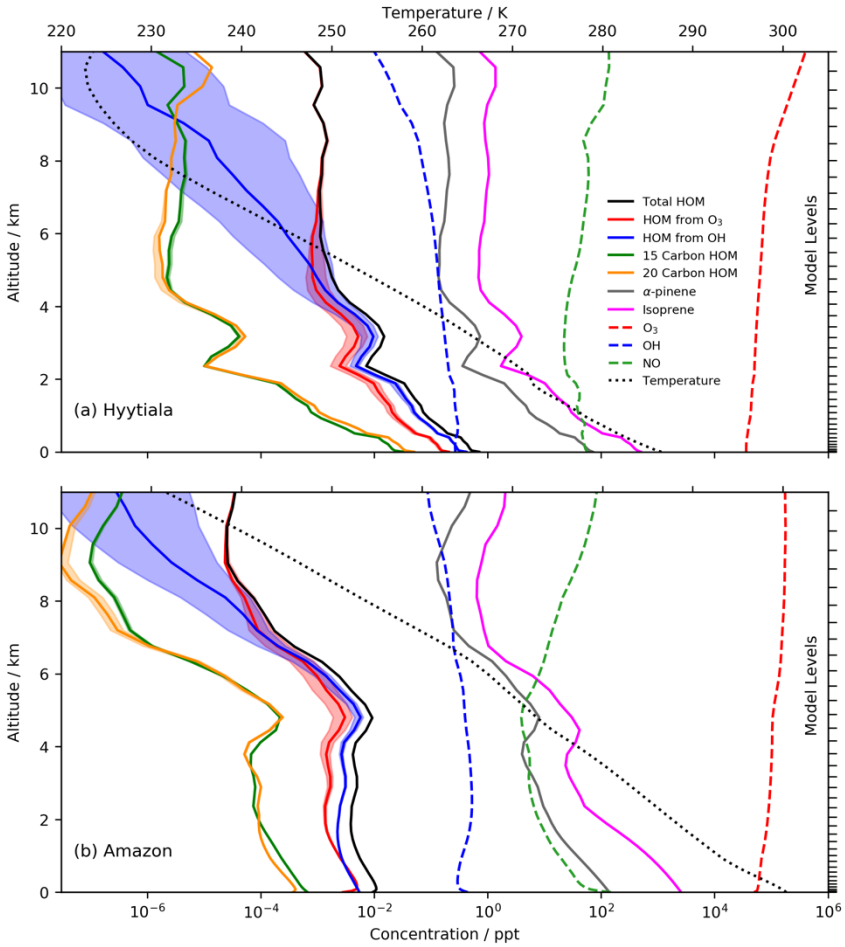


Figure 4.7. HOM profiles in June (2pm LT) above (a) Hyytiala and (b) the Amazon near Manaus. Despite higher [α-pinene], the significantly higher CS in the Amazon results in lower [HOM]. The temperature dependence (shown by the shading) is more significant at low altitude with Hyytiala's cooler temperatures. The Amazon's higher isoprene/ α-pinene ratio (~20) resulted in greater suppression of the 20-carbon accretion product than at Hyytiala.

Hyytiala and the Amazon represent very different chemical environments with the isoprene/α-pinene ratio (I/AP) playing an important role in the accretion product distribution: 15-carbon accretion products are simulated as being more abundant than 20-carbon accretion products in the Amazon with the biggest difference predicted at low altitude where I/AP is greatest. By contrast, in Hyytiala where I/AP is smaller, 20-carbon accretion products are more abundant.

Figure 4.7 highlights strong vertical profiles for the simulated [HOMs]. The simulations over the Amazon suggest a significant secondary peak in [HOMs] at around 4-5 km in altitude; in part linked to an increase in the [BVOCs] at this height. In our simulations each vertical level is represented by a different box model simulation so there is no simulation of the advection of HOMs. It will be interesting to see how future fully coupled model simulations simulate the vertical profile of [HOMs] and how this affects processes like aerosol formation and climate.

4.4.1 Nucleation Rates

Given the important role Gordon et al (2016) identified for HOMs in NPF we extend our 1-D calculations to investigate the implications of the predicted HOM profiles on nucleation rates using monthly mean climate model data from the PD and PI. Nucleation rates from two different nucleation mechanisms were studied: (i) neutral and ion-induced pure biogenic nucleation (PBN) (Kirkby et al., 2016); and (ii) activation of sulphuric acid (SA_{act}) (Kulmala et al., 2006; Sihto et al., 2006) suitable for the boundary layer. All HOMs were treated as being equally proficient at nucleating new particles, in agreement with approach and nucleation rates used by Kirkby et al (2016) and Gordon et al (2017). Recent work by Heinritzi et al (2020) suggests that 20-carbon accretion products may be better at nucleating new particles and therefore the results presented are likely to be an upper bound although nevertheless informative. Representing the different nucleation efficiencies of different HOM species will be investigated in future work. The results of the calculations of nucleation rates using these schemes are summarised in Figure 4.8. (The nucleation rate expressions are given in Appendix D.)

There exists little observational data on nucleation solely from PBN mechanisms, making model validation hard. Modelled surface sulphuric acid concentrations at Hyytiala ($2\text{-}3\times10^6$ cm^{-3}) fall within the range of observations ($3\times10^5\text{-}2\times10^7$ cm^{-3}; Boy et al., 2005; Petäjä et al., 2009). Modelled concentrations in the Amazon (3×10^4 cm^{-3}) were lower than observation ($10^5\text{-}10^6$ cm^{-3}; Wimmer et al., 2018) although the observations were taken in a pasture site downwind of Manaus surrounded by the rainforest not in the rainforest itself and are therefore likely to be higher than in-situ rainforest values. Thus, the nucleation rates we have calculated for SA_{act} are likely to be a reasonable estimate in Hyytiala and low biased in the Amazon.

Figure 4.8 shows predicted nucleation rates in the PI and PD in the Amazon and Hyytiala derived from our simulated [HOMs] vertical profile in the boundary layer and low free troposphere using June monthly mean data from a UKESM historical run taken from the PI (June average 1851-1856) and PD (June average 2009-2014). In all cases, the PBN nucleation rates decline rapidly with height above the boundary layer. In the Boreal forest the nucleation rate from PBN at very low altitudes is calculated to be around 20-25% of that from SA_{act} in the PD. However, in the PI it is comparable to the SA_{act} rate, contributing 40-80 % of the total nucleation rate in the lowest 500 m (Fig. D23). The greater relative importance of PBN in the PI, despite lower predicted [HOM], was attributed to two factors. Firstly, predicted steady state ion concentrations were higher in the PI in Finland than the PD due to the PI's lower ion CS. This increased the rate of the ion-induced pathway PBN pathway. Secondly, the considerably lower modelled concentrations of sulphuric acid in PI (around 10× lower than in the PD) reduced the importance of SA_{act}. By contrast, the lower concentrations of predicted [HOM] in the Amazon led to PBN having a much smaller contribution to the total nucleation rate (< 5% in the PD and a negligible impact in the PI). This is in agreement with multiple sources (Andreae et al., 2015; Wimmer et al., 2018; Rizzo et al., 2018). The importance of PBN in the PI atmosphere in certain locations, qualitatively in agreement with Gordon et al (2016), illustrates the potential importance including PBN in climate models could have on aerosol burden and the associated radiative effects.

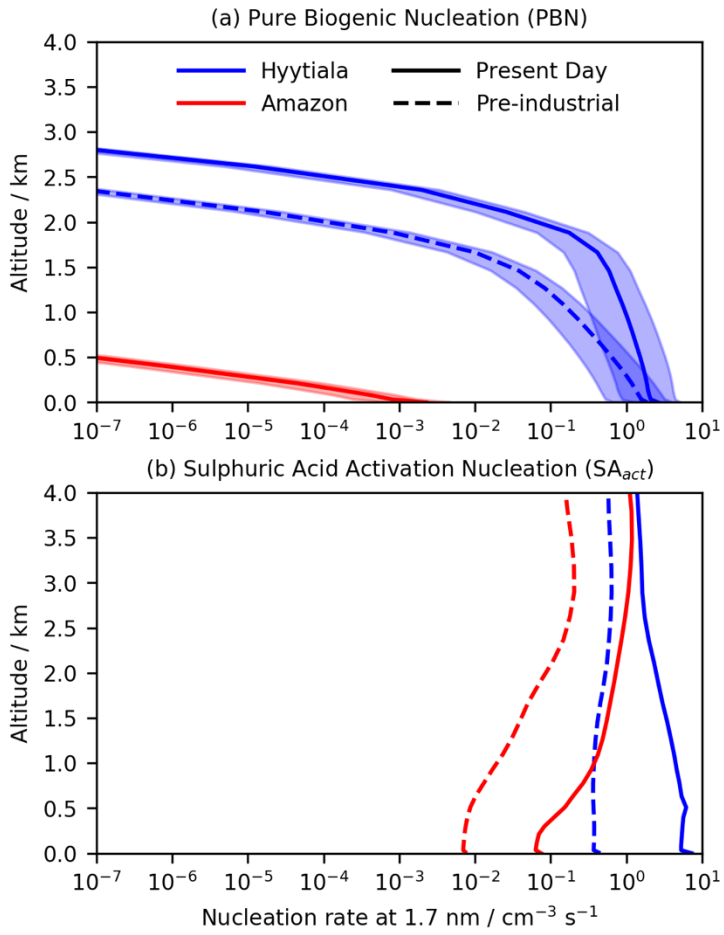


Figure 4.8. PD and PI modelled nucleation rates averaged over June for (a) summed (neutral + ion-induced) pure biogenic nucleation (assumes altitude-independent ion production rate (IPR) of 2 cm^{-3} s^{-1}; Hirsiko et al., 2011, shading shows IPR variation 0.5-5 cm^{-3} s^{-1}) and (b) nucleation from sulphuric acid only (SA$_{act}$). Both mechanisms are predicted to produce greater nucleation rates in the PD due to greater concentrations of precursor species. Importantly however, PBN at low altitude at Hyytiala is predicted to be comparable to SA nucleation in the PI due to the greater modelled ion concentration arising from a lower condensation sink and reduction in rates from SA$_{act}$ due to lower sulphuric acid concentrations. This leads to a larger increase in the total nucleation rate in the PI than the PD with potential implications for PI aerosol burden and climate.

4.5 Summary and Conclusions

We present a novel chemical mechanism, CRI-HOM, for simulating HOM formation based on the latest version of the Common Representative Intermediate scheme (CRI v2.2). Focusing on the most important natural source of HOMs, α-pinene, the CRI-HOM mechanism is one of the first HOM mechanisms ready for incorporation into existing chemistry-aerosol climate models. The scheme is much more complex than previous steady state approximations (Gordon et al., 2016) and so enables non-linear interactions and feedbacks with the chemical environment to be represented, but far more concise than other mechanisms that have been developed which treat the complex structural characteristics of the formation of HOMs (Roldin et al., 2019). The addition of 12 new

species and 66 reactions means that this scheme can be used for long term global chemistry-aerosol-climate studies.

Firstly, the mechanism was optimised against flow cell data and validated by comparison to observed HOM yields. A key result was the ability of the mechanism to reproduce observations of isoprene driving a decline in HOM peroxy radical precursors and 20-carbon accretion products (and total accretion product concentration) (McFiggans et al., 2019). The need for further research into the loss processes of the highly oxidised peroxy radicals was identified to reconcile the disparity between modelled and observed concentrations. The effect of other peroxy radicals, such as those from smaller more abundant organic species, on accretion product formation is also an area for future investigation.

After optimisation, the CRI-HOM mechanism was compared to the base mechanism (CRI v2.2) and very good agreement was observed for a wide range of atmospheric gases including O_3, OH and its precursors. This indicated that the important features of HO_x recycling and accurate O_3 representation, developed in the CRI v2.2, had been preserved in CRI-HOM.

In further tests of CRI-HOM, HOM yields and concentrations were predicted to decrease with increasing NO_x and increase with temperature, in agreement with previous theoretical and observational studies. The temperature dependence of autoxidation was investigated using activation energies spanning the range of values suggested in literature (Roldin et al., 2019, Schervish et al., 2019). Temperature dependence was predicted to have a significant effect on HOM yield at 270 K but a much smaller effect at 290 K and 310 K.

In a final experiment, vertical profiles of HOM were simulated using a pseudo 1D box model for Finland, Alabama and the Amazon using chemistry climate model data as inputs. The model performed well relative to observations in Finland and Alabama. The influence of the condensation sink (CS) value on [HOM] was shown to be significant with [HOM] predicted to be significantly lower in the Amazon, despite higher [BVOC], due to the higher CS. Improving the description of the CS within the mechanism has been identified as an important area of future work. The profiles also illustrated the dependence of HOM on the chemical environment, driven chiefly by the interaction of isoprene and monoterpenes. The higher concentrations of isoprene in the Amazon resulted in lower concentrations of the most involatile species, the 20-carbon accretion product. Simulated [HOM] were also used to probe the importance of various particle nucleation mechanisms. In Finland, pure biogenic nucleation mechanism (i.e. nucleation without sulphuric acid) at low altitude was predicted to be responsible for around 60% of new particle formation in the lowest 500 m in the pre-industrial atmosphere and around 20% in the present day, indicating the importance of HOMs, particularly in the pre-industrial, with implications for aerosol burden and climate. PBN was predicted to be less important in the Amazon given the lower simulated [HOM].

CRI-HOM can provide a framework for simulating HOMs in global chemistry-aerosol-climate studies and simulating the effects of isoprene-driven suppression of involatile biogenic-derived species and the consequences on SOA and NPF while also providing a state-of-the-art description of atmospheric chemistry. Such an effect, and the influence on the proposed “BVOC negative feedback”, is likely to be important in a warming climate with

enhanced emissions of BVOCs and determining the size and sign of the feedback. Once incorporated into a global chemistry-aerosol-climate model, assessing the effect of HOMs on pre-industrial, present day and future climate will be key area of future work.

5. Conclusions and Future Work

The fundamental aim of this thesis has been to improve the scientific understanding of how the emissions of BVOCs influence atmospheric composition and thus climate. This has centred on the recent advances in the understanding of the oxidation chemistry of the major BVOCs, isoprene and monoterpenes. These advances are not reflected in the chemical mechanisms used in most climate models. Chapter 1 detailed this chemistry, the processes by which BVOCs influence atmospheric composition and climate while highlighting the large inter-model variation in the simulated climatic impact of BVOCs, providing further motivation for improving the understanding of this topic.

5.1. How does the transition from a standard chemical mechanism to a state-of-the-art chemical mechanism affect simulated atmospheric composition?

Chapter 2 described the evaluation of the CS2 chemical mechanism, which has state-of-the-art isoprene chemistry, in UKCA. Output from UKCA using CS2 and two other mechanisms, ST and CS, were compared to observational data for a range of BVOCs and oxidants. The transition to state-of-the-art isoprene chemistry led to substantial increases (40%) in low altitude OH from the associated HO_x-recycling over tropical forestated regions compared to CS. This resulted in improvements in OH, isoprene and monoterpene diel surface profiles and isoprene column values for CS2 relative to ST and CS. However, CS2 exacerbated the existing model low bias for isoprene and monoterpenes away from the surface, suggesting potential issues with model vertical transport. The greater tropical terrestrial low altitude OH in CS2 also caused a greater fraction of BVOC oxidation (and SOA precursor formation) to occur at low altitude, with consequences for SOA which were explored in Chapter 3.

This chapter highlighted the significant impact the updates from a standard to a state-of-the-art chemical mechanism have on regional BVOC and oxidant concentrations with likely consequences for the climatic impacts of SOA, CH_4 and O_3.

5.2. How does the transition from a standard chemical mechanism to a state-of-the-art chemical mechanism affect the climatic impact of BVOCs and how might this help to explain the variation in the climatic impact of BVOCs between models?

Simulations with doubled E_{BVOC} using the ST and CS2 mechanisms were compared to respective control runs to determine the climatic impact of an increase in E_{BVOC}. For both mechanisms the forcing (and feedback factor)

was positive, indicating that doubling E_{BVOC} results in a warming in UKESM1. However, the magnitude of the forcing was 43% smaller when using CS2, illustrating the considerable influence the description of chemistry has on the simulated climatic impact of BVOCs. The disparity between ST and CS2 arose from differences in the change to atmospheric oxidising capacity following 2xE_{BVOC}. A smaller reduction in OH throughout the troposphere resulted in CS2 simulating an 16% smaller positive forcing from CH_4 increases and a 50% smaller positive CRE, the latter probably due to smaller reductions in SO_2 gas phase oxidation and CDNC. The positive forcings from CH_4, CRE and O_3 outweighed the negative IRF_{DRE} from enhanced SOA.

The net positive CRE contrasted with the findings of other E_{BVOC} perturbation studies (where the use of prescribed oxidants meant that CRE was driven solely by enhanced SOA and consequently strongly negative.

Chapter 3 also assessed the degree to which variations in simulated chemistry could explain the inter-model variations in BVOC forcing. The changes in O_3 (ϕ_{O_3}) and CH_4 (ϕ_{CH_4}) components of the forcing between ST and CS2 were comparable to the inter-model variations, suggesting differences in chemical mechanism play an important role in the model differences. However, the change in the aerosol component (ϕ_{aer}) was smaller than the inter-model variation, suggesting the change in aerosol-oxidant coupling alone cannot explain inter-model variation and that other variations, such as the aerosol and cloud parameterisations, are influential.

.

5.3. How can the chemistry of HOM formation from BVOCs be described in a form suitable for global climate modelling?

Neither ST or CS2 currently simulate HOM formation yet Gordon et al (2016) showed the introduction of HOMs into a PI atmosphere significantly increased terrestrial tropical CCN concentrations and thus reduced the negative PI-to-PD cloud forcing. However, the fixed-yield approach of Gordon et al (2016) did not capture the range of factors which influence HOM formation, prompting the final question of this thesis.

This chapter described the CRI-HOM mechanism, an addition to the CRI v2.2 mechanism which represents an improvement over the fixed-yield HOM approach, by capturing the influence of NO_x, temperature, oxidants and isoprene.

CRI-HOM added new autoxidation pathways for RO_2 produced from OH- and O_3-initiated oxidation of α-pinene, allowing production of more oxidised RO_2 which in turn could form 10-carbon HOM monomers or 15- or 20-carbon HOM dimers. The RO_2 pool used by CRI v2.2 was split into three pools for large, medium, and small RO_2, allowing the formation of HOM dimers from $RO_2 + RO_2$ reactions.

Key autoxidation and dimerisation rate constants were fitted against, flow cell observations of multiple generations of α-pinene-derived RO_2 and HOM dimers. Autoxidation temperature dependencies were also

included and CRI-HOM performed well against observational data and concurred with Gordon et al (2016) in the importance of pure biogenic nucleation in the PI.

The inclusion of CRI-HOM into the wider CRI v2.2 mechanism enables the influence of isoprene on RO_2 and 20-carbon dimers (McFiggans et al., 2019) and the suppression of HOM yield by NO_x and lower temperatures to be captured.

While further refinement of CRI-HOM is required, the mechanism describes the important chemical processes governing HOM formation and can provide a framework for simulating HOMs in global chemistry-aerosol-climate studies, facilitating a more thorough assessment of the climatic impact of BVOCs.

5.4 Future Work

The areas of important future work fall into two categories: further model development to improve the description of BVOCs, SOA and their link to climate, and the application of current modelling capabilities to answer pressing policy-relevant questions.

5.4.1 Model development

Chapter 3 demonstrated the extent to which differences in simulated chemistry could help to explain the inter-model variation in the O_3 (ϕ_{O_3}) and CH_4 (ϕ_{CH_4}) components of BVOC climate forcing. The smaller contribution of chemistry to the inter-model differences in the aerosol component (ϕ_{aer}) of BVOC climate forcing was also highlighted and attributed to fact that there are many other factors which drive the uncertainty in ϕ_{aer}, particularly the description of aerosol nucleation and thus background concentration of aerosol.

Therefore, the highest priority for model development is improvement of aerosol nucleation parameterisation including the simulations of HOMs and PBN. Such development would allow greater confidence in the simulated aerosol forcing from BVOC perturbations. In addition to aerosol nucleation, improvements to the modelling of SOA production from isoprene and sulphur chemistry are also critical for the capturing the aerosol component of BVOC climate forcing and are discussed briefly in this section.

5.4.1.1 HOMs and PBN

Using the fixed-yield HOM approach, Gordon et al (2016) demonstrated the influence of HOMs and the associated new particle formation via PBN on CCN numbers and CRE in the PI and PD (Section 1.4.5.1). New particle formation via the Metzger BLN scheme, where monoterpene oxidation products can nucleate new particles when clustering with H_2SO_4, was used in Chapter 3. However, the co-dependence on H_2SO_4 and artificial restriction of

nucleation to the boundary layer means using in the Metzger scheme as an approximation for PBN in the PI is not ideal and a dedicated HOM-PBN scheme is required.

The logical progression is first the incorporation of the fixed-yield scheme of Gordon et al (2016) and then the CRI-HOM scheme. CRI-HOM was designed to allow a semi-explicit description of HOMs, including the influence of oxidants, isoprene, NO_x, and temperature, to be included in UKCA/UKESM. Comparison of these two schemes would allow determination of the importance of the additional processes in CRI-HOM (e.g., isoprene's OH-suppression), and ultimately assessment of whether the additional complexity and computational requirements of CRI-HOM are necessary. The HOM concentrations simulated by each scheme should be evaluated against observational data to assess model performance. The simulated HOM can also be used in UKCA's aerosol code to improve the description of nucleation of aerosol particles. The role of amines in nucleation (e.g. Dunne et al., 2016) should also be included with parameterisations available from Gordon et al (2017). Again, the simulated aerosol concentrations should be compared to observational data.

The addition of PBN is likely to shift the aerosol size distribution towards a larger number of smaller particles. Predicting the climatic response to this change is not straightforward and depends strongly on the final change to the aerosol distribution (Section 1.4.6) which will be influenced by the particular model's aerosol scheme (Sporre et al., 2020). Some of the Sec_Org mass which would have condensed onto Aitken or accumulation mode particles will condense on to the additional nucleation mode particles, growing them into Aitken mode particles. Other nucleation mode particles will be lost via coagulation to Aitken mode particles. Thus, the Aitken mode number concentration is likely to increase. If the increase in Aitken mode number concentration also leads to an increase in accumulation mode concentration, the aerosol DRE and AIE will be stronger, since accumulation mode particles scatter radiation more strongly (DRE) and are better able to serve as CCN (AIE). Conversely, if the increase in Aitken mode concentrations and mass does not affect the accumulation mode as strongly, the change to DRE and AIE may be weaker or even opposite in sign. Indeed, in Sporre et al (2020), the removal of ELVOCs in NorESM (which removes PBN) led to a negative DRE forcing (i.e. inclusion of PBN would cause a positive forcing). This is because the removal of the PBN sink for organic vapours increases the vapours' concentration (increasing condensation flux). Simultaneously the reduction in small particle concentration shifts more of the condensation on to medium size particles, growing them to sizes where they can efficiently scatter radiation.
The net effect can only be determined by comparing simulations with PBN using CRI-HOM or fixed-yield HOMs to those with no nucleation and BLN. Doing so would represent one of the first applications of HOMs to a global climate model with fully interactive chemistry and be highly informative for the understanding of BVOCs' impact on climate.

5.4.1.2 Isoprene SOA

As discussed in Section 1.4.3, SOA from isoprene is significant fraction of organic aerosol and so accurately describing its production is important for accurately representing the impact of isoprene emissions on aerosol and climate. However, its simulated production at present, typically using a fixed yield, is basic in many climate models. Modelled perturbations to the SOA yield from isoprene and monoterpene influence SOA's climatic impact. When doubling (halving) SOA yield, Sporre et al (2020) calculated IRF_{DRE} values of -0.02 to -0.14 Wm^{-2} (+0.03 to +0.15 Wm^{-2}) and CRE values between -0.27 and -0.02 Wm^{-2} (+0.37 to +0.03 Wm^{-2}) across ECHAM, EC-Earth and NorESM. This illustrates the importance of capturing the influence of the parameters which control isoprene-SOA yield (e.g., NO_x, relative humidity, pH) and can lead to localised increases or decreases, relative to the standard fixed yield, of factors of 2-3 (Marais et al., 2016).

Capturing these factors could be done by explicit representation of the key species (IEPOX, HMML, glyoxal etc.,) and modelling their reactive uptake using heterogeneous reactions as used for aqueous oxidation of SO_2 by O_3 and H_2O_2. This would also require updates to the aerosol scheme to allow the aerosol pH to be diagnosed and coupled with the heterogeneous uptake (Section 1.4.3). Simple IEPOX-SOA models like Simple-GAMMA (Woo et al., 2015) would be useful references. This approach would also help to capture SOA formation further from source since SOA would not be formed immediately from isoprene but rather its derivatives (e.g. Utembe et al., 2009).

5.4.1.3 Sulphur Chemistry

Chapter 3 highlighted the importance of sulphur chemistry and SO_4 aerosol in the climatic response to BVOCs and thus the importance of using an accurate description of DMS chemistry. While the DMS scheme in CS2 from von Glasow and Crutzen (2004) is more comprehensive than ST, there remains considerable room for improvement, particularly given recent advances.

Improvements to the CS2 DMS chemistry by Cala (2021) (unavailable for this thesis) increased SO_2 yield from 29% to 65%, increasing the SO_4 aerosol burden and bringing CS2 closer to ST (Section 3.3.3.3). Other potential updates include the addition of the recently-observed DMS derivative HPMTF which may participate in aerosol growth and nucleation (Veres et al., 2020; Wollesen de Jonge et al., 2021).

Once better constrained, it would be informative to examine how this chemistry alters the responses of SO_4 and CRE to BVOC-driven oxidant depletion.

5.4.2 Using Current Modelling Capabilities

5.4.2.1 Influence of the chemical mechanism on other climate feedbacks

The impact of switching from ST to CS2 on the climatic impact of BVOCs, particularly for the CH_4 component, invites the question: "how sensitive are other chemistry-climate feedbacks to simulated chemistry?".

5.4.2.2 The influence of atmospheric state on BVOC climatic impact

Another important progression from this thesis is to investigate how the climatic impact of BVOCs depends on atmospheric state. Specifically, what will the sign and magnitude of the forcing be from an E_{BVOC} increase in a present day or future atmosphere? This is particularly relevant for future climate predictions and policy. Land use change and E_{BVOC} projections vary widely between SSPs and between models (Figs 1.4, A1) while little analysis has been done into the specific contribution from the attendant E_{BVOC} changes. Climate change mitigation strategies such as re/afforestation will increase regional E_{BVOC} and the benefits from CO_2 sequestration should be weighed against the impact of changes to E_{BVOC} and surface albedo. The location of E_{BVOC} perturbation can also be important, as highlighted in Unger (2014a) who found that tropical E_{BVOC} had 40% stronger warming effect than temperate E_{BVOC}. The importance of albedo change is amplified when dark boreal trees cover land which would otherwise be covered in snow for a substantial fraction of the year while cropland also typically has a higher albedo than forest (Unger., 2014b).

As introduced in Section 3.4.6, the changes which have occurred to atmospheric composition and background aerosol from the PI to the PD are likely to influence how an E_{BVOC} perturbation will impact climate. There are multiple factors to consider, including oxidising capacity and background aerosol concentrations, and changes in the different forcing components may partially offset. Karset et al (2018), Unger (2014a), Scott et al (2014) and Sporre et al (2019) provide some suggestions as to how the response may differ.

When using PD oxidants, Karset et al (2018) found aerosol precursors were less dispersed before forming aerosol, resulting in a shorter lifetime compared to the PI. Therefore, an E_{BVOC} perturbation in PD or future atmospheres with higher oxidising capacities will probably lead to more SOA formation at low altitude and diminished dispersion compared to the same perturbation in the PI, resulting in a smaller IRF_{DRE} (as found for $CS2_{\Delta}$ relative to ST_{Δ} in Chapter 3).

The change to CRE is complex. The PI-to-PD increases in the background aerosol concentration mean the addition of extra organic aerosol in the PD will probably have a smaller radiative impact than in the PD. As an example of lower sensitivity in the PD, Scott et al (2014) showed that increasing SOA production in a PD atmosphere led to a 19% smaller negative CRE than in a PI atmosphere due to smaller fractional increases in CCN and absolute increases in CDNC. Karset et al (2018) also highlighted the stronger CRE in the PI due to the lower background aerosol while Sporre et al (2019) found that switching from PD to PI aerosol emissions led to 53% stronger negative CRE from an increase in E_{BVOC} due to the lower background aerosol and the fact the increase in cloud albedo for a given CDNC increase is greater at low CDNC (Fig 3.13(b)). Therefore, the negative CRE from a SOA increase is likely to be smaller in a PD or future atmosphere (unless aerosol emissions drop sharply).

Another factor, discussed in Chapter 3 but not considered in detail by previous studies, is the contribution to the CRE from SO_4 aerosol. The sources of SO_4 aerosol have increased significantly from the PI to the PD. As a result, SO_4 aerosol and CDNC have increased from the PI to the PD (e.g., Gordon et al., 2016) and E_{BVOC}-driven

perturbations to the SO_4 burden and flux of $SO_2 + OH \rightarrow H_2SO_4$ are likely to be smaller in relative terms and have a smaller positive radiative effect, again due to the non-linear relationship between aerosol number and change in albedo. The addition of anthropogenic SO_2 sources will also change the spatial relationship between SO_2 and BVOC-driven oxidant changes (Section 3.3.3.3), further affecting the oxidant-aerosol coupling.

The CH_4 forcing will be partially buffered by the opposing factors that the higher CH_4 concentrations in the PD (~1870 ppb vs. ~800 ppb) will lead to a greater absolute reduction in CH_4 oxidation flux following an E_{BVOC} increase but the higher PD CH_4 and N_2O (273 ppb vs. 331 ppb; Gulev et al., 2021) concentrations mean the forcing per unit change in CH_4 concentration will be lower (~65% of PI value; Etminan et al., 2016). The higher oxidising capacity of the PD atmosphere is also likely to reduce the relative depletion of OH compared to the PI, while the higher temperatures and greater specific humidity of the PD atmosphere will also facilitate somewhat greater CH_4 oxidation. For the same E_{BVOC} change, Unger (2014a) found the positive forcing from CH_4 was significantly larger in the PI (143 mWm^{-2}) than the PD (22 mWm^{-2}).

PD and future atmospheres are likely to produce more O_3 with an increase in E_{BVOC} due to their greater NO_x concentrations. However, from a climatic perspective the location of O_3 increase is also crucial (Section 3.4.1.1). Changes to O_3 precursors (e.g. HCHO which forms HO_2) around the tropical tropopause (TT) where O_3's radiative efficiency is highest, will be particularly important. While the greater NO_x of the PD atmosphere is likely to result in a larger increase in O_3, the greater oxidising capacity of the PD atmosphere could, in a similar manner to $CS2_\Delta$ relative to ST_Δ in Chapter 3, lead to smaller increases in O_3-precursor around the TT, buffering the O_3 increase. Unger (2014a) simulated a 22% greater forcing from O_3 in the PD (712 mWm^{-2}) than the PI (583 mWm^{-2}) (same E_{BVOC} change) although these changes are considerably larger than the AerChemMIP mean $SARF_{O3}$.

The complex factors governing each component's response and the potential for components to offset makes prediction of the net result difficult. Ultimately runs with similar setups to Chapter 3 using PD and future conditions (e.g., 2050 conditions from different ScenarioMIP pathways) are required to determine these effects.

5.4.2.3 The impact of co-located changes to physical parameters

Chapter 3 considered the impact of E_{BVOC} changes without changes to land use (vegetation simply produced double E_{BVOC}). However, if future E_{BVOC} changes are driven partly by changes to forest cover (Fig A2), a range of other climatically-relevant variables such as albedo (Section 5.4.2.2) and evapotranspiration will also change.

Evapotranspiration, the sum of the evaporation and transpiration of water vapour from the surface to the atmosphere, decreases when areas are deforested (Boysen et al., 2020). Local reductions in the water vapour column yields a SW cooling while the attendant reduction in latent heat fluxes can lead to local warming. The reduction of water vapour in the atmosphere also reduces cloud cover (a SW warming) and precipitation. These effects were considered in the CMIP6 multi-model idealised global deforestation study (Boysen et al., 2020). This study concluded that boreal deforestation led to a net negative forcing due to an increase in albedo (increased

snow cover) while in the tropics a warming was simulated due to reduction in latent heat fluxes from lower evapotranspiration.

The global multi-model mean temperature change from non-CO_2 changes was -0.22°C while the reduction in the terrestrial carbon sink was simulated to cause a warming of 0.46°C. Therefore, deforestation was simulated to cause a net warming. However, no consideration was given to changes to O_3, CH_4, aerosol and clouds driven by E_{BVOC} changes.

Given that forests dominate E_{BVOC} (96% and 99.5% of isoprene and monoterpene emissions respectively; Sindelarova et al., 2014) such that complete deforestation would reduce biogenic isoprene and monoterpene emissions to almost zero, the forcing from the 2xE_{BVOC} simulations of Chapter 3 (Table 3.4) can be used to estimate the BVOC-forcing. Assuming a climate sensitivity of 0.5 K $(Wm^{-2})^{-1}$ (Eq 1.1) (Forster et al., 2021) and that removal of E_{BVOC} has the opposite effect to doubling them, the BVOC-forcing associated with complete PI deforestation would lead to a cooling of 0.15°C (ST) or 0.08°C (CS2), a considerable fraction of the non-CO_2 change of Boysen et al (2020). Furthermore, the localised changes in SOA could combine with the changes in water vapour from evapotranspiration to perturb cloud formation with consequences not considered in the CMIP6 deforestation study.

This is a first approximation: the response of PI and PD atmospheres will likely differ (Section 5.4.2.2) and removing E_{BVOC} is unlikely to have the exact opposite effect of a doubling. Nevertheless it highlights the importance of employing a comprehensive approach to policy relevant questions, such as the viability of reforestation as a climate change mitigation strategy, by considering changes to the whole Earth System, including atmospheric composition.

This thesis has presented the incorporation and evaluation of the state-of-the-art BVOC mechanism CS2 in Chapter 2 and the development of the CRI-HOM mechanism, suitable for UKESM, in Chapter 4. These tools along with the analysis of BVOC forcing and the role of simulated chemistry in Chapter 3 will enable detailed investigation of these policy relevant questions.

References

Abdul-Razzak, H., Ghan, S.J. and Rivera-Carpio, C.: A parameterization of aerosol activation: 1. Single aerosol type. Journal of Geophysical Research: Atmospheres, 103. 6123-6131, https://doi.org/10.1029/97JD03735, 1998.

Abraham, N. L., Archibald, A. T., Cresswell, P., Cusworth, S., Dalvi, M., Matthews, D., Wardle, S., and Whitehouse, S.: Using a virtual machine environment for developing, testing, and training for the UM-UKCA composition-climate model, using Unified Model version 10.9 and above, Geosci. Model Dev., 11, 3647–3657, https://doi.org/10.5194/gmd-11-3647-2018, 2018.

Albrecht, B.A., 1989. Aerosols, cloud microphysics, and fractional cloudiness. Science, 245, 1227-1230, DOI: 10.1126/science.245.4923.1227, 1989.

Allan, J. D., Morgan, W. T., Darbyshire, E., Flynn, M. J., Williams, P. I., Oram, D. E., Artaxo, P., Brito, J., Lee, J. D., and Coe, H.: Airborne observations of IEPOX-derived isoprene SOA in the Amazon during SAMBBA, Atmos. Chem. Phys., 14, 11393–11407, https://doi.org/10.5194/acp-14-11393-2014, 2014.

Andreae, M. O. and Gelencsér, A.: Black carbon or brown carbon? The nature of light-absorbing carbonaceous aerosols, Atmos. Chem. Phys., 6, 3131–3148, https://doi.org/10.5194/acp-6-3131-2006, 2006.

Andreae, M. O., Acevedo, O. C., Araùjo, A., Artaxo, P., Barbosa, C. G. G., Barbosa, H. M. J., Brito, J., Carbone, S., Chi, X., Cintra, B. B. L., da Silva, N. F., Dias, N. L., Dias-Júnior, C. Q., Ditas, F., Ditz, R., Godoi, A. F. L., Godoi, R. H. M., Heimann, M., Hoffmann, T., Kesselmeier, J., Könemann, T., Krüger, M. L., Lavric, J. V., Manzi, A. O., Lopes, A. P., Martins, D. L., Mikhailov, E. F., Moran-Zuloaga, D., Nelson, B. W., Nölscher, A. C., Santos Nogueira, D., Piedade, M. T. F., Pöhlker, C., Pöschl, U., Quesada, C. A., Rizzo, L. V., Ro, C.-U., Ruckteschler, N., Sá, L. D. A., de Oliveira Sá, M., Sales, C. B., dos Santos, R. M. N., Saturno, J., Schöngart, J., Sörgel, M., de Souza, C. M., de Souza, R. A. F., Su, H., Targhetta, N., Tóta, J., Trebs, I., Trumbore, S., van Eijck, A., Walter, D., Wang, Z., Weber, B., Williams, J., Winderlich, J., Wittmann, F., Wolff, S., and Yáñez-Serrano, A. M.: The Amazon Tall Tower Observatory (ATTO): overview of pilot measurements on ecosystem ecology, meteorology, trace gases, and aerosols, Atmos. Chem. Phys., 15, 10723–10776, https://doi.org/10.5194/acp-15-10723-2015, 2015.

Archer-Nicholls, S., Abraham, N.L., Shin, Y.M., Weber, J., Russo, M.R., Lowe, D., Utembe, S., O'Connor, F.M., Kerridge, B., Latter, B. and Siddans, R.: The Common Representative Intermediates Mechanism version 2 in the United Kingdom Chemistry and Aerosols Model. Journal of Advances in Modeling Earth Systems, 13,https://doi.org/10.1029/2020MS002420, 2021.

Archibald, A. T., O'Connor, F. M., Abraham, N. L., Archer-Nicholls, S., Chipperfield, M. P., Dalvi, M., Folberth, G. A., Dennison, F., Dhomse, S. S., Griffiths, P. T., Hardacre, C., Hewitt, A. J., Hill, R. S., Johnson, C. E., Keeble, J., Köhler, M. O., Morgenstern, O., Mulcahy, J. P., Ordóñez, C., Pope, R. J., Rumbold, S. T., Russo, M. R., Savage, N. H., Sellar, A., Stringer, M., Turnock, S. T., Wild, O., and Zeng, G.: Description and

evaluation of the UKCA stratosphere–troposphere chemistry scheme (StratTrop vn 1.0) implemented in UKESM1, Geosci. Model Dev., 13, 1223–1266, https://doi.org/10.5194/gmd-13-1223-2020, 2020a.

Archibald, A.T., Abraham, N.L., Bellouin, N., Boucher, O., Braesicke, P., Bushell, A., Carslaw, K., Collins, B., Dalvi, M., Emmerson, K. and Folberth, G., 2019. Unified Model Documentation Paper No. 84: United Kingdom Chemistry and Aerosol (UKCA) Technical Description MetUM Version 11.3. UK Met Office, Exeter, UK.

Archibald, A.T., Levine, J.G., Abraham, N.L., Cooke, M.C., Edwards, P.M., Heard, D.E., Jenkin, M.E., Karunaharan, A., Pike, R.C., Monks, P.S. and Shallcross, D.E.:. Impacts of HOx regeneration and recycling in the oxidation of isoprene: Consequences for the composition of past, present and future atmospheres. Geophysical Research Letters, 38, https://doi.org/10.1029/2010GL046520, 2011

Archibald, A.T., Neu, J.L., Elshorbany, Y.F., Cooper, O.R., Young, P.J., Akiyoshi, H., Cox, R.A., Coyle, M., Derwent, R.G., Deushi, M. and Finco, A.:. Tropospheric Ozone Assessment ReportA critical review of changes in the tropospheric ozone burden and budget from 1850 to 2100. Elementa: Science of the Anthropocene, 8, https://doi.org/10.1525/elementa.2020.034, 2020b.

Atkinson, R. and Arey, J.: Atmospheric degradation of volatile organic compounds. Chemical reviews, 12, 4605-4638, doi.org/10.1021/cr0206420, 2013.

Atkinson, R. and Arey, J.: Gas-phase tropospheric chemistry of biogenic volatile organic compounds: a review. Atmospheric Environment, 37,197-219, https://doi.org/10.1016/S1352-2310(03)00391-1, 2003.

Bannan, T. J., Le Breton, M., Priestley, M., Worrall, S. D., Bacak, A., Marsden, N. A., Mehra, A., Hammes, J., Hallquist, M., Alfarra, M. R., Krieger, U. K., Reid, J. P., Jayne, J., Robinson, W., McFiggans, G., Coe, H., Percival, C. J., and Topping, D.: A method for extracting calibrated volatility information from the FIGAERO-HR-ToF-CIMS and its experimental application, Atmos. Meas. Tech., 12, 1429–1439, https://doi.org/10.5194/amt-12-1429-2019, 2019.

Bannan, T.J., Booth, A.M., Bacak, A., Muller, J.B., Leather, K.E., Le Breton, M., Jones, B., Young, D., Coe, H., Allan, J. and Visser, S.: The first UK measurements of nitryl chloride using a chemical ionization mass spectrometer in central London in the summer of 2012, and an investigation of the role of Cl atom oxidation. Journal of Geophysical Research: Atmospheres, 120, 5638-5657, https://doi.org/10.1002/2014JD022629, 2015.

Bates, K. H. and Jacob, D. J.: A new model mechanism for atmospheric oxidation of isoprene: global effects on oxidants, nitrogen oxides, organic products, and secondary organic aerosol, Atmos. Chem. Phys., 19, 9613–9640, https://doi.org/10.5194/acp-19-9613-2019, 2019.

Bellouin, N., Quaas, J., Gryspeerdt, E., Kinne, S., Stier, P., Watson-Parris, D., Boucher, O., Carslaw, K.S., Christensen, M., Daniau, A.L. and Dufresne, J.L.: Bounding global aerosol radiative forcing of climate change. Reviews of Geophysics, 58, p.e2019RG000660, https://doi.org/10.1029/2019RG000660, 2020.

Benson, D.R., Young, L.H., Kameel, F.R. and Lee, S.H.: Laboratory-measured nucleation rates of sulfuric acid and water binary homogeneous nucleation from the SO2+ OH reaction. Geophysical research letters, 35, 11, https://doi.org/10.1029/2008GL033387, 2008.

Berndt, T., Richters, S., Jokinen, T., Hyttinen, N., Kurtén, T., Otkjær, R.V., Kjaergaard, H.G., Stratmann, F., Herrmann, H., Sipilä, M. and Kulmala, M.: Hydroxyl radical-induced formation of highly oxidized organic compounds. Nature communications, 1, 1-8, 10.1038/ncomms13677, 2016.

Berndt, T., Scholz, W., Mentler, B., Fischer, L., Herrmann, H., Kulmala, M. and Hansel, A.: Accretion Product Formation from Self-and Cross-Reactions of RO2 Radicals in the Atmosphere. Angewandte Chemie International Edition, 57, 3820-3824, doi.org/10.1002/anie.201710989, 2018a.

Berndt, T., Mentler, B., Scholz, W., Fischer, L., Herrmann, H., Kulmala, M. and Hansel, A.: Accretion product formation from ozonolysis and OH radical reaction of α-pinene: mechanistic insight and the influence of isoprene and ethylene. Environmental science & technology, 52,11069-11077, doi.org/10.1021/acs.est.8b02210, 2018b.

Bianchi, F., Kurtén, T., Riva, M., Mohr, C., Rissanen, M.P., Roldin, P., Berndt, T., Crounse, J.D., Wennberg, P.O., Mentel, T.F. and Wildt, J.: Highly oxygenated organic molecules (HOM) from gas-phase autoxidation involving peroxy radicals: A key contributor to atmospheric aerosol. Chemical reviews, 119, 3472-3509, doi.org/10.1021/acs.chemrev.8b00395, 2019.

Bondy, A., Craig, R., Zhang, Z., Gold, A., Surratt, J., Ault, A.: Isoprene-Derived Organosulfates: Vibrational Mode Analysis by Raman Spectroscopy, Acidity-Dependent Spectral Modes, and Observation in Individual Atmospheric Particles Thermodynamic Model of the System H+−NH4+−SO42-−NO3-−H2O at Tropospheric Temperatures 122, 303 – 315, https://doi.org/10.1021/acs.jpca.7b10587, 2017.

Boucher, O., D. Randall, P. Artaxo, C. Bretherton, G. Feingold, P. Forster, V.-M. Kerminen, Y. Kondo, H. Liao, U. Lohmann, P. Rasch, S.K. Satheesh, S. Sherwood, B. Stevens and X.Y. Zhang, 2013: Clouds and Aerosols. In: Climate Change 2013: The Physical Science Basis. Contribution of Working Group I to the Fifth Assessment Report of the Intergovernmental Panel on Climate Change [Stocker, T.F., D. Qin, G.-K. Plattner, M. Tignor, S.K. Allen, J. Boschung, A. Nauels, Y. Xia, V. Bex and P.M. Midgley (eds.)]. Cambridge University Press, Cambridge, United Kingdom and New York, NY, USA, pp. 571–658, doi:10.1017/CBO9781107415324.016.

Boy, M., Kulmala, M., Ruuskanen, T. M., Pihlatie, M., Reissell, A., Aalto, P. P., Keronen, P., Dal Maso, M., Hellen, H., Hakola, H., Jansson, R., Hanke, M., and Arnold, F.: Sulphuric acid closure and contribution to nucleation mode particle growth, Atmos. Chem. Phys., 5, 863–878, doi.org/10.5194/acp-5-863-2005, 2005.

Boysen, L. R., Brovkin, V., Pongratz, J., Lawrence, D. M., Lawrence, P., Vuichard, N., Peylin, P., Liddicoat, S., Hajima, T., Zhang, Y., Rocher, M., Delire, C., Séférian, R., Arora, V. K., Nieradzik, L., Anthoni, P., Thiery, W., Laguë, M. M., Lawrence, D., and Lo, M.-H.: Global climate response to idealized deforestation in CMIP6 models, Biogeosciences, 17, 5615–5638, https://doi.org/10.5194/bg-17-5615-2020, 2020.

Budisulistiorini, S. H., Li, X., Bairai, S. T., Renfro, J., Liu, Y., Liu, Y. J., McKinney, K. A., Martin, S. T., McNeill, V. F., Pye, H. O. T., Nenes, A., Neff, M. E., Stone, E. A., Mueller, S., Knote, C., Shaw, S. L., Zhang, Z., Gold, A., and Surratt, J. D.: Examining the effects of anthropogenic emissions on isoprene-derived secondary organic aerosol formation during the 2013 Southern Oxidant and Aerosol Study (SOAS) at the Look Rock, Tennessee ground site, Atmos. Chem. Phys., 15, 8871-8888, 10.5194/acp-15-8871-2015, 2015.

Butler, T. M., Taraborrelli, D., Brühl, C., Fischer, H., Harder, H., Martinez, M., Williams, J., Lawrence, M. G., and Lelieveld, J.: Improved simulation of isoprene oxidation chemistry with the ECHAM5/MESSy chemistry-climate model: lessons from the GABRIEL airborne field campaign, Atmos. Chem. Phys., 8, 4529–4546, https://doi.org/10.5194/acp-8-4529-2008, 2008.

Cala, B. A. 2021. Updating and improving DMS oxidation chemistry in Earth system models. MPhil thesis. University of Cambridge.

Cao, Y., Yue, X., Liao, H., Yang, Y., Zhu, J., Chen, L., Tian, C., Lei, Y., Zhou, H. and Ma, Y.: Ensemble projection of global isoprene emissions by the end of 21st century using CMIP6 models. Atmospheric Environment, 118766, https://doi.org/10.1016/j.atmosenv.2021.118766, 2021.

Carslaw, K. S., Boucher, O., Spracklen, D. V., Mann, G. W., Rae, J. G. L., Woodward, S., and Kulmala, M.: A review of natural aerosol interactions and feedbacks within the Earth system, Atmos. Chem. Phys., 10, 1701-1737, doi.org/10.5194/acp-10-1701-2010, 2010

Chen, J. (2016). Merged data file for SEAC4RS, Flight 01 (20130806), on the dc8 platform. (Last access 9th April 2021)

Chen, J., Liu, Y., Zhang, M. and Peng, Y.:. New understanding and quantification of the regime dependence of aerosol-cloud interaction for studying aerosol indirect effects. Geophysical Research Letters, 43, 1780-1787, https://doi.org/10.1002/2016GL067683, 2016.

Chung, E.-S., and Soden, B.J.: An assessment of methods for computing radiative forcing in climate models, Environ. Res. Lett., 10, 074004, https://doi.org/10.1088/1748-9326/10/7/074004, 2015.

Claeys, M. and Maenhaut, W.: Secondary Organic Aerosol Formation from Isoprene: Selected Research, Historic Account and State of the Art. Atmosphere, 12, 728, https://doi.org/10.3390/atmos12060728, 2021.

Collins, W. J., Lamarque, J.-F., Schulz, M., Boucher, O., Eyring, V., Hegglin, M. I., Maycock, A., Myhre, G., Prather, M., Shindell, D., and Smith, S. J.: AerChemMIP: quantifying the effects of chemistry and aerosols in CMIP6, Geosci. Model Dev., 10, 585–607, https://doi.org/10.5194/gmd-10-585-2017, 2017.

Crounse, J.D., Paulot, F., Kjaergaard, H.G. and Wennberg, P.O.: Peroxy radical isomerization in the oxidation of isoprene. Physical Chemistry Chemical Physics, 13, 13607-13613, https://doi.org /10.1039/C1CP21330J, 2011.

Crounse, J.D., Nielsen, L.B., Jørgensen, S., Kjaergaard, H.G. and Wennberg, P.O.: Autoxidation of organic compounds in the atmosphere. The Journal of Physical Chemistry Letters, 4, 3513-3520, doi.org/10.1021/jz4019207, 2013.

Dal Maso, M., Kulmala, M., Lehtinen, K.E., Mäkelä, J.M., Aalto, P. and O'Dowd, C.D.: Condensation and coagulation sinks and formation of nucleation mode particles in coastal and boreal forest boundary layers. Journal of Geophysical Research: Atmospheres, D19, PAR-2, doi.org/10.1029/2001JD00053, 2002.

de Sá, S. S., Palm, B. B., Campuzano-Jost, P., Day, D. A., Newburn, M. K., Hu, W., Isaacman-VanWertz, G., Yee, L. D., Thalman, R., Brito, J., Carbone, S., Artaxo, P., Goldstein, A. H., Manzi, A. O., Souza, R. A. F., Mei, F., Shilling, J. E., Springston, S. R., Wang, J., Surratt, J. D., Alexander, M. L., Jimenez, J. L., and Martin, S. T.: Influence of urban pollution on the production of organic particulate matter from isoprene epoxydiols in central Amazonia, Atmos. Chem. Phys., 17, 6611–6629, https://doi.org/10.5194/acp-17-6611-2017, 2017.

DeCarlo, P.F., Kimmel, J.R., Trimborn, A., Northway, M.J., Jayne, J.T., Aiken, A.C., Gonin, M., Fuhrer, K., Horvath, T., Docherty, K.S. and Worsnop, D.R.: Field-deployable, high-resolution, time-of-flight aerosol mass spectrometer. Analytical chemistry, 78, 8281-8289, https://doi.org/10.1021/ac061249n, 2006.

Dee, D.P., Uppala, S.M., Simmons, A.J., Berrisford, P., Poli, P., Kobayashi, S., Andrae, U., Balmaseda, M.A., Balsamo, G., Bauer, P., Bechtold, P., Beljaars, A.C.M., van de Berg, L., Bidlot, J., Bormann, N., Delsol, C., Dragani, R., Fuentes, M., Geer, A.J., Haimberger, L., Healy, S.B., Hersbach, H., Hólm, E.V., Isaksen, L., Kållberg, P., Köhler, M., Matricardi, M., McNally, A.P., Monge-Sanz, B.M., Morcrette, J.-J., Park, B.-K., Peubey, C., de Rosnay, P., Tavolato, C., Thépaut, J.-N. and Vitart, F.: The ERA-Interim reanalysis: configuration and performance of the data assimilation system. Q.J.R. Meteorol. Soc., 137: 553-597, https://doi.org/10.1002/qj.828, 2011.

Donahue, N. M., Kroll, J. H., Pandis, S. N., and Robinson, A. L.: A two-dimensional volatility basis set – Part 2: Diagnostics of organic-aerosol evolution, Atmos. Chem. Phys., 12, 615–634, https://doi.org/10.5194/acp-12-615-2012, 2012.

Dunne, E.M., Gordon, H., Kürten, A., Almeida, J., Duplissy, J., Williamson, C., Ortega, I.K., Pringle, K.J., Adamov, A., Baltensperger, U. and Barmet, P.: Global atmospheric particle formation from CERN CLOUD measurements. Science, 354, 1119-1124, https://doi.org/10.1126/science.aaf2649, 2016.

Edwards, P. M., Evans, M. J., Furneaux, K. L., Hopkins, J., Ingham, T., Jones, C., Lee, J. D., Lewis, A. C., Moller, S. J., Stone, D., Whalley, L. K., and Heard, D. E.: OH reactivity in a South East Asian tropical rainforest during the Oxidant and Particle Photochemical Processes (OP3) project, Atmos. Chem. Phys., 13, 9497–9514, https://doi.org/10.5194/acp-13-9497-2013, 2013.

Ehn, M., Kleist, E., Junninen, H., Petäjä, T., Lönn, G., Schobesberger, S., Dal Maso, M., Trimborn, A., Kulmala, M., Worsnop, D. R., Wahner, A., Wildt, J., and Mentel, Th. F.: Gas phase formation of extremely oxidized pinene reaction products in chamber and ambient air, Atmos. Chem. Phys., 12, 5113–5127, https://doi.org/10.5194/acp-12-5113-2012, 2012.

Ehn, M., Thornton, J.A., Kleist, E., Sipilä, M., Junninen, H., Pullinen, I., Springer, M., Rubach, F., Tillmann, R., Lee, B. and Lopez-Hilfiker, F.: A large source of low-volatility secondary organic aerosol. Nature, 506, 476-479, 865 https://doi.org/10.1038/nature13032, 2014.

Etminan, M., Myhre, G., Highwood, E.J. and Shine, K.P.: Radiative forcing of carbon dioxide, methane, and nitrous oxide: A significant revision of the methane radiative forcing. Geophysical Research Letters, 43, 12-614, https://doi.org/10.1002/2016GL071930, 2016.

Eyring, V., Bony, S., Meehl, G. A., Senior, C. A., Stevens, B., Stouffer, R. J., and Taylor, K. E.: Overview of the Coupled Model Intercomparison Project Phase 6 (CMIP6) experimental design and organization, Geosci. Model Dev., 9, 1937–1958, https://doi.org/10.5194/gmd-9-1937-2016, 2016.

Fares, S., Mahmood, T., Liu, S., Loreto, F., and Centritto, M. :Influence of growth temperature and measuring temperature on isoprene emission, diffusive limitations of photosynthesis and respiration in hybrid poplars. Atmospheric Environment, 45,155– 161, https://doi.org/10.1016/j.atmosenv.2010.09.036, 2011.

Fiore, A. M., Dentener, F. J., Wild, O., Cuvelier, C., Schultz, M. G., Hess, P., Textor, C., Schulz, M., Doherty, R. M., Horowitz, L. W., MacKenzie, I. A., Sanderson, M. G., Shindell, D. T., Stevenson, D. S., Szopa, S., Van Dingenen, R., Zeng, G., Atherton, C., Bergmann, D., Bey, I., Carmichael, G., Collins, W. J., Duncan, B. N., Faluvegi, G., Folberth, G., Gauss, M., Gong, S., Hauglustaine, D., Holloway, T., Isaksen, I. S. A., Jacob, D. J., Jonson, J. E., Kaminski, J. W., Keating, T. J., Lupu, A., Manner, E., Montanaro, V., Park, R. J., Pitari, G., Pringle, K. J., Pyle, J. A., Schroeder, S., Vivanco, M. G., Wind, P., Wojcik, G., Wu, S., and Zuber, A.: Multimodel estimates of intercontinental source-receptor relationships for ozone pollution, J. Geophys. Res., 114, D04301, https://doi.org/10.1029/2008JD010816, 2009.

Forster, P., Ramaswamy, V., Artaxo, P., Berntsen, T., Betts, R., Fahey, D.W., Haywood, J., Lean, J., Lowe, D.C., Myhre, G., Nganga, J., Prinn, R., Raga, G., Schulz, M., & Van Dorland, R. Miller, H.L. (Ed.). (2007). Changes in Atmospheric Constituents and in Radiative Forcing Chapter 2. United Kingdom: Cambridge University Press.

Forster, P., T. Storelvmo, K. Armour, W. Collins, J. L. Dufresne, D. Frame, D. J. Lunt, T. Mauritsen, M. D. Palmer, M. Watanabe, M. Wild, H. Zhang, 2021, The Earth's Energy Budget, Climate Feedbacks, and Climate Sensitivity. In: Climate Change 2021: The Physical Science Basis. Contribution of Working Group I to the Sixth Assessment Report of the Intergovernmental Panel on Climate Change [Masson-Delmotte, V., P. Zhai, A. Pirani, S. L. Connors, C. Péan, S. Berger, N. Caud, Y. Chen, L. Goldfarb, M. I. Gomis, M. Huang, K. Leitzell, E. Lonnoy, J. B. R. Matthews, T. K. Maycock, T. Waterfield, O. Yelekçi, R. Yu and B. Zhou (eds.)]. Cambridge University Press. In Press.

Forster, P.M., Richardson, T., Maycock, A.C., Smith, C.J., Samset, B.H., Myhre, G., Andrews, T., Pincus, R. and Schulz, M., 2016. Recommendations for diagnosing effective radiative forcing from climate models for CMIP6. Journal of Geophysical Research: Atmospheres, 121, 2-460, https://doi.org/10.1002/2016JD025320, 2016.

Frege, C., Ortega, I. K., Rissanen, M. P., Praplan, A. P., Steiner, G., Heinritzi, M., Ahonen, L., Amorim, A., Bernhammer, A.-K., Bianchi, F., Brilke, S., Breitenlechner, M., Dada, L., Dias, A., Duplissy, J., Ehrhart, S., El-Haddad, I., Fischer, L., Fuchs, C., Garmash, O., Gonin, M., Hansel, A., Hoyle, C. R., Jokinen, T., Junninen, H., Kirkby, J., Kürten, A., Lehtipalo, K., Leiminger, M., Mauldin, R. L., Molteni, U., Nichman, L., Petäjä, T., Sarnela, N., Schobesberger, S., Simon, M., Sipilä, M., Stolzenburg, D., Tomé, A., Vogel, A. L., Wagner, A. C., Wagner, R., Xiao, M., Yan, C., Ye, P., Curtius, J., Donahue, N. M., Flagan, R. C., Kulmala, M., Worsnop, D. R., Winkler, P. M., Dommen, J., and Baltensperger, U.: Influence of temperature on the molecular composition of ions and charged clusters during pure biogenic nucleation, Atmos. Chem. Phys., 18, 65–79, doi.org/10.5194/acp-18-65-2018, 2018.

Fu, T.M., Jacob, D.J., Wittrock, F., Burrows, J.P., Vrekoussis, M. and Henze, D.K., 2008. Global budgets of atmospheric glyoxal and methylglyoxal, and implications for formation of secondary organic aerosols. Journal of geophysical research: atmospheres, 113, https://doi.org/10.1029/2007JD009505, 2008.

Gaston, C.J., Riedel, T.P., Zhang, Z., Gold, A., Surratt, J.D. and Thornton, J.A.: Reactive uptake of an isoprene-derived epoxydiol to submicron aerosol particles. Environmental science & technology, 48, 11178-11186, https://doi.org/10.1021/es5034266, 2014.

Ghan, S. J.: Technical Note: Estimating aerosol effects on cloud radiative forcing, Atmos. Chem. Phys., 13, 9971–9974, https://doi.org/10.5194/acp-13-9971-2013, 2013.

Gordon, H., Sengupta, K., Rap, A., Duplissy, J., Frege, C., Williamson, C., Heinritzi, M., Simon, M., Yan, C., Almeida, J., and Tröstl, J.: Reduced anthropogenic aerosol radiative forcing caused by biogenic new particle formation, P. Natl. Acad. Sci. USA, 113, 12053–12058, https://doi.org/10.1073/pnas.1602360113, 2016.

Gordon, H., Kirkby, J., Baltensperger, U., Bianchi, F., Breitenlechner, M., Curtius, J., Dias, A., Dommen, J., Donahue, N.M., Dunne, E.M. and Duplissy, J.: Causes and importance of new particle formation in the present-day and preindustrial atmospheres. Journal of Geophysical Research: Atmospheres, 122, 8739-8760, doi.org/10.1002/2017JD026844, 2017.

Gregory, J.M., Ingram, W.J., Palmer, M.A., Jones, G.S., Stott, P.A., Thorpe, R.B., Lowe, J.A., Johns, T.C. and Williams, K.D.: A new method for diagnosing radiative forcing and climate sensitivity. Geophysical research letters, 31, https://doi.org/10.1029/2003GL018747, 2004.

Griffiths, P. T., Murray, L. T., Zeng, G., Shin, Y. M., Abraham, N. L., Archibald, A. T., Deushi, M., Emmons, L. K., Galbally, I. E., Hassler, B., Horowitz, L. W., Keeble, J., Liu, J., Moeini, O., Naik, V., O'Connor, F. M., Oshima, N., Tarasick, D., Tilmes, S., Turnock, S. T., Wild, O., Young, P. J., and Zanis, P.: Tropospheric ozone in CMIP6 simulations, Atmos. Chem. Phys., 21, 4187–4218, https://doi.org/10.5194/acp-21-4187-2021, 2021.

Guenther, A., Hewitt, C.N., Erickson, D., Fall, R., Geron, C., Graedel, T., Harley, P., Klinger, L., Lerdau, M., McKay, W.A. and Pierce, T.: A global model of natural volatile organic compound emissions. Journal of Geophysical Research: Atmospheres, 100, 8873-8892, https://doi.org/10.1029/94jd02950, 1995.

Guenther, A., Karl, T., Harley, P., Wiedinmyer, C., Palmer, P. I., and Geron, C.: Estimates of global terrestrial isoprene emissions using MEGAN (Model of Emissions of Gases and Aerosols from Nature), Atmos. Chem. Phys., 6, 3181–3210, https://doi.org/10.5194/acp-6-3181-2006, 2006.

Guenther, A. B., Jiang, X., Heald, C. L., Sakulyanontvittaya, T., Duhl, T., Emmons, L. K., and Wang, X.: The Model of Emissions of Gases and Aerosols from Nature version 2.1 (MEGAN2.1): an extended and updated framework for modeling biogenic emissions, Geoscientific Model Development, 5, 1471–1492, https://doi.org/10.5194/gmd-5-1471-2012, 2012.

Gulev, S. K., P. W. Thorne, J. Ahn, F. J. Dentener, C. M. Domingues, S. Gerland, D. Gong, D. S. Kaufman, H. C. Nnamchi, J. Quaas, J. A. Rivera, S. Sathyendranath, S. L. Smith, B. Trewin, K. von Shuckmann, R. S. Vose, 2021, Changing State of the Climate System. In: Climate Change 2021: The Physical Science Basis. Contribution of Working Group I to the Sixth Assessment Report of the Intergovernmental Panel on Climate Change [Masson- Delmotte, V., P. Zhai, A. Pirani, S. L. Connors, C. Péan, S. Berger, N. Caud, Y. Chen, L. Goldfarb, M. I. Gomis, M. Huang, K. Leitzell, E. Lonnoy, J. B. R. Matthews, T. K. Maycock, T. Waterfield, O. Yelekçi, R. Yu and B. Zhou (eds.)]. Cambridge University Press. In Press.

Hallquist, M., Wenger, J. C., Baltensperger, U., Rudich, Y., Simpson, D., Claeys, M., Dommen, J., Donahue, N. M., George, C., Goldstein, A. H., Hamilton, J. F., Herrmann, H., Hoffmann, T., Iinuma, Y., Jang, M., Jenkin, M. E., Jimenez, J. L., Kiendler-Scharr, A., Maenhaut, W., McFiggans, G., Mentel, Th. F., Monod, A., Prévôt, A. S. H., Seinfeld, J. H., Surratt, J. D., Szmigielski, R., and Wildt, J.: The formation, properties and impact of secondary organic aerosol: current and emerging issues, Atmos. Chem. Phys., 9, 5155–5236, https://doi.org/10.5194/acp-9-5155-2009, 2009.

Heald, C. L., Wilkinson, M. J., Monson, R. K., Alo, C. A., Wang, G., and Guenther, A.: . Response of isoprene emission to ambient CO_2 changes and implications for global budgets. Global Change Biology, 15,1127–1140, https://doi.org/10.1111/j.1365-2486.2008.01802.x, 2009.

Heinritzi, M., Dada, L., Simon, M., Stolzenburg, D., Wagner, A. C., Fischer, L., Ahonen, L. R., Amanatidis, S., Baalbaki, R., Baccarini, A., Bauer, P. S., Baumgartner, B., Bianchi, F., Brilke, S., Chen, D., Chiu, R., Dias, A., Dommen, J., Duplissy, J., Finkenzeller, H., Frege, C., Fuchs, C., Garmash, O., Gordon, H., Granzin, M., El Haddad, I., He, X., Helm, J., Hofbauer, V., Hoyle, C. R., Kangasluoma, J., Keber, T., Kim, C., Kürten, A., Lamkaddam, H., Laurila, T. M., Lampilahti, J., Lee, C. P., Lehtipalo, K., Leiminger, M., Mai, H., Makhmutov, V., Manninen, H. E., Marten, R., Mathot, S., Mauldin, R. L., Mentler, B., Molteni, U., Müller, T., Nie, W., Nieminen, T., Onnela, A., Partoll, E., Passananti, M., Petäjä, T., Pfeifer, J., Pospisilova, V., Quéléver, L. L. J., Rissanen, M. P., Rose, C., Schobesberger, S., Scholz, W., Scholze, K., Sipilä, M., Steiner, G., Stozhkov, Y., Tauber, C., Tham, Y. J., Vazquez-Pufleau, M., Virtanen, A., Vogel, A. L., Volkamer, R., Wagner, R., Wang, M., Weitz, L., Wimmer, D., Xiao, M., Yan, C., Ye, P., Zha, Q., Zhou, X., Amorim, A., Baltensperger, U., Hansel, A., Kulmala, M., Tomé, A., Winkler, P. M., Worsnop, D. R., Donahue, N. M., Kirkby, J., and Curtius, J.: Molecular understanding of the suppression of new-particle formation by isoprene, Atmos. Chem. Phys., 20, 11809–11821, https://doi.org/10.5194/acp-20-11809-2020, 2020.

Hardacre, C., Mulcahy, J. P., Pope, R., Jones, C. G., Rumbold, S. R., Li, C., and Turnock, S. T.: Evaluation of SO2, SO42− and an updated SO2 dry deposition parameterization in UKESM1, Atmos. Chem. Phys. Discuss., https://doi.org/10.5194/acp-2021-238, in review, 2021.

Hewitt, C. N., Lee, J. D., MacKenzie, A. R., Barkley, M. P., Carslaw, N., Carver, G. D., Chappell, N. A., Coe, H., Collier, C., Commane, R., Davies, F., Davison, B., DiCarlo, P., Di Marco, C. F., Dorsey, J. R., Edwards, P. M., Evans, M. J., Fowler, D., Furneaux, K. L., Gallagher, M., Guenther, A., Heard, D. E., Helfter, C., Hopkins, J., Ingham, T., Irwin, M., Jones, C., Karunaharan, A., Langford, B., Lewis, A. C., Lim, S. F., MacDonald, S. M., Mahajan, A. S., Malpass, S., McFiggans, G., Mills, G., Misztal, P., Moller, S., Monks, P. S., Nemitz, E., Nicolas-Perea, V., Oetjen, H., Oram, D. E., Palmer, P. I., Phillips, G. J., Pike, R., Plane, J. M. C., Pugh, T., Pyle, J. A., Reeves, C. E., Robinson, N. H., Stewart, D., Stone, D., Whalley, L. K., and Yin, X.: Overview: oxidant and particle photochemical processes above a south-east Asian tropical rainforest (the OP3 project): introduction, rationale, location characteristics and tools, Atmos. Chem. Phys., 10, 169–199, https://doi.org/10.5194/acp-10-169-2010, 2010.

Hirsikko, A., Nieminen, T., Gagné, S., Lehtipalo, K., Manninen, H. E., Ehn, M., Hõrrak, U., Kerminen, V.-M., Laakso, L., McMurry, P. H., Mirme, A., Mirme, S., Petäjä, T., Tammet, H., Vakkari, V., Vana, M., and Kulmala, M.: Atmospheric ions and nucleation: a review of observations, Atmos. Chem. Phys., 11, 767–798, doi.org/10.5194/acp-11-767-2011, 2011.

Hobbs, P.V. 2000. Introduction to atmospheric chemistry. Cambridge University Press.

Hoesly, R. M., Smith, S. J., Feng, L., Klimont, Z., Janssens-Maenhout, G., Pitkanen, T., Seibert, J. J., Vu, L., Andres, R. J., Bolt, R. M., Bond, T. C., Dawidowski, L., Kholod, N., Kurokawa, J.-I., Li, M., Liu, L., Lu, Z., Moura, M. C. P., O'Rourke, P. R., and Zhang, Q.: Historical (1750–2014) anthropogenic emissions of reactive gases and aerosols from the Community Emissions Data System (CEDS), Geosci. Model Dev., 11, 369–408, https://doi.org/10.5194/gmd-11-369-2018, 2018.

H olmes, C.D., 2018. Methane feedback on atmospheric chemistry: Methods, models, and mechanisms. Journal of Advances in Modeling Earth Systems, 10, 1087-1099, https://doi.org/10.1002/2017MS001196, 2018.

Huang, X.-F., He, L.-Y., Hu, M., Canagaratna, M. R., Kroll, J. H., Ng, N. L., Zhang, Y.-H., Lin, Y., Xue, L., Sun, T.-L., Liu, X.-G., Shao, M., Jayne, J. T., and Worsnop, D. R.: Characterization of submicron aerosols at a rural site in Pearl River Delta of China using an Aerodyne High-Resolution Aerosol Mass Spectrometer, Atmos. Chem. Phys., 11, 1865–1877, https://doi.org/10.5194/acp-11-1865-2011, 2011.

Iglesias-Suarez, F., Kinnison, D. E., Rap, A., Maycock, A. C., Wild, O., and Young, P. J.: Key drivers of ozone change and its radiative forcing over the 21st century, Atmos. Chem. Phys., 18, 6121–6139, https://doi.org/10.5194/acp-18-6121-2018, 2018.

IUPAC Task Group on Atmospheric Chemical Kinetic Data Evaluation, (http://iupac.pole-ether.fr), accessed 17th May 2020.

Jardine, K.J., Chambers, J.Q., Holm, J., Jardine, A.B., Fontes, C.G., Zorzanelli, R.F., Meyers, K.T., De Souza, V.F., Garcia, S., Gimenez, B.O. and Piva, L.R.D.O., 2015. Green leaf volatile emissions during high temperature and drought stress in a central amazon rainforest. Plants, 4, 678-690, https://doi.org/10.3390/plants4030678, 2015.

Jenkin, M.E., Saunders, S.M. and Pilling, M.J.: The tropospheric degradation of volatile organic compounds: a protocol for mechanism development. Atmospheric Environment, 31, 81-104, doi.org/10.1016/S1352-2310(96)00105-7, 1997.

Jenkin, M.E. and Clemitshaw, K.C.: Ozone and other secondary photochemical pollutants: chemical processes governing their formation in the planetary boundary layer. Atmospheric Environment, 34, 2499-2527, https://doi.org/10.1016/S1352-2310(99)00478-1, 2000.

Jenkin, M. E.: Modelling the formation and composition of secondary organic aerosol from α- and β-pinene ozonolysis using MCM v3, Atmos. Chem. Phys., 4, 1741–1757, https://doi.org/10.5194/acp-4-1741-2004, 2004.

Jenkin, M.E., Watson, L.A., Utembe, S.R. and Shallcross, D.E.:. A Common Representative Intermediates (CRI) mechanism for VOC degradation. Part 1: Gas phase mechanism development. Atmospheric Environment, 42,7185-7195, https://doi.org/10.1016/j.atmosenv.2008.07.028, 2008.

Jenkin, M. E., Young, J. C., and Rickard, A. R.: The MCM v3.3.1 degradation scheme for isoprene, Atmos. Chem. Phys., 15, 11433–11459, https://doi.org/10.5194/acp-15-11433-2015, 2015.

Jenkin, M. E., Khan, M. A. H., Shallcross, D. E., Bergström, R., Simpson, D., Murphy, K. L. C., and Rickard, A. R.: The CRI v2. 2 reduced degradation scheme for isoprene, Atmos. Environ., 212, 172–182, https://doi.org/10.1016/j.atmosenv.2019.05.055, 2019a.

Jenkin, M. E., Valorso, R., Aumont, B., and Rickard, A. R.: Estimation of rate coefficients and branching ratios for reactions of organic peroxy radicals for use in automated mechanism construction, Atmos. Chem. Phys., 19, 7691–7717, doi.org/10.5194/acp-19-7691-2019, 2019b.

Jenkin. M, Watson. L, Utembe. S, Richard A. (2019) Chemical mechanistic information taken from the CRI mechanism, CRI v2.2 (Jenkin et al., 2019), via the Master Chemical Mechanism and CRI websites: http://mcm.york.ac.uk/ and http://cri.york.ac.uk/home.htt (Last access 1st July 2021).

Jo, D. S., Hodzic, A., Emmons, L. K., Tilmes, S., Schwantes, R. H., Mills, M. J., Campuzano-Jost, P., Hu, W., Zaveri, R. A., Easter, R. C., Singh, B., Lu, Z., Schulz, C., Schneider, J., Shilling, J. E., Wisthaler, A., and Jimenez, J. L.: Future changes in isoprene-epoxydiol-derived secondary organic aerosol (IEPOX SOA) under the Shared Socioeconomic Pathways: the importance of physicochemical dependency, Atmos. Chem. Phys., 21, 3395–3425, https://doi.org/10.5194/acp-21-3395-2021, 2021.

Johnson, D. and Marston, G.: The gas-phase ozonolysis of unsaturated volatile organic compounds in the troposphere. Chemical Society Reviews, 4, 699-716, doi.org/10.1039/B704260B, 2018.

Jokinen, T., Sipilä, M., Richters, S., Kerminen, V.M., Paasonen, P., Stratmann, F., Worsnop, D., Kulmala, M., Ehn, M., Herrmann, H. and Berndt, T.: Rapid autoxidation forms highly oxidized RO2 radicals in the atmosphere. Angewandte Chemie International Edition, 53, 14596-14600, doi.org/10.1002/anie.201408566, 2014.

Jokinen, T., Berndt, T., Makkonen, R., Kerminen, V.M., Junninen, H., Paasonen, P., Stratmann, F., Herrmann, H., Guenther, A.B., Worsnop, D.R. and Kulmala, M.: Production of extremely low volatile organic compounds from biogenic emissions: Measured yields and atmospheric implications. Proceedings of the National Academy of Sciences, 112, 7123-7128, doi.org/10.1073/pnas.1423977112, 2015.

Karset, I. H. H., Berntsen, T. K., Storelvmo, T., Alterskjær, K., Grini, A., Olivié, D., Kirkevåg, A., Seland, Ø., Iversen, T., and Schulz, M.: Strong impacts on aerosol indirect effects from historical oxidant changes, Atmos. Chem. Phys., 18, 7669–7690, https://doi.org/10.5194/acp-18-7669-2018, 2018.

Kelly, J. M., Doherty, R. M., O'Connor, F. M., and Mann, G. W.: The impact of biogenic, anthropogenic, and biomass burning volatile organic compound emissions on regional and seasonal variations in secondary organic aerosol, Atmos. Chem. Phys., 18, 7393–7422, https://doi.org/10.5194/acp-18-7393-2018, 2018.

Kesselmeier, J. and Staudt, M.: Biogenic volatile organic compounds (VOC): an overview on emission, physiology and ecology. Journal of atmospheric chemistry, 33, 23-88, https://doi.org/10.1023/A:1006127516791, 1999.

Khan, M.A.H., Percival, C.J., Caravan, R.L., Taatjes, C.A. and Shallcross, D.E., 2018. Criegee intermediates and their impacts on the troposphere. Environmental Science: Processes & Impacts, 20(3), 437-453, https://doi.org/10.1039/C7EM00585G, 2018.

Khan, M.A.H., Schlich, B.L., Jenkin, M.E., Cooke, M.C., Derwent, R.G., Neu, J.L., Percival, C.J. and Shallcross, D.E.:. Changes to simulated global atmospheric composition resulting from recent revisions to isoprene oxidation chemistry. Atmospheric Environment, 244, 117914, https://doi.org/10.1016/j.atmosenv.2020.117914, 2020

Kiendler-Scharr, A., Wildt, J., Dal Maso, M., Hohaus, T., Kleist, E., Mentel, T.F., Tillmann, R., Uerlings, R., Schurr, U. and Wahner, A.:. New particle formation in forests inhibited by isoprene emissions. Nature, 461,381-384, https://doi.org/10.1038/nature08292, 2009, 2009.

Kirkby, J., Curtius, J., Almeida, J. et al:. Role of sulphuric acid, ammonia and galactic cosmic rays in atmospheric aerosol nucleation. Nature 476, 429–433, https://doi.org/10.1038/nature10343, 2011.

Kirkby, J., Duplissy, J., Sengupta, K., Frege, C., Gordon, H., Williamson, C., Heinritzi, M., Simon, M., Yan, C., Almeida, J., and Tröstl, J.: Ion-induced nucleation of pure biogenic particles, Nature, 533, 521–526, https://doi.org/10.1038/nature17953, 2016.

Knote, C., Tuccella, P., Curci, G., Emmons, L., Orlando, J.J., Madronich, S., Baró, R., Jiménez-Guerrero, P., Luecken, D., Hogrefe, C. and Forkel, R.: Influence of the choice of gas-phase mechanism on predictions of key gaseous pollutants during the AQMEII phase-2 intercomparison. Atmospheric Environment, 115, 553-568, /doi.org/10.1016/j.atmosenv.2014.11.066, 2015.

Kuhn, U., Andreae, M. O., Ammann, C., Araújo, A. C., Brancaleoni, E., Ciccioli, P., Dindorf, T., Frattoni, M., Gatti, L. V., Ganzeveld, L., Kruijt, B., Lelieveld, J., Lloyd, J., Meixner, F. X., Nobre, A. D., Pöschl, U., Spirig, C., Stefani, P., Thielmann, A., Valentini, R., and Kesselmeier, J.: Isoprene and monoterpene fluxes from Central Amazonian rainforest inferred from tower-based and airborne measurements, and implications on the atmospheric chemistry and the local carbon budget, Atmos. Chem. Phys., 7, 2855–2879, doi.org/10.5194/acp-7-2855-2007, 2007.

Kulmala M., Nieminen T., Chellapermal R., Makkonen R., Bäck J., Kerminen VM.: Climate Feedbacks Linking the Increasing Atmospheric CO_2 Concentration, BVOC Emissions, Aerosols and Clouds in Forest Ecosystems. In: Niinemets Ü., Monson R. (eds) Biology, Controls and Models of Tree Volatile Organic Compound Emissions. Tree Physiology, vol 5. Springer, Dordrecht, doi.org/10.1007/978-94-007-6606-8_17, 2013.

Kulmala, M., Laaksonen, A. and Pirjola, L.: Parameterizations for sulfuric acid/water nucleation rates. Journal of Geophysical Research: Atmospheres, 103, 8301-8307, doi.org/10.1029/97JD03718, 1998.

Kulmala, M., Lehtinen, K. E. J., and Laaksonen, A.: Cluster activation theory as an explanation of the linear dependence between formation rate of 3nm particles and sulphuric acid concentration, Atmos. Chem. Phys., 6, 787–793, doi.org/10.5194/acp-6-787-2006, 2006.

Kurtén, T., Rissanen, M.P., Mackeprang, K., Thornton, J.A., Hyttinen, N., Jørgensen, S., Ehn, M. and Kjaergaard, H.G.: Computational study of hydrogen shifts and ring-opening mechanisms in α-pinene ozonolysis products. The Journal of Physical Chemistry A, 119, 11366-11375, doi.org/10.1021/acs.jpca.5b08948, 2015.

Kurtén, T., Tiusanen, K., Roldin, P., Rissanen, M., Luy, J.N., Boy, M., Ehn, M. and Donahue, N., 2016.: α-Pinene autoxidation products may not have extremely low saturation vapor pressures despite high O: C ratios. The Journal of Physical Chemistry A, 120, 2569-2582, oi.org/10.1021/acs.jpca.6b02196, 2016.

Lacis, A.A., Wuebbles, D.J. and Logan, J.A:. Radiative forcing of climate by changes in the vertical distribution of ozone. Journal of Geophysical Research: Atmospheres, 95, 9971-9981, https://doi.org/10.1029/JD095iD07p09971,1990.

Le Breton, M., Wang, Y., Hallquist, Å. M., Pathak, R. K., Zheng, J., Yang, Y., Shang, D., Glasius, M., Bannan, T. J., Liu, Q., Chan, C. K., Percival, C. J., Zhu, W., Lou, S., Topping, D., Wang, Y., Yu, J., Lu, K., Guo, S., Hu, M., and Hallquist, M.: Online gas- and particle-phase measurements of organosulfates, organosulfonates and nitrooxy organosulfates in Beijing utilizing a FIGAERO ToF-CIMS, Atmos. Chem. Phys., 18, 10355–10371, https://doi.org/10.5194/acp-18-10355-2018, 2018.

Lee, B. H., Lopez-Hilfiker, F. D., Mohr, C., Kurtén, T., Worsnop, D. R., and Thornton, J. A.: An Iodide-Adduct High-Resolution Time-of-Flight Chemical-Ionization Mass Spectrometer: Application to Atmospheric Inorganic and Organic Compounds, Environmental Science & Technology, 48, 6309-6317, https://doi.org/10.1021/es500362a, 2014

Lee, S.H., Uin, J., Guenther, A.B., de Gouw, J.A., Yu, F., Nadykto, A.B., Herb, J., Ng, N.L., Koss, A., Brune, W.H. and Baumann, K.: Isoprene suppression of new particle formation: Potential mechanisms and implications. Journal of Geophysical Research: Atmospheres, 121,14-621, doi.org/10.1002/2016JD024844, 2016.

Lehtipalo, K., Yan, C., Dada, L., Bianchi, F., Xiao, M., Wagner, R., Stolzenburg, D., Ahonen, L.R., Amorim, A., Baccarini, A. and Bauer, P.S.: Multicomponent new particle formation from sulphuric acid, ammonia, and biogenic vapors. Science advances, 4, p.eaau5363, 10.1126/sciadv.aau5363, 2018.

Lelieveld, J., Butler, T.M., Crowley, J.N., Dillon, T.J., Fischer, H., Ganzeveld, L., Harder, H., Lawrence, M.G., Martinez, M., Taraborrelli, D. and Williams, J.: Atmospheric oxidation capacity sustained by a tropical forest. Nature, 452, 737-740, https://doi.org/10.1038/nature06870, 2008.

Liu, Y., Brito, J., Dorris, M.R., Rivera-Rios, J.C., Seco, R., Bates, K.H., Artaxo, P., Duvoisin, S., Keutsch, F.N., Kim, S. and Goldstein, A.H.: Isoprene photochemistry over the Amazon rainforest. Proceedings of the National Academy of Sciences, 113, 6125-6130, https://doi.org/10.1073/pnas.1524136113, 2016.

Liu, Z., Nguyen, V.S., Harvey, J., Müller, J.F. and Peeters, J.: Theoretically derived mechanisms of HPALD photolysis in isoprene oxidation. Physical Chemistry Chemical Physics, 19, 9096-9106, https://doi.org/ 10.1039/C7CP00288B, 2017.

Lopez-Hilfiker, F. D., Mohr, C., Ehn, M., Rubach, F., Kleist, E., Wildt, J., Mentel, Th. F., Lutz, A., Hallquist, M., Worsnop, D., and Thornton, J. A.: A novel method for online analysis of gas and particle composition: description and evaluation of a Filter Inlet for Gases and AEROsols (FIGAERO), Atmos. Meas. Tech., 7, 983–1001, https://doi.org/10.5194/amt-7-983-2014, 2014.

Loreto, F., Ciccioli, P., Cecinato, A., Brancaleoni, E., Frattoni, M., and Tricoli, D.: Influence of environmental factors and air composition on the emission of α-pinene from Quercus ilex leaves, Plant Physiology, 110, 267–275, https://doi.org/10.1104/pp.110.1.267, 1996.

Makkonen, R., Asmi, A., Kerminen, V.-M., Boy, M., Arneth, A., Guenther, A., and Kulmala, M.: BVOC-aerosol-climate interactions in the global aerosol-climate model ECHAM5.5-HAM2, Atmos. Chem. Phys., 12, 10077–10096, https://doi.org/10.5194/acp-12-10077-2012, 2012.

Mann, G. W., Carslaw, K. S., Spracklen, D. V., Ridley, D. A., Manktelow, P. T., Chipperfield, M. P., Pickering, S. J., and Johnson, C. E.: Description and evaluation of GLOMAP-mode: a modal global aerosol microphysics model for the UKCA composition-climate model, Geosci. Model Dev., 3, 519–551, https://doi.org/10.5194/gmd-3-519-2010, 2010.

Marais, E. A., Jacob, D. J., Jimenez, J. L., Campuzano-Jost, P., Day, D. A., Hu, W., Krechmer, J., Zhu, L., Kim, P. S., Miller, C. C., Fisher, J. A., Travis, K., Yu, K., Hanisco, T. F., Wolfe, G. M., Arkinson, H. L., Pye, H. O. T., Froyd, K. D., Liao, J., and McNeill, V. F.: Aqueous-phase mechanism for secondary organic aerosol formation from isoprene: application to the southeast United States and co-benefit of SO_2 emission controls, Atmos. Chem. Phys., 16, 1603–1618, https://doi.org/10.5194/acp-16-1603-2016, 2016.

McFiggans, G., Mentel, T.F., Wildt, J., Pullinen, I., Kang, S., Kleist, E., Schmitt, S., Springer, M., Tillmann, R., Wu, C. and Zhao, D.: Secondary organic aerosol reduced by mixture of atmospheric vapours. Nature, 565, 587-593, https://doi.org/10.1038/s41586-018-0871-y, 2019..

Mentel, T. F., Springer, M., Ehn, M., Kleist, E., Pullinen, I., Kurtén, T., Rissanen, M., Wahner, A., and Wildt, J.: Formation of highly oxidized multifunctional compounds: autoxidation of peroxy radicals formed in the ozonolysis of alkenes – deduced from structure–product relationships, Atmos. Chem. Phys., 15, 6745–6765, doi.org/10.5194/acp-15-6745-2015, 2015.

Metzger, A., Verheggen, B., Dommen, J., Duplissy, J., Prevot, A.S., Weingartner, E., Riipinen, I., Kulmala, M., Spracklen, D.V., Carslaw, K.S. and Baltensperger, U.: Evidence for the role of organics in aerosol particle formation under atmospheric conditions. Proceedings of the National Academy of Sciences, 107,6646-6651, https://doi.org/10.1073/pnas.0911330107, 2010

Møller, K.H., Bates, K.H. and Kjaergaard, H.G.: The importance of peroxy radical hydrogen-shift reactions in atmospheric isoprene oxidation. The Journal of Physical Chemistry A, 123, 920-932, https://doi.org/10.1021/acs.jpca.8b10432, 2019.

Molteni, U., Simon, M., Heinritzi, M., Hoyle, C.R., Bernhammer, A.K., Bianchi, F., Breitenlechner, M., Brilke, S., Dias, A., Duplissy, J. and Frege, C.:. Formation of Highly Oxygenated Organic Molecules from α-Pinene Ozonolysis: Chemical Characteristics, Mechanism, and Kinetic Model Development. ACS Earth and Space Chemistry, 3, 873-883,doi.org/10.1021/acsearthspacechem.9b00035, 2019.

Morgenstern, O., Braesicke, P., O'Connor, F. M., Bushell, A. C., Johnson, C. E., Osprey, S. M., and Pyle, J. A.: Evaluation of the new UKCA climate-composition model – Part 1: The stratosphere, Geosci. Model Dev., 2, 43–57, https://doi.org/10.5194/gmd-2-43-2009, 2009.

Mulcahy, J. P., Johnson, C., Jones, C. G., Povey, A. C., Scott, C. E., Sellar, A., Turnock, S. T., Woodhouse, M. T., Abraham, N. L., Andrews, M. B., Bellouin, N., Browse, J., Carslaw, K. S., Dalvi, M., Folberth, G. A., Glover, M., Grosvenor, D. P., Hardacre, C., Hill, R., Johnson, B., Jones, A., Kipling, Z., Mann, G., Mollard, J., O'Connor, F. M., Palmiéri, J., Reddington, C., Rumbold, S. T., Richardson, M., Schutgens, N. A. J., Stier, P., Stringer, M., Tang, Y., Walton, J., Woodward, S., and Yool, A.: Description and evaluation of aerosol in UKESM1 and HadGEM3-GC3.1 CMIP6 historical simulations, Geosci. Model Dev., 13, 6383–6423, https://doi.org/10.5194/gmd-13-6383-2020, 2020.

Müller, J.-F., Stavrakou, T., and Peeters, J.: Chemistry and deposition in the Model of Atmospheric composition at Global and Regional scales using Inversion Techniques for Trace gas Emissions (MAGRITTE v1.1) – Part 1: Chemical mechanism, Geosci. Model Dev., 12, 2307–2356, https://doi.org/10.5194/gmd-12-2307-2019, 2019.

Natural Environment Research Council; Hewitt. N, Edwards. P, Helfter. C, Irwin. M, Karunaharan. A, Lee. J. D, Newton. H, Robinson. N, Ryder. J. (2010): OP3 Project: Airborne and Ground-based Meteorological Instruments Records as part of the Oxidant and Particle Photochemical Processes above a South-East Asian tropical rain forest. NCAS British Atmospheric Data
Centre. http://catalogue.ceda.ac.uk/uuid/9279c7e807a2ef0eb78a03c3821e62c4 (Last access 27th March 2021)

Natural Environment Research Council; Hewitt. N, Edwards. P, Helfter. C, Irwin. M, Karunaharan. A, Lee. J. D, Newton. H, Robinson. N, Ryder. J. (2010): OP3 Project: Airborne and Ground-based Meteorological Instruments Records as part of the Oxidant and Particle Photochemical Processes above a South-East Asian tropical rain forest. NCAS British Atmospheric Data
Centre. http://catalogue.ceda.ac.uk/uuid/9279c7e807a2ef0eb78a03c3821e62c4 (Last access 27th March 2021)

Ng, N. L., Kroll, J. H., Chan, A. W. H., Chhabra, P. S., Flagan, R. C., and Seinfeld, J. H.: Secondary organic aerosol formation from m-xylene, toluene, and benzene, Atmos. Chem. Phys., 7, 3909–3922, https://doi.org/10.5194/acp-7-3909-2007, 2007

Nguyen, T. B., Coggon, M. M., Bates, K. H., Zhang, X., Schwantes, R. H., Schilling, K. A., Loza, C. L., Flagan, R. C., Wennberg, P. O., and Seinfeld, J. H.: Organic aerosol formation from the reactive uptake of isoprene epoxydiols (IEPOX) onto non-acidified inorganic seeds, Atmos. Chem. Phys., 14, 3497–3510, https://doi.org/10.5194/acp-14-3497-2014, 2014.

Nguyen, T.B., Bates, K.H., Crounse, J.D., Schwantes, R.H., Zhang, X., Kjaergaard, H.G., Surratt, J.D., Lin, P., Laskin, A., Seinfeld, J.H. and Wennberg, P.O.: Mechanism of the hydroxyl radical oxidation of methacryloyl peroxynitrate (MPAN) and its pathway toward secondary organic aerosol formation in the atmosphere. Physical Chemistry Chemical Physics, 17, 17914-17926, https://doi.org/10.1039/C5CP02001H, 2017.

Novelli, A., Vereecken, L., Bohn, B., Dorn, H.-P., Gkatzelis, G. I., Hofzumahaus, A., Holland, F., Reimer, D., Rohrer, F., Rosanka, S., Taraborrelli, D., Tillmann, R., Wegener, R., Yu, Z., Kiendler-Scharr, A., Wahner, A., and Fuchs, H.: Importance of isomerization reactions for OH radical regeneration from the photo-oxidation of isoprene investigated in the atmospheric simulation chamber SAPHIR, Atmos. Chem. Phys., 20, 3333–3355, https://doi.org/10.5194/acp-20-3333-2020, 2020.

O'Connor, F. M., Abraham, N. L., Dalvi, M., Folberth, G. A., Griffiths, P. T., Hardacre, C., Johnson, B. T., Kahana, R., Keeble, J., Kim, B., Morgenstern, O., Mulcahy, J. P., Richardson, M., Robertson, E., Seo, J., Shim, S., Teixeira, J. C., Turnock, S. T., Williams, J., Wiltshire, A. J., Woodward, S., and Zeng, G.: Assessment of pre-industrial to present-day anthropogenic climate forcing in UKESM1, Atmos. Chem. Phys., 21, 1211–1243, https://doi.org/10.5194/acp-21-1211-2021, 2021.

O'Neill, B. C., Tebaldi, C., van Vuuren, D. P., Eyring, V., Friedlingstein, P., Hurtt, G., Knutti, R., Kriegler, E., Lamarque, J.-F., Lowe, J., Meehl, G. A., Moss, R., Riahi, K., and Sanderson, B. M.: The Scenario Model Intercomparison Project (ScenarioMIP) for CMIP6, Geosci. Model Dev., 9, 3461–3482, https://doi.org/10.5194/gmd-9-3461-2016, 2016.

Olivier, J. G. J., Peters, J., Granier, C., Petron, G., Muller, J.-F., and Wallens, S.: Present and future surface emissions of atmospheric compounds, POET Report #3, EU project EVK2-1999-00011, available at: http://www.aero.jussieu.fr/projet/ACCENT/Documents/del2_final.doc, 2003.

Otkjær, R.V., Jakobsen, H.H., Tram, C.M. and Kjaergaard, H.G.: Calculated hydrogen shift rate constants in substituted alkyl peroxy radicals. The Journal of Physical Chemistry A, 122, 8665-8673, doi.org/10.1021/acs.jpca.8b06223, 2018.

Pacifico, F., Harrison, S. P., Jones, C. D., Arneth, A., Sitch, S., Weedon, G. P., Barkley, M. P., Palmer, P. I., Serça, D., Potosnak, M., Fu, T.-M., Goldstein, A., Bai, J., and Schurgers, G.: Evaluation of a photosynthesis-based biogenic isoprene emission scheme in JULES and simulation of isoprene emissions under present-day climate conditions, Atmos. Chem. Phys., 11, 4371–4389, https://doi.org/10.5194/acp-11-4371-2011, 2011.

Pacifico, F., Folberth, G.A., Jones, C.D., Harrison, S.P. and Collins, W.J.: Sensitivity of biogenic isoprene emissions to past, present, and future environmental conditions and implications for atmospheric chemistry. Journal of Geophysical Research: Atmospheres, 117, https://doi.org/10.1029/2012JD018276, 2012.

Peeters, J., Nguyen, T.L. and Vereecken, L.: HOx radical regeneration in the oxidation of isoprene. Physical Chemistry Chemical Physics, 11, 5935-5939, https://doi.org/10.1039/B908511D, 2009.

Petters, M. D. and Kreidenweis, S. M.: A single parameter representation of hygroscopic growth and cloud condensation nucleus activity, Atmos. Chem. Phys., 7, 1961–1971, https://doi.org/10.5194/acp-7-1961-2007, 2007.

Peeters, J., Müller, J.F., Stavrakou, T. and Nguyen, V.S.:. Hydroxyl radical recycling in isoprene oxidation driven by hydrogen bonding and hydrogen tunneling: The upgraded LIM1 mechanism. The Journal of Physical Chemistry A, 118, 8625-8643, https://doi.org/10.1021/jp5033146, 2014.

Petäjä, T., Mauldin, III, R. L., Kosciuch, E., McGrath, J., Nieminen, T., Paasonen, P., Boy, M., Adamov, A., Kotiaho, T., and Kulmala, M.: Sulphuric acid and OH concentrations in a boreal forest site, Atmos. Chem. Phys., 9, 7435–7448, doi.org/10.5194/acp-9-7435-2009, 2009.

Pétron, G., Granier, C., Khattatov, B., Lamarque, J. F., Yudin, V., Muller, J. F., & Gille, J.: Inverse modeling of carbon monoxide surface emissions using Climate Monitoring and Diagnostics Laboratory network observations. Journal of Geophysical Research Atmospheres, 107, https://doi.org/10.1029/2001JD001305, 2002.

Pöschl, U., Von Kuhlmann, R., Poisson, N. and Crutzen, P.J., 2000. Development and intercomparison of condensed isoprene oxidation mechanisms for global atmospheric modeling. Journal of Atmospheric Chemistry, 37, 29-52, https://doi.org/10.1023/A:1006391009798, 2000.

Praske, E., Otkjær, R.V., Crounse, J.D., Hethcox, J.C., Stoltz, B.M., Kjaergaard, H.G. and Wennberg, P.O.: Atmospheric autoxidation is increasingly important in urban and suburban North America. Proceedings of the National Academy of Sciences, 115, 64-69, doi.org/10.1073/pnas.1715540115, 2018.

Prather, M. J.: Photolysis rates in correlated overlapping cloud fields: Cloud-J 7.3c, Geosci. Model Dev., 8, 2587–2595, https://doi.org/10.5194/gmd-8-2587-2015, 2015.

Priestley, M., Le Breton, M., Bannan, T.J., Leather, K.E., Bacak, A., Reyes-Villegas, E., De Vocht, F., Shallcross, B.M., Brazier, T., Anwar Khan, M. and Allan, J.: Observations of Isocyanate, Amide, Nitrate, and Nitro Compounds From an Anthropogenic Biomass Burning Event Using a ToF-CIMS. Journal of Geophysical Research: Atmospheres, 123, 7687-7704, https://doi.org/10.1002/2017JD027316, 2018.

Pye, H.O., D'Ambro, E.L., Lee, B.H., Schobesberger, S., Takeuchi, M., Zhao, Y., Lopez-Hilfiker, F., Liu, J., Shilling, J.E., Xing, J. and Mathur, R.: Anthropogenic enhancements to production of highly oxygenated molecules from autoxidation. Proceedings of the National Academy of Sciences, 14, 6641-6646, doi.org/10.1073/pnas.1810774166, 2018.

Quéléver, L. L. J., Kristensen, K., Normann Jensen, L., Rosati, B., Teiwes, R., Daellenbach, K. R., Peräkylä, O., Roldin, P., Bossi, R., Pedersen, H. B., Glasius, M., Bilde, M., and Ehn, M.: Effect of temperature on the formation of highly oxygenated organic molecules (HOMs) from alpha-pinene ozonolysis, Atmos. Chem. Phys., 19, 7609–7625, doi.org/10.5194/acp-19-7609-2019, 2019.

Ranjithkumar, A., Gordon, H., Williamson, C., Rollins, A., Pringle, K., Kupc, A., Abraham, N. L., Brock, C., and Carslaw, K.: Constraints on global aerosol number concentration, SO_2 and condensation sink in UKESM1 using ATom measurements, Atmos. Chem. Phys., 21, 4979–5014, https://doi.org/10.5194/acp-21-4979-2021, 2021.

Rap, A., Scott, C.E., Reddington, C.L., Mercado, L., Ellis, R.J., Garraway, S., Evans, M.J., Beerling, D.J., MacKenzie, A.R., Hewitt, C.N. and Spracklen, D.V. Enhanced global primary production by biogenic aerosol via diffuse radiation fertilization. Nature Geoscience, 11, 640-644, https://doi.org/10.1038/s41561-018-0208-3., 2018.

Riahi, K., Van Vuuren, D.P., Kriegler, E., Edmonds, J., O'Neill, B.C., Fujimori, S., Bauer, N., Calvin, K., Dellink, R., Fricko, O. and Lutz, W.: The Shared Socioeconomic Pathways and their energy, land use, and greenhouse gas emissions implications: An overview. Global environmental change, 42,153-168, https://doi.org/10.1016/j.gloenvcha.2016.05.009, 2017.

Riccobono, F., Schobesberger, S., Scott, C.E., Dommen, J., Ortega, I.K., Rondo, L., Almeida, J., Amorim, A., Bianchi, F., Breitenlechner, M. and David, A.: Oxidation products of biogenic emissions contribute to nucleation of atmospheric particles. Science, 344, 717-721, doi:10.1126/science.1243527 , 2014.

Rinne, H.J.I., Guenther, A.B., Greenberg, J.P. and Harley, P.C.: Isoprene and monoterpene fluxes measured above Amazonian rainforest and their dependence on light and temperature. Atmos Env, 36, 2421-2426. doi.org/10.1016/S1352-2310(01)00523-4, 2002

Rizzo, V, L., Roldin, P., Brito, J., Backman, J., Swietlicki, E., Krejci, R., Tunved, P., Petäjä, T., Kulmala, M. and Artaxo, P.: Multi-year statistical and modeling analysis of submicrometer aerosol number size distributions at a rain forest site in Amazonia. Atmospheric Chemistry and Physics, 18,10255-10274, /doi.org/10.5194/acp-18-10255-2018, 2018.

Roldin, P., Ehn, M., Kurtén, T., Olenius, T., Rissanen, M.P., Sarnela, N., Elm, J., Rantala, P., Hao, L., Hyttinen, N. and Heikkinen, L..: The role of highly oxygenated organic molecules in the Boreal aerosol-cloud-climate system. Nature communications, 10, 1-15, doi.org/10.1038/s41467-019-12338-8, 2019.

Sander, R., Baumgaertner, A., Cabrera-Perez, D., Frank, F., Gromov, S., Grooß, J.-U., Harder, H., Huijnen, V., Jöckel, P., Karydis, V. A., Niemeyer, K. E., Pozzer, A., Riede, H., Schultz, M. G., Taraborrelli, D., and Tauer, S.: The community atmospheric chemistry box model CAABA/MECCA-4.0, Geosci. Model Dev., 12, 1365–1385, https://doi.org/10.5194/gmd-12-1365-2019, 2019.

Sarnela, N., Jokinen, T., Duplissy, J., Yan, C., Nieminen, T., Ehn, M., Schobesberger, S., Heinritzi, M., Ehrhart, S., Lehtipalo, K., Tröstl, J., Simon, M., Kürten, A., Leiminger, M., Lawler, M. J., Rissanen, M. P., Bianchi, F., Praplan, A. P., Hakala, J., Amorim, A., Gonin, M., Hansel, A., Kirkby, J., Dommen, J., Curtius, J., Smith, J. N., Petäjä, T., Worsnop, D. R., Kulmala, M., Donahue, N. M., and Sipilä, M.: Measurement–model comparison of stabilized Criegee intermediate and highly oxygenated molecule production in the CLOUD chamber, Atmos. Chem. Phys., 18, 2363–2380, doi.org/10.5194/acp-18-2363-2018, 2018.

Sato, K.: Detection of nitrooxypolyols in secondary organic aerosol formed from the photooxidation of conjugated dienes under high-NOx conditions. Atmospheric Environment, 42, 6851-6861, https://doi.org/10.1016/j.atmosenv.2008.05.010, 2008.

Saunders, S. M., Jenkin, M. E., Derwent, R. G., and Pilling, M. J.: Protocol for the development of the Master Chemical Mechanism, MCM v3 (Part A): tropospheric degradation of non-aromatic volatile organic compounds, Atmos. Chem. Phys., 3, 161–180, doi.org/10.5194/acp-3-161-2003, 2003.

Schervish, M. and Donahue, N. M.: Peroxy Radical Chemistry and the Volatility Basis Set, Atmos. Chem. Phys. Discuss., doi.org/10.5194/acp-2019-509, 2019.

Schwantes, R. H., Charan, S. M., Bates, K. H., Huang, Y., Nguyen, T. B., Mai, H., Kong, W., Flagan, R. C., and Seinfeld, J. H.: Low-volatility compounds contribute significantly to isoprene secondary organic aerosol (SOA)

under high-NO_x conditions, Atmos. Chem. Phys., 19, 7255–7278, https://doi.org/10.5194/acp-19-7255-2019, 2019.

Schwantes, R. H., Emmons, L. K., Orlando, J. J., Barth, M. C., Tyndall, G. S., Hall, S. R., Ullmann, K., St. Clair, J. M., Blake, D. R., Wisthaler, A., and Bui, T. P. V.: Comprehensive isoprene and terpene gas-phase chemistry improves simulated surface ozone in the southeastern US, Atmos. Chem. Phys., 20, 3739–3776, https://doi.org/10.5194/acp-20-3739-2020, 2020.

Schulz, C., Schneider, J., Amorim Holanda, B., Appel, O., Costa, A., de Sá, S. S., Dreiling, V., Fütterer, D., Jurkat-Witschas, T., Klimach, T., Knote, C., Krämer, M., Martin, S. T., Mertes, S., Pöhlker, M. L., Sauer, D., Voigt, C., Walser, A., Weinzierl, B., Ziereis, H., Zöger, M., Andreae, M. O., Artaxo, P., Machado, L. A. T., Pöschl, U., Wendisch, M., and Borrmann, S.: Aircraft-based observations of isoprene-epoxydiol-derived secondary organic aerosol (IEPOX-SOA) in the tropical upper troposphere over the Amazon region, Atmos. Chem. Phys., 18, 14979–15001, https://doi.org/10.5194/acp-18-14979-2018, 2018.

Scott, C. E., Rap, A., Spracklen, D. V., Forster, P. M., Carslaw, K. S., Mann, G. W., Pringle, K. J., Kivekäs, N., Kulmala, M., Lihavainen, H., and Tunved, P.: The direct and indirect radiative effects of biogenic secondary organic aerosol, Atmos. Chem. Phys., 14, 447–470, https://doi.org/10.5194/acp-14-447-2014, 2014.

Scott, C.E., Monks, S.A., Spracklen, D.V., Arnold, S.R., Forster, P.M., Rap, A., Äijälä, M., Artaxo, P., Carslaw, K.S., Chipperfield, M.P. and Ehn, M.: Impact on short-lived climate forcers increases projected warming due to deforestation. Nature Communications, 9, 1-9, https://doi.org/10.1038/s41467-017-02412-4, 2018a.

Scott, C.E., Arnold, S.R., Monks, S.A., Asmi, A., Paasonen, P. and Spracklen, D.V:. Substantial large-scale feedbacks between natural aerosols and climate. Nature Geoscience, 11, 44-48, https://doi.org/10.1038/s41561-017-0020-5, 2018b.

Sellar, A.A., Walton, J., Jones, C.G., Wood, R., Abraham, N.L., Andrejczuk, M., Andrews, M.B., Andrews, T., Archibald, A.T., de Mora, L. and Dyson, H., 2020. Implementation of UK Earth system models for CMIP6. Journal of Advances in Modeling Earth Systems, 12,https://doi.org/10.1029/2019MS001946, 2020.

Sengupta, K., Pringle, K., Johnson, J. S., Reddington, C., Browse, J., Scott, C. E., and Carslaw, K.: A global model perturbed parameter ensemble study of secondary organic aerosol formation, Atmos. Chem. Phys., 21, 2693–2723, https://doi.org/10.5194/acp-21-2693-2021, 2021.

Sheil, D: Forests, atmospheric water and an uncertain future: The new biology of the global water cycle. Forest Ecosystems, 5, 19. https://doi.org/10.1186/s4066 3-018-0138-y, 2018

Shrivastava, M., Andreae, M.O., Artaxo, P., Barbosa, H.M., Berg, L.K., Brito, J., Ching, J., Easter, R.C., Fan, J., Fast, J.D. and Feng, Z.:. Urban pollution greatly enhances formation of natural aerosols over the Amazon rainforest. Nature communications, 10, 1-12, https://doi.org/10.1038/s41467-019-08909-4 , 2019.

Shrivastava, M., Cappa, C.D., Fan, J., Goldstein, A.H., Guenther, A.B., Jimenez, J.L., Kuang, C., Laskin, A., Martin, S.T., Ng, N.L. and Petaja, T., 2017. Recent advances in understanding secondary organic aerosol: Implications for global climate forcing. Reviews of Geophysics, 55, 509-559, doi.org/10.1002/2016RG000540, 2017.

Sihto, S.-L., Kulmala, M., Kerminen, V.-M., Dal Maso, M., Petäjä, T., Riipinen, I., Korhonen, H., Arnold, F., Janson, R., Boy, M., Laaksonen, A., and Lehtinen, K. E. J.: Atmospheric sulphuric acid and aerosol formation: implications from atmospheric mea- surements for nucleation and early growth mechanisms, Atmos. Chem. Phys., 6, 4079–4091, doi:10.5194/acp-6-4079-2006, 2006

Simon, M., Dada, L., Heinritzi, M., Scholz, W., Stolzenburg, D., Fischer, L., Wagner, A. C., Kürten, A., Rörup, B., He, X.-C., Almeida, J., Baalbaki, R., Baccarini, A., Bauer, P. S., Beck, L., Bergen, A., Bianchi, F., Bräkling, S., Brilke, S., Caudillo, L., Chen, D., Chu, B., Dias, A., Draper, D. C., Duplissy, J., El-Haddad, I., Finkenzeller, H., Frege, C., Gonzalez-Carracedo, L., Gordon, H., Granzin, M., Hakala, J., Hofbauer, V., Hoyle, C. R., Kim, C., Kong, W., Lamkaddam, H., Lee, C. P., Lehtipalo, K., Leiminger, M., Mai, H., Manninen, H. E., Marie, G., Marten, R., Mentler, B., Molteni, U., Nichman, L., Nie, W., Ojdanic, A., Onnela, A., Partoll, E., Petäjä, T., Pfeifer, J., Philippov, M., Quéléver, L. L. J., Ranjithkumar, A., Rissanen, M. P., Schallhart, S., Schobesberger, S., Schuchmann, S., Shen, J., Sipilä, M., Steiner, G., Stozhkov, Y., Tauber, C., Tham, Y. J., Tomé, A. R., Vazquez-Pufleau, M., Vogel, A. L., Wagner, R., Wang, M., Wang, D. S., Wang, Y., Weber, S. K., Wu, Y., Xiao, M., Yan, C., Ye, P., Ye, Q., Zauner-Wieczorek, M., Zhou, X., Baltensperger, U., Dommen, J., Flagan, R. C., Hansel, A., Kulmala, M., Volkamer, R., Winkler, P. M., Worsnop, D. R., Donahue, N. M., Kirkby, J., and Curtius, J.: Molecular understanding of new-particle formation from α-pinene between −50 and +25 °C, Atmos. Chem. Phys., 20, 9183–9207, https://doi.org/10.5194/acp-20-9183-2020, 2020.

Simpson, D., Winiwarter, W., Börjesson, G., Cinderby, S., Ferreiro, A., Guenther, A., Hewitt, C.N., Janson, R., Khalil, M.A.K., Owen, S. and Pierce, T.E.: Inventorying emissions from nature in Europe. Journal of Geophysical Research: Atmospheres, 104, 8113-8152, https://doi.org/10.1029/98JD02747, 1999.

Sindelarova, K., Granier, C., Bouarar, I., Guenther, A., Tilmes, S., Stavrakou, T., Müller, J.-F., Kuhn, U., Stefani, P., and Knorr, W.: Global data set of biogenic VOC emissions calculated by the MEGAN model over the last 30 years, Atmos. Chem. Phys., 14, 9317–9341, https://doi.org/10.5194/acp-14-9317-2014, 2014.

Skeie, R. B., Myhre, G., Hodnebrog, Ø., Cameron-Smith, P. J., Deushi, M., Hegglin, M. I., Horowitz, L. W., Kramer, R. J., Michou, M., Mills, M. J., Olivié, D. J. L., O'Connor, F. M., Paynter, D., Samset, B. H., Sellar, A., Shindell, D., Takemura, T., Tilmes, S., and Wu, T.: Historical total ozone radiative forcing derived from CMIP6 simulations, npj Climate and Atmospheric Science, 3, 32, https://doi.org/10.1038/s41612-020-00131-0, 2020.

Sporre, M. K., Blichner, S. M., Karset, I. H. H., Makkonen, R., and Berntsen, T. K.: BVOC–aerosol–climate feedbacks investigated using NorESM, Atmos. Chem. Phys., 19, 4763–4782, https://doi.org/10.5194/acp-19-4763-2019, 2019.

Sporre, M. K., Blichner, S. M., Schrödner, R., Karset, I. H. H., Berntsen, T. K., van Noije, T., Bergman, T., O'Donnell, D., and Makkonen, R.: Large difference in aerosol radiative effects from BVOC-SOA treatment in three Earth system models, Atmos. Chem. Phys., 20, 8953–8973, https://doi.org/10.5194/acp-20-8953-2020, 2020.

Spracklen, D. V., Pringle, K. J., Carslaw, K. S., Chipperfield, M. P., and Mann, G. W.: A global off-line model of size-resolved aerosol microphysics: I. Model development and prediction of aerosol properties, Atmos. Chem. Phys., 5, 2227–2252, https://doi.org/10.5194/acp-5-2227-2005, 2005.

Squire, O. J., Archibald, A. T., Griffiths, P. T., Jenkin, M. E., Smith, D., and Pyle, J. A.: Influence of isoprene chemical mechanism on modelled changes in tropospheric ozone due to climate and land use over the 21st century, Atmos. Chem. Phys., 15, 5123–5143, https://doi.org/10.5194/acp-15-5123-2015, 2015.

Stocker, T. F., Qin, D., Plattner, G.-K., Alexander, L. V., Allen, S. K., Bindoff, N. L., Br\'on, F.-M., Church, J. A., Cubasch, U., Emori, S., Forster, P., Friedlingstein, P., Gillett, N., Gregory, J. M., Hartmann, D. L., Jansen, E., Kirtman, B., Knutti, R., Kumar, K. K., Lemke, P. et al (2013) Technical summary. In: Climate Change 2013: The Physical Science Basis. Cambridge University Press. ISBN 9781107661820

Stolzenburg, D., Fischer, L., Vogel, A.L., Heinritzi, M., Schervish, M., Simon, M., Wagner, A.C., Dada, L., Ahonen, L.R., Amorim, A. and Baccarini, A.: Rapid growth of organic aerosol nanoparticles over a wide tropospheric temperature range. Proceedings of the National Academy of Sciences, 115, 9122-9127, doi.org/10.1073/pnas.1807604115, 2018.

Surratt, J.D., Chan, A.W., Eddingsaas, N.C., Chan, M., Loza, C.L., Kwan, A.J., Hersey, S.P., Flagan, R.C., Wennberg, P.O. and Seinfeld, J.H., 2010. Reactive intermediates revealed in secondary organic aerosol formation from isoprene. Proceedings of the National Academy of Sciences, 107, 6640-6645, https://doi.org/10.1073/pnas.0911114107, 2010.

Tai, A.P., Martin, M.V. and Heald, C.L., 2014. Threat to future global food security from climate change and ozone air pollution. Nature Climate Change, 4, 817-821, https://doi.org/10.1038/nclimate2317, 2014.

Tan, Z., Rohrer, F., Lu, K., Ma, X., Bohn, B., Broch, S., Dong, H., Fuchs, H., Gkatzelis, G. I., Hofzumahaus, A., Holland, F., Li, X., Liu, Y., Liu, Y., Novelli, A., Shao, M., Wang, H., Wu, Y., Zeng, L., Hu, M., Kiendler-Scharr, A., Wahner, A., and Zhang, Y.: Wintertime photochemistry in Beijing: observations of ROx radical concentrations in the North China Plain during the BEST-ONE campaign, Atmos. Chem. Phys., 18, 12391–12411, doi.org/10.5194/acp-18-12391-2018, 2018.

Telford, P. J., Abraham, N. L., Archibald, A. T., Braesicke, P., Dalvi, M., Morgenstern, O., O'Connor, F. M., Richards, N. A. D., and Pyle, J. A.: Implementation of the Fast-JX Photolysis scheme (v6.4) into the UKCA component of the MetUM chemistry-climate model (v7.3), Geosci. Model Dev., 6, 161–177, https://doi.org/10.5194/gmd-6-161-2013, 2013.

Teng, A.P., Crounse, J.D. and Wennberg, P.O.:. Isoprene peroxy radical dynamics. Journal of the American Chemical Society, 139,5367-5377, https://doi.org/10.1021/jacs.6b12838, 2017

Thornhill, G. D., Collins, W. J., Kramer, R. J., Olivié, D., Skeie, R. B., O'Connor, F. M., Abraham, N. L., Checa-Garcia, R., Bauer, S. E., Deushi, M., Emmons, L. K., Forster, P. M., Horowitz, L. W., Johnson, B., Keeble, J., Lamarque, J.-F., Michou, M., Mills, M. J., Mulcahy, J. P., Myhre, G., Nabat, P., Naik, V., Oshima, N., Schulz, M., Smith, C. J., Takemura, T., Tilmes, S., Wu, T., Zeng, G., and Zhang, J.: Effective radiative forcing from emissions of reactive gases and aerosols – a multi-model comparison, Atmos. Chem. Phys., 21, 853–874, https://doi.org/10.5194/acp-21-853-2021, 2021a.

Thornhill, G., Collins, W., Olivié, D., Skeie, R. B., Archibald, A., Bauer, S., Checa-Garcia, R., Fiedler, S., Folberth, G., Gjermundsen, A., Horowitz, L., Lamarque, J.-F., Michou, M., Mulcahy, J., Nabat, P., Naik, V., O'Connor, F. M., Paulot, F., Schulz, M., Scott, C. E., Séférian, R., Smith, C., Takemura, T., Tilmes, S., Tsigaridis, K., and Weber, J.: Climate-driven chemistry and aerosol feedbacks in CMIP6 Earth system models, Atmos. Chem. Phys., 21, 1105–1126, https://doi.org/10.5194/acp-21-1105-2021, 2021b.

Tilmes, S., Lamarque, J.-F., Emmons, L. K., Conley, A., Schultz, M. G., Saunois, M., Thouret, V., Thompson, A. M., Oltmans, S. J., Johnson, B., and Tarasick, D.: Technical Note: Ozonesonde climatology between 1995 and 2011: description, evaluation and applications, Atmos. Chem. Phys., 12, 7475–7497, https://doi.org/10.5194/acp-12-7475-2012, 2012.

Toon, O.B., Maring, H., Dibb, J., Ferrare, R., Jacob, D.J., Jensen, E.J., Luo, Z.J., Mace, G.G., Pan, L.L., Pfister, L. and Rosenlof, K.H.:. Planning, implementation, and scientific goals of the Studies of Emissions and Atmospheric Composition, Clouds and Climate Coupling by Regional Surveys (SEAC4RS) field mission. Journal of Geophysical Research: Atmospheres, 121, 4967-5009, https://doi.org/10.1002/2015JD024297,2016 .

Turnock, S.T., Mann, G.W., Woodhouse, M.T., Dalvi, M., O'Connor, F.M., Carslaw, K.S. and Spracklen, D.V.: The impact of changes in cloud water pH on aerosol radiative forcing. Geophysical Research Letters, 46, 4039-4048, https://doi.org/10.1029/2019GL082067, 2019.

Twomey, S.: Pollution and the planetary albedo. Atmospheric Environment), 8, 1251-1256, https://doi.org/10.1016/0004-6981(74)90004-3, 1974.

Twomey, S.: Aerosols, clouds and radiation. Atmospheric Environment. Part A. General Topics, 25, 2435-2442, https://doi.org/10.1016/0960-1686(91)90159-5, 1991.

Unger, N.: On the role of plant volatiles in anthropogenic global climate change. Geophysical Research Letters, 41, 8563-8569, https://doi.org/10.1002/2014GL061616, 2014a.

Unger, N.: Human land-use-driven reduction of forest volatiles cools global climate. Nature Climate Change, 4, 907-910, https://doi.org/10.1038/NCLIMATE2347, 2014b.

Utembe, S.R., Watson, L.A., Shallcross, D.E. and Jenkin, M.E.: A Common Representative Intermediates (CRI) mechanism for VOC degradation. Part 3: Development of a secondary organic aerosol module. Atmospheric Environment, 43, 1982-1990, doi.org/10.1016/j.atmosenv.2009.01.008, 2009.

Utembe, S.R., Cooke, M.C., Archibald, A.T., Jenkin, M.E., Derwent, R.G. and Shallcross, D.E.:. Using a reduced Common Representative Intermediates (CRIv2-R5) mechanism to simulate tropospheric ozone in a 3-D Lagrangian chemistry transport model. Atmospheric Environment, 441609-1622, https://doi.org/10.1016/j.atmosenv.2010.01.044, 2010.

Naik, V., Szopa, S., B. Adhikary, P. Artaxo, T. Berntsen, W.D. Collins, S. Fuzzi, L. Gallardo, A. Kiendler Scharr, Z. Klimont, H. Liao, N. Unger, and P. Zanis, 2021: Short-Lived Climate Forcers. In Climate Change 2021: The Physical Science Basis. Contribution of Working Group I to the Sixth Assessment Report of the Intergovernmental Panel on Climate Change [Masson-Delmotte, V., P. Zhai, A. Pirani, S.L. Connors, C. Péan, S. Berger, N. Caud, Y. Chen, L. Goldfarb, M.I. Gomis, M. Huang, K. Leitzell, E. Lonnoy, J.B.R. Matthews, T.K. Maycock, T. Waterfield, O. Yelekçi, R. Yu, and B. Zhou (eds.)]. Cambridge University Press. In Press.

van Marle, M. J. E., Kloster, S., Magi, B. I., Marlon, J. R., Daniau, A.-L., Field, R. D., Arneth, A., Forrest, M., Hantson, S., Kehrwald, N. M., Knorr, W., Lasslop, G., Li, F., Mangeon, S., Yue, C., Kaiser, J. W., and van der Werf, G. R.: Historic global biomass burning emissions for CMIP6 (BB4CMIP) based on merging satellite observations with proxies and fire models (1750–2015), Geosci. Model Dev., 10, 3329–3357, https://doi.org/10.5194/gmd-10-3329-2017, 2017.

van Meeningen, Y., Schurgers, G., Rinnan, R., and Holst, T.: Isoprenoid emission response to changing light conditions of English oak, European beech and Norway spruce, Biogeosciences, 14, 4045–4060, https://doi.org/10.5194/bg-14-4045-2017, 2017.

Van Vuuren, D.P., Edmonds, J.A., Kainuma, M., Riahi, K. and Weyant, J., 2011. A special issue on the RCPs. Climatic Change, 109, 1-4, https://doi.org/10.1007/s10584-011-0157-y, 2011.

Vereecken, L., Carlsson, P.T.M., Novelli, A., Bernard, F., Brown, S.S., Cho, C., Crowley, J.N., Fuchs, H., Mellouki, W., Reimer, D. and Shenolikar, J., 2021. Theoretical and experimental study of peroxy and alkoxy radicals in the NO 3-initiated oxidation of isoprene. Physical Chemistry Chemical Physics, 23, 5496-5515, https://doi.org/10.1039/D0CP06267G, 2021.

Veres, P.R., Neuman, J.A., Bertram, T.H., Assaf, E., Wolfe, G.M., Williamson, C.J., Weinzierl, B., Tilmes, S., Thompson, C.R., Thames, A.B. and Schroder, J.C.: Global airborne sampling reveals a previously unobserved dimethyl sulfide oxidation mechanism in the marine atmosphere. Proceedings of the National Academy of Sciences, 117, 4505-4510, https://doi.org/10.1073/pnas.1919344117, 2020.

Walters, D., Baran, A. J., Boutle, I., Brooks, M., Earnshaw, P., Edwards, J., Furtado, K., Hill, P., Lock, A., Manners, J., Morcrette, C., Mulcahy, J., Sanchez, C., Smith, C., Stratton, R., Tennant, W., Tomassini, L., Van Weverberg, K., Vosper, S., Willett, M., Browse, J., Bushell, A., Carslaw, K., Dalvi, M., Essery, R., Gedney, N.,

Hardiman, S., Johnson, B., Johnson, C., Jones, A., Jones, C., Mann, G., Milton, S., Rumbold, H., Sellar, A., Ujiie, M., Whitall, M., Williams, K., and Zerroukat, M.: The Met Office Unified Model Global Atmosphere 7.0/7.1 and JULES Global Land 7.0 configurations, Geosci. Model Dev., 12, 1909–1963, https://doi.org/10.5194/gmd-12-1909-2019, 2019.

Watson, L.A., Shallcross, D.E., Utembe, S.R. and Jenkin, M.E., 2008. A Common Representative Intermediates (CRI) mechanism for VOC degradation. Part 2: Gas phase mechanism reduction. Atmospheric Environment, 42, 7196-7204, https://doi.org/10.1016/j.atmosenv.2008.07.034,2008.

Watson, L.A., Shallcross, D.E., Utembe, S.R. and Jenkin, M.E.: A Common Representative Intermediates (CRI) mechanism for VOC degradation. Part 2: Gas phase mechanism reduction. Atmospheric Environment, 42, 7196-7204, doi.org/10.1016/j.atmosenv.2008.07.034, 2008.

Weber, J., & Bannan, T. (2021). Z2F Brazil Observational used for CRI-STRAT 2 Evaluation [Dataset]. https://doi.org/10.17863/CAM.65133 (last access: 9th April 2021)

Weber, J., Shin, Y.M., Staunton Sykes, J., Archer-Nicholls, S., Abraham, N.L. and Archibald, A.T.:. Minimal Climate Impacts From Short-Lived Climate Forcers Following Emission Reductions Related to the COVID-19 Pandemic. Geophysical research letters, 47, https://doi.org/10.1029/2020GL090326 , 2020a.

Weber, J., Archer-Nicholls, S., Griffiths, P., Berndt, T., Jenkin, M., Gordon, H., Knote, C., and Archibald, A. T.: CRI-HOM: A novel chemical mechanism for simulating highly oxygenated organic molecules (HOMs) in global chemistry–aerosol–climate models, Atmos. Chem. Phys., 20, 10889–10910, https://doi.org/10.5194/acp-20-10889-2020, 2020b.

Wells, K.C., Millet, D.B., Payne, V.H., Deventer, M.J., Bates, K.H., de Gouw, J.A., Graus, M., Warneke, C., Wisthaler, A. and Fuentes, J.D.:. Satellite isoprene retrievals constrain emissions and atmospheric oxidation. Nature, 585,225-233, https://doi.org/10.1038/s41586-020-2664-3, 2020.

Wennberg, P.O., Bates, K.H., Crounse, J.D., Dodson, L.G., McVay, R.C., Mertens, L.A., Nguyen, T.B., Praske, E., Schwantes, R.H., Smarte, M.D. and St Clair, J.M.:. Gas-phase reactions of isoprene and its major oxidation products. Chemical reviews, 118,3337-3390, https://doi.org/10.1021/acs.chemrev.7b00439

Whalley, L. K., Edwards, P. M., Furneaux, K. L., Goddard, A., Ingham, T., Evans, M. J., Stone, D., Hopkins, J. R., Jones, C. E., Karunaharan, A., Lee, J. D., Lewis, A. C., Monks, P. S., Moller, S. J., and Heard, D. E.: Quantifying the magnitude of a missing hydroxyl radical source in a tropical rainforest, Atmos. Chem. Phys., 11, 7223–7233, https://doi.org/10.5194/acp-11-7223-2011, 2011.

Williamson, C.J., Kupc, A., Axisa, D., Bilsback, K.R., Bui, T., Campuzano-Jost, P., Dollner, M., Froyd, K.D., Hodshire, A.L., Jimenez, J.L. and Kodros, J.K.: A large source of cloud condensation nuclei from new particle formation in the tropics. Nature, 574, 399-403, doi.org/10.1038/s41586-019-1638-9, 2019.

Wimmer, D., Buenrostro Mazon, S., Manninen, H.E., Kangasluoma, J., Franchin, A., Nieminen, T., Backman, J., Wang, J., Kuang, C., Krejci, R. and Brito, J., 2018. Ground-based observation of clusters and nucleation-mode particles in the Amazon. Atmospheric Chemistry and Physics, 18,13245-13264, 10.5194/acp-18-13245-2018, 2018.

Wollesen de Jonge, R., Elm, J., Rosati, B., Christiansen, S., Hyttinen, N., Lüdemann, D., Bilde, M., and Roldin, P.: Secondary aerosol formation from dimethyl sulfide – improved mechanistic understanding based on smog chamber experiments and modelling, Atmos. Chem. Phys., 21, 9955–9976, https://doi.org/10.5194/acp-21-9955-2021, 2021.

Woo, J. L. and McNeill, V. F.: simpleGAMMA v1.0 – a reduced model of secondary organic aerosol formation in the aqueous aerosol phase (aaSOA), Geosci. Model Dev., 8, 1821–1829, https://doi.org/10.5194/gmd-8-1821-2015, 2015.

Wu, Z., Hu, M., Liu, S., Wehner, B., Bauer, S., Ma ßLing, A., Wiedensohler, A., Petaejae, T., Dal Maso, M. and Kulmala, M: New particle formation in Beijing, China: Statistical analysis of a 1-year data set. Journal of Geophysical Research: Atmospheres, D9, doi.org/10.1029/2006JD007406, 2007.

Xu, L., Møller, K.H., Crounse, J.D., Otkjær, R.V., Kjaergaard, H.G. and Wennberg, P.O.:. Unimolecular reactions of peroxy radicals formed in the oxidation of α-pinene and β-pinene by hydroxyl radicals. The Journal of Physical Chemistry A, 123, 1661-1674, doi.org/10.1021/acs.jpca.8b11726, 2019.

Yáñez-Serrano, A. M. (2020). VOC observational data from ATTO tower. (Last access 1st April 2021)

Yáñez-Serrano, A. M., Nölscher, A. C., Williams, J., Wolff, S., Alves, E., Martins, G. A., Bourtsoukidis, E., Brito, J., Jardine, K., Artaxo, P., and Kesselmeier, J.: Diel and seasonal changes of biogenic volatile organic compounds within and above an Amazonian rainforest, Atmos. Chem. Phys., 15, 3359–3378, https://doi.org/10.5194/acp-15-3359-2015, 2015.

Yáñez-Serrano, A. M., Nölscher, A. C., Williams, J., Wolff, S., Alves, E., Martins, G. A., Bourtsoukidis, E., Brito, J., Jardine, K., Artaxo, P., and Kesselmeier, J.: Diel and seasonal changes of biogenic volatile organic compounds within and above an Amazonian rainforest, Atmos. Chem. Phys., 15, 3359–3378, https://doi.org/10.5194/acp-15-3359-2015, 2015.

Yáñez-Serrano, A. M., Nölscher, A. C., Williams, J., Wolff, S., Alves, E., Martins, G. A., Bourtsoukidis, E., Brito, J., Jardine, K., Artaxo, P., and Kesselmeier, J. Diel and seasonal changes of biogenic volatile organic compounds within and above an Amazonian rainforest, Atmos. Chem. Phys., 15, 3359–3378, doi.org/10.5194/acp-15-3359- 2015, 2015.

Young, P.J., Naik, V., Fiore, A.M., Gaudel, A., Guo, J., Lin, M.Y., Neu, J.L., Parrish, D.D., Rieder, H.E., Schnell, J.L. and Tilmes, S. Tropospheric Ozone Assessment Report: Assessment of global-scale model performance for global and regional ozone distributions, variability, and trends. Elementa: Science of the Anthropocene, 6 ,10, https://doi.org/10.1525/elementa.265, 2018.

Zhang, Y.-Q., Chen, D.-H., Ding, X., Li, J., Zhang, T., Wang, J.-Q., Cheng, Q., Jiang, H., Song, W., Ou, Y.-B., Ye, P.-L., Zhang, G., and Wang, X.-M.: Impact of anthropogenic emissions on biogenic secondary organic aerosol: observation in the Pearl River Delta, southern China, Atmos. Chem. Phys., 19, 14403–14415, https://doi.org/10.5194/acp-19-14403-2019, 2019.

Zhang, Z., Lin, Y.-H., Zhang, H., Surratt, J. D., Ball, L. M., and Gold, A.: Technical Note: Synthesis of isoprene atmospheric oxidation products: isomeric epoxydiols and the rearrangement products cis- and trans-3-methyl-3,4-dihydroxytetrahydrofuran, Atmos. Chem. Phys., 12, 8529–8535, https://doi.org/10.5194/acp-12-8529-2012, 2012.

Zhao, B., Shrivastava, M., Donahue, N.M., Gordon, H., Schervish, M., Shilling, J.E., Zaveri, R.A., Wang, J., Andreae, M.O., Zhao, C. and Gaudet, B.: High concentration of ultrafine particles in the Amazon free troposphere produced by organic new particle formation. Proceedings of the National Academy of Sciences, 117, 25344-25351, https://doi.org/10.1073/pnas.2006716117, 2020.

Zhao, Y., Thornton, J.A. and Pye, H.O.: Quantitative constraints on autoxidation and dimer formation from direct probing of monoterpene-derived peroxy radical chemistry. Proceedings of the National Academy of Sciences, 48, 12142-12147, doi.org/10.1073/pnas.1812147115, 2018.

Zhao, B., Shrivastava, M., Donahue, N.M., Gordon, H., Schervish, M., Shilling, J.E., Zaveri, R.A., Wang, J., Andreae, M.O., Zhao, C. and Gaudet, B.: High concentration of ultrafine particles in the Amazon free troposphere produced by organic new particle formation. Proceedings of the National Academy of Sciences, 117, 25344-25351, https://doi.org/10.1073/pnas.2006716117, 2020.

Zhu, Z., Piao, S., Myneni, R.B., Huang, M., Zeng, Z., Canadell, J.G., Ciais, P., Sitch, S., Friedlingstein, P., Arneth, A. and Cao, C., 2016. Greening of the Earth and its drivers. Nature climate change, 6, 791-795, https://doi.org/10.1038/nclimate3004., 2016.

Zhu, J., Penner, J.E., Yu, F., Sillman, S., Andreae, M.O. and Coe, H.:. Decrease in radiative forcing by organic aerosol nucleation, climate, and land use change. Nature communications, 10, 1-7, https://doi.org/10.1038/s41467-019-08407-7,2019.

Appendix A

This appendix corresponds to Chapter 1.

A1 Relationship between CDNC and cloud albedo

The optical thickness, τ, can be described as a function of cloud thickness h, droplet effective radius, r_{eff}, and cloud droplet number concentration, N:

$$\tau = 2\pi h r_{eff}^2 N \quad \text{(A1)}$$

The liquid water content, LWC, can also be described:

$$LWC = \frac{4}{3}\pi r_{eff}^3 \rho_L h N \quad \text{(A2)}$$

Where ρ_L is the density of liquid water.

Rearranging A1 and A2 yields:

$$\tau = \frac{3}{2}\frac{LWC}{\rho_L r_{eff}} \quad \text{(A3)}$$

The optical thickness is related to the cloud albedo, A, in Eq. A4 (Hobbs., 1993):

$$A = \frac{\tau}{\tau + 6.7} \quad \text{(A4)}$$

Combining A3 and A4:

$$A = \frac{\frac{3}{2}\frac{LWC}{\rho_L r_{eff}}}{\frac{3}{2}\frac{LWC}{\rho_L r_{eff}} + 6.7} \quad \text{(A5)}$$

Rearranging A2 to express r_{eff} in terms of N (A6):

$$r_{eff} = \left(\frac{3LWC}{4\pi\rho_l h}\frac{1}{N}\right)^{\frac{1}{3}} = k\, N^{-\frac{1}{3}} \quad \text{(A6)}$$

Where $k = \left(\frac{3LWC}{4\pi\rho_l h}\right)^{\frac{1}{3}}$

Therefore, the albedo, A, can be expressed in terms of N for a given LWC.

$$A = \frac{\frac{3}{2}\frac{LWC}{\rho_L k}N^{\frac{1}{3}}}{\frac{3}{2}\frac{LWC}{\rho_L k}N^{\frac{1}{3}} + 6.7} = \frac{CDNC^{\frac{1}{3}}}{N^{\frac{1}{3}} + \frac{13.4}{3}\frac{\rho_l k}{LWC}}$$

$$A = \frac{N^{\frac{1}{3}}}{N^{\frac{1}{3}} + B} \quad \text{(A7)}$$

Where $B = \frac{13.4}{3}\frac{\rho_l k}{LWC} = \frac{13.4}{3}\frac{\rho_l}{LWC}\left(\frac{3LWC}{4\pi\rho_l h}\right)^{\frac{1}{3}}$ and is a constant for fixed LWC.

Eq A7 demonstrates that for a given LWC (i.e., fixed B), the cloud albedo will increase with droplet number concentration with a steeper increase at lower N.

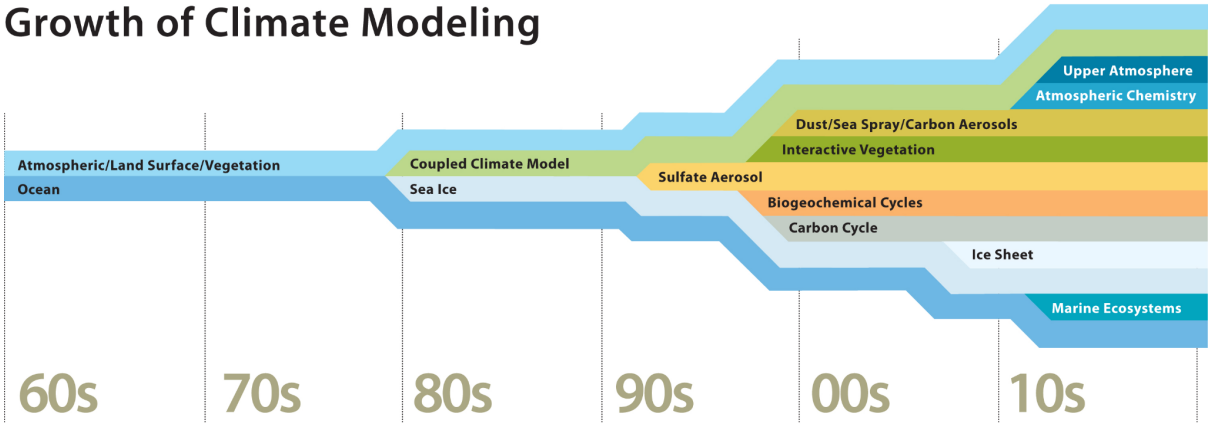


Figure A2. Schematic showing development of climate models over the last 60 years. Taken directly from NCAR [https://news.ucar.edu/sites/default/files/news/2011/predictFlow2.jpg, last accessed 21st October 2021]

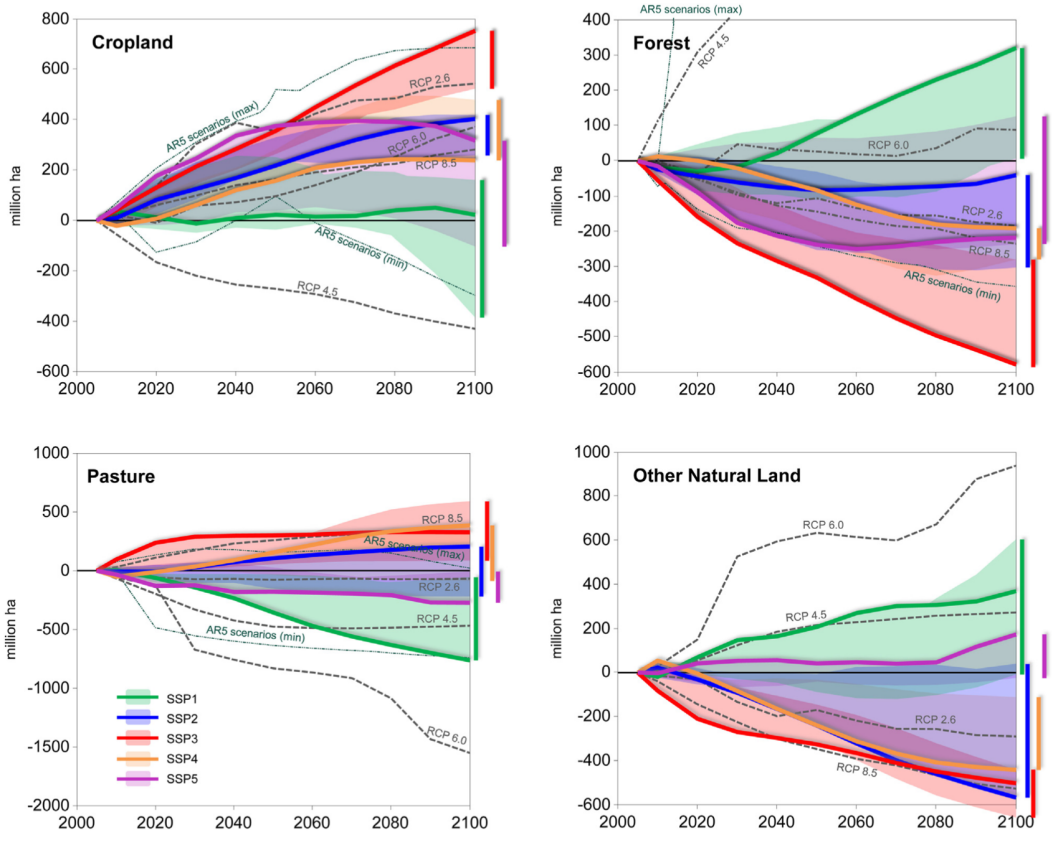


Figure A2. Evolution of cropland, pasture, forest and other natural land over the 21st Century relative to base year 2010. Taken directly from Riahi et al (2017).

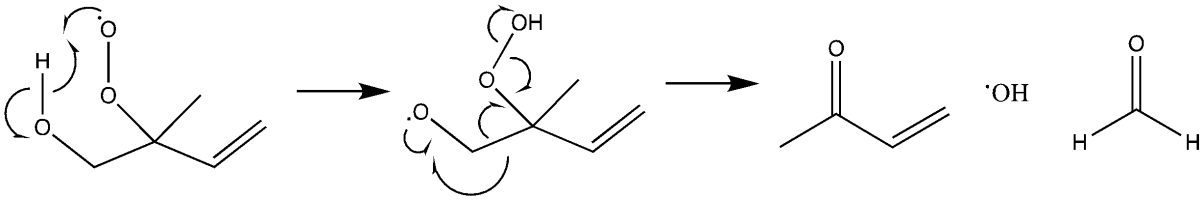


Figure A3. 1,5 H-shift of sequence β 1-OH, 2-OO ISOPOO. Adapted from Wennberg et al (2018).

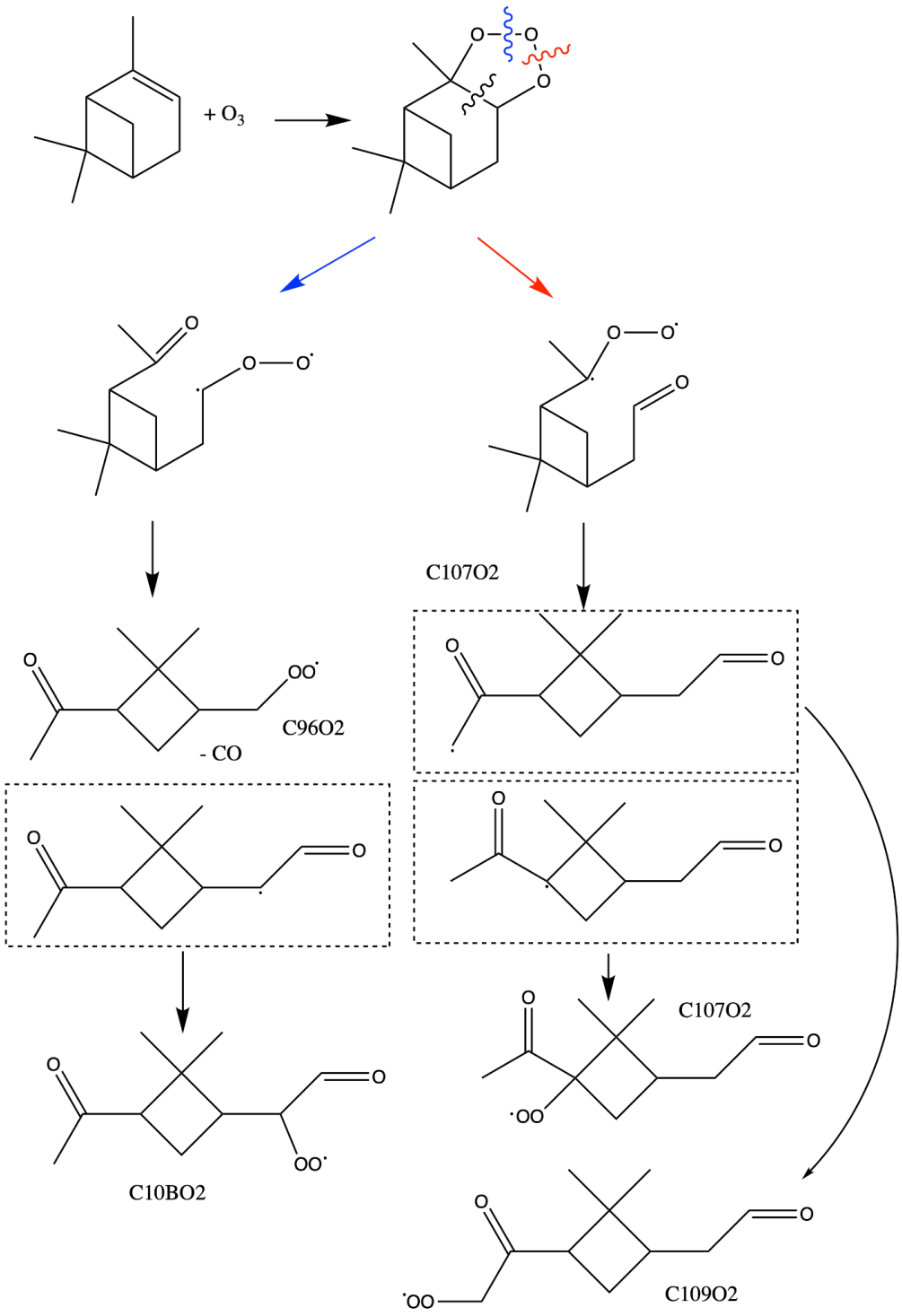


Figure A4. Production routes for peroxy radicals from alpha-pinene ozonolysis.

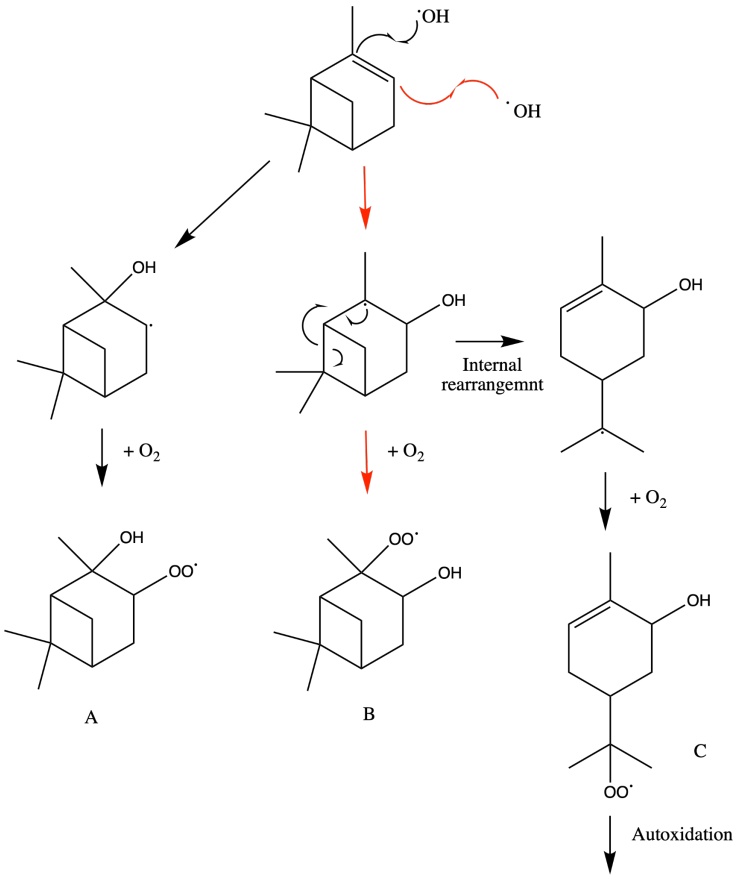


Figure A5. OH-initiated oxidation of α-pinene and subsequent formation of peroxy radicals. Adapted from Xu et al (2018).

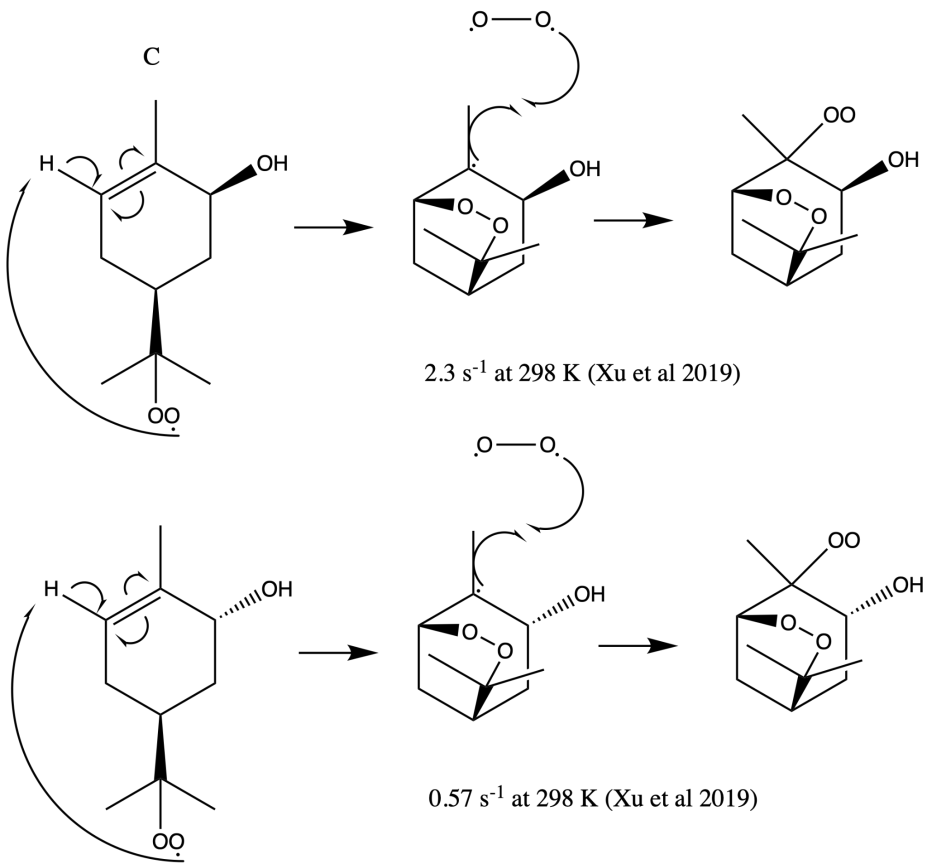


Figure A6. Autoxidation mechanism for isomer C (Fig A5)

Appendix B

This appendix corresponds to Chapter 2 and comprises the supplementary information to the published paper (GMD Weber et al., 2021) (Sections B1-B6) and additional section (B7) added for the thesis.

Supplementary Information: Improvements to the representation of BVOC chemistry-climate interactions in UKCA with the CRI-Strat 2 mechanism: Incorporation and Evaluation

Section B1

B1.1 Updates to CS to produce CS2

CRI-STRAT (CS) reactions are shown in black, CRI-STRAT 2 (CS2) reactions in red. Pairings show a direct swap while struck-through black reactions indicate CS reactions which were removed with no direct replacement. Red reactions without a black partner reaction are new reactions to the CS2. For termolecular reactions, complex rate constants are used and in these cases the low pressure limit (k_0), high pressure limit (k_1) and F_C value are specified.

Termolecular Reactions

O(3P) + NO = NO2: $k_0 = 9 \times 10^{-32}[M](T/300)^{-1.5}$, $k_1 = 3 \times 10^{-11}$ $F_C = 0.6$

O(3P) + NO = NO2: $k_0 = 1 \times 10^{-31}[M](T/300)^{-1.6}$, $k_1 = 5 \times 10^{-11}(T/300)^{-0.3}$ $F_C = 0.85$

O(3P) + NO2 = NO3: $k_0 = 9 \times 10^{-32}[M](T/300)^{-2}$, $k_1 = 2.2 \times 10^{-11}$ $F_C = 0.6$

O(3P) + NO2 = NO3: $k_0 = 1.30 \times 10^{-31}[M](T/300)^{-1.5}$, $k_1 = 2.30 \times 10^{-11}(T/300)^{0.24}$ $F_C = 0.6$

HO2 + NO2 = HO2NO2: $k_0 = 1.80 \times 10^{-31}[M](T/300)^{-3.2}$, $k_1 = 4.70 \times 10^{-12}$ $F_C = 0.6$

HO2 + NO2 = HO2NO2: $k_0 = 1.40 \times 10^{-31}[M](T/300)^{-3.1}$, $k_1 = 4.00 \times 10^{-12}$ $F_C = 0.4$

OH + NO = HONO: $k_0 = 7.40 \times 10^{-31}[M](T/300)^{-2.4}$, $k_1 = 3.30 \times 10^{-11}(T/300)^{-0.3}$ $F_C = e^{-T/1420}$

OH + NO = HONO: $k_0 = 7.40 \times 10^{-31}[M](T/300)^{-2.4}$, $k_1 = 3.30 \times 10^{-11}(T/300)^{-0.3}$ $F_C = 0.81$

OH + NO2 = HONO2: $k_0 = 2.60 \times 10^{-30}[M](T/300)^{-3.2}$, $k_1 = 2.40 \times 10^{-11}(T/300)^{-1.3}$ $F_C = 0.6$

OH + NO2 = HONO2: $k_0 = 3.20 \times 10^{-30}[M](T/300)^{-4.5}$, $k_1 = 3.00 \times 10^{-11}$ $F_C = 0.41$

MeCO3 + NO2 = PAN: $k_0 = 8.50 \times 10^{-29}[M](T/300)^{-6.50}$, $k_1 = 1.10 \times 10^{-11}(T/300)^{-1.0}$ $F_C = 0.60$

MeCO3 + NO2 = PAN: $k_0 = 3.28 \times 10^{-28}[M](T/300)^{-6.87}$, $k_1 = 1.125 \times 10^{-11}(T/300)^{-1.105}$ $F_C = 0.30$

EtCO3 + NO2 = PPAN: $k_0 = 8.50 \times 10^{-29}[M](T/300)^{-6.50}$, $k_1 = 1.10 \times 10^{-11}(T/300)^{-1.0}$ $F_C = 0.60$

EtCO3 + NO2 = PPAN: $k_0 = 3.28 \times 10^{-28}[M](T/300)^{-6.87}$, $k_1 = 1.125 \times 10^{-11}(T/300)^{-1.105}$ $F_C = 0.30$

NO2 + NO3 = N2O5: $k_0 = 2.20 \times 10^{-30}[M](T/300)^{-3.90}$, $k_1 = 1.50 \times 10^{-12}(T/300)^{-0.7}$ $F_C = 0.60$

NO2 + NO3 = N2O5 : $k_0 = 3.60 \times 10^{-30}[M](T/300)^{-4.10}$, $k_1 = 1.90 \times 10^{-12}(T/300)^{-0.2}$ $F_C = 0.35$

HOCH2CO3 + NO2 = PHAN : $k_0 = 8.50 \times 10^{-29}[M](T/300)^{-6.50}$, $k_1 = 1.10 \times 10^{-11}(T/300)^{-1.0}$ $F_C = 0.60$

HOCH2CO3 + NO2 = PHAN : $k_0 = 3.28 \times 10^{-28}[M](T/300)^{-6.87}$, $k_1 = 1.125 \times 10^{-11}(T/300)^{-1.105}$ $F_C = 0.30$

RTN26O2 + NO2 = RTN26PAN : $k_0 = 6.14 \times 10^{-29}[M](T/300)^{-6.87}$, $k_1 = 7.94 \times 10^{-12}(T/300)^{-1.0}$ $F_C = 0.60$
RTN26O2 + NO2 = RTN26PAN : $k_0 = 2.368 \times 10^{-28}[M](T/300)^{-6.50}$, $k_1 = 8.123 \times 10^{-11}(T/300)^{-1.105}$ $F_C = 0.30$

~~RU12O2 + NO2 = RU12PAN~~ : $k_0 = 5.19 \times 10^{-30}[M](T/300)^{-6.50}$, $k_1 = 6.71 \times 10^{-13}(T/300)^{-1.00}$ $F_C = 0.60$
~~RU12PAN = RU12O2 + NO2~~ : $k_0 = 1.10 \times 10^{-5}[M]e^{-10100/T}$, $k_1 = 1.90 \times 10^{17}e^{-14100/T}$ $F_C = 0.30$

RU12O2 = DHCARB9 + CO + OH : $k = 2.40 \times 10^{5}e^{-5300/T}$

MACO3 + NO2 = MPAN : $k_0 = 3.28 \times 10^{-28}[M](T/300)^{-6.87}$, $k_1 = 1.125 \times 10^{-11}(T/300)^{-1.105}$ $F_C = 0.60$

MPAN = RU10O2 + NO2 : $k_0 = 1.105 \times 10^{-5}[M]e^{-10100/T}$, $k_1 = 1.90 \times 10^{17}e^{-14100/T}$ $F_C = 0.30$
MPAN = MACO3 + NO2 : $k = 1.60 \times 10^{16}e^{-13500/T}$

RU14O2 = 0.5DHPR12O2 + 0.5 HPUCARB12 + 0.5 HO2 : $k = 2.76 \times 10^{7}e^{-6597/T}$*
RU14O2 = UCARB10 + OH + CO: $k = 1.24 \times 10^{11}e^{-9570/T}$
DHPR12O2 = DHPCARB9 + CO + OH: $k = 3.0 \times 10^{7}e^{-5300/T}$
RU10AO2 = CARB7 + CO + OH: $k = 3.0 \times 10^{7}e^{-5300/T}$

*This reaction, along with 4 bimolecular reactions, allows the $k_{bulk1,6H}$ rate constant to be represented in the framework of UKCA.

Photolysis Reactions

CARB3 + PHOTON = CO + CO + HO2 + HO2 : 9.46*jhchoa
CARB3 + PHOTON = CO + CO + HO2 + HO2 : Glyxla from Prather et al (2013)
CARB3 + PHOTON = CO + CO + H2 : Glyxlb from Prather et al (2013)
CARB3 + PHOTON = HCHO + HO2 : Glyxlc from Prather et al (2013)

~~TNCARB12 + PHOTON = RN9O2 + HOCH2CO3 : 5.47e-4*jno2~~
~~TNCARB11 + PHOTON = RTN10O2 + CO + HO2 : 0.015*jno2~~

UCARB12 + PHOTON = MeCO3 + HOCH2CHO + CO + HO2 : jhchoa
UCARB12 + PHOTON = MeCO3 + HOCH2CHO + CO + HO2 : 0.25*jhchoa
UCARB12 + PHOTON = RU12O2 + HO2 : 0.5*jmacr
UCARB12 + PHOTON = CARB7 + CO + CO + HO2 + HO2 : 0.25*jmacr

NUCARB12 + PHOTON = NOA + CO + CO + HO2 : jmacr
NUCARB12 + PHOTON = HUCARB9 + CO + NO2 : 0.6066*jno2

NRU12OOH + PHOTON = NOA + CO + HO2 + OH: jmhp
NRU12OOH + PHOTON = NOA + CARB3 + HO2 + OH: jmhp

RU14NO3 + PHOTON = UCARB10 + HCHO + HO2 + NO2 : jiprn
RU12NO3 + PHOTON = CARB6 + HOCH2CHO + HO2 + NO2 : 7.583e-3*jno2
RU10NO3 + PHOTON = MeCO3 + HOCH2CHO + NO2 : 1.213e-3*jno2

HPUCARB12 + PHOTON = HUCARB9 + CO + OH + OH : 91.65*jmacr
HPUCARB12 + PHOTON = CARB7 + CO + CO + HO2 + OH : 91.65*jmacr
HUCARB9 + PHOTON = CARB6 + CO + HO2 + OH : 91.65*jmacr

DHPR12OOH + PHOTON = DHPCARB9 + CO + OH + HO2 : jetcho
DHPR12OOH + PHOTON = CARB3 + RN8OOH + OH + OH : 3*jmhp

DHCARB9 + PHOTON = CARB7 + CO + HO2 + HO2 : jetcho

NUCARB12 + PHOTON = CARB7 + CO + CO + HO2 + NO2 : 6.066e-3*jno2

Bimolecular Reactions

A significant number of the RO_2 + NO and RO_2 + NO_3 reactions changed only in their rate constants (rate constant changes shown below) and these changes are not listed here. Where the reactions changed in the branching ratio and/or products, the reactions are shown.

CS: $k_{APNO} = 8.1 \times 10^{-12} e^{290/T}$
CRI v2.2 $k_{APNO} = 7.5 \times 10^{-12} e^{290/T}$

CS: $k_{RO2+NO} = 2.4 \times 10^{-12} e^{360/T}$
CRI v2.2 $k_{RO2+NO} = 2.7 \times 10^{-12} e^{360/T}$

CS: $k_{RO2+NO_3} = 2.5 \times 10^{-12}$
CRI v2.2 $k_{RO2+NO_3} = 2.3 \times 10^{-12}$

O(1D) + H2O = OH + OH : $k = 2.20 \times 10^{-10}$ cm^3 molecules^{-1} s^{-1}
O(1D) + H2O = OH + OH : $k = 2.14 \times 10^{-10}$ cm^3 molecules^{-1} s^{-1}

O(1D) + N2 = OH + OH : $k = 1.80 \times 10^{-10} e^{110/T}$ cm^3 molecules^{-1} s^{-1}
O(1D) + N2 = OH + OH : $k = 2.00 \times 10^{-11} e^{130/T}$ cm^3 molecules^{-1} s^{-1}

O(1D) + O2 = OH + OH : $k = 3.20 \times 10^{-11} e^{70/T}$ cm^3 molecules^{-1} s^{-1}
O(1D) + O2 = OH + OH : $k = 3.20 \times 10^{-11} e^{67/T}$ cm^3 molecules^{-1} s^{-1}

HO2 + NO = OH + NO2 : $k = 3.60 \times 10^{-12} e^{270/T}$
HO2 + NO = OH + NO2 : $k = 3.45 \times 10^{-12} e^{270/T}$

OH + HO2NO2 = H2O + NO2 + O2 : $k = 1.90 \times 10^{-12} e^{270/T}$
OH + HO2NO2 = H2O + NO2 + O2 : $k = 3.20 \times 10^{-13} e^{690/T}$

OH + PAN = HCHO + CO + NO2 : $k = 9.50 \times 10^{-13} e^{-650/T}$
OH + PAN = HCHO + CO + NO2 : $k = 3.40 \times 10^{-14}$

OH + MPAN = CARB7 + CO + NO2 : $k = 3.60 \times 10^{-12}$
OH + MPAN = CARB7 + CO + NO2 : $k = 6.38 \times 10^{-12}$

OH + MeONO2 = HCHO + NO2 + H2O: $k = 1.00 \times 10^{-14} e^{-1060/T}$
OH + MeONO2 = HCHO + NO2 + H2O: $k = 4.00 \times 10^{-13} e^{-845/T}$

MeOO + NO + O2 = HCHO + NO2 + HO2: $k = 3.00 \times 10^{-12} e^{-280/T}$
MeOO + NO + O2 = HCHO + NO2 + HO2: $k = 2.298 \times 10^{-12} e^{-360/T}$

MeOO + NO = MeONO2 : $k = 3.00 \times 10^{-15} e^{-280/T}$
MeOO + NO = MeONO2 : $k = 2.30 \times 10^{-15} e^{-360/T}$

MeOO + NO3 = HO2 + HCHO + NO2 : $k = 1.00 \times 10^{-12}$
MeOO + NO3 = HO2 + HCHO + NO2 : $k = 1.20 \times 10^{-12}$

NO3 + C5H8 = NRU14O2 : $k = 3.0 \times 10^{-12} e^{-466/T}$
NO3 + C5H8 = NRU14O2 : $k = 3.15 \times 10^{-12} e^{-450/T}$

O3 + C5H8 = UCARB10 + CO + HO2 + OH : $k = 2.12 \times 10^{-15} e^{-1913/T}$
O3 + C5H8 = UCARB10 + HCOOH : $k = 5.74 \times 10^{-15} e^{-1913/T}$
O3 + C5H8 = UCARB10 + CO + HO2 + OH : $k = 1.288 \times 10^{-15} e^{-1995/T}$
O3 + C5H8 = HCHO + MeOO + CO + HO2 : $k = 9.79 \times 10^{-16} e^{-1995/T}$
O3 + C5H8 = UCARB10 + HCOOH : $k = 1.80 \times 10^{-15} e^{-1995/T}$
O3 + C5H8 = UCARB10 + HCHO + H2O2 : $k = 3.97 \times 10^{-15} e^{-1995/T}$
O3 + C5H8 = MeCO3 + HCHO + CO + OH : $k = 1.29 \times 10^{-15} e^{-1995/T}$
O3 + C5H8 = UCARB10 + CO : $k = 9.785 \times 10^{-16} e^{-1995/T}$

OH + C5H8 = RU14O2 : $k = 2.54 \times 10^{-12} e^{410/T}$
OH + C5H8 = RU14O2 : $k = 2.70 \times 10^{-12} e^{390/T}$

OH + UCARB10 = RU10O2 : $k = 2.50 \times 10^{-11}$
OH + UCARB10 = RU10O2 : $k = 3.84 \times 10^{-12} e^{533/T}$

NO3 + UCARB10 = RU10O2 + HONO2 : $k = 1.44 \times 10^{-12} e^{-1862/T}$
NO3 + UCARB10 = RU10O2 + HONO2: $k = 5.98 \times 10^{-13} e^{-1862/T}$

O3 + UCARB10 = HCHO + MeCO3 + CO + OH : $k = 1.68 \times 10^{-18}$
O3 + UCARB10 = HCHO + MeCO3 + CO + OH : $k = 3.84 \times 10^{-16} e^{-1710/T}$

O3 + UCARB10 = HCHO + CARB6 + H2O2 : $k = 1.17 \times 10^{-18}$
O3 + UCARB10 = HCHO + CARB6 : $k = 8.16 \times 10^{-16} e^{-1710/T}$

OH + UCARB12 = RU10O2 : $k = 4.52 \times 10^{-11}$
OH + UCARB12 = RU10O2 : $k = 6.42 \times 10^{-11}$

NO3 + UCARB12 = RU10O2 : $k = 4.52 \times 10^{-11}$
NO3 + UCARB12 = RU10O2 : $k = 6.42 \times 10^{-11}$

O3 + UCARB12 = HOCH2CHO + MeCO3 + CO + OH : $k = 2.14 \times 10^{-17}$
O3 + UCARB12 = HOCH2CHO + MeCO3 + CARB3 + OH : $k = 6.00 \times 10^{-18}$

O3 + UCARB12 = HOCH2CHO + CARB6 + H2O2 : $k = 2.64 \times 10^{-18}$
O3 + UCARB12 = CARB6 + CO + OH + HO2 : $k = 1.20 \times 10^{-17}$

OH + RU14OOH = UCARB12 + OH: $k = 7.51 \times 10^{-11}$
OH + RU14OOH = 0.09UCARB12 + 0.94OH + 0.85IEPOX + 0.06RU14O2: $k = 7.14 \times 10^{-11}$

OH + RU12OOH = RU12O2 + H2O: $k = 3.00 \times 10^{-11}$
OH + RU12OOH = RU10OOH + CO + HO2: $k = 3.50 \times 10^{-11}$

OH + RU10OOH = RU10O2 + H2O: $k = 3.00 \times 10^{-11}$
OH + RU10OOH = CARB7 + CO + OH: $k = 3.84 \times 10^{-11}$

MPAN + OH = HMML + NO3: $k = 2.262 \times 10^{-11}$

RU10O2 + NO3 = CARB7 + HCHO + HO2 + NO2 : $k = 5.00 \times 10^{-13}$
RU10AO2 + NO3 = CARB7 + HCHO + HO2 + NO2 : $k = 2.30 \times 10^{-12}$

RU10O2 + RO2 = CARB7 + HCHO + HO2 : $k = 4.00 \times 10^{-13}$
RU10AO2 + RO2 = CARB7 + CO + HO2 : $k = 3.60 \times 10^{-13}$

RU10AO2 + NO = CARB7 + CO + HO2 : $k = 2.665 \times 10^{-12} e^{360/T}$

RU10AO2 + HO2 = RU10OOH + CO + HO2 : $k = 1.819 \times 10^{-13} e^{1300/T}$

OH + CARB3 = CO + OH : $k = 6.2 \times 10^{-13} e^{340/T}$

DHPR12O2 + NO = CARB3 + RN8OOH + OH + NO2 : $k = 2.70 \times 10^{-12} e^{360/T}$;
DHPR12O2 + NO3 = CARB3 + RN8OOH + OH + NO2 : $k = 2.30 \times 10^{-12}$;
DHPR12O2 + HO2 = DHPR12OOH : $k = 2.91 \times 10^{-13} e^{1300/T}$ *0.706 ;
DHPR12O2 + RO2 = CARB3 + RN8OOH + OH : $k = 7.60 \times 10^{-13}$;

OH + HUCARB9 = CARB6 + CO + HO2 : $k = 5.78 \times 10^{-11}$;

OH + DHCARB9 = CARB6 + HO2 : $k = 3.42 \times 10^{-11}$;

OH + DHPCARB9 = RN8OOH + CO + OH : $k = 3.64 \times 10^{-11}$

RU12O2 + NO = CARB7 + HOCH2CO3 + NO2 : $k = 4.59 \times 10^{-13} e^{360/T}$
RU12O2 + NO3 = CARB7 + HOCH2CO3 + NO2 : $k = 4.05 \times 10^{-13}$

OH + IEPOX = RU12O2 : $k = 1.16 \times 10^{-11}$

OH + HMML = CARB6 + OH : $k = 4.33 \times 10^{-12}$*0.7 ;
OH + HMML = HCOOH + CH3CO3 : $k = 4.33 \times 10^{-12}$*0.3 ;
OH + DHPR12OOH = DHPCARB9 + CO + OH : $k = 5.64 \times 10^{-11}$;

OH + RU12NO3 = CARB7 + CARB3 + NO2 : $k = 2.50 \times 10^{-12}$;
OH + RU10NO3 = CARB7 + CO + NO2 : $k = 5.26 \times 10^{-13}$;

RU10AO2 + NO = RU10NO3 : $k = 2.70 \times 10^{-12} e^{360/T}$ *0.013 ;
RU10AO2 + NO = CARB7 + CO + HO2 + NO2 : $k = 2.70 \times 10^{-12} e^{360/T}$ *0.987 ;
RU10AO2 + NO3 = CARB7 + CO + HO2 + NO2 : $k = 2.30 \times 10^{-12}$;
RU10AO2 + HO2 = RU10OOH : $k = 2.91 \times 10^{-13} e^{1300/T}$ *0.625 ;
RU10AO2 + RO2= CARB7 + CO + HO2 : $k = 3.60 \times 10^{-13}$

MACO3 + NO = CH3O2 + CO + HCHO + HO2 + NO2 : $k = 7.50 \times 10^{-12} e^{290/T}$ *0.65 ;
MACO3 + NO = CH3CO3 + HCHO + HO2 + NO2 : $k = 7.50 \times 10^{-12} e^{290/T}$ *0.35 ;
MACO3 + NO3 = CH3O2 + CO + HCHO + HO2 + NO2 : $k = 2.30 \times 10^{-12}$*1.74*0.65 ;
MACO3 + NO3 = CH3CO3 + HCHO + HO2 + NO2 : $k = 2.30 \times 10^{-12}$*1.74*0.35 ;
MACO3 + HO2 = RU10OOH : $k = 5.20 \times 10^{-13} e^{980/T}$ *0.56 ;
MACO3 + HO2 = CH3O2 + CO + HCHO + OH : $k = 5.20 \times 10^{-13} e^{980/T}$ *0.44 ;

OH + HPUCARB12 = HUCARB9 + CO + OH : $k = 5.20 \times 10^{-11}$;
O3 + HPUCARB12 = CARB3 + CARB6 + OH + OH : $k = 2.4 \times 10^{-17}$;
NO3 + HPUCARB12 = HUCARB9 + CO + OH + HNO3 : $k = 1.44 \times 10^{-12} e^{-1862/T}$ * 4.25 ;

NRU12O2 + NO = NOA + CARB3 + HO2 + NO2 : $k = 1.35 \times 10^{-12} e^{360/T}$
NRU12O2 + NO3 = NO3 + CARB3 + HO2 + NO2 : $k = 1.15 \times 10^{-12}$;
NRU12O2 + RO2 = NOA + CARB3 + HO2 + NO2 : $k = 4.80 \times 10^{-13}$;
RU12O2 + RO2 = CARB7 + HOCH2CO3 : $k = 7.392 \times 10^{-14}$
HOCH2CO3 + HO2 = HCHO + HO2 + OH : $k = 2.288 \times 10^{-13} e^{980/T}$

RU14NO3 + OH = RU12NO3 + HO2 : $k = 5.40 \times 10^{-12}$
RU14NO3 + OH = RU10NO3 + HCHO + HO2 : $k = 1.44 \times 10^{-11}$

*RU14O2 + NO = 0.5HPUCARB12 + 0.5HO2 + 0.5DHPR12O2 + NO : $k = 1.399 \times 10^{-15} e^{1668/T}$
*RU14O2 + NO3 = 0.5HPUCARB12 + 0.5HO2 + 0.5DHPR12O2 + NO3: $k = 1.191 \times 10^{-15} e^{1308/T}$
*RU14O2 + HO2 = 0.5HPUCARB12 + 0.5HO2 + 0.5DHPR12O2 + HO2 : $k = 1.064 \times 10^{-15} e^{2608/T}$
*RU14O2 + RO2 = 0.5HPUCARB12 + 0.5HO2 + 0.5DHPR12O2 + RO2 : $k = 6.527 \times 10^{-16} e^{1308/T}$

*These reactions, when combined with the unimolecular reaction RU14O2 = 0.5HPUCARB12 + 0.5HO2 + 0.5DHPR12O2, represents the $k_{bulk1,6H}$ rate constant in the framework of UKCA.
EtOO + NO + O2 = MeCHO + HO2 + NO2: $k = 2.58 \times 10^{-12} e^{365/T}$
EtOO + NO = RU10NO3 + HCHO + HO2 : $k = 2.53 \times 10^{-12} e^{380/T}$

EtCO3 + HO2 = EtCO3H + O2: $k = 4.40 \times 10^{-13} e^{980/T}$
EtCO3 + HO2 = 0.56EtCO3H + 0.44EtOO +0.44OH+ O2: $k = 5.20 \times 10^{-13} e^{980/T}$

EtOO + HO2 = EtOOH + O2: $k = 7.50 \times 10^{-13} e^{700/T}$
EtOO + HO2 = EtOOH + O2: $k = 4.30 \times 10^{-13} e^{870/T}$

MeCO3 + HO2 = MeCO3H : $k = 4.31 \times 10^{-13} e^{1040/T}$

MeCO3 + HO2 = 0.56MeCO3H + 0.44MeOO + 0.44OH : $k = 5.2 \times 10^{-13} e^{980/T}$

NO + HO2 = NO2 + OH : $k = 3.60 \times 10^{-12} e^{270/T}$
NO + HO2 = NO2 + OH : $k = 3.45 \times 10^{-12} e^{270/T}$

MeOO + NO + O2 = HCHO + HO2 + NO2 : $k = 3.00 \times 10^{-12} e^{280/T}$
MeOO + NO + O2 = HCHO + HO2 + NO2 : $k = 2.298 \times 10^{-13} e^{360/T}$

MeOO + NO = MeONO2 : $k = 3.00 \times 10^{-15} e^{280/T}$
MeOO + NO = MeONO2 : $k = 2.30 \times 10^{-15} e^{360/T}$

MeOO + NO3 = HO2 + HCHO + NO2 : $k = 1.00 \times 10^{-12}$
MeOO + NO3 = HO2 + HCHO + NO2 : $k = 1.20 \times 10^{-12}$

HCHO + NO3 + O2 = HONO2 + HO2 + CO : $k = 5.80 \times 10^{-16}$
HCHO + NO3 + O2 = HONO2 + HO2 + CO : $k = 5.50 \times 10^{-16}$

MeCHO + NO3 + O2 = HONO2 + HO2 + CO : $k = 1.44 \times 10^{-12} e^{-1862/T}$
MeCHO + NO3 + O2 = HONO2 + HO2 + CO : $k = 1.40 \times 10^{-12} e^{-1860/T}$

EtCHO + OH = H2O + EtCO3 : $k = 1.96 \times 10^{-11}$
EtCHO + OH = H2O + EtCO3 : $k = 4.90 \times 10^{-12}$

MeCHO + OH = H2O + MeCO3 : $k = 5.55 \times 10^{-12} e^{311/T}$
MeCHO + OH = H2O + MeCO3 : $k = 4.70 \times 10^{-12} e^{345/T}$

MeOOH + OH = H2O + HCHO + OH : $k = 1.02 \times 10^{-12} e^{190/T}$
MeOOH + OH = H2O + HCHO + OH : $k = 2.12 \times 10^{-12} e^{190/T}$

O3 + C2H4 = H2O + HCHO + OH : $k = 1.19 \times 10^{-15} e^{-2580/T}$
O3 + C2H4 = H2O + HCHO + OH : $k = 1.18 \times 10^{-15} e^{-2850/T}$
O3 + C2H4 = HCHO + HCOOH : $k = 7.95 \times 10^{-15} e^{-2580/T}$
O3 + C2H4 = HCHO + HCOOH : $k = 7.91 \times 10^{-15} e^{-2850/T}$

NO3 + C2H4 = NRN6O2 : $k = 2.10 \times 10^{-16}$
NO3 + C2H4 = NRN9O2: $k = 3.30 \times 10^{-12} e^{-2880/T}$

OH + TOLUENE + O2 = AROH17 + HO2 : $k = 3.26 \times 10^{-13} e^{338/T}$
OH + TOLUENE + O2 = AROH17 + HO2 : $k = 3.24 \times 10^{-12} e^{340/T}$

OH + TOLUENE + O2 = RA16O2 : $k = 1.48 \times 10^{-12} e^{338/T}$
OH + TOLUENE + O2 = RA16O2 : $k = 1.48 \times 10^{-12} e^{340/T}$

NO3 + APINENE + O2= NRTN28O2 : $k = 1.19 \times 10^{-12} e^{490/T}$
NO3 + APINENE + O2= NRTN28O2 : $k = 1.20 \times 10^{-12} e^{490/T}$

O3 + APINENE + O2= OH + Me2CO + RN18AO2 : $k = 8.08 \times 10^{-16} e^{-732/T}$

O3 + APINENE + O2= OH + Me2CO + RN18AO2 : $k = 6.44 \times 10^{-16} e^{-644/T}$

O3 + APINENE = TNCARB26 + H2O2 : $k = 7.57 \times 10^{-17} e^{-732/T}$
O3 + APINENE = TNCARB26 + H2O2 : $k = 1.41 \times 10^{-16} e^{-644/T}$

O3 + APINENE = RCOOH25 : $k = 1.26 \times 10^{-16} e^{-732/T}$
O3 + APINENE = RCOOH25 : $k = 2.01 \times 10^{-17} e^{-644/T}$

O3 + BPINENE = RTX24O2 + OH : $k = 5.25 \times 10^{-18}$
O3 + BPINENE = RTX24O2 + OH : $k = 4.73 \times 10^{-16} e^{-1270/T}$

O3 + BPINENE = HCHO + TXCARB24 + H2O2 : $k = 3.00 \times 10^{-18}$
O3 + BPINENE = HCHO + TXCARB24 + H2O2 : $k = 2.70 \times 10^{-16} e^{-1270/T}$

O3 + BPINENE = HCHO + TXCARB22 : $k = 3.75 \times 10^{-18}$
O3 + BPINENE = HCHO + TXCARB22 : $k = 3.38 \times 10^{-16} e^{-1270/T}$

O3 + BPINENE = CO + TXCARB24 : $k = 3.00 \times 10^{-18}$
O3 + BPINENE = CO + TXCARB24 : $k = 2.70 \times 10^{-16} e^{-1270/T}$

OH + BENZENE + O2= RA13O2 : $k = 1.10 \times 10^{-12} e^{-193/T}$
OH + BENZENE+ O2 = RA13O2 : $k = 1.08 \times 10^{-12} e^{-190/T}$

OH + BENZENE + O2= AROH14 + HO2 : $k = 1.23 \times 10^{-12} e^{-193/T}$
OH + BENZENE + O2= AROH14 + HO2: $k = 1.22 \times 10^{-12} e^{-190/T}$

OH + n-PrOH = EtCHO + HO2 : $k = 2.71 \times 10^{-12}$
OH + n-PrOH = EtCHO + HO2: $k = 2.27 \times 10^{-12} e^{70/T}$

OH + n-PrOH = RN9O2 : $k = 2.82 \times 10^{-12}$
OH + n-PrOH = RN9O2 : $k = 2.33 \times 10^{-12} e^{70/T}$

RU10O2 + NO3 = CARB7 + HCHO + HO2 + NO2 : $k = 5.00 \times 10^{-13}$
RU10AO2 + NO3 = CARB7 + HO2 + CO + NO2 : $k = 2.30 \times 10^{-13}$

HOCH2CO3 + HO2 = HOCH2CO3H : $k = 4.30 \times 10^{-13} e^{1040/T}$
HOCH2CO3 + HO2 = HOCH2CO3H : $k = 2.912 \times 10^{-13} e^{980/T}$

NRU14O2 + HO2 = NRU14OOH : $k = 2.24 \times 10^{-13} e^{1300/T}$
NRU14O2 + HO2 = NRU14OOH : $k = 2.05 \times 10^{-13} e^{1300/T}$

NRU12O2 + HO2 = NRU12OOH : $k = 1.82 \times 10^{-13} e^{1300/T}$
NRU12O2 + HO2 = NRU12OOH : $k = 2.05 \times 10^{-13} e^{1300/T}$

RTN26O2 + HO2 = RTN26OOH : $k = 2.66 \times 10^{-13} e^{1300/T}$
RTN26O2 + HO2 = 0.56RTN26OOH + 0.44RTN25O2 + 0.44OH : $k = 5.20 \times 10^{-13} e^{980/T}$

CH3O2 + RO2 + O2 = HCHO + HO2 : $k = 6.01 \times 10^{-14} e^{416/T}$
CH3O2 + RO2 + O2 = HCHO : $k = 6.01 \times 10^{-14} e^{416/T}$
CH3O2 + RO2 + O2 = MeOH : $k = 6.01 \times 10^{-14} e^{416/T}$

$k_{CH3O2} = 1.03 \times 10^{-13} e^{365/T}$
CH3O2 + RO2 = HCHO + HO2 : $2*k_{CH3O2}*7.18*e^{-885/T}$
CH3O2 + RO2 = HCHO : $2*k_{CH3O2}*0.5*(1-7.18*e^{-885/T})$
CH3O2 + RO2 = CH3OH : $2*k_{CH3O2}*0.5*(1-7.18*e^{-885/T})$;

RU14O2 + HO2 = RU14OOH + O2 : $k = 2.24 \times 10^{-13} e^{1300/T}$
RU14O2 + HO2 = RU14OOH + O2: $k = 2.05 \times 10^{-13} e^{1300/T}$

RU14O2 + RO2 = UCARB12 + HO2 : $k = 4.31 \times 10^{-13}$
RU14O2 + RO2 = UCARB12 + HO2 : $k = 1.26 \times 10^{-13}$

RU14O2 + RO2 = UCARB10 + HCHO + HO2 : $k = 1.28 \times 10^{-12}$
RU14O2 + RO2 = UCARB10 + HCHO + HO2 : $k = 1.13 \times 10^{-12}$

RU12O2 + RO2 = MeCO3 + HOCH2CHO : $k = 1.40 \times 10^{-12}$
RU12O2 + RO2 = MeCO3 + HOCH2CHO : $k = 1.772 \times 10^{-13}$

RU12O2 + RO2 = HO2 + CARB7 + CARB3 : $k = 6.00 \times 10^{-13}$
RU12O2 + RO2 = HO2 + CARB7 + CARB3 : $k = 1.668 \times 10^{-13}$

RU10O2 + RO2 = MeCO3 + HOCH2CHO : $k = 1.00 \times 10^{-12}$
RU10O2 + RO2 = MeCO3 + HOCH2CHO : $k = 1.28 \times 10^{-13}$

RU10O2 + RO2 = CARB6 + HCHO + HO2 : $k = 6.00 \times 10^{-13}$
RU10O2 + RO2 = CARB6 + HCHO + HO2 : $k = 5.49 \times 10^{-13}$

RU10O2 + RO2 = CARB7 + CO + HO2 : $k = 4.00 \times 10^{-13}$
RU10AO2 + RO2 = CARB7 + CO + HO2 : $k = 3.60 \times 10^{-13}$

NRU12O2 + RO2 = NOA + CO + HO2 : $k = 9.60 \times 10^{-13}$
NRU12O2 + RO2 = NOA + CO + HO2 : $k = 4.80 \times 10^{-13}$

RTN26O2 + RO2 = RTN25O2 : $k = 2.00 \times 10^{-12}$
RTN26O2 + RO2 = RTN25O2 : $k = 1.00 \times 10^{-11}$

RTN26O2 + RO2 = RTN25O2 : $k = 2.00 \times 10^{-12}$
RTN26O2 + RO2 = RTN25O2 : $k = 1.00 \times 10^{-11}$

OH + CARB3 + O2 = CO + CO + HO2 : $k = 1.14 \times 10^{-11}$
OH + CARB3 + O2 = CO + CO + HO2 : $k = 2.48 \times 10^{-12}$

OH + CARB6 + O2 = MeCO3 + CO : $k = 1.72 \times 10^{-11}$
OH + CARB6 + O2 = CO + CO + HO2 : $k = 1.90 \times 10^{-12} e^{575/T}$

OH + NOA = CARB6 + NO2 : $k = 1.30 \times 10^{-13}$

OH + NOA = CARB6 + NO2 : $k = 6.70 \times 10^{-13}$

OH + RU14NO3 = UCARB12 + NO2 : $k = 5.55 \times 10^{-11}$
OH + RU14NO3 = UCARB12 + NO2 : $k = 1.02 \times 10^{-11}$

OH + RN8OOH = CARB6 + OH : $k = 4.42 \times 10^{-12}$
OH + RN8OOH = CARB6 + OH : $k = 1.02 \times 10^{-11}$

RTN23O2 + NO = RTN23NO3 : $k = 2.83 \times 10^{-13} e^{360/T}$
RU12O2 + NO = RN12NO3 : $k = 9.45 \times 10^{-14} e^{360/T}$

~~RTN23O2 + OH = Me2CO + TNCARB12 + NO2 : $k = 5.37 \times 10^{-12}$~~
~~TNCARB12 + OH = TNCARB11 + HO2 : $k = 3.22 \times 10^{-12}$~~
~~TNCARB11 + OH = RTN10O2 + HO2 : $k = 1.33 \times 10^{-11}$~~
~~TNCARB11 + NO3 = RTN10O2 + CO + HONO2 : $k = 7.92 \times 10^{-12} e^{-1862/T}$~~

Wet Deposition Parameters

Table B1 - New or updated wet deposition parameters. Text/figures in parentheses show values used in CRI-STRAT (Archer-Nicholls et al., 2021)

Species	Surrogate	Reference	k(298K)	$-\Delta H/R$
HOC2H4OOH	HOC2H4OOH (EtOOH)	Schwantes et al (2020)	1.9e6 (3.4e2)	6.01e3 (5.70e3)
CARB7	Hydroxyacetone (Hydroxyacetone)	Schwantes et al (2020)	1.46e3 (1.4e2)	6.01e3 (5.70e3)
CARB10	Hydroxyacetone (Hydroxyacetone)	Schwantes et al (2020)	1.46e3 (1.4e2)	6.01e3 (5.70e3)
CARB13	Hydroxyacetone (Hydroxyacetone)	Schwantes et al (2020)	1.46e3 (1.4e2)	6.01e3 (5.70e3)
CARB16	Hydroxyacetone (Hydroxyacetone)	Schwantes et al (2020)	1.46e3 (1.4e2)	6.01e3 (5.70e3)
CARB3	Glyoxal (Methylglyoxal)	Schwantes et al (2020)	4.19e5 (3.5e3)	7.48e3 (7.2e3)
RA13NO3	RU14NO3 (no wet dep before)	Schwantes et al (2020)	8.34e3 (N/A)	6.01e3 (N/A)
RA16NO3	RU14NO3 (no wet dep before)	Schwantes et al (2020)	8.34e3 (N/A)	6.01e3 (N/A)
RA19NO3	RU14NO3 (no wet dep before)	Schwantes et al (2020)	8.34e3 (N/A)	6.01e3 (N/A)
RN8OOH	Hydroperoxy acetone (EtOOH)	Schwantes et al (2020)	1.16e4 (3.4e2)	6.01e3 (5.70e3)
RN11OOH	Hydroperoxy acetone (EtOOH)	Schwantes et al (2020)	1.16e4 (3.4e2)	6.01e3 (5.70e3)

RN14OOH	Hydroperoxy acetone (EtOOH)	Schwantes et al (2020)	1.16e4 (3.4e2)	6.01e3 (5.70e3)
RN17OOH	Hydroperoxy acetone (EtOOH)	Schwantes et al (2020)	1.16e4 (3.4e2)	6.01e3 (5.70e3)
RU14OOH	RU14OOH (EtOOH)	Schwantes et al (2020)	3.5e6 (3.4e2)	6.01e3 (5.70e3)
RU12OOH	MVKOOH (EtOOH)	Schwantes et al (2020)	1.24e6 (3.4e2)	6.01e3 (5.70e3)
RU10OOH	MVKOOH (EtOOH)	Schwantes et al (2020)	1.24e6 (3.4e2)	6.01e3 (5.70e3)
NRU14OOH	ISOPNOOH (EtOOH)	Schwantes et al (2020)	8.75e4 (3.4e2)	6.01e3 (5.70e3)
NRU12OOH	MVKN (EtOOH)	Schwantes et al (2020)	1.84e5 (3.4e2)	6.01e3 (5.70e3)
RN9OOH	HOC3H7OOH (EtOOH)	Schwantes et al (2020)	1.5e6 (3.4e2)	6.01e3 (5.70e3)
RA13OOH	BENZOOH (EtOOH)	Schwantes et al (2020)	2.3e3 (3.4e2)	6.01e3 (5.70e3)
RA16OOH	BENZOOH (EtOOH)	Schwantes et al (2020)	2.3e3 (3.4e2)	6.01e3 (5.70e3)
RA19OOH	BENZOOH (EtOOH)	Schwantes et al (2020)	2.3e3 (3.4e2)	6.01e3 (5.70e3)
RTN28OOH	Hydroperoxy acetone (EtOOH)	Schwantes et al (2020)	1.16e4 (3.4e2)	6.01e3 (5.70e3)
RTN26OOH	Hydroperoxy acetone (EtOOH)	Schwantes et al (2020)	1.16e4 (3.4e2)	6.01e3 (5.70e3)
RTN25OOH	Hydroperoxy acetone (EtOOH)	Schwantes et al (2020)	1.16e4 (3.4e2)	6.01e3 (5.70e3)
RTN14OOH	Hydroperoxy acetone (EtOOH)	Schwantes et al (2020)	1.16e4 (3.4e2)	6.01e3 (5.70e3)
RTX28OOH	Hydroperoxy acetone (EtOOH)	Schwantes et al (2020)	1.16e4 (3.4e2)	6.01e3 (5.70e3)
RTX24OOH	Hydroperoxy acetone (EtOOH)	Schwantes et al (2020)	1.16e5 (3.4e2)	6.01e3 (5.70e3)
RTX28OOH	Hydroperoxy acetone (EtOOH)	Schwantes et al (2020)	1.16e4 (3.4e2)	6.01e3 (5.70e3)

RTN26PAN	TERPA2PAN (no wet dep before)	Schwantes et al (2020)	9.59e3 (N/A)	6.01e3 (N/A)
RTN23NO3	Beta Isoprene hydroxy nitrate (no wet dep before)	Schwantes et al (2020)	8.34e3 (N/A)	6.01e3 (N/A)
RN9NO3	HONITR (no wet dep before)	Schwantes et al (2020)	2.64e3 (N/A)	6.01e3 (N/A)
RN12NO3	HONITR (no wet dep before)	Schwantes et al (2020)	2.64e3 (N/A)	6.01e3 (N/A)
RN15NO3	HONITR (no wet dep before)	Schwantes et al (2020)	2.64e3 (N/A)	6.01e3 (N/A)
RN18NO3	HONITR (no wet dep before)	Schwantes et al (2020)	2.64e3 (N/A)	6.01e3 (N/A)
RU14NO3	Beta Isoprene hydroxy nitrate (no wet dep before)	Schwantes et al (2020)	8.34e3 (N/A)	6.01e3 (N/A)
RTN28NO3	Beta Isoprene hydroxy nitrate (no wet dep before)	Schwantes et al (2020)	8.34e3 (N/A)	6.01e3 (N/A)
RTN25NO3	Beta Isoprene hydroxy nitrate (no wet dep before)	Schwantes et al (2020)	8.34e3 (N/A)	6.01e3 (N/A)
RTX28NO3	Beta Isoprene hydroxy nitrate (no wet dep before)	Schwantes et al (2020)	8.34e3 (N/A)	6.01e3 (N/A)
RTX22NO3	Beta Isoprene hydroxy nitrate (no wet dep before)	Schwantes et al (2020)	8.34e3 (N/A)	6.01e3 (N/A)
AROH14	Phenol (MeOH)	Schwantes et al (2020)	2.84e3 (2.3e2)	2.70e3 (4.9e3)
ARNOH14	Nitrophenol (MeOH)	Guo and Brimblecombe (2007)	8.5e1 (2.3e2)	6.27e3 (4.9e3)
AROH17	Phenol (MeOH)	Schwantes et al (2020)	5.67e2 (2.3e2)	5.80e3 (4.9e3)
ARNOH17	Nitrophenol (MeOH)	Guo and Brimblecombe (2007)	8.5e1 (2.3e2)	6.27e3 (4.9e3)
IEPOX	IEPOX (new species)	Schwantes et al (2020)	3.0e7 (N/A)	6.01e3 (N/A)
HMML	HMML (new species)	Schwantes et al (2020)	2.3e5 (N/A)	6.01e3 (N/A)
HUCARB9	Unsaturated	Schwantes et al	1.1e5 (N/A)	6.00e3 (N/A)

	hydroxy carbonyl (new species)	(2020)		
HPUCARB12	HPALD (new species)	Schwantes et al (2020)	2.3e5 (N/A)	6.01e3 (N/A)
DHPCARB9	DHPMPAL (new species)	Schwantes et al (2020)	9.37e7 (N/A)	6.01e3 (N/A)
DHPR12OOH	DHPMPAL (new species)	Schwantes et al (2020)	9.37e7 (N/A)	6.01e3 (N/A)
DHCARB9	Hydroxy acetone (new species)	Schwantes et al (2020)	1.46e3 (N/A)	4.9e3 (N/A)
RU12NO3	MVKN (new species)	Schwantes et al (2020)	1.84e5 (N/A)	6.00e3 (N/A)
RU1NO3	MVKN (new species)	Schwantes et al (2020)	1.84e5 (N/A)	6.00e3 (N/A)

Table B2 - Emitted species and their sources. All biogenic emissions are 2011-201 MEGAN-MACC climatologies and oceanic emissions are POET 1990 emissions.

Species	Source(s)
SO_2	Natural, anthropogenic (surface and high)
DMS	Natural, biomass burning
C_2H_4	Anthropogenic, biomass burning, biogenic, oceanic
C_2H_6	Anthropogenic, biomass burning, biogenic, oceanic
C_3H_6	Anthropogenic, biomass burning, biogenic, oceanic
C_3H_8	Anthropogenic, biomass burning, biogenic, oceanic
C_4H_{10}	Anthropogenic, biomass burning, biogenic, oceanic
C_5H_8	Biomass burning, biogenic
CO	Anthropogenic, biomass burning, biogenic, oceanic
EtCHO (propionaldehyde)	Anthropogenic, biomass burning, biogenic
EtOH	Anthropogenic, biomass burning, biogenic
HCHO	Anthropogenic, biomass burning, biogenic
HCOOH (methanoic acid)	Anthropogenic, biomass burning, biogenic
MEK (methyl ethyl ketone)	Anthropogenic, biomass burning, biogenic
Me_2CO (acetone)	Anthropogenic, biomass burning, biogenic
MeCHO (acetaldehyde)	Anthropogenic, biomass burning, biogenic

$MeCO_2H$ (ethanoic acid)	Anthropogenic, biomass burning, biogenic
MeOH (methanol)	Anthropogenic, biomass burning, biogenic
TBUT2ENE (trans but-2-ene)	Anthropogenic, biomass burning, biogenic
Toluene	Anthropogenic, biomass burning, biogenic
NO	Anthropogenic, biomass burning, biogenic, soil
NH_3	Anthropogenic, biomass burning, biogenic, oceanic
Alpha pinene	Biomass burning, biogenic
Beta pinene	Biomass burning, biogenic
Black Carbon	Biofuel, biomass burning (surface and high), fossil fuels
Benzene	Biomass burning, anthropogenic
C_2H_2	Biomass burning, anthropogenic
CH_4^*	Biomass burning
$HOCH_2CHO$	Biomass burning
Organic carbon	Biofuel, biomass burning (surface and high), fossil fuels
Toluene	Biogenic, anthropogenic, biomass burning
Oxylene	Anthropogenic, biomass burning

* Lower boundary condition imposed in model

For the observation-model comparisons, the CS and CS2 runs used anthropogenic timeseries emissions for all runs up to and including 2014 and 2014 timeslice emissions for the runs in 2016 due to a current lack of post-2014 emissions for CRI. All emissions were based on the CMIP6 CEDS inventories (Hosely et al. 2018). The ST runs used timeseries anthropogenic emissions based on the CMIP6 CEDS inventories for all runs up to 2014 and then time series emissions based on SSP370 for runs in 2016.

Section B2 Sensitivity Test Changes

CRI v2.2 reactions are shown in red, the changes made for each sensitivity test are shown in black. For termolecular reactions, complex rate constants are used and in these cases the low pressure limit (k_0), high pressure limit (k_1) and F_C value are specified.

CRI_v2_2_o1d

O(1D) + H2O = OH + OH : $k = 2.14 \times 10^{-10}$ cm^3 $molecules^{-1}$ s^{-1}

O(1D) + H2O = OH + OH : $k = 2.20 \times 10^{-10} cm^3$ $molecules^{-1}$ s^{-1}

O(1D) + N2 = OH + OH : $k = 2.00 \times 10^{-11} e^{130/T}$ cm^3 molecules^{-1} s^{-1}
O(1D) + N2 = OH + OH : $k = 1.80 \times 10^{-10} e^{110/T}$ cm^3 molecules^{-1} s^{-1}

O(1D) + O2 = OH + OH : $k = 3.20 \times 10^{-11} e^{67/T}$ cm^3 molecules^{-1} s^{-1}
O(1D) + O2 = OH + OH : $k = 3.20 \times 10^{-11} e^{70/T}$ cm^3 molecules^{-1} s^{-1}

CRI_v2_2_inorgN

O(3P) + NO = NO2: $k_0 = 1 \times 10^{-31}[M](T/300)^{-1.6}$, $k_1 = 5 \times 10^{-11}(T/300)^{-0.3}$ $F_C = 0.85$
O(3P) + NO = NO2: $k_0 = 9 \times 10^{-32}[M](T/300)^{-1.5}$, $k_1 = 3 \times 10^{-11}$ $F_C = 0.6$

O(3P) + NO2 = NO3: $k_0 = 1.30 \times 10^{-31}[M](T/300)^{-1.5}$, $k_1 = 2.30 \times 10^{-11}(T/300)^{0.24}$ $F_C = 0.6$
O(3P) + NO2 = NO3: $k_0 = 9 \times 10^{-32}[M](T/300)^{-2}$, $k_1 = 2.2 \times 10^{-11}$ $F_C = 0.6$

HO2 + NO2 = HO2NO2: $k_0 = 1.40 \times 10^{-31}[M](T/300)^{-3.1}$, $k_1 = 4.00 \times 10^{-12}$ $F_C = 0.4$
HO2 + NO2 = HO2NO2: $k_0 = 1.80 \times 10^{-31}[M](T/300)^{-3.2}$, $k_1 = 4.70 \times 10^{-12}$ $F_C = 0.6$

OH + NO = HONO: $k_0 = 7.40 \times 10^{-31}[M](T/300)^{-2.4}$, $k_1 = 3.30 \times 10^{-11}(T/300)^{-0.3}$ $F_C = 0.81$
OH + NO = HONO: $k_0 = 7.40 \times 10^{-31}[M](T/300)^{-2.4}$, $k_1 = 3.30 \times 10^{-11}(T/300)^{-0.3}$ $F_C = e^{-T/1420}$

OH + NO2 = HONO2: $k_0 = 3.20 \times 10^{-30}[M](T/300)^{-4.5}$, $k_1 = 3.00 \times 10^{-11}$ $F_C = 0.41$
OH + NO2 = HONO2: $k_0 = 2.60 \times 10^{-30}[M](T/300)^{-3.2}$, $k_1 = 2.40 \times 10^{-11}(T/300)^{-1.3}$ $F_C = 0.6$

MeCO3 + NO2 = PAN: $k_0 = 3.28 \times 10^{-28}[M](T/300)^{-6.87}$, $k_1 = 1.125 \times 10^{-11}(T/300)^{-1.105}$ $F_C = 0.30$
MeCO3 + NO2 = PAN: $k_0 = 8.50 \times 10^{-29}[M](T/300)^{-6.50}$, $k_1 = 1.10 \times 10^{-11}(T/300)^{-1.0}$ $F_C = 0.60$

EtCO3 + NO2 = PPAN: $k_0 = 3.28 \times 10^{-28}[M](T/300)^{-6.87}$, $k_1 = 1.125 \times 10^{-11}(T/300)^{-1.105}$ $F_C = 0.30$
EtCO3 + NO2 = PPAN: $k_0 = 8.50 \times 10^{-29}[M](T/300)^{-6.50}$, $k_1 = 1.10 \times 10^{-11}(T/300)^{-1.0}$ $F_C = 0.60$

NO2 + NO3 = N2O5 : $k_0 = 3.60 \times 10^{-30}[M](T/300)^{-4.10}$, $k_1 = 1.90 \times 10^{-12}(T/300)^{-0.2}$ $F_C = 0.35$
NO2 + NO3 = N2O5: $k_0 = 2.20 \times 10^{-30}[M](T/300)^{-3.90}$, $k_1 = 1.50 \times 10^{-12}(T/300)^{-0.7}$ $F_C = 0.60$

HOCH2CO3 + NO2 = PHAN : $k_0 = 3.28 \times 10^{-28}[M](T/300)^{-6.87}$, $k_1 = 1.125 \times 10^{-11}(T/300)^{-1.105}$ $F_C = 0.30$
HOCH2CO3 + NO2 = PHAN : $k_0 = 8.50 \times 10^{-29}[M](T/300)^{-6.50}$, $k_1 = 1.10 \times 10^{-11}(T/300)^{-1.0}$ $F_C = 0.60$

RTN26O2 + NO2 = RTN26PAN : $k_0 = 2.368 \times 10^{-28}[M](T/300)^{-6.50}$, $k_1 = 8.123 \times 10^{-11}(T/300)^{-1.105}$ $F_C = 0.30$
RTN26O2 + NO2 = RTN26PAN : $k_0 = 6.14 \times 10^{-29}[M](T/300)^{-6.87}$, $k_1 = 7.94 \times 10^{-12}(T/300)^{-1.0}$ $F_C = 0.60$

Note that RU12PAN, which exists in CS but not in CS2, was not added back into the mechanism for this test. In addition, the formation of MPAN, which involves RU10O2+NO2 in CS but MACO3+NO2 in CS2, was kept as MACO3+NO2 but the CS value of KFPAN was used. These changes are unlikely to have a significant impact since PAN dominated the total concentration of all PAN-type species.

MACO3 + NO2 = MPAN : $k_0 = 3.28 \times 10^{-28}[M](T/300)^{-6.87}$, $k_1 = 1.125 \times 10^{-11}(T/300)^{-1.105}$ $F_C = 0.30$
MACO3 + NO2 = MPAN : $k_0 = 8.50 \times 10^{-29}[M](T/300)^{-6.50}$, $k_1 = 1.10 \times 10^{-11}(T/300)^{-1.0}$ $F_C = 0.60$

HO2 + NO = OH + NO2 : $k = 3.45 \times 10^{-12}\ e^{270/T}$
HO2 + NO = OH + NO2 : $k = 3.60 \times 10^{-12}\ e^{270/T}$

OH + HO2NO2 = H2O + NO2 + O2 :$k = 3.20 \times 10^{-13}\ e^{690/T}$
OH + HO2NO2 = H2O + NO2 + O2 :$k = 1.90 \times 10^{-12}\ e^{270/T}$

OH + PAN = HCHO + CO + NO2 : $k = 3.40 \times 10^{-14}$
OH + PAN = HCHO + CO + NO2 : $k = 9.50 \times 10^{-13} e^{-650/T}$

OH + MPAN = CARB7 + CO + NO2 : $k = 6.38 \times 10^{-12}$
OH + MPAN = CARB7 + CO + NO2 : $k = 3.60 \times 10^{-12}$

OH + MeONO2 = HCHO + NO2 + H2O: $k = 4.00 \times 10^{-13} e^{-845/T}$
OH + MeONO2 = HCHO + NO2 + H2O: $k = 1.00 \times 10^{-14} e^{-1060/T}$

MeOO + NO = HCHO + NO2 + HO2: $k = 2.298 \times 10^{-12} e^{-360/T}$
MeOO + NO = HCHO + NO2 + HO2: $k = 3.00 \times 10^{-12} e^{-280/T}$

MeOO + NO = MeONO2 : $k = 2.30 \times 10^{-15} e^{-360/T}$
MeOO + NO = MeONO2 : $k = 3.00 \times 10^{-15} e^{-280/T}$

MeOO + NO3 = HO2 + HCHO + NO2 : $k = 1.20 \times 10^{-12}$
MeOO + NO = HO2 + HCHO + NO2 : $k = 1.00 \times 10^{-12}$

CRI_v2_2_isoprene

In this branch, changes were made to the isoprene oxidation scheme to bring it as close as was practicable to that used in CRI-STRAT. The major changes were the removal of the isomerisation reactions of the isoprene peroxy radical, RU14O2, and the updated oxidation pathway of the species UCARB10 which represents the major isoprene oxidation products methacrolein (MACR) and methyl vinyl ketone (MVK).

In this branch RU14O2 only underwent reactions with HO2, NO, NO3 and RO2. This meant the production of 10 of the 12 new CRI v2.2 species (IEPOX, HMML, HPUCARB12, HUCARB9, DHPR12OOH, DHPCARB9, DHCARB9, MACO3, DHPR12O2 and RU10AO2) and their subsequent reactions, which are key in the HOx-recycling process, were removed from the mechanism. Note that the production of two new organonitrate species, RU12NO3 and RU10NO3, and their subsequent reaction

were maintained as these had much less to do with the HOx-recycling feature under examination. It should also be noted that where there was a difference between the rate constants in CS and CS2 for a given reaction (e.g. changes in the RO2+NO and RO2+NO3 rate constants), the rate constant from CRI v2.2 was used to minimise the other drivers for difference that was observed between this branch and the full CRI v2.2 branch.

In addition, all isoprene oxidation reactions with OH, O3 and NO3 were reverted to those in CS.

NO3 + C5H8 = NRU14O2 : $k = 3.15 \times 10^{-12} e^{-450/T}$
NO3 + C5H8 = NRU14O2 : $k = 3.0 \times 10^{-12} e^{-466/T}$

O3 + C5H8 = UCARB10 + CO + HO2 + OH : $k = 1.288 \times 10^{-15} e^{-1995/T}$
O3 + C5H8 = HCHO + MeOO + CO + HO2 : $k = 9.79 \times 10^{-16} e^{-1995/T}$
O3 + C5H8 = UCARB10 + HCOOH : $k = 1.80 \times 10^{-15} e^{-1995/T}$
O3 + C5H8 = UCARB10 + HCHO + H2O2 : $k = 3.97 \times 10^{-15} e^{-1995/T}$
O3 + C5H8 = MeCO3 + HCHO + CO + OH : $k = 1.29 \times 10^{-15} e^{-1995/T}$
O3 + C5H8 = UCARB10 + CO : $k = 9.785 \times 10^{-16} e^{-1995/T}$
O3 + C5H8 = UCARB10 + CO + HO2 + OH : $k = 2.12 \times 10^{-15} e^{-1913/T}$
O3 + C5H8 = UCARB10 + HCOOH : $k = 5.74 \times 10^{-15} e^{-1913/T}$

OH + C5H8 = RU14O2 : $k = 2.70 \times 10^{-12} e^{390/T}$
OH + C5H8 = RU14O2 : $k = 2.54 \times 10^{-12} e^{410/T}$

OH + UCARB10 = RU10O2 : $k = 3.84 \times 10^{-12} e^{533/T}$
OH + UCARB10 = RU10O2 : $k = 2.50 \times 10^{-11}$

NO3 + UCARB10 = RU10O2 + HONO2: $k = 5.98 \times 10^{-13} e^{-1862/T}$
NO3 + UCARB10 = RU10O2 + HONO2 : $k = 1.44 \times 10^{-12} e^{-1862/T}$

O3 + UCARB10 = HCHO + MeCO3 + CO + OH : $k = 3.84 \times 10^{-16} e^{-1710/T}$
O3 + UCARB10 = HCHO + MeCO3 + CO + OH : $k = 1.68 \times 10^{-18}$

O3 + UCARB10 = HCHO + CARB6 : $k = 8.16 \times 10^{-16} e^{-1710/T}$
O3 + UCARB10 = HCHO + CARB6 + H2O2 : $k = 1.17 \times 10^{-18}$

OH + UCARB12 = RU10O2 : $k = 6.42 \times 10^{-11}$
OH + UCARB12 = RU10O2 : $k = 4.52 \times 10^{-11}$

NO3 + UCARB12 = RU10O2 : $k = 6.42 \times 10^{-11}$
NO3 + UCARB12 = RU10O2 : $k = 4.52 \times 10^{-11}$

O3 + UCARB12 = HOCH2CHO + MeCO3 + CARB3 + OH : $k = 6.00 \times 10^{-18}$
O3 + UCARB12 = HOCH2CHO + MeCO3 + CO + OH : $k = 2.14 \times 10^{-17}$

O3 + UCARB12 = CARB6 + CO + OH + HO2 : $k = 1.20 \times 10^{-17}$
O3 + UCARB12 = HOCH2CHO + CARB6 + H2O2 : $k = 2.64 \times 10^{-18}$

UCARB12 = MeCO3 + HOCH2CHO + CO + HO2:0.25 $*$ $jmacr$
UCARB12 = MeCO3 + HOCH2CHO + CO + HO2: $jmacr$

UCARB12 = RU12O2 + HO2:0.5 $*$ $jmacr$
No replacement

UCARB12 = RU12O2 + CARB7 + CO :0.25 $*$ $jmacr$
No replacement

NRU12OOH = NOA + CARB3 + HO2 + OH: $jhmp$
NRU12OOH = NOA + CO + HO2 + OH : $jhmp$

NUCARB12 = HUCARB9 + CO + NO2 + OH: $jmacr$
NUCARB12 = NOA + 2*CO + 2*HO2 : $jmacr$

NUCARB12 = CARB7 + CO + HO2 + NO2:8 $*$ $jnoa$
No replacement

All reactions of HUCARB9, HPUCARB12, DHCARB9, DHPCARB9, RU10AO2, MACO3, DHPR12O2, DHPR12OOH and IEPOX and HMML were removed. Reactions which produced these species reverted to their CS equivalents.

OH + RU14OOH = 0.09UCARB12 + 0.94OH + 0.85IEPOX + 0.06RU14O2: $k = 7.14 \times 10^{-11}$
OH + RU14OOH = UCARB12 + OH: $k = 7.51 \times 10^{-11}$

OH + RU12OOH = RU10OOH + CO + HO2: $k = 3.50 \times 10^{-11}$
OH + RU12OOH = RU12O2: $k = 3.00 \times 10^{-11}$

OH + RU10OOH = CARB7 + CO + OH: $k = 3.84 \times 10^{-11}$
OH + RU10OOH = RU10O2: $k = 3.00 \times 10^{-11}$

MPAN + OH = HMML + NO3: $k = 2.262 \times 10^{-11}$
No replacement

MPAN = MACO3 + NO2: $k = 1.60 \times 10^{16} e^{-13500/T}$
MPAN = RU10O2 + NO2: $k_0 = 1.10 \times 10^{-5} e^{-10100/T}$, $k_1 = 1.90 \times 10^{17} e^{-14100/T}$ $F_C = 0.30$

MACO3 + NO2 = MPAN : $k_0 = 3.28 \times 10^{-28}[M](T/300)^{-6.87}$, $k_1 = 1.125 \times 10^{-11}(T/300)^{-1.105}$ $F_C = 0.30$
MACO3 + NO2 = MPAN : $k_0 = 8.50 \times 10^{-29}[M](T/300)^{-6.50}$, $k_1 = 1.10 \times 10^{-11}(T/300)^{-1.0}$ $F_C = 0.60$

RU14O2 = UCARB10 + HCHO + OH
No replacement

RU14O2 = 0.5 HPUCARB12 + 0.5 HO2 + 0.5 DHPR12O2
No replacement

RU10AO2 + NO3 = CARB7 + HCHO + HO2 + NO2 : $k = 2.30 \times 10^{-12}$
RU10O2 + NO3 = CARB7 + HCHO + HO2 + NO2 : $k = 5.00 \times 10^{-13}$

RU10AO2 + RO2 = CARB7 + CO + HO2 : $k = 3.60 \times 10^{-13}$
RU10O2 + RO2 = CARB7 + HCHO + HO2 : $k = 4.00 \times 10^{-13}$

RU12O2/RU10O2 - aside from changes from RU10AO2 to RU10O2, no other changes made

CRI_v2_2_RO2_N

The only change made to the mechanism for this test was reversion of the rate constants of RO2 with NO and NO3. Where branching ratios had changed between CS and CS2, the CRI v2.2 were maintained with rate constants scaled accordingly. The red rate constants below were changed to those in black:

kRO2NO: $k = 2.70 \times 10^{-12} e^{360/T}$
kRO2NO: $k = 2.40 \times 10^{-12} e^{360/T}$

kRO2NO3: $k = 2.30 \times 10^{-12}$
kRO2NO:3 $k = 2.50 \times 10^{-12}$

Five acyl peroxy species in CRI featured a different RO2 + NO rate constant, kAPNO, which decreased by 7.5% in CRI v2.2.

kAPNO: $k = 7.50 \times 10^{-12} e^{290/T}$
kAPNO:3 $k = 8.10 \times 10^{-12} e^{290/T}$

Section B3 iBVOC and Megan-MACC Emissions

The difference between two possible BVOC emissions approaches, the iBVOC approach and the non-interactive MEGAN-MACC emission approach, was considered. Globally, the annual average non-interactive isoprene emissions were 5.9% higher (576.9 Tg yr^{-1} vs. 545.0 Tg yr^{-1}) while MT emissions were 29% lower (97.5 Tg yr^{-1} v. 137.3 Tg yr^{-1}, cf 95±3 Tg yr^{-1} Sindelarova et al., 2014) (Fig. S1). Emissions at three of the surface observational sites, ATTO, Z2F and Borneo, were also compared with a specific focus on the months where model-observational comparisons were performed. At the ATTO and Z2F sites monthly MEGAN-MACC isoprene emissions were lower than iBVOC emissions (~ 40% for the months considered). Non-interactive MT emissions at the ATTO sites were also lower than iBVOC emissions (35% Feb and 25% Sept) but slightly higher in June for the Z2F site. In Borneo, MEGAN-MACC isoprene and MT emissions were ~25% and ~15% lower than iBVOC over the April-July period respectively.

A spatial comparison of the emission approaches was also performed (Fig. S2). Annually averaged, iBVOC exhibited greater isoprene emissions in the northern part of South America but lower emissions at more southern latitudes as well as general southern migration of isoprene emissions in Africa. Isoprene emissions in

Australia were significantly lower. These differences were more pronounced in the June-July-August (JJA) period while in the December-January-February (DJF) period iBVOC also exhibited increased emissions over China and South East Asia and the northern hemisphere boreal forests but lower emissions over the South East USA. For monoterpenes, iBVOC simulated greater JJA emissions in the boreal forest, South East USA and South East Asia and greater DJF emissions in much of South America.



Figure B1. Global emissions of (a) isoprene and (b) MT from the non-interactive MEGAN-MACC (MM) dataset and iBVOC (shading shows standard deviations in iBVOC emissions over period 2005-2013). Emissions per unit area for isoprene and MT at the ATTO (c, d), Bannan (e, f) and Borneo (g, h) observational sites. Black dots indicate months when model-observational comparisons were performed at the corresponding site.

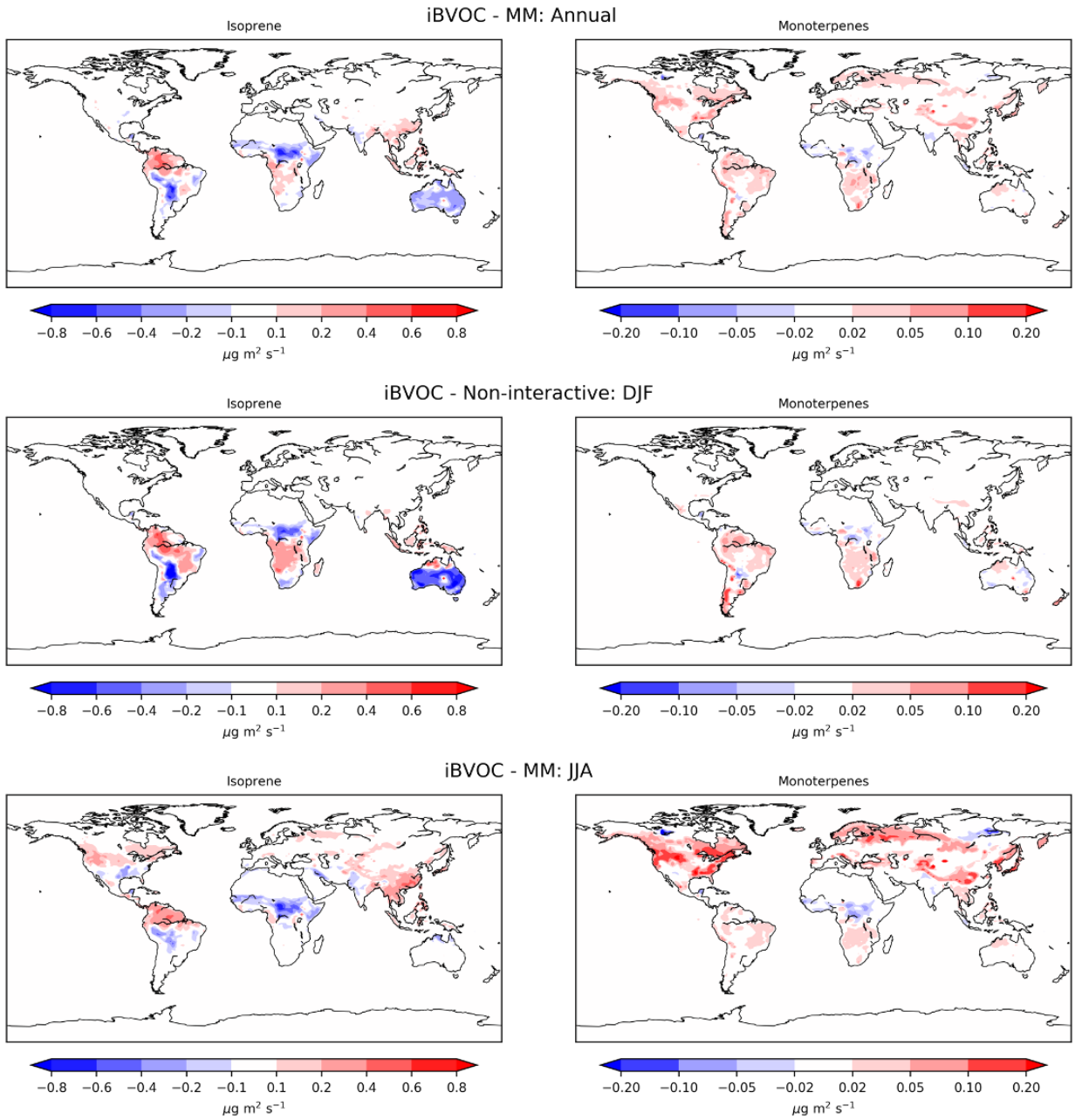


Figure B2. Difference in emissions between the iBVOC and MEGAN-MACC 2001-2010 climatologies (MM) emission approaches for isoprene and monoterpenes. Annual average (top panels), DJF average (middle panels) and JJA average (lower panels).

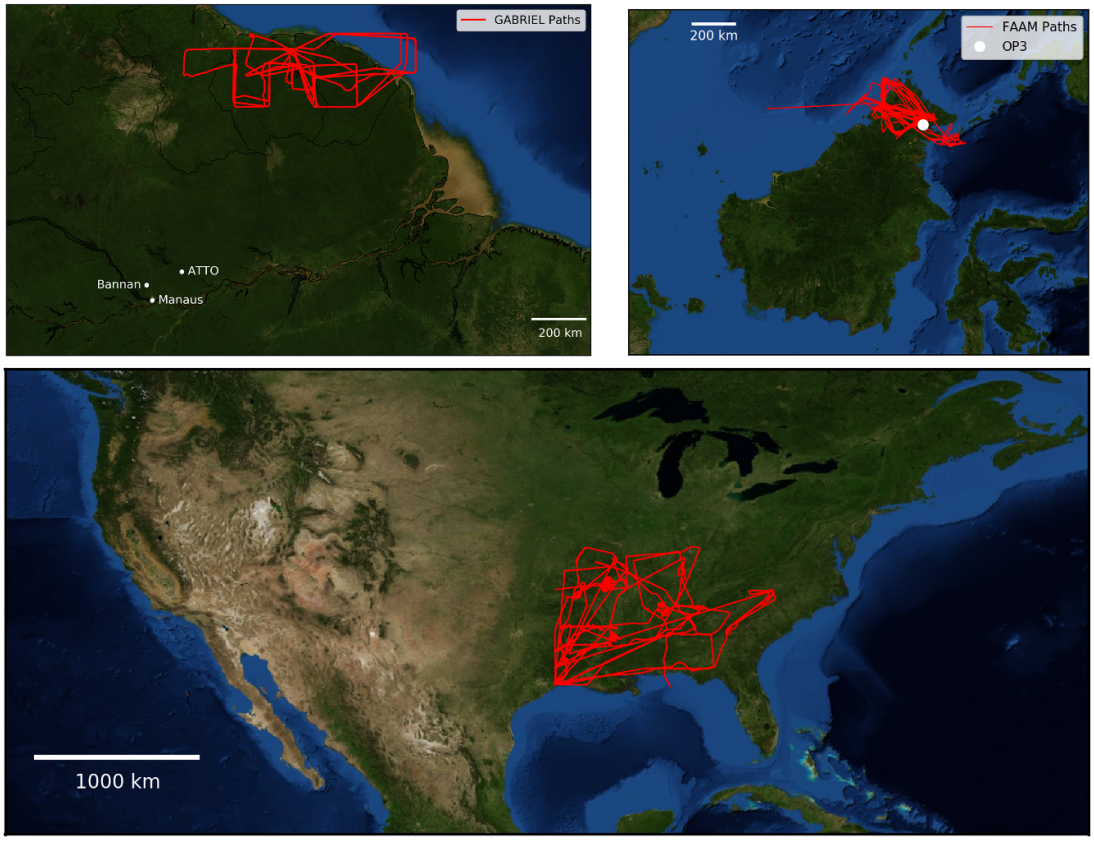


Figure B3. Location of the two in-situ Amazon observation sites (Bannan and ATTO), city of Manuas and GABRIEL aircraft campaign paths (upper left), OP3 observation tower and FAAM aircraft campaign flights over Borneo (upper right) and SEAC^{4}RS flight campaign over the South East USA (lower). Map Sources: Esri, DigitalGlobe, GeoEye, i-cubed, USDA FSA, USGS, AEX, Getmapping, Aerogrid, IGN, IGP, swisstopo, and the GIS User Community

Table B3. Additional information regarding observational data

Dataset	**Notes**
SEAC^{4}RS	All data points below limit of detection set to zero
GABRIEL	Estimated LODs: Isoprene 0.1 ppb, MVK 0.09 ppb, Acetone 0.09 ppb Non-zero data points below the LOD were not removed.
FAAM	Estimated LOD: Isoprene 0.1 ppb Data marked as low quality was ignored
Borneo	Data marked as low quality was ignored
ATTO	Monoterpene LOD: 0.05 ppb (Sept 2013) 0.06 ppb (March 2014) Isoprene LOD: 0.09 ppb (Feb 2013), 0.1 ppb (Sept 2013) Acetone LOD: 0.03 ppb (Feb 2013), 0.05 ppb (Sept 2013) Isoprene oxidation products LOD: 0.13 ppb (Feb 2013), 0.07 ppb (Sept 2013) LOD estimated as 2σ of the background average. Non-zero data points below the LOD were not removed.

Section B4 Overview of field Brazil ZF2 measurements

Note that this section was written by Tom Bannan (University of Manchester) as stated in the author contributions section of Weber et al (2021) and in Chapter 2.

A suite of online measurement techniques was deployed in Central Amazonia, at the ZF2 site located 61 km north upwind of Manaus (60°11'W, 2°5'S) in June and July 2016. This is a site that at the transition between wet and dry seasons that is mostly influenced by natural biogenic emissions, with virtually no biomass burning and no anthropogenic pollution at the time of experiment. A high-resolution TOF-CIMS using iodide-adduct ionization was coupled to an Aerodyne Research Incorporated FIGAERO (Lee et al., 2014, Lopez-Hilfiker et al., 2015, Bannan et al., 2019), and was utilized for the semi-simultaneous measurement of a range of oxygenated species in the gas and particle phase. An Aerodyne ACSM (Aerosol Chemical Speciation Monitor) monitored the bulk submicron organic and inorganic aerosol composition and a PTR-MS (proton transfer reaction mass spectrometer) was used to measure isoprene and a subset of isoprene oxidation products. Routine measurements including NO_x, SO_2 and O_3 and key meteorological conditions were also made. Further details of all aspects of the field measurements are given in the sections that follow.

TOF-CIMS technique

Configuration and operating technique

The gas-phase measurements of the Manchester time-of-flight chemical ionization mass spectrometer (TOF-CIMS) instrument have been described in detail previously (Priestley *et al*, 2015) but the specific setup and operation procedures used in the present work is described herein. The instrument comprises an Aerodyne FIGAERO inlet attached to a reduced pressure ion molecule reaction (IMR) region in front of a Tofwerk atmospheric pressure interface high resolution time-of-flight mass spectrometer (Lopez-Hilfiker et al., 2015) together these facilitate simultaneous gas and particle phase measurements. In the present work, a Tofwerk X-Ray ionization source was used in place of the Po-210 source normally used with iodine CIMS. The instrument performance was tracked daily by monitoring the baseline, single ion signal measurements, m/z calibrations, regular gas-phase calibrations and high-frequency filter and gas-phase background measurements.

The Aerodyne FIGAERO is a two-port inlet with the first dedicated to gas sampling (PFA Teflon tubing, 20 SLM measured flow rate) and the second to aerosol sampling (stainless steel inlet,10 SLM measured flow rate). The sampling lines were situated at an altitude just above the canopy to avoid sampling being compromised by trees or structures. Recently, Liu *et al. (2016)* discussed in detail the effect of inlets on species quantification - the inlets used in the present work were chosen due to the limitations of the measurement site.

The FIGAERO couples both inlets with the chemical ionization region of the mass spectrometer and operates in two modes: (A) ambient air sampling for trace gas analysis using CIMS and simultaneous particle collection on a PFTE filter via a separate inlet, and, (B) thermal desorption of the collected particles in nitrogen, allowing detection of the desorbed vapors via CIMS.

The IMR was held at a constant pressure by a scroll pump (Agilent SH-112), regulated with a servo control valve placed between the scroll pump and IMR. The ionizing reagent, I-, was generated via X-ray ionization of CH_3I. 10 sccm of N_2 was flowed over a methyl iodide (CH_3I) permeation tube (held at 40°C) and the resultant CH_3I-entrained N_2 carried by a 2 SLM N_2 flow through the X-ray ionizer into the IMR, orthogonally to the sample flow. The ionizer and ambient air flows were allowed to mix, such that trace chemical species within the ambient air sample were ionized by I-, generating iodine adducts. The resultant flow was sampled via a critical orifice into the first of four differentially pumped chambers in the TOF-CIMS. The first chamber was held at a set pressure (1.6 mbar) by a scroll pump (Triscroll 600) and the subsequent chambers were pumped by a split flow turbo molecular drag pump. Quadrupole ion guides transmitted the ions through these chambers while simultaneously providing additional collisional cooling and energetic homogenization of the ions as they entered the extractor region. The electric fields were set to optimize the total ion signal and transmission of the iodide adducts.

CIMS Calibrations and background measurements

Mass calibration was performed using 5 known masses (I^-, $I^-.H_2O$, $I^-.HCOOH$, I_2^- and I_3^-) that cover a range of m/z 127 to 380. The mass calibration was fitted by a 3rd order polynomial and was accurate to within 1 ppm, ensuring peak identification for all species was accurate below 1 ppm. The Tofware-specific FIGAERO-CIMS analysis software (version 3.1) was utilized to attain high-resolution 1Hz time series of all of the species identified here, in both the gas- and particle-phases. Further analysis was done using software developed in-house.

Gas-phase background measurements were made once every 30 minutes for 30 seconds by overflowing the IMR just above the pinhole with wetted high-purity nitrogen. Data was background-subtracted using an interpolation of the two background measurements recorded either-side of data collection. An example of the data processing for an arbitrary mass is shown in Figure B4.

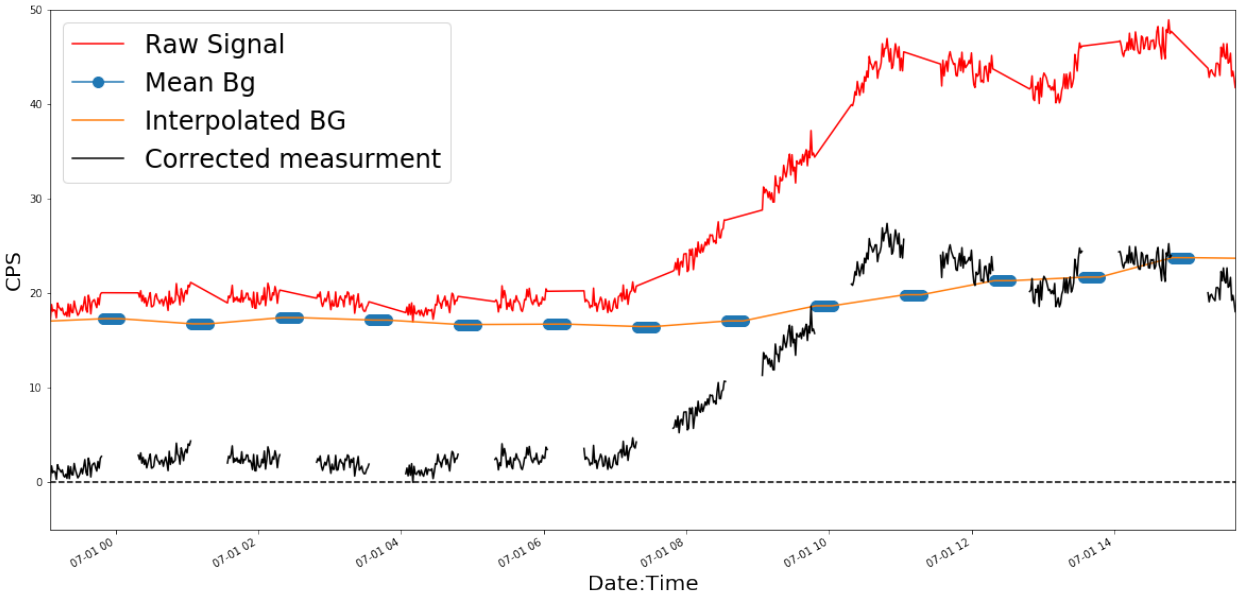


Fig. B4 Retrieval of background-corrected data from raw data for a subset of the measurement campaign for an arbitrary mass. The background counts obtained during the background period (blue dots) are interpolated to yield the interpolated background data (orange line). This is subtracted from the raw signal (red line) to obtain the corrected measurement (black line). All data are in units of counts per second (CPS).

Background filter measurements comprised a ramp, soak and cool cycle matching that of the ambient air sampling method. Each background measurement was applied to the thermogram measurements made until the next background filter measurement was recorded. In the event of a break in FIGAERO-CIMS measurements (i.e., due to temporary failure or power shortages), a new filter was placed into the instrument. The new filter was cleaned by ramping the temperature to 200°C for a duration of 20 mins and subsequently cooled, with a complete cycle immediately after. Where there was no break in the measurements for ~2 days, the cleaning process was undertaken for the existing installed filter. Detailed analysis during the measurements was undertaken to ensure that all of the collected material was being volatilized during normal operation.

Offline calibrations after the field work campaign were performed specific to the isoprene oxidation species that were observed at the ZF2 site. 2-Methyltetrols, 2-methylglyceric acid, and IEPOX were synthesized by the University of North Carolina, Department of Environmental Sciences & Engineering according to procedures outline in Bondy et al. (2018), Budisulistiorini et al. (2015), and Zhang et al. (2012), respectively. These standards were dissolved in acetone at known concentrations and using a micro-syringe were deposited on the FIGAERO filter and thermally desorbed using a known continuous flow of nitrogen over the filter. This was performed following the methodology devised in Lee et al. (2014). The measured sensitivities for $C_5H_{10}O_3$, $C_4H_8O_4$, $C_5H_{12}O_4$ varied by a maximum of 25% from each other with the mean sensitivity of the 3 isoprene oxidation standards being only 8% higher than that of acetic acid. The mean sensitivity of the 3 isoprene oxidation standards in the gas and particle phase is therefore applied to the full data set presented here.
All species sensitivities reported herein were deduced assuming a linear response between reported and formic

acid calibrations in the field (where day-to-day calibrations were performed) and the laboratory. A range of other species were calibrated for after the campaign, and relative calibration factors were derived using the measured formic acid sensitivity during these calibrations, as has been performed previously (Le Breton *et al.*, 2018; Bannan et al., 2015)

Supporting measurements

Several supporting measurements were made that allow for interpretation of the TOF-CIMS measurements. These include gas-phase measurements of biogenic volatile organic compounds (BVOCs) from a proton transfer time-of-flight mass spectrometer (PTR-ToF-MS; Ionicon Analytik) and particle-phase measurements using an aerosol chemical speciation monitor (ACSM)(DeCarlo *et al.*, 2006). Operation and analysis procedures are outlined elsewhere for the PTR-TOFMS (Liu *et al.*, 2016) and for the ACSM (de Sá *et al., 2017)*. The chemical composition of submicrometer aerosols was measured on-line by mass spectrometry using an Aerosol Chemical Speciation Monitor (ACSM). The aerosol mass spectrometer was used to characterize a wide range of non-refractory sub-micron aerosol particles such as organics, nitrate, sulfate, ammonium, and chloride in real-time with time-resolution of <15 minutes. Sulfur dioxide, NO_x and O_3 mixing ratios were monitored at both sites using trace gas analyzers (Thermo 43i-TLE, Thermo 42i and Thermo 49i, respectively). Meteorological parameters were measured using two different automatic weather stations (HOBO U30 Station GSM-UDP). Meteorological measurements comprised: temperature (± 0.3 °C), humidity (± 3–5%), rain amount (± 5% for daily accumulation), wind speed (0.3–0.5 ms-1) and direction (± 3°), where the resolution and accuracy are stated in parenthesis.

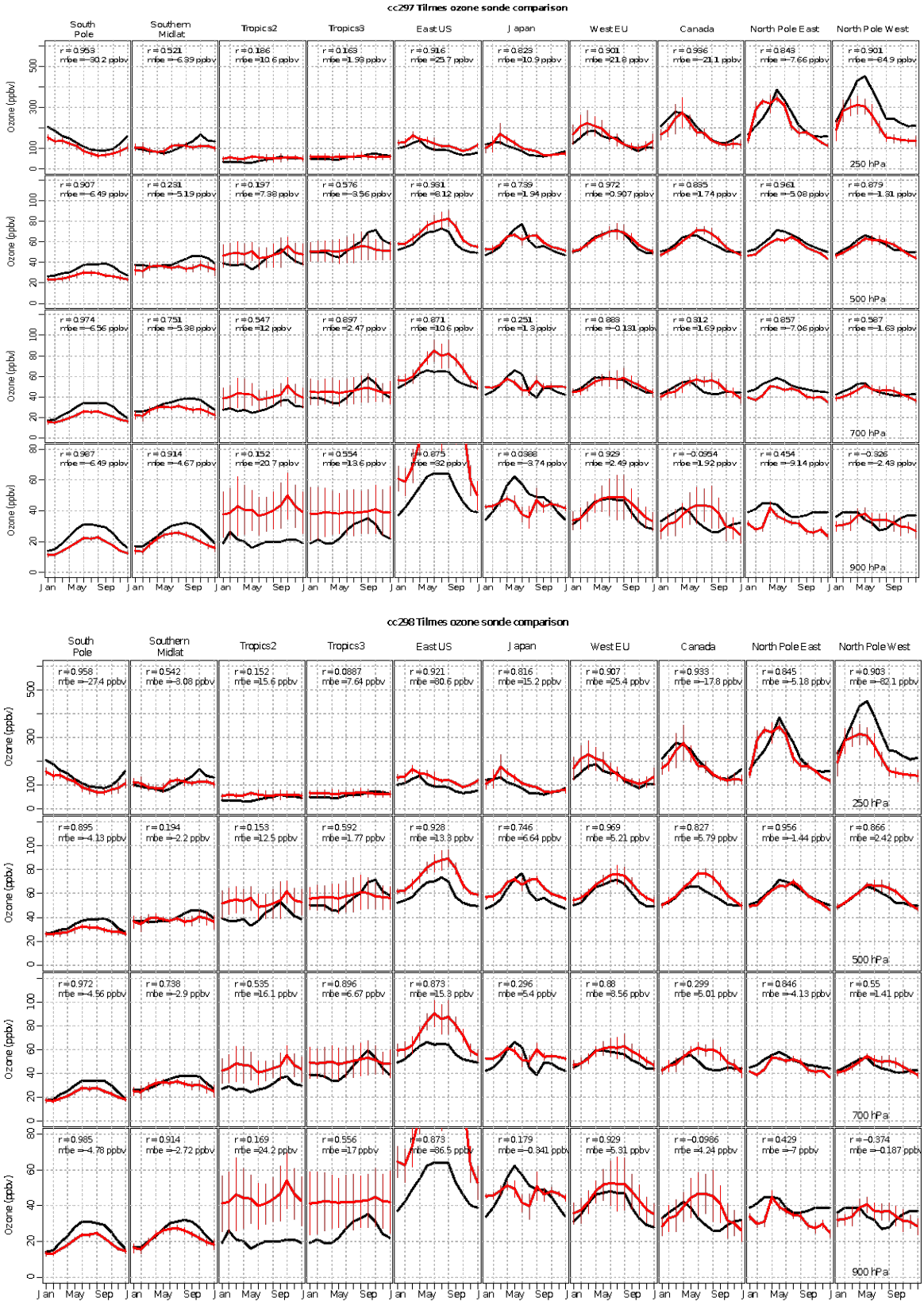


Figure B5. Monthly mean ozone from observations (black) and CS (cc297 upper plot, red) and CS2 (cc298 lower plot, red) runs at 10 sites and 4 pressure levels (250 hPa – 1st row, 500 hPa – 2nd row, 700 hPa – 3rd row, 900 hPa – 4th row) .

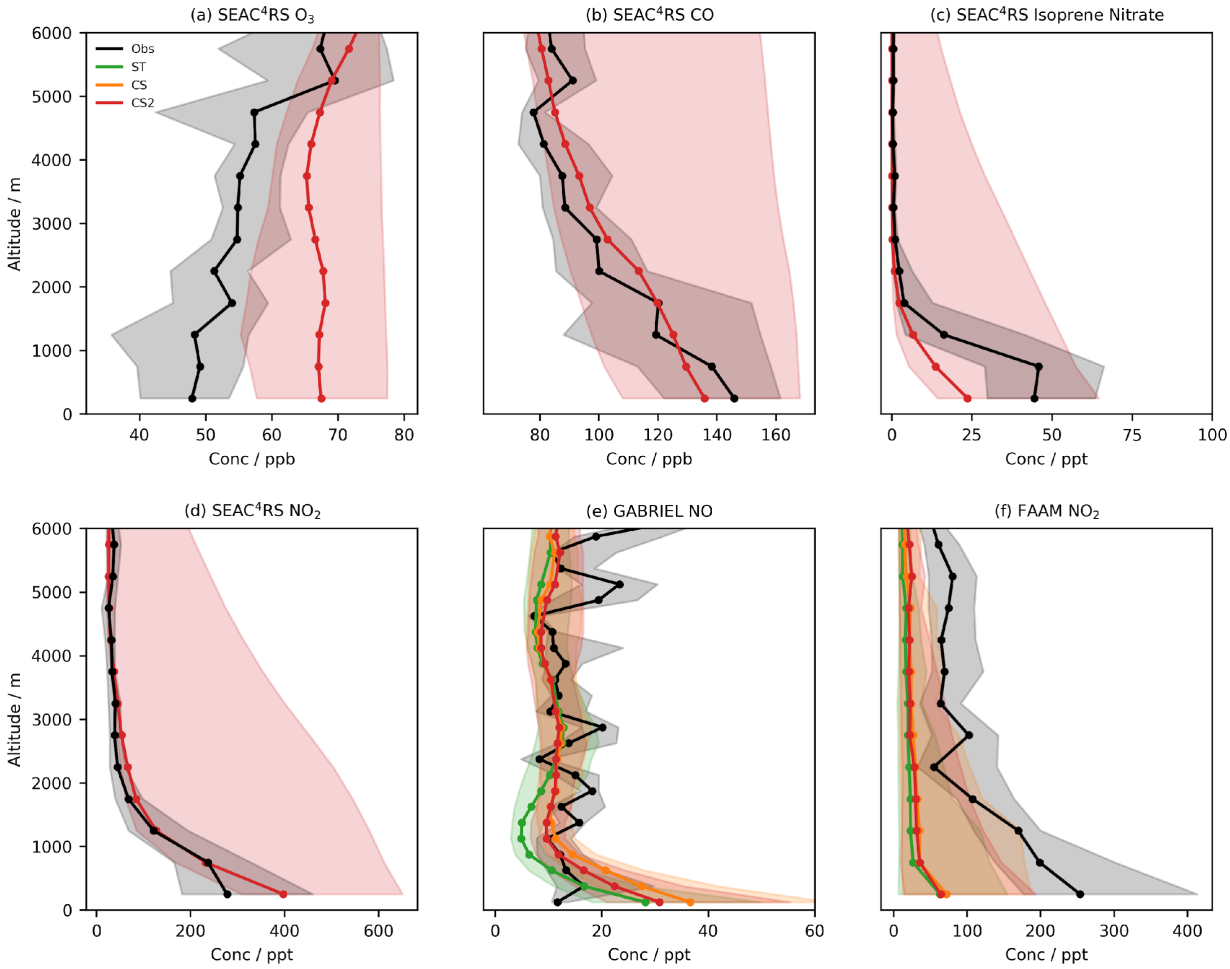


Figure B6. Median observed and model (CS2) concentrations for (a) O_3, (b) CO, (c) Isoprene nitrate, (d) NO_2 from the SEAC⁴RS flight campaign. Panels (e) and (f) show median observed NO (GABRIEL) and NO_2 (FAAM) concentrations from observations and all mechanisms. Shading shows IQR.

Section B5 Other Species

CO

As discussed in the context of HO_x, Borneo modelled surface CO was high biased for all mechanisms (Fig. S7) with CS and CS2 exhibiting a bias 50-60 ppb in July when observations were low (~100 ppb) and ST a bias of 27 ppb. ST and CS were low and high biased respectively by around 13 ppb while CS2 was high biased by 27 ppb (Fig. S10). Over the Amazon CS and CS2 exhibit a smaller low bias than ST while over Borneo, ST and CS perform well with ST high biased by 10-15 ppb (Fig. 3). The CO profile from CS2 performs well against SEAC⁴RS data (Fig. S5).

Monthly mean surface CO from the longer CS2 runs show a consistent increase across multiple locations in CO concentration compared to CS but, due to the spatially-varying performance of CS (high bias in certain regions and low bias in others), CS2 appeared no better or worse than CS on a global scale. A small increase in low altitude CO was also seen in the annual mean CO vertical profiles.

$HONO_2$

Tropospheric vertical profiles of annual mean nitric acid at multiple locations show a small increase in CS2 in a few locations (<~50 ppt) relative to CS, slightly increasing the general model high bias. In the stratosphere, $HONO_2$ was slightly (0.25-0.5 ppb) lower than CS in the 20-30 km increasing the model low bias.

Benzene and SO_2

In the Amazon CS and CS2 show reasonable agreement for benzene while all mechanisms have a daytime low bias for SO_2 (Fig. S10).

PAN

PAN is high biased in Borneo (Fig S7), with CS and CS2 worse than ST. The increase in PAN in CS is documented by Archer-Nicholls et al (2021) and the general reduction from CS to CS2 is discussed in Section 2.5.

HCHO

The model high bias for HCHO in Borneo (Fig. S7) increased from ST to the CS due to additional secondary production (Archer-Nicholls et al., 2021) while above the Amazon, CS2 (Fig. S10) did yield an improvement relative to CS at low altitudes (< 1km). The general reduction in HCHO in CS2 relative to CS is discussed further in Section 2.5.

Acetone and Acetaldehyde

All mechanisms are significantly high biased for acetone and acetaldehyde in Borneo and for acetone in the Amazon (Figs S7, S8). Above the Amazon, the three mechanisms are broadly similar for acetone displaying high bias at low altitude (greatest in the CRI mechanisms due to enhanced secondary production) and much smaller bias above ~ 2km. This highlights the importance of the ongoing work to update the photolysis of acetone and acetaldehyde species. These updates which are yet to be incorporated in UKCA have been noted to increase acetone photolysis frequency by 3-5x in the lowest 5km (Prather et al., 2013) and so should help to reduce model high bias.

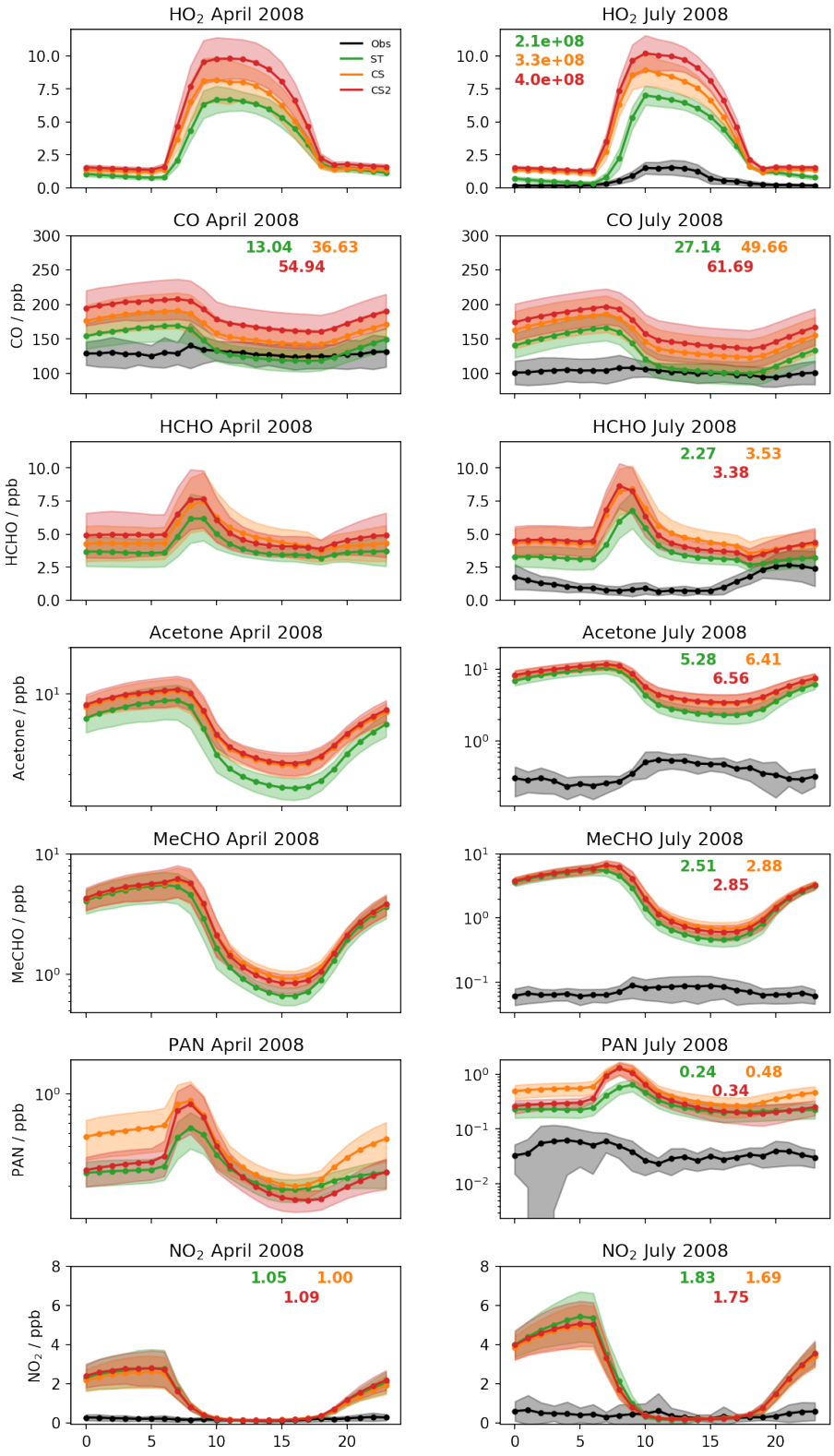


Figure B7. Mean modelled (ST, CS and CS2) and observed diurnal profiles of HO_2, CO, HCHO, Acetone, MeCHO, PAN and NO_2 profiles from Borneo. Observations are from the OP3 tower (ref) and model output from the most relevant grid cell. Shading indicates ±1 standard deviation from the mean and the numbers in bold show the mean diurnal model bias (model - observations) for species/locations where observations were recorded.

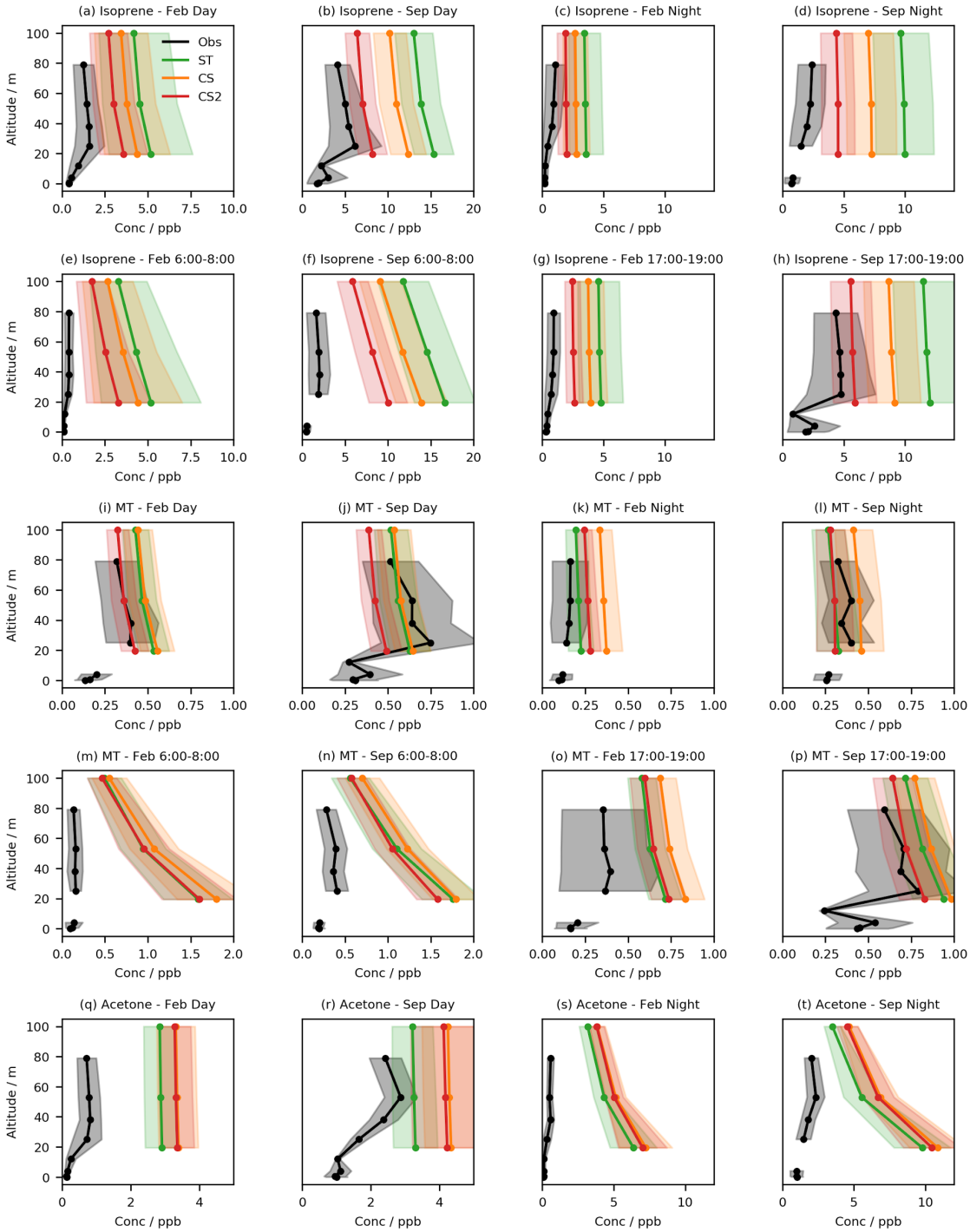


Figure B8. Mean vertical profiles of isoprene, monoterpenes from observations taken at the ATTO tower (Yanez-Serrano et al., 2015) and model output from ST, CS and CS2. Daytime and nighttime periods are taken as 9:00-15:00 and 21:00-03:00 respectively. Shaded regions indicate ± 1 standard deviation from the mean.

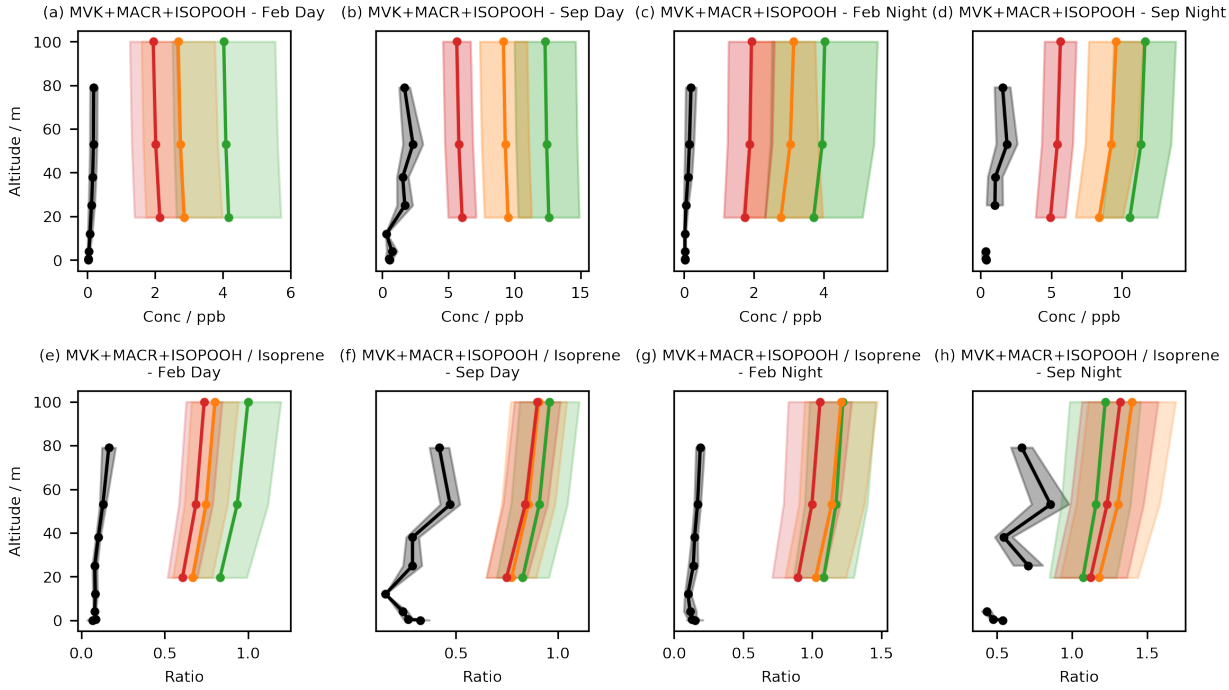


Figure B9. Mean vertical profiles of the isoprene oxidation products MVK+MACR+ISOPOOH and the ratio of MVK+MACR+ISOPOOH to isoprene from observations taken at the ATTO tower (Yanez-Serrano et al., 2015) and model output from ST, CS and CS2. Daytime and nighttime periods are taken as 9:00-15:00 and 21:00-03:00 respectively. Shaded regions indicate ± 1 standard deviation from the mean.

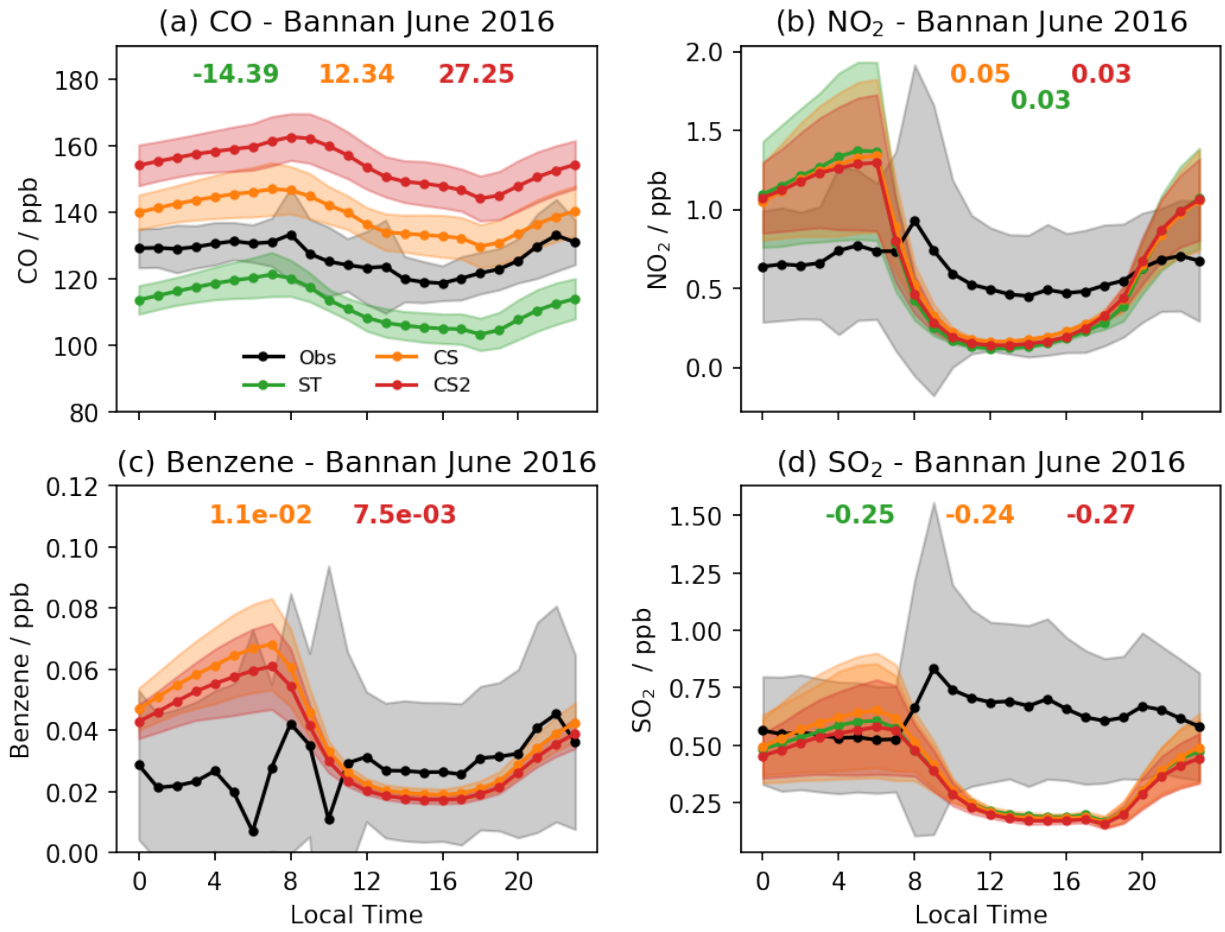


Figure B10. Mean modelled (ST, CS and CS2) and observed diurnal profiles of CO, NO2, Benzene and SO2 from the Bannan site in the Amazon. Shading indicates ±1 standard deviation from the observation mean and the numbers in bold show the mean diurnal model bias (model - observations). (Note that the ST mechanism does include benzene as a species.).

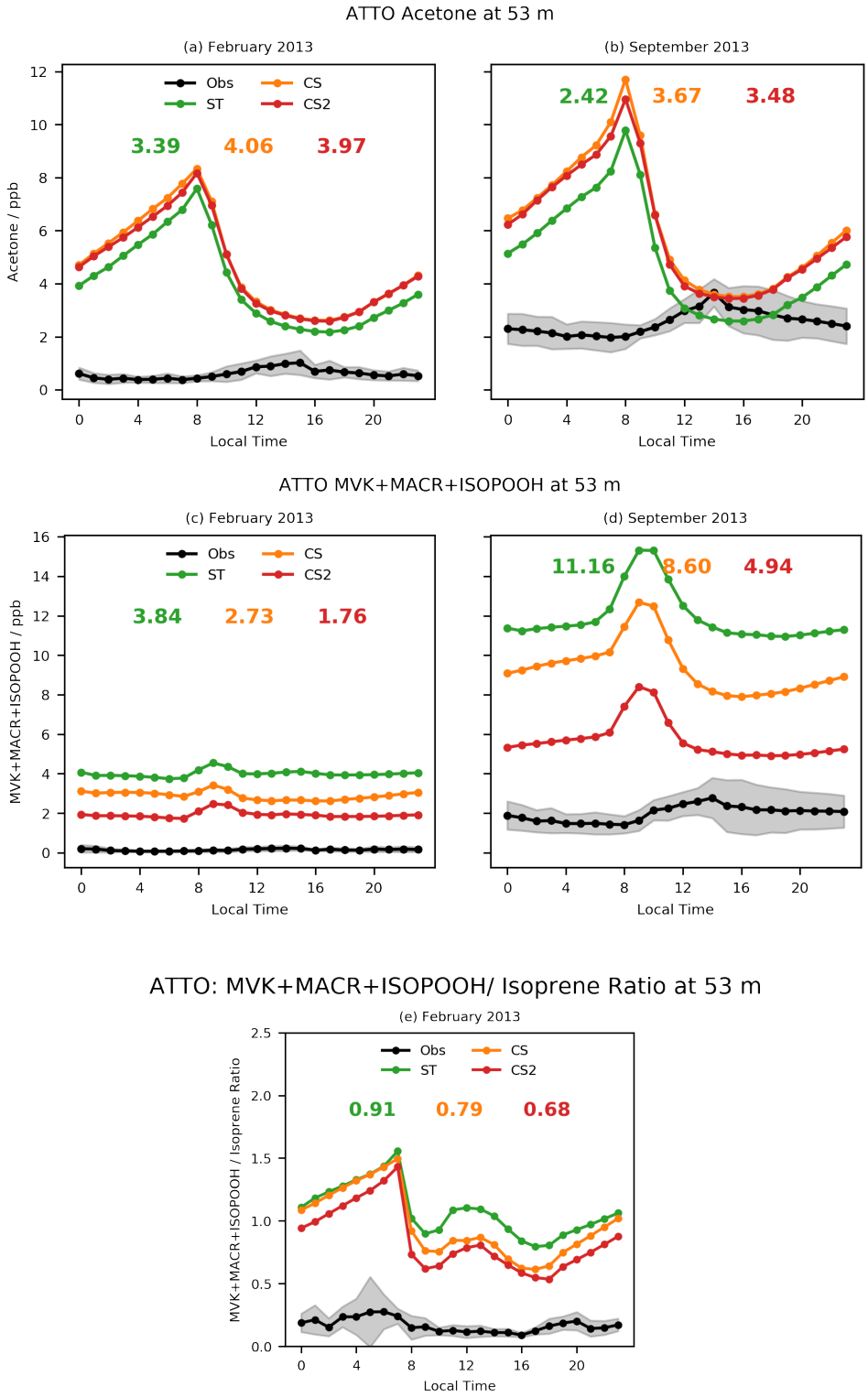


Figure B11. Mean modelled (ST, CS, CS2) and observed diurnal profiles of acetone, MVK+MACR+ISOPOOH at the ATTO tower. Observations are from the OP3 tower (e.g. Hewitt et al., 2010, Table 3) and model output from the most relevant grid cell. Shading indicates ±1 standard deviation from the observation mean and the numbers in bold show the mean diurnal model bias (model - observations).

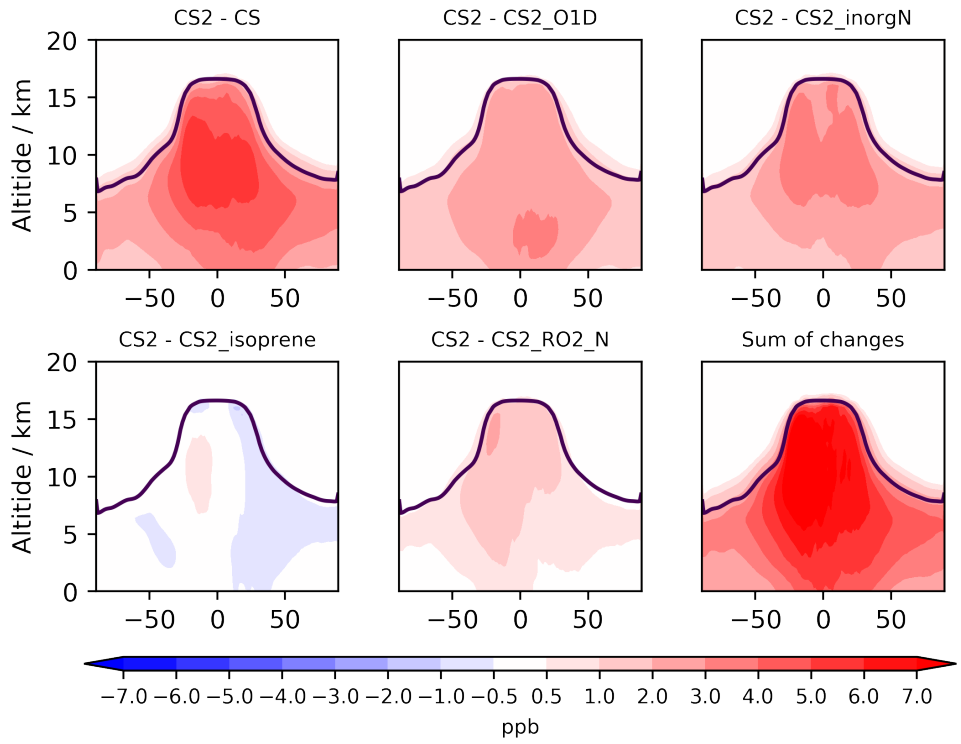


Figure B12. Zonal mean change in ozone mixing ratio for 2006 for CS2 and CS (top left), CS2 and the respective sensitivity tests and the sum of the changes from the sensitivity tests. The purple line shows the mean tropopause height.

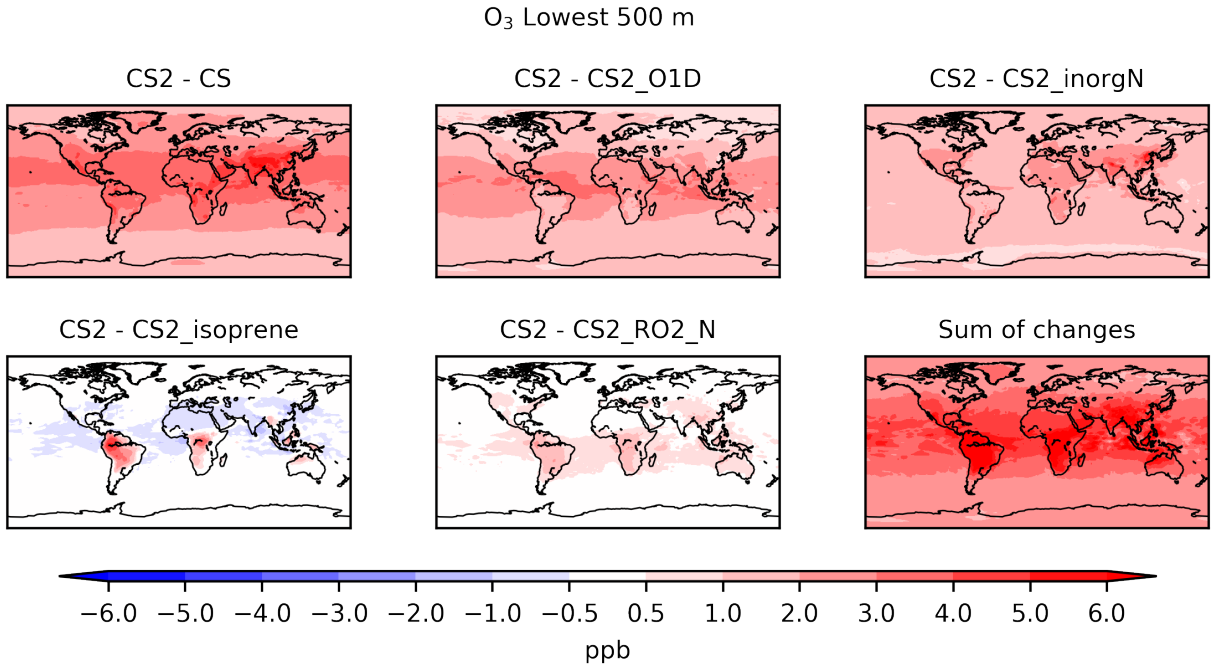


Figure B13. Mean change in ozone mixing ratio for the lowest ~500 m for 2006 for CS2 and CS (top left), CS2 and the respective sensitivity tests and the sum of the changes from the sensitivity tests.

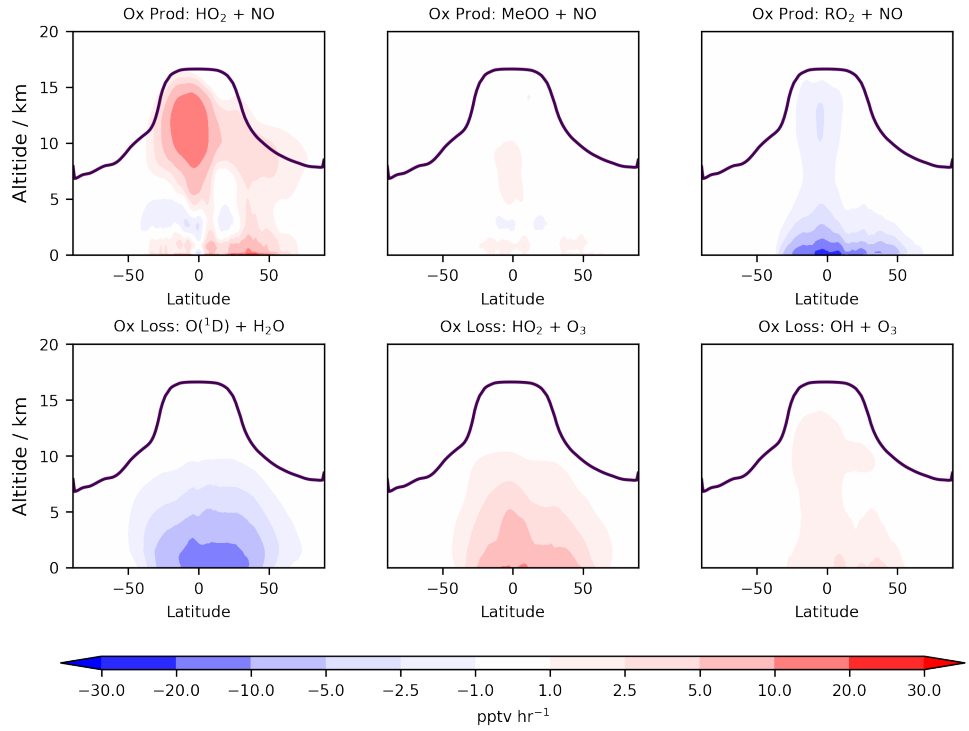


Figure B14. Tropospheric zonal mean change in the major production and loss Ox fluxes for CS2 - CS. These fluxes make up over 99%and 95% of total production and loss fluxes, respectively.

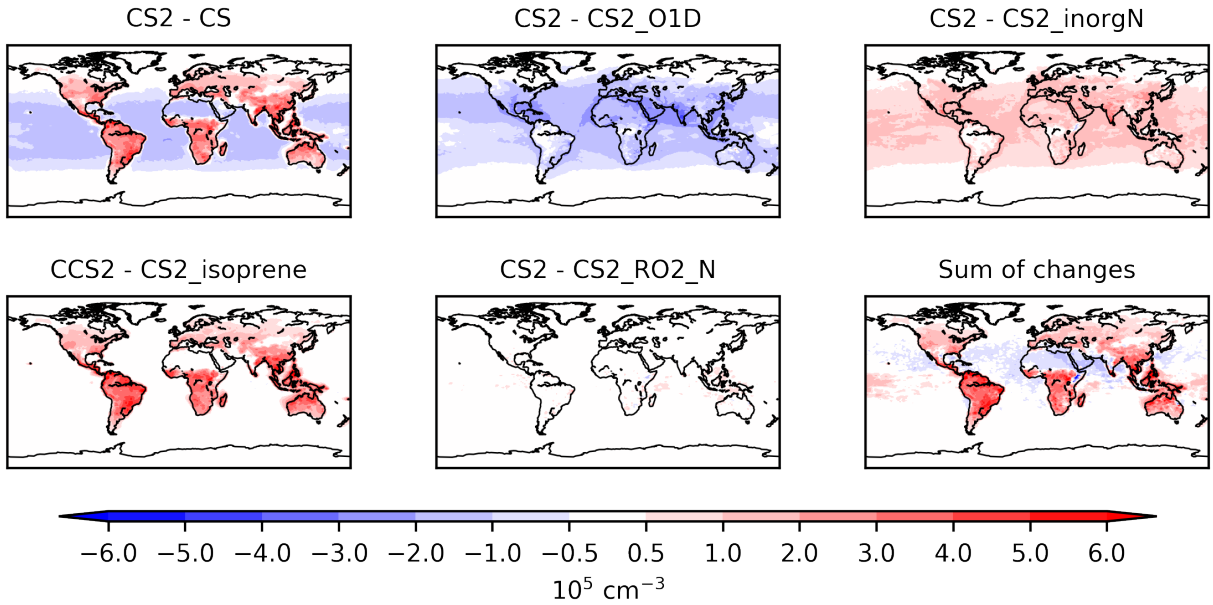


Figure B15. Mean change in OH concentration for the lowest ~500 m for 2006 for CS2 and CS (top left), CS2 and the respective sensitivity tests and the sum of the changes from the sensitivity tests.

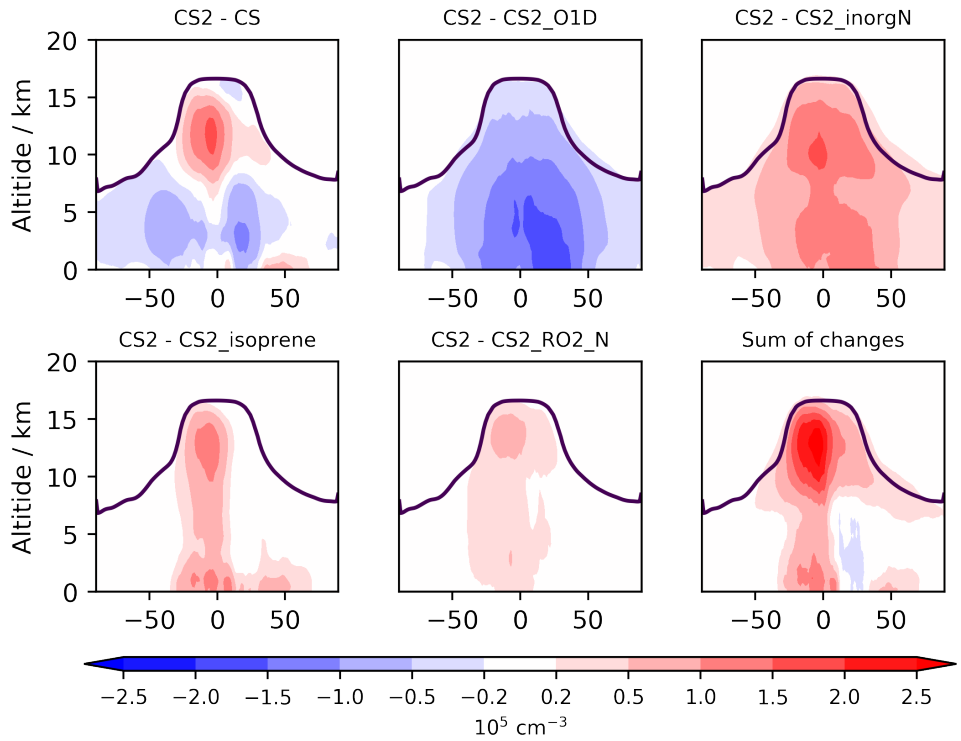


Figure B16. Tropospheric zonal mean change in OH for 2006 for CS2 and CS (top left), CS2 and the respective sensitivity tests and the sum of the changes from the sensitivity tests. The purple line shows the mean tropopause height.

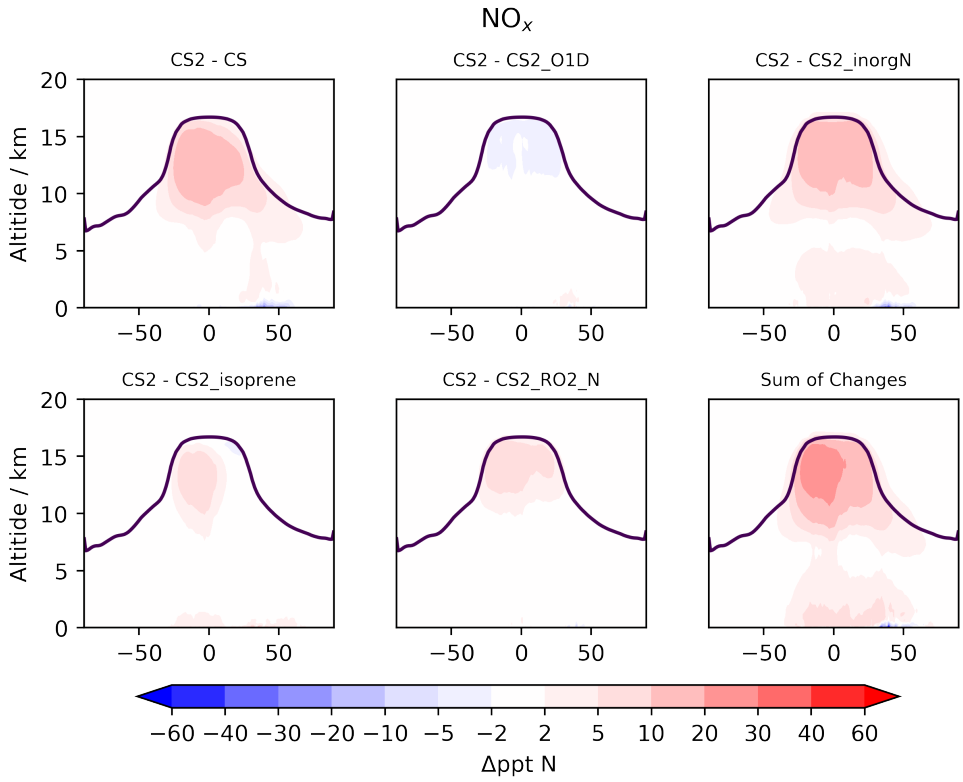


Figure B17. Zonal mean change in NOx for CS2 and CS (top left), CS2 and the respective sensitivity tests and the sum of the changes from the sensitivity tests. The purple line shows the mean tropopause height.

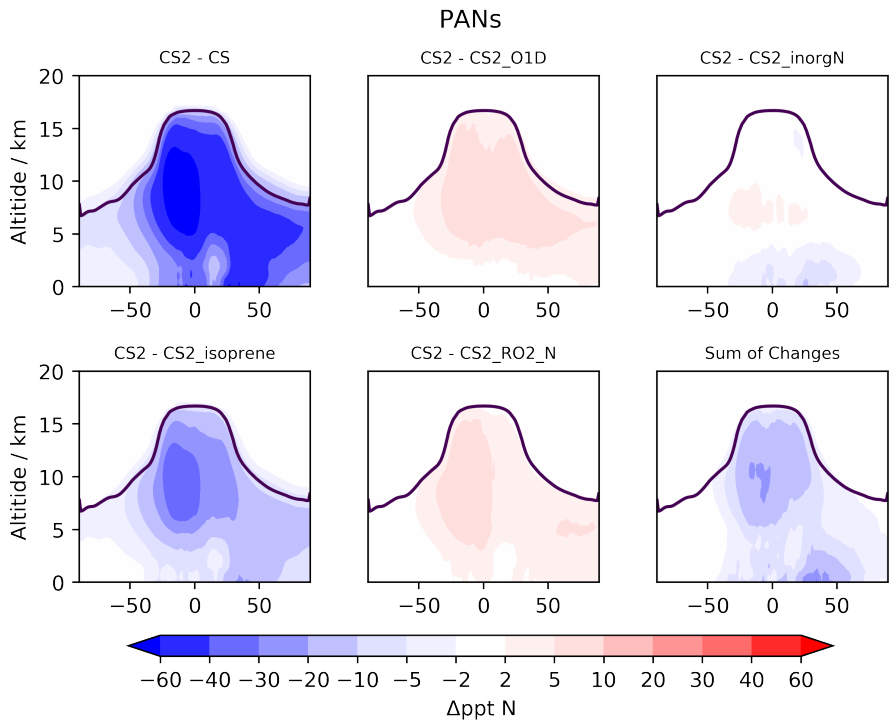


Figure B18. Tropospheric zonal mean change in PANs for CS2 and CS (top left), CS2 and the respective sensitivity tests and the sum of the changes from the sensitivity tests. The purple line shows the mean tropopause height.

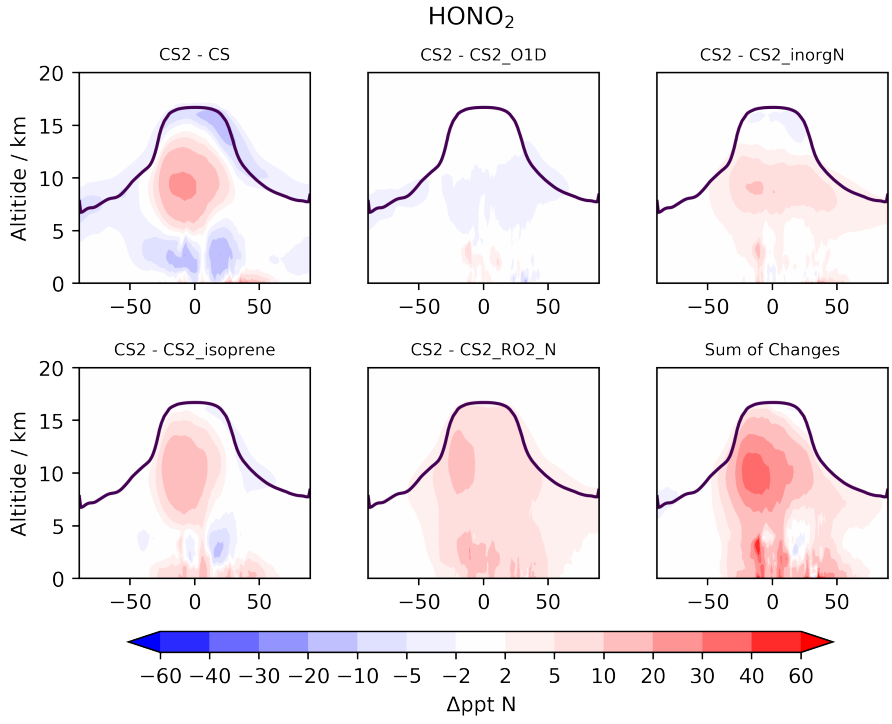


Figure B19. Zonal mean change in $HONO_2$ for CS2 and CS (top left), CS2 and the respective sensitivity tests and the sum of the changes from the sensitivity tests. The purple line shows the mean tropopause height.

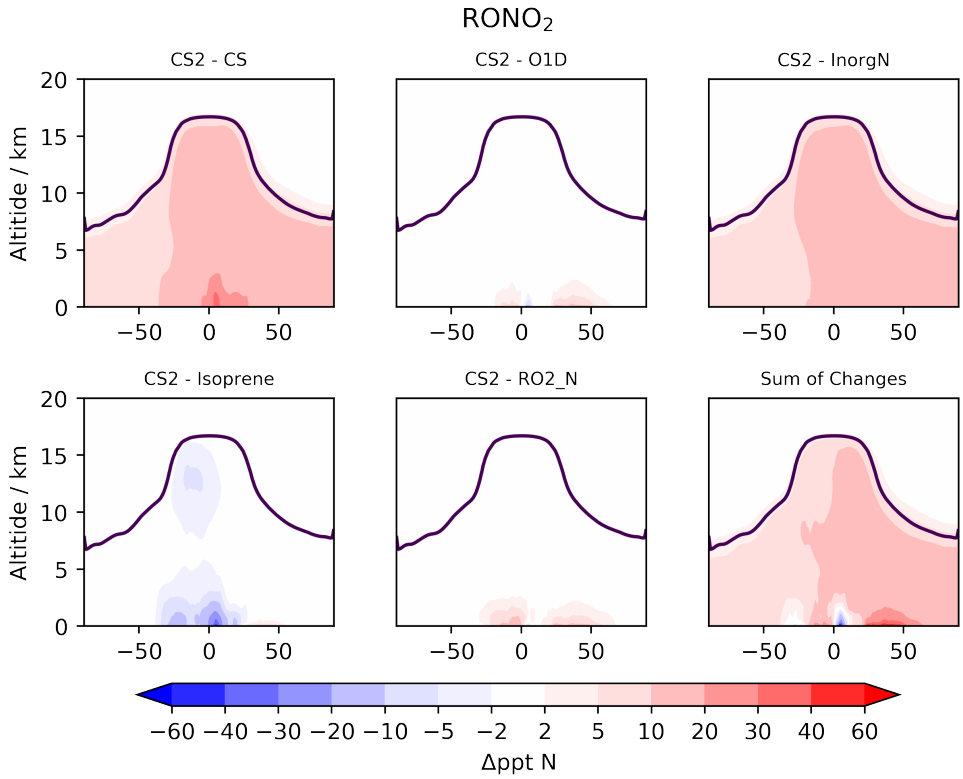


Figure B20. Zonal mean change in $RONO_2$ for CS2 and CS (top left), CS2 and the respective sensitivity tests and the sum of the changes from the sensitivity tests. The purple line shows the mean tropopause height.

Table B4. Annual mean Ox diagnostics for CS, CS2 and sensitivity tests. Note that these data refer to the single year of analysis used for the sensitivity tests rather than the 4 year mean as in Table 2.4 so the absolute values for CS and CS2 may differ from Table 2.4.

	CS	CS2	CRI_v2_2_O1D	CRI_v2_2_inorgN	CRI_v2_2_isoprene	CRI_v2_2_RO2_N
O_3 Burden (Tg)	324	351	334	334	353	345
O_x Lifetime (days)	17.23	18.63	17.28	18.73	18.62	18.61
Chemical Production (Tg year^{-1})	**6579**	**6585**	**6780**	**6217**	**6650**	**6478**
HO_2 + NO	4100	4231	4347	4009	4200	4165
MeOO + NO	1575	1585	1659	1468	1565	1549
NO + RO_2	852	720	721	694	833	718
Other	51	49	52	47	52	46
Chemical Loss (Tg year^{-1})	**5837**	**5761**	**6003**	**5446**	**5828**	**5669**
$O(^1D)$ + H_2O	3168	2939	3221	2830	2956	2906
HO_2 + O_3	1659	1812	1760	1700	1814	1781
OH + O_3	739	796	809	711	785	772
O_3 + Alkene	167	101	94	100	162	99
Other	105	113	109	104	112	110
Deposition (Tg year^{-1})	**1129**	**1202**	**1155**	**1155**	**1200**	**1183**

Section B5

CO

The CO burden increased by 3.2% from 343 Tg in CS to 354 Tg in CS2 with gains of 4-5 ppb in the SH low altitudes and 2-4 ppb in much of the troposphere (Fig. 10). Tropospheric destruction of CO by OH increased by 3.2% (~100 Tg yr^{-1}) with increases of 5-10% in the tropical and midlatitude PBL driven by the enhanced oxidising capacity and greater CO production. However, this increased destruction was outweighed by a 4.4%

increase in chemical production, driven primarily by the updates to the isoprene scheme, illustrated by the large column increases occurring over the regions with high BVOC emissions (Fig. S26).

Table B5. Annual mean CO diagnostics for CS and CS2.

	CRI-STRAT	**CRI-STRAT 2**
CO burden / Tg	326.8	337.9
CO lifetime / days	38.1	38.3
Production / Tg CO year^{-1}	**3227.5**	**3326.7**
Emissions / Tg CO year^{-1}	1110.2	1110.7
HCHO + OH/NO_3 / Tg CO year^{-1}	589.3	555.3
HCHO + hv / Tg CO year^{-1}	1228.6	1239.4
Other Chemistry / Tg CO year^{-1}	86.2	179.7
Other Photolysis / Tg CO year^{-1}	213.1	242.2
Loss / Tg CO year^{-1}	**3158.2**	**3254.2**
CO + OH / Tg CO year^{-1}	2994.6	3086.6
CO Dry Dep / Tg CO year^{-1}	163.6	167.6
Net production / Tg CO year^{-1}	**69.3**	**72.5**

HCHO

The HCHO burden decreased by 10% in CS2 (1.20 Tg to 1.08 Tg), driven primarily by the change to isoprene chemistry with a small contribution from the increased HCHO photolysis flux. Added competition from ISOPO2 isomerisation leads to the production of methylglyoxal (CARB6) and hydroxy acetone (CARB7), at the expense of methacrolein and methyl vinyl ketone (lumped together as UCARB10). The former species tend to produce less HCHO than the latter, resulting in the greatest reduction in HCHO column over the regions with the greatest biogenic emissions (Fig. S26).

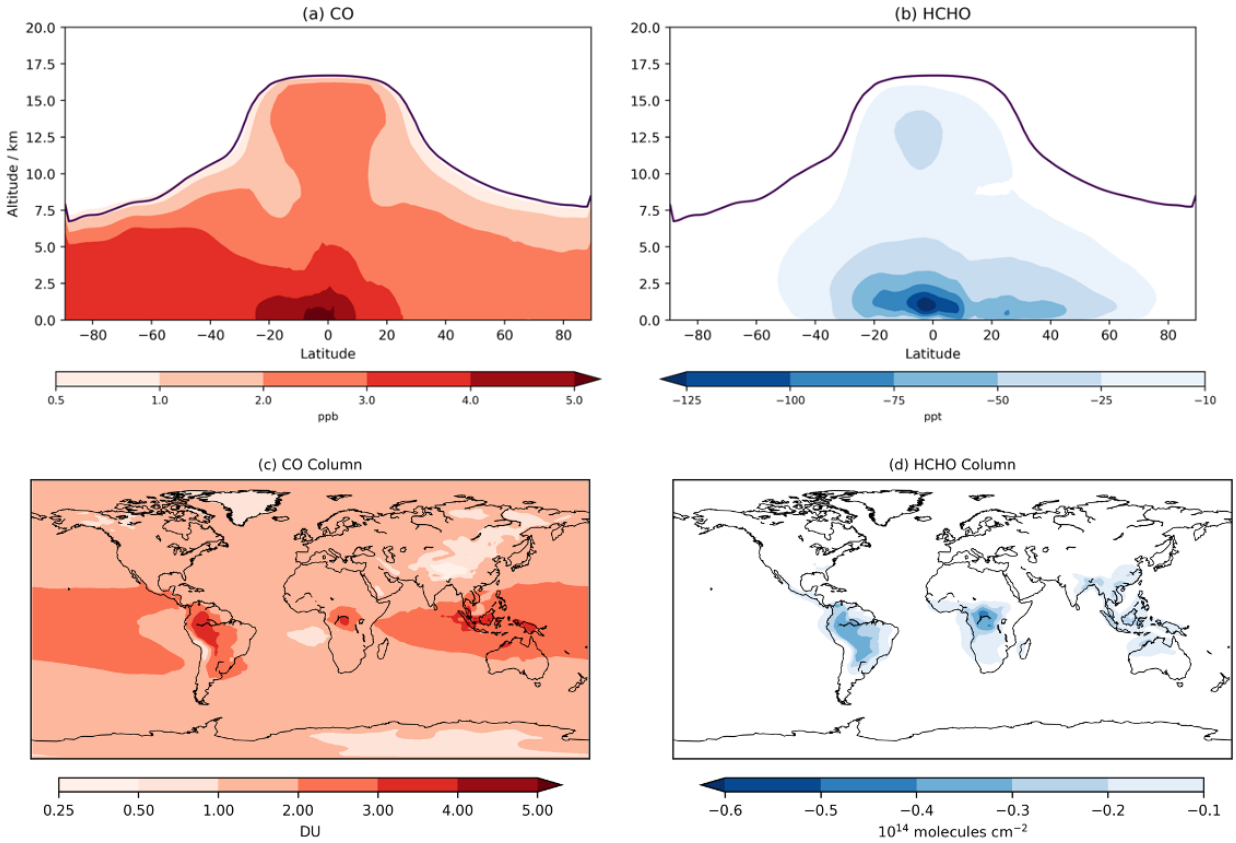


Figure B21. Annual zonal mean changes in (a) CO and (b) HCHO and annual column changes in (c) CO and (d) HCHO.

Section B6 Impact of Photolysis Changes

The CS2 mechanism featured the updates to photolysis described in Section 2.2. To isolate the impacts of these changes on tropospheric ozone and OH, a further run was performed using the CS2 mechanism but with photolysis parameters from the CS mechanism. This run was run for 2 years with the 2nd year analysed and compared to the same year in the longer CS2 run.

The change in photolysis had produced minor changes in tropospheric oxidants. The tropospheric O_3 burden decreased by 0.09% (0.32 Tg). Changes in most of the troposphere were below 0.2 ppb (~1%), at least an order of magnitude lower than the simulated changes between CS and CS2 (with updated photolysis) while larger increases of 0.5-1.5 ppb (0.5-1%) were observed around the tropical tropopause (Fig. S27). Therefore, we can conclude the change in O_3 between CS and CS2 s being driven predominantly by the change in chemistry rather than photolysis.

Updating the photolysis increased the air mass-weighted OH concentration by 0.98% (1.0 x 10^4 cm^{-3}), compared to a decrease of 1.55% between in CS2 relative to CS. Spatially, OH increased in most of the troposphere by less than 2.0 x 10^4 cm^{-3} (0.2-0.5%) (Fig S28) with the largest absolute increases in at low altitude 40S-50N. By comparison, OH is simulated to decrease from CS to CS2 in the bulk of the troposphere by at least

2.0 x 10^4 cm^{-3} and more than 5.0 x 10^4 cm^{-3} in tropical and midlatitudes (excluding the tropopause). Therefore, the update to the photolysis, by increasing OH in CS2, actually reduces the change in OH from CS to CS2 rather than being a cause of the mechanistic difference.

An important caveat to this is low altitude northern hemisphere midlatitude OH which increased from CS to CS2 and also from the base to updated photolysis setup. The impact on OH of the photolysis update must be compared to the impact of the changes to the chemistry, notably isoprene HOx recycling and changes to $O(^1D)$'s reaction pathways. Crucially, we see that the change in OH averaged over the lowest 500m from CS to CS2 is significantly larger than the change arising from the photolysis update, particularly over the regions with significant BVOC emissions such as the Amazon and other tropical regions (Fig. S28). That said, the impact of updated photolysis may be more significant over the parts of Europe and North America where the OH increase between CS and CS2 is smaller. Overall however we can conclude that the update to the photolysis is not a major driver of the significant changes to low altitude OH, rather the update in chemistry between CS and CS2 is the major driver.

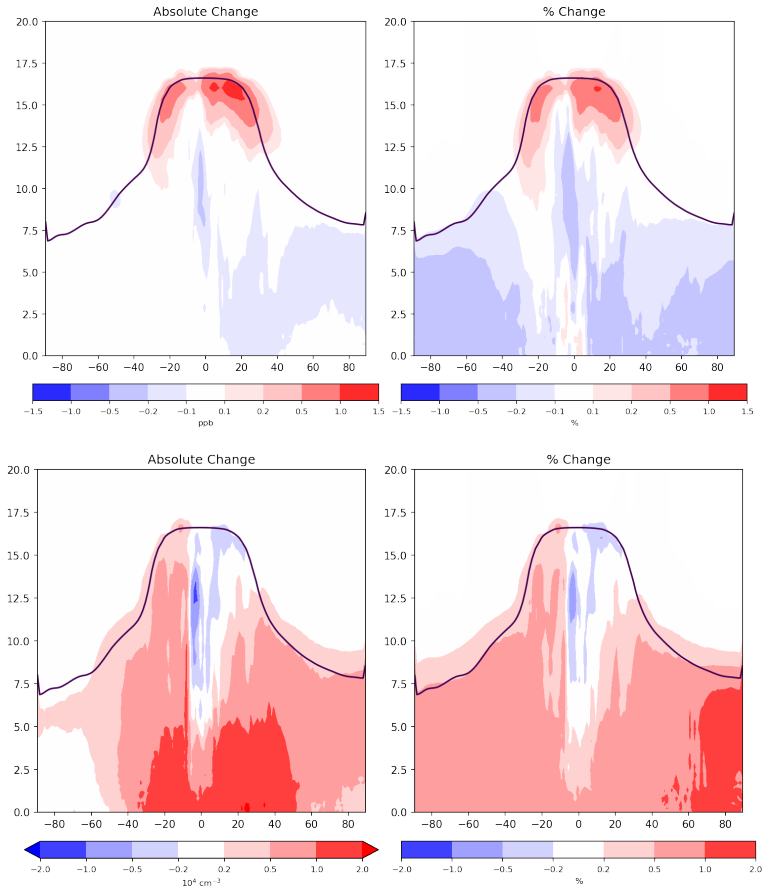


Figure B22. Zonal mean changes in O_3 (upper panels) and OH (lower panels) between CS2 and CRI_v2_2_photo. The purple line shows the mean tropopause height.

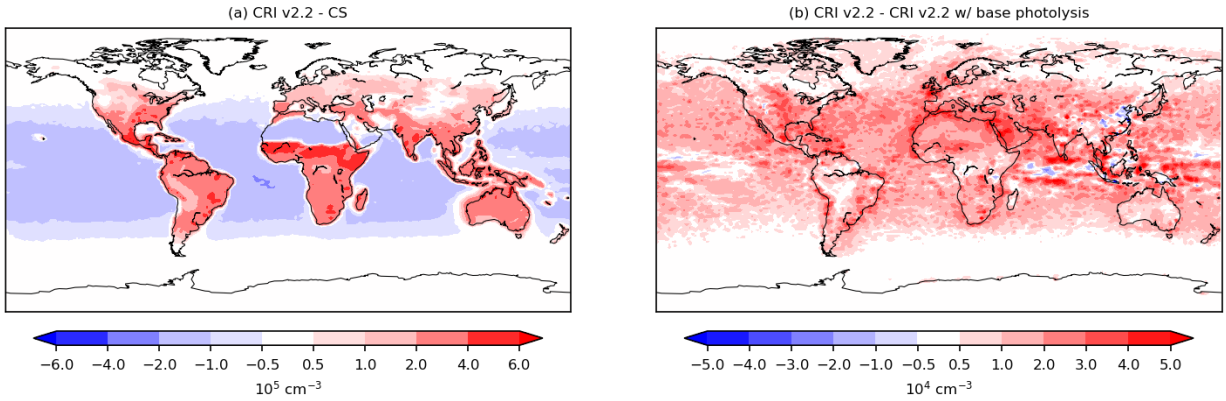


Figure B23. Change in OH averaged over lowest ~500m between (a) CS2 and CS and (b) CS2 and CRI_v2_2_photo. Note that the scale of (a) is an order of magnitude greater than (b).

Section B7 - Comparison of ST and CS2

As previously mentioned, the broad mechanism comparison of CS and CS2 was designed to complement the earlier comparison of ST and CS by Archer-Nicholls et al (2021). However, the study in Chapter 3 uses the ST and CS2 mechanisms to increase the relevance of the results, as explained in 3.2. Therefore, present day 2-year nudged runs (1 year spin, 1 year analysis) are also performed with ST and CS2 mechanisms to allow a brief comparison between the mechanisms, building on the earlier comparisons of ST and CS2 in the observational data comparison (Section 2.4 and Figs 2.1-2.3). Figure B24 shows side-by-side comparisons of the differences between CS and CS2 and ST and CS2 for low altitude O_3, tropospheric O3, low altitude OH, tropospheric OH and tropospheric NO_x.

As with CS, CS2 differs from ST in both the chemistry and the emissions used. While the differences in chemistry between CS and CS2 are investigated thoroughly in this chapter, the influence of the additional VOC emissions are not because both CRI mechanisms use identical emissions. The impact of the emission differences in the context of the ST vs. SC2 comparison is also considered below.

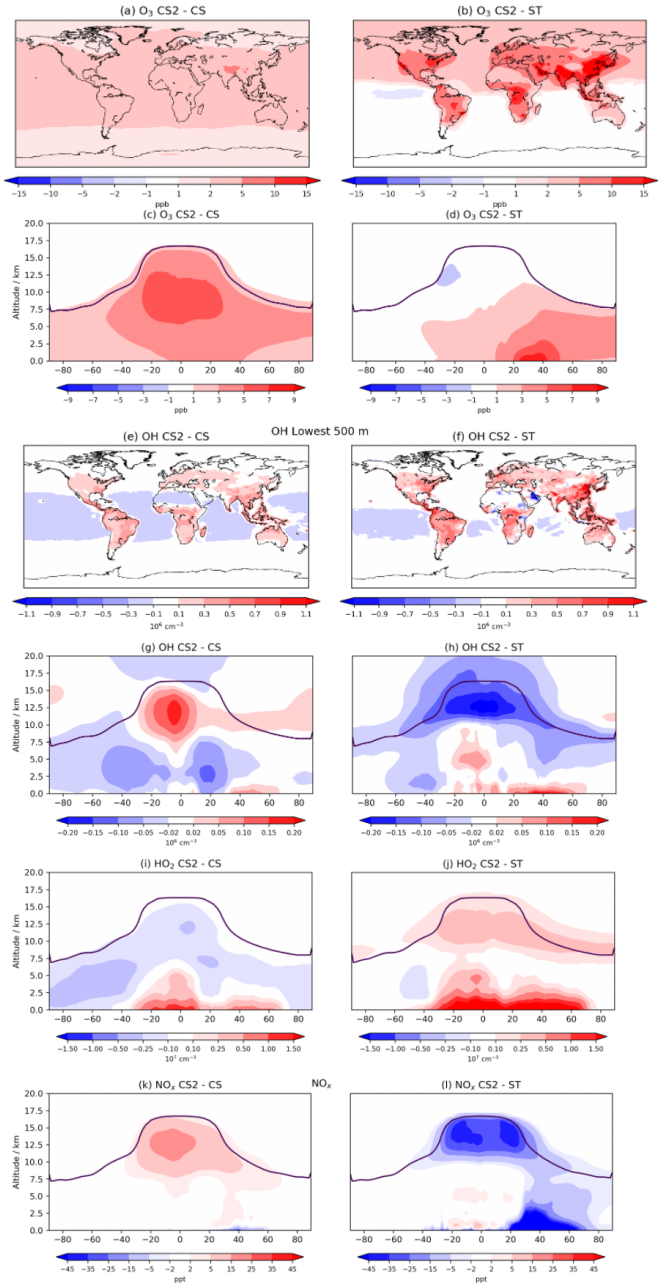


Figure B24. Difference between CS and CS2 (left) and ST and CS2 (right) for (a, b) low altitude (<500m) O_3, (c, d) zonal mean O_3, (e, f) low altitude (<500m) OH, (g, h) zonal mean OH, (i, j) zonal mean HO_2 and (k, l) zonal mean NO_x.

O_3

A major difference in the O_3 distribution between CS and CS2 is driven by the greater flux in CS through the $O(^1D)$ + H_2O reaction which represents a loss of O_3. This leads to CS simulating lower O_3 throughout the troposphere compared to CS2 (Fig 2.4) and ST (Fig 6, Archer-Nicholls et al., 2021). This flux through this reaction is strongly influenced by the rate constants of $O(^1D)$ with O_2, N_2 and H_2O. The updates to the IUPAC preferred values in CS2 mean these rate constants are significantly different between CS and CS2. This difference results

in a smaller fraction of $O(^1D)$ reacting with H_2O in CS2 and has a strong influence on PBL and free troposphere O_3 differences (illustrated by the CS2_O1D sensitivity test, Figs B12, B13).

However, the IUPAC updates in CS2 bring these rate constants much closer to those used in ST. Therefore, the O_3 difference caused by this pathway will be much smaller between ST and CS2. The difference in marine boundary layer and free troposphere O_3 between ST and CS2 will also be smaller than it is between ST and CS (Fig B24 (c,d)).

However, the larger quantity of VOC emissions in CS2 will also play a role in the difference in O_3 between the mechanisms. Archer-Nicholls et al (2021) compared O_3 between ST and CS (using the full VOC emissions set) and, separately, between ST and a CS run using the same VOC emissions as ST (CRI_EMISS_ST). The O_3 burdens in the CS and CRI_EMISS_ST runs were 8 Tg and 29 Tg lower than ST respectively. Furthermore, while the CS run exhibited greater low altitude O_3 (<1 km) than ST, particularly in the terrestrial NH where increases exceeded 5 ppb (5-10%) in most areas, CRI_EMISS_ST generally simulated lower O_3 (2-5%) in the same regions. Thus, under present day conditions the additional VOC emissions used by the CS (and CS2) mechanism increased the O_3 burden by 21 Tg (7%) and boundary layer O_3 concentrations in terrestrial regions (Figs B24 (a-d)).

Therefore, for CS2 the combination of the reduced O_3 loss via $O(^1D) + H_2O$ (compared to CS) and enhanced O_3 from the greater VOC emissions (compared to ST) means that CS2, under present day conditions, will simulate greater O_3 than ST. This is in agreement with the ST and CS2 data seen in the observational comparisons where CS2 is universally higher than ST by up to 10 ppb (Figs 2.1 (f-j), 2.2 (b, f)).

HO_x

In tropical terrestrial regions, the increase in OH from ST to CS2 is even greater than between CS and CS2, exceeding 100% during daytime peaks in some locations (Fig 2.1 (a-e)). This trend of an even greater increase in OH between ST and CS2 applies throughout the terrestrial tropical boundary layer where HO_x-recycling from isoprene is very important (Figs B24(e, f)).

However, in oceanic regions, the difference in OH between CS and CS2 is largely determined by the fraction of $O(^1D)$ which forms OH. This fraction is lower in CS2, leading to lower OH in the marine boundary layer and much of the free troposphere (Fig 2.6). As previously mentioned, the relevant rate constants for this process in CS2 are much closer to ST than CS. Therefore, the difference between low altitude oceanic OH will be smaller between ST and CS2 (Figs B24 (e,f)). and the influence of this process in the difference of lower free troposphere OH will also be smaller (Figs B24 (g,h)).

The larger quantity of VOC emissions in CS2 also play a role in the difference between the mechanisms. Considering again the comparisons of ST vs. CS and ST vs. CRI_EMISS_ST of Archer-Nicholls et al (2021), CS and CRI_EMISS_ST both simulated greater OH in the tropical PBL and lower troposphere than ST, but the difference was smaller in CRI_EMISS_ST (Fig 2.12 (a,b)). In other words, the additional emissions used in CS (and CS2) also contribute to greater OH in the tropical PBL and lower troposphere. Archer-Nicholls et al (2021)

noted that the greater OH in CS was driven enhanced by HO_x production from CS's greater low altitude O_3 and the wider range of O_3 + alkene reactions, which produce OH.

HO_2 was also higher in the tropical PBL and lower free troposphere in CS than ST, again due to higher VOC emissions (Fig B25 (c,d)), and the further increase in HO_2 from CS to CS2 simulated in this chapter (Fig 2.6(b)) means HO2 is higher in CS2 than ST in the lower troposphere (Fig B24(j)).

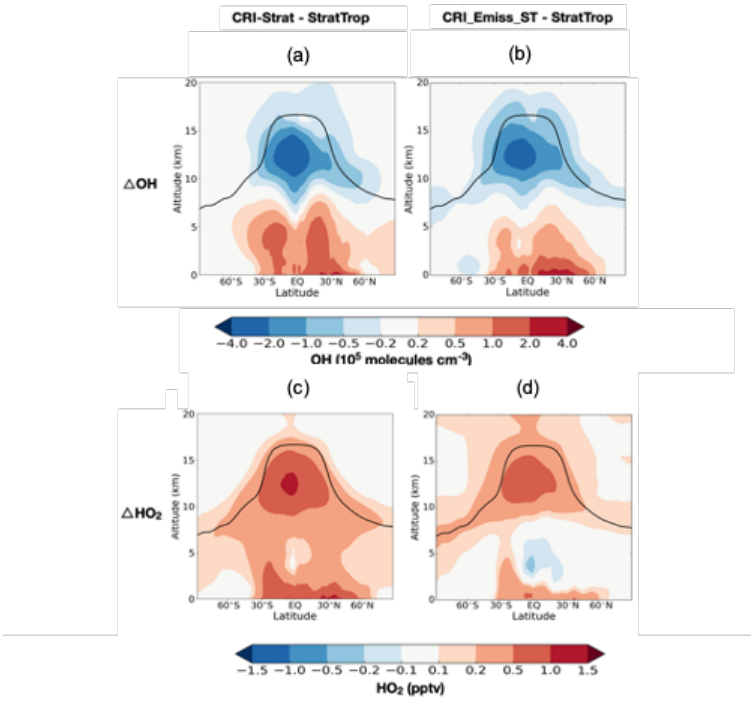


Figure B25. Zonal mean differences in OH between (a) CS and ST and (b) CRI_Emiss_ST and ST. Zonal mean differences in HO_2 between (c) CS and ST and (d) CRI_Emiss_ST and ST. Black lines show average tropopause height over simulation period. Adapted from Archer-Nicholls et al (2021).

2.7.3 BVOCs and SOA

As the burden and dispersion of isoprene and monoterpene is largely controlled by atmospheric oxidising capacity in the source regions, the greater OH in CS2 will result in lower BVOCs concentrations as demonstrated in Figs 2.1 (k-t) & 2.3. The vertical difference in BVOC oxidation and SOA precursor formation (Fig 2.9) will be even more pronounced between ST and CS2.

2.7.4 NO_y

The major difference between the NO_y distribution in CS and CS2 (Section 2.5.5) is the significant reduction in PANs in CS2 (28.2% vs. 33.7%) and attendant increases in NO_x (as less of it is being sequestered into PANs) and $HONO_2$ (since there is more NO_x). This was driven by updates to the rate constants of multiple inorganic nitrogen reactions such as those forming species with the peroxy acyl nitrate moiety, termed PAN-type, and and, and

changes to the major PAN precursor $MeCO_3$. The difference between CS and CS2 mirrors that of ST and CS where Archer-Nicholls et al (2021) showed that a much greater fraction of NO_y was in the form of PANs in CS. Therefore, the global NO_y distribution in CS2 is more similar to ST than CS is.

However, some of the differences simulated between ST and CS remain in the ST and CS2 comparison. NH boundary layer NOx is lower in CS2 than ST (Figs B24(j)), also seen in Fig 13 of Archer-Nicholls et al (2021), due to the greater array of NO_x reservoirs such as $RONO_2$ in the CRI mechanisms and the greater emissions of VOCs which provide more opportunities for the formation of NO_x reservoirs. The lower NOx around the tropical tropopause in both CRI mechanisms is in part driven by the presence of MeO_2NO_2 which does not exist in ST.

The lower NOx in the upper tropical tropopause in CS2 compared to ST contributes to the co-located lower OH (Fig B24(h)) via the reaction $HO_2 + NO$.

Appendix C

This appendix corresponds to Chapter 3.

C1: Methane Lifetime Forcing Calculation

The methane lifetime with respect to loss to OH, τ_{OH}, is defined in Eq C1.

$$\tau_{OH} = \frac{B_{CH_4}}{F_{OH+CH_4}} \quad \text{(C1)}$$

Where B_{CH_4} is the whole atmosphere CH_4 burden and F_{OH+CH_4} is the tropospheric flux of OH + CH_4. τ_{OH} is combined with the lifetimes of methane with respect to soil loss (120 years) and stratospheric loss (160 years) (O'Connor et al., 2020) to calculate the overall methane lifetime, τ_{CH_4}, for each simulation. As in Eq 3.10 of Chapter 3, the change in overall τ_{CH_4} between two simulations, $\Delta\tau_{CH_4}$, is then used along with a feedback factor of 1.28 (O'Connor et al., 2020) to calculate the change in concentration ΔC which would have occurred had methane concentration been allowed to respond (Eq C2).

$$\frac{\Delta C}{C} = \left(\frac{\Delta\tau}{\tau} + 1\right)^{f} - 1 \quad \text{(C2)}$$

Finally, this change in concentration is applied to the CH_4 forcing equation in Table 1 of Etminan et al (2016) with a scaling of 1.52 applied to account for additional chemical production of O_3 and stratospheric water vapour, as in Thornhill et al (2021).

C2: Forcing and feedback factor error calculation

The error in the forcing is the error in the 30-year mean and a scaling is applied for CH_4 (1.14) or O_3 (1.15) to account for uncertainty in the kernel estimate (Thornhill et al., 2021).

The uncertainty in the feedback factors for the different components is calculated by adding the fractional errors in γ_{BVOC}, the forcing and ΔE_{BVOC} in quadrature.

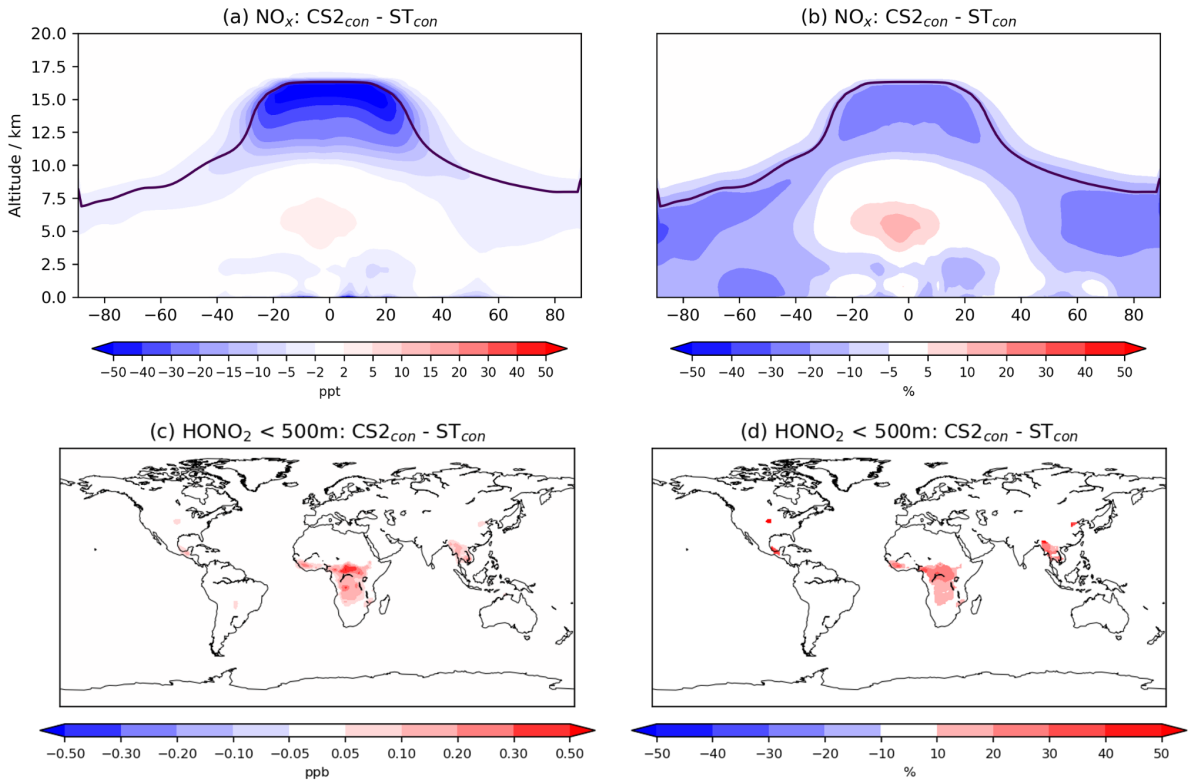


Figure C1. Absolute (a) and percentage (b) differences in NOx between $CS2_{con}$ and ST_{con}. Absolute (c) and percentage (d) differences in $HONO_2$ averaged over the lowest ~500 m between $CS2_{con}$ and ST_{con}.

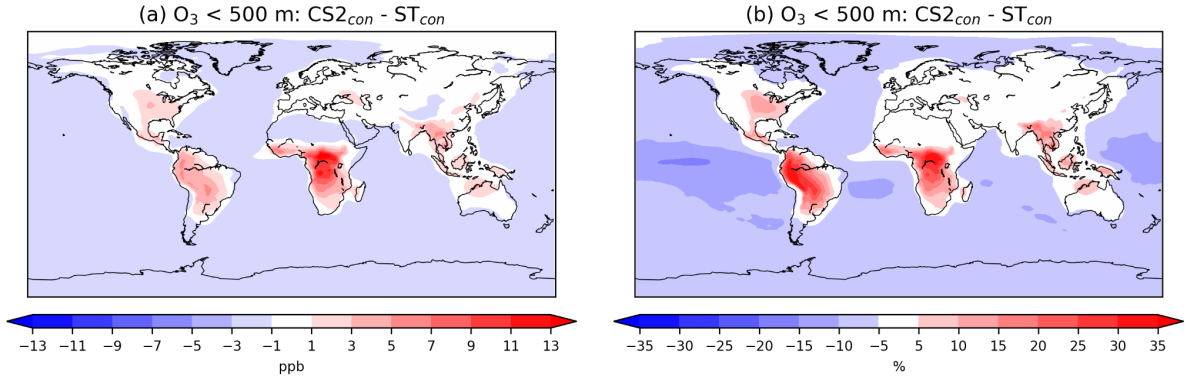


Figure C2. Absolute (a) and percentage (b) difference in low altitude O_3 between $CS2_{con}$ and ST_{con}.

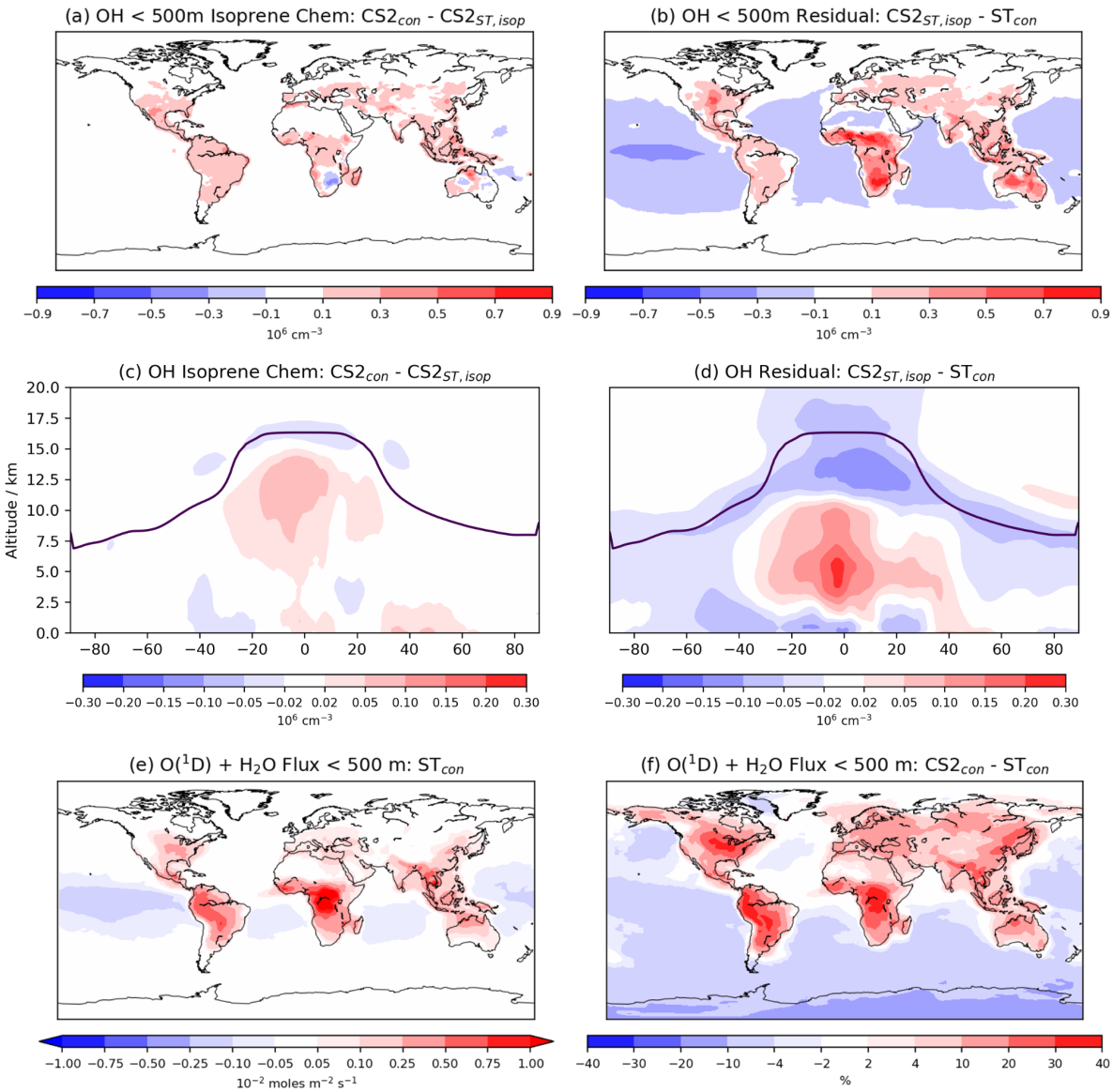


Figure C3. Difference in low altitude OH (< 500m) between (a) CS2$_{con}$ and CS2$_{ST,isop}$ and (b) CS2$_{ST,isop}$ and ST$_{con}$. Zonal mean difference in OH between (c) CS2$_{con}$ and CS2$_{ST,isop}$ and (d) CS2$_{ST,isop}$ and ST$_{con}$. Absolute (e) and percentage (f) difference in primary production of low altitude OH (< 500 m) between CS2$_{con}$ and ST$_{con}$.

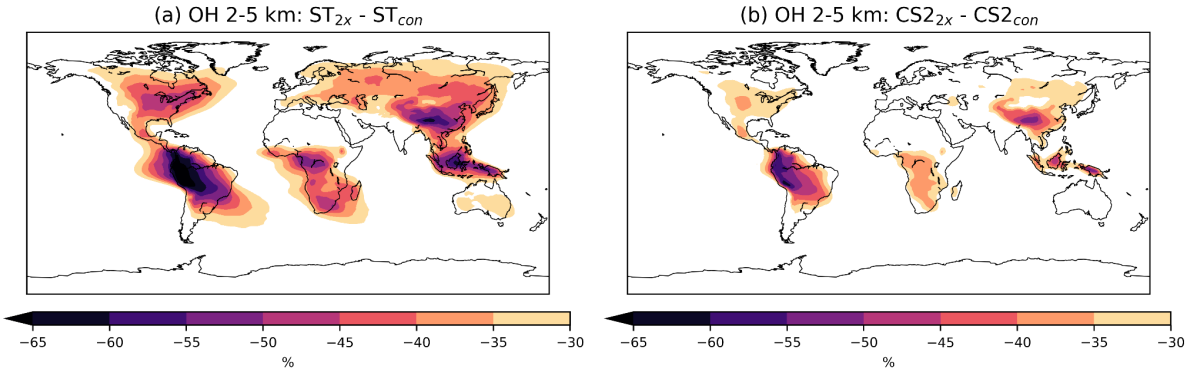


Figure C4. Difference in OH between 2 and 5 km for (a) ST$_\Delta$ and and (b) CS2$_\Delta$.

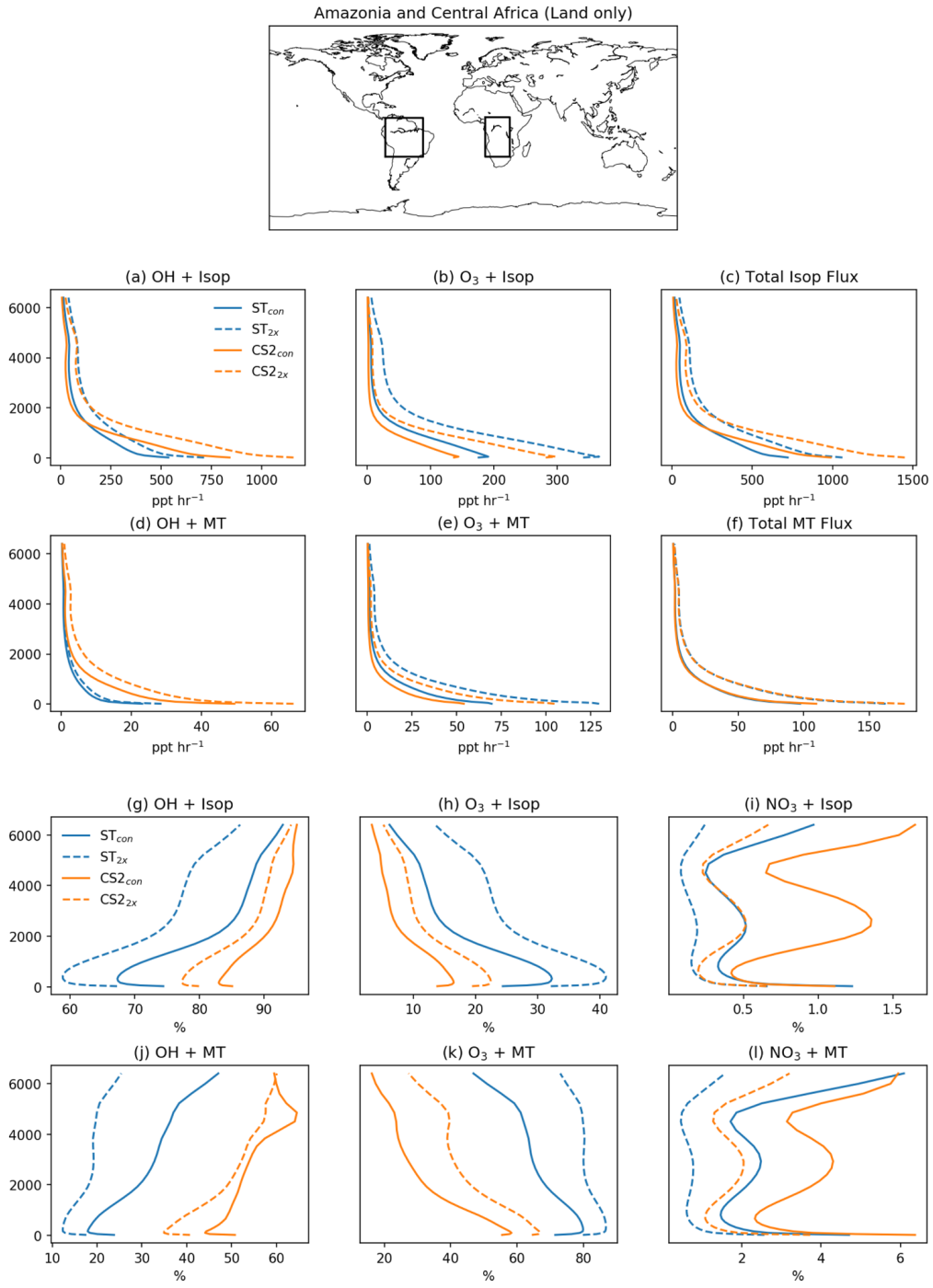


Figure C5. (Top) Map plot indicating regions considered as Amazonia and Central Africa (only grid cells over land were considered for analysis). Absolute fluxes for OH, O_3 and NO_3 oxidation of isoprene and monoterpenes with altitude over Amazonia (a-f). Percentage of total isoprene and monoterpene oxidation flux contributed by each oxidation pathway over Amazonia (g-l).

Table C1. Primary Organic Aerosol, Black Carbon Aerosol and Sea Salt aerosol burdens. Values in parentheses show percentage change in $2xE_{BVOC}$ experiment relative to corresponding control run while values in square brackets show percentage difference between ST_{con} and $CS2_{con}$.

Burden / Tg	ST_{con}	ST_{2x}	$CS2_{con}$	$CS2_{2x}$
POA	0.878	0.806 (-8%)	0.879 [+0.01%]	0.801 (-8.6%)
BC	0.072	0.067 (-7.1%)	0.073	0.067 (-7.3%)
SS	7.51	7.44 (-0.9%)	7.49 [-0.1%]	7.49 (-0.07%)

Table C2. SOA mode burdens. Values in parentheses show percentage difference in $2xE_{BVOC}$ experiment relative to corresponding control run and values in square brackets show percentage difference between ST_{con} and $CS2_{con}$.

Tg	ST_{con}	ST_{2x}	$CS2_{con}$	$CS2_{2x}$
Nucleation (SOA_{nuc})	0.00152	0.00137 (-9%)	0.00145 [-4%]	0.00133 (-9%)
Aitken (SOA_{ait})	0.175	0.346 (+97%)	0.123 [-30%]	0.236 (+91%)
Accumulation (SOA_{acc})	0.344	0.806 (+134%)	0.343 [-0.3%]	0.766 (+123%)
Coarse (SOA_{coa})	0.0032	0.008 (+141%)	0.003 [-9%]	0.007 (+120%)

Table C3. SO4 aerosol mode burdens. Values in parentheses show percentage difference in $2xE_{BVOC}$ experiment relative to corresponding control run and values in square brackets show percentage difference between ST_{con} and $CS2_{con}$.

Tg	ST_{con}	ST_{2x}	$CS2_{con}$	$CS2_{2x}$
Nucleation	0.0078	0.0048 (-38%)	0.0055 [-30%]	0.0034 (-38%)
Aitken	0.284	0.210 (-26%)	0.185 [-35%]	0.148 (-20%)
Accumulation	0.530	0.537 (+1.6%)	0.365 [-31%]	0.361 (-1%)
Coarse	0.0071	0.006 (-11%)	0.006 [-11%]	0.006 (-4%)

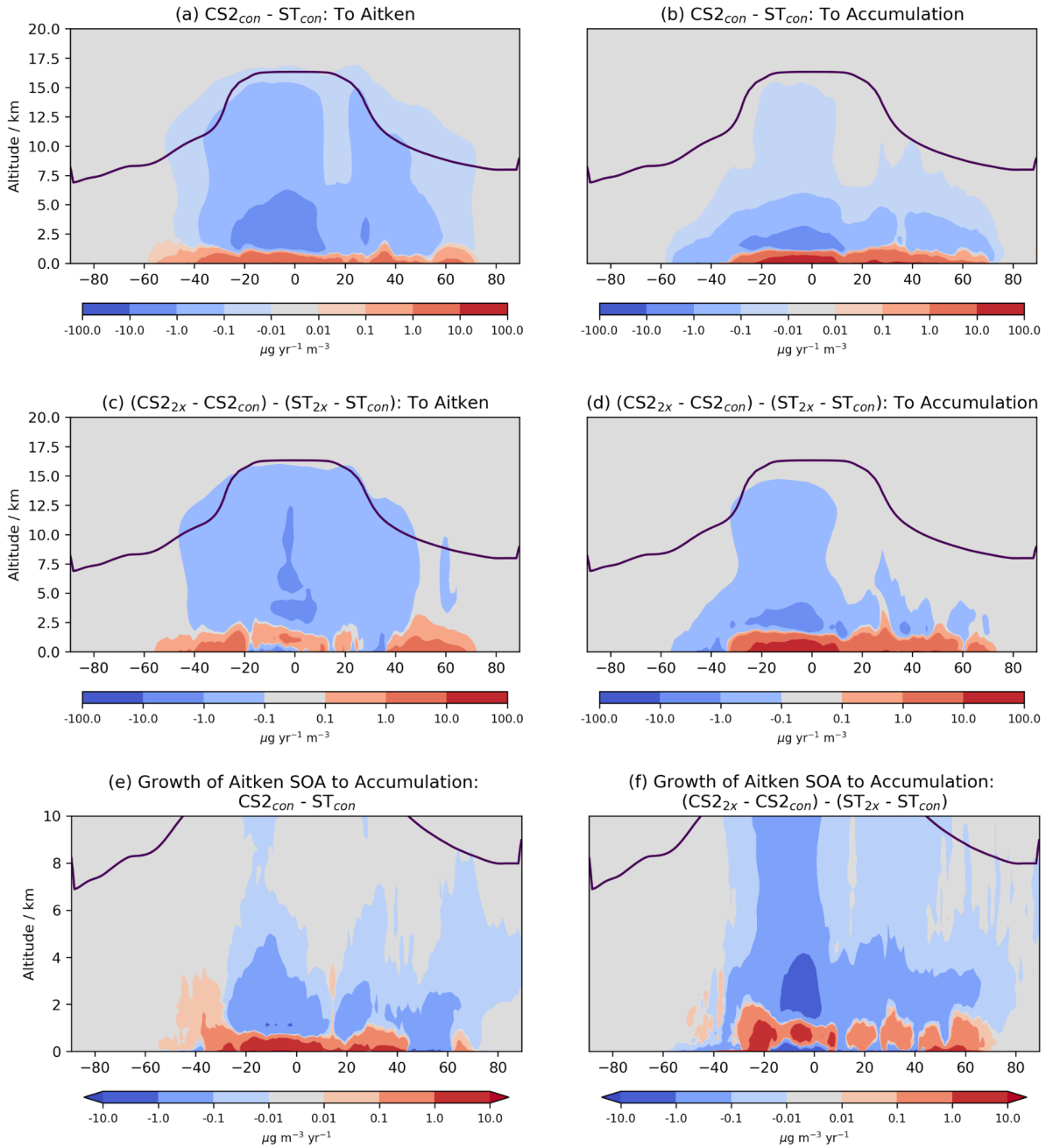


Figure C6. Zonal mean difference in condensational flux of Sec_Org between ST$_{con}$ and CS2$_{con}$ to (a) Aitken mode and (b) accumulation mode particles. Zonal mean difference in condensational flux of Sec_Org between ST$_{\Delta}$ and CS2$_{\Delta}$ to (c) Aitken mode and (d) accumulation mode particles. Zonal mean difference in growth of Aitken mode particles to accumulation particles between (e) ST$_{con}$ and CS2$_{con}$ and (f) ST$_{\Delta}$ and CS2$_{\Delta}$. (Note logarithmic scales)

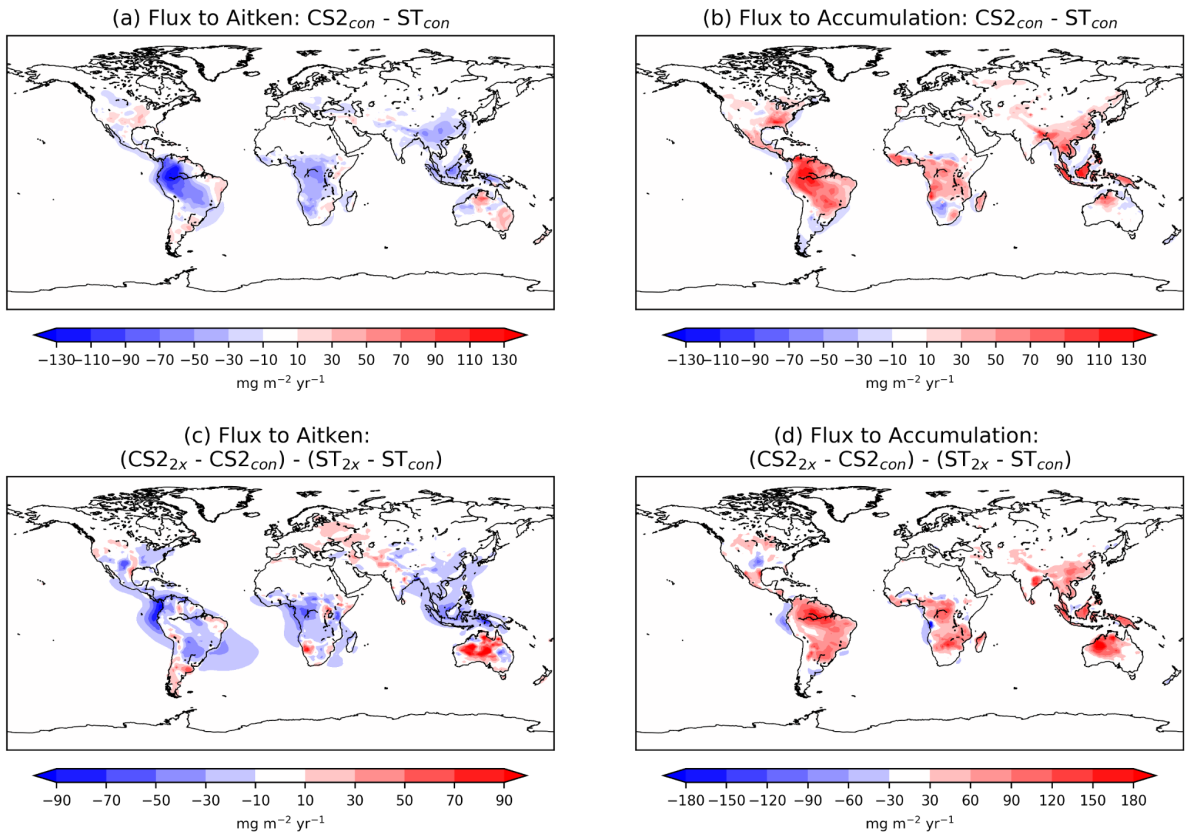


Figure C7. Difference in column condensational flux to (a) Aitken mode and (b) accumulation mode between ST_{con} and $CS2_{con}$. Difference in column condensational flux to (a) Aitken mode and (b) accumulation mode between ST_{Δ} and $CS2_{\Delta}$.

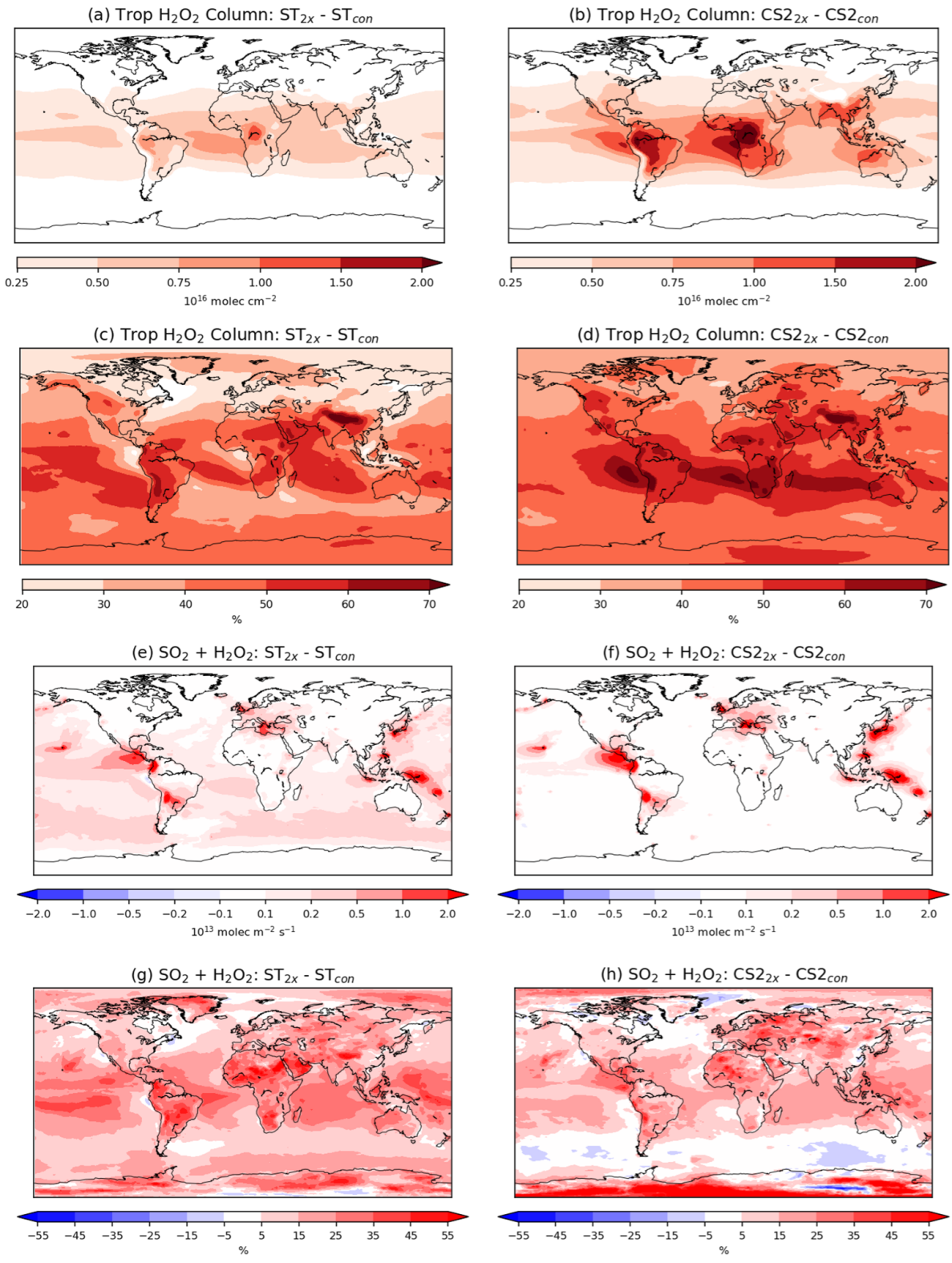


Figure C8. Absolute (a,b) and percentage changes (c,d) in H2O2 tropospheric column in response to $2xE_{BVOC}$ for ST and CS2. Absolute (e,f) and percentage (g,h) changes in SO2 + H2O2 column flux for ST_{Δ} and $CS2_{\Delta}$.

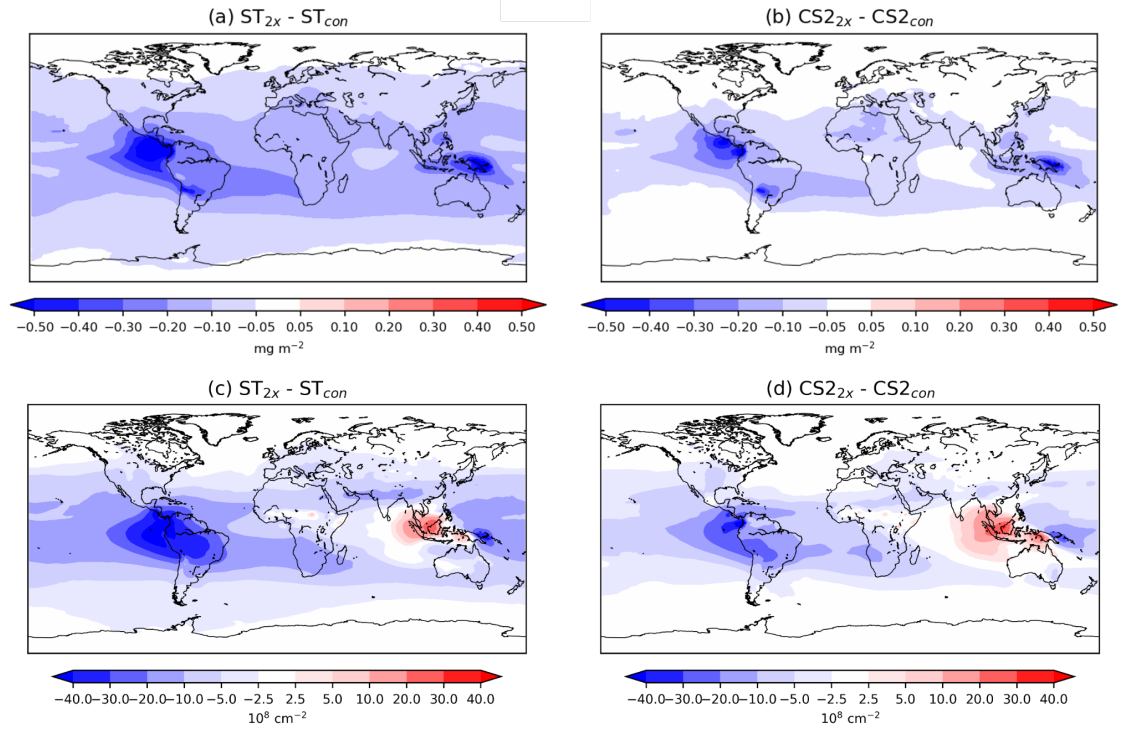


Figure C9. Change in SO4 Aitken mode column for (a) ST_{Δ} and (b) $CS2_{\Delta}$ and total Aitken mode number concentration column for (c) ST_{Δ} and (d) $CS2_{\Delta}$.

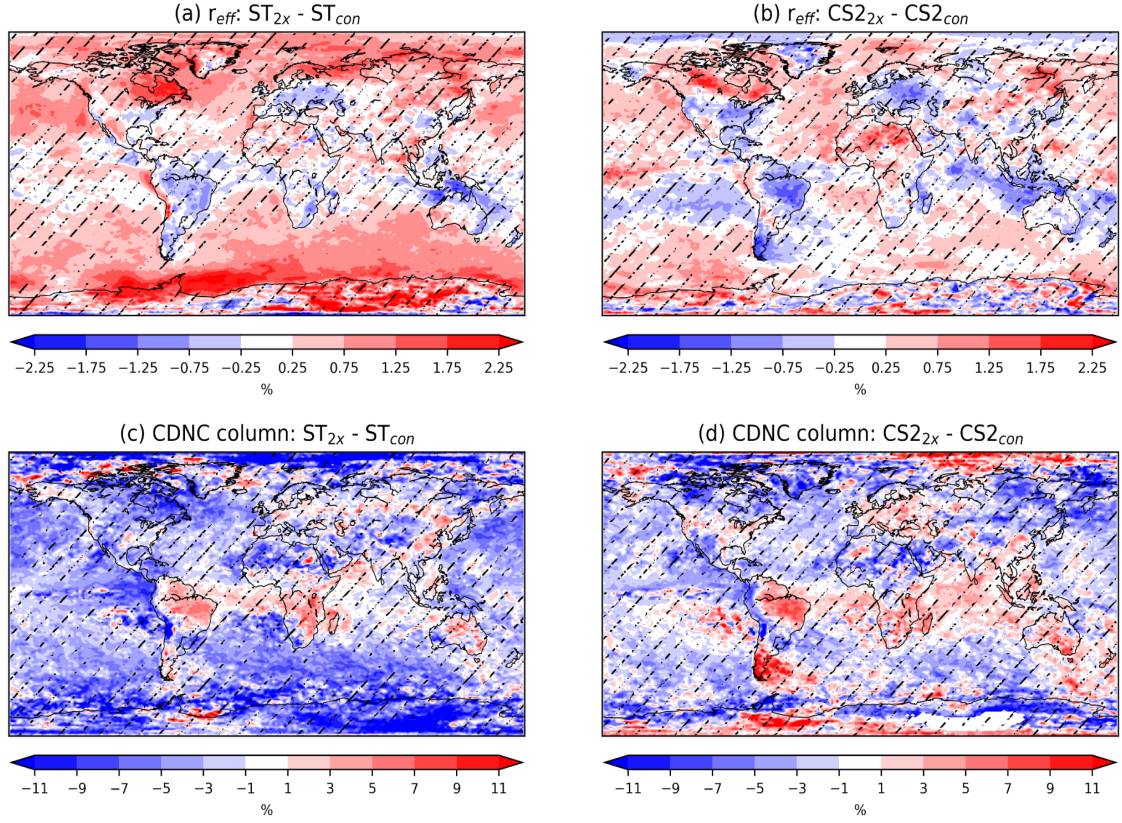


Figure C10. Percentage change in (a, b) cloud droplet effective radius (r_{eff}) and (c, d)CDNC column for ST_{Δ} and $CS2_{\Delta}$. Hatching shows regions which are statistically significant at the 95% confidence level.

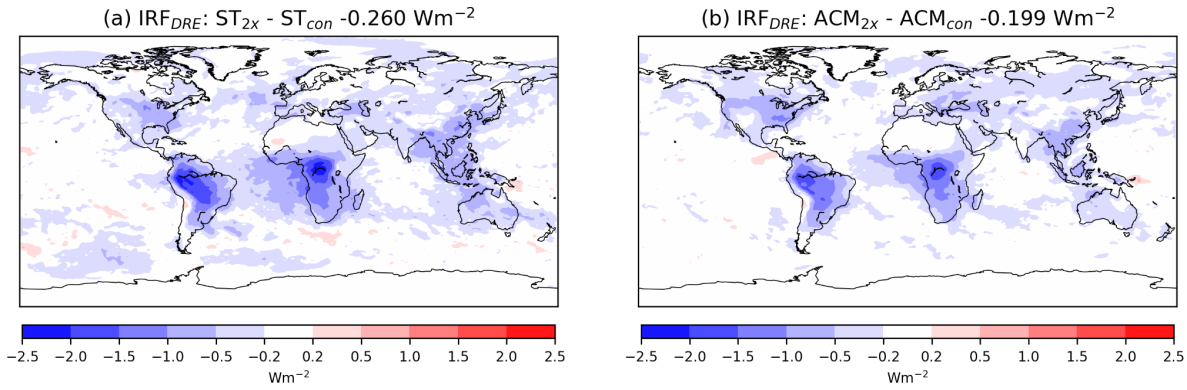


Figure C11. IRF$_{DRE}$ forcing for (a) ST$_{\Delta}$ and (b) ACM$_{\Delta}$.

Appendix D

This appendix corresponds to Chapter 4 and comprises the supplementary information of the corresponding published paper (ACP; Weber et al., 2020).

Supplementary Information: CRI-HOM: A novel chemical mechanism for simulating Highly Oxygenated Organic Molecules (HOMs) in global chemistry-aerosol-climate models.

Table D1. Summary of RO_2-RO_2 rate coefficients

Reaction	Rate Coefficient / cm^3 $molecules^{-1}$ s^{-1}	Reference	Comments
All O3RO2 + $RO2_b$ = 0.5 C20d	$0.97 - 3.6 \times 10^{-11}$ (See full reaction list)	Berndt et al., 2018b	Derived from data from Berndt et al., 2018b
All OHRO2 + $RO2_b$ = 0.5 C20d	$0.4 - 3.5 \times 10^{-11}$ (See full reaction list)	Berndt et al., 2018b	Derived from data from Berndt et al., 2018b
All O3RO2 + $RO2_b$ = C10x/CARB16	1.68×10^{-12}	Molteni et al., 2019	
All O3RO2 + $RO2_b$ = Closed shell + peroxy radical	1.68×10^{-12}	Molteni et al., 2019 Jenkin et al., 2019a	
RN26BO2 + $RO2_m$, $RO2_s$ = C10x/TNCARB26	8.3×10^{-13}	Jenkin et al., 2019a*	Weighted average of rate coefficients
RTN28AO2 + $RO2_b$, $RO2_m$, $RO2_s$ = Closed shell	5.9×10^{-13}	MCM	Weighted average of RO2 rate coefficients for species APINAO2 and APINBO2
RTN28BO2 + $RO2_m$, $RO2_s$ = Closed shell + peroxy radical	6.70×10^{-15}	MCM	MCM value for species APINCO2
2nd – 5th gen O3RO2 + $RO2_m$, $RO2_s$ = Closed shell + peroxy radical	$5 \times 10^{-12} – 1 \times 10^{-11}$ (See full reaction list)	Roldin et al., 2019	Increases with increasing O3RO2 functionality
2nd – 5th gen OHRO2 + $RO2_b$, $RO2_m$, $RO2_s$ =	$5 \times 10^{-12} – 1 \times 10^{-11}$ (See full reaction list)	Roldin et al., 2019	Increases with increasing OHRO2 functionality

Closed shell + peroxy radical			
All O3RO2 + $RO2_m$ = C15d	**3.9 - 7.5× 10^{-12} (See full reaction list)**	**Berndt et al., 2018b**	**Based on Berndt et al, then fitted to data**
All OHRO2 + $RO2_m$ = C15d	**1.8 - 3.75 × 10^{-12} (See full reaction list)**	**Berndt et al., 2018b**	**Based on Berndt et al, then fitted to data**

* The rate coefficient for the production of the closed shell and alkoxy radical from reaction of the first generation O3RO2 species, RN26BO2, with $RO2_m$ and $RO2_s$ was taken to be the average of the rate coefficients of the three actual species (C107O2, C109O2 and C10BO2 using the notation of Molteni et al (2019)), weighted by the branching ratio of their production. The rate coefficients for C107O2, C109O2 and C10BO2 were calculated using the methodology of Jenkin et al (2019a).

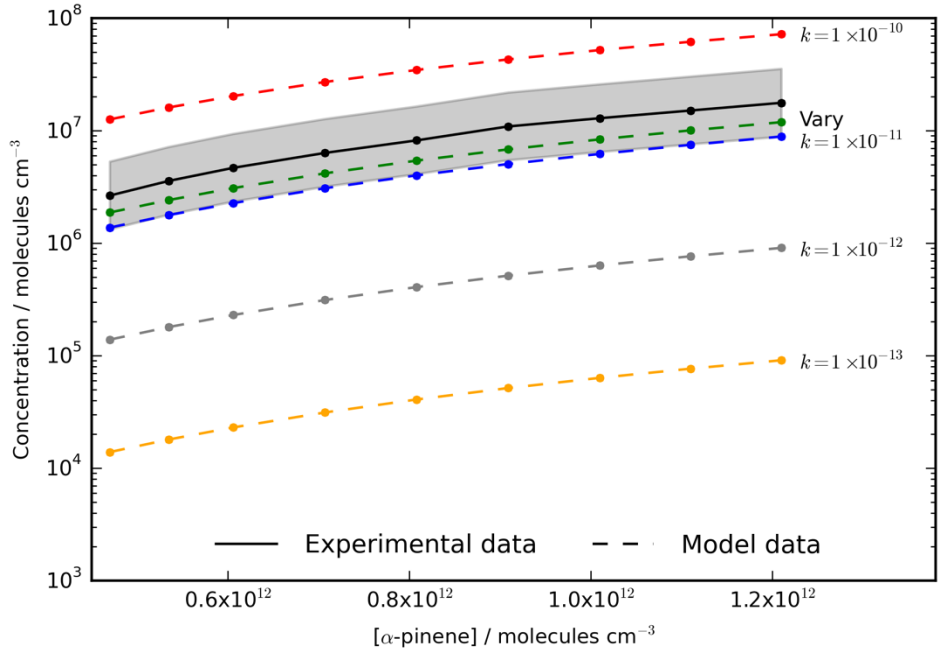


Figure D1. Effect of C20d formation rate coefficient on model performance compared to observations from Berndt et al (2018b) under varying initial conditions of α-pinene (Simulation A, Table 4.3). The model was able to reproduce observed concentrations within experimental error (shaded region) here and in Fig 4.5 when the rate coefficients were increased with increasing peroxy radical functionalisation (line marked "Vary"). The lines with k= 1×10^{-10}, 1×10^{-11}, 1×10^{-12} and 1×10^{-13} show model performance when the specified rate coefficient (in units of cm^3 $molecules^{-1}$ s^{-1}) was used for all O3RO2 and OHRO2. The simulations with accretion formation rate coefficients suggested by Roldin et al (2019) (~ 10^{-13}-10^{-12} cm^3 $molecules^{-1}$ s^{-1}) produced significantly lower C20d concentrations while using rate coefficients suggested by Molteni et al (2019) (≥ 10^{-10} cm^3 $molecules^{-1}$ s^{-1}) overpredicted C20d concentrations.

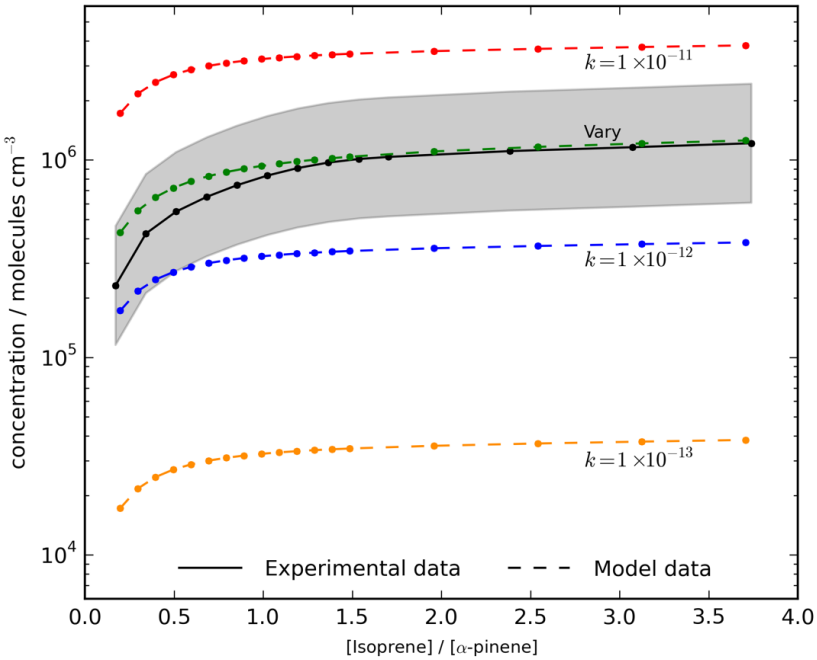


Figure D2. Effect of C15d formation rate coefficient on model performance compared to observations from Berndt et al (2018b) under conditions of fixed initial α-pinene concentration and varying initial isoprene concentration (Simulation B, Table 4.3). The model was able to replicate the general trend of increasing C15d with isoprene when the rate coefficients were increased with increasing peroxy radical functionalisation (line marked "Vary"), reproducing observation within experimental error (shaded region). The lines with k=1×10^{-11}, 1×10^{-12} and 1×10^{-13} show model performance when the specified rate coefficient (in units of cm^3 molecules^{-1} s^{-1}) was used for all O3RO2 and OHRO2.

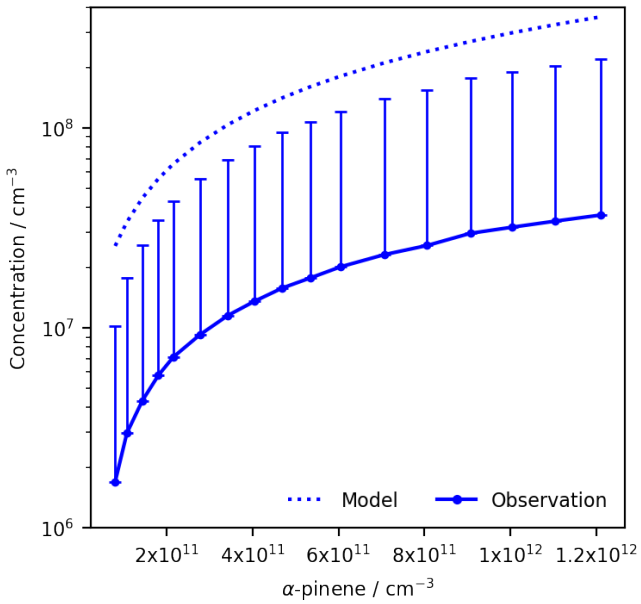


Figure D3. 1st generation OHRO2 observation (Berndt et al., 2018b) and modelled with estimated experimental underprediction of factor of 5. Reasons for observation-model discrepancy are discussed in the main text.

Table D2. Summary of HOM mechanisms and autoxidation activation energies

Mechanism	Autoxidation Activation Energy / K	Comments
HOM_{TI}	N/A - temperature independent	Autoxidation coefficients based on fitting from data from Berndt et al (2018b) at 297K
HOM_{6000}	6000	Representing possible lower bound of activation energy
HOM_{9000}	9000	Representing possible middle value of activation energy
HOM_{12077}	12077	Value suggested by Roldin et al (2019)

HOM Yield Equations

The yields for 10-carbon HOMs from ozonolysis (γ_{C10z}), OH oxidation (γ_{C10x}) and the total HOM yield (γ_{total}) are given by Eq. D1, Eq. D2 and Eq. D3 respectively.

$$\gamma_{C10x} = \frac{[C10x](k_{OH+HOM}+CS+J)}{k_{OH}[OH][AP]} \quad \text{(D1)}$$

$$\gamma_{C10z} = \frac{[C10z](k_{OH+HOM}+CS+J)}{k_{O_3}[O_3][AP]} \quad \text{(D2)}$$

$$\gamma_{total} = \frac{([C10z]+[C10x])(k_{OH+HOM}+CS+J)}{\left(k_{O_3}[O_3]+k_{OH}[OH]\right)[AP]} \quad \text{(D3)}$$

where $[O_3]$, $[OH]$, $[C10z]$ and $[C10x]$ are the concentrations of O_3, OH and the 10-carbon HOMs formed from ozonolysis and OH oxidation respectively, k_{OH+HOM} is the rate coefficient for the reactions of HOMs with OH, CS is the HOM condensation sink, J is the HOM photolysis frequency and k_{O_3} and k_{OH} are the reaction rate coefficients of α-pinene with O_3 and OH respectively.

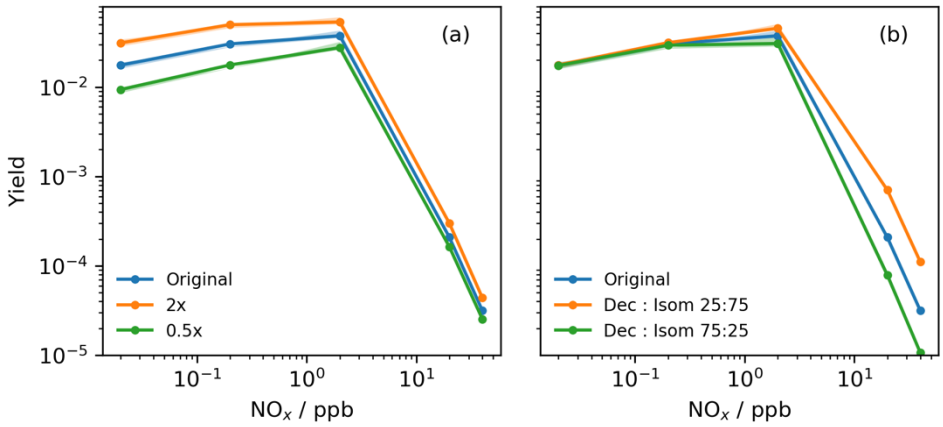


Figure D4. Modelled HOM yield at 290 K showing with (a) scaling of k14, k15 rate coefficients and (b) perturbations of the alkoxy decomposition-isomerisation branching ratio (originally 50:50).

Comparison to CRI v2.2

The new mechanism and the CRI v2.2 were run in a box model (Simulation D, Table 4.3) for 8 days with varying temperature (298 K average, amplitude of 4 K) and emissions of isoprene and α-pinene varying sinusoidally (Fig D3). Time-independent base NO emissions of 4.7×10^{9} molecules m^{-2} s^{-1} were used with scaling factors of 1, 3, 10, 30, 100 and 200 employed in a manner consistent with Jenkin et al (2015). Time dependent isoprene emissions reached a maximum of $1.1\text{x}10^{12}$ molecules m^{-2} s^{-1} at 13:00 local time and had an average of $7.1\text{x}10^{11}$ molecules m^{-2} s^{-1} over the period 06:00 to 18:00, similar to emissions used in Jenkin et al (2015) and Bates et al (2019). Time dependent base α-pinene emissions with a mean of $3.23\text{x}10^{9}$ molecules m^{-2} s^{-1} and maximum of $5.30\text{x}10^{9}$ molecules m^{-2} s^{-1} at 1500 hours were applied. Further runs were performed with α-pinene emissions scaled by factors of 10^{-3}, 10^{-2}, 0.1, 0.2, 0.5, 1, 2, 3 and 5 to investigate the model's performance. Initial conditions of CH_4 (1.8 ppm), CO (100 ppb), O_3 (20 ppb) and HCHO (300 ppt) were applied.

Photolysis frequencies simulating conditions at the equator also varied in the diurnal cycle. The box model simulated an instantaneously well-mixed planetary boundary with mixing with the free troposphere (with same composition of initial conditions) represented by the box height increasing from 250 m at night to 1500 m at midday before collapsing back to 250 m at 2100 hours.

The "concentration" of a species was taken to be the mean daytime concentration on the 8th day, the metric used by Jenkin et al (2015) and Bates et al (2019). The performance of all the HOM mechanisms (HOM_{TI}, HOM_{6000}, HOM_{9000} and HOM_{12077}) was compared to the CRI v2.2.

The HOM mechanisms matched the CRI extremely well for OH, O_3, NO, NO_2, HO_2, α-pinene and isoprene as well as the hydroperoxides and nitrates derived from isoprene, methyl vinyl ketone and methacrolein, and the important SOA precursor isoprene epoxy diol (IEPOX)).

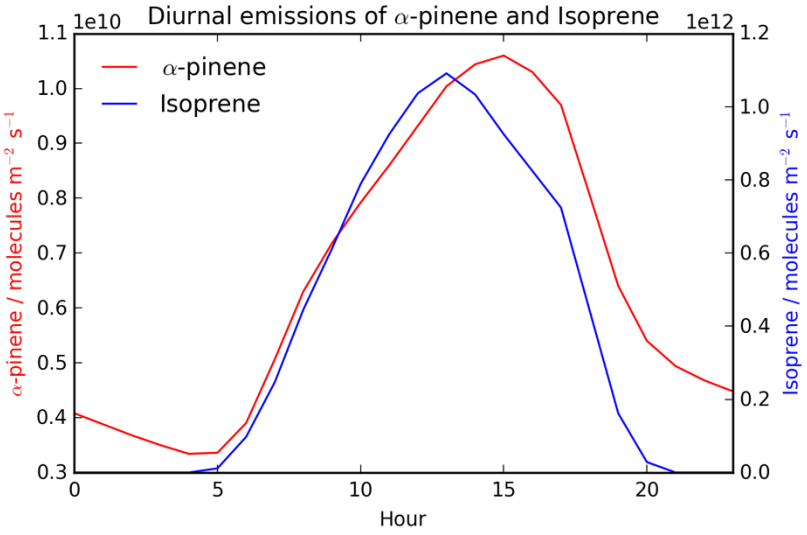


Figure D5. Diurnal cycle of emissions of α-pinene and isoprene for 8-day comparison of CRI v2.2 R5 with HOM mechanism versions.

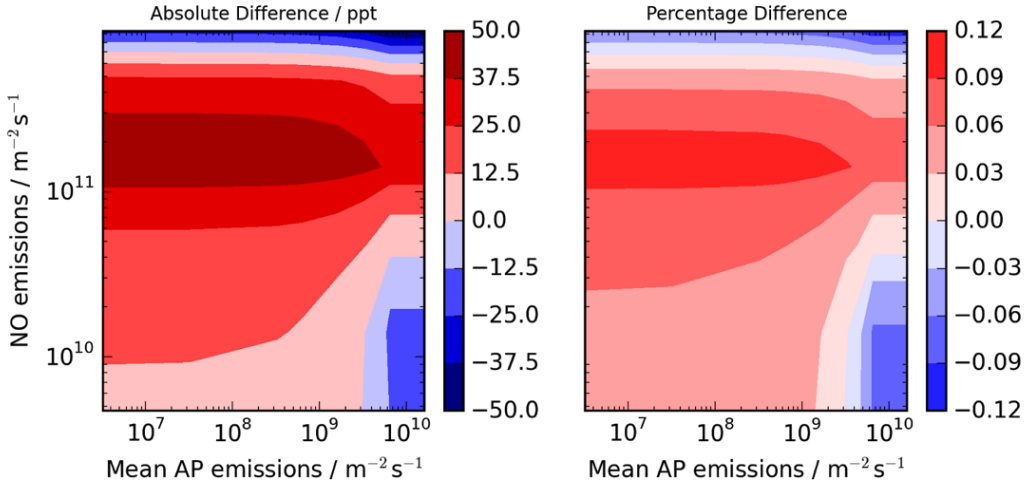


Figure D6. Absolute and percentage difference in 8th day daylight mean O_3 between the CRI v2.2 R5 and the HOM_{9000} mechanism. The difference between mechanisms is less than ±0.05 ppb.

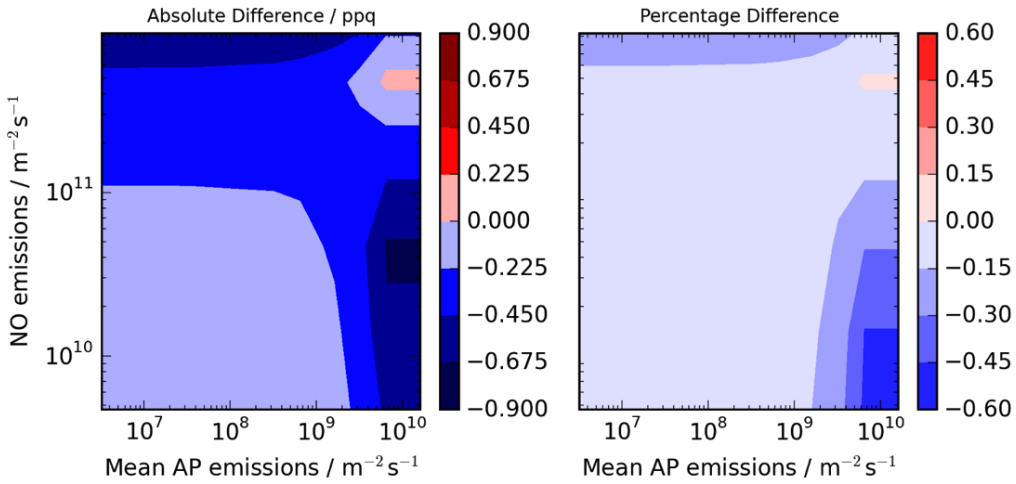


Figure D7. Absolute and percentage difference in 8th day daylight mean OH between the CRI v2.2 R5 and the HOM_{9000} mechanism. The difference between mechanisms is less than ±0.3% for the vast majority of the emissions space with the difference exceeding this only under very high emissions of α-pinene.

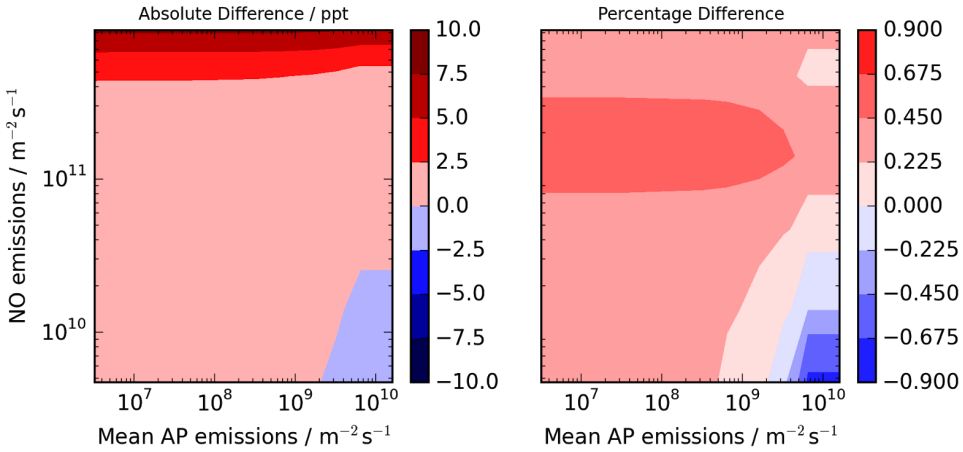


Figure D8. Absolute difference in 8th day daylight mean NO between the CRI v2.2 R5 and the HOM_{9000} mechanism. The difference between mechanisms is less than ±2.5 ppt for the vast majority of the emissions space with the difference exceeding this only under very high emissions of NO and α-pinene.

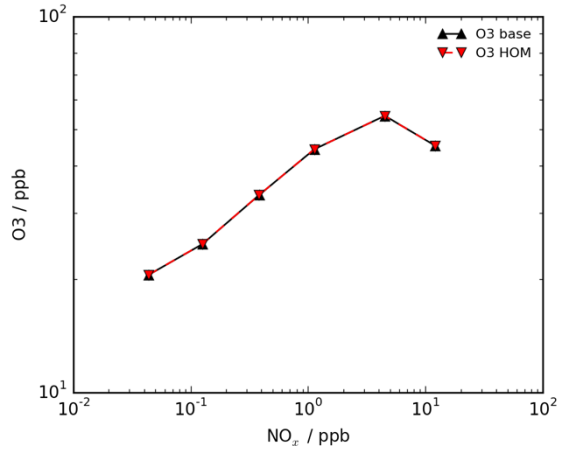


Figure D9. 8th day daylight mean O_3 in CRI v2.2 R5 and HOM_{9000} model

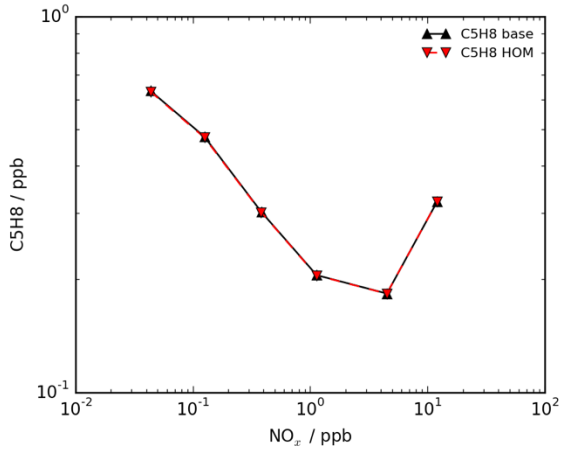


Figure D10. 8th day daylight mean isoprene in CRI v2.2 R5 and HOM_{9000} model

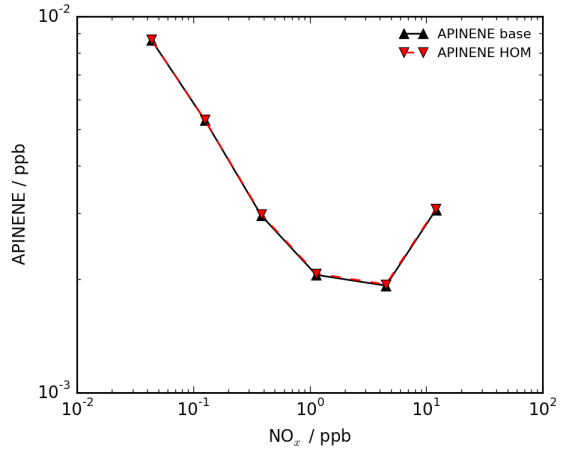


Figure D11. 8th day daylight mean α-pinene in CRI v2.2 R5 and HOM_{9000} model

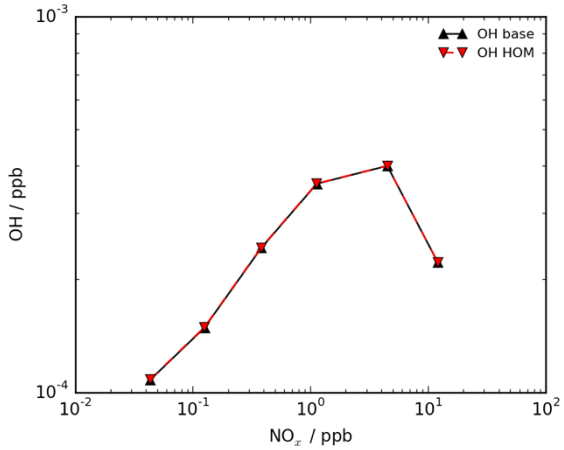


Figure D12. 8th day daylight mean OH in CRI v2.2 R5 and HOM$_{9000}$ model

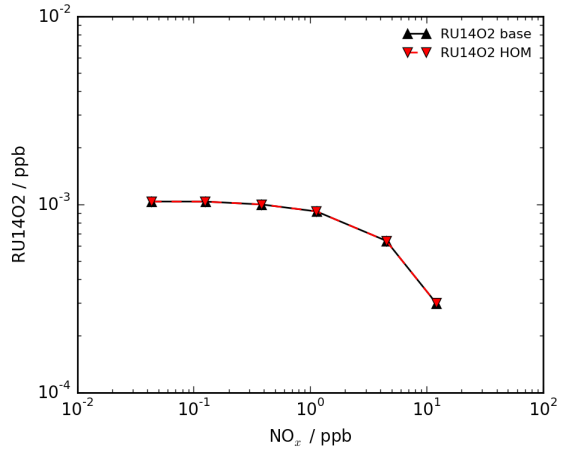


Figure D13. 8th day daylight mean 1st generation isoprene peroxy radical in CRI v2.2 R5 and HOM$_{9000}$ model

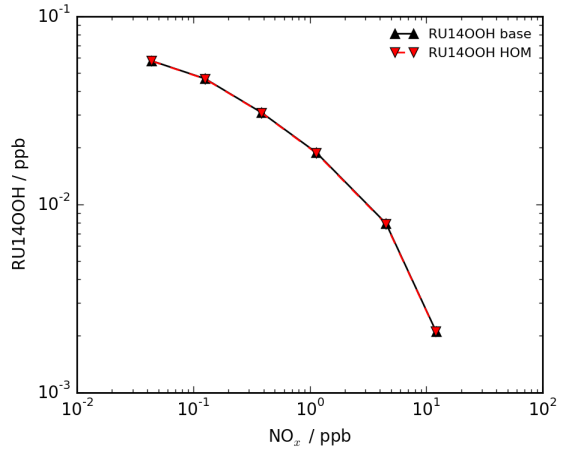


Figure D14. 8th day daylight mean 1st generation isoprene hydroperoxide in CRI v2.2 R5 and HOM$_{9000}$ model

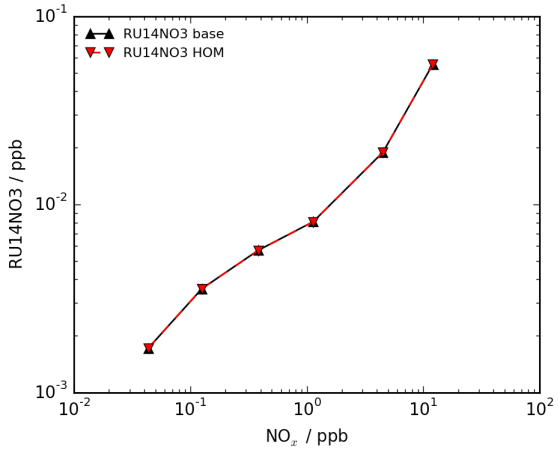


Figure D15. 8th day daylight mean 1st generation isoprene nitrate in CRI v2.2 R5 and HOM$_{9000}$ model

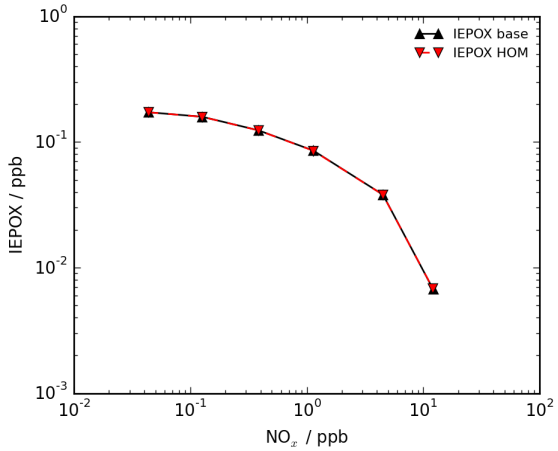


Figure D16. 8th day daylight mean isoprene epoxydiol in CRI v2.2 R5 and HOM$_{9000}$ model

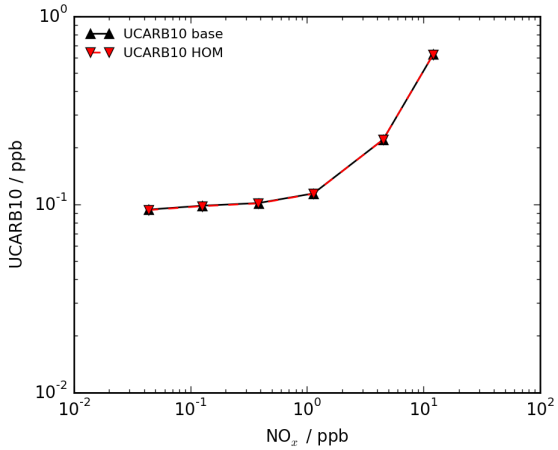


Figure D17. 8th day daylight mean combined methyl vinyl ketone and methacrolein in CRI v2.2 R5 and HOM$_{9000}$ model

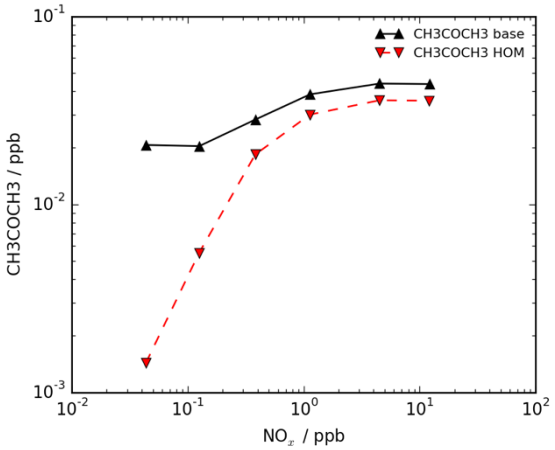


Figure D18. 8th day daylight mean combined acetone in CRI v2.2 R5 and HOM$_{9000}$ model. The difference was attributed to the added competition supplied by the autoxidation pathways, diverting the degradation of α-pinene away from the traditional pathways which form acetone. However, this discrepancy between mechanisms did not led to significant disagreement between the HOM mechanism and CRI v2.2 R5 for O_3 and OH concentrations.

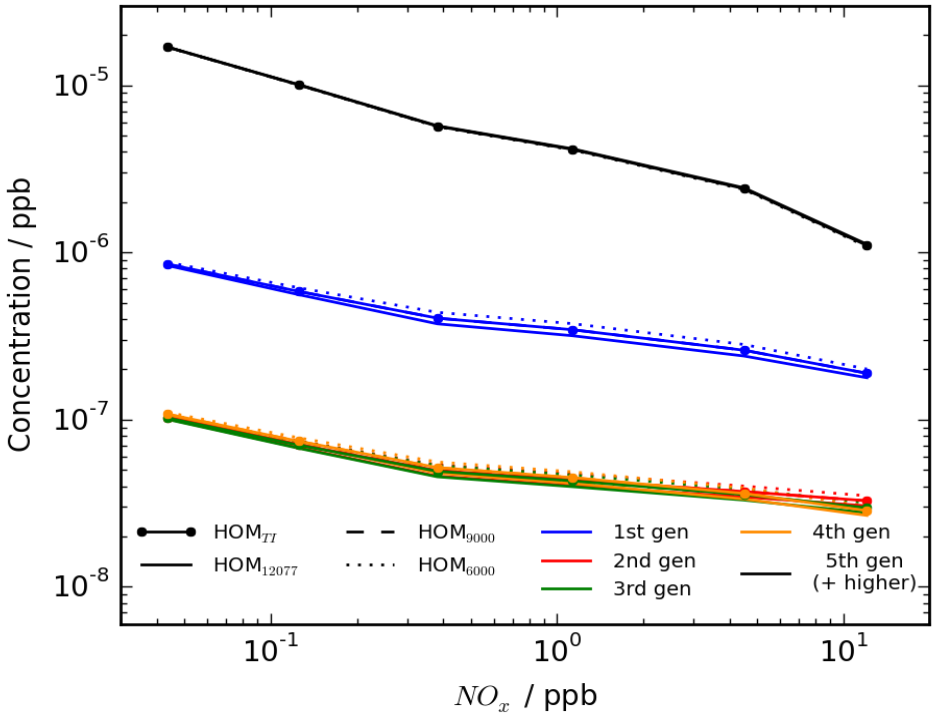


Figure D19. Peroxy radicals from ozonolysis (O3RO2) exhibiting a decrease with NO_x and the clear dominance of the highest generation peroxy radical. Negligible difference is observed between the 4 HOM mechanisms for each peroxy radical.

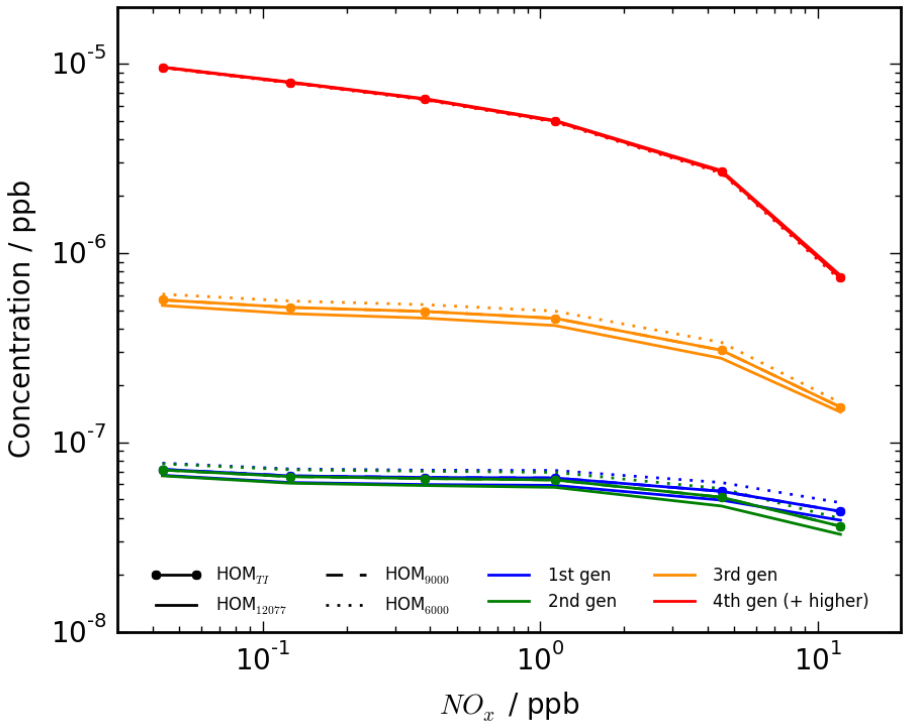


Figure D20. Peroxy radicals from OH oxidation (OHRO2) exhibiting a decrease with NO_x and the clear dominance of the highest generation peroxy radical. Negligible difference is observed between the 4 HOM mechanisms for each peroxy radical.

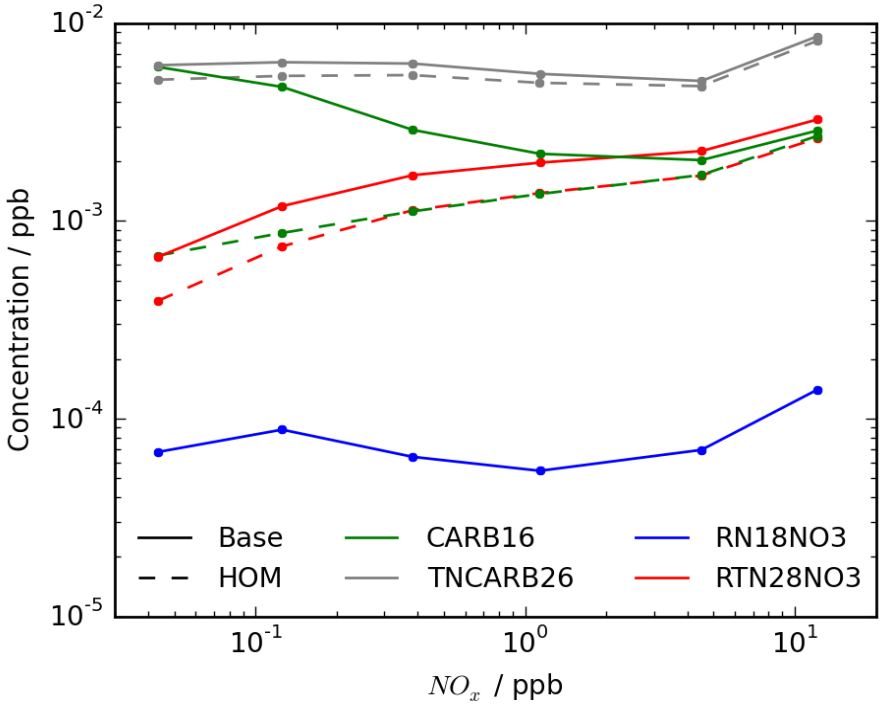


Figure D21. Closed shell species in base mechanism compared to HOM_{TI} mechanism. The lower concentrations of TNCARB26, CARB16 and RTN28NO3 were attributed to the increased competition from the autoxidation pathways in the HOM mechanism. RN18NO3 was significantly lower in the HOM mechanisms (not shown) as discussed in the main text.

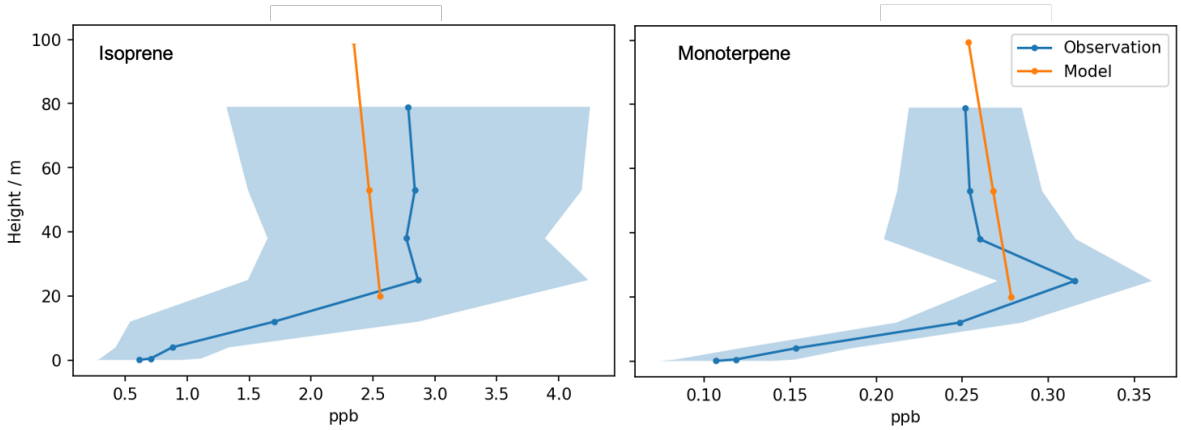


Figure D22. Observed concentrations of isoprene (left) and monoterpene (right) at the ATTO tower at 1:30-2:30 pm in June 2013 (Yáñez-Serrano et al., 2015) (shading shows standard deviation of observational data) and modelled concentrations of species.

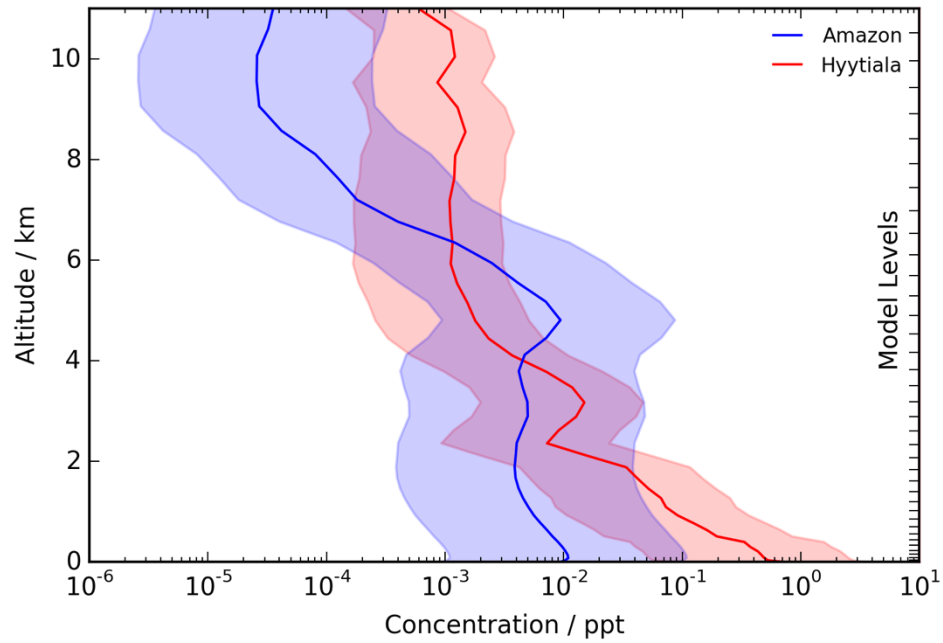


Figure D23. Total HOM concentrations in Amazon and Hyytiala with shaded region showing the effect of increasing/decreasing CS by a factor of 10. The value of the CS has a significant influence on HOM concentrations.

Table D3. Species and physical parameters used in the HOM altitude profile modelling. Note that for nucleation calculations, the same input species and parameters were used but all data were monthly means.

Data from UKCA run (2pm 16th June, averaged over 2010-2104)	**Data from UKESM Historical**
Temperature, pressure, O_3, OH, isoprene, monoterpene*, NO, NO_2, NO_3, N_2O_5, CO, HO_2, H_2O	CH_4, CO, HCHO, CH_3O_2, $C_2H_5O_2$, isoprene nitrate and hydroperoxides, H_2O_2, CH_3OOH, HONO, C_2H_6, C_2H_5OOH, CH_3CHO, PAN, C_3H_8, C_3H_7OOH, C_2H_5CHO, CH_3NO_3, Methacrolein, Methylglyoxal, HCOOH, CH_3CO_3, $C_3H_7O_2$, $C_2H_5CO_3$, CH_3OH

* The modelled monoterpene concentration was halved to approximate the α-pinene concentration (Rinne et al., 2002)

Table D4. Values of surface level CS and local time of run used for HOM altitude profiles (Lee et al., 2016)

	Location		
	Hyytiala	**Manaus**	**Brent, Alabama**
CS / s^{-1}	0.004	0.9	0.012 ± 0.006
Local time	14:00	14:00	12:00

Nucleation Parameterisations

The rates of neutral and ion-induced pure biogenic nucleation (J_n and J_{iin} respectively) are described by the parameterisations (Kirkby et al (2016)) in Eq. D4 and Eq. D5:

$$J_n = a_1[HOM]^{a_2+\frac{a_5}{[HOM]}} \text{ (D4)}$$

$$J_{iin} = a_3[HOM]^{a_4+\frac{a_5}{[HOM]}}[n_{\pm}] \text{ (D5)}$$

Where $a_i$are fitted parameters and $[n_{\pm}]$ the concentration of ions calculated by method described Kirkby et al (2016). In this work, no distinction was made between the different HOM species; the [HOM] term was taken as the sum of all HOM species. In reality, the larger accretion products are likely to be better at nucleating due to their lower volatility and even among 10-carbon HOMs, more oxidised species will also be more proficient at new particle formation. The condensation sink for ions was calculated by summing over aerosol modes and (Eq. D6).

$$CS = \frac{2kT\mu}{e}\sum(wd \times c) \times 10^6 \text{ (D6)}$$

Where k is the Boltzmann constant, T temperature (in Kelvin), μ=1.2 x 10^{-4} m^2 V^{-1} s^{-1}, e =1.6022 x 10^{-19} C, wd is the wet diameter (in m) of the aerosol mode and c the mode's particle concentration (per cm^3) (wd and c were taken from UKCA run).

The ion loss rate, X, was then calculated as the sum of the condensation and nucleation sinks (Eq. D7).

$$X = CS + a_3[HOM]^{a_4+\frac{a_5}{[HOM]}} \text{ (D7)}$$

The recombination coefficient, α, is given by Eq. D8:

$$\alpha = 6 \times 10^{-8} \sqrt{\frac{300}{T}} + 6 \times 10^{-26} c_{air} \left(\frac{300}{T}\right)^4 \text{ (D8)}$$

Where c_{air} is the concentration of air in molecules per cm^3.

$$[n_{\pm}] = \frac{\sqrt{(X^2 - 4\alpha q)} - X}{2\alpha} \text{ (9D)}$$

Where q is the rate of ion-pair production in cm^{-3} s^{-1}.

The sulphuric acid activation parameterisation used was that developed by Kulmala et al (2006) with coefficient from Sihto et al (2006) as used by Scott et al (2014) (Eq. 10).

$$J_{act} = A[H_2SO_4] \text{ (D10)}$$

Where A=2x10^{-6} s^{-1}

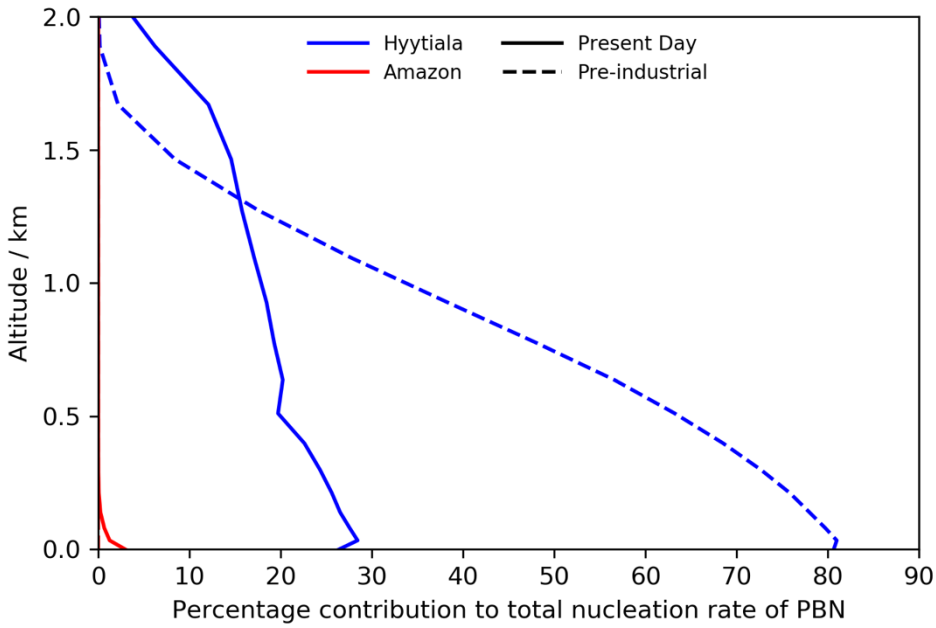


Figure D24. Percentage contribution to total nucleation rate (PBN + SA$_{act}$) of PBN. Significant increase is predicted for the PI Hyytiala case in particular, indicating the important implications of including PBN in climate models.

Changes to CRI v2.2 R5 mechanism

Simple rate coefficients (e.g. kRO2NO) and photolysis frequencies (e.g. J41) were taken from CRI (Jenkin et al., 2008, Jenkin et al., 2019b). Unless otherwise stated, unimolecular rate coefficients have units of s^{-1}. The peroxy radical pools (RO2$_b$, RO2$_m$, RO2$_s$ and RO2) represent the total concentration of peroxy radicals falling within the respective pool. In the mechanism used in modelling, certain reactions were lumped together with product fractions weighted by relative rate coefficients to reduce the total number of reactions. For clarity, reactions have been decomposed below. The autoxidation coefficients provided are those fitted at 297 K. Table D5 shows the expressions for the autoxidation coefficients in the 3 temperature dependent mechanisms.

The standard reactions rate coefficients used by the CRI are as follows:

KRO2NO = 2.7D-12*EXP(390/TEMP)

KRO2HO2 = 2.91D-13*EXP(1300/TEMP)

KRO2NO3 = 2.3D-12

Reactions removed from CRI v2.2 R5 mechanism

Ozonolysis of alpha pinene and treatment of resulting peroxy radical RN18AO2

APINENE + O3=OH+CH3COCH3+RN18AO2 : 8.05D-16*EXP(-640/TEMP)*0.80 ;

APINENE + O3 = TNCARB26 + H2O2 : 8.05D-16*EXP(-640/TEMP)*0.175 ;

APINENE + O3 = RCOOH25 : 8.05D-16*EXP(-640/TEMP)*0.025 ;

RN18AO2 + NO = CARB16 + HO2 + NO2 : KRO2NO*0.946 ;

RN18AO2 + NO = RN18NO3 : KRO2NO*0.054 ;

RN18AO2 + NO3 = CARB16 + HO2 + NO2 : KRO2NO3 ;

RN18AO2 + HO2 = RN18OOH : KRO2HO2*0.770 ;

RN18AO2 = CARB16 + HO2 : 8.80D-13*RO2 ;

OH oxidation of alpha pinene and treatment of resulting peroxy radical RTN28O2

APINENE + OH = RTN28O2 : 1.20D-11*EXP(444/TEMP) ;

RTN28O2 + NO = TNCARB26 + HO2 + NO2 : KRO2NO*0.767*0.915 ;

RTN28O2 + NO = CH3COCH3 + RN19O2 + NO2 : KRO2NO*0.767*0.085 ;

RTN28O2 + NO = RTN28NO3 : KRO2NO*0.233 ;

RTN28O2 + NO3 = TNCARB26 + HO2 + NO2 : KRO2NO3 ;

RTN28O2 + HO2 = RTN28OOH : KRO2HO2*0.914 ;

RTN28O2 = TNCARB26 + HO2 : 2.85D-13*RO2 ;

Reactions added

Ozonolysis of α-pinene producing 1st generation O3RO2, RN26BO2 - branching ratio set to 50% based on experimental observations of Berndt et al (2018b)

1. APINENE + O3 = 0.175TNCARB26 + 0.025RCOOH25 + 0.8OH + 0.5RN26BO2 + 0.3RTN2402: 8.05E-16*EXP(-640/TEMP);

Reactions of RN26BO2

Reaction with HO2 forms hydroperoxide species already in CRI, not a HOM due to insufficient oxygens.

2. RN26BO2 + HO2 = RTN26OOH + O2: KRO2HO2*0.9;

Reaction with NO, NO_3 forms next generation O3RO2 via alkoxy radical isomerisation and fragmentation products (smaller RO2, RN9O2, and closed shell species, CARB16) at 50:50 branching ratio). NO also forms small yield of RN18NO3, estimated from original CRI v2.2 R5.

3. RN26BO2 + NO = 0.025RTN28NO3 + 0.487RN25BO2O2 + 0.487CARB16 + 0.487RN9O2 + 0.975NO2: KRO2NO;

4. RN26BO2 + NO3 = 0.5RN25BO2O2 + 0.5CARB16 + 0.5RN9O2 + NO2 : KRO2NO3 ;

Autoxidation of RN26BO2 to 2nd generation O3RO2, RN25BO2O2

5. RN26BO2 + O2 = RN25BO2O2 : 0.206 ;

Reactions of RN25BO2O2

Reaction with HO2 forms HOM monomer C10z as product has sufficient oxygens. Reaction with NO, NO_3 follows the same principle as RN26BO2.

6. RN25BO2O2 + HO2 = C10z + O2: KRO2HO2*0.914;

7. RN25BO2O2 + NO = 0.5RN24BO4O2+ 0.5CARB16 + 0.5RN8O2 + NO2: KRO2NO

8. RN25BO2O2 + NO3 = 0.5RN24BO4O2+ 0.5CARB16 + 0.5RN8O2 + NO2 : KRO2NO3 ;

Autoxidation of RN25BO2O2 to 3rd generation O3RO2, RN24BO4O2

9. RN25BO2O2 + O2 = RN24BO4O2 : 1.7;

Reactions of RN24BO4O2

10. RN24BO4O2 + HO2 = C10z + O2: KRO2HO2*0.914;

11. RN24BO4O2 + NO = 0.5RN23BO6O2+ 0.5CARB16 + 0.5RN8O2 + NO2: KRO2NO

12. RN24BO4O2 + NO3 = 0.5RN23BO6O2+ 0.5CARB16 + 0.5RN8O2 + NO2 : KRO2NO3 ;

Autoxidation of RN24BO4O2 to 4th generation O3RO2, RN23BO6O2

13. RN24BO4O2 + O2 = RN23BO6O2 : 1.7 ;

Reactions of RN23BO6O2

14. RN23BO6O2 + HO2 = C10z + O2: KRO2HO2*0.914;

15. RN23BO6O2 + NO = 0.5RNxBOyO2 + 0.5CARB16 +0.5RN8O2 + NO2: KRO2NO ;

16. RN23BO6O2 + NO3 = 0.5RNxBOyO2 + 0.5CARB16 +0.5RN8O2 + NO2: KRO2NO3 ;

Autoxidation of RN23BO6O2 to lumped "5th generation and higher" O3RO2, RNxBOyO2

17. RN23BO6O2 + O2 = RNxBOyO2 : 1.6;

Reactions of RNxBOyO2 - no further autoxidation

18. RNxBOyO2 + HO2 = C10z + O2: KRO2HO2*0.914;

19. RNxBOyO2 + NO = 0.5RNxBOyO2 + 0.5CARB16 + 0.5RN8O2 + NO2: KRO2NO ;

20. RNxBOyO2 + NO3 = 0.5RNxBOyO2 + 0.5CARB16 + 0.5RN8O2 + NO2: KRO2NO3 ;

Reactions of O3RO2 with big peroxy radical pool (RO2_b)

All reactions with $RO2_b$ produce a 20-carbon accretion product at a rate coefficient from fitting to experimental data (Berndt et al., 2018b). Reactions also produce, with equal rate coefficients (from Molteni et al., 2019), closed shell species which are classified as HOMs for all cases (except for the reaction of RN26BO2 which is not sufficiently oxidised) and alkoxy radicals which go on to react as previously described in this work.

21. RN26BO2 = 0.5 C20d : 0.97E-11 $RO2_b$;

22. RN26BO2 = 0.5TNCARB26 + 0.25RN25BO2O2 + 0.25CARB16 + 0.25RN8O2 : 3.36E-12*RO2_b ;

23. RN25BO2O2 = 0.5 C20d : 2.5E-11 $RO2_b$;

24. RN25BO2O2 = 0.5C10z + 0.25RN24BO4O2 + 0.25CARB16 + 0.25RN8O2 : 3.36E-12*RO2_b;

25. RN24BO4O2 = 0.5 C20d : 3.4E-11 $RO2_b$;

26. RN24BO4O2 = C10z + 0.5 RN23BO6O2 + 0.5 CARB16 + 0.5 RN8O2 : 1.68E-12 $RO2_b$;

26. RN24BO4O2 = 0.5C10z + 0.25RN23BO6O2 + 0.25CARB16 + 0.25RN8O2 : 3.36E-12*RO2_b ;

27. RN23BO6O2 = 0.5 C20d : 3.6E-11 $RO2_b$;

28. RN23BO6O2 = 0.5C10z + 0.25RNxBOyO2 + 0.25CARB16 + 0.25RN8O2 : 3.36E-12*RO2_b ;

29. RNxBOyO2= 0.5 C20d : 3.6E-11 $RO2_b$;

30. RNxBOyO2 = 0.5C10z + 0.25RNxBOyO2 + 0.25CARB16 + 0.255RN8O2 : 3.36E-12*RO2_b ;

Reactions of O3RO2 with medium and small peroxy radical pools ($RO2_m$ and $RO2_s$)

Reaction of RN26BO2 is based on corresponding species in MCM.

31. RN26BO2 = 0.5RN25BO2O2 + 0.5CARB16 + 0.5RN9O2 : 8.13E-13 ($RO2_s$+$RO2_m$) ;

Rate coefficient and branching ratios of later generation O3RO2 with medium and small peroxy radical pools taken from Roldin et al (2019). The alkoxy radical produced goes on to react as described earlier in this work.

32. RN25BO2O2 = 0.3RN24BO4O2 + 0.3CARB16 + 0.3RN8O2 + 0.4C10z: 5E-12 ($RO2_s$+$RO2_m$) ;

33. RN24BO4O2 = 0.2RN23BO6O2 + 0.2CARB16 + 0.2RN8O2 + 0.6C10z: 7E-12 ($RO2_s$+$RO2_m$);

34. RN23BO6O2 = 0.1RNxBOyO2 +0.1CARB16 +0.1RN8O2 + 0.8C10z : 9E-12 ($RO2_s$+$RO2_m$) ;

35. RNxBOyO2 = 0.1RNxBOyO2+0.1CARB16+0.1RN8O2+0.8C10z : 1E-11 ($RO2_s$+$RO2_m$) ;

Rate coefficient of O3RO2 with isoprene-derived peroxy radical from fitting of model to experimental data (Berndt et al, 2018b).

36. RN26BO2 = 0.667C15d : 3.9E-12 $RO2_m$;

37. RN25BO2O2 = 0.667C15d : 5.2E-12 $RO2_m$;

38. RN24BO4O2 = 0.667C15d : 6.5E-12 $RO2_m$;

39. RN23BO6O2 = 0.667C15d : 6.5E-12 $RO2_m$;

40. RNxBOyO2 = 0.667C15d : 7.5E-12 $RO2_m$;

OH oxidation of alpha pinene producing two OHRO2 - RTN28AO2 + RTN28BO2

41. APINENE + OH = 0.78 RTN28AO2 + 0.22 RTN28BO2: 1.20E-11*EXP(440/TEMP);

Reactions of RTN28AO2 are the same as for RTN28O2 in original CRI v2.2 R5 except for accretion product formation. RTN28AO2 does not undergo autoxidation.

42. RTN28AO2 + NO = 0.23RTN28NO3 + 0.77TNCARB26 + 0.77NO2: 2.7D-12*EXP(360/TEMP)*0.767 ;

43. RTN28AO2 + HO2 = RTN28OOH : 2.91D-13*EXP(1300/TEMP)*0.914 ;

44. RTN28AO2 + NO3 = TNCARB26 + HO2 + NO2 : 2.3D-12 ;

45. RTN28AO2 = TNCARB26: 6.65E-13*RO2 ;

46. RTN28AO2 = 0.5 C20d : 0.4E-11*RO2_b ;

47. RTN28AO2 = 0.667C15d : 1.8E-12*RO2_m ;

Reactions of RTN28BO2

Reaction with HO2 forms hydroperoxide species already in CRI, not a HOM due to insufficient oxygens.

48. RTN28BO2 + HO2 = RTN28OOH + O2: KRO2HO2*0.914 ;

Reaction with NO, NO_3 forms next generation OHRO2 via alkoxy radical isomerisation and fragmentation products (smaller RO2, RN9O2, and closed shell species, CARB16) at 50:50 branching ratio). NO also forms small yield of RN18NO3, estimated from original CRI v2.2 R5.

49. RTN28BO2 + NO = 0.125*RTN28NO3 + 0.875CH3COCH3 + 0.875RN19O2 + 0.875NO2: KRO2NO ;

50. RTN28BO2 + NO3 = CH3COCH3 + RN17O2 + NO2 : KRO2NO3 ;

Autoxidation of RTN28BO2 to produce 2nd generation OHRO2, RTN27BO2O2

51. RTN28BO2 + O2 = RTN27BO2O2 : 2.1 ;

Reactions of RTN27BO2O2

Reaction with HO2 forms hydroperoxide species already in CRI, not a HOM due to insufficient oxygens.

52. RTN27BO2O2 + HO2 = RTN28OOH + O2: KRO2HO2*0.914 ;

53. RTN27BO2O2 + NO = 0.5RTN26BO4O2+0.5CARB16 + 0.5RN9O2 +NO2: KRO2NO ;

54. RTN27BO2O2 + NO3 = 0.5RTN26BO4O2+0.5CARB16 + 0.5RN9O2 +NO2: KRO2NO3 ;

Autoxidation of RTN27BO2O2 to produce 3rd generation OHRO2, RTN26BO4O2

55. RTN27BO2O2 + O2 = RTN26BO4O2 : 2.1 ;

Reactions of RTN26BO4O2

Hydroperoxide from RTN26BO4O2 has sufficient oxygens to be classified as a HOM.

56. RTN26BO4O2 + HO2 = C10x + O2: KRO2HO2*0.914 ;

57. RTN26BO4O2 + NO = 0.5RTNxBOyO2 + 0.5CARB16 + 0.5RN8O2 +NO2: KRO2NO ;

58. RTN26BO4O2 + NO3 = 0.5RTNxBOyO2+0.5CARB16 + 0.5RN8O2 +NO2: KRO2NO3 ;

Autoxidation of RTN26BO4O2 to produce "4th generation and higher" OHRO2, RTNxBOyO2

59. RTN26BO4O2 + O2 = RTNxBOyO2 : 0.25 ;

Reactions of RTNxBOyO2 - no further autoxidation occurs

60. RTNxBOyO2 + HO2 = C10x + O2: KRO2HO2*0.914 ;

61. RTNxBOyO2 + NO = 0.5RTNxBOyO2 + 0.5CARB16 + 0.5RN8O2 +NO2: KRO2NO ;

62. RTNxBOyO2 + NO3 = 0.5RTNxBOyO2 + 0.5CARB16 + 0.5RN8O2 +NO2: KRO2NO3 ;

Reactions of OHRO2 with big peroxy radical pool ($RO2_b$)

Rate coefficient from fitting of model to experimental data (Berndt et al, 2018b).

63. RTN28BO2 = 0.5 C20d : 0.4E-11 $RO2_b$;

64. RTN27BO2O2 = 0.5 C20d : 2.5E-11 $RO2_b$;

65. RTN26BO4O2 = 0.5 C20d : 5.5E-11 $RO2_b$;

66. RTNxBOyO2 = 0.5 C20d : 3.5E-11 $RO2_b$;

Reactions of OHRO2 with medium, small and total peroxy radical pools ($RO2_m$, $RO2_s$ and RO2)

67. RTN28BO2 = 0.7TNCARB26 + 0.3CH3COCH3 + 0.3RN17O2 : 6.7E-15*RO2

68. RTN27BO2O2 = 0.4TNCARB26 + 0.3RTN26BO4O2 + 0.3CARB16 + 0.3RN10O2 : 5E-12*RO2 ;

69. RTN26BO4O2 = 0.4C10x + 0.3RTNxBOyO2 + 0.3CARB16 + 0.3RN9O2: 8E-12*RO2 ;

70. RTNxBOyO2 = 0.8C10x + 0.1RTNxBOyO2 + 0.1CARB16 + 0.1RN8O2 : 1E-11*RO2 ;

Rate coefficient of OHRO2 with isoprene-derived peroxy radical from fitting of model to experimental data (Berndt et al, 2018b).

71. RTN28BO2 = 0.667C15d : 1.8E-12 $RO2_m$;

72. RTN27BO2O2 = 0.667C15d: 3.75E-12 $RO2_m$;

73. RTN26BO4O2 = 0.667C15d: 3.75E-12 $RO2_m$;

74. RTNxBOyO2 = 0.667C15d : 3.75E-12 $RO2_m$;

Photolysis of HOMs

Photolysis of peroxide linkage and carbonyl linkages were considered using MCM frequencies J41 and J22 respectively. The KPP parameter "SUN" was used in experiments where the photolysis frequency was varied. Photolysis of peroxide linkage in HOM monomer produces one OH and one alkoxy radical which behaves as previously discussed (50% decomposition, 50% isomerisation). As the extent of oxidation of the HOM is unknown, isomerisation produces second generation peroxy radical by default.

75. C10z = 0.5CARB16 + 0.5RN9O2 + 0.5RN25BO2O2 + OH : J41;

76. C10x = 0.5CARB16 + 0.5RN9O2 + 0.5RTN27BO2O2 + OH: J41;

Photolysis of C20d produces two alkoxy radicals. The isomerisation products are 2nd gen OHRO2 and 2nd gen O3RO2.

77. C20d = 0.5RN25BO2O2 + 0.5RTN27BO2O2 + RN9O2 + CARB16 : J41;

Photolysis of C15d produces two alkoxy radicals. The isoprene-derived alkoxy radical produces UCARB12 (as inCRI v2.2 R5) while the alkoxy radical from alpha pinene forms next generation peroxy radicals via isomerisation (50 % OHRO2 and 50% O3RO2) and fragmentation products.

78. C15d = UCARB12 + 0.25RN25BO2O2 + 0.25RTN27BO2O2 + 0.5RN9O2 + 0.5CARB16: J41;

Photolysis of carbonyl linkage produces an acyl radical and an alkyl radical which will form peroxy radicals. It is assumed that one of these peroxy radicals is big enough to be considered (2nd generation) O3RO2 or OHRO2

79. C10z = RN25BO2O2 : J22;

80. C10x = RTN27BO2O2: J22;

81. C20d = RN25BO2O2 + RTN27BO2O2 : J22;

For C15d, one of the two peroxy radicals formed is assumed to be of medium size and produce UCARB12 which isomerisation (as occurs for isoprene-derived peroxy radicals).

82. C15d = 0.5RN25BO2O2 + 0.5RTN27BO2O2 + UCARB12: J22;

HOM loss to OH

All HOM species are lost to OH with same rate coefficient as that for large hydroperoxide RTN28OOH in CRI v2.2 R5. The products, closed shell CRI species CARB10 and CARB15, were chosen under the assumption that the HOM fragments and the sum of CRI indices of the product is close to the CRI index of the peroxy radical which formed the HOM (23-27). The reaction of C15d also produces a product featured in the oxidation pathway of isoprene, UCARB10.

83. C10z + OH = CARB10 + CARB15 + OH : 2.38E-11 ;

84. C10x + OH = CARB10 + CARB15 + OH : 2.38E-11 ;

85. C15d + OH = CARB10 + CARB15 + UCARB10+ OH : 2.38E-11 ;

86. C20d + OH = 2CARB10 + 2CARB15 + OH : 2.38E-11 ;

Table D5. Temperature dependencies used for 3 temperature dependent mechanism versions.

Species	HOM_{6000}	HOM_{9000}	HOM_{12077}
RN26BO2	1.223E8*EXP(-6000/T)	2.981E12*EXP(-9000/T)	9.413E16*EXP(-12077/T)
RN25BO2O2	1.009E9*EXP(-6000/T)	2.460E13*EXP(-9000/T)	7.768E17*EXP(-12077/T)
RN24BO4O2	1.009E9*EXP(-6000/T)	2.460E13*EXP(-9000/T)	7.768 E17*EXP(-12077/T)
RN23BO6O2	9.500E8*EXP(-6000/T)	2.315E13*EXP(-9000/T)	7.311E17*EXP(-12077/T)
RTN28BO2	1.247E9*EXP(-6000/T)	3.038E13*EXP(-9000/T)	9.595E17*EXP(-12077/T)
RTN27BO2O2	1.247E9*EXP(-6000/T)	3.038E13*EXP(-9000/T)	9.595E17*EXP(-12077/T)
RTN26BO4O2	1.484E8*EXP(-6000/T)	3.617E12*EXP(-9000/T)	1.142E17*EXP(-12077/T)

The uncertainty in the autoxidation coefficients was estimated by further box models simulations where an autoxidation coefficient was adjusted so that the corresponding species was simulated at the upper and lower concentrations values given the experimental uncertainty.

Table D6. References for model parameters and confidence

Parameter	Value(s)	Source	Confidence
Autoxidation Coefficients	Detailed in Table 4.4	Derived in this work*	Estimated uncertainty in Table 4.4
Rate coefficients for C20d formation (k13)	Section 2.3.1 and reaction list: 21, 23, 25, 27, 29, 46, 63, 64, 65, 66	Derived in this work	Sensitivity tests suggested uncertainty range of +100% / - 35% (scalings of 0.65-2)
Rate coefficients for C15d formation (k16)	Section 2.3.2 and reaction list: 36, 37, 38, 39, 40, 47, 71, 72, 73, 74	Derived in this work	Sensitivity tests suggested uncertainty range of ±50% (scalings of 0.5-1.5)
Closed Shell / Alkoxy radical from a specific big RO_2 reacting with RO_2b pool (k14, k15)	Section 2.3.1 and reaction list: 22, 24, 26, 28, 30, 32-35	Molteni et al (2019), Roldin et al (2019)	Scaling by factors of 10 and 0.1 did not affect rate coefficients fitted for autoxidation or accretion product formation. HOM yield greater sensitivity with universal scalings of +100% and –50% resulting in a doubling and halving of HOM yield respectively.
k14/k15 branching ratio	50:50	Ratio similar to Jenkin et al (2019a) values of 40:60 (1°, 2° RO_2), 20:80 (3° RO_2)	Sensitivity tests with ratios of 40:60 and 20:80 did not affect rate coefficients fitted for autoxidation or accretion product formation and had minor effects on HOM yield.
HOM + OH rate coefficient	2.38×10^{-11} molecules^{-1} cm^3 s^{-1}	Based on comparable species in CRI v2.2, RTN28OOH	Increasing rate coefficient to collision limit (as suggested by Bianchi et al., 2019) had negligible affect
Alkoxy radical decomposition-isomerisation branching ratio	50:50	Estimate	Sensitivity tests with ratios of 75:25 and 25:75 did not affect rate coefficients fitted for autoxidation or accretion product formation. HOM yield below 200 ppt NOx was unaffected and at 2 ppb NOx, uncertainty in autoxidation temperature dependence dwarfed this uncertainty. Ratio more important at higher NOx but this coincided with drastically reduced HOM yield.

*Note that the autoxidation rate coefficient for the 1st generation species RTN28BO2 was taken from Xu et al (2018)

Breakdown of Peroxy Radical Pools In CRI-HOM

Large Peroxy Radical Pool (8 or more carbons)

RTN28AO2, RTN28BO2, RTN27BO2O2, RTN26BO4O2, RTNxBOyO2, RN26BO2, RTN24O2, RN25BO2O2, RN24BO4O2, RN23BO6O2, RNxBOyO2, NRTN28O2, RA19CO2, RTX28O2, NRTX28O2, RTN26O2, RTN25O2, RTX22O2, RTN24O2, RTN23O2

Medium Peroxy Radical Pool (4-7 carbons)

RU12O2, NRU12O2, RN13O2, RN12O2, NRN12O2, RA13O2, DHPR12O2, RN11O2, RA16O2, RU10O2, RU10AO2, MACO3, RN13AO2, RU12O2, NRU12O2, RTN14O2, RN16AO2, RN14O2, RTN10O2, RN17O2, RN15AO2, RN15O2, RN18AO2, RN16O2, RN18O2, RN19O2

Small Peroxy Radical Pool (3 or fewer carbons)

CH3O2, C2H5O2, HOCH2CH2O2, CH3CO3, C2H5CO3, ICH3H7O2, RN10O2, HOCH2CO3, NRN6O2, RN9O2, NRN9O2, RN8O2